Research and Technology 1991

Annual Report of the Marshall Space Flight Center

NASA TM - 103554

National Aeronautics and
Space Administration

George C. Marshall Space Flight Center
Marshall Space Flight Center, Alabama 35812

BUILDING FOR THE FUTURE

We at the Marshall Space Flight Center are actively involved in building the Nation's future in space. We firmly believe that our past successes and our current strong capabilities have been made possible by our continuing emphasis on research and technology. We look forward to forthcoming challenges with confidence that our research and technology is providing a firm base for continuing success.

This report describes a select representative sampling of the research and technology work in progress at the Marshall Space Flight Center. These examples not only show what is being accomplished today, but also our investment in technical leadership for the future.

T. J. Lee

T.J. Lee
Director, Marshall Space Flight Center

Acknowledgements

The point of contact and coordinator at MSFC for this report is T.S. Dollman (ER01/(205) 544–6568). He was assisted by an editorial committee consisting of G.F. McDonough, C.R. Chappell, S.H. Morgan, W.C. Snoddy, and G.R. Wallace. Detailed editorial support and production assistance was provided by MSI, a Division of The Bionetics Corporation. The research and technology work at MSFC is a cooperative effort, but, because of space restrictions, it is impossible to list all those involved in the projects described in this report.

To assist the reader, the MSFC contact, office code, telephone number, and sponsoring organization are included at the end of each article. Please note that some sponsoring organizations have implemented organizational name changes. An alphabetical index of all contacts is presented at the end of this report.

Contents

Research Programs

Earth Science and Applications

Technology Programs

Propulsion

Structures and Dynamics

Index of Key Words

NOTE — Each keyword in bold-face type is a project, program or initiative that benefits from the application of the results from the R&T activity which uses that keyword. Additionally, many of the activities described herein are sponsored by program offices which benefit from the results of those activities.

Building for the Future

ADVANCED STUDIES

The advanced systems and missions we are investigating today build the future for MSFC and NASA. In these studies blueprints are developed that draw on the research and technology foundation and that identify future challenges for the research and technology community. Space Station Freedom *evolution, missions to and from planet Earth, the transportation systems necessary to accomplish these programs, and the supporting science are vital building blocks in sustaining the progress we have made in space.*

Earth-monitoring satellites and shuttle missions will provide scientific data on global changes to our ecosystem and atmosphere. An understanding of chemical composition and temperature changes is the first step in taking responsibility for our environment and our future. Precise navigational systems for aircraft, ships, and even automobiles will require more accurate knowledge of the Earth's gravitational and magnetic fields. An understanding of the Sun and solar flares will help protect our communications and power networks both in space and on Earth. Low Earth orbit and the Geostationary Earth Observatory (GEO) mission analysis, science, platforms, and small spacecraft studies are being pursued.

The challenge of returning to the Moon and then going to Mars requires a new generation of space transportation. Utilization of the National Launch System as a building block, evolutionary launch vehicles, and a variety of propulsion concepts are being studied. Transfer vehicles and landers that reach lunar and planetary surfaces are being defined, as well as recovery systems that return reusable components for refurbishment. Lunar and planetary science activities are investigating astrophysics, space physics, and other science disciplines. Advanced studies are the first step in building our future in space.

C.R. Darwin
Director, Program Development

Transportation Systems

Advanced Recovery Systems

Recovery, refurbishment, and reuse of major launch vehicle components are desirable and have been shown in a number of studies to be technically and economically feasible as a means to conserve resources and improve operational schedules. Studies and technology efforts are ongoing to define and test systems that combine vehicle propulsion and avionics into a relatively compact package called the **propulsion/avionics (P/A) module** for ease of installation on the vehicle, separation from the vehicle after use, and return to Earth for straightforward refurbishment. A large fabric **parafoil** is now being tested that represents one approach to soft landing at the refurbishment site. Plans are continuing with test weights approaching the full-scale **P/A module** and will later incorporate fully automatic landing capability. This system has other far-reaching potential, including Space Station *Freedom* crew emergency return, routine personnel rotation, and cargo and payload **recovery**.

Engines and avionics systems are among the most expensive and complex systems of a launch vehicle. Over the last few years, extensive studies have shown that these systems can be conveniently packaged into a **P/A module** that streamlines prelaunch operations and facilitates reuse. Key value components are rapidly returned to the launch site and reused, reducing launch costs compared to an expendable launch vehicle. Two concepts being considered include a high lift-to-drag (L/D) ratio module for ordinary runway landing and a ballistic (low L/D) configuration requiring some type of parachute system. The runway landing configuration (fig. 1) has conventional control surfaces and landing avionics, uses

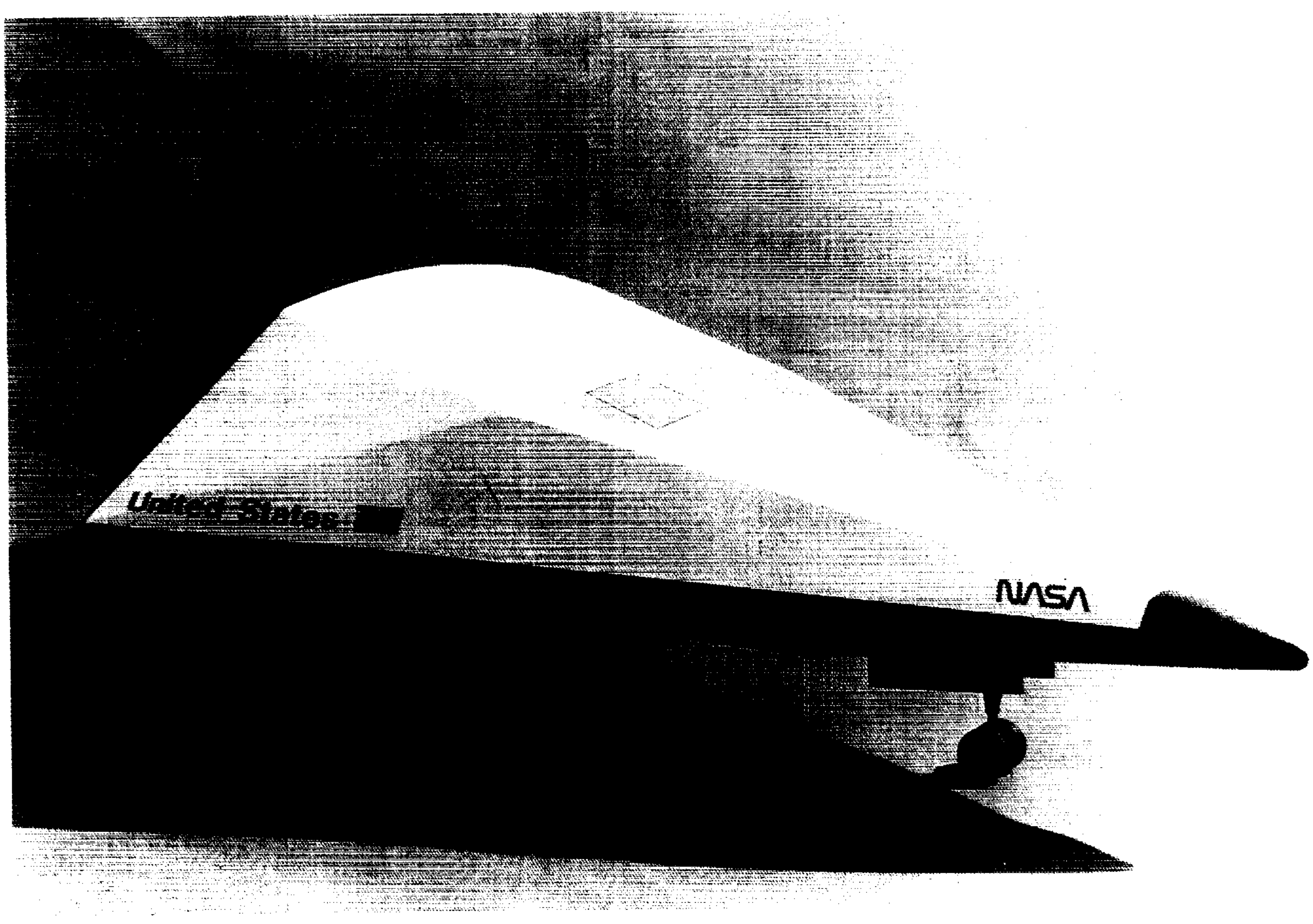

FIGURE 1.—High L/D propulsion avionics module.

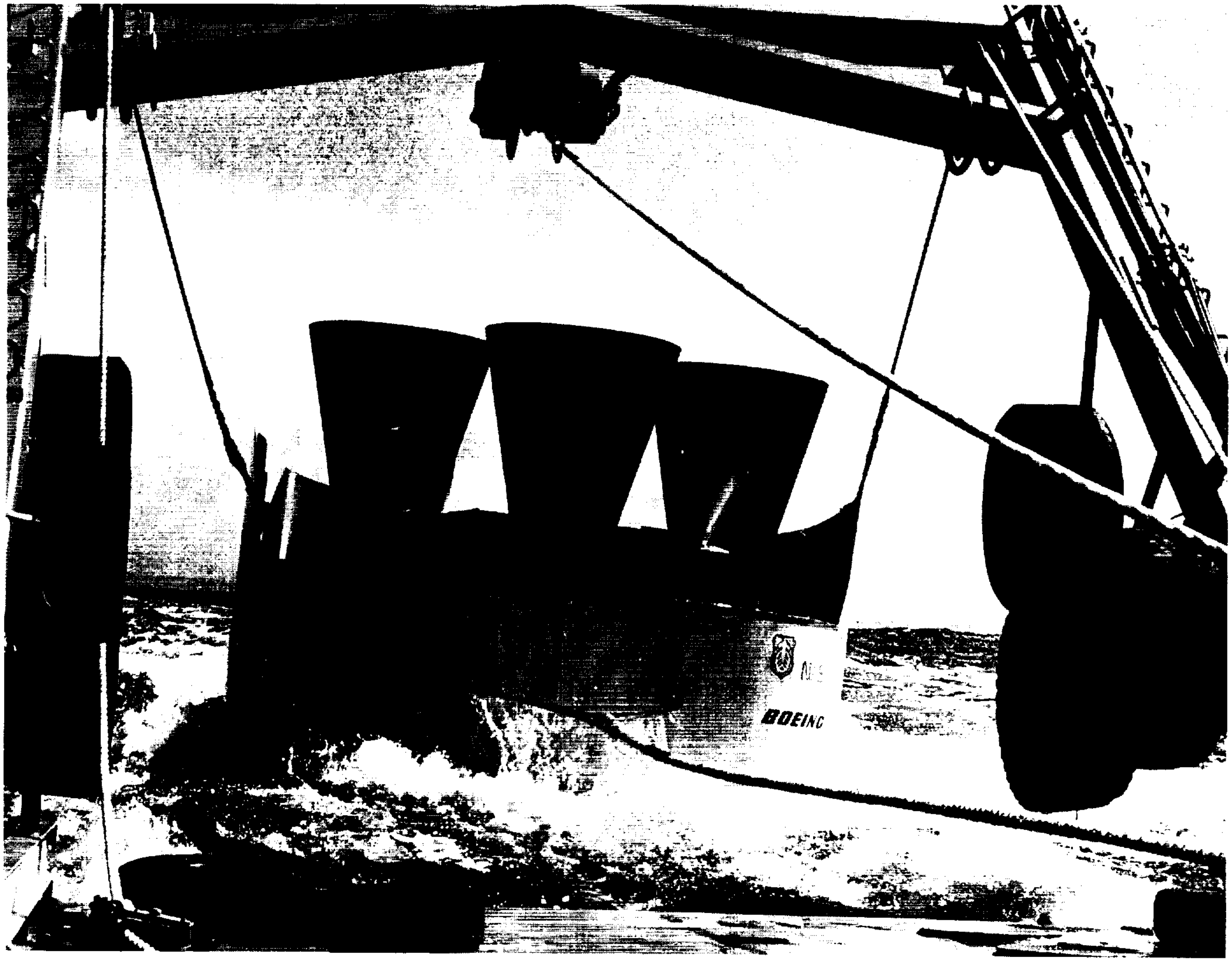

FIGURE 2.— Ballistic P/A module in water recovery test.

existing landing fields, and has high cross-range capability. The ballistic module (fig. 2) shown being recovered from the sea by a ship in recent tests conducted by Boeing may also be recovered on land. Either approach may be utilized with booster or core stage **recovery**. Booster **recovery** and landing typically require turbojet assist for return to the launch site because of downrange staging. The core stage module attains orbit and can be selectively deorbited for relatively straightforward return to a chosen ground site.

Both configurations have recently undergone testing of scaled models. Wind tunnel tests have been conducted to determine control parameters and performance at a variety of speeds ranging from hypersonic to low subsonic. Control surface variations, such as canards, were tested to determine the preferred control methods. Thermal tests were also conducted at hypersonic speeds, and **recovery** operations from the water were demonstrated for the ballistic configuration. Land-based water tank testing on small scales and ocean **recovery** on models as large as 50 percent of full scale were conducted. Results show that a buoyant ramp is the preferred method of shipboard **recovery**. Of vital importance to **recovery** of **P/A modules** is a precision **recovery** gliding parachute system for soft touchdown on land, which is currently being developed. This program, called the advanced **recovery** system (ARS), has a target landing capacity of more than 27,000 kg (60,000 lb), which represents a significant increase in the weight capability of **parafoils**. The program is jointly sponsored by the U.S. Air Force, NASA, and the U.S. Army for application to the National

ORIGINAL PAGE
BLACK AND WHITE PHOTOGRAPH

Launch System and for use in heavy-weight cargo offset delivery. It is of considerable interest to the Space Station *Freedom* assured crew return vehicle and the personnel launch system. Many other applications are also possible.

The ARS began in 1986 with phase I study contracts to define a system for the safe land **recovery** of large, high-cost launch vehicle components. The result was a ram-air gliding parachute, also known as the **parafoil**. The **parafoil** required for a 27,000–kg (60,000–lb) payload was defined to be a 985–m^2 (10,600–ft^2) system.

Phase II extended the effort to include a scaled demonstration of the concept. This program is currently under way at the Yuma Proving Grounds in Arizona and is scheduled to end in mid-FY92. Phase II has included two series of wind tunnel tests at the NASA Ames Research Center's National Full-Scale Aerodynamics Complex. The first series was conducted in September 1988, and the second series was completed in April 1990. The major portion of the program includes a series of 11 aircraft drop tests with weights ranging from 4,500 to 9,000 kg (10,000 to 20,000 lb). The **parafoil** and weights being used are about one-third scale, so the tests represent wing loadings representative of a full-scale payload. Man-in-the-loop steering controls have been incorporated for turns and flared landings.

To date, nine drop tests have been attempted, with eight of the tests being totally successful. Deployment of the large **parafoil**, using a unique mid-span reefing technique developed by Pioneer Aerospace Corporation, has been reliably demonstrated. Steering has been incorporated on the last three tests and works as planned. The system is shown in figure 3 in a recent drop test. To date, the heaviest weight tested has been approximately 6,400 kg (14,000 lb), which represents almost triple the weight successfully flown before.

During the first half of FY91, the program was relatively inactive due to funding limitations. However, the program was resumed in April 1991 and will continue through December 1991.

G.W. Johnson/PT21
(205) 544–0636
Sponsors: Office of Space Flight, National Launch Systems Joint Program Office, and U.S. Army Natick Research, Development, and Engineering Center

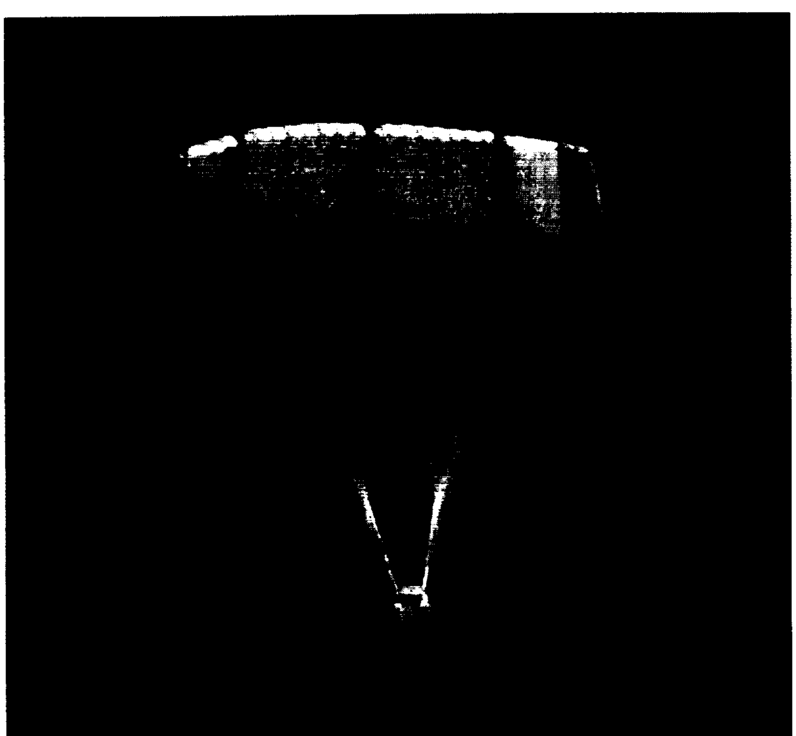

FIGURE 3.— Large parafoil in gliding flight with 14,000-lb weight.

Integrated Earth-to-Orbit Transportation

NASA is currently analyzing alternatives to establish the desired path for future **unmanned** and **manned launch vehicles**. This activity is directed at satisfying the civil needs requirements, including those that the Space Exploration Initiative (SEI) will place on the **Earth-to-orbit (ETO) transportation** systems early in the next century. The SEI requirements will dictate the need for new **heavy-lift launch vehicle (HLLV)** capabilities. Studies will be conducted over the next few years to determine the best path to follow, both technically and programmatically, to develop the capability to meet these requirements. These studies will examine the entire **ETO** infrastructure, including ground processing, supporting facilities, as well as the launch vehicles themselves. Specific areas to be addressed are resiliency/assured access, safety, operability, and affordability. The results of these studies will be used to formulate credible ETO infrastructures needed to satisfy both the manned and unmanned space transportation requirements.

The launch vehicle systems will encompass those derived from the proposed National Launch System (NLS), as well as "clean sheet" designs. Emphasis will be placed on evolving current capabilities into systems required to meet the new heavy-lift requirements in excess of 150,000 lb to low Earth orbit (LEO) (fig. 4). A modular

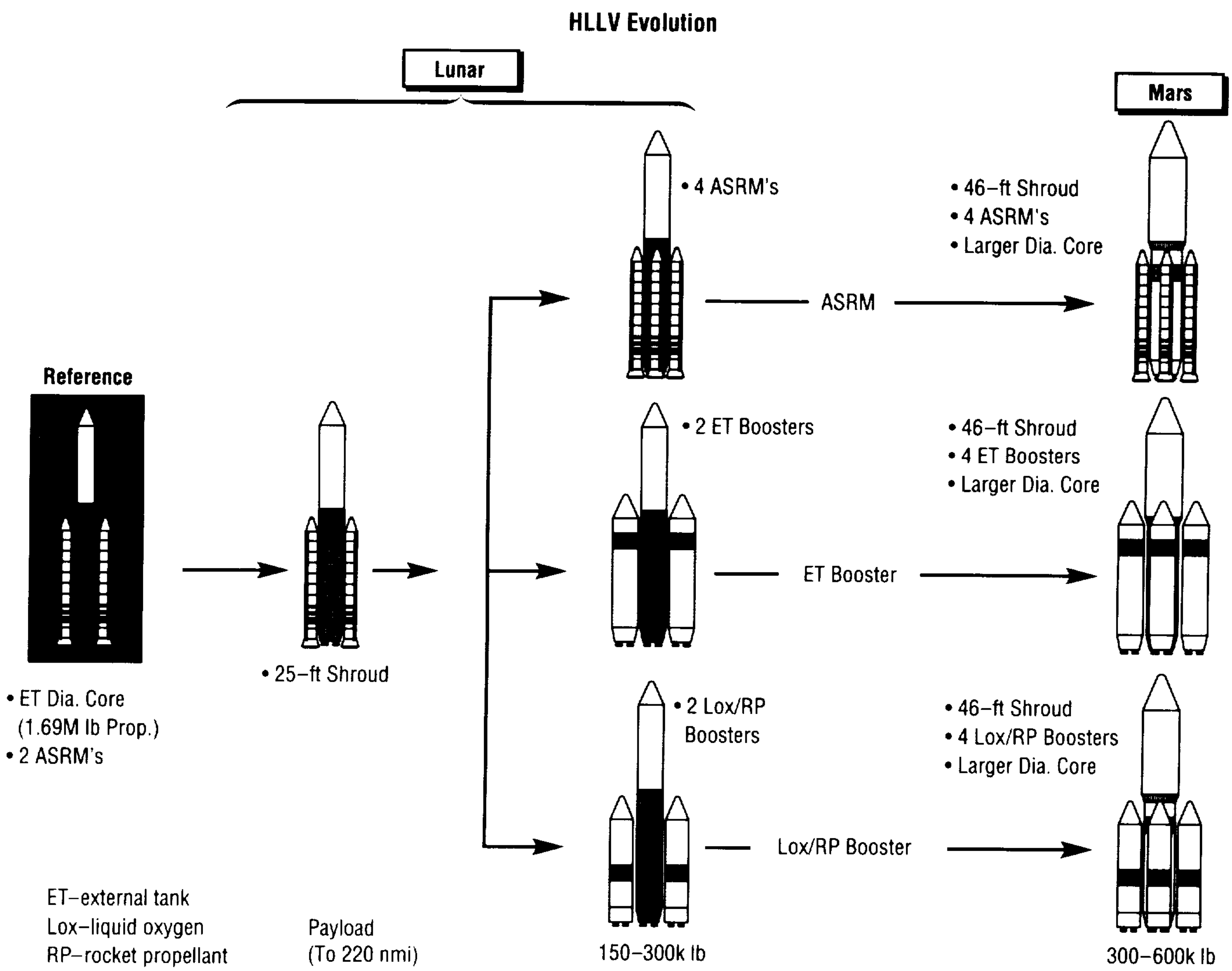

FIGURE 4.— HLLV evolution.

building block approach will be incorporated in which common components will be used to build a family of launch vehicles capable of meeting a wide range of requirements. The NLS "common core" is used as the basic building block across the entire family of launch vehicles (fig. 5). The "clean sheet" designs will take maximum advantage of new technologies, processes, and facilities to reduce recurring launch vehicle costs. This approach offers several long-term advantages, but it requires a large up-front nonrecurring investment to put these new systems in place.

The manned launch systems studies generally fall into one or more of the following three paths: space shuttle evolution, the personnel launch system (PLS), and the advanced manned launch system (AMLS). Shuttle evolution deals with major block changes to the space shuttle, as opposed to the current shuttle improvements under way. A near-term block change is the planned incorporation of the advanced solid rocket motors (ASRM's). Future changes being studied are advanced avionics, use of electromechanical actuators, use of aluminum-lithium, etc. The PLS study is assessing the feasibility of separating man from cargo. The potential of launching a manned capsule or a cargo return vehicle (CRV) on existing and/or new launch vehicles is being studied. The launch vehicle options include the NLS 1.5-stage vehicle. The AMLS will be the next-generation reusable manned transportation system to replace the existing space shuttle. The vehicle may be capable of transporting both crew and cargo to LEO. However, its cargo-carrying capability may be less than the shuttle since alternate unmanned vehicles will be available for heavier payloads.

R.C. Armstrong/PT21
(205) 544–1863
Sponsor: Office of Space Flight

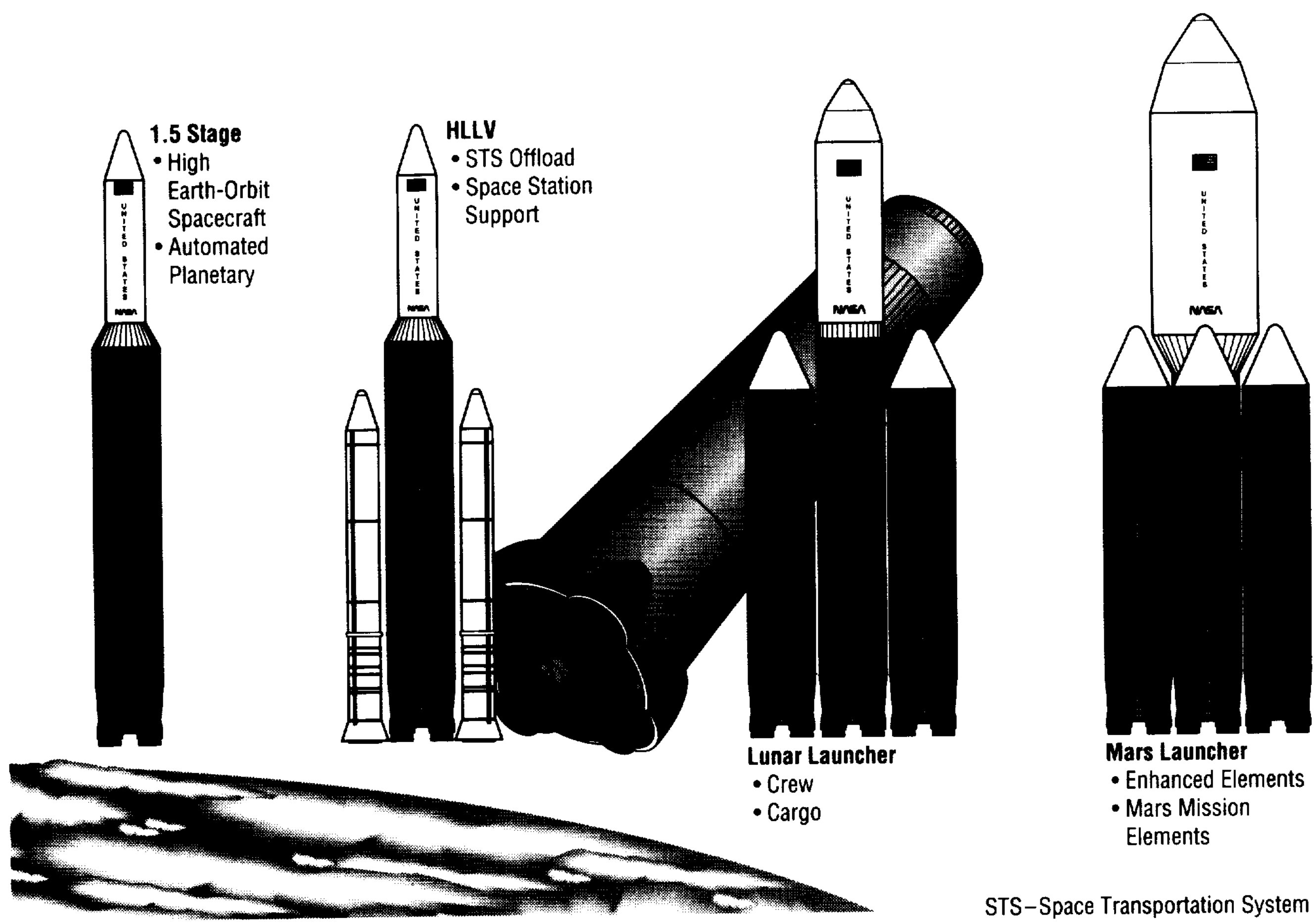

FIGURE 5.—NLS "common core" as modular building block for evolution.

Space Exploration Initiative

The nationwide outreach process announced on May 31, 1990, has been completed. This search for ideas, concepts, and technologies that might benefit the Space **Exploration** Initiative (SEI) was implemented to ensure that all reasonable space **exploration** alternatives have been considered. Hundreds of suggestions ranging from individual components to complete architectures were received. A group under the leadership of Lt. General Tom Stafford (U.S. Air Force, retired), which was formed to synthesize the inputs from the outreach program, began its work in the fall of 1990 and released its report in June 1991. This synthesis group was chartered to identify alternative architectures to implement the SEI, to prioritize the technology thrusts that have the greatest leverage to benefit SEI, and to identify near-term SEI milestones.

In connection with the outreach/synthesis process, MSFC has continued its assigned role to analyze integrated space **transportation** concepts and options to implement the SEI. The scope of these study activities includes launch vehicles and the transfer systems to move people and cargoes between near-Earth environs and the surfaces of the **Moon** and **Mars**. Additionally, MSFC supports the lunar and **Mars** science definition activities and the planetary surface areas for habitation modules and manned surface rover vehicles.

Launch vehicle concepts under consideration to carry out the SEI include evolutionary versions of the National Launch System (NLS) and new conceptual designs based on liquid-hydrogen-fueled boosters, as well as concepts utilizing hydrocarbon fuel.

Lunar **transportation** systems concepts include both expendable and partially reusable vehicles. Configuration options include integrated transfer and lander vehicles along with multistage concepts. Figure 6 depicts a representative piloted lander with its cargo as it approaches a landing site on the **Moon**. Cryogenic and storable propellants are viable candidates for lunar vehicle application. Mission options include direct launches to the lunar surface, as well as Earth-orbit rendezvous and lunar-orbit rendezvous approaches.

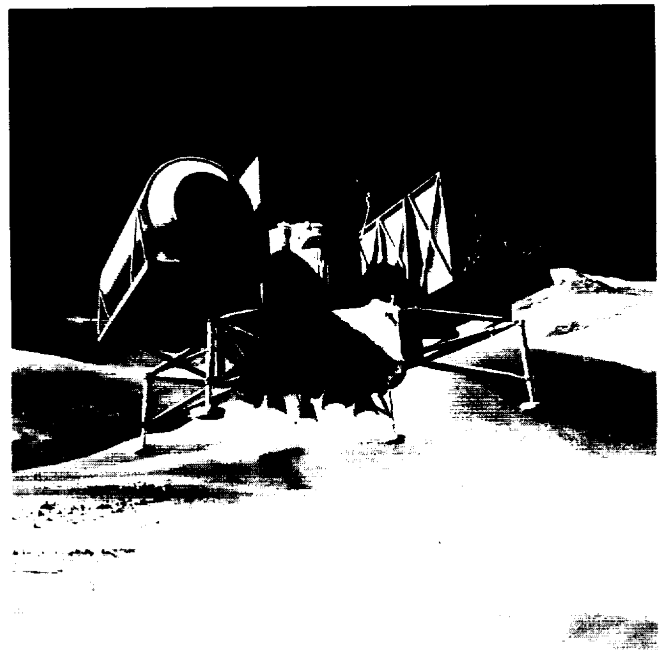

FIGURE 6.— A representative piloted lander with its cargo as it approaches a landing site on the Moon.

A range of **propulsion** concepts that are potentially applicable to the **Mars transportation** system is being studied. These concepts include the chemical/aerobrake system considered during NASA's 90-d study, nuclear thermal **propulsion**, nuclear and solar electric **propulsion**, and other advanced concepts. Each of these technologies presents unique advantages and challenges. Transit time, required mass in Earth orbit, operational and design complexity, technology maturity, safety, and cost are among the important criteria to be considered in comparing alternative concepts. Figure 7 depicts a **Mars** transfer vehicle concept utilizing nuclear thermal **propulsion** as it might appear in **Mars** orbit. As seen, one of two landers returning from the surface is approaching the vehicle to

FIGURE 7.— A Mars transfer vehicle concept utilizing nuclear thermal propulsion as it might appear in Mars orbit.

dock. A second lander, intended for visiting a separate site, can be seen with its landing aerobrake still attached. In addition to alternative **propulsion** concepts, a wide range of configuration and mission trades and analyses is being performed.

These **transportation** studies are building a data base that will be utilized to assess and compare the architectures contained in the forthcoming synthesis report. The next several years will concentrate on analyzing and evolving these architectures, leading to options from which a final selection of an architecture to implement the SEI can be made.

J.P. Sumrall/PT41
(205) 544-8491
Sponsor: Office of Space Exploration

SPACE TRANSPORTATION MAIN ENGINE

The **space transportation main engine** (STME) will provide **Earth-to-orbit (ETO) main propulsion** for the next generation of U.S. launch vehicles. The **STME** phase A concept study began in 1986 to support NASA/U.S. Air Force space transportation architecture studies. Current **STME** phase B studies are providing engine designs and program plans to support the joint NASA/U.S. Air Force **National Launch System** (NLS) definition. **STME** has followed a new approach to rocket engine concept definition that utilizes concurrent engineering to consider cost, producibility, operations, and other factors from the beginning of the program, leading to high reliability, low-cost, and producible designs.

NLS has three vehicle configurations defined to utilize the **STME**: a six-engine vehicle, and a four-engine vehicle that is augmented by shuttle advanced solid rocket boosters, both of which will be developed in parallel, followed by a single-engine vehicle to be developed beginning in the late 1990's. The **STME** will provide reliable, economical, core propulsion across the **NLS** family. With **STME**, the **NLS** family will be able to launch payload masses from 10,000 to 73,000 kg (20,000 to 160,000 lb) per mission. The versatile **STME** can also provide economical propulsion well into the Nation's future by adaptation to a variety of additional applications including liquid rocket boosters and **NLS**-growth vehicles. A baseline **gas generator (GG) cycle engine** configuration, which can be applied to either expendable or reusable vehicle configurations, was selected to allow thorough investigation of design features and program plans. Development of preliminary power balances and transient models continue in support of system and component design.

STME will set new standards for high reliability, low cost, and robust features in a high-performance liquid hydrogen/liquid oxygen propellant rocket engine system. Engine features may include dual-thrust capability, and engine-out failure coverage throughout the mission for applicable vehicle and payload combinations. Total quality management techniques (e.g., continuous process improvement, quality function deployment, and variability reduction) combined with new processes (e.g., investment castings, plasma-spray metal application, automated joining, automated assembly, and advanced materials) exemplify technologies under consideration to help make program cost and reliability goals a reality.

To develop, verify, and validate these manufacturing and design technologies, an extensive advanced development program has been established in support of **STME** studies. Full-scale piece parts for turbopumps, thrust chambers, and control hardware will be built and tested to provide confidence in the results of **STME** phase A and B studies. Test facilities at the Air Force Phillips Laboratory and MSFC have been upgraded to perform thrust chamber firings, and a new Component Test Facility (CTF) is under construction at Stennis Space Center (SSC) to provide turbopump testing.

Development of the **STME** is planned to begin in mid-FY92. A rigorous component testing program is planned on the existing advanced development program (ADP) facilities prior to engine systems testing. Initial engine systems testing will be performed on the Advanced Engine Test Facility at MSFC. Engine system testing is planned for FY95. Engine system and major component testing during full-scale development and production will be performed at SSC. The SSC CTF will be used to meet turbopump testing requirements; some current propulsion test facilities will be converted for **STME** use; and the currently existing stand will be converted to dual-position capability for single-engine development testing. The development program will be a 90-mo effort that will include research and development testing of engine components and systems, followed by a complete, rigorous verification and certification program. Studies in support of **NLS** have identified nonengine propulsion hardware as a major contributor to reliability. Therefore, **STME** testing will include parallel development of many traditional vehicle hardware elements, such as flexible interface lines, thrust-vector control hardware, heat shields, and flight configuration feedlines. This integrated development approach will culminate in core and booster cluster tests at SSC. The full-scale development effort will culminate with one test flight of an **NLS** vehicle projected to occur no earlier than late 1999, with full production of the **STME** beginning in 2001.

H.A. Cikanek/HA31
(205) 544–1461
Sponsors: Office of Space Flight,
U.S. Air Force/Space Systems Division,
and Strategic Defense Initiative
Organization

Space Systems

Geostationary Earth Observatory Program

The **Geostationary Earth Observatory** (GEO) program is a major element of NASA's Mission to Planet Earth (MTPE) initiative, which has the goal of establishing the scientific basis for understanding global change processes. Geostationary observations complement polar and other specialized low-Earth-orbit observations by providing nearly continuous views and opportunities for acquiring data on atmosphere, sea, and land interactive processes. To accomplish these observations, **GEO** will consist of a series of multi-instrument satellites placed in orbit over given points on the ground resulting in unprecedented global and temporal coverage. The current baseline **GEO** mission scenario consists of five **geostationary satellites** orbiting the Earth over a mission lifetime of 15 yr. No on-orbit servicing is planned. Each **GEO** satellite lifetime is 5 yr and replacement satellites are placed on-orbit at 5-yr intervals. Current planning is that three **GEO**'s will be developed by the United States, with the other two developed by Europe and Japan. Current technology and engineering studies indicate the first **GEO** satellite can be ready for launch shortly after the year 2000.

MSFC continued in-house and contracted studies on the **GEO** program and baselined an MSFC-developed concept for the initial observatory. In addition, several government, industry, and university teams, under contract to MSFC, completed concept studies (phase A) on a number of instruments provisionally selected to meet the required scientific observational goals. The baseline **GEO** concept and instrument list are shown in figure 8. Note that there are three types of instruments: facility (F) instruments that are multidisciplinary in nature; principal investigator (PI) instruments for specific measurements of Earth-system processes; and operational (O) or precursor operational instruments that could fulfill the next generation National Oceanic and Atmospheric Administration (NOAA) operational geostationary sensor requirements.

The MSFC baseline **GEO** configuration is a three-axis stabilized spacecraft that utilizes an asymmetric, stiff structure design to meet the instrument accommodation requirements. Passive radiant coolers have been baselined due to lifetime concerns with cryogenic mechanical coolers. The single-wing solar array configuration provides the instruments with cold detector requirements an unobstructed view of cold space for maximum radiative cooling. The unsymmetrical design does, however,

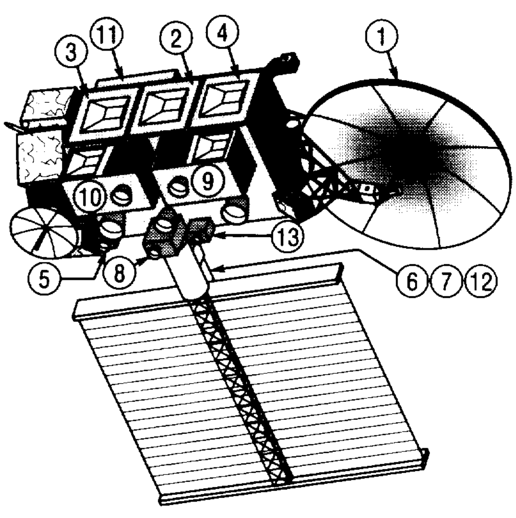

Type	#	Instrument Name
F	1	Geostationary Microwave Precipitation Radiometer
F	2	Geostationary Atmospheric Profiler
F	3	Geostationary Earth Processes Spectrometer
F	4	Higher-Resolution Earth Processes Imager
F	5	Advanced Lightning Mapper
PI	6	Solar Total Irradiance Monitor
PI	7	Solar Spectral/Irradiance Monitor
PI	8	Geostationary Earth Climate Sensor
O	9	Geostationary Operational Imager
O	10	Geostationary Operational Sounder
O	11	Space Environment Monitor
O	12	Solar X-Ray Imager
O	13	Geostationary Data Collection Platform

Figure 8.— Geostationary Earth Observatory (GEO).

require larger than normal reaction wheels to compensate for the unbalanced torques produced by the solar wind. Note that the cryogenic passive radiant coolers for the infrared detectors are located on the side of the spacecraft opposite the solar array, whereas, the higher temperature passive radiant coolers used to dissipate heat from the electronics are located on the solar array side of the spacecraft.

A 180° yaw maneuver of the spacecraft every 6 mo is necessary to keep the Sun on the solar array side of the spacecraft. This maneuver minimizes the requirement for bulky sunshades on the cryogenic radiant coolers and allows a shorter, stiffer solar array boom. A maneuver of this type will be utilized on the upper atmosphere research satellite (UARS) scheduled for launch later this year.

In the MSFC baseline **GEO** concept, three of the larger facility instruments are recessed into the spacecraft structure to maximize Earth-looking **platform** surface area. The **GEO** spacecraft has a total mass of 5,150 kg (11,355 lb) and can be launched with either the Titan IV/Centaur expendable launch vehicle or the planned National Launch System (NLS), if the system becomes available in the required timeframe. The Titan IV/Centaur, with its planned solid rocket motor upgrade, is capable of lifting 5,760 kg (12,700 lb) to geostationary orbit. The 4.5–m (15–ft) diameter by 12.2–m (40–ft) cylindrical length of the Titan IV payload envelope is adequate for the baseline **GEO** spacecraft.

Meeting the instrument pointing stability requirements remains a major design driver on the **GEO** pointing, navigation, and control subsystem. The baseline **GEO** achieves 1 arc sec/s stability. Studies are continuing on control concepts that will result in the sub-arc sec stability over periods of up to 15 s.

Effort is also being expended on a **GEO** data and information system. Wherever possible, the **GEO** data system architecture will utilize commonality with the Earth observation satellite data and information system (EOSDIS), which is presently under development. Due to the nature of the **GEO** measurements, there is very strong science interest and justification in distributing data to the users in near real time. A variety of concepts are under investigation to achieve this goal, including satellite linking and ground system linking. At least to the user, archival and retrieval of the **GEO** data from the archive should be identical to the EOSDIS.

R.G. Beranek/PS01
(205) 544–0624
Sponsor: Office of Space Science and Applications

Space Station Advanced Programs

In 1991, MSFC continued its participation in intercenter **advanced programs** activities on the **space station**, supporting the Level I **Space Station** Engineering Office at NASA Headquarters. This effort was focused on the timeframe after **Space Station** *Freedom* (S.S. *Freedom*) becomes operational, and emphasis was placed on early identification of "hooks and scars" necessary for S.S. *Freedom* to accommodate **growth/evolution**.

Other studies in progress at MSFC and elsewhere are defining advanced payloads and missions that are potential users of the **space station**. Some of these will require increased S.S. *Freedom* capabilities, and the usefulness of S.S. *Freedom* in the timeframe after its initial implementation will depend, in large measure, on its ability to accommodate such payloads and missions.

One effect of the S.S. *Freedom* restructuring activity in 1991 was to underscore the need for S.S. *Freedom* to have flexibility to adjust to reasonable degrees of change in mission emphasis, as well as to accommodate a reasonable degree of **evolution/growth**. To help achieve such flexibility while minimizing impacts to S.S. *Freedom*, the Level I/II requirements for **evolution** were reworked, based partly on data from the intercenter studies. The main thrust was to ensure that S.S. *Freedom's* main features would not preclude **evolution**, while stopping short of requiring full built-in **evolution/growth** capability.

MSFC's module **evolution** studies assessed the implications of **growth** of the integrated subsystems, including hooks/scars such as volume, weight, and resources. **Evolution** studies on the environmental control and life support system (ECLSS) dealt with the incorporation of potential improvements to the ECLSS, including selected advanced technologies. The associated hooks/scars external to racks were also identified.

MSFC's advanced development work was also continued in automation of (1) portions of the ECLSS and (2) the module power management and distribution (PMAD) subsystem. Computer models were completed in both of these areas; they were utilized to perform fault diagnoses and to identify corrective actions in these systems. Data from the MSFC ECLSS and PMAD breadboards were used as inputs to these computer models.

J.M. Butler/PS04
(205) 544–4833
Sponsor: Office of Space Flight, Space Station *Freedom*

Space Station *Freedom* Utilization

The advent of Space Station *Freedom* (S.S. *Freedom*) opens up a new era of opportunities and challenges to space **payload operations**. The cumulative resources available to S.S. *Freedom* **payload operations,** in terms of **payload** mass on orbit, time to operate, and **payload** power, offer an increase (more than two orders of magnitude) over a typical year of shuttle missions. The challenge is how to integrate and operate these **payloads** so that this tremendous increase in resources is fully utilized.

Under the auspices of NASA Headquarters, MSFC is sponsoring work that will:

- Improve the convenience of **payload integration** both on the ground and in space
- Develop a family of **adapters** and **containers** that will adapt current shuttle and other **payloads** to S.S. *Freedom*
- Improve safety
- Provide for on-orbit servicing and checkout
- Facilitate sample exchange.

Current **payload adapters** and associated **payload containers** are in the mock-up or engineering model stages. The system (fig. 9) is composed of a **payload** carrier (rack and drawers) and associated **payload containers.** The rack/carrier will accommodate middeck lockers, experiment apparatus containers (EAC's), universal small experiment containers (USEC's), and improved experiment apparatus containers (IEAC's).

Plans are to refine these concepts through actual simulated ground and space **integration** and **operations**, and to add additional items as required.

K.R. Taylor/PS05
(205) 544–0640
Sponsors: Office of Space Science and Applications
and Office of Commercial Programs

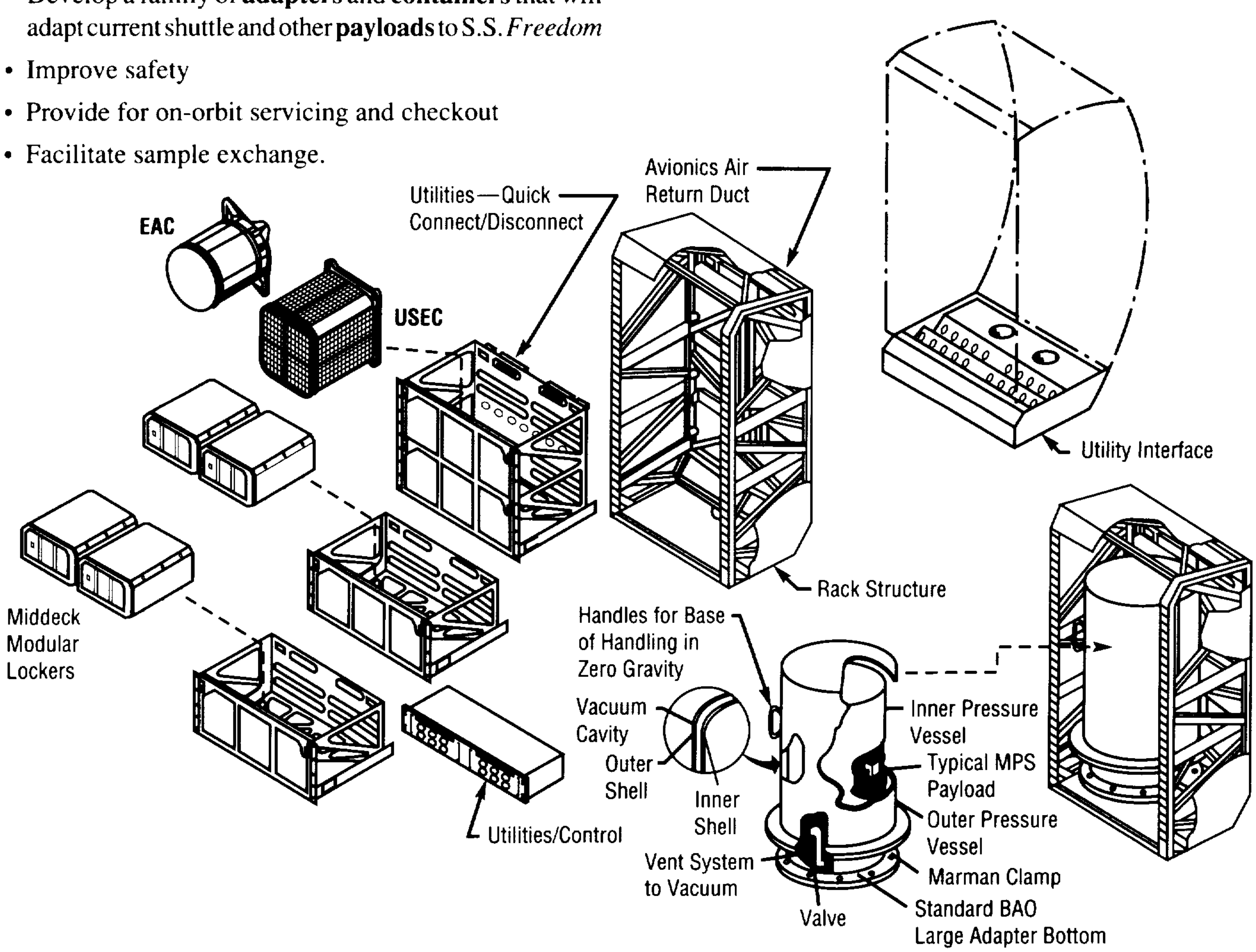

FIGURE 9.—Space station payload adaptation system (SSPAS).

Tether Applications in Space

Tether applications in space (TAS) activities are aimed at developing ways to use **tethers** in space. During 1991, planning/definition of advanced payloads for the **tethered satellite system (TSS)** continued under the auspices of the international TAS Working Group. **TSS** is a large (approximately 1,818 kg (4,000 lb)) shuttle orbiter-based deployable/retrievable **tether** system scheduled for initial flight in 1992.

The greater part of MSFC's TAS effort was spent in planning and defining advanced payloads for the **small expendable deployer system** (**SEDS**). **SEDS** is a low-cost, light-weight (approximately 38.6 kg (85 lb)) deployment-only **tether** system, designed for launch as a secondary payload on a Delta II vehicle. The initial launch of **SEDS** is scheduled to occur in 1992.

Recent TAS activities include developing television instrumentation for viewing the **tether**, developing **SEDS**–2 control laws, and increasing telemetry capacity. Near-term follow-on **SEDS** missions are being readied, including one that deploys a student-developed payload upward and one that deploys a short electrodynamic **tether** to study Space Station *Freedom* (S.S. *Freedom*) charging effects such as sputtering, arcing, and the generation of electromagnetic interference. Planning is continuing for other flight experiments, such as a small artificial gravity facility (SAGF) experiment and a small reentry capsule.

Upgraded versions of **SEDS** have potential for deorbiting trash and scientific samples from S.S. *Freedom*. The orbital momentum removed from the trash or sample packages by the deploying **tether** would be transferred to S.S. *Freedom*, raising its orbit and saving considerable reboost propellant.

Successful first flights of the **TSS** and **SEDS** will pave the way for these future applications.

C.C. Rupp/PS04
(205) 544–0627
Sponsor: Office of Space Flight

Space Science

Gravity Probe-B

Gravity Probe-B (GP–B) is an experiment in fundamental physics that requires flight in Earth orbit for its execution. Its primary goal is to perform two very precise tests of **Einstein**'s general theory of relativity, which is the basis for an understanding of the large-scale structure of the universe. Today, despite important progress in the last 25 yr, **general relativity** remains a very imperfectly tested theory. Through observations of the spin axes of **gyroscopes** in a **drag-free** satellite in polar orbit around the Earth, GP–B will provide (1) a measurement for the first time, with high precision (~0.3 percent), of one of the most challenging predictions of **Einstein's** theory—the dragging of the inertial frame of space by rotating matter, and (2) a measurement to approximately 1 part in 10^5 of the geodetic precession of a gyroscope due to its motion through the curved space-time around the Earth. The latter furnishes, by far, the most precise test of any of the positive predictions of **general relativity** yet performed. In a polar orbit, the two effects are at right angles and amount to 0.042 and 6.6 arc sec/yr, respectively.

The GP–B **gyroscopes** (fig. 10) are 38–mm diameter fused quartz spheres, round to better than 10 nm, coated with superconducting niobium, and electrically suspended in a vacuum. They spin at 10,000 r/min, and any shift in their spin axis is measured with a precision of 0.1 m-arc sec by means of superconducting circuits. Four such **gyroscopes**, together with a **drag-free** proof mass and a high-precision telescope, will be mounted in a **dewar** containing 2,000 L of superfluid helium at a temperature 1.8 K above absolute zero. The mission will fly in a carefully trimmed 650–km polar orbit and will last approximately 18 mo. Throughout that time, the spacecraft will point at a single guide star (Rigel) and will slowly roll about the line of sight. Relativity and geodesy data will be gathered continuously, stored onboard, and transmitted to Earth every few orbits. An important aspect of the experiment is an elaborate series of in-flight calibration and validation checks to assure the reliability of the final results.

In CY84, the NASA Administrator approved the engineering development phase for GP–B known as the shuttle test of the relativity experiment (STORE). The first phase of STORE culminated in June 1990 with the successful completion of first integrated systems test (FIST), a full-scale prototype science instrument mounted in an engineering development **dewar** (EDD). A follow-on test is scheduled for CY92, and a second advanced prototype instrument is under construction. Also under construction is the shuttle test unit (STU), which is scheduled to be launched in CY95. (See table 1 for a summary of GP–B status.)

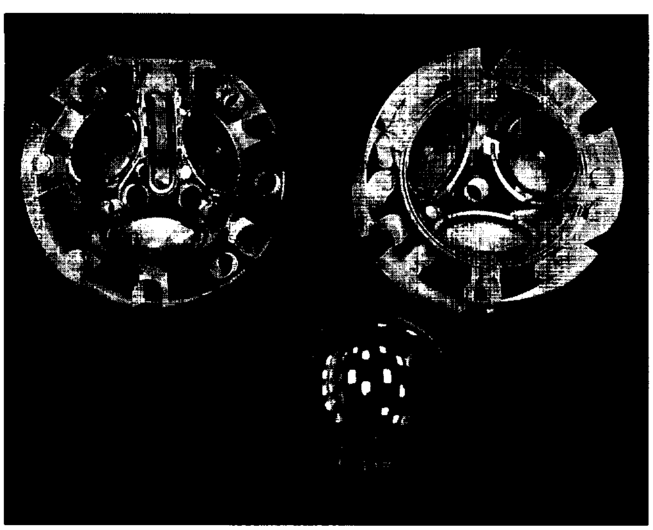

FIGURE 10.—The Gravity Probe-B gyroscopes.

TABLE 1.—*Summary of GP–B status*

- The shuttle test of the relativity experiment (STORE) engineering development program initiated FY85
- Ground test unit currently under systems test
- Two competitive spacecraft studies completed in CY91
- Science mission start FY93/FY94
- Shuttle engineering test flight of gyro subassembly CY94
- Science mission launch CY98/CY99

R. Ise/JA91
(205) 544–1962
Sponsors: Office of Space Science and Applications

Hydrogen Maser Clock

The **hydrogen maser** clock is an atomic clock experiment to demonstrate the long-term accuracy and stability of **hydrogen maser** clocks in space. Highly accurate time references are required to support applications for future in-space investigations such as astrophysics, space-borne, radio, astronomical, very long baseline interferometry, and worldwide time synchronization.

The atomic **hydrogen maser** is the most stable frequency standard currently available for measurement intervals ranging from seconds to weeks. For time measurements made at intervals of about 11 h, time resolution is about 3×10^{-16}. Establishing the clock stability at these accuracies will require the spacecraft position along its path to be known within a few meters and its velocity to be known within a few millimeters per second. This position and velocity determination will be established with NASA's satellite laser ranging and tracking stations (fig. 11).

The extreme accuracy and resolution of this instrument is affected by minute changes caused by radiation magnetic fields and low gravity in the **orbital** environment. Parameters such as applied coating degradation, hydrogen atom and molecular flow, and instrumentation techniques will be evaluated.

This experiment is currently planned for flight on the European retrievable carrier (EURECA). The EURECA spacecraft is carried to low Earth orbit by the space shuttle, released, and then boosted into a 500–km orbit. After approximately 6 mo at this orbit, the mission is completed by deorbiting to an altitude where the space shuttle retrieves the spacecraft and returns it to Earth.

The experiment was selected for a 1–yr definition activity, which started in CY91. Approval of the development effort is anticipated in CY92.

B.J. Schrick/JA93
(205) 544–1976
Sponsors: Office of Space Science and Applications

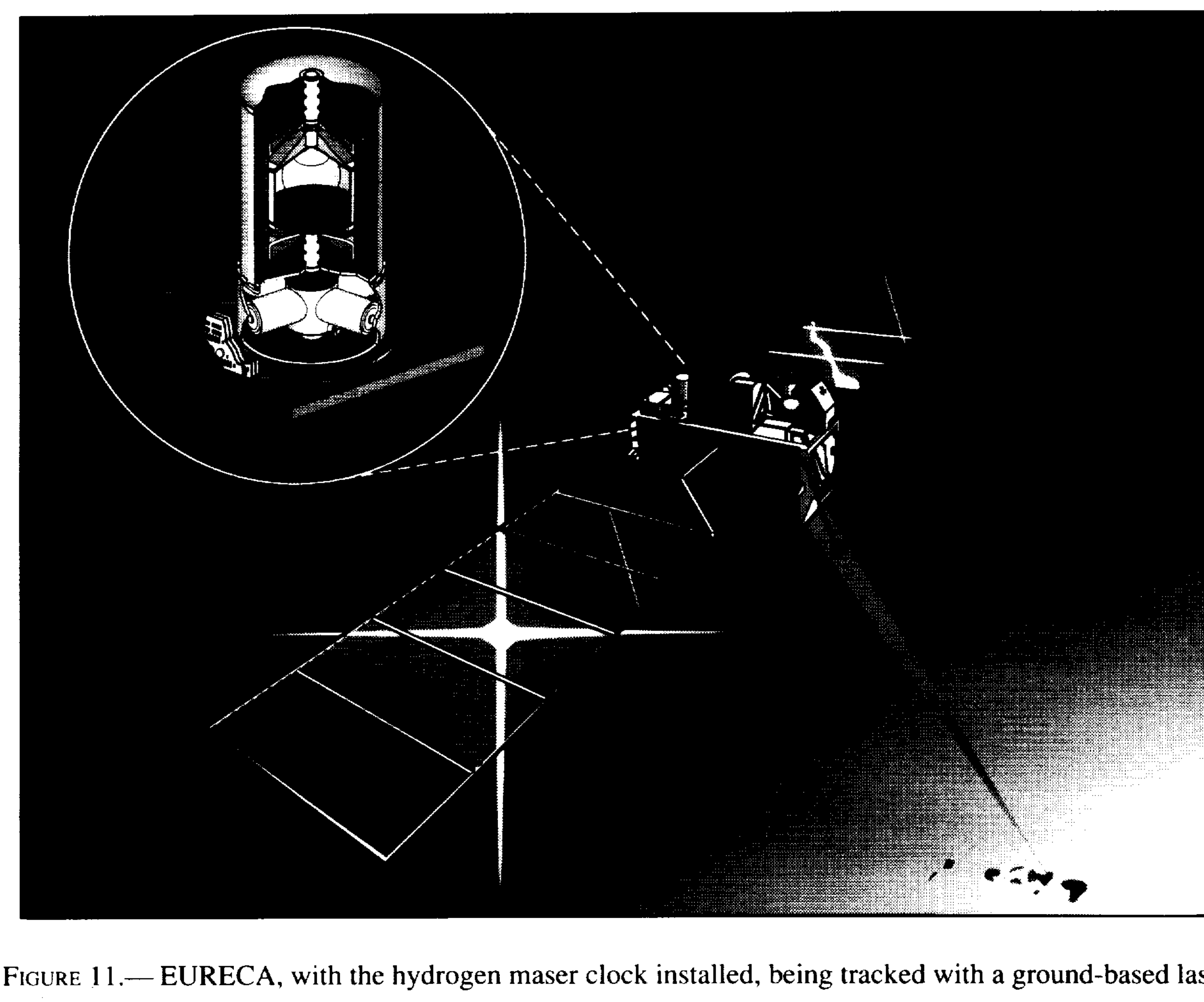

Figure 11.— EURECA, with the hydrogen maser clock installed, being tracked with a ground-based laser.

Inner Magnetosphere Imager

MSFC initiated an engineering feasibility study for an "Explorer-class" mission to globally image the Earth's **magnetosphere** from space. Progress in magnetospheric physics has shown that a static model built up over time from single-point measurements alone cannot adequately describe the complexity of the magnetospheric system. Further progress is contingent upon global observations of the entire system, in conjunction with microscale measures from single- or multipoint sensor systems. A program to image the inner **magnetosphere**, combined with internal measurements conducted previously and planned as a part of the International Solar Terrestrial Program, will significantly enhance the understanding of magnetospheric processes.

Recently developed techniques will allow satellite imaging of important charged particle populations in the **magnetosphere** (in addition to methods for imaging vacuum ultraviolet and visible signatures). Techniques to image the ring current with **energetic neutral atoms** have been demonstrated and can be optimized for satellite use. The imaging of low-energy magnetospheric plasmas using solar radiation resonantly scattered from singly ionized helium has also been demonstrated. The further possibility of O^+ imaging of the plasmasphere and extended imaging of the near-Earth plasma sheet also appear to be feasible.

A mission to (1) image the global ring current, plasmasphere, inner edges of the plasma and auroral regions, (2) globally map the fields and currents from low altitudes to the equatorial regions, and (3) globally image the substorm injections is being defined at MSFC with the support of the Space Physics Division of the Office of Space Science and Applications.

Several candidate imaging measurements were identified for the mission at a series of workshops sponsored by MSFC. Instruments for performing these measurements are to be developed once the mission is approved for a phase B study. The instrument candidates for performing these measurements are:

- Energetic neutral atom imager (with low- and high-energy heads)
- Plasmasphere imager
- Far ultraviolet (FUV) imager
- Geocoronal imager
- Proton **aurora** imager
- Electron precipitation imager.

A science working group was formed to define the specific science goals and to develop a strawman instrument complement for the inner **magnetosphere** imager (IMI) mission. MSFC led a preliminary study to examine the feasibility of accommodating these strawman instruments on an existing spacecraft bus for a potential launch in the late 1990's. The preliminary instrument configuration for a free-flying spacecraft is illustrated in figure 12.

C.L. Johnson/PS02
(205) 544–0614
Sponsor: Office of Space Science and Applications

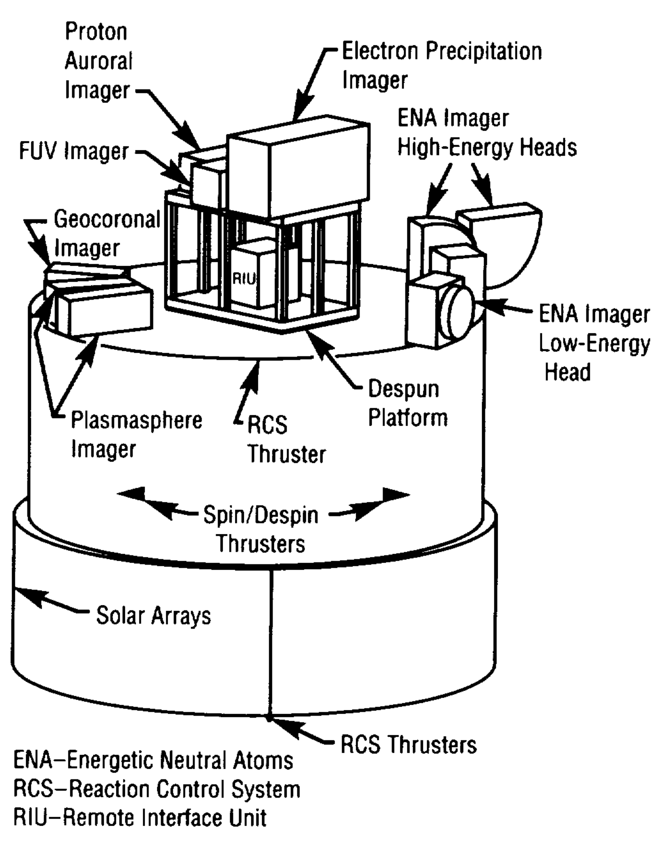

FIGURE 12.—IMI instrument configuration.

Pinhole/Occulter Facility

The **Pinhole/Occulter Facility (P/OF)** was selected for study as an "attached payload" for the space station. When the payload pointing system (PPS) was dropped from the space station infrastructure, the **P/OF** and other pointing payloads could no longer be supported by the space station. The **P/OF** scientific goals are still highly relevant and can be accomplished as a **free-flying spacecraft** or as a **lunar surface observatory**. The goals of the **P/OF** are the high-resolution imaging of the Sun in hard x rays and gamma rays. Other planned instruments and spacecraft will be capable of some **high-energy imaging** of the Sun and the celestial sphere, but the resolution of such imaging is directly related to the physical dimensions of the instruments.

The basic instrument uses a large structure to separate an aperture plate from x-ray sensors on the detector plane. The x rays (and gamma rays) are imaged by two different techniques. A large field-of-view coded-aperture array uses multiple pinholes in a pseudo-random repetitive pattern; total aggregate open area typically approaches 50 percent of the total plate area. The x-ray sensitive detector is typically a multiwire gas proportional counter. Actual spatial resolution is dependent upon separation of the elements and the plate scale of the detectors, but is typically on the order of a few arc seconds.

The other system uses a series of slits of varying width and angular orientation that generates the Fourier-transform (F–T) elements of the x-ray image. These slits comprise grids that are mounted in pairs, one mounted on the detectors with the other at the distal end of the structure. Image elements are formed as Morie fringes and measured by scintillator arrays. The spatial resolution of the F–T imager is on the order of sub-arc seconds.

In FY91, work was under way to complete the computer model of the F–T imaging technology, and studies were made of the requirements of a lunar surface **P/OF**.

J.R. Dabbs/PS02
(205) 544–0623
Sponsor: Office of Space Science and Applications

Space Exploration Initiative Science Missions

In the next century, return to the Moon for scientific exploration, and as a waypoint for travel to Mars, will become a reality. The lunar surface provides a stable base and suitable environment for large-area science projects that otherwise cannot be accomplished either on the Earth or in space with free-flying spacecraft. Among the chief advantages of the lunar surface are low gravity, slow rotation, reduced terrestrial radio emissions, a dark sky (no airglow), and the ultrahigh vacuum of space. Several missions have been identified as candidates for lunar emplacement as a part of the **Space Exploration Initiative (SEI)**.

MSFC is nearing completion of in-house engineering studies that examine the feasibility of placing a large lunar telescope (LLT) and a precursor lunar transit telescope (LTT) on the Moon. Large lunar-based telescopes have the potential for spectacular scientific returns. Such telescopes will be capable of sensitivities, speeds, and spatial resolutions that are orders of magnitude better than current systems. An LLT with a 16–m aperture will have a resolution of 10 m-arc sec making it possible to observe structures at scales of 100 parsecs within all known galaxies. In addition, it will be capable of detecting the presence of Earth-like planets around other stars. The in-house LLT study identified some of the critical issues relating to the telescope's fabrication and emplacement on the lunar surface. A small teleoperated telescope, such as the proposed LLT, was also investigated as a potential precursor and test-bed for the LLT. The LTT would land on the Moon and become operational without the need for manned assembly. Such a precursor mission would provide first-class science and serve to answer technical questions pertaining to the operation of science instruments on the Moon. The LTT concept is illustrated in figure 13.

Several additional science instruments are being examined for lunar emplacement, although at a lower level of detail than the LLT or the LTT. However, many of the issues identified and resolved for the aforementioned telescopes are directly applicable to these other missions.

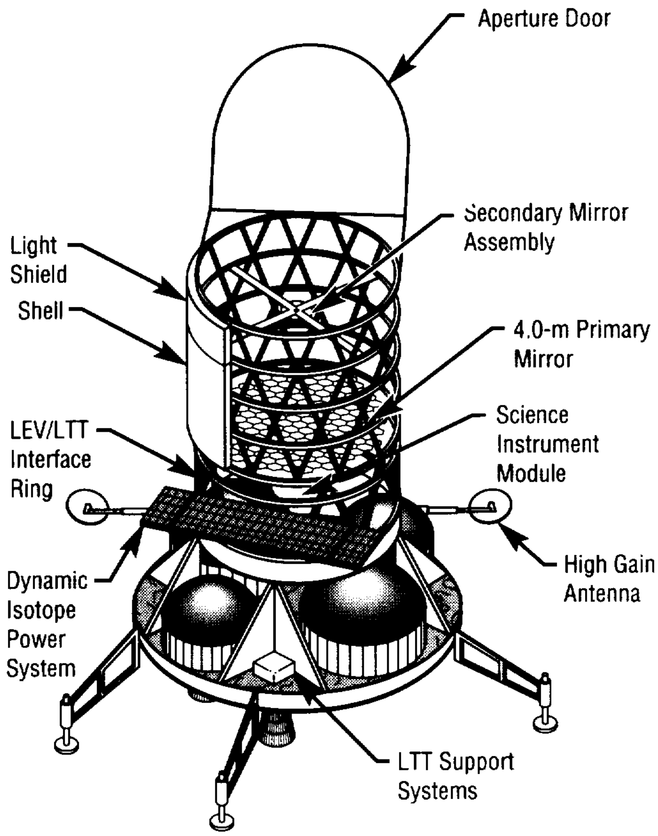

FIGURE 13.—Lunar transit telescope (LTT) concept.

The lunar calorimeter will explore the composition of cosmic-ray nuclei with energies in excess of 1,015 eV and aid in the determination of the sources and acceleration mechanisms of the highest-energy **cosmic rays**. The calorimeter will consist of layers of plastic scintillator counters viewed by photomultiplier tubes. Each layer will be separated by approximately 35 cm (14 in) of lunar regolith. The detector is to be position-sensitive for trajectory and time-of-flight measurements.

The **neutrino** telescope will search for a diffuse flux of heavy **neutrinos**, a directional flux of weakly interacting massive particle annihilation products from the Sun and from discrete sources of cosmic **neutrinos**. Fabrication of a telescope with sufficient area to detect **neutrino** events will be a daunting task. A detector with a surface area of 100 to 1,000 m^2 (10,764 ft^2) buried in a lunar lava tube for **cosmic-ray** background attenuation is likely to be required. The detector would consist of gas-filled chambers supported on a mesh structure and would be oriented to allow for up/down discrimination.

A lunar-based magnetospheric imaging system would be able to image the entire **magnetosphere** globally from the unique external vantage point offered by the Moon. The imager would consist of a thin foil time-of-flight sensor and would require a pointing accuracy of approximately 3 arc min. The detector is estimated to have a mass of 200 kg and an aperture of approximately 2 m.

The goal of a lunar-based magnetopause sounder includes active sounding of the magnetopause boundary using dipole transceiver arrays with pulse-coded outputs located kilometers apart on the lunar surface. The sounder would step in frequency from 5 to 100 kHz in 5–kHz steps. The receiving antenna would be large: 9 dipole arrays, each 2,500–m (8,202–ft) long and mounted on a short mast to yield an effective aperture of 20,000 m (65,617 ft).

A lunar solar observatory would include a variety of instrumentation to investigate the basic plasma physics processes responsible for the metastable and impulsive energy releases in solar flares. More fundamental research might also be conducted into the cause of the solar activity cycle. Such a facility would consist of several instruments including a solar vector magnetograph and possibly an evolutionary pinhole occulter facility. In addition to fundamental science, such an observatory could provide the functional capability of flare alert and warning for the proposed lunar base.

Nein, M.E., and Davis, B., "Systems Concept for a Large Lunar Telescope," SPIE *Proceedings*, OE/Aerospace Sensing, vol. 1494, Orlando, FL, 1–5 April, 1991.

McGraw, J., "The Lunar Transit Telescope (LTT)," *AIP Conference Proceedings 207*, Astrophysics From the Moon, Annapolis, MD, 1990.

Johnson, C.L., and Dietz, K.L., "Effects of the Lunar Environment on Optical Telescopes and Instruments," *SPIE Proceedings*, OE/Aerospace Sensing, vol. 1494, Orlando, FL, 1–5 April, 1991.

C.L. Johnson/PS02
(205) 544–0614
Sponsor: Office of Space Science and Applications

Superconducting Gravity Gradiometer

Accurate knowledge of the Earth's **gravity** field is fundamental to geophysics, oceanography, and **geodesy**. Limited **gravity** field information has been obtained in the past primarily through the measurement of satellite perturbations. In the last 25 yr, efforts have been made to develop highly accurate, moving base gradiometers. Under the sponsorship of NASA and the Department of Defense, a spaceborne gradiometer utilizing superconducting technology has been under development. MSFC is examining two superconducting **gravity** gradiometer (SGG) mission options for possible implementation in the latter part of this decade. The first option, a short-duration engineering test of the instrument, is being investigated for flight aboard the European retrievable carrier (EURECA). An Earth-probe mission class science mission is also being assessed.

The SGG instrument, which has been under development at the University of Maryland since 1980, has an intrinsic accuracy of 10–4 E $Hz^{-1/2}$ (where E represents the unit of **gravity** gradient (1 E = 1 Eotvos = 10^{-9} s^{-2})). Under parallel development by the university is a superconducting six-axis **accelerometer** (SSA) with an accuracy of 10^{-13} g_E $Hz^{-1/2}$ in linear acceleration and 10^{-11} rad s^{-2} $Hz^{-1/2}$ in angular acceleration. The instrument will be able to measure the Earth's global **gravity** field to 2– to 3–mgal (1 gal = 10^{-2} m s^{-2}) precision and 50–km (31–mi) resolution. Newton's inverse square law of gravitation might also be tested by the SGG instrument during the mission.

Several versions of the SGG instrument have been demonstrated in the last few years. With each new model, significant improvements in performance have been achieved. In the last year, progress has been made in upgrading the SGG model IIA (with a demonstrated intrinsic sensitivity of 0.01 E $Hz^{-1/2}$) to a model IIB (sensitivity of 5×10^{-4} E $Hz^{-1/2}$). The model IIB SGG uses state-of-the-art commercial superconducting quantum interference devices (SQUID's) to enhance its performance. The model III SGG is currently undergoing tests at the University of Maryland. The model III instrument is theoretically capable of achieving a sensitivity of 10^{-4} E$Hz^{-1/2}$.

In the last year, the feasibility of accommodating the SGG instrument aboard the EURECA spacecraft for an engineering flight test was examined by MSFC through a contract to GE Astro Space. The EURECA spacecraft is, as its name implies, a retrievable carrier launched by the space shuttle for 6–mo orbital missions. The SGG will require only 50 percent of the available area on the EURECA flight deck and will allow additional payloads to be flown concurrently. Figure 14 illustrates the accommodation of the SGG instrument module aboard the EURECA spacecraft.

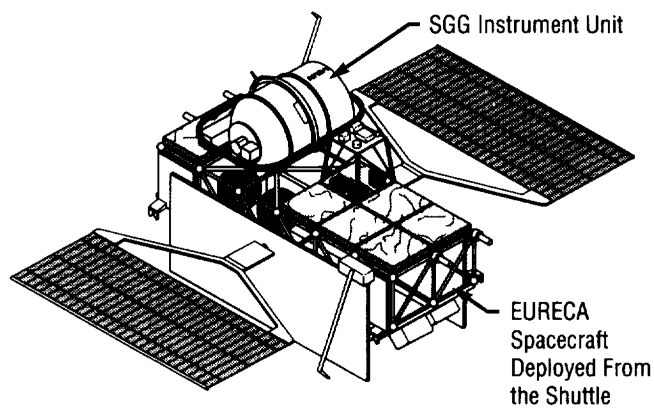

Figure 14.—Superconducting gravity gradiometer aboard the EURECA.

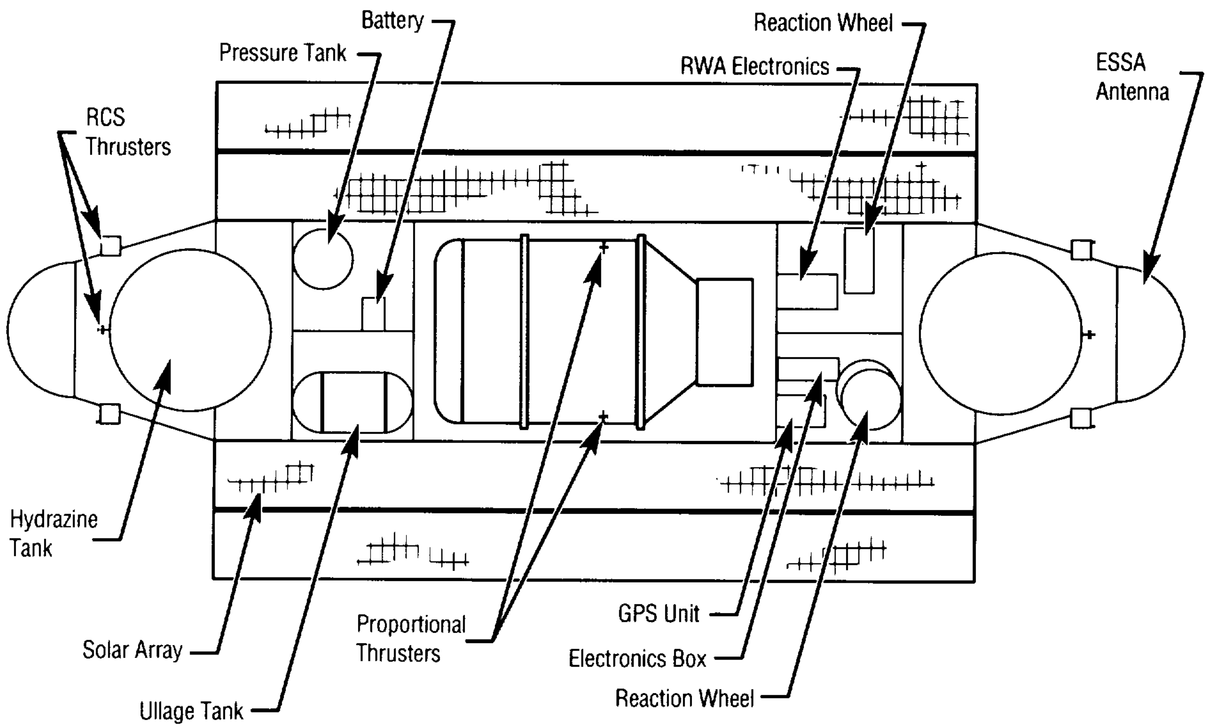

FIGURE 15.—Superconducting gravity gradiometer "Earth-probe" configuration.

The SGG Earth-probe mission is envisioned to fly in the 1998 timeframe just before the next solar maximum. An MSFC in-house engineering feasibility study of this mission was completed in 1991. The timing of the mission is critical since the SGG instrument must fly at an altitude less than or equal to 200 km (124 mi) in order to achieve the desired measurement accuracy. The mission spacecraft is designed to minimize drag and vibrational disturbances to the instrument. An Earth-fixed orientation is desired to fulfill the basic physics experiments of the mission. This orientation imposes orders of magnitude, more stringent control requirements, or much high-accuracy attitude rate knowledge on the spacecraft. The SGG instrument will be flown in a superfluid helium dewar similar in design to that being developed for the **Gravity** Probe-B mission. The experiment module will be free-floating within the spacecraft and will use helium-boiloff thrusting for vernier control, drag compensation, and vibration isolation. An engineering concept design for the SGG Earth-probe mission spacecraft has been developed by MSFC and is shown in figure 15.

Moody, M.V., Chan, H.A., and Paik, H.J., "Superconducting Gravity Gradiometer for Space and Terrestrial Applications," Journal of *Applied Physics*, vol. 60, No. 12, 1986, pp. 4308–4315.

Johnson, C.L., Morgan, S.H., Schelkopf, J., and Ransom, S., "Space Flight Options for a Superconducting Gravity Gradiometer," Proceedings of the International Association of Geodesy Symposium, No. 3, Vienna, Austria, 1991.

C.L. Johnson/PS02
(205) 544–0614
Sponsor: Office of Space Science and Applications

Building for the Future

RESEARCH PROGRAMS

By providing the means for extending the frontiers of space exploration, today's research lays the groundwork for tomorrow's space ventures. MSFC's scientific research program includes four major discipline areas of space science: microgravity science, astrophysics, Earth science, and solar-terrestrial physics. Within each of these, the Center maintains scientific cells of excellence to support major NASA flight programs.

The focus of the Microgravity Science Program is materials science. Using the low-gravity laboratory of space, this area promises exciting improvements in electronic and optical devices, and in eventually providing information for drug design.

Astrophysics research is primarily devoted to the high-energy spectral region. In the x-ray region, emphasis is on support of the Advanced X-Ray Astrophysics Facility (AXAF) mission and the study of celestial x-ray sources and radiation mechanisms. Gamma-ray research emphasizes the study of gamma-ray bursts and transient gamma-ray events.

Marshall's Earth science role involves support of the Mission to Planet Earth program through modeling and the development of diagnostic, analytical, and simulation systems and instruments that provide an integrated understanding of the Earth system.

The major theme of solar-terrestrial research is to obtain an understanding of the solar-terrestrial connection, i.e., how the Earth space environment is driven by solar extreme ultraviolet (EUV) photons and energetic particles.

E.A. Tandberg-Hanssen
Director, Space Science Laboratory

MICROGRAVITY SCIENCE

As a center of excellence for microgravity science and applications, combined with developing programs in regional universities (i.e., The University of Alabama in Huntsville; Alabama A&M University; the University of Alabama, Birmingham; and Vanderbilt University), MSFC has become a focus for microgravity research. In an effort to study the influence of weightlessness on basic materials science and biotechnology, a number of ground-based microgravity research and flight programs is continuing at a high level of activity. MSFC scientists and engineers are utilizing microgravity opportunities on the KC–135 aircraft, the MSFC drop tube, and space shuttle to conduct research and checkout of potential flight hardware and experiments. More than 20 principal investigators have had proposals selected as a result of peer reviews in MSFC-managed microgravity ground-based disciplines. MSFC scientists and engineers are preparing state-of-the-art experiments for a number of flight programs aimed at the U.S. Microgravity Laboratory (USML), the International Microgravity Laboratory (IML) -1 and -2, the U.S. Materials Pallet (USMP), Space Station Freedom, *and other shuttle flight opportunities. The results of these efforts have been the selection of 14 MSFC scientists as experiment principal investigators, and 8 MSFC scientists have been selected as flight hardware development project scientists or assistant mission scientists for these flights during 1992. Such experiments will clarify how the absence of gravity-driven convection and sedimentation can beneficially influence solidification and crystallization processes for inorganic and organic materials.*

ELECTRONIC MATERIALS

A broad scope of research and development in the area of **electronic and photonic materials** is carried out at MSFC. This includes the investigation of fundamental concepts related to the growth processes of these materials, especially those related to gravitationally influenced phenomena, and the development of the technology required for spaceflight furnaces to grow these materials. All materials of current interest are crystals grown by either **directional solidification** or **physical vapor transport**.

During the past year, a flight experiment to grow HgZnTe in the crystal growth furnace (CGF) on the first U.S. Microgravity Laboratory (USML–1) Spacelab mission has been brought to full development including flight simulations in the Ground Control Experiment Laboratory (GCEL) and the flight unit of the CGF. This mission is currently scheduled for a mid-1992 launch date. Development of the advanced automated **directional solidification** furnace (AADSF) flight experiment to grow HgCdTe has continued and that experiment is now scheduled to fly aboard the U.S. Microgravity Pallet (USMP–2) in 1993. Both of these flight experiments are **directional solidification** or **Bridgman crystal experiments**.

A third flight experiment, which will be carried out in the Boeing vapor CGF, will be the growth by **physical vapor transport** of CdTe. This flight experiment opportunity has been provided by Boeing with the support being provided by the Microgravity Science and Applications Division at NASA Headquarters as part of a concurrent ground-based research and technology objectives and plans (RTOP) project.

Under the Center Director's Discretionary Fund (CDDF) and Office of Space Science and Applications Advanced Technology Development (ATD) project support, a high-pressure furnace has been developed and is in the late stages of testing preparatory to using it for crystal growth and phase diagram determination of HgCdTe, HgZnTe, and related alloys.

PRECEDING PAGE BLANK NOT FILMED

A 5–T superconducting magnet with a 25–cm room temperature bore has been installed, and a furnace has been developed as part of the ATD effort to test the effects of magnetic fields on vertical Bridgman crystal growth. The magnetic field will retard the convective fluid flows always present in this type of growth process and, thus, to some extent, will simulate the reduction of the gravitational field.

A new project to expand from II–VI materials into the III–V area has been initiated under a CDDF project funded during the year. The initial material to be investigated will be GaAs, which is a superior, but more costly, alternative to silicon for high-speed electronic device applications.

S.L. Lehoczky/ES75
(205) 544–7758
Sponsor: Office of Space Science and Applications

Alloy Directional Solidification Experiments

Metallic alloy and composite solidification is strongly influenced by buoyancy-driven convection and Stokes flow in the melt. Commonly used metallic alloys are multiphase, multicrystalline, solidify with complex solid/liquid interfacial morphology, and are often cast into complex three-dimensional geometries. Because of the commercial and strategic importance of metals and **metallic alloys**, their solidification processes have been intensely studied by both the commercial and academic communities. However, because of the complexity of the solidification processes and the largely uncontrollable influence of gravity-driven flows, few models of **metallic alloy** solidification are advanced enough to be utilized extensively in commercial processes. Consequently, commercial processing of metallic alloys is still largely an empirical science. Research in low gravity has the advantage of greatly simplifying the solidification process. Buoyancy-dependent variables can be isolated, quantified, and incorporated into the solidification models. Because of the geometrical and physical complexity of **metallic alloy** solidification, castings with unique microstructure and properties can be made in low gravity that can be impossible to duplicate on Earth.

Directional solidification of **metallic alloys** during continuous KC–135 aircraft **low-gravity** maneuvers provides useful data, since convection and Stokes flow damping time is within the first quarter of the **low-gravity** period. Such research has been conducted on the **metallic alloy** of aluminum, copper, and lead (Al-Cu-Pb) (4.12, 70.63, 25.24 weight percent, respectively). This **metallic alloy** is of the **monotectic** type, i.e., it has an **immiscible** phase present in its melt. This **immiscible** phase, the hypermonotectic phase, usually settles quickly to the crucible bottom in normal gravity. The Al-Cu-Pb **immiscible** alloy **directional solidification** experiments at 5 mm/min have shown that volume fraction of the hypermonotectic phase was directly correlatible to the magnitude of gravity during **directional solidification** (fig. 16). These results show quite graphically the dramatic effect that gravity can have on the microstructure of monotectic alloys. Previous studies of **monotectic** alloys solidified in this manner have shown that even subtle, buoyancy-influenced changes in the composition and structure can have dramatic influence on the alloy electrical properties. This work forms the basis of a proposal reviewed by the European Space Agency (ESA) in which the highest priority was given for a flight experiment in the European advanced gradient heating furnace.

P.A. Curreri/ES75
(205) 544-7763
Sponsors: Office of Space Science and Applications and Office of Commercial Programs

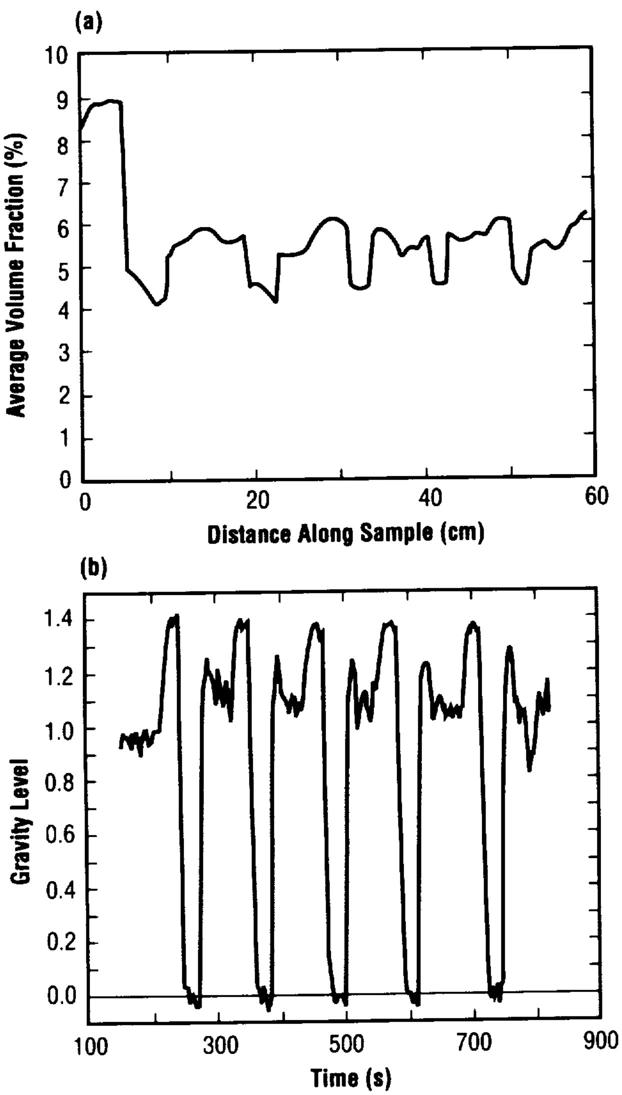

FIGURE 16.— (a) Plot of volume fraction of the hypermonotectic phase versus distance solidified. (b) Plot of gravity level versus distances solidified.

MSFC 105-m Drop Tube Undercooling and Nucleation Studies

In order to improve present metals and alloys through space processing, it is necessary to first understand the effect of low-gravity processing on the structure and properties of the material. The effect of low gravity coupled with **containerless processing** is being studied using the MSFC 105-m drop tube facility. This environment, achieved in both the drop tube and during a containerless space flight, is conducive to large degrees of undercooling before solidification of the metal occurs. Therefore, the MSFC 105-m drop tube facility provides an ideal environment for undercooling and **nucleation studies** of undercooled metals.

In the past year, effort has been directed at the measurement of the nucleation temperatures of over 500 high-purity niobium samples. A histogram of nucleation temperatures revealed a Poisson distribution from which the nucleation rate and most probable nucleation temperature could be readily determined. The results of this nucleation study will be compared to results obtained during space flight with the TEMPUS electromagnetic levitator to be flown aboard the International Microgravity Laboratory-2 (IML-2) shuttle mission. In addition, the results have been compared to samples processed by this group in the drop tube located in Grenoble, France.

Additional studies of undercooled samples have involved the measurement of dendritic solidification velocities. It has been found that the solidification velocities measured for pure metals are considerably less than the theoretical predictions. Further research is continuing.

Hofmeister, W.H., Bayuzick, R.J., and Robinson, M.B., "Non-Contact Temperature Measurement of a Falling Drop," *International Journal of Thermophysics*, vol. 10, No. 1, January 1989.

Robinson, M.B., Bayuzick, R.J., and Hofmeister, W.H., "A Review of Drop Tube and Drop Tower Facilities and Research," *Space Commercialization: Platforms and Processing*, edited by F. Shahrokhi, G. Hazelrigg, and R. Bayuzick, vol. 127 of Progress in Astronautics and Aeronautics, AIAA, Washington, DC ISBN 0-930403-76-2.

Rathz, T.J., Robinson, M.B., Hofmeister, W.H., and Bayuzick, R.J., "The Marshall Space Flight Center Drop Tube Facility," *Review of Scientific Instruments*, vol. 61, No. 12, December 1990.

M.B. Robinson/ES75
(205) 544–7774
Sponsor: Office of Space Science and Applications, Microgravity Science and Applications Division

Diacetylenes for Nonlinear Optical Applications

In recent years, **polymers** made from **diacetylenes** have been of great interest as **non-linear optical materials.** Polydiacetylenes have some of the largest measured non-resonant, third-order, nonlinear susceptibilities, which are proportional to the intensity-dependent index of refraction. Moreover, the response time of their optical nonlinearity is believed to be less than a picosecond. In the past year, MSFC has been investigating **diacetylene** derivatives of **pyrrole** as candidate materials to test some computer models that predict the chemical and nonlinear optical properties of these compounds.

One **diacetylene** of interest has been the following:

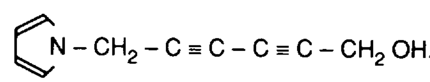

This compound was synthesized in approximately four steps starting from **pyrrole** and propargyl alcohol. Purification is accomplished using column chromatography on silica gel. A very unique and novel feature of this **diacetylene** is that it exists as a liquid at room temperature. (The freezing point is approximately 5 °C (41 °F).) Most **diacetylenes** commonly studied for nonlinear optical applications are solid at room temperature.

The purpose for making this **diacetylene** was to grow thin crystalline films of the compound by vapor deposition, which were then polymerized by ultraviolet (UV) light (in the solid state) to form polydiacetylene films having interesting nonlinear optical properties. Thin crystalline monomer films were grown on quartz or glass overnight at 30 to 35 °C/20 μm Hg, using a condenser temperature of –20 °C (–4 °F); a condenser temperature much lower than the freezing point is needed because of undercooling. The **monomer** film was then polymerized by exposure to intense long wavelength UV radiation (around 365 nm) for 2 to 3 d. These somewhat extreme conditions for polymerization (as compared to those for certain other diacetylenes) were predicted by one of the computer models, thus illustrating the potential utility of such models. The resulting polydiacetylene film is currently being characterized, i.e., its nonlinear optical properties are being determined. In microgravity, the quality of the films produced should be better than that of those produced in 1g because of the lack of buoyancy-driven convection, which interferes with vapor deposition of the crystalline **monomer** films.

One very interesting result that has been obtained is that the **diacetylene monomer** itself has exhibited good nonlinear optical properties. Solutions of the **monomer** in acetone show very good third-order effects such as self-focusing and defocusing, self-phase modulation, and phase conjugation. Figure 17 shows the interference pattern caused by optical-field-induced refractive index changes in an acetone solution of the **diacetylene monomer**. The symmetry is initially circular, but quickly changes to semicircular due to convection. The remaining pattern is due to stable density gradients. Figure 18 shows "fanning" of the laser light, in the same solution, due to these third-order effects. These properties make the compound potentially very useful for **signal processing**. Currently, thin films of polymethyl methacrylate are being prepared at MSFC that contain the **diacetylene monomer**, which will show all of the nonlinear effects seen in solution, and, additionally, can be used as waveguides. Such films would be very useful for device fabrication.

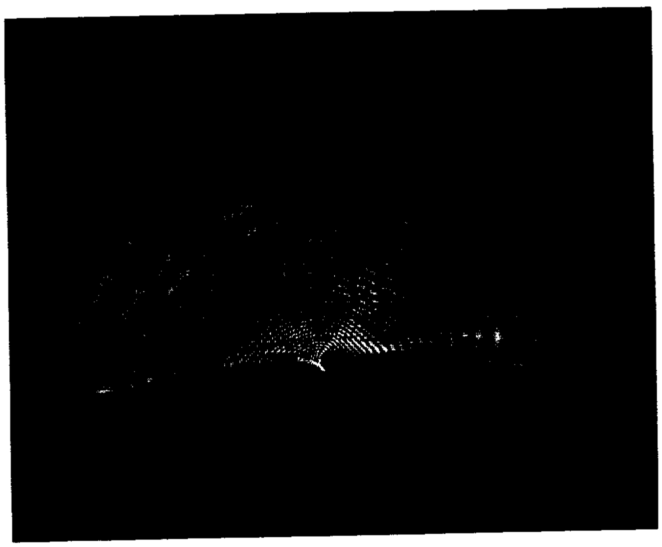

FIGURE 17.—Transient multiple diffraction ring pattern in pyrrole derivative of diacetylene with half-circular symmetry (due to convection) caused by optical-field-induced refractive index changes.

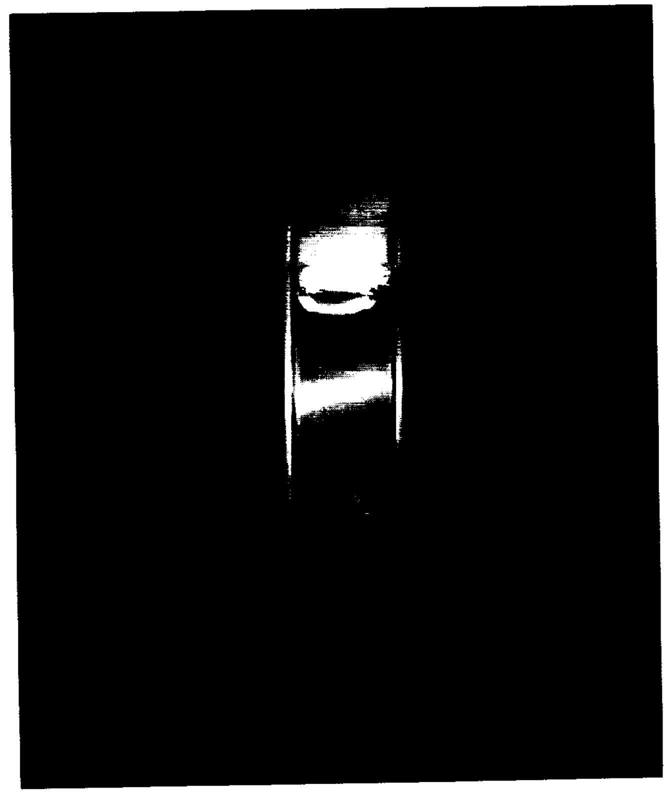

FIGURE 18.—Fanning in dilute acetone solution of diacetylene pyrrole derivative.

Lastly, because the **diacetylene** is liquid at room temperature, MSFC is investigating the possibility of polymerizing thin films of the diacetylene in the liquid state to see how such films compare to those produced in the solid state. Polymerization in the liquid state may offer advantages over polymerization in the solid state because of the lack of complications due to crystal imperfections in the solid state.

McManus, S.P., Frazier, D.O., and Paley, M.S., "Synthesis, Vapor Growth, and Polymerization of Thin Films of Novel Liquid Diacetylenes for Nonlinear Optical Applications," Patent Disclosure.

Penn, B.G., Cardelino, B.J., Moore, C.E., Shields, A.W., and Frazier, D.O., "Growth of Bulk Single Crystals of Organic Materials for Nonlinear Optical Devices: An Overview," *Prog. Crystal Growth and Charact.*, vol. 22, 1991, pp. 19–51.

Moore, C.E., and Cardelino, B.H., "Static Second-Order Polarizabilities of Aminobenzophenones and Nitrobenzophenones," *Journal of Molecular Structure*, (Theochem), June 1991.

D.O. Frazier/ES74
(205) 544–7825
Sponsor: Office of Space Science and Applications

Rotating Chamber Microgravity Simulators

At MSFC, four different versions of rotating chamber reactors are now available for use in ground-based microgravity simulator tests applicable to fluid-fluid and fluid-particle suspensions investigations. All four versions are similar in that each consists of a sample chamber in the form of a right circular cylinder that is rotated about its horizontal axis while housed within a temperature-controlled environment. Particles or fluids of dissimilar densities can be maintained in suspension for long periods of time, subject to Stokes Law, through rotation of this chamber. If particles such as monodisperse latex microspheres are suspended in fluid such as water, and are rotated within one of these chambers, the particle orbits are approximate circles with centers displaced horizontally from the axis of rotation. At high rotation rates, the particles spiral outward or inward (depending on whether their density is more or less than the fluid) too quickly; at low rotation rates, displacement of orbit centers from the rotation axis is excessive in relation to the chamber radius. A test program has recently been completed using the **enhanced latex rotary reactor** to determine the rotation rates that maximize the number of particles remaining in suspension and describe the motion of the particles within the chamber. Typically, the optimum rotation rates were found to be close to or slightly above 1 r/min, and the four rotating chamber reactors described here have been designed to operate within this range. The four types of rotating chamber reactors are described below.

The **prototype latex rotary reactor** (fig. 19) contains a 240–mL chamber (4×2.25–in diameter), which is rotatable between approximately 2 to 12 r/min, and is housed within a constant-temperature water bath. The chamber has a Pyrex glass wall, a stainless steel piston at one end, and a temperature probe and optional stirrer at the other end. All interior metal parts are plated with gold, allowing use with caustic fluids. A linear variable differential transducer (LVDT) is attached to the piston, so that volume-change data can be recorded during operation. This apparatus has been used to support the **monodisperse latex reactor (MLR)** shuttle flight experiment and the zeolite crystal growth (ZCG) experiment.

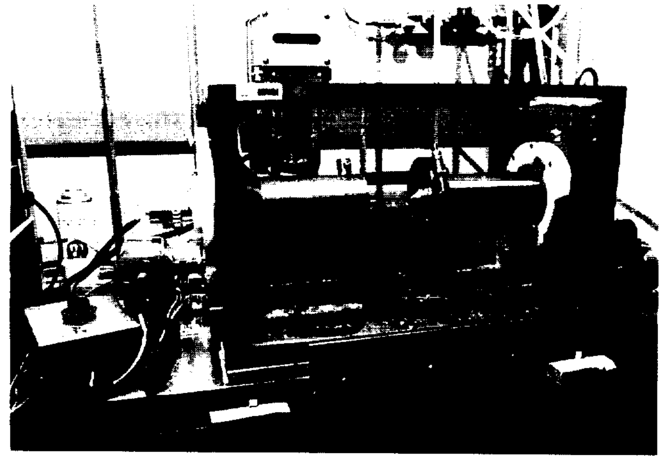

FIGURE 19. — Prototype latex rotary reactor.

The **enhanced latex rotary reactor** (fig. 20) contains a 230–mL chamber (4×2.13–in diameter), which is rotatable between approximately 1 to 23 r/min, and is housed within a constant-temperature water bath. The entire water bath and chamber are designed to be tilted from horizontal to vertical to facilitate chamber loading and sample removal. The chamber has a Pyrex glass wall, a steel piston with LVDT, an optional stirrer at one end, and a Pyrex glass window at the opposite end. A rotoscope (a device to optically subtract angular movement) is mounted outside the end window to allow observation and photography along the axis of rotation. A rotary valve allows injection or sampling of fluid along the axis while the chamber is rotating. Three temperature probes record within the chamber. The **enhanced latex rotary reactor** has been used for a variety of tests, including phase partitioning, and for a recently completed study to develop a computer model to optimize the operating parameters of this type of rotating system. This reactor will also be used for the spherical dye laser project.

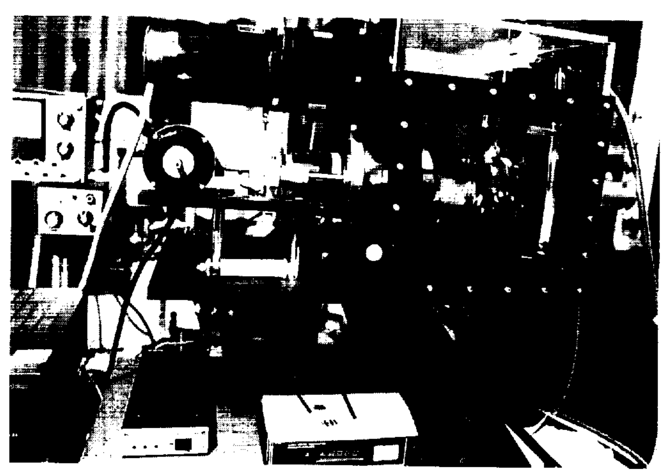

FIGURE 20. — Enhanced latex rotary reactor.

The **rotating chamber crystallizer** (fig. 21) contains an 800–mL chamber (4×4–in diameter), which is rotatable between approximately 1 to 12 r/min, and is housed within a constant-temperature water bath. This apparatus is a larger version of the previous reactor, including rotoscope and all its other features. In addition to the larger diameter chamber, this version is fitted with an optical mirrored piston and a laser illuminator and lens system to provide schlierin and shadowgraph capability through the end window. Seed crystals can be grown while attached to a sting projecting along the center axis of the chamber; crystals can also be initiated and grown in bulk while the LVDT provides a volume-change readout sensitive enough to provide phase-change information. All interior metal parts are coated with black Teflon, allowing use with acidic fluids. This apparatus is currently being used to support the triglycine sulfate (TGS) nucleation and crystal growth experiment.

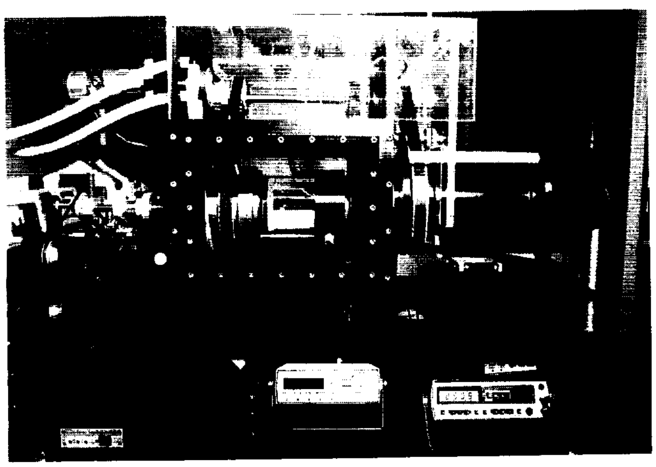

FIGURE 21.—Rotating chamber crystallizer.

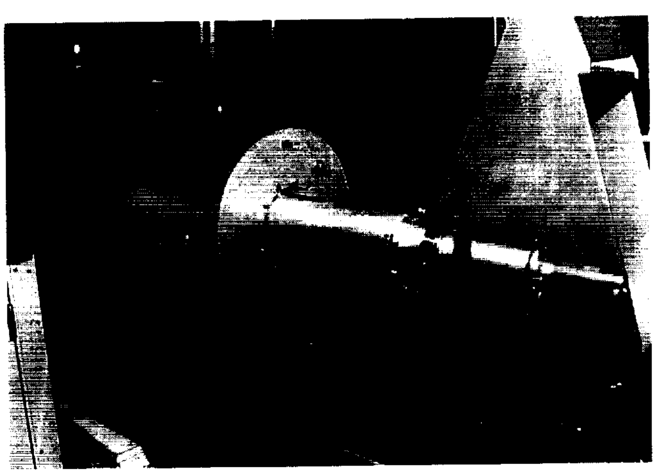

FIGURE 22.—Pilot-plant latex rotary reactor.

The **pilot-plant latex rotary reactor** (fig. 22) contains a 2–L chamber (8.5×4.5–in diameter), which is rotatable between approximately 1 to 10 r/min. This apparatus is an all-metal, industrial-type design, using an insulated, electrically heated jacket and heat-sink for temperature control between ambient temperature and 90 °C (194 °F). An LVDT/piston assembly and temperature probes allow chamber fluid volume and temperature measurements. This sturdy design can also be used as flight hardware, if needed. This apparatus, which only recently became available at MSFC, will be used to support a variety of projects, including the ZCG experiment and the spherical dye laser project.

Roberts, G.O., Kornfeld, D.M., and Fowlis, W.W., "Particle Orbits in a Rotating Liquid," *J. Fluid Mech.*, vol. 229, 1991, pp. 555–567.

Kornfeld, D.M., "Rotary Reactor Makes Large Latex Particles," NASA Technical Briefs, vol. 12 , No. 3, May 1988, p. 76.

D.M. Kornfeld/ES74
(205) 544–7808
Sponsor: Technology Utilization Program

Protein Crystal Nucleation

Nucleation is a complicated process that is not very well understood, even for small molecules. With **proteins**, there exists an opportunity to study this process in systems with considerably more experimental access to the nucleating molecules. Light scattering, while difficult with small molecules, is relatively easy with **proteins**. Most **proteins** have at least one fluorescent amino acid or can be readily derivitized with specific fluorescent probes. **Protein** molecules can be cross-linked while still retaining their function, which can also be exploited in **nucleation** studies. The approach taken by MSFC is designed to exploit these strengths of **protein**-based systems.

Initial experimental work has been done using the **protein** lysozyme, a well-characterized and easily crystallized material. Knowledge of the phase behavior is fundamental to any **nucleation** and **crystal** growth research effort. The tetragonal and 50 percent of the orthorhombic solubility diagrams from pH 4.0 to 5.4 in 0.2 pH unit steps have now been completed. Figure 23 shows the combined diagrams for pH 4.6. Note that the tetragonal form predominates below approximately 25 °C (77 °F), while orthorhombic form is found above this region. The tetragonal portion of this work has been completed and is being submitted for publication. In an effort to expand these studies, MSFC has also prepared solubility diagrams for alpha chymotrypsinogen and concanavalin-A.

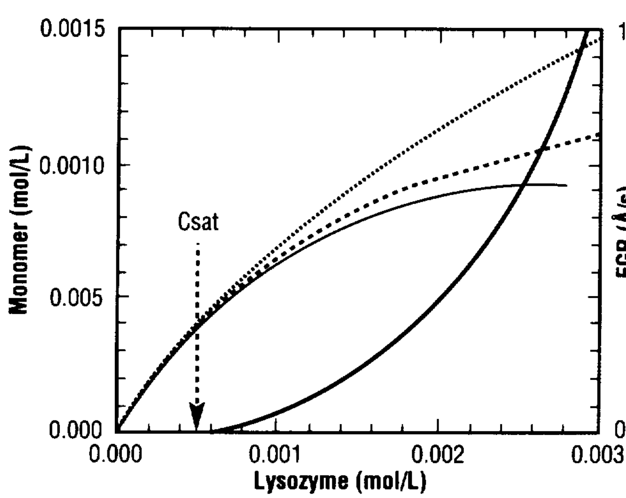

FIGURE 23.— The combined tetragonal and orthorhombic solubility of the protein lysozyme at pH 4.6.

Light scattering was initially proposed for following the **aggregation** process for nuclei formation. However, recent experience has shown that the results obtained are not as straightforward as expected. While continuing with these studies, MSFC has also developed a novel **dialysis kinetics**-based technique that is conceptually and experimentally simpler and enables us to estimate monomer (and larger) size populations in solutions that would be experimentally inaccessible to light-scattering techniques. The technique is based on following the rate at which **protein** passes through a **dialysis** bag that has a defined molecular weight cutoff. For example, with a 15,000 molecular weight cutoff, only monomeric lysozyme can get through the bag. The **dialysis** rate itself is followed by continuously cycling the **dialysis** buffer through an ultraviolet detector at 280 µm. This makes it possible to follow **protein** flux rates as low as 1×10^{-7} mg/s in real time. Figure 24 shows a summary of the data obtained so far with lysozyme at 20 °C, 3.0 percent NaCl, pH 4.0. The plot shows the monomer concentration calculated assuming a monomer-dimer-only **aggregation** and a monomer-dimer-tetramer **aggregation** pathway versus the total added **protein** concentration. The saturation concentration is 7.14 mg/mL and is indicated by an arrow. Also shown in figure 24 are the

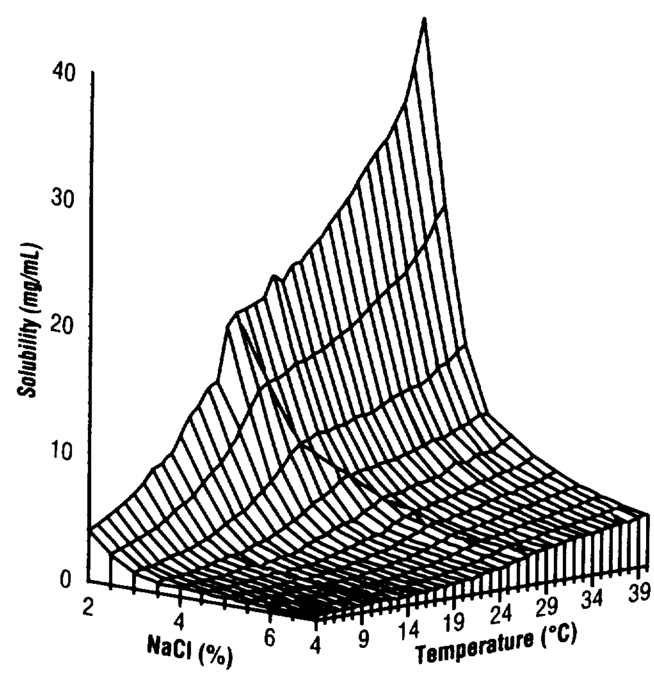

FIGURE 24.— Monomer concentrations as measured using dialysis kinetics in under- and oversaturated solutions (–0–).

expected face growth rates (110) under these conditions (shown by the solid lines). (The short dashed line and long dashed lines are the calculated monomer concentrations using 1→2 and 1→2→4 aggregation models, respectively.) Note that the measured monomer concentration quickly levels off by approximately three times the saturation concentration, and that only aggregate population and changes in its concentration do not seem to correlate with the changing growth rate. While the absolute values are not the same as those previously found using relative light scattering, the overall trends still very much support the conclusions that tetragonal lysozyme **crystal** growth proceeds by the addition of aggregates preformed in the solution. Subsequent experiments using the **dialysis kinetics** technique should enable us to dissect the **aggregation** pathway through the tetramer, and possibly through the ocatamer, **aggregation** levels.

Pusey, M.L., "Estimation of the Initial Equilibrium Constants in the Formation of Tetragonal Lysozyme Nuclei," *J. Crystal Growth*, vol. 109/110, 1991 (in press).

Cacioppo, E., Munson, S., and Pusey, M.L., "Protein Solubilities Determined by a Rapid Technique and Modification of that Technique to a Micro-Method," *J. Crystal Growth*, vol. 109/110, 1991 (in press).

Cacioppo, E., and Pusey, M.L., "Tetragonal Lysozyme Solubilities from pH 4.0 to 5.4," Manuscript to be submitted to *J. Biological Chem.*

M.L. Pusey/ES76
(205) 544–7823
Sponsor: Office of Space Science and Applications

Solution Crystal Growth

Research is continuing on the growth of **crystals** from solution. This effort includes both ground-based laboratory studies and flight experiments. It is directed toward increased understanding of the basic processes of **crystal growth**, **nucleation**, and growth techniques, and their applications and relations to a **microgravity** environment.

One activity centers around designing and carrying out experiments on Spacelab missions utilizing the Glovebox experiment module (GEM). This is a facility in which small experiments will be contained and isolated from the Spacelab crew environment and that can be manipulated by use of inserted gloves. An experiment has been designed and built for this facility, and it has been approved for flight on U.S. Microgravity Laboratory Flight-1 (USML–1). The experiment is entitled "**Nucleation** of **Crystals** from Solution in a Low-Gravity Environment." It will study crystal **nucleation** from solution using a new technique designed specifically for application in the **microgravity** environment. This technique, which involves localized injection of a heated, highly supersaturated solution into a host growth solution, is designed to control the onset, location, and character of **nucleation** when applied in a **microgravity** environment. A **nucleation** cell, injection mechanism, solution reservoir, and optical system have been built

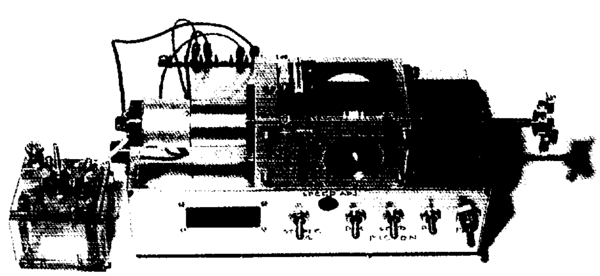

FIGURE 25.—USML–1 Glovebox experiment.

(fig. 25) and will be tested; it will interface with the Glovebox facility. Supporting ground-based research is being carried out to evaluate several candidate **crystal growth** solutions and their nucleating properties for suitability in this experiment.

In the laboratory, there is continued emphasis on supporting research to measure and study the physical properties of solutions from which **crystals** are grown. Basic properties such as viscosity, density, thermal conductivity, and mass diffusivity are measured. Techniques have been developed for studying synthesis, purification, solubility, and **nucleation** of new materials for crystallization. The internal structure of solutions at or above supersaturation concentration is not well understood. An internal reflectance cell is being used to investigate the structure of such solutions using infrared spectroscopy.

A new research activity is the partial simulation of **microgravity crystal growth** conditions achieved by growing a **crystal** in a cylindrical rotating solution chamber. In this apparatus, the concentration depletion region surrounding the growing crystal is not swept away by buoyancy, but is spiraled around the growing **crystal**, forming a depletion region similar in appearance to what occurs in a **microgravity** growth situation. This solution chamber will also be used to investigate injection **nucleation**. The rotation of the solution chamber keeps the injected fluid positioned along its axis and allows **nucleation** to occur in the interior of the chamber instead of on a wall, which would be the case if rotation was not maintained.

Wide use is made of optical techniques both for enhanced visualization and for specific measurements. Schlieren and shadowgraph images are made of growing **crystals** to image their growth or dissolution plumes. Holograms and interferometric images are used for detailed measurements of growth rates, concentration depletion regions surrounding growing **crystals**, and density gradients due to temperature or concentration variations in a growth solution. A laser scattering microscope is used to map microscopic defects in **crystals**. Index of refraction measurements are made on solutions for direct concentration determination and for use in analysis of interferograms.

Ground-based research is also focusing on new candidate growth materials that have high-technology applications. Particular emphases is being placed on nonlinear optical and infrared detector materials.

Kroes, R.L., and Reiss, D.A., "Development of New Techniques for the Characterization of Crystals and Their Growth Solutions," NASA TM–100371, June 1989.

Kroes, R.L., Reiss, D.A., and Facemire, B., "Concepts for Microgravity Experiments Utilizing Gloveboxes," NASA TM–100378, September 1989.

R.L. Kroes/ES74
(205) 544–7770
Sponsor: Office of Space Science and Applications

Decisive Gravity Test of Bioconvective Patterns

The remarkable phenomenon of **pattern formation** in dense cell cultures has been known for more than 150 yr. Its study has attracted physicists, biologists, and mathematicians, with each discipline favoring a different explanation of what causes biological patterns or, as it is sometimes called, bioconvection. The patterns themselves form rapidly (in seconds), repeatedly, and spontaneously. Their appearance is composed of alternatingly dense and sparse regions of cells that generate a fine network spanning up to 50 cm and connecting the movements of a third of a billion swimming cells (fig. 26). A typical cell is the protozoa, *Tetrahymena*, which is prominently featured in anticancer studies. Among 24 cell types tested for sensitivity to **anti-tumor drugs**, *Tetrahymena* rated as the optimal performer. The cause of macroscopic patterns in bioconvecting cells remains a disputed subject. The aim of these investigations was to identify and study the cause of spontaneous biological **pattern formation**.

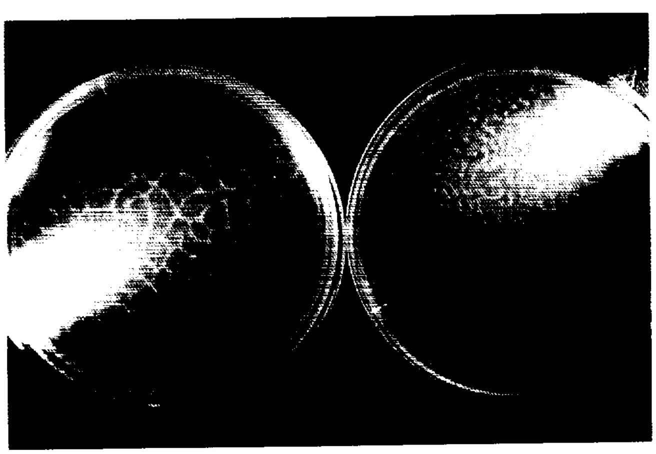

FIGURE 26. — Top view of bioconvective patterns in two shallow dishes of cell cultures. Cell density approximately 1M/mL.

To explain the cause of bioconvection, three hypotheses are offered: (1) the gravity hypothesis, which states that cells swim upward against gravity and, since they are heavier than water, subsequently turn over or stir their fluid culture into elaborate networks of rising and sinking cells; this is akin to Benard cells of thermal convection; (2) the drafting hypothesis, which states that cells draft or otherwise become linked together in their swimming by fluid viscosity; and (3) the chemical hypothesis, which states that cells detect and self-assemble in response to chemical gradients (e.g., oxygen) near their neighbors. Previous attempts to isolate and study these causes without at least one other mechanism interfering have failed. For example, the preparation of equidensity, isopycnic cultures introduces changes in both fluid density (gravity hypothesis) and viscosity (drafting hypothesis) with uncertain effects on the cells' chemistry (chemical hypothesis). However, by observing **pattern formation** in modulated gravity during parabolic flights of the KC-135 aircraft, the cause of bioconvection can be identified decisively.

Flight results indicate that those cells biologically capable of remaining active at extremely high concentrations (e.g., 10 billion cells per milliliter) form patterns by drafting for each other, while cells at lower concentrations (e.g., 1 M cells per milliliter) form patterns by sinking and rising in response to gravity. The chemical mechanism did not generally lead to **pattern formation** in the absence of gravity or drafting. The study of **pattern formation** in modulated gravity yielded uniquely decisive results.

Ground work suggests that bioconvective patterns make up the basis for novel pharmacological studies and **cell separations.** For example, bioconvective patterns have been used successfully here to monitor cadmium toxicity in polluted water and to construct strategies to counter cadmium's lethal activity by supplementing protective calcium, nickel, or copper. In addition to cell separations, 200 to 300 percent fractional splits have been obtained routinely in a rotating spectrometer in a single pass on bioconvecting cultures.

Noever, D.A., "Fractal Dimension of Bioconvective Patterns," *J. Phys. Soc. Japan*, vol. 59, 1990, pp. 10–13.

Noever, D.A., "Bioconvective Patterns, Synchrony, and Survival," *Phys. Rev. Lett.*, vol. 65, 1990, pp. 1953–1956.

Noever, D.A., "A Rotating Spectrometer to Concentrate and Separate Microorganisms," *Reviews of Scientific Instruments*, vol. 62, 1991, pp. 229–235.

H.C. Matsos/ES76
(205) 544-7814
Sponsor: Center Director's Discretionary Fund

ASTRONOMY AND ASTROPHYSICS

Astronomy and astrophysics have been a major part of the scientific space program since its beginning. Observations of the universe from above the Earth's atmosphere have brought exciting scientific discoveries and have opened new disciplines of research such as x-ray astronomy and gamma-ray astronomy. Historically, MSFC has been actively involved in various areas of astronomy and astrophysics with flight experiments, scientific payloads, and missions. The Center has had an increasing role in developing scientific instruments and managing major science projects starting with Skylab, including the Apollo Telescope mount, followed by the three High-Energy Astronomy Observatories, the Hubble Space Telescope, Spacelab experiments, and the ASTRO 1 mission. Responsibilities for future missions include the ASTRO 2 mission and the Advanced X-Ray Astrophysics Facility (AXAF).

The Astrophysics Division of the Space Science Laboratory has strong research programs in several areas of astrophysics and astronomy including x-ray astronomy, gamma-ray astronomy, cosmic-ray research, and infrared astronomy. Research activities cover theoretical and experimental research, development of new detector systems, scientific instruments, and flight experiments. Advanced technology work in support of scientific instrument development is being carried out in several areas, including low-temperature physics and cryogenic systems. A balloon flight experiment program in cosmic-ray research and x-ray astronomy is being conducted for high-energy astrophysics research and to test new detector systems and instruments. Presently, one of the major science operations involves data acquisition and data analysis from the Burst and Transient Source Experiment (BATSE) on the orbiting Compton Observatory (formerly the Gamma Ray Observatory).

FIRST GAMMA-RAY BURST OBSERVATIONS BY THE COMPTON OBSERVATORY

The **Compton Observatory** (formerly the **Gamma Ray Observatory**) was deployed into Earth orbit on April 7, 1991. It is the second of the four great observatories in space astronomy planned by NASA for the 1990's. The burst and transient source experiment (BATSE) is one of four experiments on the **Compton Observatory**. BATSE was designed, assembled, and tested by the in-house engineering and technical staff of the Science and Engineering Directorate of MSFC. The primary scientific objective of BATSE is the study of **gamma-ray bursts**. BATSE consists of eight detector modules arranged on the corners of the **Compton Observatory** to provide the maximum unobstructed view of the celestial sphere. It will allow the observation and location of hundreds of **gamma-ray bursts** each year with unprecedented sensitivity for performing spectral observations and rapid temporal variability studies. Two **gamma-ray bursts** detected early in the mission are shown in figures 27 and 28. In addition, the locations of some stronger bursts will

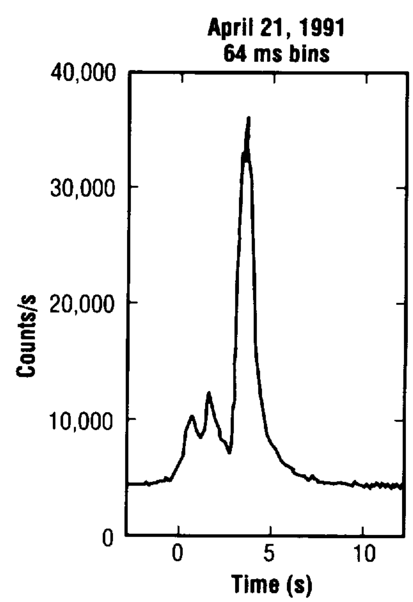

FIGURE 27.—The first gamma-ray burst observed by BATSE-Compton Observatory on April 21, 1991.

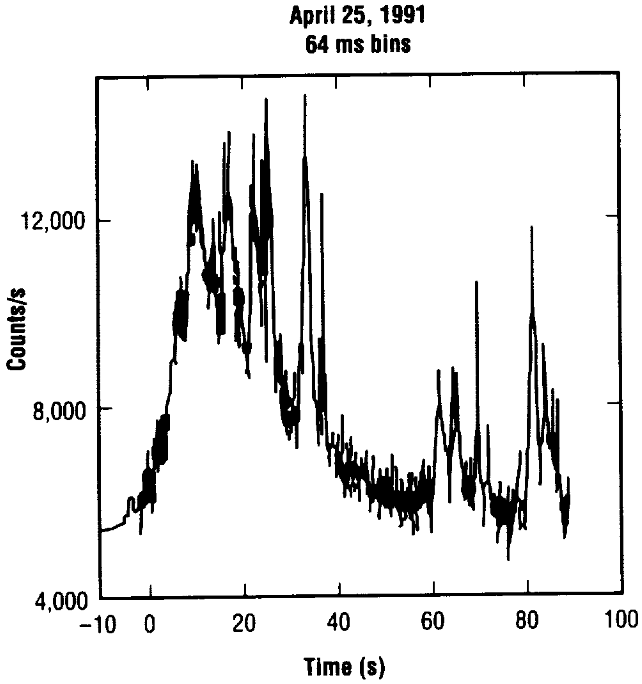

FIGURE 28. — Example of a strong gamma-ray burst detected by BATSE-Compton Observatory.

be determined quicker than previously possible, so that longer-lived emission at other wavelengths can be searched. BATSE also provides a **gamma-ray burst** signal and a solar flare trigger signal to the other experiments on the **Compton Observatory**.

Gamma-ray bursts remain one of the least understood phenomena in astrophysics. Although many theories of **gamma-ray bursts** have been proposed, the explanation of **gamma-ray bursts** is still quite speculative. Most recent theories propose that **gamma-ray bursts** are associated with old neutron stars within the galaxy. Initial attempts to identify the bursts with known objects have not succeeded. It is now recognized that there are distinct types of **gamma-ray bursts** that probably have different spatial distributions, emission mechanisms, and, perhaps, different central objects. Some types of bursts may be extragalactic, such as the March 5, 1979 burst. The soft, repeating **gamma-ray bursts** are associated with the central galactic bulge. The objective of burst classification and the determination of the spatial distribution of the different classes of **gamma-ray bursts** can be met through the detection and localization of many hundreds of **gamma-ray bursts** by BATSE. The spatial distribution of bursts in galactic coordinates or the association of certain types of bursts with extragalactic objects such as the LMC, M31, or the Virgo cluster would immediately provide the much sought-after distance scale needed to provide luminosities. Sensitive observations by the BATSE large-area detectors will provide the required large population sample along with the single-spacecraft determination of these burst locations.

G.J. Fishman/ES62
(205) 544-7691
Sponsor: Office of Space Science and Applications

Radiation Analysis of the LDEF Spacecraft

The **Long Duration Exposure Facility** (LDEF), retrieved by STS-32 after nearly 6 yr in orbit, is the focus of a broad-based study of the **radiation** environment in low Earth orbit and its effects on materials. Since its return to Earth in January of 1990, studies have concentrated on the use of **induced radioactivity**, dosimetry, and other passive methods to sample the effects of corpuscular **radiation** on the spacecraft. Over 400 samples of materials taken from different locations on the spacecraft, and detectors from a number of experiments are being analyzed at several national facilities. The results are being studied and compiled at MSFC for future use.

Magnitudes of proton and neutron exposure are being determined using low-level background measurement of residual gamma-ray activity. Various nuclides with half-lives in the range of 20 d to 5 yr have been detected in the spacecraft. The magnitudes of these activities are consistent with dosage received from the trapped proton flux encountered in the South Atlantic anomaly. Due to the gravity-gradient stabilization of the **LDEF**, it was possible to sample the anisotropy of the trapped component of the **radiation**. The activity for Na-22 in aluminum is shown in figure 29 as a function of angle from the leading edge of the spacecraft. Na-22, with a half-life of 2.6 yr, is formed from proton- and secondary neutron-induced reactions with Al-27, the stable isotope of aluminum. A calculation using the anisotropy model of watts, normalized to the predicted isotropic flux (AP8), is represented by the solid curve. The effect of the proton anisotropy is seen as a maximum in the activity at approximately 200° away from the leading direction (east). This is produced by atmospheric attenuation for geomagnetically trapped protons. The protons that encounter the spacecraft on its east side must travel in the atmosphere at lower altitudes, and tend to scatter out of their bound orbits.

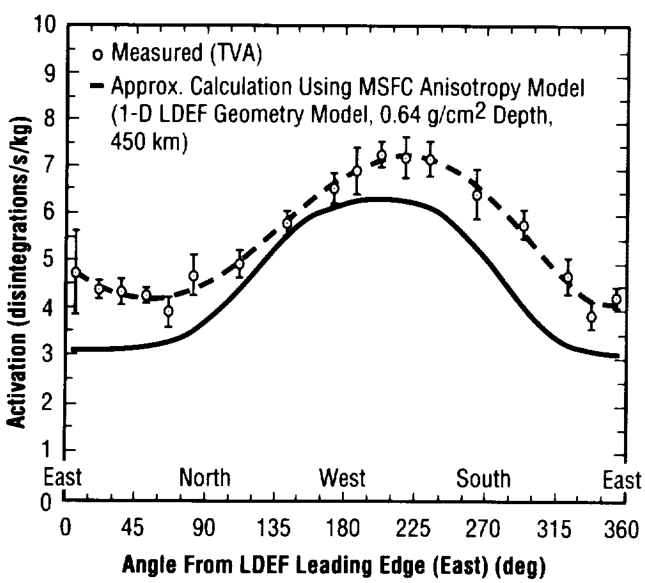

FIGURE 29.— 22Na activation of LDEF aluminum tray clamps.

A number of **LDEF** experiments carried thermoluminescent dosimeters (TLD's), which measured the absorbed dose at various locations and shielding depths. TLD's in three experiments (P0006, P0004, and M0004) have been analyzed. Experiments P0006 and P0004 were near the trailing (west) side of **LDEF** and M0004 was on the leading side. The dose (in rads) is displayed as a function of shielding depth for those detectors in figure 30. Also shown in the figure are calculations of the dose performed with an omnidirectional proton flux model (AP8) and two simple shielding geometries. The east-west effect of dose from the trapped protons is apparent in the data. Also obvious is the failure of the omnidirectional flux model to match all the data. The anisotropy model for the trapped protons will be used in an attempt to more accurately describe the directional dependence observed in the dosimeter experiments.

Directionality of dose and radioactivity, depth dependence, shielding, and other components of the **space radiation** environment affecting **LDEF**, such as galactic protons, thermal neutrons, and heavy charged particles, are currently under investigation. The length of the **LDEF** mission, the size and stability of the spacecraft, and its orbital configuration have made it quite valuable as a "laboratory" for long-term **space radiation** effects. It is expected that these studies will help to improve the predictive power of **radiation** environmental/transport codes currently being used in the design of other long-duration missions such as Space Station *Freedom*.

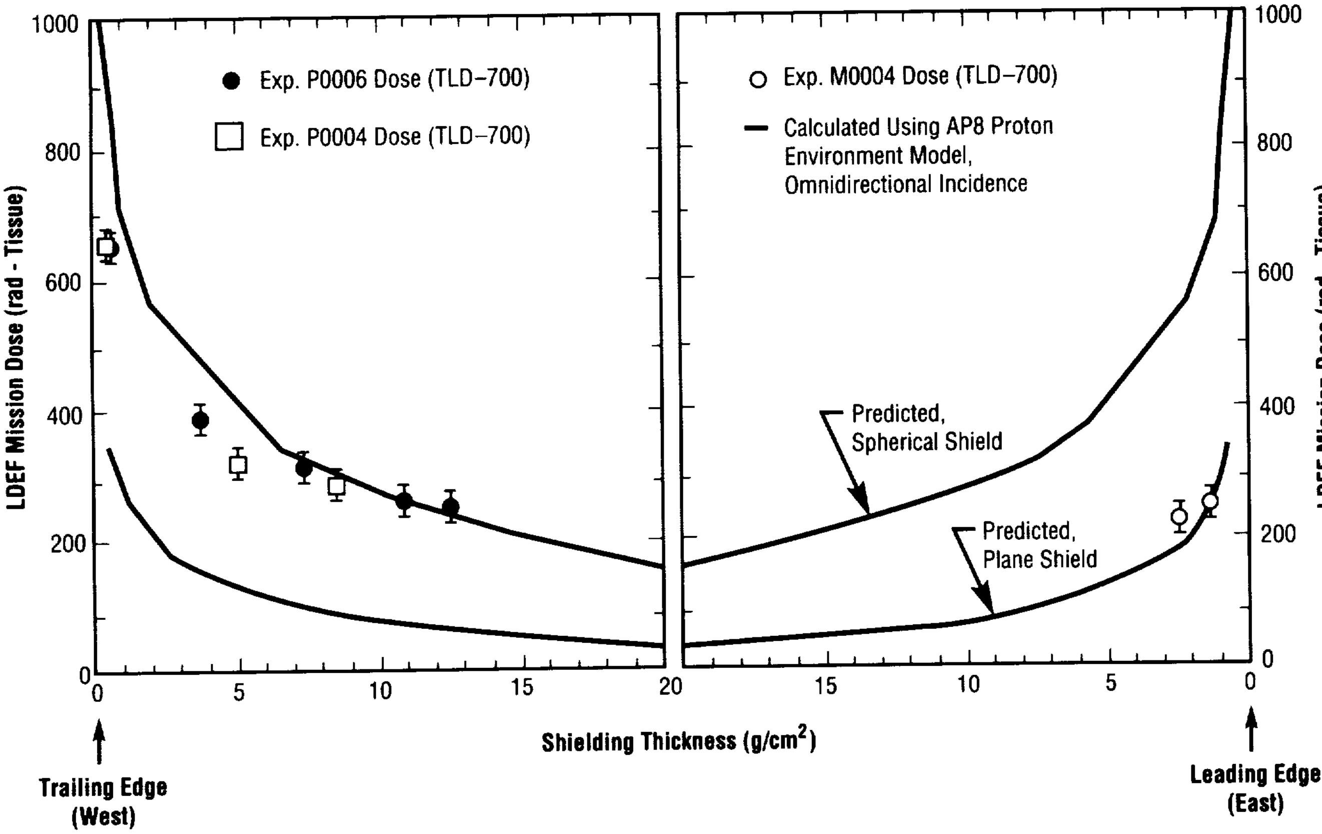

FIGURE 30. — Data from experiments P0006 and M0004, showing the dose performed with an omnidirectional proton flux model (AP8) and two simple shielding geometries.

Fishman, G.J., Parnell, T.A., and Harmon, B.A., "Long Duration Exposure Facility (LDEF) Induced Radioactivity Analysis Plan," NASA TM–103545, August 1991.

Watts, J.W., Parnell, T.A., and Hechman, H.H., "High-Energy Radiation Background in Space," AIP *Conf. Proc.*, vol. 186, Sanibel, FL, 1989, pp. 75–85.

Benton, E.V., et al., "Ionizing Radiation Exposure of LDEF (Pre-Recovery Estimates)," University of San Francisco Report USF–TR–77, 1990.

B.A. Harmon/ES62
(205) 544–4924

Sponsors: Office of Aeronautics, Exploration and Technology and Office of Space Science and Applications

Observation of ^{7}Be on the Surface of the LDEF Spacecraft

The **Long Duration Exposure Facility** (LDEF), an orbiting unmanned satellite, was recently returned to Earth after almost 6 yr in space. From **radioactivity** measurements, significant quantities of the isotope ^{7}Be (**atmospheric beryllium**) were found on the leading side surfaces of the **LDEF**. Quantitative results for ^{7}Be surface concentrations have been reported recently in the British scientific journal *Nature*.

Following the return of **LDEF** to the Kennedy Space Center for postretrieval processing, gamma spectra were obtained along each side of the spacecraft using germanium detectors from the Naval Research Laboratory. The gamma-ray line at 478 keV from the radioactive decay of ^{7}Be was unambiguously observed to emanate from the leading side of the spacecraft, as shown in figure 31. Individual components of the **LDEF** were also brought to MSFC to quantify the residual **radioactivity**. A high-purity germanium detector in the low-level background facility at MSFC was used to obtain spectra of small aluminum and steel samples taken from the leading and trailing sides. Gamma-ray spectra of two identical aluminum plates taken from the leading and trailing sides of the spacecraft are shown in figure 32. A clear ^{7}Be signal was seen on the leading side, with little or no signal above background on the trailing side.

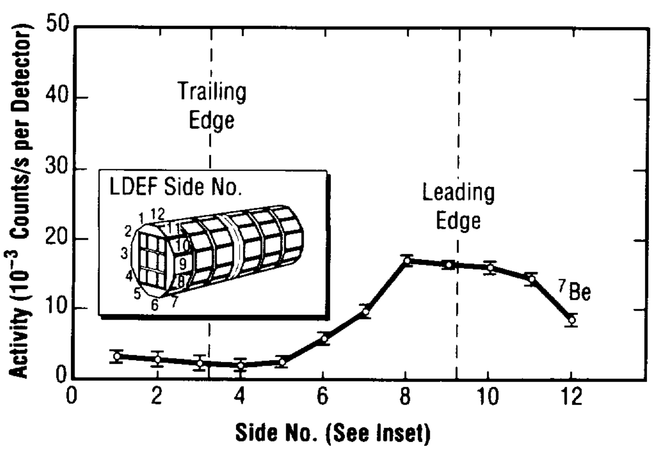

FIGURE 31.— LDEF acquired ^{7}Be radioactivity as a function of side number.

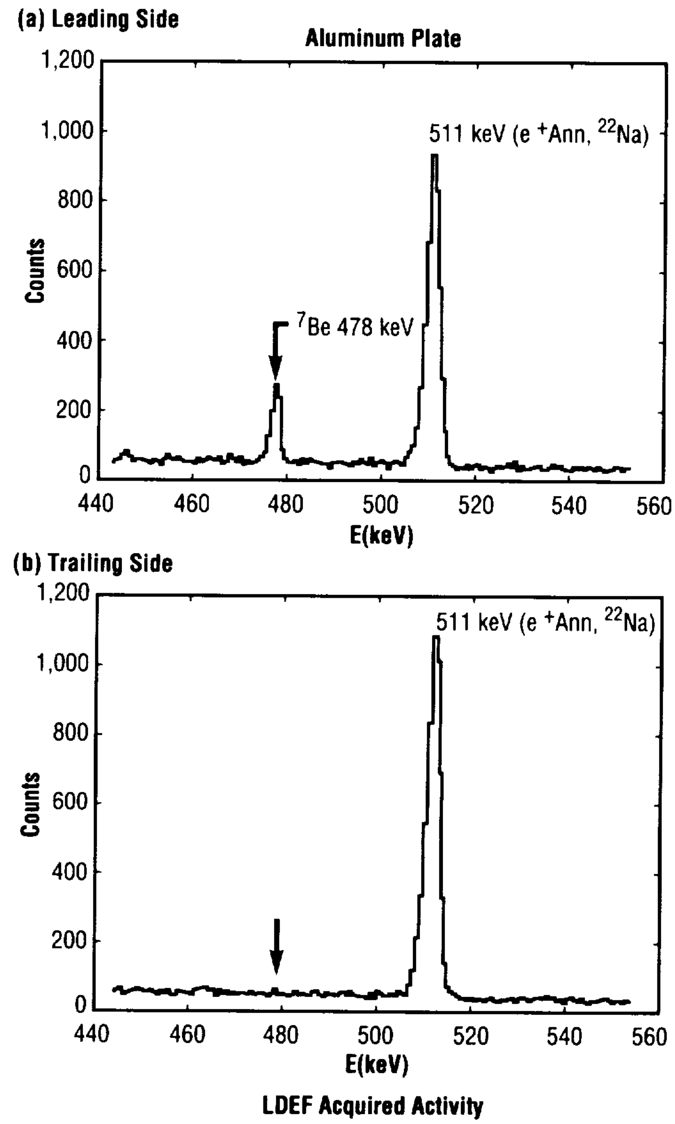

FIGURE 32.— LDEF ^{7}Be activity on experiment AO114 aluminum plates.

A series of wipe, stripping, and etch tests of a polished aluminum plate, which is used as a thermal control surface in **LDEF** experiment A0114, were performed to determine the depth of penetration and the form of deposition of the ^{7}Be. An acid etch removed several tens of microns of material from the metal surface, and most of the ^{7}Be activity. This suggests that the ions are trapped in the metal oxide surface layer, although the mechanism by which they adhere to the surface is not understood.

The low-level gamma-ray measurements of the areal density of ^{7}Be atoms on the leading side surfaces of **LDEF** yielded a value of ~5×10^{5} atoms/cm^2 (3×10 atoms/in^2), independent of metal type. The amount of ^{7}Be implied by these measurements, which is about two orders of magnitude higher than the contribution expected for reactions with the incident protons on aluminum and its surface distribution, leads to the conclusion that the ion must have accumulated on the spacecraft surfaces from the ambient atmosphere.

The concentration of ^{7}Be at the retrieval altitude of **LDEF** (310 km), calculated from the areal density, is about 3.8×10^{6} atoms per gram of air, with a density of 1.1×10^{-7} atoms/cm^3 (1.8×10^{-6} atoms/in^3). This result is three to four orders of magnitude in excess of what would be expected from conventional atmospheric transport and mixing models. The peak production region of ^{7}Be by cosmic ray bombardment is ~20 km (12 mi), and could feed the upper atmospheric burden of ^{7}Be. It is not understood, however, how the observed concentration at 310 km (190 mi) could be built up from the peak production region at much lower altitudes; this is now under study by a number of groups.

Fishman, G.J., *et al.*, *Nature*, vol. 349, 1991, p. 678.

B.A. Harmon/ES62
(205) 544–4924
Sponsors: Office of Aeronautics, Exploration and Technology and Office of Space Science and Applications

X-Ray Astronomy Research

A major portion of the experimental effort in x-ray astronomy has been devoted to developing advanced detectors, particularly for the hard x-ray energy region. These instruments are large-area imaging proportional counters that incorporate many new techniques to improve both sensitivity and resolution. These techniques include fluorescence gating, multistep operation, and the use of Penning gas mixtures, all of which have been developed and successfully demonstrated in the laboratory.

A flight instrument has been constructed that utilizes fluorescence gating. This technique makes use of the fact that true x-ray events usually lead to fluorescence of the detector gas, whereas charged particle **background** event interactions do not. The **background** can be effectively discriminated against by accepting only those events that cause fluorescence.

The first flight of this instrument was in May 1989, from Alice Springs, Australia, as part of NASA's SN1987A campaign (fig. 33). This flight, a collaboration with Harvard College Observatory/Harvard-Smithsonian Center for Astrophysics (HCO/CfA), revealed that a major portion of the residual instrument **background** was produced through the interaction of high-energy atmospheric photons with the thick aluminum detector body. A complete redesign of the detector has since taken place, and a new, molybdenum-bodied instrument is

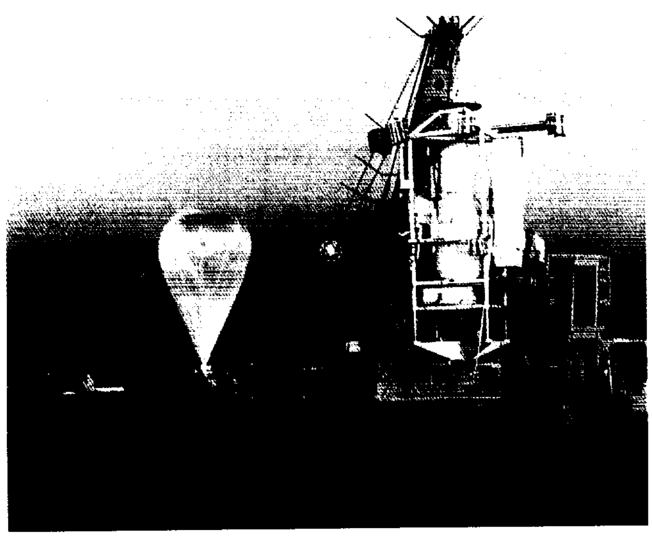

FIGURE 33.—The HCO/CfA/MSFC balloon payload.

currently being assembled for a flight in the fall of 1991. It is anticipated that, as a direct result of this change in material, the **background** count rate will be a factor of 20 lower than with the previous, aluminum-bodied instrument.[1]

In addition to the flight program, work continues on new instruments and techniques. Optical imaging of charge avalanches produced by alpha particle has recently been demonstrated as a first step towards an all-optical, x-ray detector. This offers the benefit of improved spatial resolution and charged particle rejection over the conventional charge readout instrument. Tests with a prototype mirror system for hard x-ray astronomy have also produced encouraging results. Initial images with ultraviolet light have demonstrated high-accuracy alignment between individual reflecting elements, paving the way for subsequent x-ray tests.

A further area of interest is x-ray **polarimetry**. The measurement of the polarization of cosmic x-ray sources will provide an important probe of the physical processes occurring in these systems. However, so far there exists only one unambiguous detection of linear polarization of x-radiation from a cosmic source, namely the orbiting solar observatory (OSO−8) measurement of 19-percent linear polarization from the Crab nebula. This one detection did provide strong confirmation that the x-ray emission process in this source was synchrotron radiation. The lack of additional positive detections is due to the inherent inefficiency of the polarimeters flown aboard OSO−8 and Ariel V in the mid 1970's, and the absence of flight opportunities since then. The stellar x-ray polarimeter (SXRP) experiment,[2] with the participation of the MSFC x-ray astronomy group in an international consortium led by Columbia University, will increase the number of objects observed with meaningful sensitivity to at least 100, including rotation and accretion powered x-ray pulsars, black hole candidates, other supernova remnants, and active galactic nuclei. X-ray **polarimetry** with the 1-percent sensitivity planned for SXRP requires precise modeling of systematic instrumental effects. A suite of detailed Monte Carlo simulations carried out by the MSFC x-ray astronomy group has provided important inputs into the design of the Bragg crystal and scattering polarimeter components of the SXRP experiment. As components for the flight experiment are assembled and tested, this suite of results is continuously consulted in order to assess the impact on performance and sensitivity of necessary engineering modifications to the original design. An example is the recent modification of the beryllium housing for the lithium scattering block. The MSFC x-ray astronomy group has also provided inputs into the design of the support structure for the Bragg crystal polarimeter and has coordinated environmental testing of an engineering model. The SXRP experiment, scheduled for launch in late 1994 on the Spectrum-X-Gamma mission, will make a dramatic impact on x-ray astronomy.

[1]Ramsey, B.D., Bower, C.R., Dietz, K.L., and Weisskopf, M.C., "The Background in a Balloon-Borne, Fluorescence-Gated Proportional Counter," *SPIE*, vol. 1344, 1990, pp. 82–90.

[2]Weisskopf, M.C., Elsner, R.F., Novick, R., Kaaret, P., and Silver, E., "Predicted Performance of the Lithium Scattering and Graphite Crystal Polarimeter for the Spectrum-X-Gamma Mission," *SPIE*, vol. 1343, 1990, pp. 457–468.

M.C. Weisskopf/ES65
(205) 544–7740
Sponsors: Office of Space Science and Applications
and Center Director's Discretionary Fund

RELATIVISTIC ELECTRODYNAMICS

An experiment at the European Center for Nuclear Studies (CERN) has produced new information concerning the production of **electron-positron pairs** along the track of an **ultrarelativistic heavy ion**. The experiment involved the exposure of **nuclear track emulsions** to beams of oxygen and sulfur nuclei at 60 and 200 billion electronvolts per nucleon, and subsequent analysis—both experimental and theoretical. The experiment, designated EMU04 at CERN, was led by scientists at MSFC in collaboration with members of The University of Alabama in Huntsville, the University of Tennessee, and a Japanese group under the sponsorship of the Institute for Cosmic Ray Research, University of Tokyo. MSFC performed theoretical calculations, microscope data measurements, and the synthesis of the data analysis.

The phenomenon under investigation is the production of an **electron positron** pair by an ion passing through a medium (an "absorber"). For a heavy ion at high energy (the lorentz factor, = $1/\sqrt{1-v^2/c^2} >> 1$), this energy loss channel becomes noticeable, and has a logarithmic slope that has no bound with energy. The interest in the direct coulomb pair phenomenon has several avenues. First, it is a rare **electrodynamic** channel in most experimental settings, and past measurements have produced conflicting results about its frequency. Second, it is the only **electrodynamic** phenomenon that might be used to measure primary particle energies above 10^{14} ev. Third, it is the process that provides the fundamental limit to beam intensity at colliding heavy ion accelerators now under construction, or being proposed.

The EMU04 consortium has made extensive microscope measurements of the linear frequency of $e^{\pm}$ pairs emanating from the oxygen and sulfur ion tracks in nuclear emulsion plates exposed at CERN. At the same time, calculations from theory have been made of the effect including linear frequency (mean free path), and the angular and energy distribution of the pairs. The EMU04 measurements of the mean free path are compared to the calculations in figure 34. The results indicate promise in the application of this phenomenon in heavy ion measurements at extreme energies, and provide results for the design of heavy ion accelerators.

Derrickson, J.H., et al., 21st International Cosmic Ray Conference, University of Adelaide, Adelaide, Australia ,1990, Section HE 3.1–16.

Moon, K.H., et al., 22nd International Cosmic Ray Conference, Trinity College, Dublin, Ireland, 1991, Abstract.

King, D.T., et al., 22nd International Cosmic Ray Conference, Trinity College, Dublin, Ireland, 1991, Abstract.

T.A. Parnell/ES62
(205) 544–7690

Sponsor: Office of Space Science and Applications

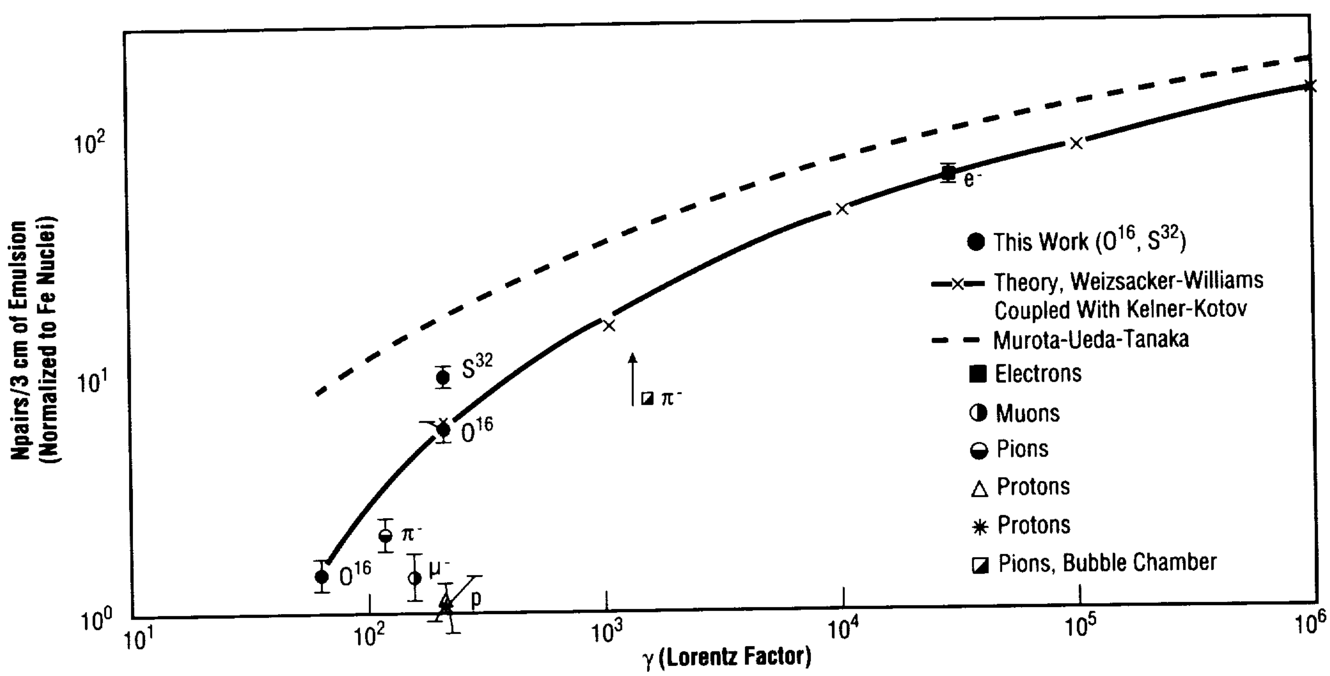

FIGURE 34.—Direct electron pair yield from accelerator measurements.

Infrared Astronomy and Space Research

In 1991, **infrared** (**IR**) astronomy at MSFC has focused on two research areas: the extensive observation of star-forming regions in other **galaxies** and of **protoplanetary disks** around other stars using the previously developed MSFC mid-**IR** camera, and the scientific and technical participation in the European Space Agency's (ESA's) **Infrared Space Observatory** (**ISO**) program.

The mid-**IR** camera, with 20 extremely sensitive bolometer detectors, has been operational for 6 yr. This camera has permitted a broad range of astronomical observations at major observatories, including the only extensive program to map regions of star formation in other **galaxies**. During the last year, the famous "starburst" galaxy, M82, was imaged at the NASA **IR** Telescope Facility (IRTF) on Mauna Kea, Hawaii. The **IR** radiation from starburst **galaxies** like M82 is emitted by dust grains that have been heated by extremely luminous populations of very young stars that are still buried deep within the clouds of gas and dust from which they formed. Observations of M82 have permitted the development of a picture of how the fantastic starburst probably started.

In late 1990, because of its outstanding sensitivity, the MSFC mid-**IR** camera made the first detection, also at the IRTF, of the "silicate feature" from a protoplanetary disk. This broad spectral feature in the mid-**IR** is a signature of silicate dust grains, and is an important diagnostic of particle sizes and evolutionary histories. The discovery of this feature from the disk around the star Beta Pictoris opens the way to a better understanding of the evolution of a disk that may be in the process of forming planets.

In parallel with the **IR** observational and instrumental programs, the MSFC **IR** astronomy program has continued to contribute to the development of the **ISO** spectrophotometer (ISOPHOT), an **IR** spectrophotometer that will be one of four **IR** instruments to be flown aboard ESA's **ISO** scheduled for launch in 1993. **ISO** will be the next major **IR** space experiment, and will be available to all American astronomers for guest observations.

Telesco, C.M., Campins, H., Joy, M., Dietz, K., and Decher, R., "Infrared Mapping of M82: A Starburst in an Edge-On Barred Galaxy," Astrophys. J., vol. 369, 1991, p. 135.

Telesco, C.M., and Knacke, R.F., "Detection of Silicates in the Beta Pictoris Disk," Astrophys. J., vol. 372, 1991, p. L29.

C.M. Telesco/ES63
(205) 544–7723
Sponsor: Office of Space Science and Applications

Superconducting Magnetic Suspension Systems and Bearings

The advantages of superconducting magnetic suspensions and bearings over their mechanical counterparts were described in the 1990 Research and Technology Report. Studies of suspensions of small masses of **high-temperature superconducting** materials were reported at that time along with studies of free-air suspensions of 0.1–kg magnetic rotors using a liquid-helium cryostat system. At the time of those studies, the best reported load-bearing capabilities had been observed for liquid-helium-cooled low-temperature superconducting materials and were approximately4 lb/in^2. A number of researchers were concerned that **high-temperature superconductors**, which had only recently shown sufficient **flux pinning** to have applications, could not match this 4–lb/in^2 load limit. Fortunately, recent **high-temperature superconducting** materials have not only met the previous record, but have exceeded it. The best reported load-bearing capabilities are now several times that of the previous report, and reports of **magnetic measurements** on newer materials suggest that over 50 lb/in^2 may be forthcoming. Such rapid advances in load-bearing capability indicate that many practical applications will soon follow.

At MSFC, it has been demonstrated that sizeable rotors at room temperature can be suspended by the compound $YBa_2Cu_3O_x$ at 77 K. These rotors can be spun to high speed and exhibit low drag if the flux distribution has the correct symmetry, or they exhibit multistable positions similar to those of stepper motors if alternating magnetic poles are used. By varying the level of flux trapping and adjusting component geometries, tradeoffs between suspension stiffness, load-bearing capabilities, and vibration isolation can be realized. For relatively large masses and low-suspension stiffness (low natural frequency), moderate to high frequencies are greatly attenuated by the suspension, as demonstrated by vibrating either the 77 K superconductor or the magnet and observing the relative vibrational amplitude of the other. Damping of any vibrations that are transmitted by the magnetic suspension can be accomplished by eddy current generation in properly designed normal metal surfaces, or by use of other loss mechanisms, such as flux vortex motion, etc. Again, however, nondamping of desired displacements, such as intentional rotations, requires careful design of the normal metal geometry and field distributions. To minimize eddy current drag associated with desired displacements, fields through the normal conductor should remain constant during these displacements. However, the field changes and damping that occur with undesired displacements should be large to accomplish the desired selective damping. A number of geometries have been investigated that provide the above characteristics.

Although many tasks could be accomplished with designs based on existing load bearing capabilities (especially in the "weightless" environment in orbit), development of materials with hundreds of pounds-per-square-inch load-bearing capability is desirable for bearings applied to engine cryopumps or similar hardware. To develop high load bearings, better understanding of material properties such as magnetic **flux pinning**, critical currents, fields, and temperatures, and their relation to the magnetization of the materials must be obtained. In addition to the more uniform microscopic pinning of individual flux quantum, many present materials exhibit rather large inhomogeneous properties associated with their magnetic properties. Several types of hardware have been developed to investigate these larger-scale inhomogeneities, including a scanning force measurement apparatus. Results for diamagnetic

FIGURE 35.— Diamagnetic repulsion on a submillimeter magnet scanned across a 1-in diameter yttrium-barium-copper-oxide (YBCO) superconductor at 77 K.

repulsion of a fractional millimeter magnet are shown in figure 35. (Measurements using steps of 0.5-mm spacing have been smoothed to give the magnetic inhomogeneity observed in the figure.) Corresponding flux trapping measurements using forces measured on fractional millimeter nickel spheres have been made, and rapid production of patterns by decoration with ferrimagnetic particles gives similar qualitative results. Scanning magnetometry results are also being developed to separate fields and their gradients, both of which contribute to the forces. Compositional, structural, electrical, and thermal properties are also measured for correlation to the magnetic properties. Measurements are being performed on both in-house and out-of-house prepared samples.

P.N. Peters/ES63
(205) 544-7728
Sponsors: Office of Aeronautics, Exploration and Technology and Center Director's Discretionary Fund

Solar Physics

The Sun has an 11–yr cycle of activity familiarly known as the sunspot cycle from the cyclical behavior of sunspots. Sunspots are large concentrations of magnetic fields whose frequency of occurrence waxes and wanes over an 11–yr period. Although knowledge of how this cycle is generated deep within the Sun, and how and why it varies from cycle to cycle, is limited, more awareness of how the Sun's variability affects the solar-terrestrial environment is developing. It has been shown that the total radiative output of the Sun varies slightly over the 11–yr cycle. However, the different spectral ranges, and especially the shorter wavelengths in the extreme ultraviolet (UV) vary much more dramatically; it is these radiations that directly affect the chemistry and thermodynamics of the upper atmosphere. The variations in atmospheric chemistry induced by these cyclical changes have profound implications for the problems of global warming and ozone layer maintenance. Increases in the UV emission also warm and expand the Earth's outer atmosphere, increasing the drag and shortening the orbital lifetime or time between reboosts of the large space observatories and the space station. To learn more about these variations, MSFC is studying the requirements for a space mission called SOURCE (Solar Ultraviolet Radiation and Correlative Emissions), which would accurately measure the UV flux over a 3–yr period and would identify proxies for these emissions that can be measured from the ground.

The solar magnetic fields are continually being pushed and jostled by the convective motions present in the Sun's outer layers. These motions can create instabilities in the structures of the outer atmosphere that can collapse, releasing energy in the form of high-energy radiation and particles. The latter propagate outward, reaching the orbit of Earth in times of tens of minutes to hours. The particles are prevented from penetrating to the Earth's surface, except at the poles, by the Earth's magnetic field. But outside this protection, for instance between the Earth and the Moon or Mars, or on the lunar surface, the flux of these particles can present a serious threat to the health and safety of astronauts.

Understanding solar activity of all forms is inexorably linked to the physics of the solar magnetic field, which forms the basis of solar research at MSFC. Through direct observation of the vector field, a capability developed at MSFC that is still quite unique, there has been considerable success in understanding how the energy stored in the magnetic field by the convective motions of the Sun's atmosphere is released. Currently, MSFC personnel are testing a data-based algorithm to locate, in real time, those magnetic regions that will give rise to large flares. Also, currently under development is an experimental vector magnetograph that will be used as a test-bed for advanced technologies including improved polarimeters and large focal plane arrays with high-speed readouts. Plans include development of a balloon-borne instrument based on these ideas as a precursor to a satellite mission.

Beyond the search for scientific knowledge, MSFC personnel are also studying methods to predict solar flares. A satisfactory method, which generates few false alarms, is essential if MSFC is to accept the President's challenge to undertake the manned exploration of the inner solar system. The development of an understanding of the underlying physics of energy storage and release in solar flares will form the focus of solar research at MSFC during the next decade.

EXPLOSIVE EVENTS IN THE QUIET SUN

New observations continue to reveal a diverse range of dynamic phenomena in the so-called "quiet" **Sun**, i.e., in the ordinary regions of the **Sun** away from the large concentrations of magnetic flux that form sunspots and active regions. The energy released in individual events is fairly inconsequential; however, taken all together, these may be the primary mechanism for heating the outer solar atmosphere and driving the solar wind. Microflares have been previously observed in the quiet **Sun** as impulsive increases of **ultraviolet** (**UV**) emission, characteristic of temperatures of approximately 10^5 K. The data from the **UV** spectrometer and polarimeter (UVSP), onboard the solar maximum mission, showed that the microflares occur on lines of inversion of the longitudinal **magnetic field** ("neutral lines") in small magnetic bipoles scattered throughout the quiet **Sun**. In this respect, they are like regular **flares**, which occur on neutral lines of larger flux concentrations in active regions. The magnetic flux elements in the quiet **Sun** are not uniformly distributed, but are grouped together into a magnetic network at the edges of supergranular convective cells, where they have been swept by the convective motions.

Other compact, short-lived events similar to the UV microflares, but having higher material velocities, have been observed with the high-resolution telescope and spectrograph (HRTS) flown on a series of rocket flights and on Spacelab 2. From a comparison of a portion of the Spacelab 2 data with a simultaneous magnetogram, the results reported here provide the first look at the character of the **magnetic field** at the sites of these explosive events; there are some surprising distinctions from the previously studied microflares. Figure 36 shows a

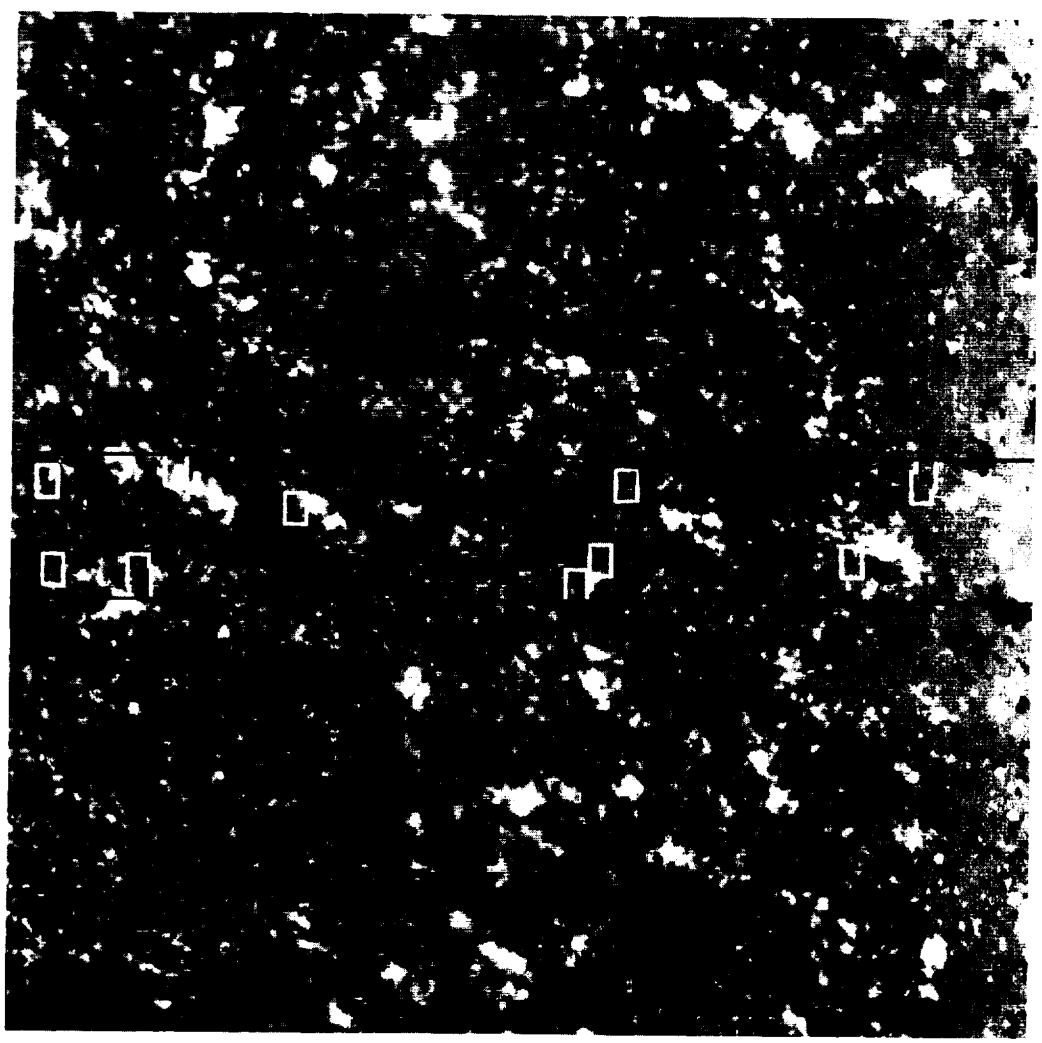

FIGURE 36.—Observed magnetic location of explosive events.

segment of the magnetogram taken at the same time as the Spacelab 2 data. Pixels (1×1–arc sec) representing **magnetic field** strengths less than 10 G make up the uniform gray background, while stronger fields are represented by lighter (positive field) and darker (negative field) shades. The HRTS field-of-view is restricted to the strip running across the middle of the figure. The sites of observed explosive events are enclosed by the white boxes.

The overlay shows that the events do occur in the magnetic network. This is significant because the magnetic loops that fill the outer solar atmosphere are rooted in the network, and the explosive events must be located here too if they are to heat the corona and generate the solar wind. However, unlike the microflares seen with the UVSP, the explosive events do not tend to lie on the more obvious magnetic bipoles in the network. A few occur at bipoles, but it is more common to find them at the edges of apparently unipolar flux patches or in weak field areas where there are no detectable flux concentrations at all. There must be systematic differences in the magnetic topology of the energy release sites in microflares and explosive events (as the difference in velocity signatures also suggests). Further work is required to determine what it is about these particular sites that leads to the explosive events. From the single magnetogram, the event sites appear fairly nondescript, in contradiction to the observed tendency of the more energetic solar phenomena to be associated with the stronger **magnetic fields**. If a time sequence of magnetograms can be obtained in conjunction with a future flight of the HRTS, it might show whether the event sites are in fact the last vestiges of larger flux concentrations as they subside beneath the solar surface, or perhaps the first manifestation of new regions as they emerge.

Porter, J.G., Moore, R.L., Reichmann, E.J., Engvold, O., and Harvey, K.L., "Microflares in the Solar Magnetic Network," *Astrophys. J.*, vol. 323, 1987, p. 380.

Porter, J.G., and Dere, K.P., "The Magnetic Network Location of Explosive Events Observed in the Solar Transition Region," *Astrophys. J.*, 370, 1991, p. 775.

J.G. Porter/ES52
(205) 544–7607
Sponsor: Office of Space Science and Applications

Solar Convection Zone Dynamics

The **solar convection** zone comprises the outermost 30 percent of the solar interior. Within this zone, the solar heat flux is carried by fluid motions. These motions are responsible for producing the Sun's magnetic field and associated activities such as sunspots, solar flares, and the 11–yr sunspot cycle. The ability to predict solar magnetic activity is handicapped by a lack of information concerning these motions and their interactions with the magnetic field elements. This research program is concerned with developing techniques for measuring the fluid motions themselves along with computer models of how these motions interact with the Sun's magnetic field.

A data analysis technique for accurately measuring the motions at the surface of the Sun was completed during this last year. The data consist of measurements of the fluid motions directed along the line-of-sight. Data are currently available from ground-based instruments at Mount Wilson Observatory and from the global oscillation network group (GONG) breadboard instrument in Tucson, AZ. The results of the analysis of data from these two instruments have revealed a broad spectrum of motions, including the Sun's rotation and differential rotation in which the equatorial regions rotate more rapidly than the higher latitude regions, a meridional circulation in which fluid at the surface flows very slowly from the equator toward the poles, and a cellular convective pattern with cell sizes ranging from more than 100,000 km (60,000 mi) down to the limits of the data resolution at about 6,000 km (3,600 mi). The observed spectrum of these motions is shown in figure 37.

A complete description of these fluid motions also requires a determination of the time evolution of the various flow components. The evolution of the convective pattern can be determined from observations taken over several days. The pattern moves and slowly changes. The motion of the pattern is determined using a technique

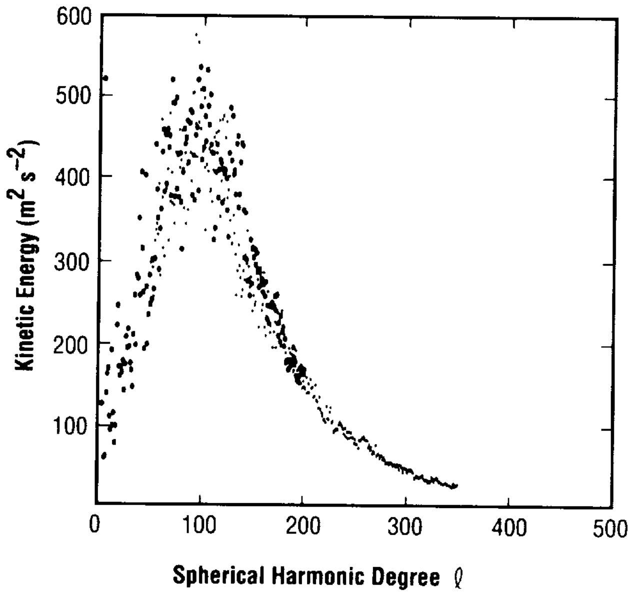

FIGURE 37.— Solar convection spectrum from the GONG breadboard instrument (large dots) and the Mount Wilson magneto-optical filter instrument (small dots).

in which the pattern is, at one time, shifted until maximum correlation is obtained with the pattern observed at a later time. The results of this analysis show that the convection cells move with the solar rotation and differential rotation. Cells near the equator rotate more rapidly than cells at higher latitudes. Comparison of the patterns at later times also provides a measure of the lifetimes of the cells. The most energetic cells, the "supergranules," have lifetimes of about 2 d. The evolution of the large-scale flows, i.e., the differential rotation and meridional circulation, can only be determined from observations taken over a much longer time period. Previous observations have indicated that there are variations in the solar rotation and differential rotation over the course of several years that is associated with the solar activity cycle.

Information on the structure of the flows below the surface of the Sun can be obtained using analysis techniques from helioseismology. In addition to the steady flows described above, there is a rich spectrum of oscillatory motions observed at the solar surface. These oscillations are due to sound waves that are produced by the convective motions and are trapped within the Sun. The characteristics of these oscillations provide information on the internal structure and fluid motions of the Sun. With the data and data analysis techniques currently available, the depth of the convection zone and the variations in the rotation and differential rotation with depth through the convection zone have been determined.

Information on the deeper layers below the convection zone would be available if the low-frequency oscillations could be observed. However, these oscillations are expected to be very slow and are difficult to separate from the convective motions themselves. In an effort to determine the chances of observing these oscillations, a simulation of the convective motions has been produced. The results of the analysis of the observed surface flows have been used as input for constructing a sequence of images representing an observation every 10 min for 20 d. This simulation will be used to determine how these convective motions influence the detection and measurement of the low-frequency oscillations. A comparison of the observed and simulated velocity fields is shown in figure 38.

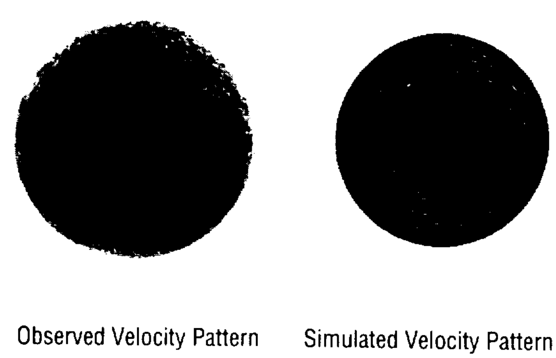

FIGURE 38.— Comparison of an observed velocity pattern (GONG breadboard instrument) and a simulated velocity pattern. (Flow toward the observer is in black; flow away from the observer is in white.)

The velocity fields that are constructed in this simulation are also being used to determine how magnetic fields are transported by these motions. Markers representing magnetic field elements are placed in the flow and their subsequent motions are followed. The results will be compared with observed magnetic field patterns to determine the veracity of the simulation and to look for missing flow field components. Previous simulations for the magnetic field evolution have not resolved the cellular motions and have used an unrealistic meridional circulation.

Additional analyses of the ground-based data will continue in anticipation of future data from the NASA/European Space Agency (ESA) solar and heliospheric observatory (SOHO) mission. The solar oscillations imager currently under development for this mission will provide a continuous stream of velocity images with high spatial resolution over the course of several years.

Hathaway, D.H., "Spherical Harmonic Analysis of Steady Photospheric Flows II," *Solar Physics*, in press, 1991.

Hathaway, D.H., Rhodes, E.J., Cacciani, A., and Korzennik, S., "The Supergranulation Spectrum," Proc. Conference on Challenges to Theories of the Structure of Moderate Mass Stars, in press, 1991.

Hathaway, D.H., Rhodes, E.J., Korzennik, S., and Cacciani, A., "Rotation Rate of the Supergranulation Pattern," *Bull. Amer. Astron. Soc.*, vol. 23 ,1991, p. 1051.

D.H. Hathaway/ES52
(205) 544–7610
Sponsor: Office of Space Science and Applications

Coronal and Interplanetary Physics

The Sun's extended outer atmosphere, the corona, is so hot that it radiates predominantly in x rays. The persistent heating that must be present to keep the corona from cooling off is a longstanding premier problem of solar physics. The Sun's coronal luminosity is of the order 10**28 erg/s. X-ray emission of this order or greater, and having the spectral and temporal character of that from the Sun, has been observed to be normal for all stars that, like the Sun, have convective envelopes. From this evidence, it is now accepted that a hot corona similar to the solar corona is a common feature of these stars, and the problem of **coronal heating** has become a focus of **solar-stellar astrophysics**.

The solar corona is permeated by a magnetic field that is rooted in, generated by, and continually changed by the convective envelope. Over much of the surface of the Sun, this magnetic field is in the form of closed loops that confine the coronal plasma. But, in some areas, the magnetic field is forced open by the pressure of the hot coronal plasma. From these open-field regions, the coronal plasma empties out to fill interplanetary space with the outflowing, expanding solar wind. These open-field, relatively empty places in the corona are seen as dark **coronal holes** in x-ray images. However, the observed solar wind flow and much more massive, but cooler, winds observed from giant stars with convective envelopes cannot be explained by the coronal gas pressure alone. An additional driver is needed to account for the observed speeds and mass fluxes of the **solar** and stellar winds. This is another major problem of **solar-stellar astrophysics**.

During the past year, a group of solar astrophysicists from MSFC, The University of Alabama in Huntsville, Applied Research, Inc., in Huntsville, and the University of Chicago have made progress on both the **coronal heating** problem and the solar/stellar wind problem by considering the reflection of **Alfvén waves** in a nonuniform medium, such as in a coronal hole.

First, a new analytical method was devised for determining the critical wave period for reflection of **Alfvén waves** in any smoothly nonuniform medium that is capable of bearing pure **Alfvén waves**. This method was then applied to the model coronal hole (fig. 39). For temperature, density, strength, and fanning out of the magnetic field (all representative of real **coronal holes**), it was found that the value of the critical period is about 5 min. **Alfvén waves** emitted up into the coronal hole from below are reflected back by the coronal hole if their periods are longer than 5 min, but pass on through to the solar wind if their periods are shorter than 5 min. The power spectrum of **Alfvén waves** is emitted up into **coronal holes** from the convection and magnetic activity (such as the explosive microflares in the magnetic network) beneath **coronal holes** peaks around 5 min. This coincidence of the peak of the **Alfvén wave** power spectrum with the critical period for reflection suggests that the temperature of **coronal holes** is regulated by heating the reflected **Alfvén waves** (those with periods longer than 5 min) and that the extra driving of the solar wind is provided by the transmitted **Alfvén waves** (those with periods shorter than 5 min). In addition, it was also realized that the **Alfven-wave** reflection process that heats the solar corona in **coronal holes** may provide the extra push needed to produce the cool massive winds observed from late-type giant and supergiant stars.

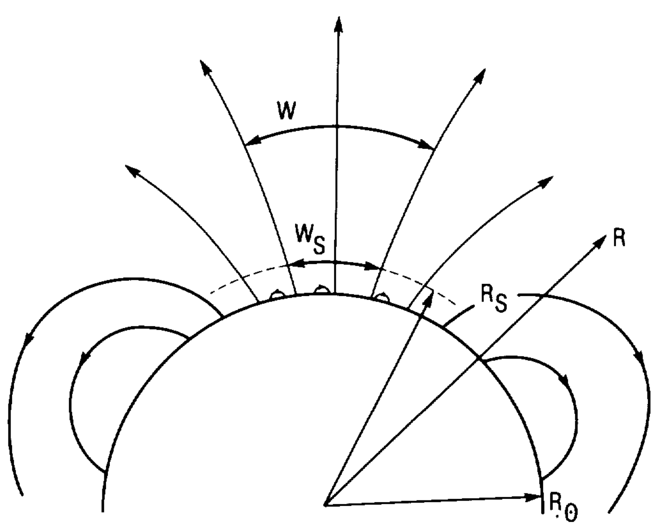

FIGURE 39.— Sketch of the Sun's magnetic field in and around a coronal hole.

Musielak, Z.E., Fontenla, J.M., and Moore, R.L., "Klein-Gordon Equation and Reflection of Alfvén Waves in Nonuniform Media," *Physics of Fluids B*, in press, 1991.

Moore, R.L., Musielak, Z.E., Suess, S.T., and An, C.H., "Alfvén Wave Trapping, Network Microflaring, and Heating in Solar Coronal Holes," *Astrophys. J.*, in press, 1991.

Rosner, R., An, C.H., Musielak, Z.E., Moore, R.L., and Suess, S.T., "Magnetic Confinement, Alfvén Wave Reflection, and the Origins of X-Ray and Mass Loss 'Dividing Lines' for Late-Type Giants and Supergiants," *Astrophys. J. Lett.*, vol. 372, 1991, p. L91.

S.T. Suess/ES52
(205) 544-7611
Sponsor: Office of Space Science and Applications

Magnetospheric Physics

Magnetospheric physics is the application of fluid dynamics and plasma kinetic theory to understand and predict the flow of matter, momentum, and energy between the Sun and the Earth. The magnetosphere is the region of space, permeated by the geomagnetic field, that makes the solar-terrestrial connection between the atmospheres of the Sun and Earth. The currents, which distort the geomagnetic field and mechanically couple the regions, are carried through geospace by the ionized gas of charged particles (plasma) that are present. As understanding of this system improves, comprehension and anticipation of the interactions between solar events, interplanetary conditions, and terrestrial responses are greater. The solar-terrestrial environment also serves as a laboratory of opportunity for in situ observations of processes that are of astrophysical importance in such situations as planetary and cometary magnetospheres and stellar atmospheres. Studies of such processes have been performed both remotely and locally. Because of these studies, an improved ability to interpret the electromagnetic radiations received from distance astrophysical plasmas has been gained.

In 1990–91 and subsequent years, the research emphasis of the Magnetospheric Physics Branch at MSFC is being broadened to a more global perspective by the initiation of a study of the inner magnetospheric imager mission. This is a new Office of Space Science and Applications (OSSA) Space Physics Division initiative that will open a new window on the plasma universe by obtaining time series of global images of the dynamic magnetosphere. The branch continues its excellence in the observation of low energy or core plasma, which originates in the ionosphere and has been found to supply plasma to the entire magnetosphere. Highlights of branch activities during the previous year include:

- *Formation of a science study team and mission study team for the OSSA/Space Physics Division inner magnetosphere imager mission*
- *A third, highly successful, sounding rocket flight of the superthermal ion composition spectrometer (STICS) in February 1991*
- *Fabrication and testing of a new ultraminiaturized thermal electron capped hemisphere spectrometer (TECHS) for a Chemical Release and Radiation Effects Study (CRRES) program sounding rocket flight in summer 1991*
- *Significant progress in the fabrication and test of the thermal ion dynamics experiment/plasma source investigation (TIDE/PSI) for the international solar terrestrial physics program (ISTP) POLAR spacecraft*
- *Initiation of the development phase for the cometary retarding ion mass spectrometer (CRIMS) for the comet rendezvous asteroid flyby (CRAF) mission*
- *Completion of post-integration test and final calibration of the research on orbital plasma electrodynamics (ROPE) investigation for the tethered satellite system (TSS)*
- *Discovery that magnetotail dynamics during auroral substorms automatically generate the high-energy particle populations of the inner magnetosphere via the induced electric fields produced*
- *Determination that the outflow of ionospheric plasma in the dayside auroral zone is strongly modulated by interplanetary conditions, especially the direction of the interplanetary magnetic field*
- *Development of an improved magnetospheric plasma specification model, that incorporates a larger base of data sets and contains a clear dusk bulge feature*
- *Development of enhanced capability for raytracing of low-frequency plasma waves within the observed distribution of plasma in the magnetosphere*
- *Achievement of a fully automated laboratory control and data acquisition system, using Labview software running on Apple Macintosh computers, with IEEE 488 interfaces to laboratory equipment*
- *Achievement of successful three-dimensional visualization of multidimensional data sets obtained from the STICS instrument and from TIDE simulation data.*

Modeling the Inner Magnetosphere

By density, the bulk of the plasma in the inner **magnetosphere** is comprised of ions with temperatures below approximately 100 eV. For the last 30 yr, these bulk or core plasmas have been observed from the ground using lightning-produced, whistler-mode waves and from space on orbiting platforms. There have been many event studies of the characteristics and processes involving plasma in the inner **magnetosphere**. As a result, a detailed understanding has developed of the microscopic processes important in many regions. More recent research efforts have focused on establishing the relationships between the various regions and processes in the **magnetosphere**.

Some point-wise, in situ observations of the **magnetosphere** have been accomplished with sufficient completeness to allow independent statistical pictures to be developed for various regions of near-Earth space. Previous work at MSFC produced one such picture. In that study, measurements from the retarding ion mass spectrometer onboard the Dynamics Explorer 1 spacecraft were used to produce an analytical description of plasmaspheric density as a function of the McIlwain L-shell parameter and local time. Other researchers have produced similar descriptions of density and temperature at geosynchronous equatorial orbit, in the polar cap, and at ionospheric altitudes.

Each of these regional, **empirical** models of the **magnetosphere** was produced independently. Most models lack sufficient measurements to be valid for wide ranges of geophysical, seasonal, or solar variations. Within certain constraints, however, it appears that some of these regional models can be combined to obtain a more global picture of the magnetospheric system. The process can be likened to the three blind men combining their independent impressions to form a more complete picture of the elephant. Naturally, the **magnetosphere** is a great deal more complex than the external characteristics of an elephant. The **magnetosphere** is strongly influenced by solar and solar-wind conditions and continuously fed by ionospheric plasmas. The **magnetosphere** is a highly dynamic system for which in situ measurements are inherently time-aliased.

In spite of these difficulties, interesting results are appearing as a direct result of joining independent **empirical** models of differing magnetospheric regions. One such preliminary result is a new picture of the equatorial shape of the plasmaspheric bulge. This new picture results from combining the analytical formalism and inner plasmasphere of Gallagher, et al. (1988), the geosynchronous description of electron density by Higel and Wu (1984), and a new work by Carpenter and Anderson (1991) that provides equatorial profiles of electron density as a function of geophysical and solar conditions. Figure 40 shows contours of equal density in the Earth's equatorial plane for four different values of the geophysical index Kp. Each panel depicts a distribution of plasma density, which includes the evening bulge of the plasmasphere. The plasmasphere is seen to have a great extent for low values of Kp, with the bulge located in the late evening. As Kp rises, the bulge region rotates Sunward and the plasmasphere shrinks.

Theoretical descriptions of plasma convection have suggested that the plasmaspheric bulge takes on a teardrop shape, oriented toward 18 h magnetic local time. Statistical observations have shown a much more rounded profile for the bulge, although still extended at evening local times. The new result is also based on statistical studies; however, the conditions in these studies were chosen to minimize blurring as a result of the ever-changing geophysical conditions. The resulting picture is strikingly like that given by theory.

Efforts to amalgamate independent regional descriptions of the **magnetosphere** will continue along with the growing emphasis toward developing a global understanding of the Earth's magnetospheric system. This **modeling** will be extended to higher latitudes and to plasma composition. The resulting composite **empirical** model will find wide-ranging uses, such as in the study of wave propagation and global magnetohydrodynamics (MHD) and in planning for future missions. One such proposed mission is the inner **magnetosphere** imager, which offers the first opportunity to directly view the Earth's constantly changing **magnetosphere** as a whole.

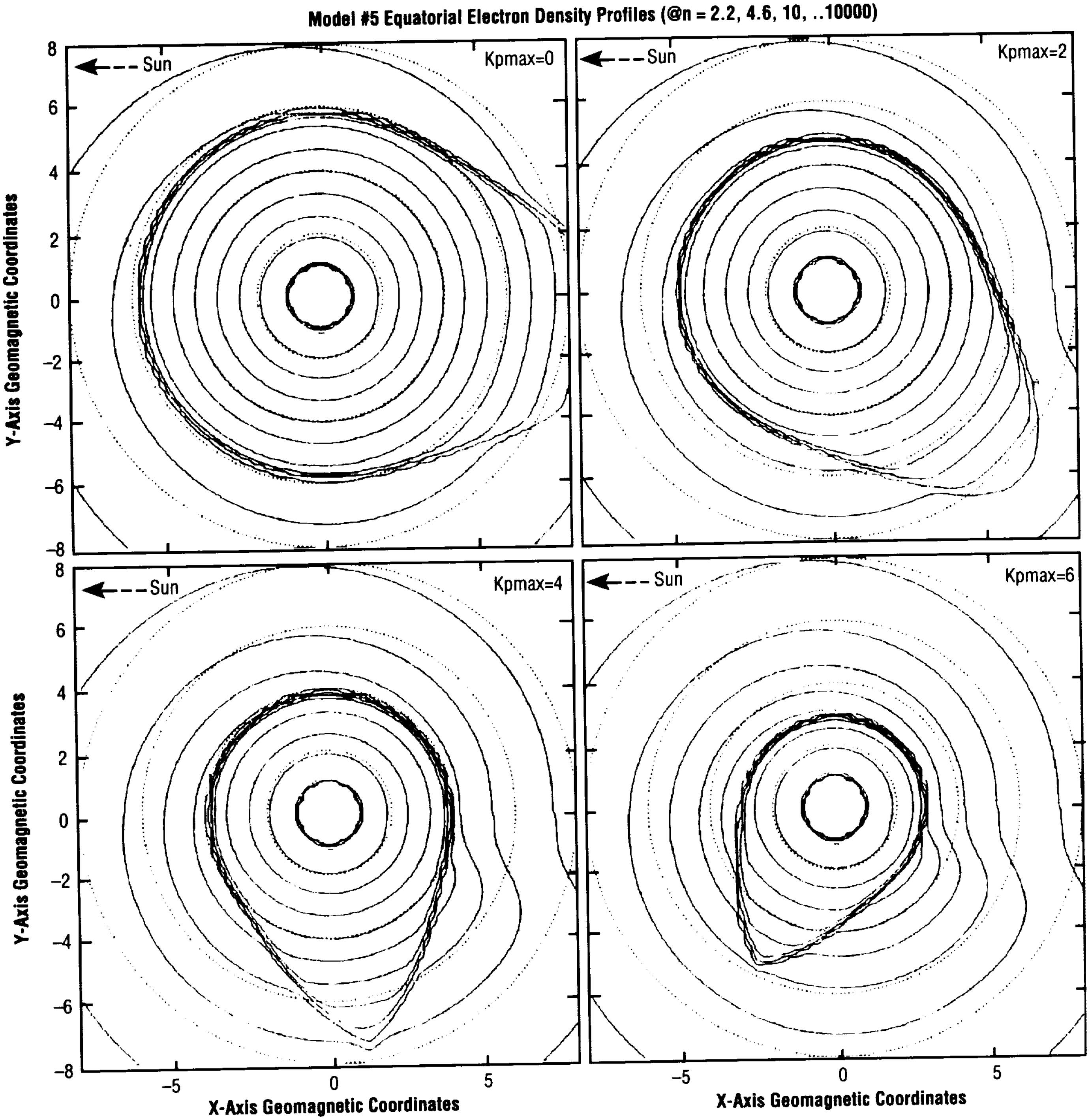

FIGURE 40.—Equatorial electron density profiles (n=2.2, 4.6, 10,...10,000).

Higel, Bernard, and Lei, Wu, "Electron Density and Plasmapause Characteristics at 6.6 Re:A Statistical Study of GEOS 2 Relaxation Sounder Data," *J. Geophys. Res.*, vol. 89, 1984, pp. 1583–1601.

Gallagher, D.L., Craven, P.D., and Comfort, R.H., "An Empirical Model of the Earth's Plasmasphere," *Adv. Space Res.*, vol. 8, 1988, pp. 15–24.

Carpenter, D.L., and Anderson, R.R., "An ISEE/Whistler Model of Equatorial Electron Density in the Magnetosphere," *J. Geophys. Res.*, in press, 1991.

D.L. Gallagher/ES53
(205) 544-7587

Sponsor: Office of Space Science and Applications

Injection of Auroral Particles by Magnetotail Collapse

The auroral **substorm** is the phenomenon that makes the magnetosphere widely visible to the naked eye in the populated areas of Earth. While **auroras** occur essentially continuously in a ring haloing each geomagnetic pole, they are greatly enhanced in brightness and equatorward extent during the convulsions of the geomagnetic field known as **substorms**, particularly on the nightside of the Earth. This brightening and broadening of the global **aurora** is produced by the transient acceleration of charged particles already present within the magnetosphere, which subsequently enter the upper atmosphere and emit auroral light by colliding with and creating excited atomic states in upper atmospheric atoms of various species.

A less visible effect of auroral **substorms** when they occur in rapid succession is the formation of an extremely hot **plasma** region encircling the Earth at a distance of roughly 3 to 6 Earth radii. This **plasma** carries a large current amounting to millions of amperes encircling the Earth in the volume of space known as the ring current. This current weakens the geomagnetic field at the Earth's surface to an easily measured degree, the characteristic signature of a full-fledged geomagnetic storm.

Recently, significant progress has been made in understanding the nature of the acceleration processes responsible for creating the bright **substorm auroras** and the ring current. The magnetic field of the magnetospheric tail, normally stretched quite noticeably downstream of the Earth by the solar wind flow, undergoes a cycle of increased stretch followed by a collapse back to its unstretched state, often referred to as "dipolarization" events. The period of increased stretch is known as the growth phase, in recognition that energy is being stored in the magnetic field by virtue of its being stretched out. The period of collapse is known as the **substorm** expansion phase, and is accompanied by the auroral brightening and broadening, especially in the nightside.

The essential new insight that has been applied to understanding **substorm** particle acceleration is that significant transient electric fields are induced by the rapid changes in the magnetic field accompanying geotail collapse. When the magnetic field is steady and unchanging, the electric field in a **plasma** is a measure of the rate of **plasma** convection across field lines. When the field lines move around due to a changing magnetic field geometry, the induced electric field is just that required to move the **plasma** with the magnetic field lines. Observations show that the magnitude of the convection field is dwarfed by the induction field produced by "dipolarization" events. This indicates a capability that is much enhanced during **substorms** to accelerate charged particles.

In order to evaluate this capability, a model has been developed that utilizes an empirical description of the magnetotail at varying degrees of "stretch." The field is assumed to relax smoothly from a more stretched to a less stretched state in a period of 1 to 2 min, which is derived from observations of the induced electric field. The induced motion of the field lines is computed and translated into an induced electric field. Individual charged particles, representative of an initial state prior to a **substorm**, are introduced at appropriate locations in the tail and released just prior to beginning the collapse process. Their motions in the combined magnetic and electric fields are then computed through the collapse period and beyond.

The near-Earth magnetotail, where **substorm** acceleration directly feeds the ring current, is thought to be directly supplied with **plasma** from the Earth's own ionosphere. This **plasma**, rich in heavy O^+ ions, flows out of the ionosphere mainly from the auroral zones and is transported to the near-Earth tail. These ions arrive in the tail with energies near 100 eV, but are accelerated as they pass through the equatorial plane of the tail by steady-state electric fields reaching energies of 1 to 10 keV, as they stream back toward the Earth, following magnetic field lines. These ions may be recognized in the upper panel of figure 41. In this figure, the initial particle energies and positions are representative of the ions delivered to the magnetotail from the dayside auroral oval by anti-Sunward flow over the polar caps of the Earth. The formation of an Earthward moving "front" of energetic particles is clearly depicted in this time sequence.

The most important result of this modeling is the dramatic acceleration of the preexisting ions produced in regions where the induced electric field changes rapidly, compared with the normal gyration of the ions about the local magnetic field. In the case of oxygen ions originating in the dayside auroral zone and supplying the near-Earth tail with energies of 1 to 10 keV, accelerations up to hundreds of kiloelectronvolts occur (fig. 41). This process leads to an extremely energetic population at energies characteristic of the ring current, and propagating Earthward in the local evening sector, as required to create a ring current.

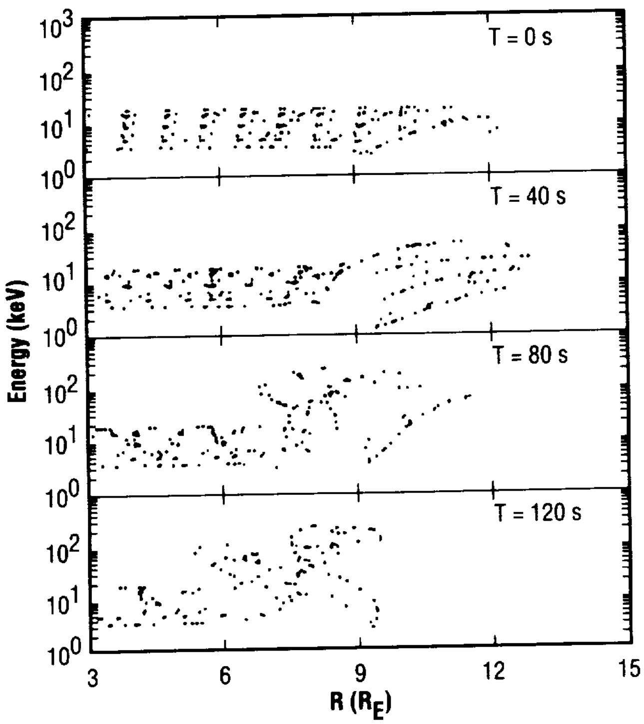

FIGURE 41.— Plots of particle energy versus radial distance down the magnetotail that show the evolution of a set of O^+ ions during a substorm "dipolarization" event.

Delcourt, D.C., Sauvaud, J.A., and Moore, T.E., "Cleft O^+ Contribution to the Ring Current," *J. Geophys. Res.*, in press, 1990, p. 95.

Moore, T.E., and Delcourt, D.C., "Merging and the Single Particle," *Modeling Magnetospheric Plasma Processes*, eds. G.R. Wilson and M.O. Chandler, in press, 1991.

Delcourt, D.C., Pedersen, A., and Sauvaud, J.A., "Gyro-Phase Effects Near the Storm-Time Boundary of Energetic Plasma," Geophys. Res. Lett., vol. 18, in press, 1991.

T.E. Moore/ES53
(205) 544-7633
Sponsor: Office of Space Science and Applications/ Space Physics Division

Ionospheric Heating by an Artificial Ion Beam

Ionospheric **ion heating** is a subject of intense interest to researchers in the fields of ionospheric and magnetospheric **plasma physics**. It has been demonstrated over recent years that the **ionosphere** provides a substantial fraction of the magnetospheric ion plasma through the escape of ionospheric ions to high altitudes.[1] This process occurs in spite of the fact that the bulk of the ionospheric plasma (oxygen ions (O^+) and nitrous oxide ions (NO^+)) is so heavy as to be gravitationally bound to low altitudes at ionospheric temperatures. Therefore, some energization mechanism must be operative on these particles in order to provide escape energy. This subject is, and will continue to be, an active area of research in space **plasma physics**. One of the approaches taken to this problem has been to actively perturb the **ionosphere** in a controlled manner and to observe the effect that this perturbation has on the ionospheric plasma. Such experiments can be carried out effectively and reasonably inexpensively using **sounding rocket** platforms from which the perturbations are initiated and their effects are observed.

A series of argon release for controlled studies (ARCS) experiments has represented an effort to perturb the ionospheric plasma by injecting an argon ion (Ar^+) beam from a rocket payload and using instrumentation on that (or a nearby) payload to measure the response in the fields and charged particle distributions of the ionospheric plasma. The first three ARCS experiments have shown that injection of Ar^+ beams into the ionospheric plasma results in the production of a spectrum of plasma waves, the acceleration of ambient ions in the direction transverse to the geomagnetic field, and, possibly, the acceleration of ambient electrons parallel to the geomagnetic field through an anomalous resistivity process.[2] Evidence was found during the ARCS–3 experiment that the gun payload charged to 100 V (one half the beam energy per charge) during beam injections perpendicular to the geomagnetic field and that no significant payload charging occurred during parallel beam injections.[3]

The fourth in the series of ARCS flights was launched from Poker Flat Research Range, Alaska, on February 23, 1990. This experiment featured a subpayload that housed the Ar^+ beam accelerator and a limited complement of particle and wave diagnostics. The main payload carried a more complete set of plasma diagnostics, including imaging electrostatic analyzers for electrons and ions, plasma wave antennae and receivers, direct current (dc) electric and magnetic field sensors, and the superthermal ion composition spectrometer (STICS), which was developed and managed at MSFC. For this experiment, STICS measured the distribution of ions as a function of mass/charge, energy, and motional direction, yielding a full three-dimensional velocity distribution of six ion species in the energy range 0.5 to 200 eV every 12 s. The experiment subpayload was separated from the main payload at 149 s after launch at an altitude of 276 km (172 mi), and the two payloads drifted apart at a relative velocity along the geomagnetic field line of 1 m/s (3.3 ft/s). The experiment geometry is illustrated in figure 42. The Ar^+ ion accelerator commenced operation 14 s after payload separation at 309–km (192–mi) altitude. The 100–mA beam was fired into a cone centered on a direction perpendicular to the geomagnetic field with a 12–s on, 10–s off duty cycle, with alternate beam events characterized by 100– and 200–V beam energy.

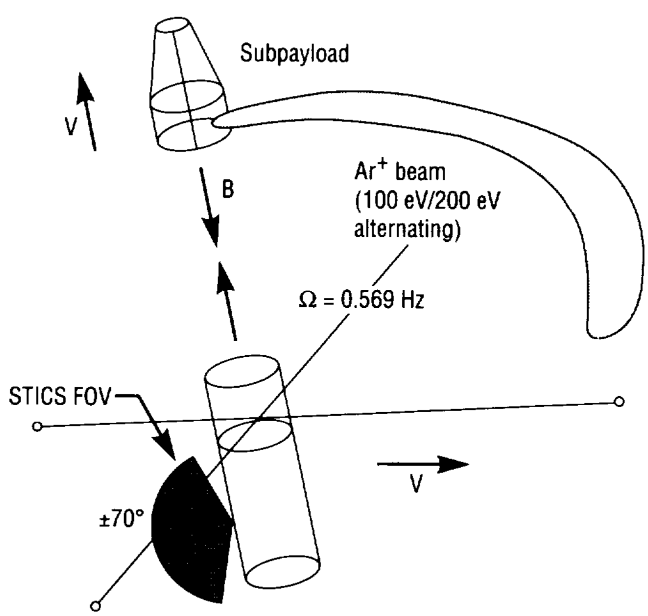

FIGURE 42.— ARCS–4/STICS deployment.

As in past flights, ions associated with beam operations were observed at the main payload through much of the flight, up to payload separation distances of near 1 km (0.6 mi). On ARCS–4, these ions were unambiguously identified using the STICS instrument as Ar^+ ions. STICS observations of the hydrogen ions (H^+) and O^+ ion distributions at the main payload during the experiment show distinct differences in the shapes of the distributions during beam-on periods, as compared with those during beam-off periods, indicating the action of **ion heating** processes associated with beam operations.

Strong heating of O^+ and moderate heating of H^+ were observed at the main payload when it was still close to the beam-emitting subpayload. This is illustrated in figure 43, which shows an H^+ energy distribution during gun-on, during a 100–eV beam event (squares), and during gun-off (circles) periods. Figure 43 also shows similar data for O^+. The heating of the ambient ion plasma is indicated by the flattening of the high-energy tails in the ion distributions.

When the payloads were further separated, heating of ambient plasma due to the Ar^+ beam was observed only in the H^+ component. In the case of preferential heating of the lighter H^+ ions far from the beam source, it can be argued that these ions with larger thermal velocity than the heavy O^+ ions are resonant with plasma waves that are themselves resonantly driven by the 200–eV Ar^+ beam. In all cases where **ion heating** was observed to take place during the ARCS–4 experiment, the heating was

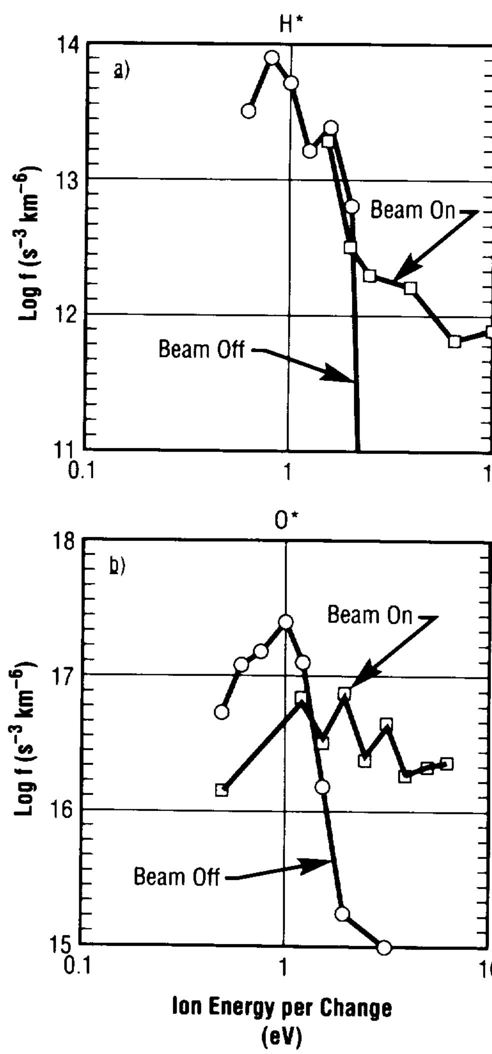

FIGURE 43.— Ion energy distributions measured on ARCS–4 main payload.

preferentially in the direction transverse to the geomagnetic field. This preferential transverse heating of ions has been observed previously in ARCS experiments and is commonly observed in nature. Such transverse heating is thought to be a strong contributor to the ejection of terrestrial ions from the **ionosphere**.

[1]Chappell, C.R., Moore, T.E., and Waite, J.H., Jr., "The Ionosphere as a Fully Adequate Source of Plasma for the Earth's Magnetosphere," *J. Geophys. Res.*, vol. 92, 1987, p. 5896.

[2]Moore, T.E., Arnoldy, R.L., Kaufmann, R.L., Cahill, L.J., Jr., Kintner, P.M., and Walker, D.N., "Anomalous Auroral Electron Distributions Due to an Artificial Ion Beam in the Ionosphere," *J. Geophys. Res.*, vol. 87, 1982, p. 7569.

[3]Pollock, C.J., Arnoldy, R.L., Erlandson, R.E., and Cahill, L.J., "Observations of the Plasma Environment During an Active Ion Beam," *J. Geophys. Res.*, vol. 93, 1988, pp. 11, 473.

C.J. Pollock/ES53
(205) 544-7638
Sponsor: Office of Space Science and Applications

The Chemical Release Mission of the Combined Release and Radiation Effects Satellite

The regions of space surrounding the Earth where matter exists in an ionized state is known as Earthspace. The ionized state has been called the "fourth state of matter," and it is unique because particles can interact through long-range electromagnetic forces, and can carry electric currents. The lower-altitude region is called the **ionosphere**, and the higher-altitude region is the magnetosphere. The **ionosphere** is the sink for energy in the magnetosphere and becomes highly structured and variable during periods of intense geomagnetic activity. The structuring in the **ionosphere** affects high-frequency radio communications and causes distortions of satellite-Earth signals; the large currents in the **ionosphere** actually couple into large-scale systems such as power grids and pipelines with destructive effects.

Active experiments involve injections of energy and matter in the forms of charged particle beams, electromagnetic waves, and chemicals. The experiments are designed to produce a controlled and known input to the space environment, and the effects are measured with arrays of diagnostic instruments.

The **combined release and radiation effects satellite (CRRES)** was a dual-mission spacecraft with a NASA mission to perform active chemical release experiments. Chemical release experiments may be broadly grouped into categories of tracer, modification, and simulation experiments. Tracer experiments inject relatively small amounts of material that can be detected by remote-sensing means, and illuminate natural dynamic processes in the environment. Larger amounts of material can be used to modify or perturb the environment in a controlled manner, and the "system response" to this perturbation is studied. A simulation experiment is designed to mimic a natural process. For example, in the active magnetospheric particle tracer experiment (AMPTE), the spacecraft released a cloud of barium vapor in the solar wind, simulating a comet.[1]

The first **CRRES** campaign, conducted in September of 1990, was designed to investigate the critical velocity mechanism. This theory, first proposed by Alfven[2] states that, under certain conditions, a neutral gas moving at high speed through a magnetized plasma will, through the action of collective plasma processes, become ionized to an extent greater than that predicted by the two-particle collision and charge-exchange cross sections. Figure 44 shows schematically how this experiment was conducted. The release had to be performed in darkness because the presence of photoionization would have invalidated the results. (The release point was 10 to 20 km below the sunlight terminator in darkness.) Yet, in order to see any ions created, they had to move upward along magnetic field lines into sunlight where they could be identified by their characteristic resonance emissions. The experiment needed to be performed near local dusk. The magnetic field geometry, coupled with the orbit characteristics placing the perigee near the dusk terminator at southerly latitudes, required that these experiments be conducted over the South Pacific. Two aircraft based in American Samoa were used to make the observations.

The high-altitude release campaign in January and February of 1991 featured a series of releases to investigate the reaction of the magnetosphere to injections of artificial ion clouds. The conjugate points, or the points where the magnetic field line from **CRRES** traced to the upper atmosphere level of 100 km, were required to be over northeastern Canada in the vicinity of Hudson Bay, so that the region would be accessible to aircraft optical observatories based in northern Michigan.

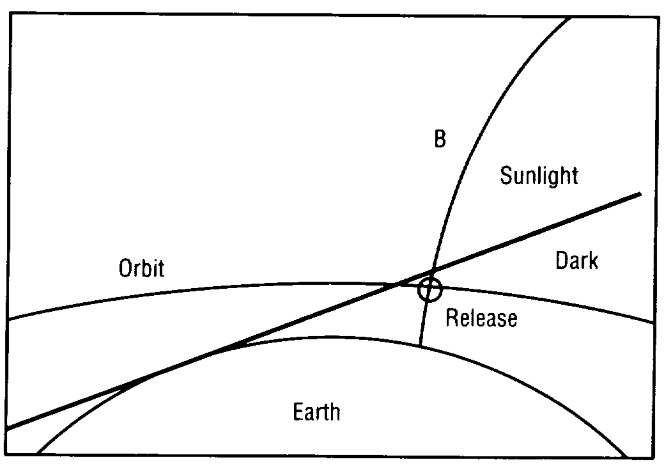

FIGURE 44. — The geometry of the critical velocity release.

At the time of this writing, the final campaign from the **CRRES** satellite will be conducted in the Caribbean in July and August of 1991, with observatories both near the releases and at the opposite end of the magnetic field line in South America. These experiments have several objectives, but may be divided into two primary areas: (1) the study of the momentum and energy coupling between fast-moving ion clouds and the ambient ionosphere, and (2) the tracing of the electric and magnetic field structure of the midlatitude magnetosphere with the injected tracer barium ions.

The critical velocity experiments showed that ionization of all three elements, barium, calcium, and strontium, did occur with a mixture of ionization mechanisms.[3] The critical velocity process operated, but only for the first few seconds following the neutral cloud injection. This is consistent with a recent theoretical simulation of the process which showed that the conditions for operation of the process were quite restrictive in terms of the ratio of the neutral cloud density to the ambient ion density. The remainder of the ionization observed could be accounted for by charge exchange and collisional ionization.

The series of small barium releases at varying altitudes showed vastly different behavior. In the lowest-altitude release at 6,000 km, the ion cloud velocity was quickly braked by close coupling to the ionosphere. The release at a 12,000–km altitude showed a time constant for braking consistent with the velocity of hydromagnetic waves (about 500 km/s) traveling from the release point to the ionosphere. These releases have yielded valuable data on the coupling between the ionosphere and the magnetosphere.

The large high-altitude barium releases produced significant modifications to the ambient particle and field environment. The magnetic field measured at the satellite was reduced to zero, and significant changes in the distributions of high-energy electrons were observed. Observations of aurora from the aircraft observatories suggest that intensifications of activity occurred following the releases, but the data are still under study to determine if an exact cause-and-effect relationship can be ascribed.

[1]Valenzuela, A., Haerendel, G., Foppl, H., Melzner, F., Nuess, H., Rieger, E., Stoecker, J., Bauer, H., Hoefner, H., and Loidl, J., "The AMPTE Artificial Comet Experiments," *Nature*, vol. 320, April 1986, pp. 700–703.

[2]Alfven, H., "On the Origin of the Solar System," Oxford Clarendon Press, 1954.

[3]Wescott, E.M., Stenbaek-Nielson, H.C., and Hampton, D., "Results from the CRRES Ba, Sr, and Ca Critical Velocity Experiments," EOS, Trans. Amer. Geophys. Union, Spring Meeting Supplement, vol. 72, April 23, 1991, p. 230.

D.L. Reasoner/ES53
(205) 544–7636
Sponsor: Office of Space Science and Applications

Map of Low-Energy Ion Distributions in the Earth's Magnetosphere

At polar latitudes, because the Earth's dipole field is nearly vertical, charged particles in the ionosphere created by photoionization or particle impact ionization are relatively free to move upward along the magnetic field lines and populate higher altitude regions of the **magnetosphere**. A significant portion of the outward flowing ionospheric plasma has been shown to have energies below 50 eV. This low-energy plasma is a very dynamic element of the **magnetosphere** system and operates as a foundation upon which plasma waves are generated and propagated to other parts of the **magnetosphere**. The low-energy particles act as charge carriers for magnetospheric and ionospheric currents, are very sensitive to small fluctuations in local magnetic and electric fields, and influence larger-scale interactions.

A statistical study of the occurrence of **low-energy ions** has been completed using measurements from the retarding ion mass spectrometer onboard the Dynamics Explorer 1 satellite. In this survey, distinction is made between ions of different mass (H^+, He^+, O^+, N^+, He^{++}, and O^{++}) and between the different ion angular distributions observed (which indicate the plasma flow characteristics). The increased statistical accuracy of the data and the added dimensions in this study relative to earlier work provide a more detailed picture of **low-energy ion** transport. Occurrence frequencies were determined as a function of spatial location and magnetic activity and were then used toproduce a "map" of the **magnetosphere's** low-energy plasma component as shown in figure 45.

Figure 45 is a cut-away view of the Earth's **magnetosphere** that illustrates regions, drawn from the results of the statistical survey, in which the low-energy ion distributions have been found to exhibit distinct flow characteristics. Region A is an area of dense, cold (<1 eV) isotropic plasma corotating with the Earth. The average radial distance for the isotropic region depends directly on magnetic activity and decreases as magnetic activity increases. Region B, involving light ions at high pitch angles, is confined within a few degrees of the magnetic equator and is associated with temperature enhancements occurring without a corresponding increase in the total ion density.

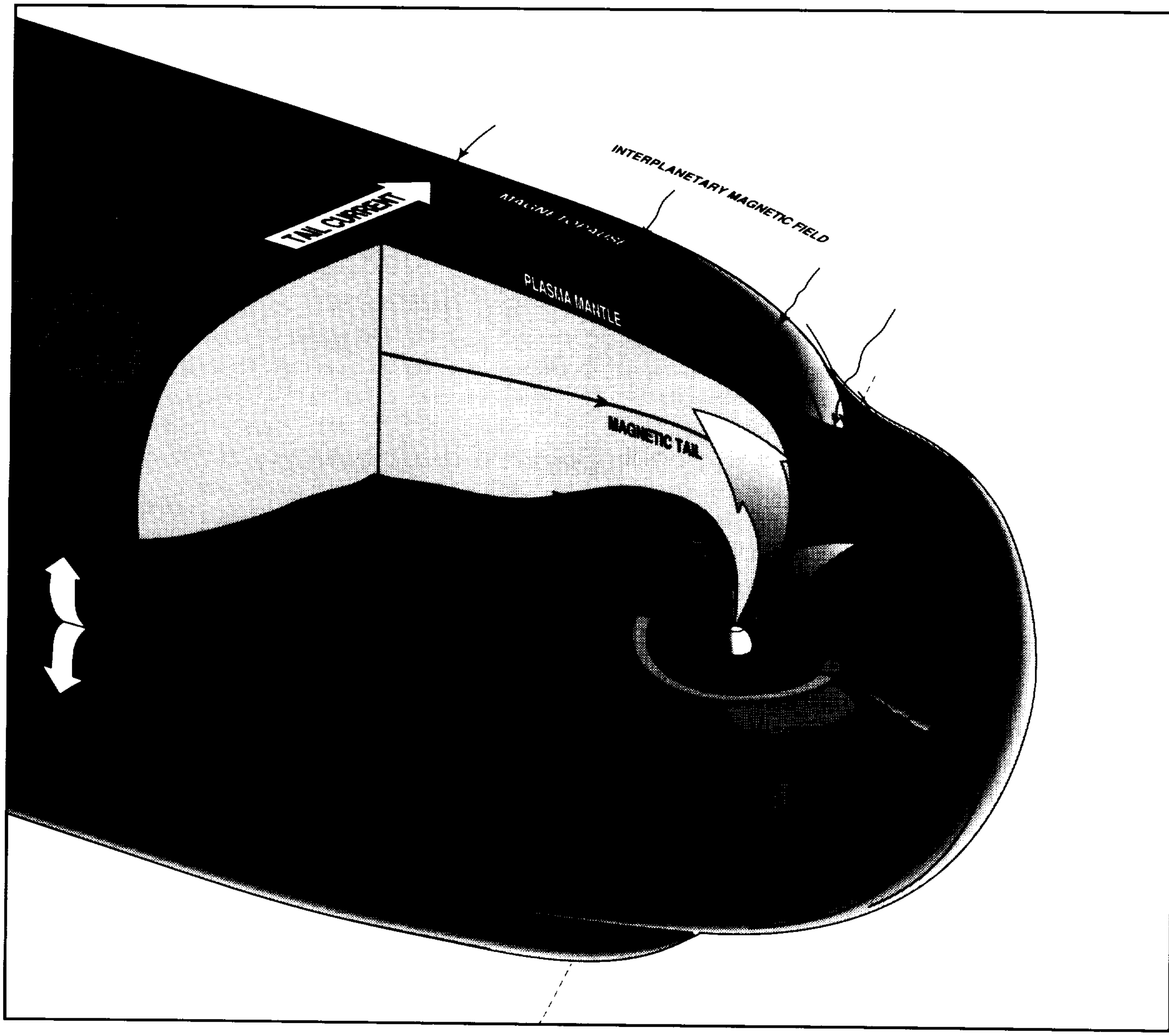

FIGURE 45.— A "map" of the magnetosphere's low-energy plasma component, created from measurements from the retarding ion mass spectrometer onboard the Dynamics Explorer 1 satellite.

Region C is an area of outflowing ions supplied from the auroral zone ionosphere and dayside polar cusp. Traveling upward, these ions flow along high-latitude magnetic field lines that are either open due to reconnection with the solar magnetic field or closed in a highly-elongated fashion such that return flow would occur over long time periods and would be disrupted by nonadiabatic processes. The statistical survey has shown that the region C auroral zone outflow occurs for all the measured ions with a probability that depends on magnetic activity consistent with the location and magnetic activity dependent expansion and contraction of the auroral oval. The occurrence frequencies peak more equatorward on the nightside than for the dayside, and peak at lower latitudes during disturbed times. In addition, there is a magnetic activity dependence on ion mass. The light ions are able to flow from ionospheric altitudes with approximately equal probability during both quiet and active magnetic periods. The heavier ions, such as oxygen and nitrogen, have little probability of being transported to higher altitudes during quiet periods. Increasing geomagnetic activity dramatically increases the number of observations of the heavier mass species. The survey also suggests a mass-dependent correlation with **interplanetary magnetic field** (**IMF**) parameters. In particular, for lighter ions, the low-altitude transverse outflows correlate with the southward (–Z) component of **IMF**, while, for heavier ions, the correlation is with increasing solar-wind magnetic pressure. The high-altitude beam outflows correlate with the northward (+Z) **IMF** component, while, for heavier ions, the correlation is, again, with increasing pressure.

The outflowing ion distributions of region C originating at very high latitudes in the midnight sector may be lost to the nightside plasma sheet region, or they may convect toward the dayside magnetopause (region F), remaining unidirectional because of a relatively short convection travel time. Those distributions originating at somewhat lower nightside latitudes have longer convection travel times and evolve into bidirectional flows (region D) during Sunward convection. The convecting plasma traveling Sunward to the magnetopause will be lost there during magnetic reconnection. The bidirectional conic distributions (region E) in the dayside tough region are thought to be evidence of loss cone formation in the bi-directional flow occurring during Sunward convection.

This study provides information well-suited to define the plasma processes that carry ionospheric ions into the **magnetosphere** region. Further study with theoretical model results is needed to determine the relationship between low- and high-altitude outflowing ion events and the mechanisms that control these outflows as the solar-wind magnetic configuration changes.

Giles, B.L., Chappell, C.R., Moore, T.E., and Comfort, R.H., "Variations in Low-Energy Ion Pitch Angle Distributions as Observed by DE–1/RIMS," to be submitted to *J. Geophys. Res.*, 1991.

Giles, B.L., Chappell, C.R., Waite, J.H., Jr., Moore, T.E., and Horwitz, J.L., "Dynamic Evolution of Low-Energy Ions in the Terrestrial Magnetosphere," *Modeling Magnetospheric Plasma*, eds. T.E. Moore, and J.H. Waite, Jr., 1988, pp. 177–183.

Delcourt, D.C., Giles, B.L., Chappell, C.R., and Moore, T.E., "Low-Energy Bouncing Ions in the Magnetosphere: A Three-Dimensional Numerical Study of Dynamics Explorer 1 Data," *J. Geophys. Res.*, vol. 93, 1988, pp. 1859–1870.

B.L. Giles/ES53
(205) 544–7637
Sponsor: Office of Space Science and Applications

Visualization of 3–D Velocity Distribution Data

Data from current **magnetospheric instruments** (e.g., super thermal ion composition spectrometer (STICS), thermal ion dynamics experiment (TIDE), retarding ion mass spectrometer (RIMS)) are multidimensional. This presents a problem in trying to analyze that data in an efficient and effective manner. Previous attempts have involved methods of taking two-dimensional (2–D) representations of these data, sometimes in subsets and sometimes via aggregating the data. The use of subsets has the limitation that one cannot see all of the data at once. The use of aggregates smears the data together obscuring the detailed features of the data.

A **data visualization** tool kit (currently **application visualization system** (AVS) on a Stardent) has been used to look at a full three-dimensional (3–D) data set for a sounding rocket experiment, STICS, and for simulated data from a model for the TIDE experiment. Each data set consists of a time series of energy/angle/spin data for six different mass species. This tool kit allows the construction of visualizations by plugging together operation modules using a graphical editor and immediately seeing the results. The standard module set has been augmented by writing a data input module that allows for the choice of the appropriate mass species and time step for display. Other modules have been written that allow custom annotation of the visualization.

This work has led to displays such as figure 46. In this figure, the physical data dimensions of the spin of the instrument about its axis and the multiple elevation look angles are represented as points on a sphere. The data dimension of the energy sweep is transformed into a radial distance from the spherical center resulting in a spherical volume coordinate system. Figure 46 is a perspective view of the full 3–D array showing the distribution function for the period from 578 to 590 s flight time of the ARCS4 (Argon Release for Controlled Studies) flight at 525–km altitude. The perspective provides a view at a 30–deg angle to the local magnetic field (Vz or polar axis). The white surface is an isosurface of constant phase space density at a level near 10^{16} $s^3 km^{-6}$.

FIGURE 46.—Toroidal O^+ velocity distribution.

The velocity distribution at each point in this coordinate system is represented in two ways using a "bubble" data indicator. First, as the data value increases the size of the bubble increases between some minimum and maximum size. Second, the color of the bubble also changes to indicate the same effect. It was discovered that neither indicator by itself was sufficient to differentiate close values over the full range. Additionally, two special cases—no data available and true zero data value—are indicated by violating the size-color correspondence. These cases use small bubble sizes coupled with different color values from the high end. Another representation method employs the use of an isosurface, the white structure in figure 46. This represents a surface of constant value in the data volume.

One of the crucial aspects of this work is the need for strong computer power coupled with graphics hardware support. It was discovered that the ability to quickly manipulate the 3–D graphics object (shown necessarily as a 2–D projection) allowed a better grasp of the data due to the mind's ability to integrate the various views into a perceived 3–D object.

Future plans for this work are numerous. These plans include the investigation of other data visualization tool kits, most notably apE, to determine appropriate display technologies. There will also be some use of a custom code to investigate display methods not provided by the tool kits. Plans to investigate the use of these tool kits on other platforms such as Sun Microsystems, Inc., Silicon Graphics, Inc. (SGI), and Digital Equipment Corp. (DEC) are scheduled. Finally, the expansion of these and other methods to view data sets beyond three-dimensions is planned. This would involve techniques for displaying multiple data values at each coordinate point.

W.J. Selig/ES53
(205) 544–7608
Sponsor: Office of Space Science and Applications

Laboratory Automation Using Networked Personal Computers

Recent advances in space plasma physics using the past generation of ion and electron instrumentation has led to instrument designs of greater complexity. Fully characterizing these instruments increases the demand on the testing and calibration procedure in the lab. The **Low-Energy Ion Facility (LEIF)** provides the ability to develop and calibrate these instruments thoroughly and efficiently through a linked network of computers and lab devices. The **LEIF** (fig. 47) features a large vacuum chamber, an ion source, personal computers, and a rotation table that enables positioning of the instrument relative to the particle beam.

For the control and data acquisition requirements in the **LEIF** lab, MSFC obtained the Macintosh IIx computer with the National Instruments LabView software that allows interfacing with all of the devices through an icon-based language called G. This software allows the development of virtual instruments, which are a set of sequential controls or measuring tasks for each lab device. These virtual instruments can then be linked together so that any measured parameter can be run as a function of another. In this way, long periods of routine testing and large amounts of data can be processed. The devices in the **LEIF** lab are typical: power supplies, counters, electrometers, motion controllers, and personal computers; and the communication interfaces of these devices vary between serial, IEEE–488, digital, and analog. With this software, there is also a library of drivers that are already written for many popular measuring instruments. Its transfer rates of up to 1 MB/s permit it to be used with the fastest IEEE–488 instrument in a wide variety of test applications.

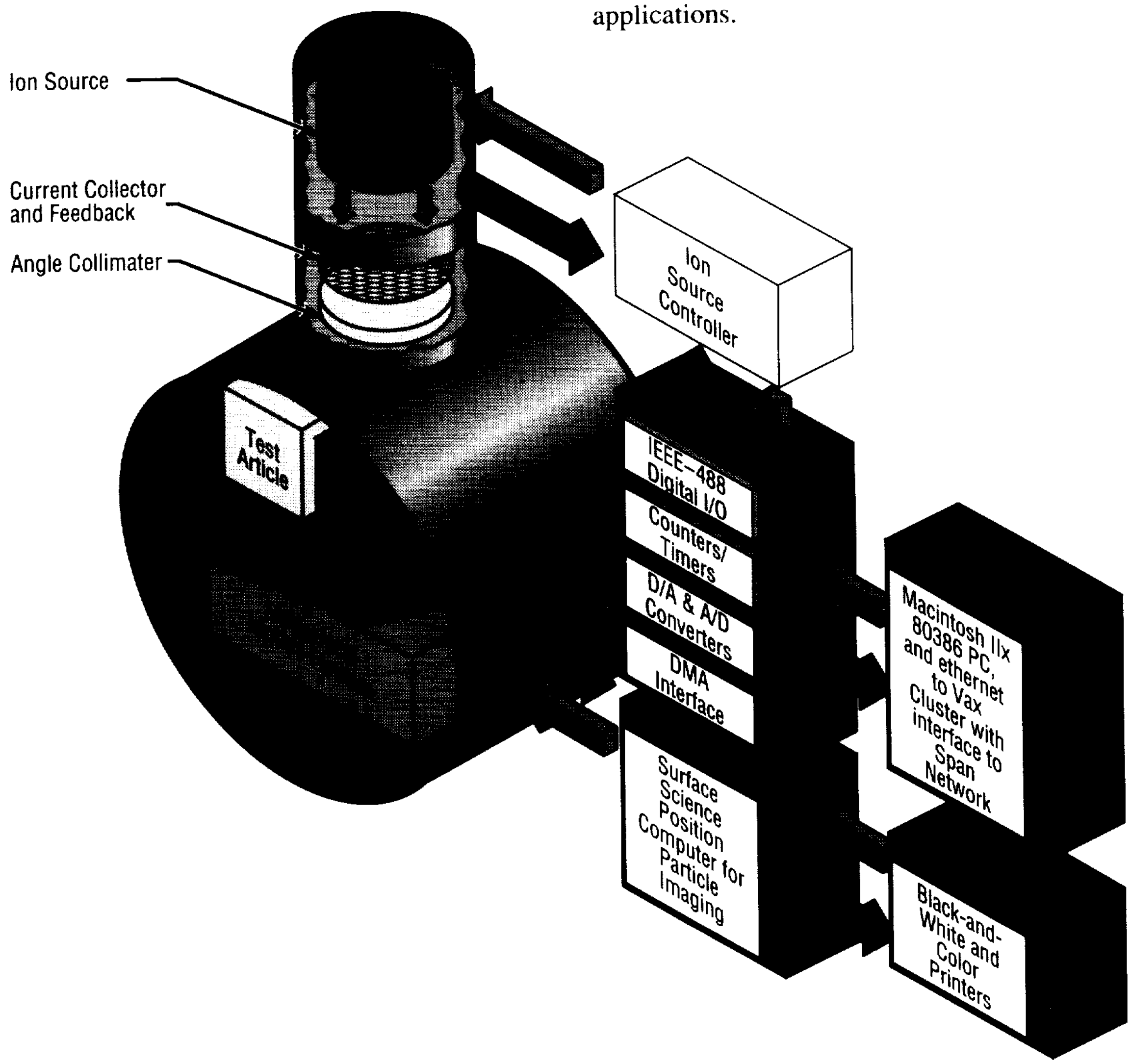

FIGURE 47.—The Low Energy Ion Facility (LEIF).

An example of the use of LabView in the lab is the testing and calibration that will be conducted for the thermal ion dynamics experiment (TIDE). The Macintosh will be interfaced serially to one computer and by IEEE–488 interface to another computer. While these computers have their own tasks during the testing, the Macintosh will act as the controller by sending and receiving information from these computers, and, based on this information, will transmit and receive information from other devices such as the ion source and the motion controller. The Macintosh is also connected to an ethernet communication line through a network router so that the large amounts of data accumulated can be passed to a larger computer or mainframe.

Manually conducting a comprehensive series of tests for a complex flight instrument over its complete range of particle energy, mass, flux, and angular acceptance is time-consuming, tedious, and not easily reproducible. With the Macintosh II and the LabView software, it is possible to perform a series of complex tests on a flight instrument and easily reproduce the test, if needed. This software is powerful in that it provides both low-level and high-level language capability for all situations and devices that may be required. The software is easy and quick to use because the code can be written in modules and can be adapted for any changes that may arise.

Biddle, A.P., and Reynolds, J. M., "An Integrated Development Facility for the Calibration of Low-Energy Charged Particle Flight Instrumentation," 1985.

Center Director's Discretionary Fund, FY90 Annual Report, November 1990.

V.N. Coffey/ES53
(205) 544–7635
Sponsor: Office of Space Science and Applications

Atomic Physics and Aeronomy

The incoming solar energetic particles and the electromagnetic radiation (photons) in the x-ray, ultraviolet (UV), visible, and infrared (IR) part of the spectrum interacts with the mixture of gases comprising the upper atmosphere. Aeronomy is the study of physical and chemical processes in the upper atmosphere arising from this interaction. The solar radiation is absorbed, emitted, and scattered by the atmospheric gases at various levels, involving electronic, vibrational, and rotational transitions, resulting in a characteristic spectrum. The photons with sufficiently high energies ionize and dissociate atmospheric molecules, producing reactive species or free radicals that interact with other molecules in a complex set of reactions. The characteristic thermal structure and the composition of the Earth's atmosphere and the planetary atmospheres is a consequence of this complex interaction.

A great deal of knowledge about the physical state of the atmospheres and the complex photochemical and dynamical processes can be obtained from the observations and analyses of atmospheric spectra in the UV and IR spectral regions. This information about the rich array of photochemical and dynamical processes that arise from the interaction of the solar radiation with the upper atmospheres is crucial to an understanding of the nature of this part of the Earth's environment. The ongoing studies involve ground-based and space-borne atmospheric observations, laboratory experiments for measurements of molecular parameters, and development of theoretical models and analytical techniques for interpretation of the observations.

Infrared Spectroscopy of Upper Atmospheres

Infrared (IR) spectroscopy has developed into a powerful remote-sensing technique for studies of the physical and chemical processes in atmospheres. The atmospheric molecular constituents absorb and emit characteristic IR radiation by rotational and vibrational transitions. An observation of the IR spectrum provides information about the vertical constituent distributions, temperature profiles, and physical and dynamical processes in atmospheres. Experimental techniques for measurement of atmospheric IR spectra from ground-based, aircraft, balloon-borne, and space-borne platforms have been well-developed along with theoretical developments of radiative transfer models and inversion techniques for interpretation of the observed data. Multidimensional photochemical models are evolving for a quantitative understanding of the physical processes and acquiring a predictive capability for the behavior of the atmosphere.

A research program for continuing development of radiative transfer models and spectral inversion techniques for **IR spectroscopy** of the Earth's atmosphere has been in progress at MSFC.[1,2] These developments include:

- An evaluation of the continuum water vapor absorptions and an empirical model suitable for use in the radiative transfer calculations in the 80 to 230 cm^{-1} spectral region

- An investigation of the methods for rapid radiative transfer and inversion calculations

- An investigation of the methods for extension of the current programs to the nonlocal thermodynamic regime of the mesosphere and the thermosphere.

The developing analytical techniques are being employed for analysis of balloon-borne stratospheric thermal emission observations in the far-IR spectral regions. The far-IR investigation is being carried out in collaboration with the group at the Harvard-Smithsonian

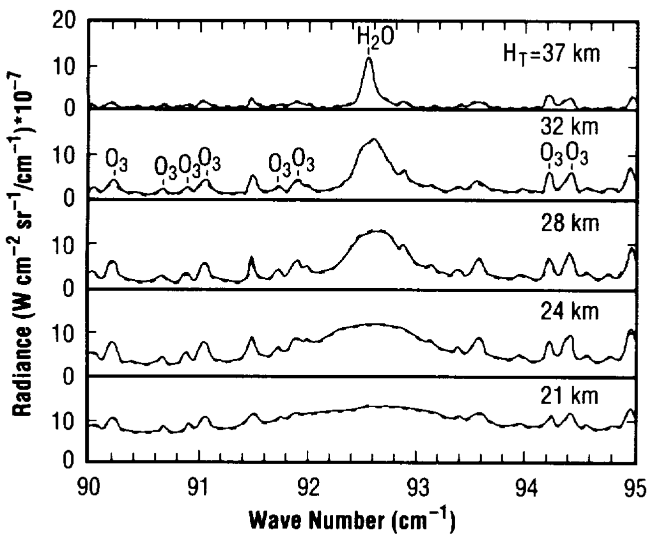

FIGURE 48.—A limb sequence of the observed thermal emission spectra (solid line) in the 90–95 cm^{-1} region for tangent heights from 21 to 37 km. The dashed line represents the calculated spectra for the retrieved constituent distribution profiles.

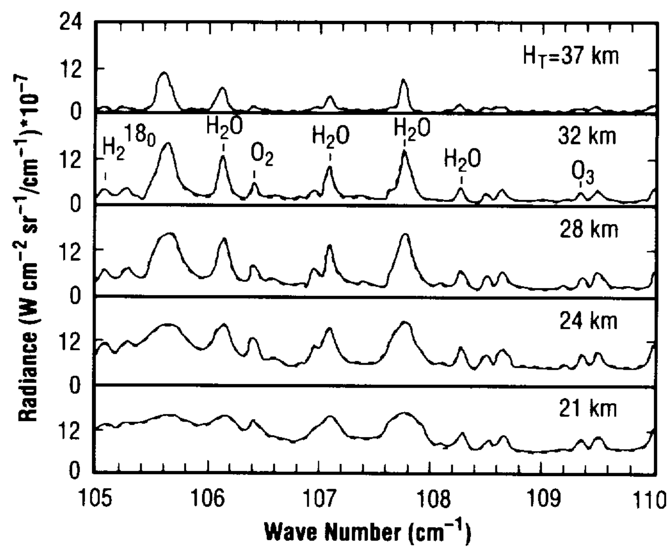

FIGURE 49.—A limb sequence of the observed thermal emission spectra (solid line) in the 105–110 cm^{-1} region. The dashed line represents the calculated spectra for the retrieved constituent distribution profiles.

Center for Astrophysics. An analysis of the observed IR thermal emission spectra in the 80 to 230 cm^{-1} region provides simultaneously determined profiles of a number of trace gases controlling the stratospheric ozone chemistry. An overview of observed spectra in the 90 to 110-cm^{-1} range is shown in figures 48 and 49 for a complete limb sequence of five angles with tangent heights varying from 20 to 37 km. The focus in the current analysis is on the vertical distributions of O_3, $H_2{}^{16}O$, $H_2{}^{17}O$, $H_2{}^{18}O$, HF, HCl, and OH. This investigation will also permit an evaluation of the variation of stratospheric OH over full diurnal cycle.

[1]Abbas, M.M., Glenn, M.J., Kunde, V.G., Brasunas, J., Conrath, B.J., Maguire, W.C., and Herman, J.R., "Simultaneous Measurement of Stratospheric O_3, H_2O, CH_4 and N_2O From Limb Thermal Emissions," *J. Geophys. Res.*, vol. 92, 1987, pp. 8343–8353.

[2]Abbas, M.M., Kunde, V.G., Brasunas, J., Herman, J.R., and Massie, S.T., "Nighttime Reactive Nitrogen Measurements for Stratospheric Infrared Thermal Emission Observations," *J. Geophys. Res.*, vol. 96, No. 10, 1991, pp. 885–10,898.

M.M. Abbas/ES55
(205) 544-7680

Sponsors: Office of Space Science and Applications and Center Director's Discretionary Fund

EARTH SCIENCE AND APPLICATIONS

The two goals of the MSFC Earth Science and Applications program are:

- *To develop and utilize space technology to observe the Earth and gain a more comprehensive understanding of the geophysical processes and their role in defining the interactions between the components of the Earth system*

- *To use the understanding of the Earth's atmosphere to define the launch environment of the space shuttle and advanced launch vehicles.*

Major research activities are conducted in support of NASA's Mission to Planet Earth and the U.S. Global Change Research Program. These activities involve theoretical and analytical model development, remote sensors development, laboratory and field experiments, development and analysis of flight payloads, and advanced information systems development. Implementation of the Hydrologic Cycle Distributed Active Archive Center is under way at MSFC, using an existing WetNet system as its foundation.

Hydrologic cycle research includes ground- and space-based measurements of Earth parameters and uses these to develop and verify analytical and theoretical models of global and mesoscale processes. Field experiments produce data required to verify the operation of air- and spaceborne sensors. Data derived from observations are used as input to model computer codes. Extensive use is also made of interactive data display and access systems to study time-dependent development of Earth system processes on all scales.

WIND/AEROSOL RESEARCH

CO_2 LIDAR BACKSCATTER EXPERIMENT

Space-based measurement of the global tropospheric wind field has been established as one of the highest priority efforts of NASA's Atmospheric Dynamics Research program. The Doppler **laser-radar (lidar)** is the most viable candidate for this effort. Key to the development of this system is the establishment of a minimum **lidar backscatter** sensitivity and optimum operating wavelength necessary to ensure scientifically meaningful data. The **Global Backscatter Experiment** (**GLOBE**) program has been designed and led by MSFC to address these needs. This effort is directed toward accomplishing well-integrated **lidar backscatter** and supporting field measurements and analyses to determine the **lidar** requirements. This is being accomplished under **GLOBE** program scientific plans by (1) using the MSFC **lidars** and related facilities to obtain measurements at selected times and global areas in collaboration with other NASA and university researchers, and (2) by conducting detailed **lidar** measurement analyses as well as quantitative intercomparisons with other NASA and university researchers.

To date, MSFC has designed and led two major **backscatter** survey missions in the remote Pacific as part of the NASA **GLOBE** program. Additionally, two deployments have been made with MSFC **lidar** and supporting instruments to a remote Pacific island for short-term monitoring of low **backscatter** conditions (Mauna Loa **backscatter** intercomparison experiment—MABIE I and II). Preliminary intercomparisons between the MSFC **lidars** and other instruments show good agreement.

It is planned to continue scientific management and to perform specific research tasks according to the **GLOBE** science plan. These plans include establishment of a **GLOBE** data base, modeling of aerosol optical properties based on Mie theory, observing system simulation experiments incorporating recently measured and modeled aerosol **backscatter**, detailed analysis of the MSFC **lidar** data, and synthesis of MSFC **lidar** data and supporting aerosol and meteorological data into a global scale model of tropospheric aerosol **backscatter** at 9.1 and 2.1 μm, and other wavelengths.

Bowdle, D.A., Rothermel, J., Vaughan, J.M., Brown D.W., and Post, M.J., "Aerosol Backscatter Measurements at 10.6 μm With Airborne and Ground-Based CO2 Lidars Over the Colorado High Plains 1. Lidar Intercomparison," *J. Geophys. Res.*, vol. 96, 1991, pp. 5,327–5,335.

Bowdle, D.A., Rothermal, J., Vaughan, J.M., and Post, M.J., "Aerosol Backscatter Measurements at 10.6 μm With Airborne and Ground-Based CO2 Lidars Over the Colorado High Plains 2. Backscatter Structure," *J. Geophys. Res.*, vol. 96, 1991, pp. 5,337–5,344.

J. Rothermel/ES43
(205) 544–1685
Sponsor: Office of Space Science and Applications

Doppler Radar Wind Profiler

The 50–MHz **Doppler wind profiler** installed at the Kennedy Space Center (KSC) by Tycho Technology was accepted by MSFC in October 1990. The **wind profiler** measures the horizontal and vertical **winds** every 3 min from 2 to 19 km (6,500 to 62,000 ft) at 150–m (500–ft) intervals. In October, MSFC began an 18–mo validation procedure to assess the wind profiler's accuracy and reliability. As part of this assessment, the **wind profiler** data will be compared to **jimsphere** data, the standard upper-level **wind** measurement system used on the day of launch. The validation procedure includes gathering and archiving simultaneous measurements of **wind profiler** and **jimsphere** data, performing statistical analyses to determine measurement differences, developing **wind profiler** reliability statistics, developing and implementing automatic quality control procedures, and providing data bases to the engineering community for space **shuttle** structural loads and performance analyses. Once the validation procedure is completed, an assessment will be made to determine the use of **wind profiler** data on the day of launch. The space **shuttle** program is interested in the **wind profiler** as a tool to monitor the upper-level **winds** prior to launch, and as input to the structural loads and performance model run on the day of launch.

An example of the **wind profiler** data versus **jimsphere** data is depicted in figure 50. The solid line represents the **jimsphere** data, and the plus signs represent the **wind profiler** data. The data are from April 5, 1991, during the launch countdown of STS–37. The profile of the **wind profiler** data was produced using a prototype median filter technique applied to the **profiler** spectral data gathered over a 15–min period ending at 1,423 Z, the same time as the **shuttle** launch. The **jimsphere** was released from the ground at 1,438 Z, 15 min after launch. The profiles of **wind** speed and direction show how well these systems compare; however, there are slight differences in the two profiles. These differences may be due to temporal and spatial differences in the measurement systems.

The temporal difference results from the different measurement techniques. The **wind profiler** measurement is an average **wind** profile over 3 min, and the **jimsphere** measurement is comprised of instantaneous measurements of the **wind** with height. For the comparison in figure 50, the temporal difference at 11 km (36,000 ft) is approximately 50 min. The spatial differences between the **wind profiler** and the **jimsphere** are a result of the physical locations of the measurement sites and the fact that the **wind profiler** radar beams are stationary and the **jimsphere** balloon is not. The **wind profiler** site is located at the **shuttle** landing facility at KSC, which is approximately 20 km (12.5 mi) north of the Cape Canaveral Balloon Facility where the **jimsphere** is released. Also, depending on the speed and direction of the upper-level **winds**, the **jimsphere** balloon can be transported downstream at distances of up to 100 km (62 mi) from the Cape Canaveral balloon facility. For this example, the **jimsphere** balloon was approximately 30 km (19 mi) downstream from the **wind profiler** site.

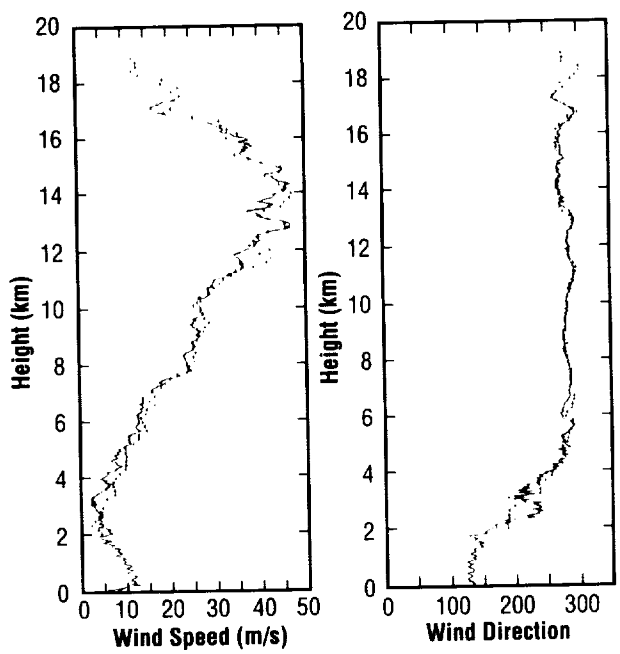

FIGURE 50.—Profiler versus jimsphere comparison.

C.C. Lapenta/ES44
(205) 544–2755
Sponsor: Office of Space Flight

WIND AND TURBULENCE SENSORS FOR SPACE SHUTTLE LAUNCHES

The research and technology in identifying wind and turbulent regions from the surface to 16 km (9.94 mi) by the space transportation system (STS–16) radar/jimsphere and the use of these wind and turbulent assessments to validate the **radar wind profiler** has been in progress. The existing technology for the past three decades (1960's, 1970's, and 1980's), and the present decade of the 1990's in measuring winds aloft for the space shuttle launch has been obtained by balloon-borne wind sensors, e.g., the **STS–16 radar/jimsphere system** (used as the standard) and the meteorological sounding system (MSS) windsonde (used as the backup). The wind profiles are measured in the lower stratosphere and troposphere of the atmosphere, 0 to 16 km (0 to 9.94 mi), for the wind load analysis of the ascent phase of the space shuttle as it passes through maximum dynamic pressure (max 8), where the loads are the greatest on the vehicle.

However, electromagnetic probing of the atmosphere by clear-air radar (**radar wind profiler**) is an emerging technology to supplement balloon-borne wind sensors because there is need for wind load data acquisition closer to lift-off for wind loads assessment. Further, the **radar wind profiler** will be an asset to calculate wind loads for the National Launch System (NLS) and the National Aerospace Plane being developed by NASA and the U.S. Air Force at the turn of the century. In addition, rapid turnaround time wind measurements will be necessary for the speed-up schedule for NASA's Space Station *Freedom* and for human space exploration of the Moon and Mars. Also, the Air Force will use the NLS as a replacement for the Titan–4 class booster for satellite insertion into Earth orbit.

The meteorological features used in describing winds and the dynamics of **turbulence** are well documented.[1] The atmospheric data obtained during the shuttle launches by the rawinsonde provide the necessary meteorological data to compute aerodynamic parameters to identify **turbulence**. One meteorological feature used in describing the dynamics of **turbulence** is the delineation between **turbulence** (T) and no **turbulence** (NT), which is the vertical gradient of kinetic energy.[2] The value of this gradient has been derived as the product of wind speed and vertical wind shear measurements obtained directly from jimsphere data. This parameter has been analyzed during the 16 space shuttle flights where the vertical gradient of kinetic energy was computed, Ke=V(dV/dH). The kinetic energy gradient plots illustrate very good results between **turbulence** (T) and no **turbulence** (NT) during shuttle launches (fig. 51(a) and (b)).

The results of the total energy, stress, and stability parameters illustrate the behavior of wind during **turbulence** and no **turbulence** in the atmosphere for STS−11 and STS−41D (fig. 52(a) and (b)). The total energy (e) obtained by the jimsphere balloon wind measurement was calculated from the following equation:

Eq. 1 $$e \equiv \frac{1}{2}(\bar{u}'^2 + \bar{v}'^2 + \bar{w}'^2).$$

The total energy is the time average of the square of the eddy velocities of u′, v′, and w′ in m^2/s^2.

The turbulent stresses are the presentation of the transfer of momentum due to turbulent fluctuations. The turbulent stress is given by the following equation:

Eq. 2 $$U^{*2} \equiv \sqrt{\bar{v}'\bar{w}'^2 + \bar{v}'\bar{w}'^2},$$

which is the square root of the time average (indicated by the bar) of the square of the eddy velocities of u′ and w′, and v′ and w′.

The stability parameter (x), obtained from the jimsphere balloon wind measurements and the temperature from the radiosonde, was calculated from the following equation:

Eq. 3 $$\xi = X/L, \text{ where } L = \frac{\bar{T}U^{*3}}{kg\, w'T'}.$$

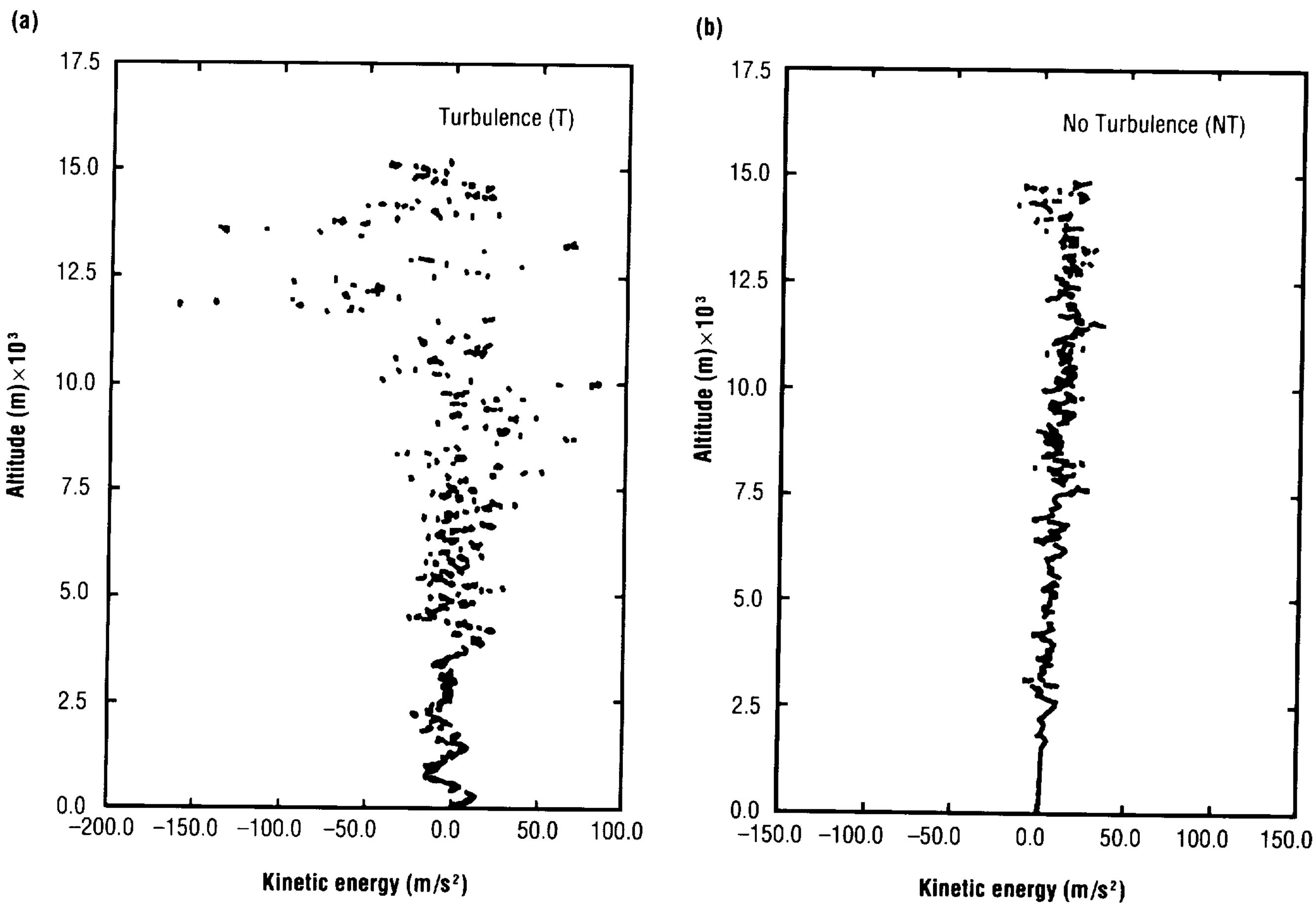

FIGURE 51.—(a) Kinetic energy versus altitude parameter for STS−11 launch, February 3, 1984. (b) Kinetic energy versus altitude parameter for STS−41D launch, August 30, 1984 (1,242 Z) at the Kennedy Space Center (KSC), FL.

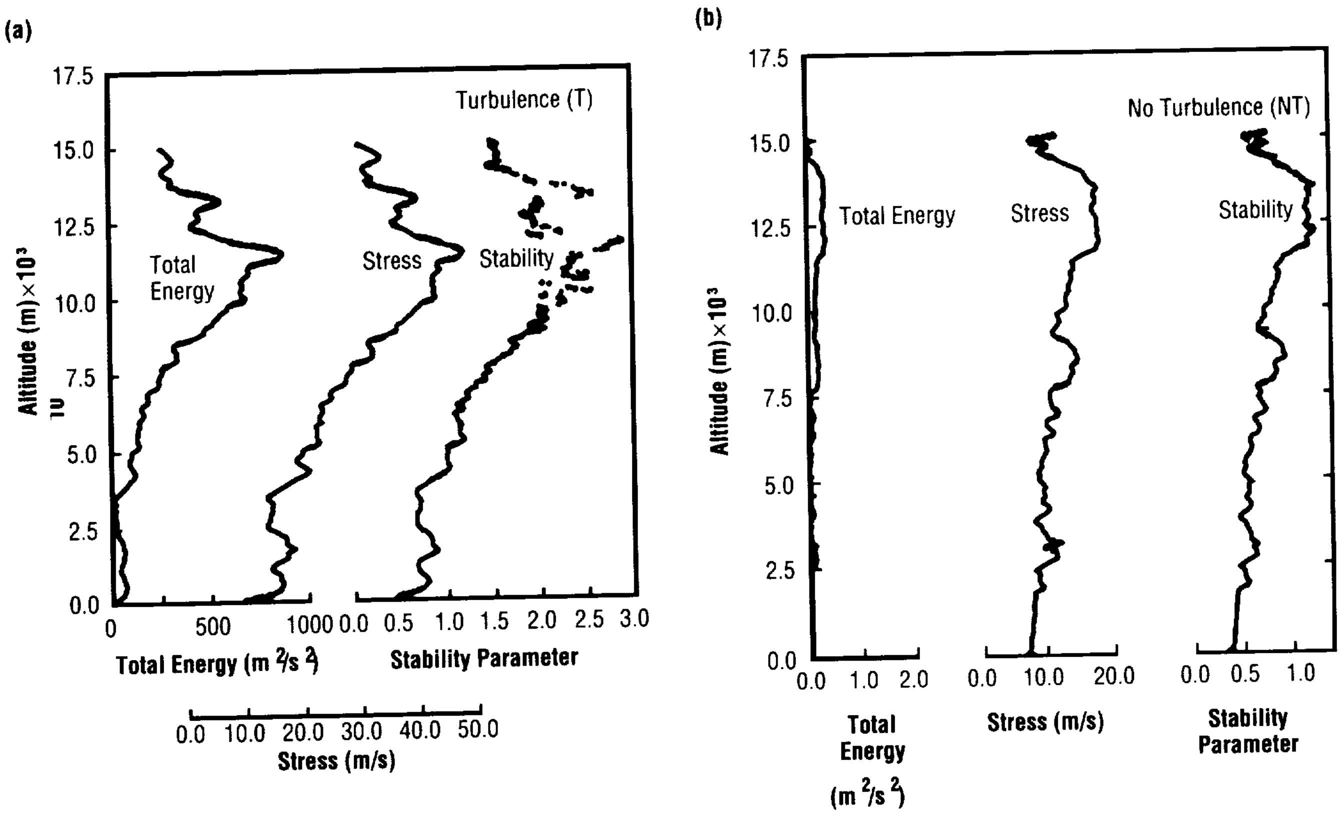

FIGURE 52.—(a) Total energy, stress, and stability versus altitude parameters during STS-11 launch, February 3, 1984 (1,300 Z) at KSC, FL. (b) Total energy, stress, and stability versus altitude parameters during STS-41D launch, August 30, 1984 (1,242 Z) at KSC, FL.

X is the scale height, T is the average temperature in kelvin, T′ is the temperature perturbations, U is the stress from the **turbulence** stress equation, k is Von Karman's constant, g is the acceleration of gravity, and w′ is the vertical velocity perturbation.

Data from the jimsphere balloon are calculated every 30 m (98.4 ft) and averaged over a scale length of 150 m (492 ft) in altitude. The length scale was made at 150-m (492-ft) intervals because the discernible wavelengths of the jimsphere are on the order of 100 to 150 m (328 to 492 ft) as noted by Smith[3] where spectra and cross-spectra of 20 pairs of dual-tracked jimsphere data were computed and averaged. In the validation of the **radar wind profiler**, the same equations and length scales that are being used to evaluate the jimsphere will be used by the **radar wind profiler**.

[1]Susko, M., "Atmospheric Turbulence Review of Space Shuttle Launches," NASA TM 4289, May 1991.

[2]Ehernberger, L.J., "High-Altitude Turbulence for Supersonic Cruise Vehicles," NASA Technical Memorandum 88285, Ames Research Center, Dryden Flight Research Facility, Edwards, CA, May 1986.

[3]Smith, S.A., "Cross Spectral Analysis to Determine the Resolutions and Precision of Jimsphere and Windsonde Wind Measurements," Third International Conference on the Aviation Weather System, Anaheim, CA, January 30–February 3, 1989, American Meteorological Society.

M. Susko/ES44
(205) 544-1660
Sponsor: Office of Space Flight

Lightning Remote Sensing Research

MSFC Shuttle Lightning Research

NASA/MSFC lightning researchers have used both the NASA high-altitude U–2 aircraft since 1978 and the early space **shuttle** missions STS–2, –4, and –6 during the 1980's to observe and photograph lightning, and to collect optical and electronic data while flying over or while viewing from space large mesoscale convective storm complexes. The main objective of these early U–2 and **shuttle** flights was to develop design criteria information for use in the design of a geostationary satellite-borne optical lightning mapper instrument. This instrumentation sensor concept to observe lightning from geostationary orbit was proposed by Dr. Bernard Vonnegut in a talk he presented during the NASA Conference entitled "Exploratory Meeting on Atmospheric Electricity and Severe Storms," April 10–11, 1978, held in Huntsville, AL. To date, objectives of the present MSFC **lightning research** program have been to develop a better understanding of the optical and electrical characteristics of lightning and to investigate the relationship between storm electrification and other underlying and interrelated phenomena, including the structure, dynamics, rain-volume production, and evolution of thunderstorms and severe weather systems.

MSFC scientists have now largely satisfied the need for acquiring a quantitative data base for the design of the geostationary lightning mapper sensor, and preliminary and conceptual designs have been developed for the sensor packages by contractors. Details of the sensor package were described in a paper by Christian, Blakeslee, and Goodman in the *Journal of Geophysical Research*. Present **shuttle lightning research** goals are now focused on understanding the behavior of lightning and the global distribution of lightning rather than characterizing the types of optical and electrical signals produced.

A new **shuttle** lightning observation program called the **mesoscale lightning experiment** (**MLE**), which was started in 1988, is now directed toward using the low-Earth-orbiting **shuttle** as a platform to observe the global distribution of lightning and the behavior of lightning with respect to other storm characteristics, and to observe other phenomena that might not be seen from the ground. This program concentrates on using the **shuttle** payload bay TV cameras at times while the crew members are asleep and/or are not available to make observations. Since the cameras are operated from the ground, longer viewing time of targets can be obtained.

The **shuttle MLE**, flown on earlier **shuttle** flights STS–26, –30, –34, and most recently flown on STS–31, –37, –35, –38, and –41, has continued to focus on obtaining additional quantitative measurements of lightning characteristics and creating a data base for use in demonstrating observation simulations for future space-borne lightning mapper systems. These flights are also providing criteria data for the design of a proposed future experiment consisting of a spectrometer and camera mounted in the middeck window area, which will be used to obtain both video and spectroscopic signatures of lightning. Figure 53 is a sequence of four video images showing a vertical discharge moving out from the top of a thunderstorm close to the limb of the Earth. The bright

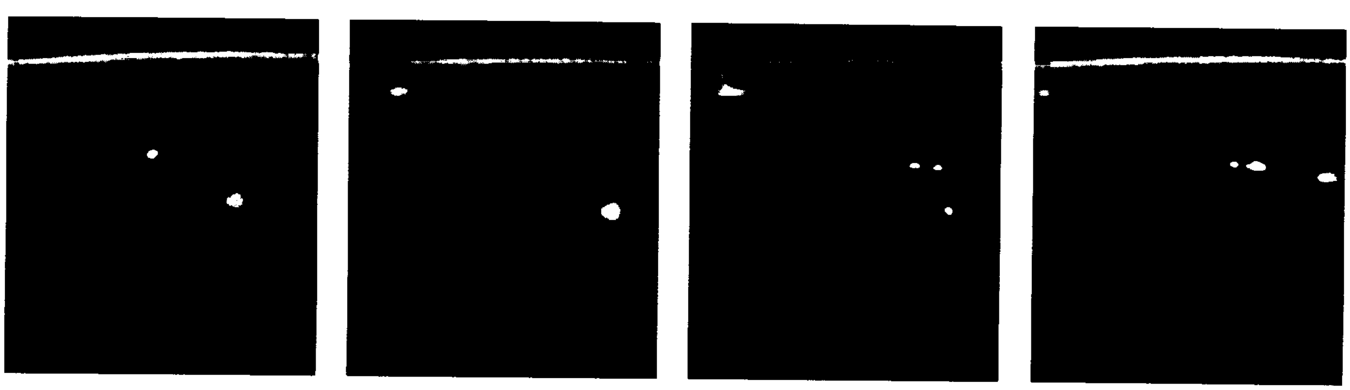

FIGURE 53.— Sequence of video images of a vertical discharge moving out from the top of a thunderstorm close to the limb of the Earth.

line across the top of the images is the Earth's airglow. This unique image was obtained using the shuttle's low light level payload bay TV camera during an orbital pass over Mauritania in northwest Africa during the STS-31 **shuttle** mission while the camera was looking southward. The approximate location of the storm cell is lat. 7.5° N. and long. 4.0° E., or about 1,275 nmi from the **shuttle**. The length of the discharge above the top of the cloud is 19 nmi. Since it is such a unique observation, MSFC is trying to develop a theory to understand how this phenomena can occur from a storm cell that has a very low flash rate. Figure 54 shows a sequence of five video images of a lightning storm in the Gulf of Mexico, south of Houston, Texas, as seen by the **shuttle** STS-31 video camera. This sequence shows how lightning is moving in the storm complex and how single storm cells are illuminated by lightning at the same time.

The **shuttle** imagery now being obtained from the **MLE** observations is analyzed for the frequency of flashes, the length of lightning discharge within the cloud, and global estimates of lightning activity in storm systems that are oblique to the **shuttle**'s orbital track on a time-available basis. These **shuttle**-type observations will continue to provide information for the development of observation simulations for an upcoming polar platform and space station instrument, the lightning imaging sensor (LIS), and the lightning mapper sensor (LMS), which is planned for the geostationary platform series in the late 1990's.

Vaughan W.W., "Exploratory Meeting on Atmospheric Electricity and Severe Storms," NASA CP-2056, July 1978.

Vaughan, O.H., "Thunderstorm Overflight Program, Atmospheric Electricity Research: An Overview Report on the Optical Lightning Experiment for Spring and Summer 1983," NASA TM-86468, November 1984.

Christian H.J., Blakeslee, R.J., and Goodman, S.J., "The Detection of Lightning from Geostationary Orbit," *J. Geophys. Res.*, vol. 94, No. D11, September 30, 1989, pp. 13, 329-13, 377.

Vaughan, O.H., "Mesoscale Lightning Experiment (MLE): A View of Lightning as Seen From Space During the STS-26 Mission," NASA TM-103513, July 1990.

O.H. Vaughan/ES43
(205) 544-1648
Sponsor: Office of Space Science and Applications

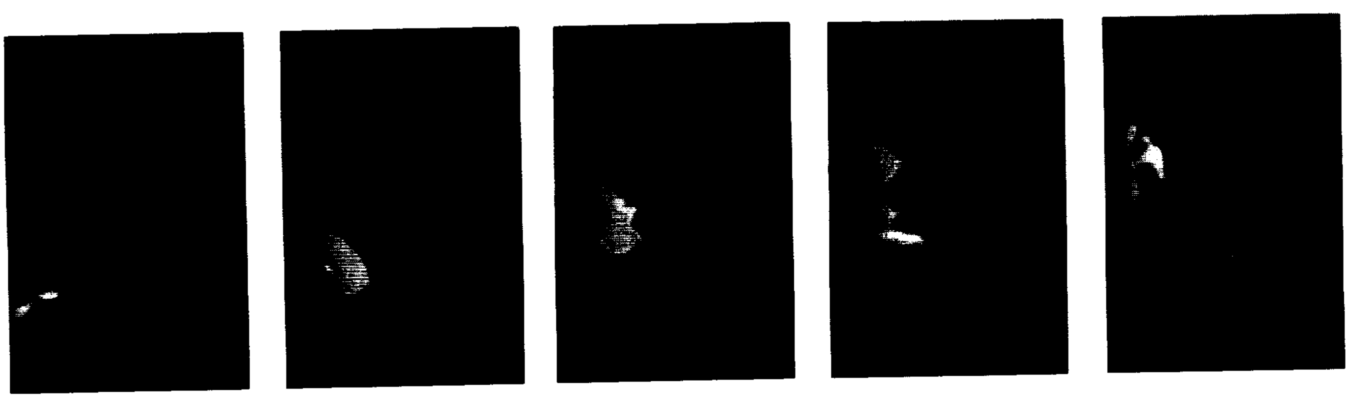

FIGURE 54.—Sequence of video images of a lightning storm as seen by the shuttle STS-31 video camera.

Lightning Instrument Package

In recent years, optical and electrical observations of **lightning** signals have been obtained over the tops of **thunderstorms** from a high-altitude U–2 aircraft using a complement of instruments called the **lightning instrument package (LIP)**. These observations have provided important new details about the temporal, spatial, and spectral characteristics of cloud-top optical emissions; have furnished data essential for the design and development of the **lightning** mapper sensor (LMS), **lightning** imaging sensor (LIS), and other proposed satellite-based **lightning** detectors; and have supported investigations of **lightning** relationships.

The focus of present **LIP** investigations is now to correlate **lightning** and storm electrification with storm characteristics and other atmospheric processes including the structure, dynamics, and evolution of **thunderstorms** and thunderstorm systems; precipitation distribution and amounts; atmospheric chemistry processes; and the global electric circuit. In particular, an emphasis will be placed on the **LIP** investigations on establishing quantitative relationships that employ **lightning** data, such as could be derived from satellite observations of optical **lightning** emissions as the independent variable.

Measurements above **thunderstorms** are still needed to develop, test, and refine relationships dependent on optical **lightning** data sets. Ground-based studies of **lightning** alone are simply not sufficient for these efforts. One reason for this is that ground-based **lightning** location networks do not identify intracloud discharges, which often represent the dominate contribution to the total **lightning**. Presently, the **ER–2** aircraft provides the best means to fly over **thunderstorms** since the **ER–2** can be easily and quickly vectored over regions of interest. The **LIP** instrumentation will enable the detection of total **lightning** and allow for easy differentiation between intracloud and cloud-to-ground **lightning**. In addition, the high-altitude aircraft platform also provides a cloud-top perspective similar to that viewed by a space sensor, albeit much closer. Further, by developing and maintaining the capability to monitor **lightning** and **thunderstorms** with the **ER–2**, NASA will also be able to provide important ground-truth verifications and calibrations when the LMS, LIS, and other **lightning** detectors begin operations in the 1990's. Finally, it should be noted that the **ER–2 LIP** will generally be flown with other sensor systems (e.g., infrared, passive microwave, Dopplar radar, etc.) to provide new understanding of **thunderstorms** and precipitation through the analysis of multiparameter data sets and support satellite simulations of storm measurements.

R.J. Blakeslee/ES43
(205) 544–1652
Sponsor: Office of Space Science and Applications

Effect of Atmospheric Buoyancy on Lightning/Rainfall Relationships

Radar, cloud-to-ground **lightning**, and sounding data are being analyzed in an attempt to define a relationship between **lightning** and **rainfall** in convective storms. The storms studied occurred during the Cooperative Huntsville Meteorological Experiment (COHMEX), which was conducted in the northern Alabama/central Tennessee region of the southeastern United States during June and July 1986. A **rainfall/lightning** relationship would allow large region **rainfall estimations** from space-based **lightning** detection systems.

The storms studied varied from individual thunderstorms to storm complexes ranging in size from 26 to 20,492 km^2. Convective **rainfall** was calculated from the radar reflectivity data using a 30-dBZ threshold over the life cycle of each storm. Then, the number of cloud-to-ground **lightning** flashes produced by each storm was tallied. Next, the average convective **rainfall** per ground discharge was calculated for each day studied. The environment was characterized by convective available potential energy (CAPE) computed from the sounding data. CAPE represents the maximum attainable updraft speed due to buoyancy and was computed from environmental soundings taken at 18:00 GMT on each day.

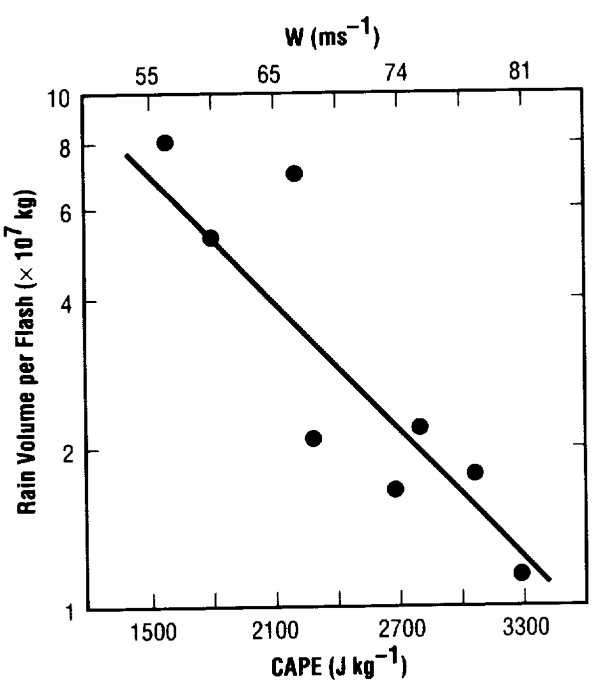

FIGURE 55.— The average radar-derived rain volume per lightning flash versus CAPE.

The average radar-derived rain volume per flash versus CAPE is shown in figure 55, which shows the average **rainfall** per ground flash decreasing as the buoyancy increases. This is attributed to stronger updrafts elevating mass to higher levels in the storm where, more frequently, ice particle interactions may play a major role in separating charge leading to enhanced **lightning** activity. Data from the upcoming CAPE experiment in east central Florida should enable the data set to be extended as well as provide total **lightning** counts to compare with the cloud-to-ground results.

Buechler, D.E. and Goodman, S.J., "1990: Lightning-Rainfall Relationships During COHMEX," Preprints, AMS Conf., on Atmospheric Electricity, Kananaskis Provincial Park, Alberta, Canada, October 22–26, 1990.

R.J. Blakeslee/ES43
(205) 544-1652
Sponsor: Office of Space Science and Applications

MICROWAVE REMOTE SENSING RESEARCH

GLOBAL ATMOSPHERIC TEMPERATURE MONITORING FROM SATELLITES

Temperature monitoring from **satellites** for both **climate** research and **global warming** monitoring is being performed with the **microwave** sounding units (MSU's) flying since late 1978 on the TIROS-N series of National Oceanographic and Atmospheric Administration (NOAA) **satellites**. The MSU's measure the thermal emission of radiation by oxygen in the atmosphere at four frequencies near 60 GHz, a region of strong interaction between radiation and the oxygen molecules. Out of a total of seven MSU's flying on seven separate spacecraft to date, two are typically operating at any one time, with newer ones replacing older ones as they are launched. Intercalibration of overlapping **satellites** to high precision is necessary to construct the long-term **climate** record. These intercomparison periods serve to document stability of the instruments.

An agreement was reached in 1990 between NASA and NOAA whereby monthly **satellite** data are sent to MSFC at the end of every month. The data are processed to obtain the global distribution of **temperature** anomalies (seasonally adjusted **temperature** trends) in three atmospheric layers. These results are used in **climate** studies at both MSFC and at other research institutions. The results are now also being sent to the National Weather Service's **Climate** Analysis Center (CAC), where they are included in a monthly bulletin of **climate** trends that is distributed worldwide.

Radiosonde (weather balloon) comparisons to the **satellite temperature** measurements were performed as an independent validation procedure. Excellent agreement was found between the 10 yr of monthly anomalies derived from the data from over 100 radiosonde stations scattered around the world and the **satellite** measurements made in the vicinity of those stations. Correlation coefficients of 0.90 to 0.95 were common at the 2.5° gridpoint level of spatial sampling, and standard errors range from about 0.15 °C (0.27 °F) in the tropics to 0.20 °C (0.36 °F) at high latitudes. No long-term drift in the intercalibrated **satellite** data set was evident from these radiosonde comparisons.

R.W. Spencer/ES43
(205) 544–1686
Sponsor: Office of Space Science and Applications

THE ADVANCED MICROWAVE PRECIPITATION RADIOMETER

The **advanced microwave precipitation radiometer (AMPR)** is an aircraft instrument originally designed to meet three primary scientific goals. The first of these goals is to investigate the vertical structure of oceanic rain systems. The second goal is to support the development and validation of current satellite precipitation retrieval algorithms, and the third is to provide information in the instrument design of future spaceborne sensors. The **AMPR** passively detects a unique combination of **microwave** frequencies, and, when mounted on a **high-altitude aircraft** platform, it also offers unparalleled surface resolution capabilities at these frequencies. The **AMPR** successfully completed an extensive series of engineering and preliminary science flights during the fall of 1990 and readily demonstrated its ability to meet its original scientific objectives. Data collected during these flights have also shown the enormous utility of the **AMPR** for use in other passive **microwave** studies concerning Earth and sea-surface characteristics.

The **AMPR** and its accompanying data acquisition systems are designed to fly aboard the NASA ER–2 **high-altitude aircraft**. The instrument is a cross-track scanning, total power **microwave** radiometer with four channels centered at 10.7, 19.35, 37.1, and 85.5 GHz. It has a dual lens antenna to accommodate two separate feedhorns. One horn is a copy of the special sensor **microwave**/imager (SSM/I) spaceborne multifrequency feedhorn, which is currently flying aboard the defense meteorological satellite program (DMSP) F8 and F10 satellites. This horn feeds the 19.35–, 37.1–, and 85.5–GHz channels, while the other **AMPR** feedhorn was designed for the 10.7–GHz frequency. The instrument is currently configured with a rotating polarization for all four channels during scanning. This polarization varies from horizontal at 45° to the right of nadir to vertical at 45° to the left of nadir. At the nadir position, the polarizations are equally mixed. The surface resolutions of the nadir-viewing footprints range in size from 2.8 km (1.7 mi) for the 10.7– and 19.35–GHz channels down to 0.64 km (.4 mi) at 85.5 GHz when collected at a **high-altitude aircraft** height of 20 km (12 mi).

The 1990 combined engineering and science **AMPR** flights conducted in Florida during October and offshore of the Oregon/Washington coastline during November have yielded useful examples of oceanic precipitation in both a warm tropical environment and a cool, maritime air mass. These data provide proof of the ability of a 10.7–GHz **microwave** signature to isolate the rain cores of oceanic storm systems. This finding had previously only been shown theoretically and will be especially useful to the design of future precipitation remote-sensing satellites. Data collected during the ER–2 ferry flight from Florida to California also produced many useful samples of land-surface features, such as the wetlands of Louisiana.

The **AMPR** is currently scheduled to be flown during the convection and precipitation/electrification (CAPE) experiment between 18 July and 17 August 1991, which is a multiagency effort taking place in the Cape Canaveral area of central Florida. Deployment of the **AMPR** during the CAPE experiment will provide the most extensive passive **microwave** aircraft and auxiliary data set ever available covering both ocean and land precipitation systems in a tropical environment. The **AMPR** has also been proposed to fly during the STORM—Scale Operation and Research Meteorology—Fronts Experiment Systems Test—1992 (STORMFEST), which is another multiagency field project planned for the winter of 1992 in the central United States. The **AMPR** research objectives for this experiment will be to investigate land-based winter rain and snow systems over varying land backgrounds.

R.E. Hood/ES43
(205) 544–5407
Sponsors: Office of Space Science and Applications and Center Director's Discretionary Fund

Hydrology/Fluid Dynamics Research

The Geophysical Fluid Flow Cell

Large-scale motions of the atmospheres of planets and in the convection zones of **rotating stars** are strongly constrained by rotation, under the action of Coriolis forces, and gravity, which is manifest in the buoyancy forces that drive thermal circulations. The resulting atmospheric structures are often surprising and continue to baffle scientists seeking fundamental understanding of such phenomena as the zonal bands of Jupiter; the numerous spots and other isolated cloud patterns on Jupiter, Saturn, and Neptune; the origin of extremely high winds in the tropics and subtropics of these bodies; and the persistent differential rotation of the Sun where the equatorial atmosphere rotates faster than that near the poles.

The geophysical fluid flow cell (GFFC) provides a means of examining **thermal convection** on a rotating sphere. The GFFC experiment simulates a wide variety of **thermal convection** phenomena on a spherical surface with a radially directed body force. By applying an electric field across a spherical capacitor filled with a dielectric liquid (low-viscosity silicon oil), a body force analogous to gravity is generated around the fluid. The force acts as buoyancy in that its magnitude is proportional to the local temperature of the fluid and is in the radial direction perpendicular to the spherical surface. In this manner, cooler fluid sinks toward the surface of the inner sphere while warmer fluid rises toward the outer sphere. The value of this artificial gravity is proportional to the square of the voltage applied across the sphere and can be imposed electronically as desired. With practical voltages, its magnitude is only a fraction of Earth's gravity and so requires a microgravity environment to be significant. A unique feature of these experiments is the latitudinal dependence of the Coriolis effect resulting in flows more relevant to geophysical applications. The experiment was flown on Spacelab 3 (SL3) and is scheduled for reflight on a future Spacelab mission. The reflight of the GFFC on Spacelab will provide the opportunities for significant fundamental scientific research in dynamic processes.

MSFC has focused on constructing multiple solutions of atmospheric baroclinic waves and of Jovian convection (for the same external parameters) using a high-resolution numerical model. Cattaneo and Hart proved that there are, in general, an infinite number of multiple states possible for problems of giant planet and stellar circulations. Numerical computations have shown that typically more than one of these is stable in both of these settings. The transition to turbulence and the nature of allowed vacillations and index cycle fluctuations are different for each type of solution. The results have a bearing on the question of multiple climate regimes and on the breakdown of banana cells in the GFFC experiments. Research is also focused on interpreting the results of these complex simulations by obtaining low-order descriptions based on the nonlinear orthogonal functions appropriate to the coherent structures in the original partial differential equation calculations. Some of our 10^4-degree-of-freedom spectral numerical simulations can be replicated by as few as six nonlinear ordinary differential equations for the amplitudes of the coherent structures. This method of reduction of a set of partial differential equations to a small number of ordinary differential equations provides a useful interpretive tool as well as an efficient predictive method.

MSFC, along with university colleagues, wishes to further investigate nonlinear **baroclinic flows**, which are important in internal climate variability. The emphasis will be on the following questions: Under what circumstances can high-resolution-model results or laboratory data be represented by a robust low-order description? What are the errors involved, data requirements, etc.? Once a low-order description is found, how can the low-order structures be interpreted physically, and perhaps arrived at beforehand from first principles?

These ideas will be applied to the columnar (banana cell) convection models of circulation in the giant planets as well. In both this and the Earth's atmosphere baroclinic instability problem, MSFC will pursue the numerical simulations of transition to chaos, fractal behavior, and effects of additional realistic physical processes like small-scale boundary layer turbulence on the same.

Brummel, N., and Hart, J.E., "Numerical Models of Columnar Convection," in preparation, 1991.

Cattaneo, F., Hurlburt, N.E., and Toomre, J., "Supersonic Convection," *Astrophys. J.*, vol. 349, 1990, pp. FL63–FL66.

Hart, J.E., "Experiments on Planetary Scale Instabilities," *Non-Linear Ocean Physics*, ed. A. Osborne, 43 pages, Italian Physical Soc., in press, 1991.

F.W. Leslie/ES42
(205) 544–1633
Sponsor: Office of Space Science and Applications

Remote Sensing Perspectives on the Global Hydrologic Cycle

The cycling of water through the geophysical environment has long been recognized as crucial to understanding the Earth's physical climate system and various biogeochemical processes. Space-based remote sensing is rapidly becoming a tool of critical importance for inventorying and understanding the global water cycle. The requirement for a perspective from space results in part from the paradox that while the distribution of water is globally extensive, the processes of phase change between vapor, liquid and ice, associated Earth radiation budget influences, and interaction with other chemical constituents all occur on scales ranging from global to molecular. While no single observing system or research tool can address the whole problem, space observations make a unique and critical contribution.

For several years, the Space Science Laboratory has focused on studies involving the atmospheric component of the hydrologic cycle. These studies have sought to understand how heat sources and sinks induced by phase condensation and evaporation modify atmospheric thermal structure and wind fields. Recently, MSFC has been analyzing passive microwave measurements of atmospheric water vapor, liquid water, and ice available from the **special sensor microwave/imager** (**SSM/I**). Global monthly distributions of column-integrated water vapor (**precipitable water**) have been generated and compared against similar measurements taken from conventional observing networks. A principal aim of this research is to understand the spatial/temporal scales of variability exhibited by atmospheric moisture. These patterns are important because they imply locations of condensation (a heat source for the atmosphere) and because they are signatures of atmospheric kinematic and dynamic processes.

During FY91, a novel approach has been evaluated that constructs consistent global analyses of water vapor and condensate through the blending of **SSM/I** precipitable water and kinematic constraints from global wind analyses. In this methodology, the global wind and

C-2

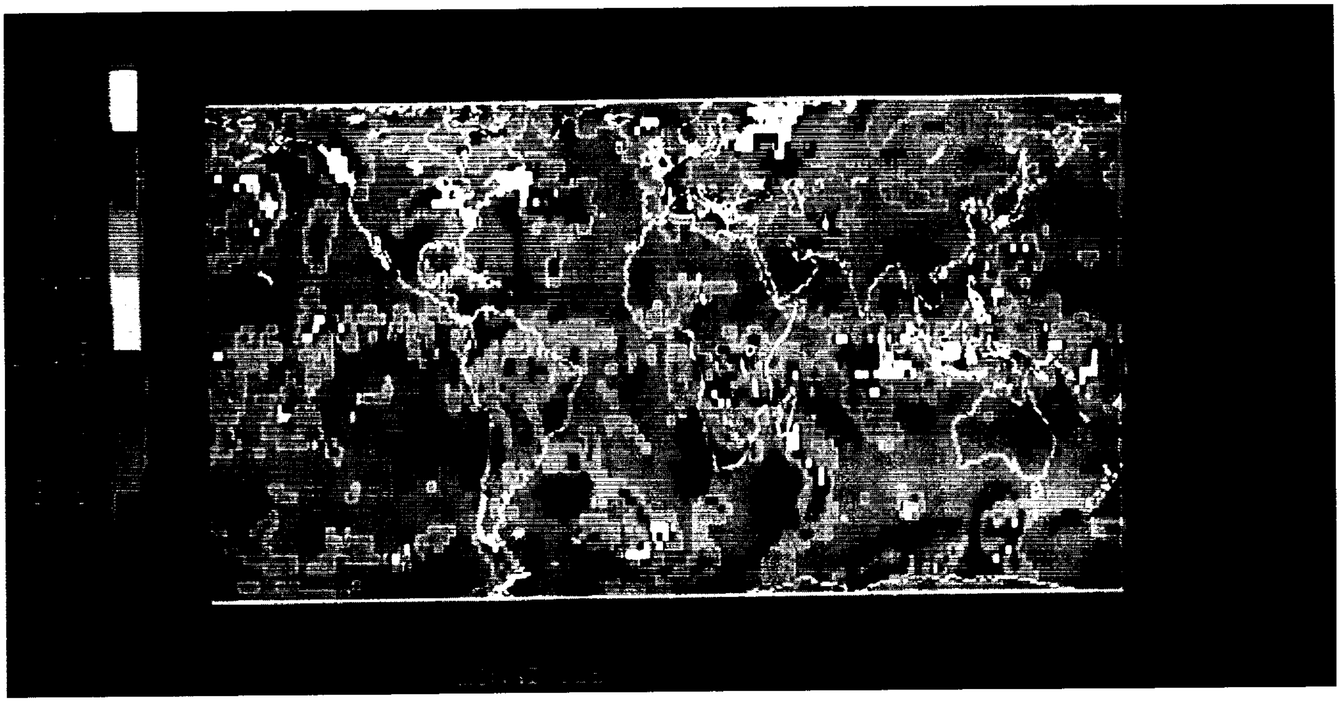

FIGURE 56.— Condensate field (mg $cm^{-2} \times 10$) produced by a diagnostic model constrained with SSM/I water vapor retrievals.

temperature analyses—those archived, for example, by the European Center for Medium-Range Weather Forecasts—are used to drive conservation equations for vapor, liquid, and ice. In addition, these evolving, predicted fields are updated, or constrained periodically by **SSM/I** precipitable water observations. Figure 56 depicts a sample output of total condensate (cloud water plus rain water) produced by this approach. Note the comma-shaped condensate features in middle latitudes that correspond to storm systems.

The initial success with this approach has led to the expansion of this effort with the aim of producing global multi-year data sets of water vapor and condensate that quantify the atmospheric hydrologic cycle. Current efforts include better representations of convective processes and derivation of an independent estimate of atmospheric vertical motion needed to drive the moisture equations. The latter effort is being pursued through analyses of **SSM/I** retrievals of precipitating ice and through **microwave sounding unit** (**MSU**) inferences on potential vorticity.

Robertson, F.R., "Global Analyses of Water Vapor, Cloud, and Precipitation Derived from a Diagnostic Assimilation of SSM/I Geophysical Retrievals," Preprints, Fifth Conference on Satellite Meteorology and Oceanography (Amer. Meteorl. Soc.), Sept. 3–7, 1990.

F.R. Robertson/ES42
(205) 544–1655
Sponsor: Office of Space Science and Applications

Global Atmospheric Modeling

Numerical models of the atmospheric general circulation are powerful tools for probing the nature of physical processes that control the dynamics of **climate**. The complex aspects of surface energy fluxes, cloud radiative forcing, and orographic influence are just a few of the important physical processes that can be studied. Several years ago, MSFC initiated a cooperative effort with the **National Center for Atmospheric Research (NCAR)** through which the **NCAR community climate model (CCM1)** would be implemented on MSFC supercomputing facilities for use in studies of the Earth's physical climate system. The **CCM1** is currently formulated as a global spectral model that predicts atmospheric temperature, winds, and moisture subject to physical laws governing hydrodynamic flow; also treated are radiative processes, cloud cover, subgrid-scale deep convection, and exchanges of energy with the underlying land or ocean.

Currently, MSFC is investigating the sensitivity of the model **climate** to lower boundary conditions. Exchanges of heat, moisture, and momentum between the surface and overlying atmosphere exert a fundamental control on **climate**. The soil/vegetation complex acts as an integrator of the high-frequency rainfall distributions from storm systems. In turn, soil moisture possesses a long autocorrelation time, especially at higher latitudes, and can force the atmosphere on low-frequency time scales. In the same way that the oceans moderate climate by absorbing heat in summer and releasing it to the atmosphere in winter, land surfaces can acquire moisture in the cool rainy season and moisten the atmosphere during summer.

Experiments to date have shown that the **CCM1 climate** is sensitive to the amount of stored water since this strongly modulates surface evaporation rate. Surface temperature, a critical **climate** variable, is strongly regulated by the fraction of the surface energy flux occurring through the evaporation process. Figure 57 shows the difference in atmospheric temperature in two experimental **CCM1** integrations, one having the standard interactive **hydrology** and one having a fixed amount of soil moisture. Both model simulations included identical sea-surface temperature (SST) anomalies in the Central Pacific in order to mimic El Niño climate anomalies. The large temperature differences in middle latitudes show

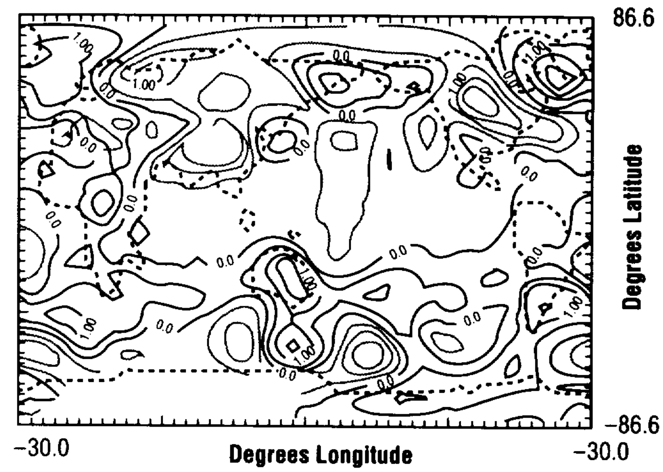

FIGURE 57. — Surface temperature difference between two CCM1 integrations. Contour interval 1.0 K (1.8 °F); negative contours are shown in dot pattern.

that, even for climate anomalies originated by anomalously warm or cold SST patterns, it is necessary to have realistic land surface hydrology in the model to fully assess the full response of atmosphere.

A key aspect of these studies is the comparison to remote observations from space. A recent compilation of global temperature structure from the **microwave sounding unit (MSU)** will provide a source for comparison to vertical mean temperature in the **CCM1** experiment. Comparison of **CCM1** computed outgoing longwave radiation (OLR) and rainfall estimates from several sources (especially the **special sensor microwave/imager (SSM/I)**) is now under way.

In the context of the Earth observing system (EOS) initiative, MSFC anticipates a variety of model studies that examine the sensitivity of short-term **climate** to interactions between the hydrologic cycle, radiation, and lower boundary. Remote sensing will play a key role both in evaluating the realism of the model simulations and specifying forcing mechanisms for model experiments.

F.R. Robertson/ES42
(205) 544–1655

Sponsor: Office of Space Science and Applications

Numerical Modeling of Explosive Oceanic Cyclogenesis

Many investigators have suggested that the warm waters of the Gulf Stream provide necessary energy for the explosive deepening that is a frequently observed characteristic of winter maritime **cyclogenesis** off the east coast of the United States and Canada. Data collected during the experiment on rapidly intensifying cyclones over the atlantic (ERICA) held during the winter of 1988–89 afford the opportunity to investigate the effect of the Gulf Stream on well-documented, rapidly developing systems.

The goal of this study is to quantify the extent to which a **sea-surface temperature** (SST) front can influence **cyclogenesis**. The approach is to use the drexel **limited-area mesoscale prediction system (LAMPS)** dynamical model to simulate **cyclogenesis** over various **SST** fields. It is easy to specify various **SST** fields and to show the differences they induce in the simulated **cyclogenesis**. However, the challenge is to specify the initial conditions of the large-scale flow and to ensure reasonable initial adjustment to the specified **SST** field. If the initial boundary layer structure and the underlying **SST** field are significantly out of balance, unrealistically large initial heat and moisture fluxes may be produced as the boundary layer tries to reach a balance. This boundary layer "spin up" may obfuscate the results of sensitivity experiments designed to determine and understand the impact of the **SST** and boundary layer on rapid **cyclogenesis**.

Research during the past year has focused on the development and testing of a four-dimensional data assimilation (FDDA) technique within **LAMPS**. The technique is a continuous dynamical assimilation where forcing terms are added to the governing model equations to gradually "nudge" the model solution toward a gridded analysis. In this study, nudging is used as a dynamic initialization tool during a 12–h preforecast to generate model-balanced initial conditions for a subsequent 24–h numerical prediction. Optimal results were obtained by nudging the u- and v-components of the wind along with the potential temperature. The nudging terms are included in the model equations for all grid points except those within the model-predicted oceanic boundary layer. This design attempts to confine changes imposed by the specified **SST** field to the oceanic boundary layer during the preforecast period.

The scheme has been tested on a real data case of extreme **cyclogenesis** during ERICA on 4–5 January 1989. A model configuration with horizontal spacing of approximately 70 km and 34 vertical levels was used. The **SST** fields were identical in all experiments while testing the assimilation scheme. Results from three experiments are shown here. Two simulations were initialized at 12 UTC (universal time) 3 January and integrated for 36 h. One run included nudging during the first 12 h while the other did not. The third simulation was initialized 12 h later at 00 UTC 4 January and was integrated for 24 h. Figure 58 shows that the simulation initialized 00 UTC 4 January produced a more intense system (curve B) than that produced when starting the model 12 h earlier (curve A). The figure shows the success of the nudging technique, which significantly improved the central pressure of the simulated cyclone in comparison with the 36–h forecast without nudging (compare curves A and C). It is also worth noting that nudging also significantly improved the storm track (not shown).

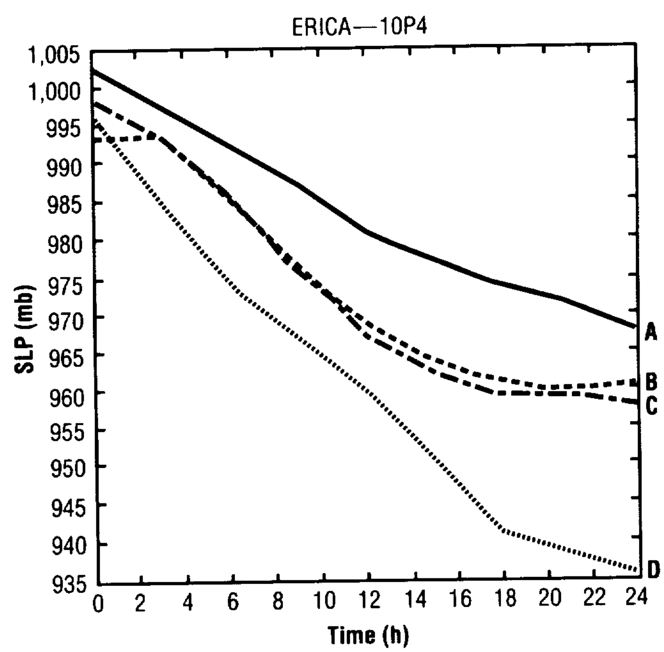

FIGURE 58.— Model-simulated and observed central pressure versus time for the time period valid 00 UTC 4 January (0 h) to 00 UTC 5 January (24 h)1989.

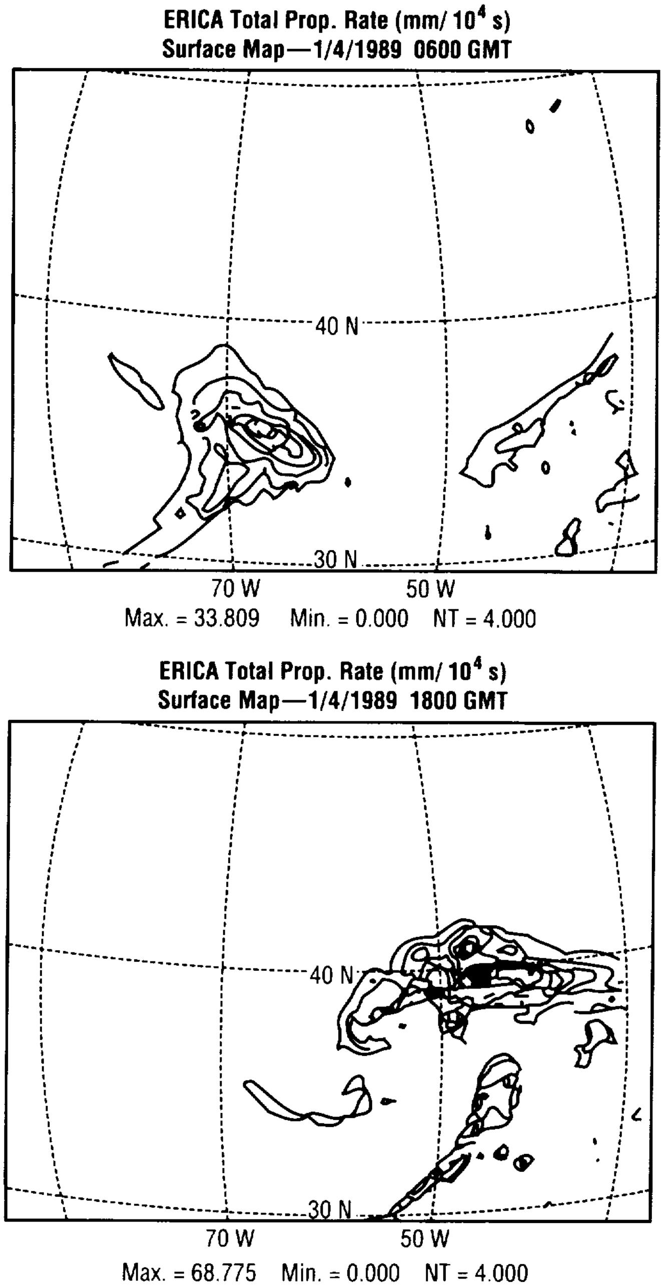

FIGURE 59.— LAMPS total precipitation rate valid at 06 and 18 UTC 4 January 1989. Contour interval is 4 mm (10^4 s)−1.

Figure 59 shows the time evolution of the simulated total **precipitation** rate valid at 06 and 18 UTC 4 January. Comparison between subjective analyses (not shown) and the **precipitation** patterns indicates the model successfully reproduced many of the mesoscale features associated with the complex event.

The next phase of the work will be to complete testing of the nudging technique. Once testing is completed, a series of experiments will be performed using variations of the **SST** fields, such as elimination of the Gulf Stream, a weakened Gulf Stream **SST** front, or idealized Gulf Stream fronts. These types of experiments will be performed on a number of ERICA cases. Other work includes comparison of the model simulations and **special sensor microwave/imager (SSM/I)** observations to aircraft radar returns and in situ measurements of atmospheric temperature, moisture, wind, and microphysics data. This will enable some verification of simulated vertical structure to the **LAMPS** condensate fields, and also help interpret more accurately the **SSM/I** data.

Perkey, D.J., Robertson, F.R., Lapenta, W.M., and Cohen, C., "Comparison of SSM/I Measurements to Numerically Simulated Cloud and Precipitation During ERICA," *Preprints*, 5th Conference on Satellite Meteorology and Oceanography, American Meteorological Society, September 3–7, 1990, London, England.

Perkey, D.J., Lapenta, W.M., Robertson, F.R., and Kreitzberg, C.W., "The Role of the Sea-Surface Temperature Distribution on Numerically Simulated Cyclogenesis During ERICA IOP-4," *Preprints*, 1st International Winter Storm Symposium, January 13–18, 1991, New Orleans, LA.

W.M. Lapenta/ES42
(205) 544–1667

Sponsor: Office of Space Science and Applications

Global Rainfall and the Hydrologic Cycle

The amount of rain falling on the Earth is perhaps the most important parameter of the **hydrologic** cycle (and input parameter to **hydrologic** models); yet, it is one of the most variable and difficult quantities to measure accurately. Weather radar estimates of rain offer good regional samplings of storms with good spatial and temporal resolution. Mesoscale convective systems (MCS's) with lifetimes greater than several hours and spatial scales of hundreds of kilometers are believed responsible for 30 to 70 percent of the warm season **rainfall** and flooding in the United States. Mesoscale weather systems are not just a phenomena peculiar to the United States, but are typical of midlatitude continental climates and are readily apparent from satellite imagery over the continents. Improved understanding of regional precipitation patterns requires substantial knowledge of microphysical and dynamical processes operating at the cloud scale and smaller.

Many empirical radar reflectivity **rainfall** rate (Z–R) relationships have been developed to estimate **rainfall** and provide validation for satellite estimates of **rainfall**. The main drawback of these relationships is that they are often only valid for the one area where the training data sets were compiled and only for certain times of the year. In some cases, radar-derived Z–R relationships might be valid for only one type of storm, e.g., isolated airmass storms versus low-precipitation supercells. One primary reason for the abundance of radar-**rainfall** relationships is the tacit assumption of a single rain-making process, which, in turn, presumes a constant, time-independent raindrop size distribution for converting radar reflectivity into **rainfall**. However, the drop size distribution (DSD) varies both spatially and temporally within mesoscale weather systems.

Recently, new **rainfall** estimation algorithms have been developed for dual-polarization radars. These techniques allow the determination of volume-median drop diameter over large areas from the difference in reflectivity factors measured at horizontal (Z_H) and vertical (Z_V) polarizations. This quantity, Z_{DR}, is defined as the ratio $Z_{DR} = 10 \, log \, (ZH/Z_V)$.

The differences in the rain rates of various cells embedded within an MCS are illustrated below. The National Center for Atmospheric Research (NCAR) CP2 S-band polarimetric radar deployed near Huntsville, AL, is used to characterize the **rainfall** field. MSFC compares and contrasts **rainfall** estimates using the single parameter Z=200R1.6 Marshall and Palmer (MP) method with the Illingworth and Caylor (ILC) (1989) dual-polarization technique. The primary differences in the rain rate estimates are shown to be associated with the differences in the DSD's derived from the ILC technique that occur within the various storms.

Figure 60 shows a low-level reflectivity scan at 2,300 UTC from the NCAR CP4 5–cm **Doppler radar** (located 10 km southwest of CP2). This scan shows a broad region of stratiform precipitation south of the radar and several regions of convective precipitation near the southern edge of the system. In figure 61, contours are 18,

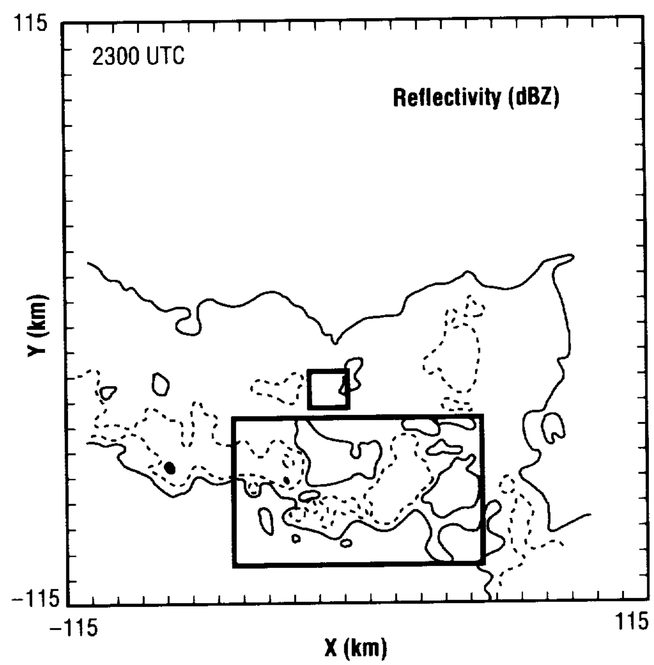

FIGURE 60.—Radar reflectivity factor in dBZ.

solid line; 30, dashed line; greater than 46, solid. All distances are relative to CP2. The area in the large box is the area of coverage in figure 61. The area in the small box is the area of stratiform rain. Figure 61 depicts an expanded view of the rain rate patterns at 2,302 UTC. Several cells are producing nearly the same MP estimated rain rates (fig. 61(a)). (Figure 61(a) shows an MP rain rate with contours of 2, 10, 22, 50, 150, and 230 mm

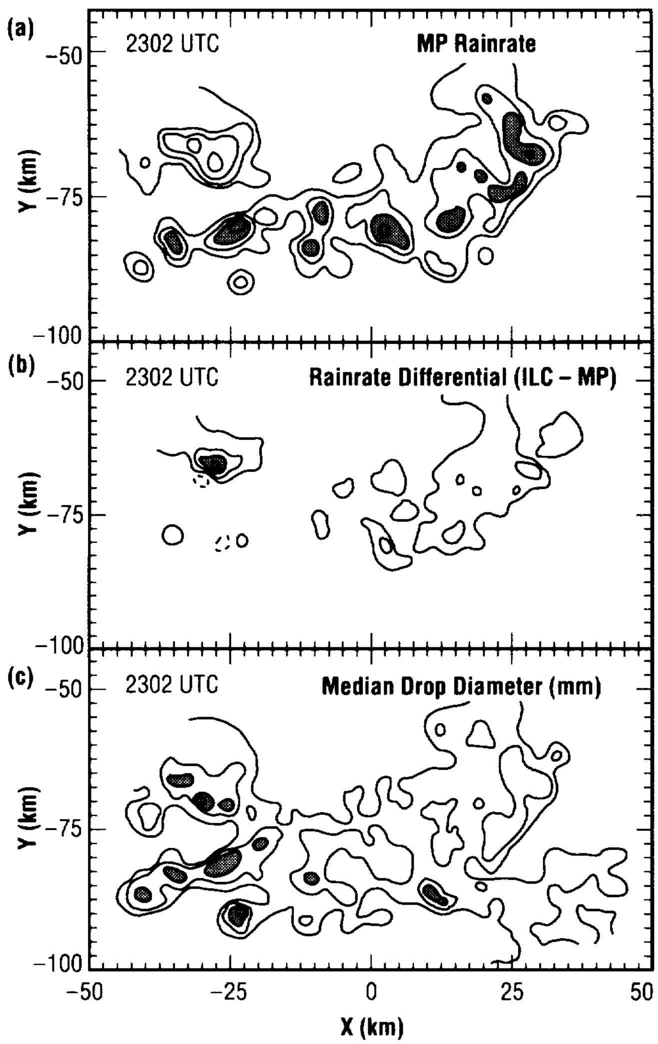

FIGURE 61.— Radar derived quantities at 2,302 UTC.

h^{-1}. Shaded regions are greater than 22 mm H^{-1}.) Figure 61(b) represents the difference between the ILC rain rate and the MP rain rate. Several storm cells are located in a region where the ILC rain rates are 15 to 30 mm h^{-1} greater than the MP estimated rain rate. In contrast, the southwest quadrant of the **rainfall** pattern can be characterized by a greater MP rain rate (ILC–MP < 0). (Figure 61(b) shows an LC minus MP rain rate with contours every 15 mm h^{-1}, solid lines positive, dashed lines negative. Shaded region greater than 45 mm h^{-1}.) Figure 61(c) shows that this region also contains the larger rain drop sizes. Since the reflectivity is proportional to the sixth power of drop diameter, D^6, the MP estimate tends to overestimate the true amount of **rainfall**. (Figure 61(c) shows an ILC volume-median drop diameter with contours every 0.5 mm from 1.0 mm up. The shaded region is greater than 2 mm.)

Illingworth, A.J., and Caylor, I.J., "Polarization Radar Estimates of Raindrop Size Spectra and Rainfall Rates," *J. Atmos. Oceanic. Technol.*, vol. 6, 1989, pp. 939–949.

Wright, P.D., and Goodman, S.J., "A Multiparameter Radar Examination of a Mesoscale Convective System," *Preprints*, 25th Conf. on Radar Meteorology, Paris, France, 24–28 June, Am. Meteor. Soc., Boston, MA.

S.J. Goodman/ES44
(205) 544–1683

Sponsor: Office of Space Science and Applications

Low-Gravity Fluids and Materials Processing Data Base

A data base documenting information on approximately 600 fluids and **materials processing** experiments performed in a low-gravity environment has been prepared at the Space Sciences Laboratory (ES42). The compilation was designed to document all such experimental efforts performed on U.S. manned space vehicles, on payloads deployed from U.S. manned space vehicles, and on all domestic and international sounding rocket programs (excluding those of the U.S.S.R. and China).

Currently, the data base identifies experiments performed by the United States (1) throughout the duration of the Mercury, Apollo, Skylab, and Apollo-Soyuz missions (1962–1975), (2) throughout the duration of the Space Processing Applications Rocket (SPAR) sounding rocket program (1975–1983), (3) during the Consort sounding rocket program prior to Consort 2 (1989), and (4) during the space transportation system (STS) shuttle program prior to and including STS–32 (January 1990). The compilation also identifies sounding rocket experiments performed (1) during the West German Technologische Experiment unter Schwerelosigkeit (TEXUS) program prior to and including TEXUS 18 (1977–1988), (2) throughout the duration of the Japanese TT–500A program (1980–1983), and (3) during the Swedish Materials Science Experiment Rocket (MASER) program prior to and including MASER 2 (1987–1988). It should be noted that, although the STS, Consort, TEXUS, MASER, and other more recently developed low-gravity programs have successfully launched missions after the above dates, these more recent experiments are not detailed within the present version of the data base. A summary of the experiment payload types encompassed within the data base is presented (table 2).

TABLE 2.—*A summary of payload types within the data base*

Payload Type	Number of Fluids and Materials Experiments Performed
Mercury/Apollo*	11
Skylab	45
Apollo-Soyuz Test Project	13
Sounding Rocket**	300
STS Spacelab***	86
STS Middeck	45
STS-Deployed Long Duration Exposure Facility (LDEF)	4
STS Payload Bay****	93

* The only missions that appear to have had such experiments were Mercury-Aurora 7, and Apollo 14, 16, and 17.

** SPAR, Consort, TEXUS, TT–500A, MASER

*** Spacelab 1, Spacelab 2, Spacelab 3, Spacelab D1

**** Includes Getaway Special (GAS) canisters and other GAS canister-type payloads, the Materials Experiment Assembly (MEA), the Materials Science Laboratory (MSL), and the STS-deployed west German shuttle pallet satellite (SPAS) free-floating platform.

The first release of the data base to users outside of MSFC will be a hardcopy compilation of the information. The hardcopy version, which should be available during the first quarter of 1992, will have a detailed summary about each of the 600 experiments and an extensive index. A typical experiment summary (abridged) from the hardcopy version is presented (fig. 62). Each summary contains (1) general information concerning principal investigators and co-investigators, mission, launch date, processing facility, etc.; (2) a detailed description outlining experiment goals, setup, and space results; (3) a list of key words that quickly identify the experiment; (4) a list of the materials or fluids employed during the experiment; (5) a short paragraph explaining the applications of the space research; (6) a list of publications that are applicable to the experiment; and (7) a point of contact for more information concerning the experiment.

Principal investigator: Luttges, M.
From: Bioserve Space Technologies, the NASA Center for Commercial Development of Space (CCDS) at the University of Colorado, Boulder, Colorado

Co-Investigator(s): Stodieck, L.S.
From: Bioserve Space Technologies, CCDS at the University of Colorado, Boulder, Colorado

Experiment origin: United States
Mission: Consort 1 (Starfire Rocket)
Date: March 1989
Launched from: White Sands Missile Range, New Mexico
Payload type: Sounding Rocket Experiment
Processing facility: Materials Dispersion Apparatus (MDA) Minilab
Builder of processing facility: Instrumentation Technology Associates, Inc., Exton, Pennsylvania

Experiment: Collagen Polymerization

The quiescent fluid environment of microgravity has been used to assess the polymerization of the protein macromolecule, collagen, into a cohesive material. The elongate molecules cross-link at specific sites through weak intermolecular forces. In the absence of gravitationally driven flows, the differences in molecular arrangements have been evaluated. The experiments used two separate reactants brought together when the microgravity environment was attained. Mixing was dependent on small convective forces induced by positioning reactants adjacent to each other. Diffusion accounted for the remaining interfacial mixing. The collagen materials, so formed, vary from those prepared in ground controls.

Key words: Biomedical applications, liquid-liquid diffusion, convection, shear forces, sedimentation, biomaterials, protein macromolecules, collagen structures, biological structures

Materials: Top wells: (a) collagen initiation buffer, (b) 2-percent gluraraldehyde fixative;
Bottom wells: solubilized collagen

Experiment applications: This investigation had commercial applications in the area of biofilms that are used for artificial skin implants, blood vessels, tendons, and other organs.

Applicable publications/references:

1) Moos, P. J., Hayes, J. W., Stodieck, L. S., and Luttges, M.W, "Macromolecular Assemblies in Reduced Gravity Environments. AIAA 28th Aerospace Sciences Meeting," January 8–11, 1990, Reno, Nevada, AIAA Paper 90–0027, 8 p. (post-flight)

2) Wessling, F.C., and Maybee, G.W., "Consort 1 Sounding Rocket Flight," Journal of Spacecraft and Rockets, vol. 26, No. 5, September-October 1989, pp. 343–351. (preflight; brief description of MDA)

3) Wessling, F. C., Lundquist, C. A., and Maybee, G. W., "Consort 1 Flight Results—A Synopsis," Presented at the IAF 40th International Astronautical Congress, October 7–13, 1989, Malaga, Spain, IAF #89–439. To be published in Acta Astronautica in 1990. (post-flight)

Contacts: Dr. Marvin Luttges or Dr. Louis Stodieck
University of Colorado Bioserve
Campus Box 429
Boulder, CO 80309

FIGURE 62.— A typical (abridged) experiment summary.

Data base information has been obtained by a number of methods, but mostly via excessive literature searches. The amount of information available on each experiment depends greatly on the quantity of descriptive documentation. Publications often do not contain specifics such as principal investigators and co-investigator designations, processed sample identifications, or even ground-based versus reduced gravity-research distinctions.

In an effort to ensure that all research efforts were accurately represented in the data base, a summary of the information available on each experiment was sent to at least one of the identified principal investigators. The investigators were asked to comment on any discrepancies and provide additional details where information was incomplete. Because very few investigators provided a descriptive experiment summary, Wyle Laboratories was contracted to aid in the writing of the remaining experiment descriptions and in the procurement of other experiment information. To date, approximately 50 experiment summaries must still be written.

When all 600 summaries are completed, principal investigators will be given an additional opportunity to review the information describing their experiment prior to the final preparation of the hardcopy version.

The Space Sciences Laboratory is also analyzing why some experimental payloads were successfully performed while others experienced experiment anomalies. A general assessment of the successes of the low-gravity efforts are being formulated.

Currently, the computational data base is maintained on a commercially available data-base software package. The data-base format was designed by the Space Sciences Laboratory. The menu-driven system is easy to use, and searching and sorting capabilities are, for the most part, extremely efficient. Computational networking data-base release options are still being reviewed by NASA Headquarters.

C.A. Winter/ES42
(205) 544–1695
Sponsor: Office of Space Science and Applications

Effects of Vegetation on Soil Moisture Distribution and Flux

Recent **climate modeling** experiments have identified a critical need for a better understanding of land surface-atmosphere interactions. In particular, **hydrological processes** that link the land surface and atmosphere are inadequately represented due to a basic lack of understanding and to the spatial variability of hydrological and soil-vegetation properties both on small and large scales. A project was initiated at MSFC to study small-scale effects of vegetation on the distribution and fluxes of **soil moisture**. This effort will provide valuable data to validate and modify small-scale models of **hydrological processes** that are embedded in larger climate models and to identify important parameters necessary for surface calibration of remote-sensing instruments designed to monitor **soil moisture**.

The field site encompasses a 1650–m^2 (18,000–ft^2) area at MSFC. The site consists of bare soil with no vegetation, grass-covered soil, and grass- and tree-covered soil. The soil is a residual sandy clay, at least 2–m (6–ft) thick, derived from limestone.

Many instruments have been installed at the field site to monitor atmospheric and soil conditions. A wind vane, an anemometer, a temperature probe, and a relative humidity probe monitor atmospheric conditions at the site. In addition, 14 tipping-bucket rain gauges monitor subcanopy throughfall and stemflow and free-field precipitation. To evaluate the spatial variability of **soil moisture** attributed to throughfall and macropore transport, 36 manually read rain gauges have been installed beneath the canopy of one tree in a 6×6 grid, with a grid spacing of 2.4 m (7.87 ft) between grid points. A sprinkler system is also present to artificially induce moisture at the site under controlled conditions for special purposes. Soil-moisture is monitored indirectly by measurements of pore water pressures with tensiometers installed in sets of three at depths of 30, 60, and 90 cm (1, 2, and 3 ft). **Soil moisture** can be sampled at five locations with sets of three suction lysimeters installed at depths of 30, 60, and 90 cm (1, 2, and 3 ft). Data acquisition for the system is controlled by three programmable data loggers that periodically upload data to solid-state storage modules, which, in turn, can be retrieved and downloaded to a computer for data analysis. The entire system is powered by batteries that are recharged by a photovoltaic array.

Preliminary results indicate that instruments at the site are yielding high-quality, time-series data. For example, comparing throughfall and free-field precipitation has revealed temporal and volumetric variations in the amount of precipitation reaching the ground. These variations are functions of the canopy storage capacity and rate of precipitation. More research is necessary to quantify this variability in relation to tree architecture and precipitation rate because interception of moisture by vegetation provides a faster pathway for cycling of moisture back to the atmosphere by reducing the amount of moisture temporarily stored in soils.

Figure 63 shows the difference in **soil moisture** response at depths of 30 and 90 cm (1 and 3 ft) resulting from the same storm event. It is readily apparent that the response to an increase in **soil moisture** is of greater magnitude and is more rapid at shallower depths. The response to individual precipitation events is also apparent at 30 cm (1 ft) depth; the high-resolution details are greatly attenuated at 90 cm (3 ft).

A higher rate of moisture loss at 30 cm (1 ft) compared to 60 and 90 cm (2 and 3 ft) is indicated by steeper gradients on the curves shown in figure 64. A higher rate of moisture loss is also observed for soils with both tree and grass cover compared to soils with only grass cover, which, in turn, have a higher rate of moisture loss than bare soils. This observation highlights the importance of

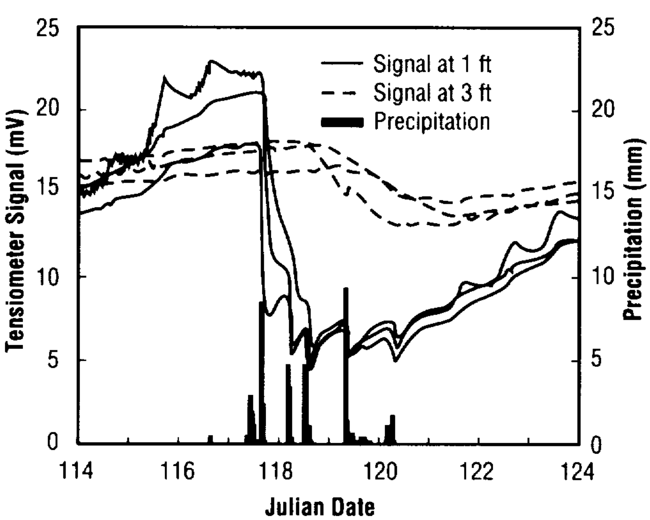

FIGURE 63. — Soil moisture response to a precipitation event as a function of depth.

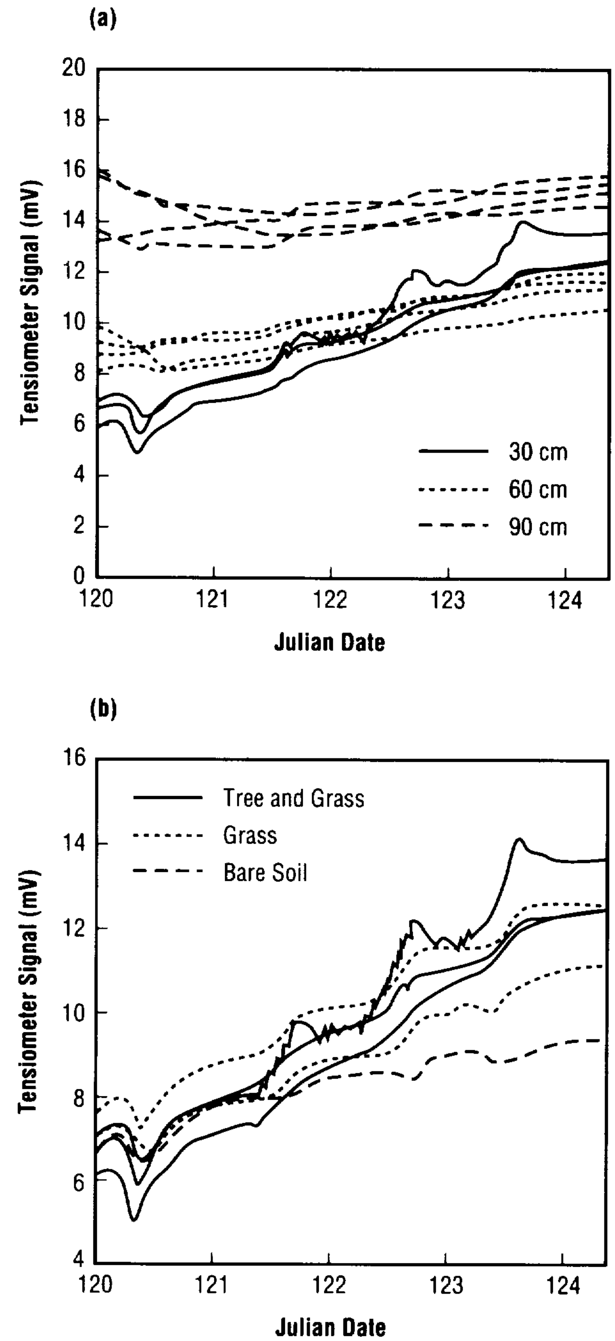

FIGURE 64. — The rate of soil moisture loss as a function of (a) depth and (b) vegetation cover.

vegetation in moisture cycling through transpiration. Further studies will be conducted to quantify the effects of vegetation on **soil moisture** flux.

Additional activities this year entail the installation and operation of a "Bowen Ratio" instrument system to measure sensible heat flux and other heat fluxes from the ground to the atmosphere to aid in computations of energy balance at the hydrologic research site.

McDonnell, J.J., and Costes, N.C., "Use of Remote Sensing in Process Hydrology at Varying Basin Scales," Paper presented at the 1st Joint USA/USRA Conference on Environmental Hydrology and Hydrogeology, Leningrad, U.S.S.R., June 18–21, 1990. Proceedings published by Kendall Hunt Publishing Company, and appearing also as American Institute of Hydrology (AIH) Special Series No. 6. The same paper was also presented in another international conference on hydrologic issues, Budapest, Hungary, June 27–29, 1990.

Costes, N.C., McDonnell, J.J., and Macari, E.J., "Experimental Techniques for Assessing Vegetation-Induced Moisture Flux," Abstract for Poster Session, Fall Meeting, American Geophysical Union, 1990.

Laymon, C.A., Macari, E.J., and Costes, N.C., "Small-Scale Field Experiment of Land Surface-Atmosphere Interactions with EOS Implications," paper accepted for presentation at an EOS symposium at SPACE 92, The Third International Conference on Engineering, Construction, and Operations in Space, Denver, CO, May 31–June 4, 1992.

N.C. Costes/ES42
(205) 544–1637
Sponsor: Center Director's Discretionary Fund

Atmospheric Remote Sensing Research

Evaluation of Thermosphere Models Using the LDEF Orbital Decay Data

Thermosphere density models are currently being evaluated by coupling these models with an orbit generation algorithm and comparing the predicted densities obtained from the models with actual densities derived from the decay of satellites. The difference in the predicted orbital density and the derived orbital density is an indication of how accurately the **thermosphere** density models predict the total density at orbital altitudes. At this time, two models—the **Marshall engineering thermosphere (MET) model** and the **mass spectrometer and incoherent scatter (MSIS) model**—are being evaluated. Both are empirical models with the **MET model** being derived from satellite decay data and the **MSIS model** derived from in situ mass spectrometer measurements. The two models require similar solar parameter inputs and both models are used to predict orbital lifetimes of satellites.

Since the development of these two models, many comparisons have been made between them, and each has been compared with various data sets. The results of these studies indicate that both models, on the average, agree with measured density data to within a standard deviation error of 15 percent. However, many of these studies were performed with data acquired during solar conditions not as extreme as are being experienced during the peak of the present solar cycle (cycle 22). For this reason, the **Long Duration Exposure Facility (LDEF)** satellite provides an opportunity to compare orbit decay data with model predictions during a time of high solar activity and to evaluate the model's performance. Of interest will be the identification of any deviations and trends that are present in the comparisons that are due to the rise of the current solar cycle.

Particular **thermosphere** phenomena that can be investigated are the **thermosphere** responses to long-term solar flux variations (solar disc component), short-term solar flux variations (active region components), and the semiannual variations. Since the decay rate is directly proportional to the **thermosphere** mass density, the variations in decay rate can be directly correlated to the density variations. If the decay rate of the LDEF is compared with solar flux indices of the same time period, it would be seen that the variations in the decay rate are primarily due to the **thermosphere** response induced by variations in the solar extreme ultraviolet (EUV) energy flux and solar wind particle flux as demonstrated by the variations in the solar 10.7-cm radio flux index and the geomagnetic index (fig. 65). For example, the approximate 27-d variations in the 10.7-cm radio flux (EUV proxy) due to solar rotation of active regions can clearly be seen in the decay rate data. Also, a major anomaly in the decay rate on March 13, 1989 (modified Julian date (MJD) 47600) can easily be identified as corresponding to one of the largest geomagnetic (Ap index) disturbances ever recorded.

The above phenomena have long been observed in satellite decay data and have been modeled in the current thermosphere models. To investigate the accuracies of the models and any anomalies associated with the current solar cycle, thermospheric densities have been derived from the decay rate of the LDEF and compared to the model calculations. The relative difference between the **thermosphere** model calculations and the densities derived from the decay rate of the LDEF have also been calculated (fig. 66). The day-to-day differences between the model calculations and the LDEF-derived values are believed to be due to short-term variations, described above, not being modeled precisely. It has been found that the day-to-day differences give an average standard deviation error of 15 percent about the running mean, which is in agreement with earlier studies. The error also shows no appreciable change with the rise of the solar cycle for either the **MET** or **MSIS model**. The running mean of the day-to-day differences provides an

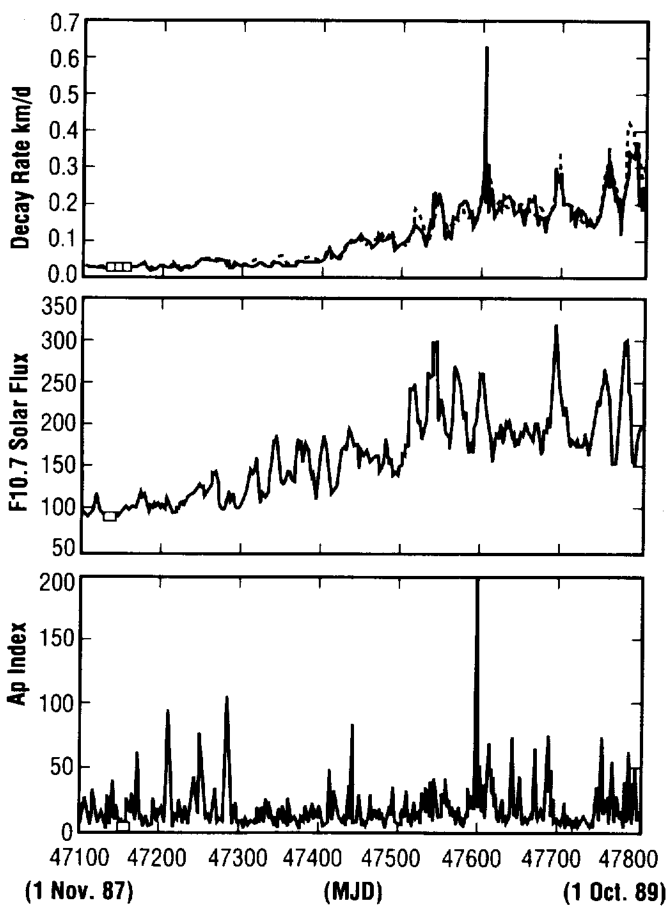

FIGURE 65.— Decay rate of LDEF (solid curve, top panel), and calculated decay rate using MET model (dashed curve, top panel), compared with solar indices.

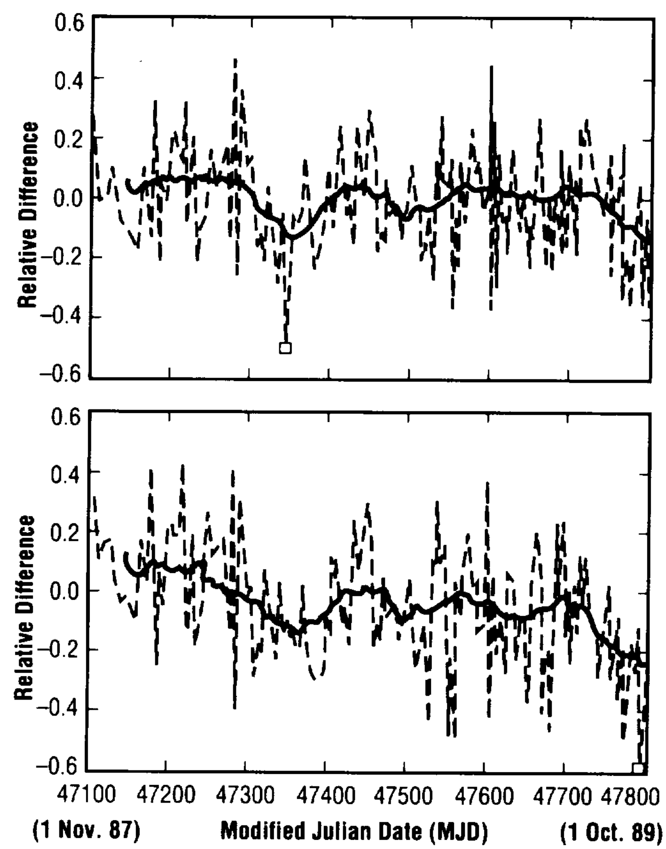

FIGURE 66.— Relative difference of densities derived from LDEF decay and calculations using MET model (top panel) and MSIS model (bottom panel).

assessment of the systematic error present in the models (fig. 66). The cause of these variations is due to long-term variations such as solar cycle and semiannual variations not being modeled precisely. These variations and departures of the models are continuing to be investigated with the goal of understanding the phenomena that are causing these departures and to incorporate better algorithms into the models that will represent the **thermosphere** density more accurately.

R.J. Suggs/ES44
(205) 544–7797
Sponsor: Office of Space Flight, Space Station *Freedom* Office

Sensor Development: Space Applications

The Remote Sensing Branch of the Earth Science and Applications Division is supporting the development of electro-optical instrumentation for space applications. Under the **Earth Observing System (EOS)** program, an optical facility is being developed to calibrate the **lightning imaging sensor (LIS)** and measure its performance through the use of realistic simulations. The **LIS** will image the large-scale distribution of lightning from low Earth orbit in a near-infrared (NIR) narrow wavelength band using a 128×128 pixel silicon charge coupled device (CCD) focal plane array. The sensor requirements include a unique combination of a 2–ms frame time, a field-of-view (FOV) of approximately 80°×80°, and a high background-to-signal ratio during daytime operation.

The **calibration** facility will consist of three distinct systems that can be defined functionally as: focal plane **calibration**, radiometric **calibration**, and lightning scene simulation. The first item, currently undergoing fabrication and assembly, will directly measure the following parameters of individual focal plane arrays:

- Responsivity versus wavelength
- Dark current and noise versus temperature
- Linearity
- Crosstalk
- Pixel uniformity
- Readout speed.

This characterization will enable the determination of **calibration** coefficients and performance parameters, such as dynamic range. The focal plane **calibration** system will utilize three sources of NIR radiation: a monochromator for responsivity measurements, a laser diode for temporal response and crosstalk measurements, and an incandescent quartz tungsten halogen lamp for background flux generation. To maintain traceable radiometric accuracy, a calibrated silicon detector reference will be utilized.

Radiometric **calibration** will be performed on each completed sensor in order to verify FOV, alignment, linearity, responsivity, and the wavelength accuracy of the **LIS** narrowband filter. A 0.5-m monochromator will be utilized to achieve the required subnanometer wavelength resolution.

The **lightning simulator (LSIM)** will use a 3-mW NIR diode laser as the source of simulated lightning. Through an acousto-optic (AO) modulator and an AO deflector, the laser beam will be pulsed and scanned across a rear projection screen to simulate a dynamic lightning scene (fig. 67). A static background image can also be projected onto the screen and its intensity varied by the use of neutral density filters. A simple combination of fresnel lenses and a meniscus collimating lens is used to place the lightning scene at the infinite conjugate plane and to obtain wide FOV coverage. The anticipated FOV coverage of the present design is greater than 60°×60°.

The Remote Sensing Branch is also beginning development of the **shuttle optical lightning imager and spectrometer (SOLIS)**, a compact instrument package for characterizing lightning on Earth from within the cabin

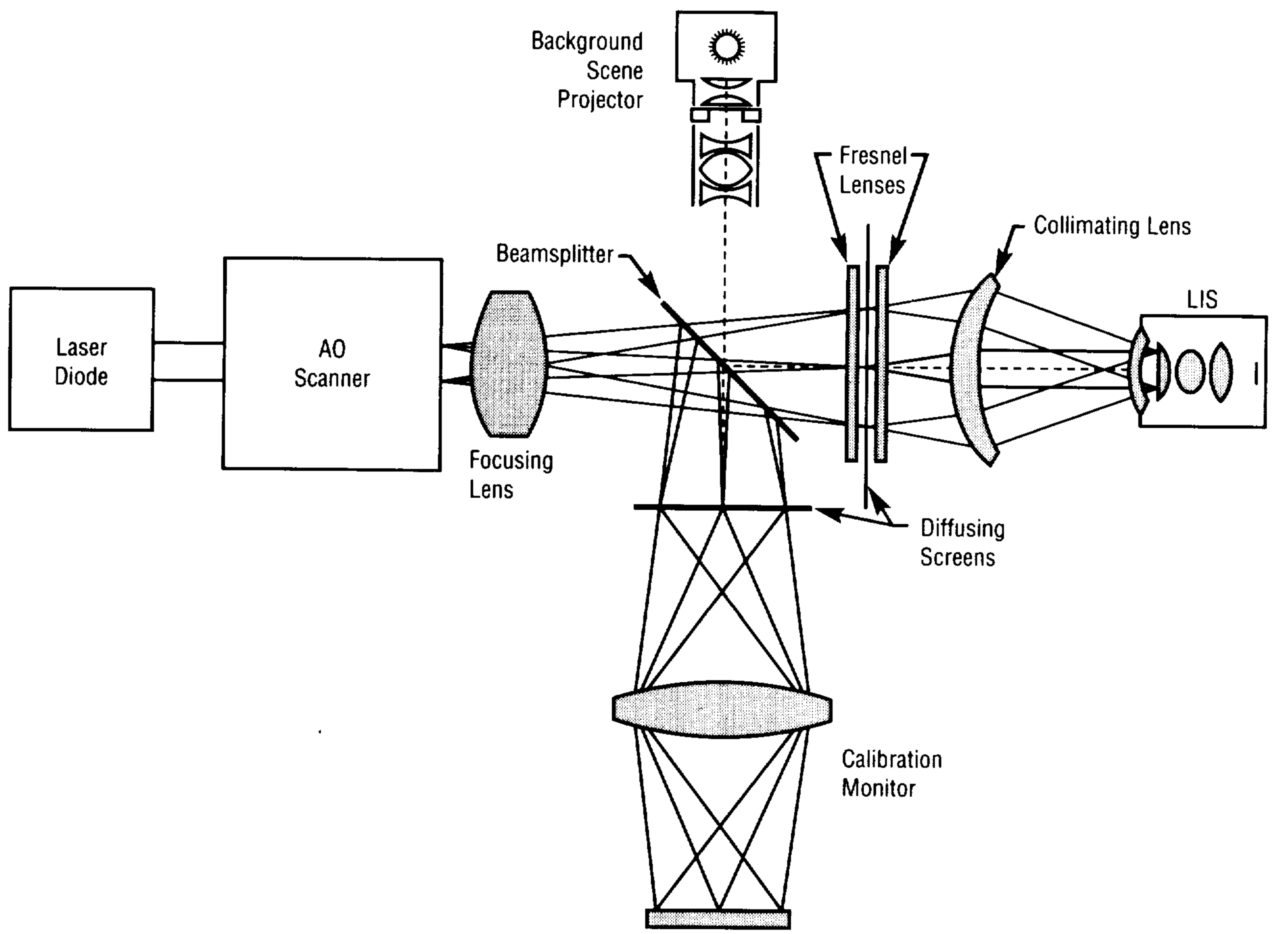

FIGURE 67.— Schematic diagram of the LSIM.

of shuttle orbiters or other manned space vehicles. The **SOLIS** is a second-generation instrument with the primary goal of gathering premission data for global lightning mapping projects such as the **LIS** and the geosynchronous lightning mapper sensor (LMS). The **SOLIS** results will also provide a comparison to similar airborne lightning data previously acquired from the ER-2 aircraft platform.

The **SOLIS** (fig. 68) comprises three distinct instruments: data storage, control electronics, and a battery power supply all in a package that will fit into a single **shuttle middeck payload** storage locker. The sensor is being designed to view lightning through the spacecraft windows, and to be operated either as a hand-held instrument or attached to a simple noninvasive window mount. The three **SOLIS** instruments are: an NIR band-limited intensified video camera for viewing the large-scale lightning spatial distribution, a low-resolution visible-NIR grating spectrometer for spectral measurements, and an NIR band-limited, high-speed silicon photometer for characterizing lightning pulse shapes.

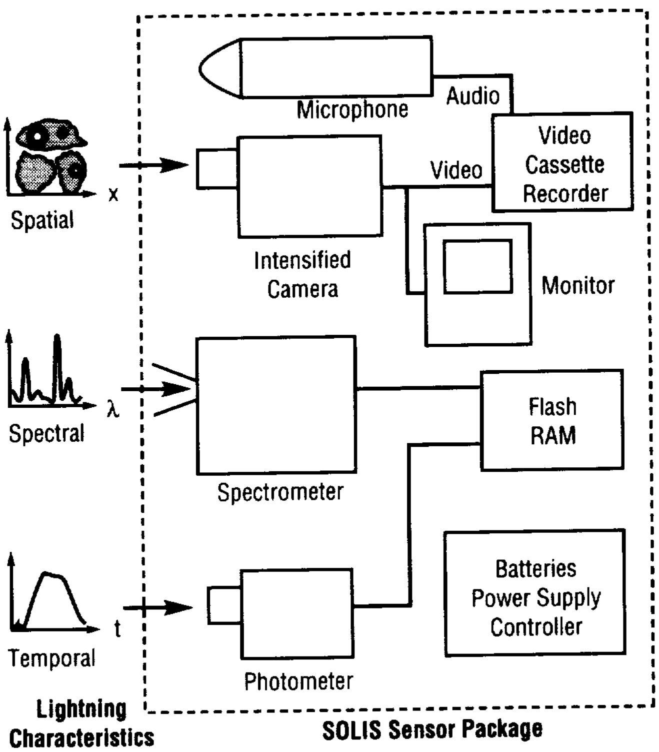

FIGURE 68.— Block diagram of the SOLIS.

M.W. James/ES43
(205) 544-5020

Sponsor: Office of Space Science and Applications

MULTISPECTRAL ATMOSPHERIC MAPPING SENSOR

NASA's **multispectral atmospheric mapping sensor (MAMS)** is a line scanner with eight visible and three infrared (IR) channels. The eight visible channels range from 0.42 μm to 1.05 μm with the four IR channels as follows.

Channel	Central Wavelength (μm)	Bandwidth (@50% response)(μm)
9	3.73	3.47-3.86
10	6.54	6.28-6.98
11	11.12	10.55-12.24
12	12.56	12.32-12.71

Only three of the IR bands are available during any configuration and the 6.54- and 3.73-μm bands cannot be used together. **MAMS** data are being used to determine atmospheric moisture variability and its importance for cloud formation and storm development at scales not available from satellites. The **MAMS** instrument is flown aboard NASA's ER-2 high-altitude aircraft where data are recorded on a 14-track, high-density instrumentation tape recorder. Further detailed information on the data analysis and instrument configurations are available from NASA TM-100352, "Improved Capabilities of the Multispectral Atmospheric Mapping Sensor."

The baseline system flown in 1985 consisted of a 5-mrad aperture that produced a ground instantaneous field-of-view (IFOV) of 50 m (164 ft). With the scan mirror rotation of 12.5 r/s, the noise equivalent change in temperature (NEΔT) ranged from 0.5 to 0.9 K. The following year, 1986, the configuration was changed to improve the NEΔT's down to the 0.3- to 0.5-K range. This resulted from having a larger aperture of 5 mrad that produced a 100-m (328-ft) IFOV at a scan rate of 6.25 r/s. The slower scan speed and larger aperture allowed more radiant energy to fall on the detectors and increased the integration period, improving the NEΔT's of the thermal channels. The scan head or primary optics used by the **MAMS** spectrometer is also used by other spectrometers such as the **thematic mapping sensor (TMS)** and the **advanced ocean color imager (AOCI)**. Several changes that directly affect data quality have been made to the scanner system to accommodate the **AOCI** spectrometer. These changes have improved data quality in all scanner applications. The axe-blade scan mirror was upgraded to a full face mirror. This change increased the amount of energy falling on the detectors, and increased the signal-to-noise ratios in all channels. With the improved dynamic range, the digitization resolution was upgraded from 8 to 10 bits for the IR channels. The averaging electronics for the blackbodies were also changed to average over more samples of the blackbodies to reduce the sensitivity of the detectors to noise. With these improvements, sensitivity became less than 0.1 K, with NEΔT less than 0.2 K. Based on current instrument performance, minimal changes are necessary for the collection of high-quality data in the future.

Recent deployments have demonstrated a deficiency in on-site data analysis capabilities for scientific evaluation of the **MAMS** data. The **quick view display (QVD)** system is being developed to address this deficiency by reading data directly from the instrumentation tape after a deployment. These data will be stored in frame format on a personal computer (PC) and will be made available for analysis with various software packages. Existing analysis software developed at MSFC for calibration, presentation, and navigation of the data is being ported to the PC for use at the deployed site.

The **QVD** system consists of a single PC form factor card that performs the bit and frame synchronization of the incoming single serial Bi–phase–L encoded data. Once the start-of-frame code is detected, five scan lines are stored in a local buffer before transfer to the PC hard disk drive is performed. Data are recorded in frames of 750 bytes with start-of-frame code, housekeeping data, scene data, and end-of-frame code comprising a single frame. Software drivers developed for the PC will read five line blocks through a direct memory access (DMA) transfer to a file that is then read by the analysis software for calibration and navigation correction.

M. W. James/ES43
(205) 544–5020
Sponsor: Office of Space Science and Applications

Thermal Response of Tropical Forest Canopies

The need for the inclusion of surface thermal process information in global-scale climate models is clearly recognized. However, far more detailed information about the thermal response characteristics of heterogeneous surface types is needed.

Remotely sensed forest canopy temperatures can be combined with other measurements to estimate the thermal response and evapotranspiration of tropical **forest canopies**. New methods in remote sensing are now available to measure forest canopy temperatures over large regions using aircraft-based, calibrated thermal sensors. Many of the world's remaining tropical forests occur in vast mountainous regions with limited access. It would be impossible to use conventional micrometeorological techniques to examine the tropical forest canopy temperatures or estimate evapotranspiration over such a vast area, yet the alteration of the tropical forest canopy can affect the regional climate and hydrologic cycle.

The study was conducted in Costa Rica along the Atlantic slopes of the Cordillera Central, an area of tropical rain forest starting at 35 m (155 ft) (La Selva Biological Station) in elevation to 2,900 m (9,514 ft) (Volcan Barva) in elevation. The area is included in the Costa Rican Braulio Carrillo National Park and is believed to be the last remaining strip of uninterrupted forest in Central America to cover such a wide range of elevations. It has also been designated as a man and biosphere (MAB) reserve. The elevational gradient passes through four life zones and two transition zones of the Holdridge Life Zone system: (1) tropical wet forest (30 to 250 m), tropical wet forest—premontane transition (250 to 600 m), premontane rain forest—perhumid transition (600 to 780 m); (2) premontane rain forest (780 to 1,450 m); (3) lower montane rain forest (1,450 to 2,500 m); and (4) montane rain forest (2,500 to 2,900 m).

The Costa Rican **thermal infrared multispectral scanner (TIMS)** flights were conducted during February 1988. Flights were flown between 7 and 9 a.m. with different flight lines. Repeated flights allowed for the calculation of temperature changes among flights for a whole series of forests along the transect and to examine the magnitude of forest canopy temperature change over time.

Analysis of **TIMS** data revealed considerable variation in forest canopy temperatures in the study area, both within and between forest types. Several factors may contribute to these differences, including changes in microclimate, forest canopy structure, and species composition, although it is difficult at present to separate the relative effects of these factors.

Because of the high spatial resolution of the **TIMS**, detailed studies of forest edges or other ecotones were possible (fig. 69). The effect of **forest canopies** on the spatial differences in surface temperature can be readily quantified using **TIMS** data. A thermal image produced from the **TIMS** in the area of La Selva Biological Station was used for temperature transects of 5–m (16–ft) pixels through various surface vegetation types (fig. 70). The transects bisected a pasture, a burn (1–mo old), and a small tree island, and back to pasture. The two lines represent duplicate **TIMS** flights taken at 7:30 a.m. (**TIMS** flight 1) and repeated approximately 17 min later (**TIMS** flight 2).

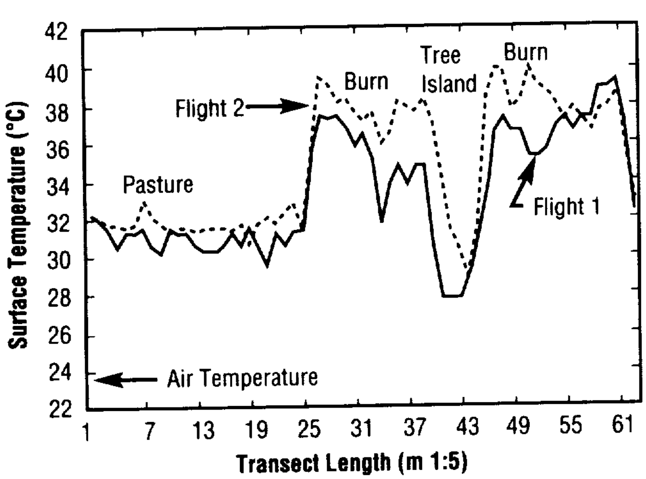

FIGURE 69.— TIMS surface temperature transects of 5–m pixels across several land surface types.

There is a large temperature range among the various surfaces. The comparatively cool tree island is about 29 °C (84 °F), and the warmest burn area is about 38 °C (100 °F). The transitions between the burn area and tree island are quite abrupt, spanning only about 3 pixels, or 15 m (49 ft). Forest edges generate steep, complex microclimate gradients, and support a dynamic assemblage of woody and herbaceous plant species. Intensive microclimate measurements across forest edges have seldom been undertaken to quantify spatial variability in forest microclimate, since conventional micrometerological techniques for studying forest energy budgets demand a large, uniform canopy. However, it is evident that **TIMS** canopy temperatures can provide information on the microclimate of forest edges.

The second **TIMS** flight (17 min later) showed the same relative temperature differences, but temperatures were shifted upward with increased input of solar radiation. The **TIMS** image is an instantaneous "look" at the surface. It is important that the relative temperature differences were maintained through time because the temperature relationships among the surfaces obtained are not unique to that time.

The difference in air temperature and surface represents the 0.5–h average ending at 8 a.m. taken at a height of 2 m (7 ft) at one location and not spatially averaged. Also, during the same time period, solar radiation was quickly increasing and warming the surface. It can readily be seen that air temperatures would be a poor predictor of canopy temperatures in these forests.

Thermal remote sensing is a potentially powerful tool for examining forest canopy thermal responses on a landscape scale, and is particularly suited for use in tropical forests where access is difficult. Understanding the impact of tropical forest alteration on climate and the hydrologic cycle is clearly enhanced. Additional work is in progress to integrate surface thermal responses with large-scale atmospheric processes.

J.C. Luvall/ES43
(205) 544–2809

Sponsor: Office of Space Science and Applications

Silicon Carbide Optics Research

The Geostationary Earth Observatory (GEO), which is an important part of NASA's **Mission to Planet Earth**, will include several optical instruments to monitor the Earth's environment from **geostationary orbit**. This orbit imposes a severe thermal environment on any optical instrument that is part of a three-axis stabilized spacecraft. At the same time, optical resolution requirements are higher in **geostationary orbit** than in low Earth orbits (for comparable ground resolution). The Earth's rotation (and the rotation of the spacecraft over the Earth) allows direct solar flux into the optical ports of these Earth-viewing instruments for several hours each day. Generally, this solar input is incident on optical elements near the **optics** port (such as scan mirrors, telescope secondaries and supports, and telescope primary mirrors).

Several approaches can be taken to minimize the optical and mechanical impacts of this flux. One is to minimize the flux input through the use of long sunshades. Another is to isolate the thermal flux from the optical subsystem as much as possible by internal baffling and dissipation of the flux to cold space. Yet another is to select materials for the **optics** and structure that are minimally reactive to this periodic solar energy.

Silicon carbide (**SiC**) is emerging as a serious alternate to beryllium for spaceborne, lightweight telescope and mirror applications due to its excellent material properties, significantly lower cost, and simpler, non-toxic fabrication processing. Recent cryogenic mirror tests indicate a maximum surface change of 0.25 wave of visible light from 300 K to 90 K. In terms of its strength to stiffness ratio, **SiC** compares favorably with beryllium (at a fraction of its cost) and it is polishable to visible and ultraviolet diffraction limited performance.

Research is under way to develop recent **SiC** advances into a telescope assembly including mirrors, structure, mounts, and baffles. Such an optical system would offer unprecedented stability and performance under the severe environment of the GEO.

R.J. Koczor/ES41
(205) 544–3078
Sponsor: Office of Commercial Programs, Small Business Innovation Research

Mars-Global Reference Atmosphere Model

The advent of such NASA projects as the **Mars** Observer, **Mars** Rover/Sample Return, and proposed manned **Mars** missions, along with the ongoing research of aerobraking techniques for aerocapture by **Mars**, has necessitated the construction of a more detailed global, climatological **model** for **Mars**—the **Mars Global Reference Atmosphere Model** (**Mars-GRAM**).

This personal computer (PC)-based **model** operates with run characteristics that are similar to MSFC's highly successful Earth-**GRAM**. Both **models** provide total density, temperature, pressure, and wind conditions for any location, any date, any time of day from the surface to 600 km (373 mi) (figs. 70 and 71). Small-scale density

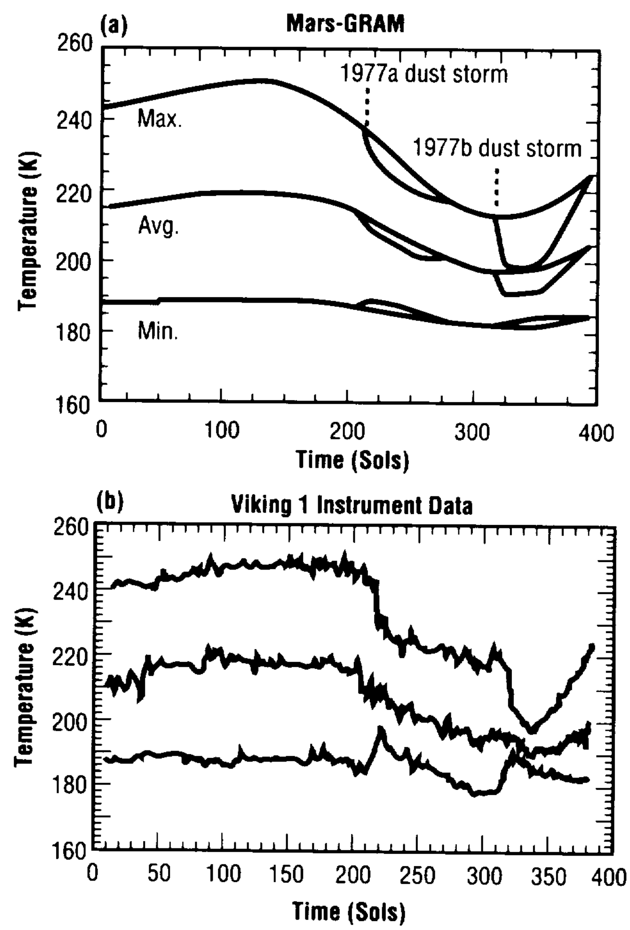

FIGURE 70.— Seasonal variation of the temperature at the Viking Lander 1 site (a) computed by Mars-GRAM, and (b) from Viking 1 instrument data.

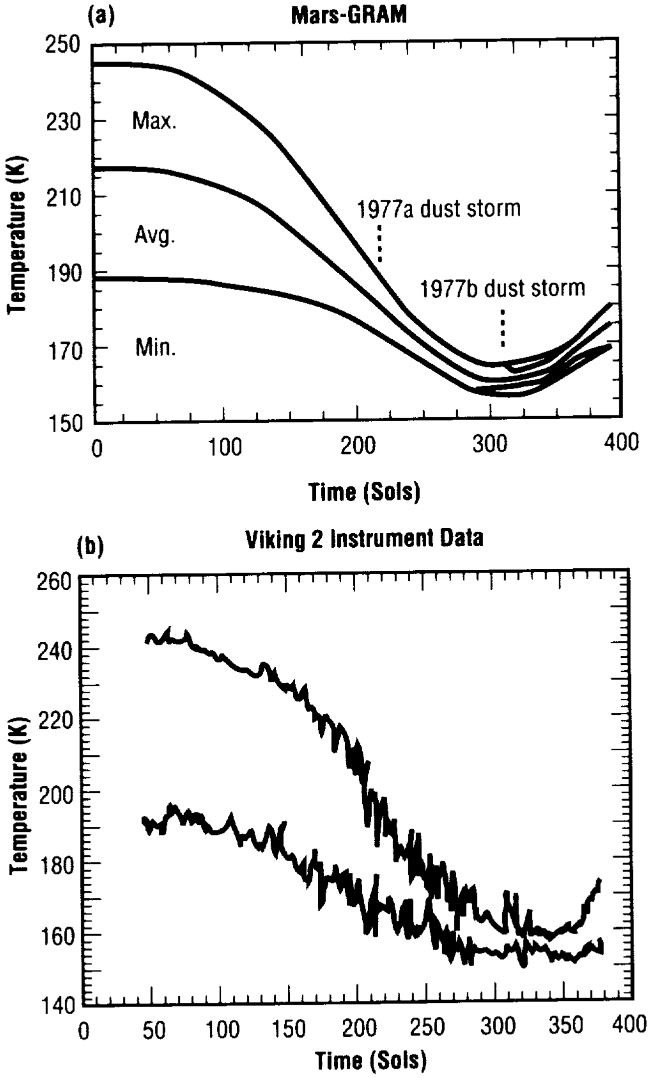

FIGURE 71.— Seasonal variation of the temperature at the Viking Lander 2 site (a) computed by Mars-GRAM, and (b) from Viking 2 instrument data.

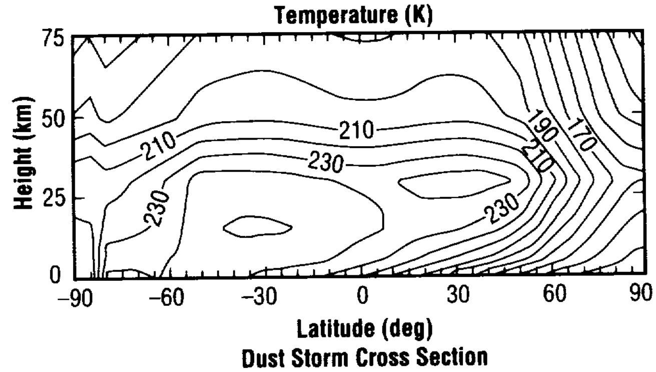

FIGURE 72.— Temperature variation at Northern Hemisphere winter solstice for a global dust storm computed by Mars-GRAM.

perturbations and long-term average density values are also calculated. **Mars-GRAM** also provides realistic **modeling** of dust storms and their effect on the thermodynamics and wind structure of the Martian atmosphere (fig. 72).

The **Mars-GRAM** couples the Culp-Stewart upper atmosphere **model** with a lower atmosphere parameterization scheme based on data received from previous **Mars** missions. To enhance areas where data were sparse, theoretical calculations were added. More than 40 different data sets were utilized throughout the empirical **modeling** process.

Since the first release version was distributed in 1989, the **model** has experienced widespread use in a variety of NASA missions. **Mars-GRAM** has been baselined for use in NASA's **Mars** Rover/Sample Return mission and is also being used for the joint U.S./Soviet **Mars** 1994 balloon mission. The **model** is also being extensively used for ongoing aerobraking research with special use of the **model**'s density perturbation **modeling**, random density profile capabilities, and mountain wave simulation features.

Currently, various upgrades to the **Mars-GRAM** are under way. Work on the second release version will be completed this year. This version will mainly incorporate two areas of enhanced **modeling**: localized dust storm capabilities and atmospheric responses to middle atmosphere waves and tides. Also, a **Mars** atmospheric data base is being assembled with the incorporation of unpublished data sets from various Mariner and Viking instruments. These data will then be incorporated into the empirical **modeling** within **Mars-GRAM**. These **modeling** efforts will provide improved **modeling** of the atmospheric characteristics of **Mars** in support of NASA's Space Exploration Initiative.

B.F. James/ES44
(205) 544-6985
Sponsor: Office of Aeronautics, Exploration and Technology

Data and Visualization Systems Research

Earth-Observing System Data and Information System

MSFC has a major role in NASA's **Earth-observing system (EOS)** program. MSFC is involved in developing, designing, and building the instruments, conducting the sponsored research programs, and collecting and processing the data.

The **EOS** is a comprehensive Earth-observing program scheduled for initial space flight in the late 1990's. NASA plans to launch a series of polar-orbiting platforms furnished with a full complement of instruments that will remotely sense the Earth's surface, atmosphere, oceans, and cryosphere. The primary goal of **EOS** is to create an integrated space-based observing system that will enable multidisciplinary study of the Earth's critical life-enabling, interrelated processes involving the atmosphere, the oceans, the land, and the solid Earth. To accomplish this goal, an extensive data and information system, including a data processing and retrieval system, must be developed. Although the space platforms will not be in operation until the end of the decade, the development of an **EOS Data and Information System (EOSDIS)** has already begun at MSFC.

The EOSDIS is a continually improving system. Throughout the lifetime of the **EOS** program, there will be several major **EOSDIS** versions (software and hardware improvements). These major versions will coincide with milestones in the **EOS** program as a whole. The initial **EOSDIS** (Version 0) is a prototype currently under development and will be based on existing data processing, archive, and distribution facilities at each of the proposed **EOSDIS** centers. The next major version change (i.e., Version 1 scheduled for operation in 1996) will be the first full-functioning system employing all the **EOSDIS** functionality. Subsequent major versions will coincide with milestones of the **EOS** instrument platform.

The EOSDIS overall system is based on an open and distributed architecture. There are seven **EOSDIS** data centers called **distributed active archive centers (DAAC's)**. Each **DAAC** specializes in some aspect of Earth science data processing (fig. 73). The seven **DAAC's** and their Earth science emphases are:

- Alaska SAR Facility (ASF)—Cryosphere studies using synthetic aperture radar (SAR) imagery
- EROS (Earth Resources Observation Systems) Data Center (EDC)/U.S. Geological Survey—Land processes
- NASA/Goddard Space Flight Center (GSFC)—Upper atmosphere, ocean biology, and meteorology
- NASA/Jet Propulsion Laboratory (JPL)—Oceanography and air-sea interaction
- NASA/Langley Research Center (LaRC)—Radiation budget and upper atmosphere
- National Snow and Ice Data Center (NSIDC)—Snow and ice studies
- NASA/MSFC—Hydrologic cycle and the dynamics of water and energy in the climate system.

A **DAAC** is composed of three subsystems that perform separate but integrated tasks. A **DAAC** consists of a product generation system (PGS), a data archive and distribution system (DADS), and an information management system (IMS). Each **DAAC** will receive the unprocessed instrument data and ancillary engineering data through high-speed communication links from the **EOS** ground terminal. The PGS will process the data into geophysical products.

DADS is the archive and distribution component of the **DAAC**. The data will be permanently archived at the site and made available for distribution to the instrument science teams and the user public.

The IMS provides the user interface to the **DAAC**'s. Through the IMS, the scientist can browse through data sets, determine data set availability, and place data orders. Therefore, the MSFC **DAAC** will become a complete data processing, archive, and distribution center.

Each of the **DAAC**'s was selected as a data center because of its commitment, history, and expertise with a particular Earth science subject. Each **DAAC** has an

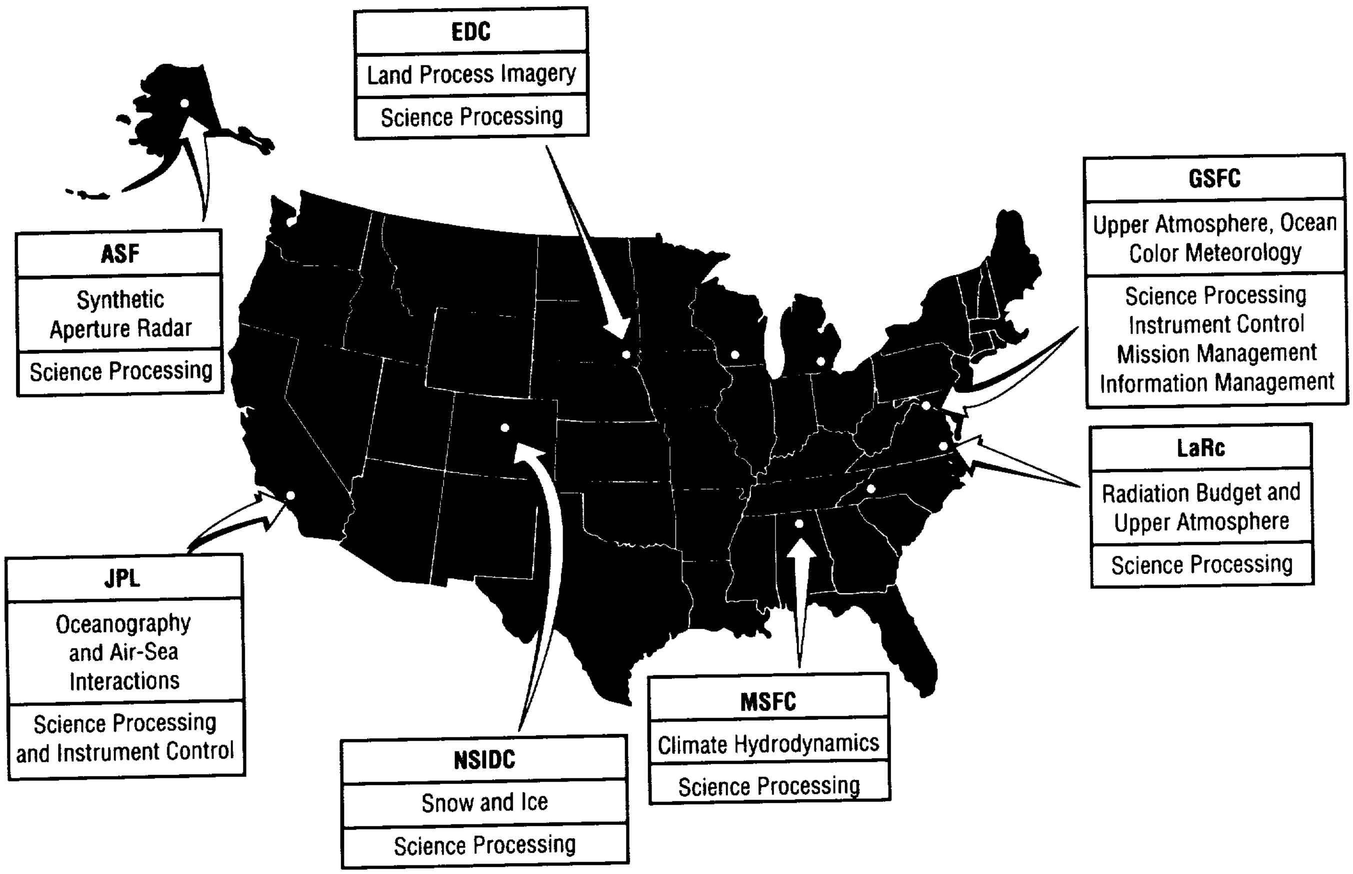

FIGURE 73.—DAAC distribution.

existing data processing system associated with its Earth science expertise. At MSFC, the existing systems that will serve as the baseline for the initial **DAAC** are the WetNet system and the interactive data integration and management system (IDIMS).

WetNet is an interdisciplinary Earth science data analysis and research project with emphasis on the study of the global hydrologic cycle through passive microwave observations. The project goals are to facilitate scientific discussion and collaboration among a selected group of science investigators by providing passive microwave data access and analysis software on a personal computer. There are currently 39 foreign and domestic principal investigators. Each investigator is provided with a WetNet workstation (hardware and software) and a continually updated archived data set.

IDIMS is a menu-driven, data-base information system that allows browsing of data set catalogues and retrievals of archived data to an active on-line state. IDIMS searches data by various criteria, such as common dates, platforms, instruments, etc., and provides summaries of the data sets and their disposition.

The EOSDIS project at MSFC will incorporate the features of WetNet and IDIMS into the design of MSFC Version 0 **DAAC**. In 1991, and following years, WetNet will expand its data base, user base, and functionality. IDIMS will be transported to a UNIX-based operating system and will be integrated with the **information systems** at the other **DAAC**'s.

H.M. Goodman/ES44
(205) 544-8006
Sponsor: Office of Space Science and Applications

Four-Dimensional Man-Computer Interactive Data Access System Technology

The **man-computer interactive data access system** (**McIDAS**) has been under development at the Space Science and Engineering Center (SSEC) of the University of Wisconsin for 20 yr. It has been used for the analysis and display of two-dimensional meteorological data, e.g., satellite imagery, temperature contours, etc. Under support from MSFC during FY91, SSEC has been developing a four-dimensional (4–D) analysis and display tool. Since the Earth-atmosphere system is a volume that is evolving in time, a tool is needed that will allow the scientist to visualize various and multiple parameters from varied viewing geometrics.

The eventual goals of this effort are to design and implement a 4–D data management system within **McIDAS** and to design and develop the software necessary for **interactive** display of Earth system data. These data consist of output from numerical models as well as remotely sensed observations. Tools to render complex 4–D fields of environmental data and long time series of remotely sensed observations are necessary. These tools will allow for the rapid integration of interdisciplinary Earth science data sets into one display. The system will be used for qualitative and quantitative interpretation.

The following tasks have been accomplished during FY91. An **interactive** display package (VIS5D) for 4–D data has been further expanded to allow for the analysis of horizontal and vertical cross section through the volume (a three-dimensional (3–D) spatial domain) on an **interactive** basis. The initial VIS5D routine allowed for the analysis of isosurfaces of user-chosen parameters. These isosurfaces were then depicted as a graphically rendered object. Wind fields are depicted as variable-length trajectory paths, with length proportional to the wind speed. A 3–D cursor has been developed to allow for **interactive** data probing into the data volume. User-placeable text labels have been created that allow the scientists to indicate features.

A tool has been developed for climate data exploration. This tool, while in its infancy, is used to animate and probe long time series of polar orbiter satellite data. It has been developed around a microwave sounder unit temperature anomaly data set. These global data may be viewed on either Mollweide or spherical projections. The application currently handles two channels and may animate at up to 10 frames per second. The application provides a color widget for interactively adjusting the false color of the two channels. The mouse may be used to control panning and continuous zooming of the Mollweide projections, and rotation of the spherical globe. The mouse can also be used to select and drag a geographical point for calculation and display of a time series of image values. The time series display also serves as a context for mouse selection of animation bounds and current displayed time.

Planned activities for FY92 include improved 4–D data **visualization** and improvement of the climate exploration tool. New methods of data depiction will be added to VIS5D, such as retrieving fields of data using the 3–D cursor, and **interactive** placement of wind trajectories using the cursor. Features will also be added to VIS5D to enhance its usefulness for producing publication-quality images. The climate explorer will be augmented to include an ability to select a geographic region and integrate values over the region, as well as an ability to correlate values from different points and regions.

P.J. Meyer/ES43
(205) 544–1654
Sponsor: Office of Space Science and Applications

Building for the Future

TECHNOLOGY PROGRAMS

In a very real sense, building for the future presents a challenge to each member of the MSFC team. Those of us involved directly with technology development at MSFC are resolved to accept the challenge and to continue to lay our foundation straight and strong for the future. In this manner, we build upon our experience of the past as we efficiently and effectively help develop the building blocks of our future in space.

This section depicts representative selections describing exciting technology development in the areas of automated and robotic systems, avionics, data systems, materials and processes, propulsion, space systems, and structures and dynamics. We realize that the future must be built soundly upon the work of today and we offer these topics as indicators of our promise for tomorrow.

G.R. Wallace
Director, Research and Technology Office

AUTOMATED AND ROBOTIC SYSTEMS

ADVANCED X-RAY ASTROPHYSICS FACILITY PERFORMANCE MODELING

The 1.2-m (48-in) diameter outermost pair of **mirrors** for the **Advanced X-Ray Astrophysics Facility (AXAF)** is to be tested at the MSFC **X-Ray** Calibration Facility in summer 1991. The test system that will be used is known as the **verification engineering test article (VETA)**. Measurements of the images at a number of **x-ray** energies are to be used as a check of the **mirror** surface quality independent of the **mirror** surface metrology used by the **mirror** manufacturer, Hughes-Danbury Optical Systems (HDOS). Also, on-orbit performance prediction is to be based both on **mirror** surface metrology and **x-ray** test image measurements. Study is continuing on maximizing the amount of information to be obtained from the test. In particular, one in-house study is continuing concerning the measurement of a focused-ring image that is formed in front of the overall best focus image of the test configuration.

Simulation of the test configuration must take into account many parameters. The effects of the **mirror** surfaces are generally modeled with an exact geometric ray-trace of **mirror** figure combined with the **x-ray scattering** distribution from **mirror** surface roughness. A ray trace program has been written in-house to deal with the narrow annular entrance aperture and the nearly cylindrical shape of **x-ray mirrors**. The **x-ray scattering** distribution is generated with the program EEGRAZ written by Paul Glenn of Bauer Associates. **X-ray** test system parameters include alignment, stability, gravity and thermal surface deformation, source size, source position, source intensity, and detector characteristics. A program has been written to simulate detector scans across the **x-ray** image.

Initial results from the **ring-focus** image study indicate that detector scans across the ring-image annulus are sensitive to certain variations in surface slope in the plane of incidence of the **x-rays** hitting the **mirror** surface. The surface-slope distribution is important to the resolution of the telescope and can be related to surface measurements. Combinations of data from this test with measurements at the test system's overall best focus are expected to help maximize the amount of information to be obtained from the **x-ray** test.

In addition to the **ring-focus** study, in-house prediction of **x-ray** test performance and on-orbit performance is being compared with performance prediction results from the Smithsonian Astrophysical Observatory and from the contractor team of TRW, Kodak, and HDOS.

Griner, D., Zissa, D., and Korsch, D., "Test Method for Telescopes Using a Point Source at a Finite Distance," NASA Technical Memorandum TM-86523, September 1985.

Zissa, D., and Korsch, D., "Experimental Evaluation of the Ring Focus Test for X-Ray Telescopes Using AXAF's Technology Mirror Assembly," NASA Technical Memorandum TM-86570, October 1986.

Glenn, P., Reid, P., Slomba, A., and Van Speybroeck, L., "Performance Prediction of the AXAF Technology Mirror Assembly Using Measured Mirror Surface Errors," *Applied Optics*, vol. 27, 1989, p. 1,539.

D.E. Zissa/EB23
(205) 544-3486

Sponsor: Office of Space Science and Applications

Anthropomorphic Teleoperation: Controlling Remote Manipulators With the DataGlove

This research evaluates the "**DataGlove**," a lightweight glove input device that can output signals in real time based on hand position, orientation, and movement. The glove's control unit can also output user-dependent, calibrated records of hand gestures.

The **DataGlove** is an innovative, state-of-the-art device that has potential applications in various MSFC programs. However, its capabilities and limitations in the field of **teleoperations** are not currently well understood. Hence, it has not been considered for applications where other more proven technologies are sufficient. In order to surmount this lack of knowledge and nonutilization, it is necessary to both develop an operational data base and demonstrate suitable applications for this innovative technology. As these capabilities are developed and demonstrated, the **DataGlove** may show potential for a number of programs, for example, the Space Station *Freedom* workstation applications (e.g., telescience) where weight and volume are critical.

Following checkout and familiarization in a virtual environment, the **DataGlove** was interfaced with the protoflight manipulator arm (PFMA), a large telerobotic arm with a 2.4–m (8–ft) reach. The PFMA has six degrees-of-freedom (DOF) plus a seventh manually indexable DOF. Subsequently, data were collected comparing the **DataGlove**'s overall capabilities to control a telerobot against currently used **hand controllers**.

The PFMA was under "position" control of the **DataGlove**, i.e., the end effector would "puppet" the movement of the **DataGlove**, translating along and/or rotating about the X, Y, and Z axes as the **DataGlove** moved along and/or about these same axes. Three gestures were employed in this study. Throughput of commands for these motions are enabled by bending the thumb. This gave added assurance that only hand movements that were intended as control inputs were, in fact, acted upon. The two other gestures selected gain for the system. One finger extended was for low gain; two fingers selected meant high gain.

Data on operator performance on the PFMA using "standard" **teleoperation** input devices have already been collected under another project. These data will be compared to **DataGlove teleoperation** performance. Data analysis is under way. Preliminary results indicate that not only can the **DataGlove** be used as a **teleoperation** input device, but that it is a very capable, natural, and intuitive interface for **teleoperation**. The training period to proficiency is relatively short and the task completion times and accuracy compare favorably to the more commonly used **teleoperation** controllers.

Work with the **DataGlove** will continue within the Man/Systems Integration Branch. There are currently two applications being planned. One is similar to this project in that it involves **teleoperations**. In this case, however, the telerobot is a small, rack-mounted robot rather than the large PFMA. The major differences are in scale and required dexterity. This robot is for payload operations and the project would explore onboard and "telescience" capabilities and limitations (e.g., time delay). The second project incorporates the **DataGlove** system as a key component in a virtual reality (VR) system. The VR system can be used not only for "virtual" **teleoperation** applications, but also for design and development activities, thus enhancing the efficiency of the development process and the quality of the design product.

J.P. Hale/EO23
(205) 544–2193
Sponsor: Center Director's Discretionary Fund

Centerline Imaging Module for External Grasping End Effector

This Small Business Innovation Research (SBIR) project will develop mechanical packaging of compact **video** imaging and lighting systems that can fit within existing external grasping **end effectors** and are adaptable to other **end effector** configurations including laser-automated guidance sensing. The first prototype imaging module (fig. 74) incorporated several subminiature incandescent bulbs, allowing direct vision of the target pin as it enters the cavity before the inflated bladder grasps it. Later test units can be equipped with laser diodes and fed into the **video** processor. The small size of the test units will allow easy integration into other applications and robots that require direct vision of the structure being captured or probed and will enable safer, more reliable rescue of free-flying satellites and apparatus.

T.C. Bryan/EB24
(205) 544–3550
Sponsor: Office of Commercial Programs, Small Business Innovation Research

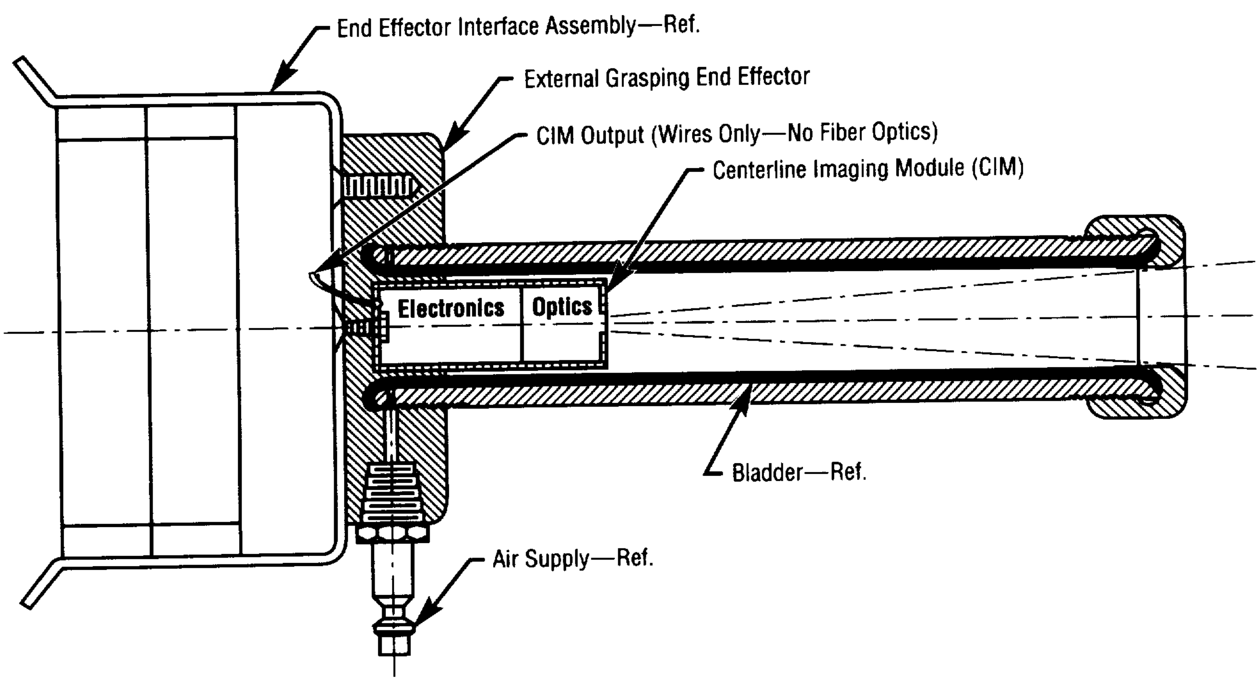

Figure 74.—Concept centerline imaging module.

Control Electronics Assembly for Automation of a Three-Point Docking Mechanism

The purpose of the control electronics assembly (fig. 75) is to provide automatic control and operation of the **three-point docking mechanisms (TPDM's)** latches during a **docking** maneuver. Requirements on the **TPDM** latches during a **docking** maneuver are to sense payload trunnion presence and direction, capture and containment of trunnion in 3.5 s or less, and close latch and preload in 60 s or less.

The objective is to fully automate the operation of the **TPDM** latches during a **docking** sequence. Each one of the three latches (fig. 76) consists of a direct current (dc) motor/dc tachometer combination for rate control, and uses a pair of **opto-electronic** sensors to provide trunnion presence and direction of travel indication. In addition, the latches are also configured to provide claw position indication by means of a rotary pot, and trunnion hard dock (locked) indication by means of a linear pot. Each one of the latches has its dedicated motor control and display electronics and can be controlled individually or simultaneously. Motor rate commands for trunnion capture and latch closure are issued independently and are front-panel adjustable.

Prior to a **docking** maneuver, the latches are preset to close and, as soon as trunnion presence is indicated by the **opto-electronic** sensors (i.e., both light beams broken), the motor is commanded to close the latch at the present "capture" rate. Should the sensors detect the trunnion escaping the capture envelope before the end of the capture sequence, the motor is commanded to open the latch. Once the capture sequence is completed, the motor closes the latch at a preset "close" rate until a hard dock indication is given by the linear pot, at which point the motor is turned off. To release a trunnion, an open command is issued at which time the motor fully opens the claw and then stops. The control electronics are configured to operate and control the latches by means of its front-panel functions or from a remote terminal.

J. Montenegro/EB24
(205) 544-3514
Sponsor: Office of Space Flight

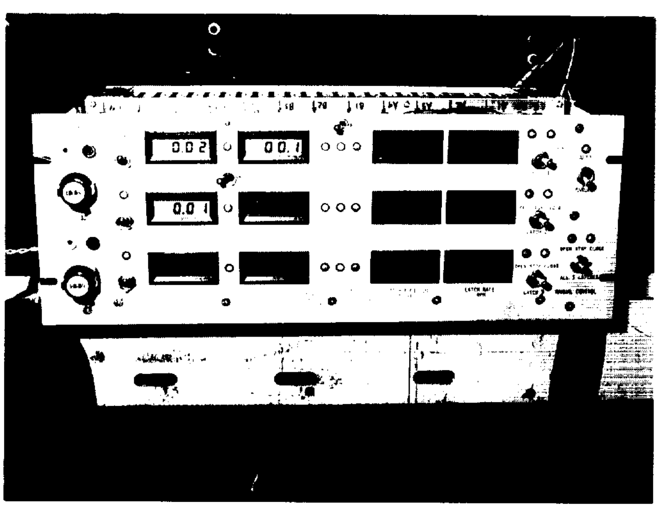

FIGURE 75.—Control electronics assembly.

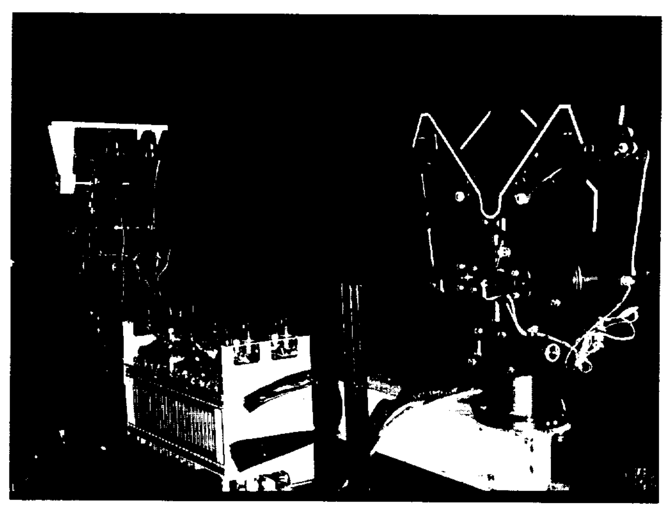

FIGURE 76.—TPDM latches.

Development of Telerobot Hands

This is a phase II Small Business Innovation Research (SBIR) contract that started in November 1989 and concludes in November 1991. This SBIR effort will develop, test, and deliver two servo-controlled **anthropomorphic telerobot** hands and appropriate controlling software. The hands will consist of two fingers and an opposing thumb whose joints will be driven directly. Each finger is an interchangeable bolt-attached module to facilitate low-cost maintenance. A glove unit will also be designed for the hand.

The **telerobot** hand's grasping capabilities are greatly improved through the use of the specially designed glove. The glove, designed by ILC Dover, consists of a rubberized palm and fingers (fig. 77). Micro Mo is the contractor supplying the motors utilized in these **telerobot** hands. Several patents could result from this contract. A patent has already been filed for the miniature linear actuator used in the hand and wrist. When design and development are complete, the **high-dexterity** hand (fig. 78) will have several applications including space station repair, satellite servicing, and even hazardous material handling.

Rosheim, M., proposal and monthly progress reports, Ross-Hime Designs, Inc., 1313 5th Street, SE, Minneapolis, MN 55414.

P.J. Nelson/EB24
(205) 544–3645
Sponsor: Office of Commercial Programs,Small Business Innovation Research

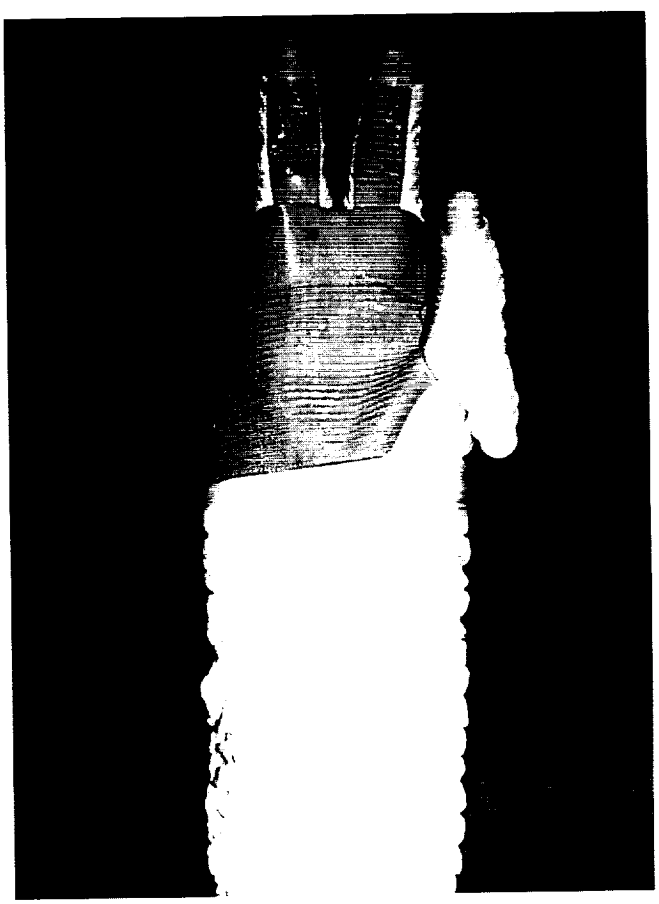

FIGURE 77.—The telerobot hand and glove, which is designed by ILC Dover.

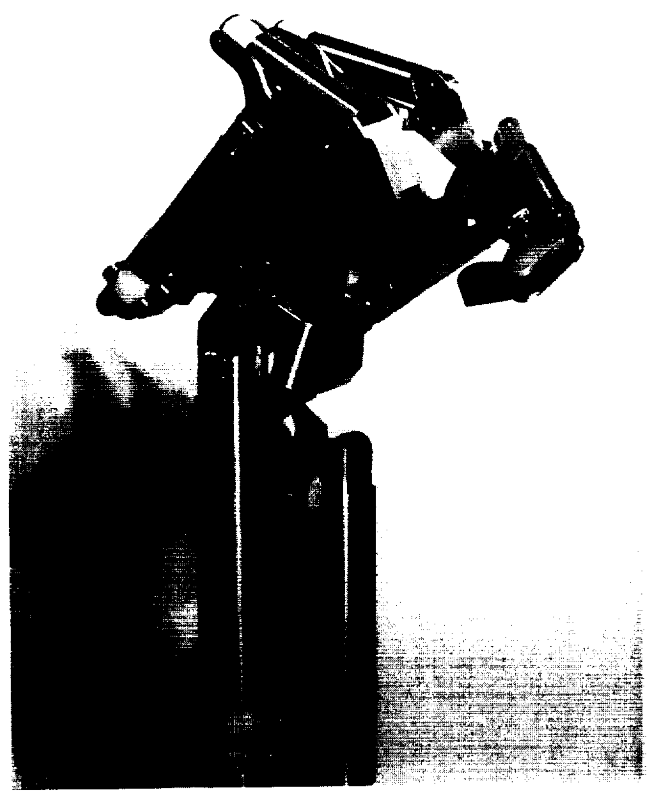

FIGURE 78.—High-dexterity telerobot hand.

ORIGINAL PAGE
BLACK AND WHITE PHOTOGRAPH

Environmental Control and Life Support System Model-Based Diagnosis

In this third year of the Space Station *Freedom* **environmental control and life support system** (ECLSS) advanced automation project, operational models of a water recovery subsystem for use by **model-based diagnosis** software have been developed at MSFC. The model-based reasoning algorithm analyzes this model, which helps in the automatic detection, diagnosis, and prediction of faults. This software forms the basis for an **ECLSS** health maintenance system. Plans this year include demonstration of the automatic fault detection and diagnosis capabilities using **ECLSS** test-bed operational data.

The models (fig. 79) consist of complex structural and behavioral relationships of the subsystem's components. Faults are detected by noting discrepancies between the subsystem and model sensor values. Fault diagnosis procedures list the parent components of the faulty value, a fault candidate list. Various operations are performed on the fault candidate list, including model inversion, to remove suspected components from the candidate list. A candidate list of one component is declared to be the faulty component.

A unique goal of the **ECLSS** health maintenance system is to include chemical and biological recombinations of the air and water recovery systems in the fault diagnosis processes. Innovative and intuitive graphic user interfaces are to be used to display system, as well as model, information to the test and/or ground-support operator.

B.D. Dewberry/EB42
(205) 544–4247
Sponsor: Office of Space Flight, Space Station *Freedom* Advanced Development Program

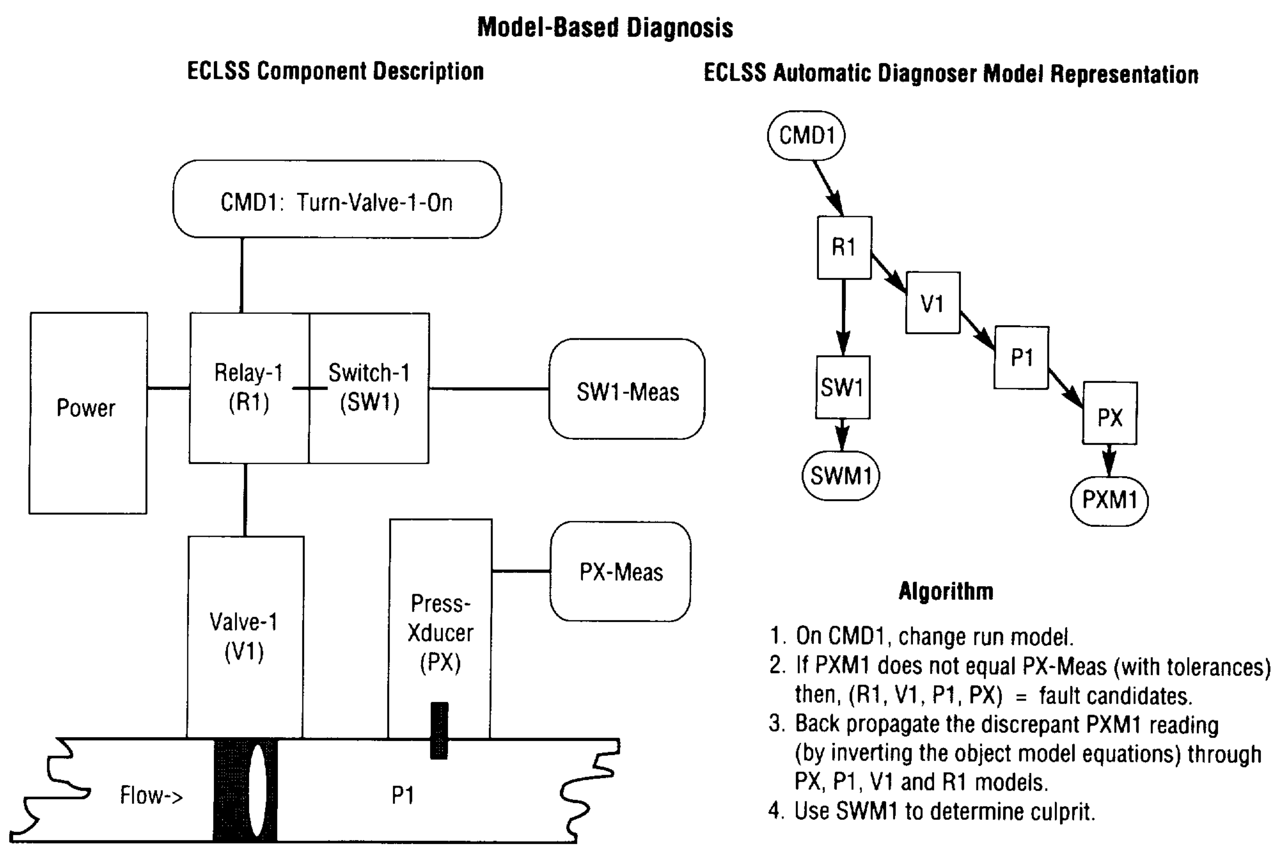

FIGURE 79.—The environmental control and life support system (ECLSS) advanced automation project.

Flexible Agricultural Robotics Manipulator System (FARMS)

A technology utilization project was established with MSFC and the University of Georgia (UGA) to develop an Earth-based, **robotic** end effector to process live plant (geranium) material that will (1) improve **productivity** and efficiency in the agricultural field (i.e., commercial nursery and greenhouses), and (2) apply this technology to NASA's presence in space, including permanently manned space stations and manned planetary communities requiring large-scale food production needs (e.g., vegetables and fruits) and automated testing of plant growth in space.

Robotics have great potential for enhancing the **productivity** and quality of the U.S. greenhouse industry. Therefore, a **robotic** workcell has been developed at the UGA Experiment Station by Dr. Ward Simonton to process geranium cuttings for propagation. The robot removes cuttings from a conveyer and performs unit operations of leaf removal, stem trimming, stem bend measurement, and plug insertion. A **flexible agricultural robotics manipulator system** (**FARMS**) is being evaluated on its ability to process geranium cuttings because tedious labor required to process these cuttings and the high-volume demand for the plant justifies an attempt to automate this sector of the greenhouse industry. The original end effector in the workcell was a pneumatic, arc-parallel mechanism. Custom fingers of aluminum, spring steel, and rubber performed adequately on cuttings with stem diameters of 6 to 10 mm. No sensing was used. Unsatisfactory aspects of this original end effector included the limited range of acceptable object sizes, variable forces applied to the objects as a function of size and shape, and occasional damage to cuttings.

The development of **FARMS** was a joint effort between NASA/MSFC and UGA. The end effector, along with the microprocessor and software, was designed and developed at the MSFC/**Productivity Enhancement Complex** to perform the following functions:

- Determine the plant cutting orientation (perpendicularity) to the surface (Z-axis)
- Grasp the cutting, using a predetermined, controlled force
- Measure the diameter of the stem
- Measure the mass of the cutting
- Trim unwanted leaves from the plant
- Trim the plant length
- Pass the cutting through "bend measurement" and orient the plant for potting
- Insert the plant in potting trays.

FARMS is composed of three subsystems: a closed-loop, force-controlled, direct current (dc), servo-actuated, two-fingered gripper; an industrial personal computer communications node; and integral fiber optic analog output sensors used for part feature recognition (fig. 80). (The MSFC/UGA end-effector controller (shown as "gripper controller" in the figure) transfers information to and accepts commands for both robot controller and supervisory computer.)

At present, cuttings are manually placed on the conveyor during test cell operations. The conveyor indexes each cutting into the field-of-view of a charge coupled device (CCD) camera, which photographs the part and transmits the vision data to a 32-bit cell computer (Heurikon). The computer calculates the position of the cutting in the XY plane defined by the surface of the conveyor belt. These data are formatted into robot commands and transmitted to the robot, which then moves to a location above the

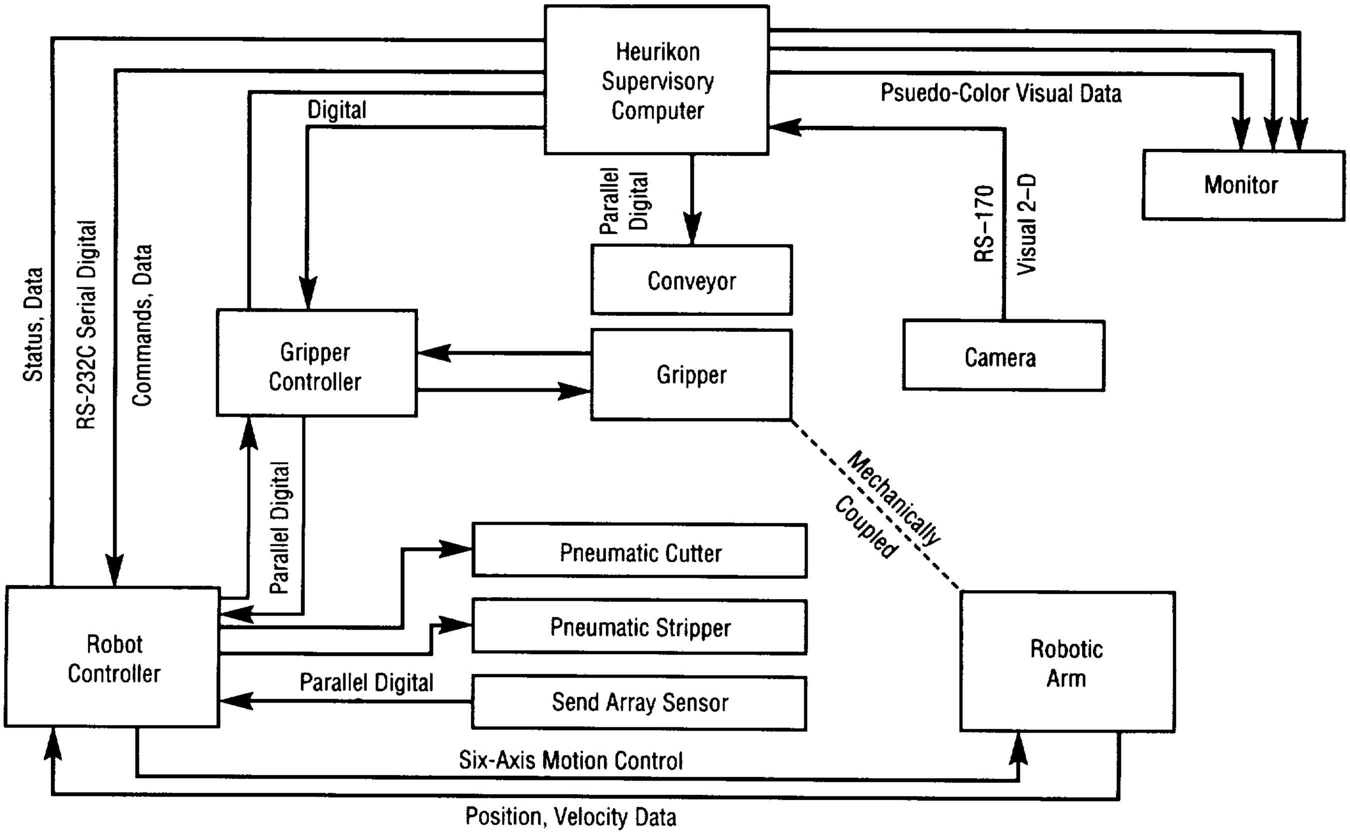

FIGURE 80.—Organization of major components in laboratory.

cutting. The arm searches along the negative Z-axis until the axial center line of the part is sensed using fiber optic distance gauges. The analog output of the fiber optic sensors is sampled by an analog-to-digital (A/D) card residing in the gripper node control. Upon recognition of the part, the gripper closes using force feedback from a load cell internal to the gripper. Once the programmed force setpoint is obtained by the gripper, the resulting finger opening is stored by the gripper node control. These system caliper data are available to the computer when needed.

The part is grasped by the gripper and carried by the arm to three fixtures that act as second hands for the robot. The first fixture removes any petioles at the base of the stem, while the second fixture trims the base of the stem. The part is then placed in a third fixture on an electronic balance. The balance is polled for the mass of the part by the gripper node control, while data are also made available to the Heurikon computer when needed. The gripper is closed under force control for a second time, grasping the part by the gripper, and carrying it by the robot arm to a stem alignment measurement station. Data from this station are used by the Heurikon to command the robot to correctly place the stem into a potting tray. Upon completion of this cycle, the gripper is "homed." The next cutting is then positioned under the camera by the conveyor and the process is repeated.

Through cooperative design, fabrication, development, testing, and evaluation of the force sensing **robotic** gripper system by NASA and Martin Marietta personnel at MSFC, the implementation of the gripper system into UGA's **robotic** workcell was successful. Test results indicate that the **force-sensing** gripper does not crush or bruise plants. The results reflected a full 90-percent successful robot cycling, although the photoelectric sensors slow the robot's cycle time by 1 to 2 s. This latter effect gives the workcell a cycle time of 8 to 9 s with sensors operating.

Simonton, W., "Robotic End Effector for Handling Greenhouse Plant Material," ASAE Technical Paper No. 097503, 1990.

P.S. Gill/EH44
(205) 544-2557
Sponsor: Office of Commercial Programs,
Technology Utilization Office

In-Flight Optical Leak Detection

Presently, there is no real-time propellant **leak detection** capability that exists for implementing closed-loop control during flight. Also, there is no ground-based propellant **leak detection** capability for flight readiness firing (FRF) with a leak location ability for the space **shuttle** main engine (SSME).

Current leak test procedures of the SSME are limited to ground-based, low-pressure inspections, postflight analysis of sampling bottles mounted in the **shuttle** engine compartment, and mass spectrometer readings taken during FRF. In-flight parameters, such as pressure, temperature, and residual gas concentrations, were obtained from data collected during **shuttle** flights using the gas bottle technique for **leak detection**; the gases in the aft fuselage are sampled at designated intervals during **shuttle** lift-off. This method has obvious disadvantages: it is single-point, it cannot be performed in real time, and it is not continuous.

Studies of many **leak detection** companies were reviewed to determine what types of hydrogen, oxygen, and water vapor detection systems were commercially available for flight-practical **leak detection** capability. Among the 13 different technologies found, 11 could identify and quantify hydrogen, oxygen, or water vapor. The remaining two technologies were unable to distinguish the species of gas they were sensing. Each technology was reviewed for compatibility with in-flight environmental conditions and additional requirements, such as real-time data analysis capabilities and flight-weight practicality.

Two **optical** techniques were identified and evaluated—**optical** absorption and **Raman** scattering. These techniques are not commercially packaged for **leak detection**, but do offer the potential of overcoming the limitations of existing techniques, and can be adapted to near real-time imaging or scanning.

Optical absorption employs a camera for imaging a leaking gas, and a light source that emits radiation at wavelengths that are strongly absorbed by the leaking gas. The beam of the light source is spread to illuminate the entire test area. A camera views the illuminated inspection area for any leaking gas. Any leaking gas absorbs the light energy and appears as a black cloud to the camera. An advantage of an **optical** absorption system lies in its ability to remotely examine large areas, which leads to pinpointing and quantifying leaks in real time. The only light sources identified for this technique would add impractical weight to the flight. This **optical** absorption method was abandoned for the **Raman** scattering technique, which was determined to be the most promising in-flight **leak detection** method.

This **optical** technique—the Raman scattering technique—is based on inelastic collisions between photons and the leaking gas molecules from which the **Raman**-scattered photons' wavelengths are shifted by an amount dependent on the cross section of the gas molecule with which they collide. The intensity of the **Raman**-scattered light provides a measure of gas concentration. This technique has the advantages of being gas-selective and pressure- and temperature-insensitive, and of providing real-time scanning or imaging capabilities. Although the **Raman**-scattered signal is very small in comparison to the intensity of the excitation source, appropriate filtering and signal processing can be employed to discriminate the **Raman** signal from any background light.

Tests were performed to measure the performance of the test fixture in detecting the presence of hydrogen. In the first set of tests, both illumination of the sampling region and collection of the scattered light were performed without the use of fiber optics. In the first of these tests, **Raman** scatter was collected from hydrogen at a total pressure of 1 at (760 torr). A strong signal corresponding to the **Raman** scatter off of hydrogen was detected at the predicted wavelength of 683 nm. At a chopper frequency of 2 kHz and a time constant of 1 s, with an illumination power of 140 mW, a signal-to-noise ratio of approximately 100 was realized. In a similar test, the holographic interference filter and the notch filter were inserted into the **optical** beam train and the entire sensitivity region of the detector was scanned to demonstrate that the only signal reaching the detector was due to **Raman** scatter from hydrogen.

Other tests demonstrated laser illumination via fiber-optic cable and fiber-optic collection. It was shown that any spontaneous or stimulated **Raman** scattering from the fiber core or cladding, or any fluorescence that might have arisen from the laser light passing through the cladding, had no material effect on the signal. As expected, the signal-to-noise level, even with the fiber-optic collection of the **Raman** scatter, was excellent.

Ongoing efforts include testing of the system to improve signal levels using fiber-optic illuminations and the fiber-optic collection without the monochromator in the beam train. With development of remote, **optical** leak measurement technologies, such as **optical** absorption and **Raman** scattering, these techniques can provide high-speed, accurate, and reliable automated **leak detection** systems that can achieve dramatic reductions in inspection times and drastically improve the reliability of in-flight leak monitoring of liquid propellants to ensure a more reliable **leak detection** system for launch readiness, in-flight monitoring, and documentation of space transportation system hardware.

M.L. Johnson/EB22
(205) 544–5519
Sponsor: Office of Aeronautics, Exploration and Technology

Intelligent Processor for Space Station Life Support

The first year of this Small Business Innovation Research contract proposes to prove the functionality of artificial **neural network** software algorithm implementation in Space Station *Freedom's* **environmental control and life support system** (ECLSS). The instrumentation in the **ECLSS** that gives multiaspect, signature-like properties has been targeted for prototype **neural network** analysis. These specific **ECLSS** applications are gas chromatography/mass spectrometry (GCMS) analysis and multiaspect fire detection instrumentation synthesis.

Significant progress has been made in analysis of GCMS mass spectra. Networks have been taught to recognize nominal cabin air makeup and to classify regenerated water compound test data into percentages of major categories (ketones, alcohols, etc.).

The GCMS spectra mass per charge (m/z) ratios are input into the network (fig. 81). Three-, four-, and five-layer back-propagation learning networks have been used to

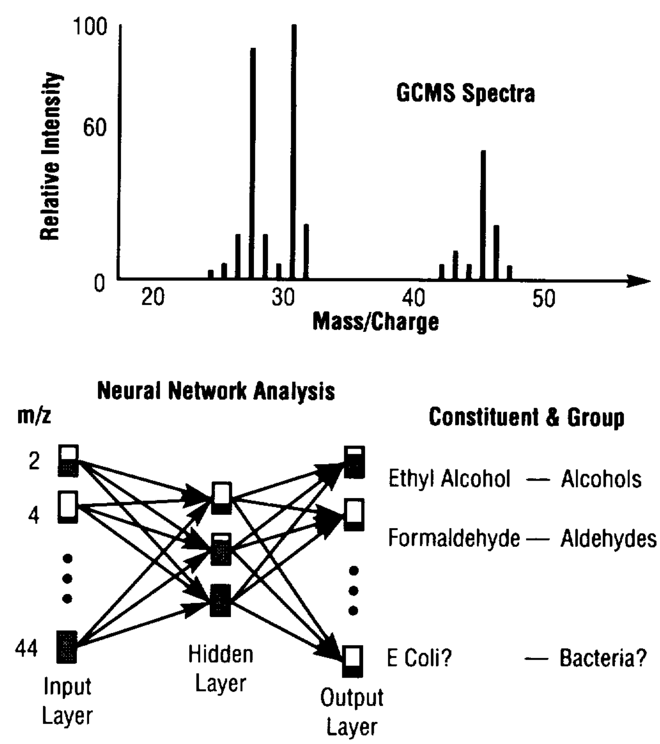

FIGURE 81.—Neutral network analysis of GCMS spectra.

determine the learning speeds and errors encountered in this application. A properly trained network is expected to output the specific constituents and/or categories of the sample from input of mass per charge ratios. The value gained by **neural network** analysis over traditional statistical table lookup methods is the speed and accuracy of the analysis when the sample is full of diverse unexpected compounds. Bacterial density information, if embedded in the GCMS spectra, may also be detectable by this analysis.

The gathering of data for real-time synthesis of multiaspect fire detection is continuing. Timelines of data from smoke (particulate), thermal, and light (ultraviolet, infrared, (IR) and visible) are being gathered for synthesis (categorization) of the type and starting time of a fire. The network is trained using typical fire sensor signatures (fig. 82). The visible, IR, particulate, and thermal aspects of fires are known to differ over time as a function of fire type. For example, a paper fire smolders at first, releasing more IR energy, until it flames, when most of the fire's energy is released through visible light.

A properly trained network may accept as input the relative intensities of fire aspects and produce the classification of the fire along with its starting time. This process should also be helpful in alleviation of false alarms, which normally have specific recognizable characteristics such as step functions.

B.D. Dewberry/EB42
(205) 544–4247
Sponsor: Office of Commercial Programs, Small Business Innovation Research

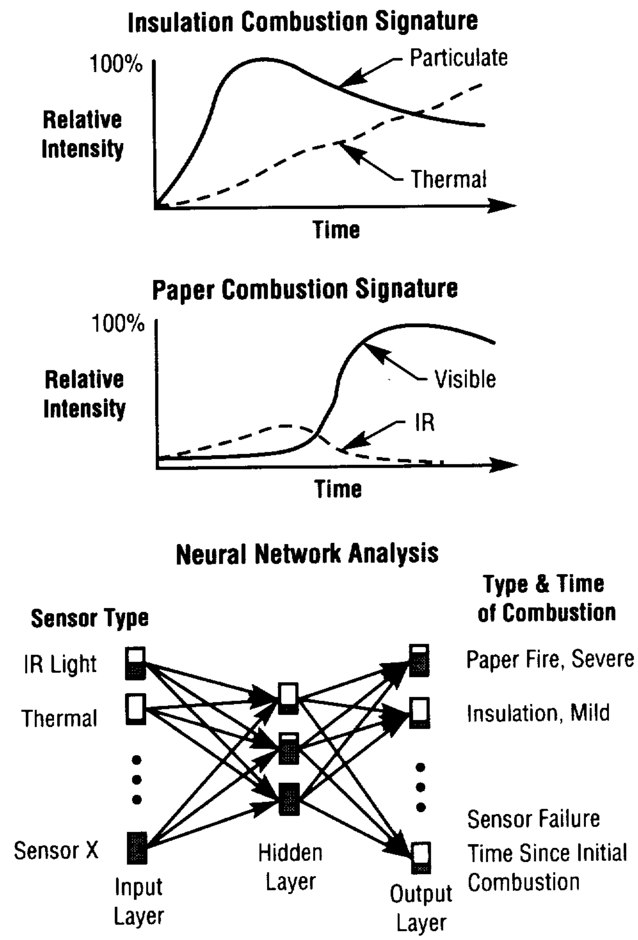

FIGURE 82.—Neutral network synthesis of combustion signatures.

Mobile Robotic Hydroblast System

The mobile **robotic hydroblast** system (MRHS) (fig. 83), which is presently in the certification and implementation stage at Kennedy Space Center, has recently been developed by NASA and United Space Boosters, Inc. (USBI), at the Productivity Enhancement Center at MSFC. The MRHS was designed to solve problems associated with manual refurbishment. The system was developed for automated removal of the thermal protection system (TPS) from the space shuttle solid rocket boosters prior to disassembly. The TPS has to be removed from field joints, the aft skirt interior, the trailing edge, the system tunnels, external tank attach ring, and other miscellaneous areas in order to expose all fasteners. The system had to be designed for minimum impact on the existing facility, yet allow access to geometrically hard-to-reach areas imposed by the sheer size of the flight hardware. The robot's extensive path **programming** also had to be developed at MSFC (700-mi away from the flight hardware) without any physical mock-up. This would not have been possible without the availability of state-of-the-art **graphic simulation/offline programming** technologies.

The MRHS was designed and built as an integrated system consisting of a six-degree-of-freedom articulated robot mounted on a transportable platform. The vehicle can be raised up to 33–in off the ground by four hydraulic cylinders for extra reachability. The carrydeck cabin was also modified to accommodate two operators and a karel robot controller. Air conditioning and soundproofing were added to the cab's watertight Plexiglas, creating an enclosure that protects equipment, operators, and the robot controller from heat, humidity, and debris. The robot itself is a GMF S–420, selected for its 120–kg (264–lb) payload capability and large reach envelope. It was waterproofed and given compatible subsystems such as a robust and adjustable end effector for high-pressure water delivery through either a dual-orifice rotary nozzle or a single-orifice nozzle. The rotary nozzle consists of twin jets fixed on a rotating hub that turns by the back pressure of the waterjet. Remote-controlled diversion valves enable easy selection of either nozzle or of the system's "dump line." Also added were an inclinometer for deck leveling, a pressure transducer to monitor water pressure, and a displacement transducer to input the deck height to the robot controller for verification and added safety. Any parameter beyond acceptable range causes an interruption so the controller can take appropriate action to safeguard personnel and flight hardware. Such action could involve diversion of water to the dump line, stopping the robot's motion, or prompting the operator for some verification.

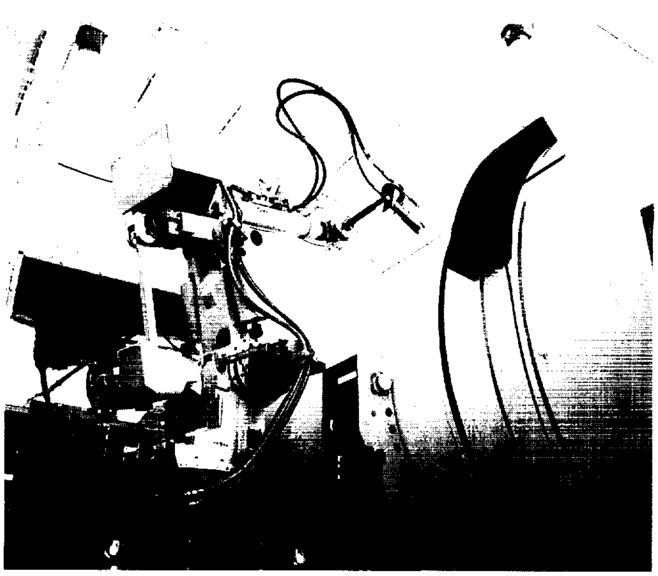

FIGURE 83.—Mobile robotic hydroblast system.

Graphic simulation has been essential for design and development of the MRHS. It has been effectively employed from the robot selection phase all the way to the establishment and orientation of tag point coordinates, as well as verification of arm reachability and evaluation of collision detection.

The MRHS becomes a portable robot that can endure long-term operation under harsh conditions, its human occupants safely activating any 1 of 48 robot path programs for a given location to remove TPS while monitoring the robot's operation. This unit, the first of its kind, can be conveniently maneuvered around the boosters while its **robotic** end effector holding the nozzles withstands the delivery of 22 gal of water per minute under 15,000–lb/in^2 pressure. The nozzle assembly moves through a smooth preprogrammed robotic path while removing the TPS with increased accuracy. Personnel and flight hardware safety is increased while, at the same time, refurbishment time is decreased. It has been conservatively estimated that the system can save 20 h of serial time per flight set. This equates to a 40–percent reduction in TPS removal time prior to SRB disassembly at estimated savings of $67k per launch.

M.K. Babai/EH44
(205) 544–2795
Sponsor: Office of Space Flight

Modeling of Lasers

Development of computer codes to model pulsed carbon dioxide (CO_2) **lasers** continues. A general purpose diffractive optics program (DOC3D) has already been written. DOC3D has been used to model a number of different types of optical **resonators**. An example is the self-filtering unstable **resonator** (SFUR), which uses an internal aperture to filter out noise. The intensity profile for SFUR is shown in figure 84. Contrasted to an ordinary unstable **resonator**, SFUR has a smooth intensity profile. Also developed is a computer code (DOC2D) for two-dimensional modeling the effects of **laser**-induced medium perturbations (LIMP). The deleterious effect of LIMP on **laser** frequency for SFUR is shown in figure 85.

Up to now, a simple saturable gain model has been used to do loaded cavity calculations. A **kinetics** code is now being developed to do a realistic simulation of the processes that lead to **laser** gain. Also being developed is a code to model the effects of the discharge on the **gas dynamics** for the flowing gas. The three computer codes—the **resonator**/optics code, the **kinetic** code, and the **gas dynamics** code—will be linked together for a complete simulation of a **laser**.

M.E. Smithers/EB23
(205) 544–3477
Sponsor: Office of Aeronautics, Exploration and Technology

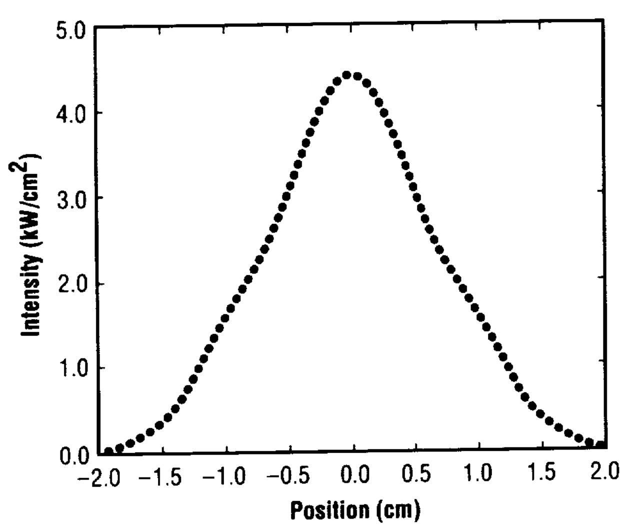

FIGURE 84.—SFUR loaded cavity.

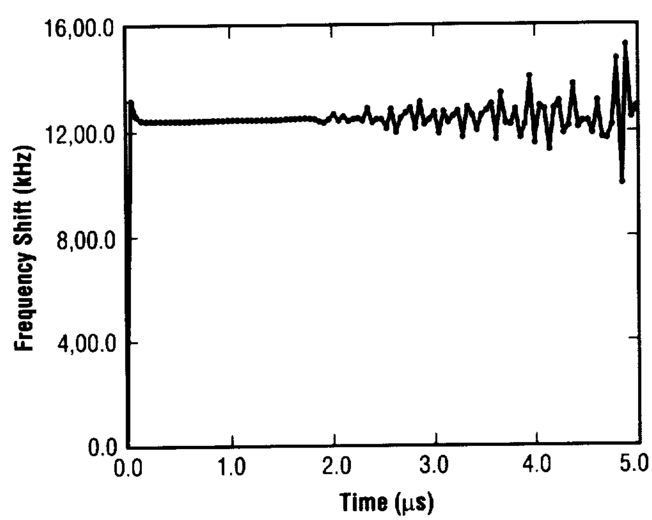

FIGURE 85.—SFUR LIMP.

ROBOSIM: A Robotic Simulator

ROBOSIM is a NASA-developed, graphics-based **robotics** simulation software package for support of both industrial and aerospace design applications. During the past year, a number of achievements have been made by the research contractor working in this area, including the development of a simulation library, a graphical editor, and the porting of ROBOSIM into the Intergraph Corporation's **computer-aided design/computer-aided manufacturing** (CAD/CAM) environment being used at MSFC.

Porting ROBOSIM to an Intergraph workstation consisted basically of two tasks: the porting of the basic ROBOSIM kernel and the porting of the simulation library. The basic ROBOSIM kernel port consisted of converting the X-windows graphic-display software, as used with the contractor's Hewlett-Packard HP350SRX workstation, to the Environ V windowing environment used with the Intergraph workstation. This consisted primarily of translating between the Move and Draw commands of the two windowing environments. The simulation library port primarily involved code changes to take advantage of the specific three-dimensional drawing routines and the input-output devices available on the Intergraph platform. This software conversion/translation has resulted in the availability of the ROBOSIM program and its simulation library on the Intergraph platform/environment used at MSFC.

Planned ROBOSIM development activities include: extended testing and demonstration of the ROBOSIM application on the Intergraph workstation, implementation of improvements and new features of the ROBOSIM advanced automation test-bed (AAT) on the Intergraph workstation environment, and development of further AAT interfaces to ROBOSIM.

ROBOSIM was used to develop industrial robotic applications for a variety of shuttle systems, control algorithms for optimal control of robotic welding systems, and modeling of robotic systems control concepts for use on **Space Station *Freedom***. The objective of this project is the further development and transfer of ROBOSIM technology for distribution within NASA, as well as among other government, industry, and academic centers.

M.K. Smith/EB44
(205) 544–3813
Sponsor: Office of Commercial Programs, Technology Utilization Office

Robotic Eddy Current Inspection System

With the increased use of carbon-carbon and graphite-epoxy materials in the aerospace industry also comes a demand for more sophisticated methods of **nondestructive evaluation** (NDE) of these types of materials. The integration of computers into **NDE** equipment, coupled with automated methods of scanning hardware, allows both inspection and interpretation of results to be performed on-line in real time. The development of these types of "smart" systems also results in shorter inspection times and a more accurate interpretation of results.

Under the direction of MSFC, The University of Alabama in Huntsville (UAH) has developed a "smart" system for **eddy current** inspection of both carbon-carbon and graphite-epoxy materials and hardware. The complete system consists of a robotic manipulator arm that holds an inspection probe, a turntable that allows automated rotation of cylindrical hardware, an **eddy current** instrument for test signal generation, and a visual interface to display results, all linked together by a supervisory computer that stores all of the test results. When this "smart" system is fully operational, the supervisory computer will also interpret the test results in real time by identifying the type and location of any defects in the carbon-carbon and graphite-epoxy specimens. A new contract has been awarded to UAH for completion of this effort, at which time the system will be turned over to the **NDE** branch at MSFC.

Preliminary laboratory tests have shown that digital **eddy current** testing may be a viable method for in-process monitoring of composite components. Once fully operational, the robotic **eddy current** inspection system will be used to perform analyses of graphite-epoxy and carbon-phenolic raw materials, in-process parts, and finished parts to identify general trends in processed materials, as well as localized changes in conductivity that might indicate changed mechanical or thermal properties. This information will be correlated with **NDE** data from other sources, such as computed tomography and ultrasonics through the integrated **NDE** data evaluation and reduction system (INDERS).

A further contribution of digital **eddy current** testing is expected to be the extrapolation of ply-orientation from three-dimensional readings of directional conductivity. This technique provides critical orientation information in a quantitative format, which can then be used to support thermostructural analyses of as-built components. Preliminary testing with carbon-carbon indicates this information is critical in predicting the failure load of composite rings and cylinders. Efforts to extract ply-orientation effects in wrinkled carbon-carbon cylinders have shown promise, but further development is required.

The information gained from this program will contribute to an increased understanding of the effects of processing on composite material properties and of the way **composite materials** fail.

C.C. Bryson/EH13
(205) 544-2553
Sponsor: Office of Space Flight

Robotic Variable Polarity Plasma Arc Welding

Variable polarity **plasma arc** (VPPA) **welding** allows defect-free welds to be made on aluminum alloys. It is an integral joining process currently used to fabricate the space shuttle external tank (ET). To date, however, VPPA **welding** has been used in production for welds that require only single-axis motion. To realize the advantages of VPPA **welding** on complex weld paths, such as those found on Space Station *Freedom* (S.S. *Freedom*) structures, multiaxis manipulation of the **welding** torch is required. To meet this need, the VPPA **welding** torch and system has been integrated with a six-axis articulated arm robot and a two-axis coordinated part positioner.

The application that fully demonstrates the capabilities of the **robotic** VPPA **welding** system is the S.S. *Freedom* node radial docking port. The radial docking port requires that a weld be made to join the large docking plate forging to a thin skin structure. The contoured weld path that is formed resembles the intersection of two right circular cylinders. Complex manipulation of the VPPA **welding** torch and radial docking port structure are required to perform this weld.

All eight axes of motion of the **robotic welding** system are required to make the radial docking port weld. This requirement is driven by two factors that have a significant influence on the VPPA **welding** process itself. These factors are the need to maintain the **welding** torch normal to the surface of the part and to progress the torch vertically up in relation to the weld path. During **welding**, the part positioner must rotate and tilt simultaneously to introduce the weld path in the desired orientation. At the same time, the robot moves simultaneously in six degrees-of-freedom. The movement of both the robot and positioner provides the necessary motion to progress the torch along the weld joint. Since the robot and positioner are servo-controlled and fully coordinated, the desired **welding** torch travel speed, relative to the weld path, is maintained by the robot system controller.

This application of **robotic** VPPA **welding** to the radial docking port structure is aided by the use of a graphic modeling and simulation system. This computer workstation is used to properly lay out the **robotic** workcell and to simulate the **robotic welding** motion before actually moving the robot and positioner. This is a very proficient way of performing much of the trial and error associated with complex **robotic** motion and results in substantial time savings.

A **robotic** VPPA **welding** cell has been set up at MSFC and is used to successfully demonstrate the radial docking port weld (fig. 86). Likewise, the technology has been transferred to Boeing and demonstrated on a flight hardware configuration. The **robotic** VPPA **welding** system is currently planned for use on approximately one-third of S.S. *Freedom* structural welds, representing seven unique configurations.

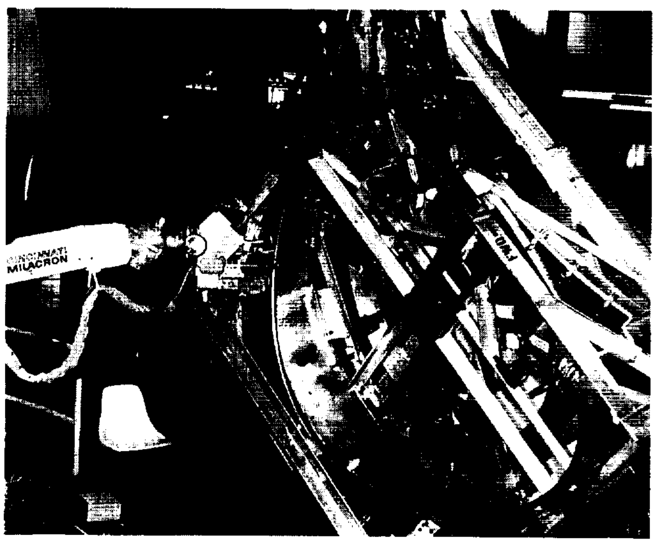

FIGURE 86.—Robotic variable polarity plasma arc welding.

D.S. Hoffman/EH42
(205) 544-2713
Sponsor: Office of Space Flight

Robotics Guidance Systems Using Specialized and Generalized Targets

As more and more robotics tasks are performed in space, robotics guidance using specialized and generalized visual targets may be needed to automate many of these tasks. Automating these tasks will give astronauts more time to perform other tasks. Robotics guidance can be separated into two areas: finding the relative location of the target from the video sensor and controlling the robot to join the sensor with the target.

Robotics control has been around for several years. Research being performed at Cybernet Systems Corporation in Ann Arbor, MI, is concentrating on relative position determination between the sensor and the target. The target itself is a **hologram** of the standard **remote manipulator system (RMS)** target. Object features are located in three spaces and matched to the known object geometry. This can be done by observing multiple sets of identical known features in several sensors. These feature-to-feature-to-object part matches can provide the numerical data needed to compute object position and orientation. While not completely eliminating the need for general feature-based vision, targets like those shown in figure 87 can reduce computation efforts

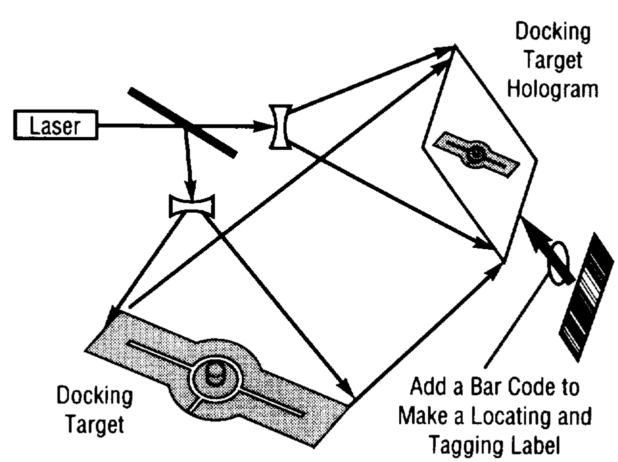

FIGURE 87.—An RMS grapple target and corresponding hologram target.

during feature extraction (i.e., **RMS** target stripes and dots are easier to extract than edges and surfaces of **halftone** objects), and can reduce matching process computations between models and features (i.e., when imaging and processing **RMS** target features, algorithms can be used that are insensitive to other geometric features or false features generated from noise, reducing processing time). Three-dimensional mapping is shown in figure 88.

M.L. Book/EB24
(205) 544–3699
Sponsor: Office of Commercial Programs, Small Business Innovation Research

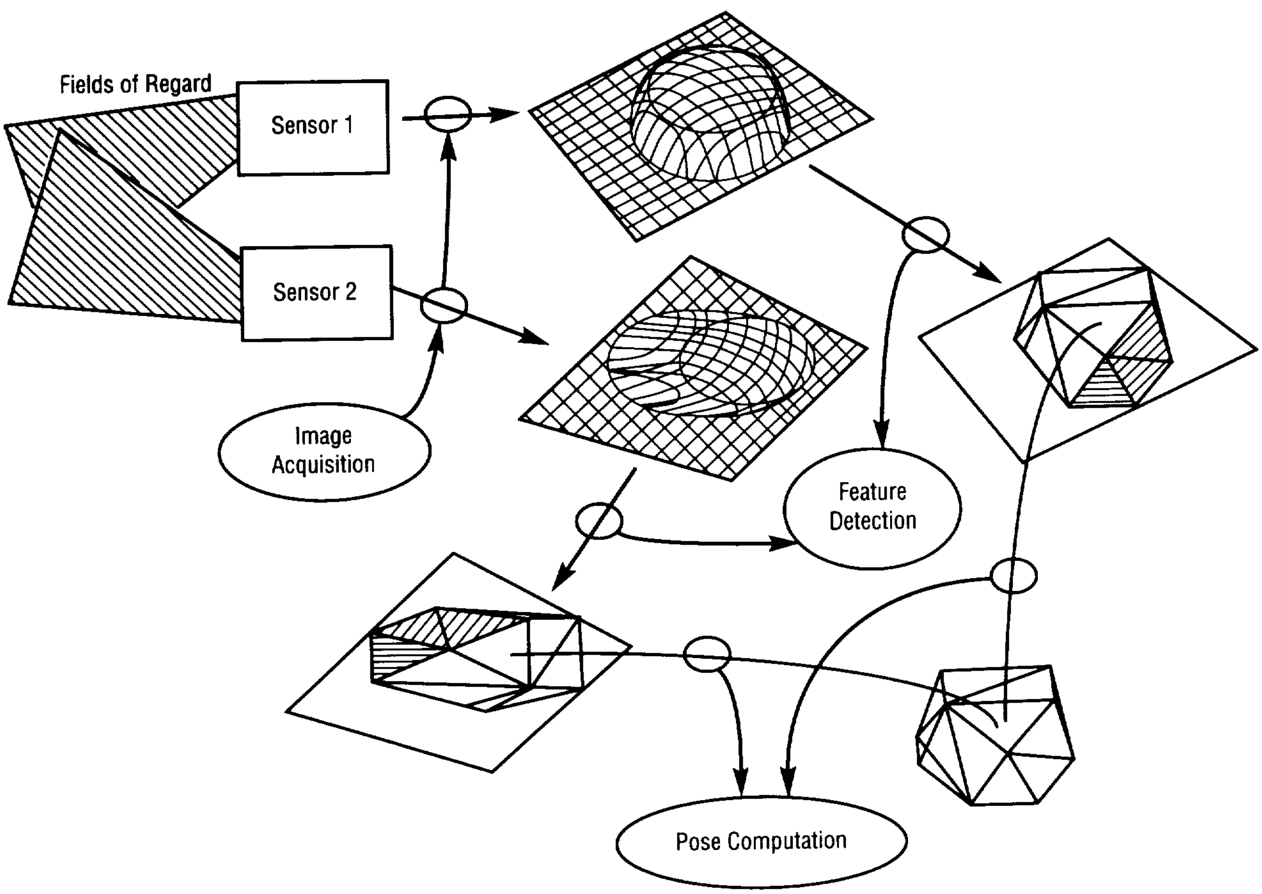

FIGURE 88.— Collocation of features derived from multiple sensors and computer-aided design (CAD) data base-coded object features to compute position and orientation.

Satellite Resupply Docking System Interface

This program is directed toward developing a standard interface to enable a service vehicle to hard dock with and to **resupply** a free-flying spacecraft. The standard interface will allow spacecraft designers, observatory, and military communications to develop and scar their spacecraft for fluid **resupply** and boosting, and allow independent development of a service vehicle such as the cargo transfer vehicle. This interface has commonality with the shuttle flight support system (for **satellite servicing**) and will incorporate flight configuration mechanisms of the orbital maneuvering vehicle (OMV) three-point **docking** (TPD) system and the universal **resupply** interface system as well as a suitable **docking** target for automated rendezvous and **docking**.

Most of the elements of the satellite **resupply docking** system interface are nearly developed. At the cancellation of OMV, the testing and analysis of the TPD interface and mechanisms were nearly complete at MSFC and TRW. MOOG, Inc., has delivered their universal **resupply** interface system (URIS) test unit under MSFC's automated fluid interface system study. MSFC's automated **docking** sensor has repeatedly demonstrated dynamic **docking** with the TPD interface.

This current transportation-supporting development effort is focused on (1) in-house redesign and qualification of the TPD mechanisms and controls; (2) development of **docking** and latching logic; (3) environmental and functional testing of the URIS test unit for electrical, fluid, and cryogenic transfers; (4) integrated ground tests and demonstration; and (5) interface specification and validation. The effort will be coordinated with automated rendezvous and **docking** development and may evolve into a flight experiment to verify and validate the spacecraft **resupply docking** system interface. See figure 89 for placement of TPD and URIS mechanisms within the proposed interface between the satellite and the servicer/tanker.

T.C. Bryan/EB24
(205) 544–3550
Sponsor: Office of Space Flight

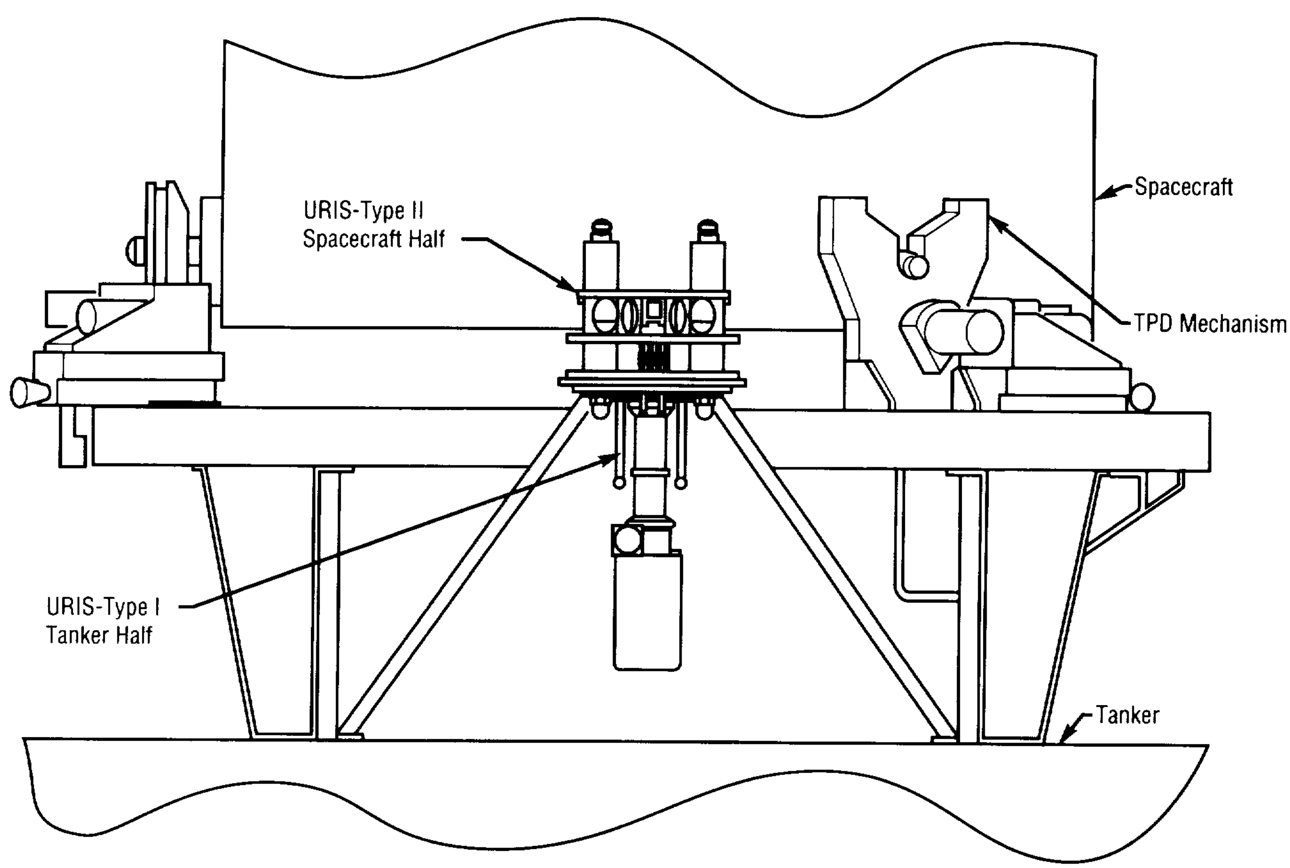

FIGURE 89.—Spacecraft resupply docking system interface.

Self-Contained Miniature Dexterous Hand

This is a phase I Small Business Innovation Research (SBIR) contract. The contract was awarded in January 1991 to Bonneville Scientific of Salt Lake City, UT. The work being performed involves a practical application of **piezoelectric** motors to **robotics**. The end result may lead to an improved end effector design. The purpose of this contract is to demonstrate the feasibility of using a small **piezoelectric** motor within a miniature dexterous robotic hand. An improved end effector design is needed that is small enough to fit in tight areas, has very simple motor construction, is reliable, and has extensive tactile sensing capabilities to allow adaptive grasping of objects. This design could be used in space station experiments and hazardous material handling.

Sufficient clamping torques at 50.6 kg (23 lb) of clamping force with only around 9– to 10–µm displacement in the clamp mechanisms is the objective of this phase I SBIR contract. The **piezoelectric actuators** are 18×2×3 mm. **Actuator** force and displacement values for the **actuators** were specified at 100 V. In this contract, the **actuators** were characterized over the maximum useful voltage range to determine if greater motor performance could be obtained. Figure 90 illustrates the displacement over a 150–V range.

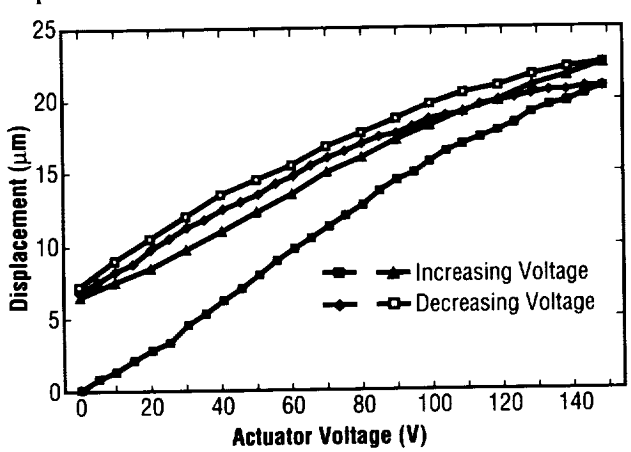

FIGURE 90.— Displacement versus voltage for 18×2×3 mm actuator.

Bonneville Scientific, Inc., bimonthly progress reports, 918 East 900 South, Salt Lake City, UT 84105.

P.J. Nelson/EB24
(205) 544–3645
Sponsor: Office of Commercial Programs, Small Business Innovation Research

Space Station Module/ Power Management and Distribution

The space station module/**power management and distribution** (SSM/PMAD) breadboard (fig. 91) models the power distribution within a Space Station *Freedom* Habitation or laboratory module. In addition to power hardware, the system includes computer control through a hierarchy of processors. The lowest level processor is fast, simple (from a computer standpoint), and switchgear capable of quickly safing the system. The next level contains local load center processors, called lowest level processors (LLP's), which execute scheduling, perform redundant switching, and shed loads that draw more than scheduled power. The level above the LLP's contains a communication and algorithmic controller that coordinates communications with the highest level of control. This level contains three cooperating **artificial intelligence** (**AI**) systems that handle load prioritization, scheduling, load shedding, and fault recovery and management. The systems, working together, provide an excellent venue for developing and examining advanced **automation** techniques.

The work that led to the SSM/PMAD breadboard began in 1984. The present test-bed, which models the Space Station *Freedom* **power subsystem**, consists of three load centers powered by two power distribution control units in a 120–Vdc star bus configuration (fig. 92). The LLP's are 80386–based microcomputers with an Ethernet

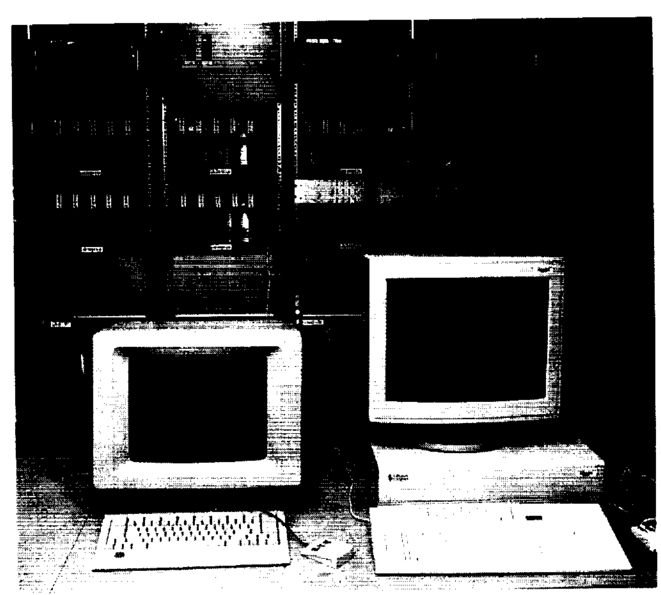

FIGURE 91.—SSM/PMAD test-bed.

communications board. The three **AI** systems are installed on a Solbourne 5/501 workstation and a Symbolics 3620–D **AI** workstation. The user interface and the communications gateway are installed on the Solbourne workstation with all high-level communications being performed on an Ethernet local area network. Two of the three **AI** systems reside in a knowledge-based management system (KBMS) called KNOMAD. KNOMAD makes the knowledge in the system more explicit and groups the knowledge into modular groups of rules. It also serves as an overall framework to expedite improvement of the cooperation between the three **AI** systems in the breadboard. The third **AI** system, which resides in the Symbolics workstation, functions in a server mode under the control of KNOMAD. As a result, the three **AI** systems operate in a near real-time mode and can analyze **power system** problems much faster than a **power systems** engineer(s).

As the breadboard matures, several efforts are under way to make the breadboard even more robust. The first effort involves continuous enhancement of the advanced man-machine interface to make it more graphic and user-supportive. The next effort involves adding intermediate levels of autonomy in order for the system operator to be "in the loop." This will allow an override capability without having the operator to take complete control of the breadboard. Another effort will involve evaluating the system in order push as many functions as possible down the levels of hierarchy. This could help in the reduction of some of the data management requirements for an autonomous system such as the SSM/PMAD. Finally, a link to the Lewis Research Center autonomous **power system** has been implemented with further enhancements being investigated.

Lollar, L.F., "Automating a Spacecraft Electrical Power System Using Expert Systems," NASA Technical Paper No. TP3161, August 1991.

L.F. Lollar/EB12
(205) 544–3306
Sponsors: Office of Space Flight, Space Station *Freedom*, and Office of Aeronautics, Exploration and Technology

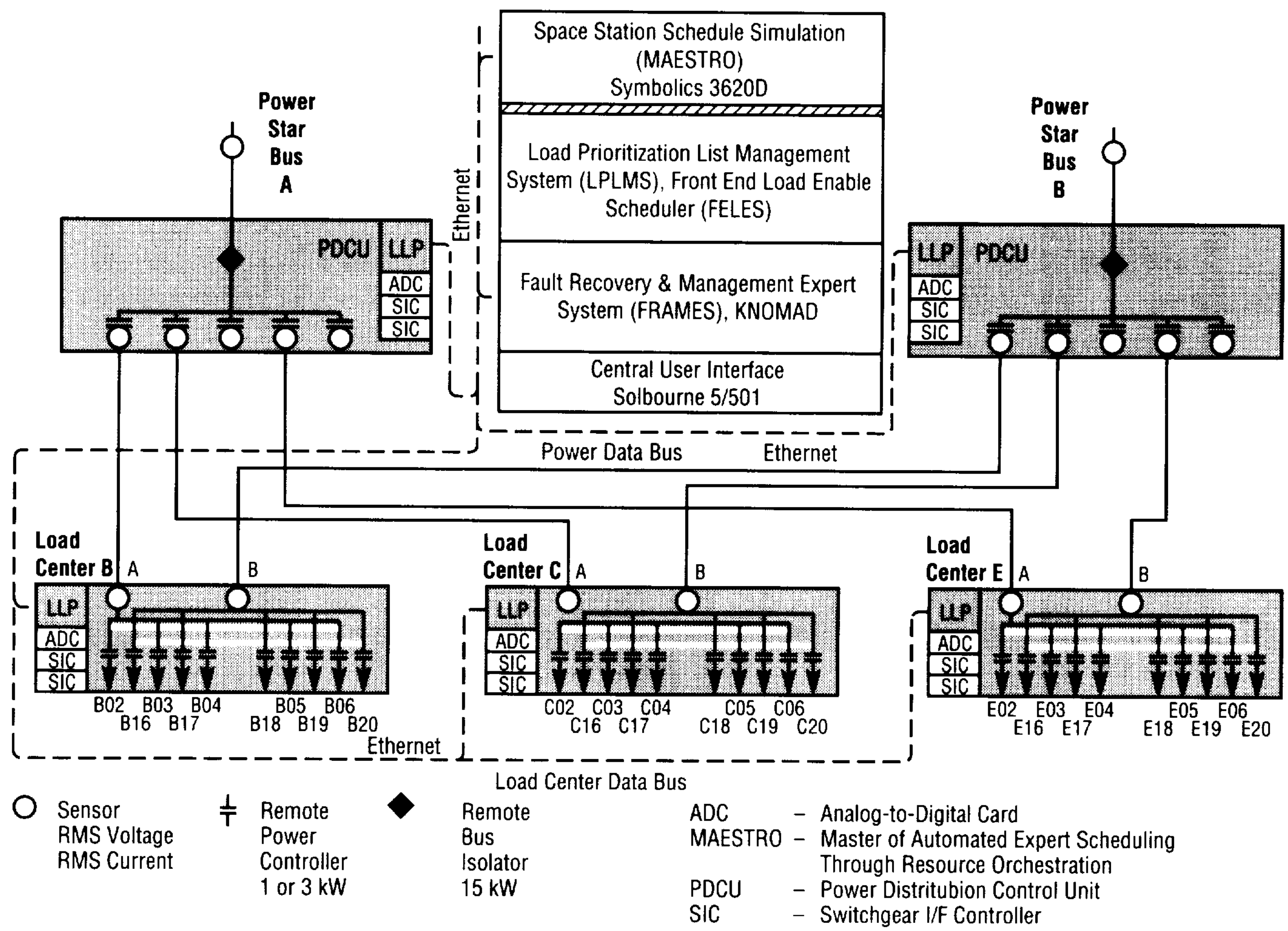

FIGURE 92.—SMM/PMAD system schematic.

Task-Level Planning and Diagnosis for an Intelligent Robot

This phase II Small Business Innovation Research (SBIR) effort by University Faculty Associates (UFA), Inc., will end in June 1991. In the 1990–91 timeframe, the contractor has developed a graphical simulation of a general intelligent **path planner** for robotic **satellite servicing**. Figure 93 shows a user interface window to the **knowledge base** and a view of the satellite model. This simulation has been demonstrated on a Silicon Graphics 4D70 workstation and has been further enhanced by interfacing the planner with ROBOSIM, a dynamic robotic simulation package developed jointly by NASA and Vanderbilt University. The software effort has been developed using the NASA/National Bureau of Standards (NBS) standard reference model for telerobot control system architecture (NASA standard reference model (NASREM) architecture) as a reference hierarchical approach to developing high-level **artificial intelligence** (AI) task planning.

The **path planner** is implemented using a **knowledge base** that keeps track of the robot location, commanded destination for the task, and any obstructing equipment along a path for collision avoidance. This **knowledge base** can be modified for different scenarios and robotic task configurations. Subsystems failure analysis is simulated for three robotic tasks using the **knowledge base** and associated rules in the diagnosis model that is currently being developed. The diagnosis model uses knowledge about mock subsystems such as communications, solar power system, and thermal control system to diagnose likely failures based on symptoms and then plans the path to investigate and repair the failure.

These path-planning and diagnosis modules could be incorporated into a robotic system as a portion of an automated or human-tended servicing system. An intelligent aid such as this, with a properly robust and complete **knowledge base**, could offload some of the simpler, repetitive robotic tasks to a more automated system with the intelligence to maintain system safety. This could improve system efficiency as well as reduce operator fatigue.

C.A. Coker/EB24
(205) 544–3541
Sponsor: Office of Commercial Programs Small Business Innovation Research

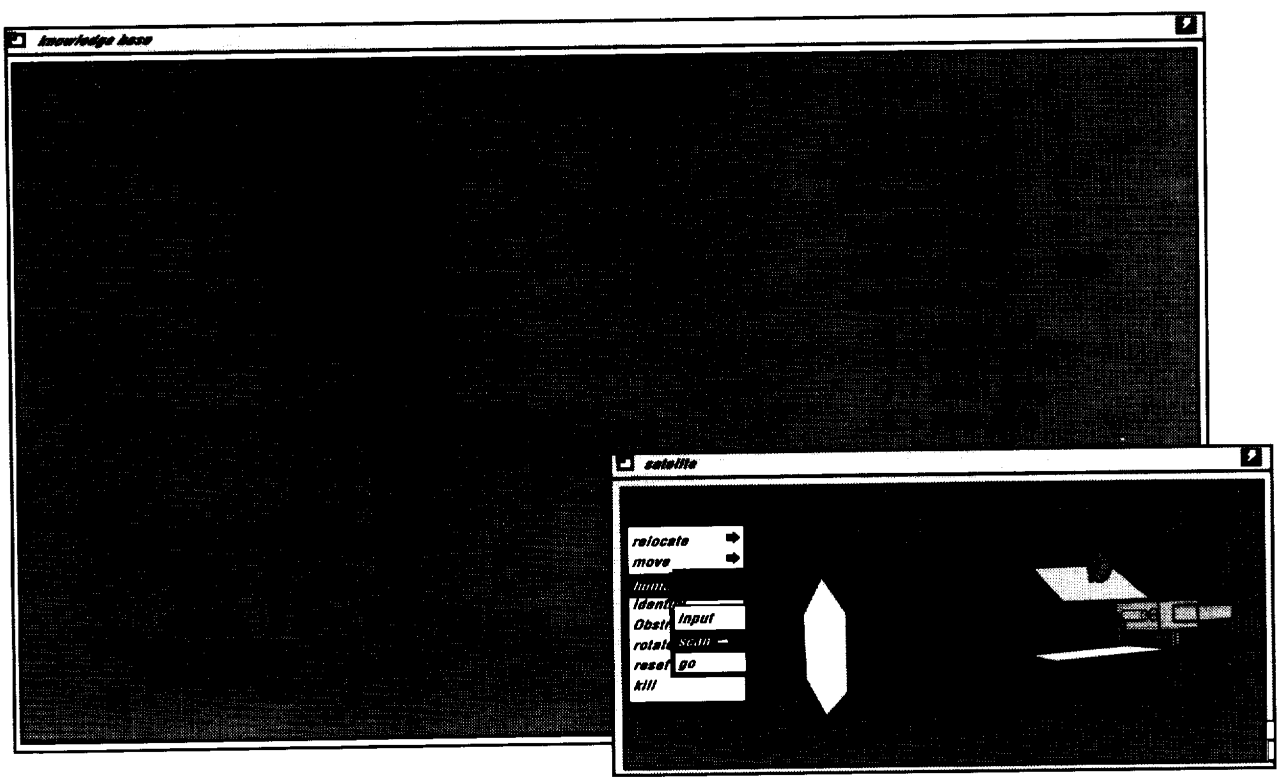

FIGURE 93.—Knowledge base user interface and simplified robotic servicing scenario.

The Use of Virtual Reality for Controlling a Robot

For remote tasks, such as many space operations, an operator is very far away from the actual task site. The operator is then controlling some kind of device, such as a robot, to actually perform the task. Many factors can combine to make task performance difficult since the operator has limited information as to the conditions of the environment at the remote site. Time delay can compound difficulties by providing the operator with late and limited information.

Virtual reality allows the operator to "experience" a realistic simulation of the remote environment through a combination of sensory inputs. This better enables a human's perceptive ability to aid in accomplishing the task.

This Small Business Innovation Research (SBIR) project is currently in the first phase. The **virtual reality** system is being designed to interface with a robot in the MSFC Flight Robotics Facility test-bed. The system will incorporate a computer-linked glove, heads-on display, graphics workstation, controller, and video and graphics displays. Software for updating the virtual environment and simulating the robot arm(s) is being developed. The simulation software uses a modular design to allow easy updating and customizing of the world of robot model parameters.

This research is conducted under an SBIR contract by KMS Fusion of Ann Arbor, MI.

E.M. Hinman/EB24
(205) 544–3519
Sponsor: Office of Commercial Programs, Small Business Innovation Research

Trace Atmospheric Carbon Monoxide Sensor

Carbon monoxide (CO) is an odorless, colorless, toxic **gas** found in closed environments such as the space station and long-duration manned spacecraft. It is difficult to detect at trace levels with usual multigas analysis techniques. A nondispersive infrared sensor dedicated to CO monitoring would provide a method for **CO** detection. The **trace** atmospheric **CO sensor** (TACOS) is such a **sensor** with a CO-specific light source. This specific light source greatly increases sensitivity as compared to conventional blackbody source absorption technology.

Initial **CO sensor** development efforts have focused on the **CO**-emission lamp design. The **CO**-emission lamp is composed of a small sealed quartz cell filled with a quantity of **CO gas**. This lamp is then surrounded with resistively heated nichrome wire and a thick layer of insulation. The **gas** in the cell, which can be heated to temperatures in excess of 1,000 K, emits radiation as lines, which is characteristic of **CO**. A second component of the lamp emission comes from thermal emission by the hot walls of the quartz cell. This thermal emission has been reduced by changing the lamp's size and shape. This reduction in thermal emission increases the sensitivity of the sensor and reduces the lamp power consumption. This lamp is then incorporated into the breadboard system.

Emission from a molecular line lamp is sent through a high-speed chopper and a filter wheel containing alternating **gas** samples of **CO** and **nitrogen** (**N_2**), then focused into and through a white cell and onto a photodetector. (The white cell is the area from the lamp window to the detector that contains the sample gases being analyzed.) Comparison of the signal through the two filter samples yields the **CO** concentration.

A breadboard **sensor** has been designed and fabricated, and a brassboard **sensor** is presently being fabricated with NASA/MSFC specifications included. The results from the breadboard testing show that a **CO** sensitivity of less than 1 part per million can be achieved with the **sensor's** physical dimensions and weight down to the size of a shoe box weighing approximately 10 lb.

M.L. Johnson/EB22
(205) 544–5519
Sponsor: Office of Commercial Programs, Small Business Innovation Research

WELDSMART: A Vision-Based Weld Quality Assurance System

WELDSMART is a system being developed to apply computer analysis to images of **welds** for the purpose of evaluation. Certain types of faults can be classified, and an overall evaluation of success or failure of the weld can be ascertained. Histograms are used in software analysis to preprocess the original images to aid in fault detection. The resultant images effectively highlight defects such as cracks. Threshold imagery also highlights the edges of the **weld** and introduces some background noise in the form of randomly placed pixels. The isolational aspects of the noise and the smooth, rounded shape of the **weld** can be used to filter these pixels, resulting in a clearer image of the defect.

A number of basic image-processing routines have been coded and are currently running on a Dell Computer Systems 310 computer. A hierarchy of defects is being designed so that classification of observed defects can be implemented. **Artificial intelligence (AI)** mechanisms are being developed to take the information from the image processing modules and ultimately assess the number, nature, and severity of the observed defects.

As this work is aimed at **automating** a very common task (i.e., **visual inspection**), its results are applicable to a wide variety of applications. Two likely areas to benefit from this work are quality inspection in space and commercial/industrial quality inspection. Space Station *Freedom* will have a need for periodic inspection and maintenance. A robotic manipulator could scan an electronic camera across the surface for this purpose. Previous scans could then be compared and possible defects brought to the attention of the appropriate personnel for further checking. Commercially, quality inspection is frequently needed in hostile environments such as nuclear plants and underwater construction or maintenance. Also, mass production applications using human inspection, which is expensive and prone to error, could benefit greatly from automated **visual inspection**.

The next step after the image processing routines is that of overall quality assessment. The questions of what constitutes an acceptable workpiece or specimen, and to what extent defects may be tolerated, must be evaluated. The **C language integrated product system (CLIPS)**, which has been developed by NASA at the Johnson Space Center, is under evaluation for the purpose of making pass/fail decisions. This system allows the user to specify a collection of general rules, and to define a collection of facts relating to the problem(s) at hand. The **CLIPS** inference engine iteratively compares the rules against the facts, derives sets of new facts, and continues until no further deductions can be made. A small **expert system** was constructed to examine the feasibility of determining which process faults contributed to the observed weld defects. This system performed acceptably.

In looking at a cast-iron part (fig. 94), sometimes a serious crack can be almost invisible. Through the use of computer-aided image processing, the magnetic particle test technique, and using an edge-detection algorithm, an enhanced image of the crack can be obtained (fig. 95). Additionally, a thresholding technique can be used on the resulting image to further separate the crack image from the background surface (fig. 96).

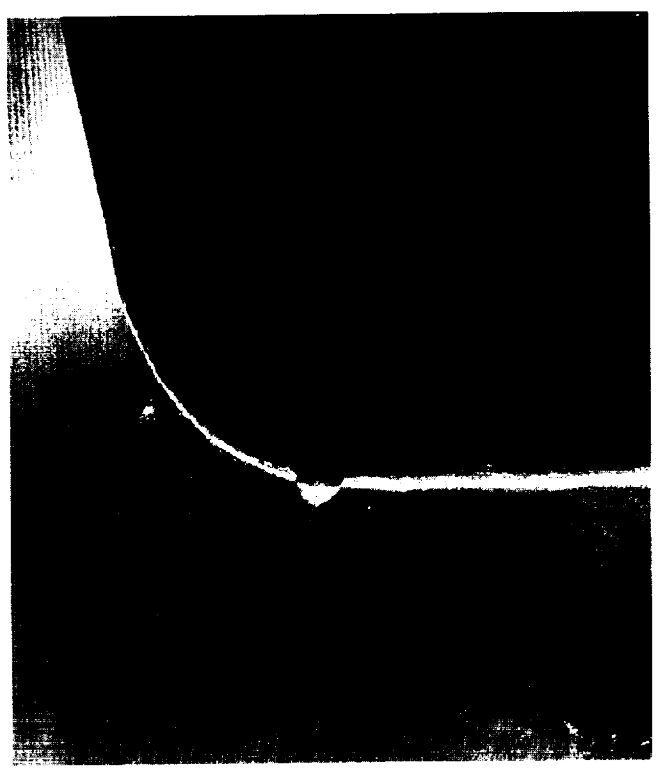

FIGURE 94.— An unenhanced image of a cast-iron part showing a barely visible crack on the right-hand side.

ORIGINAL PAGE
BLACK AND WHITE PHOTOGRAPH

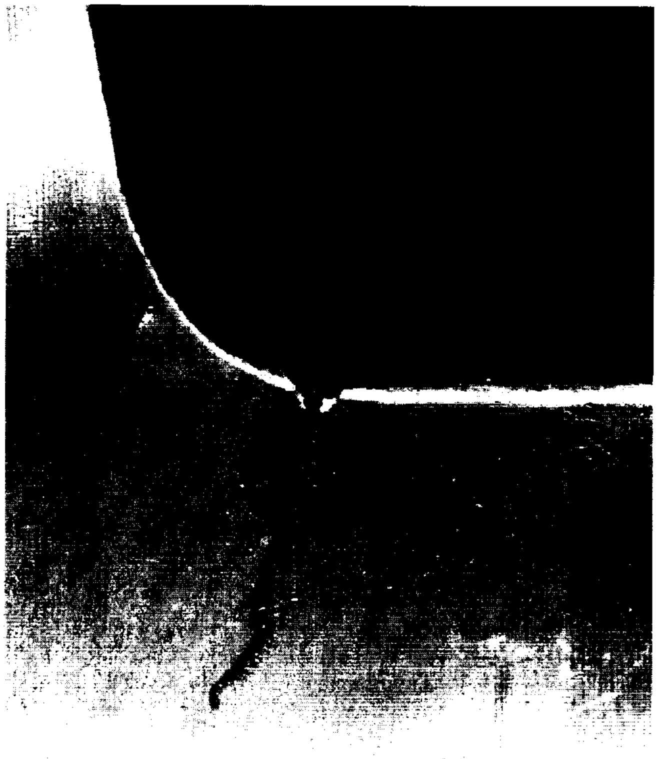

FIGURE 95.— An enhanced image of the cracked part shown in figure 94.

FIGURE 96.— A further enhanced image of the cracked part, which utilized a thresholding technique.

W.L. Boglio/EB44
(205) 544–3806
Sponsor: Office of Commercial Programs, Technology Utilization Office

ORIGINAL PAGE
BLACK AND WHITE PHOTOGRAPH

AVIONICS

COHERENT DOPPLER LIDAR RESEARCH AND DEVELOPMENT

During FY91, work on the coherent **Doppler laser radars (lidars)** continued in many areas. Data collected by the 9.1- and 10.6–μm **lidars** as part of the FY90 global backscatter experiment (GLOBE) survey missions were partially analyzed. The installed 9.1–μm **lidar** is shown in Figure 97. Preliminary results from this analysis were presented at the December 1990 American Geophysical Union (AGU) meeting, at the January 1991 American Meteorological Society, and at the GLOBE working group meeting in April 1991. Final data sets will be submitted to the central archive upon completion of the final analysis. The data, along with data from other experiments, will allow modeling of the performance of the laser atmospheric wind sounder (LAWS) **lidar**.

A contract between NASA and Coherent Technologies, Inc. (CTI), of Boulder, CO, was completed. Under NASA/MSFC sponsorship, operation of a pulsed 2–μm Tm,Ho:YAG eye-safe, solid-state **Doppler lidar** was demonstrated. Coherent **lidar** returns were observed from clouds, terrain, and aerosols. This is the first time that coherent **lidar** returns of this type are known to have been obtained. (These results are described in detail in NASA Contractor Report 4347.) Additional work was performed by CTI to better understand the performance of coherent **Doppler lidars**. The initial motivation for this effort was better calibration and improved sensitivity of the continuous wave (CW) **lidars** used for **atmospheric backscatter coefficient** measurements. However, the results are sufficiently general so that they may be applied to any **lidar**.

Kavaya, M., Henderson, S., and Frehlich, R., "Theory of CW Lidar Aerosol Backscatter Measurements and Development of a 2.1–μm Solid-State Pulsed Laser Radar for Aerosol Backscatter Profiling," NASA CR–4347, March 1991.

Henderson, S., Hale, C., Magee, J., Kavaya, M., and Huffaker, A., "Eye-Safe Coherent Laser Radar System at 2.1 μm Using Tm,Ho:YAG Lasers," Optics Letters, vol. 16, 1991, pp. 773–775.

W.D. Jones/EB23
(205) 544–3479
Sponsor: Office of Space Science and Applications

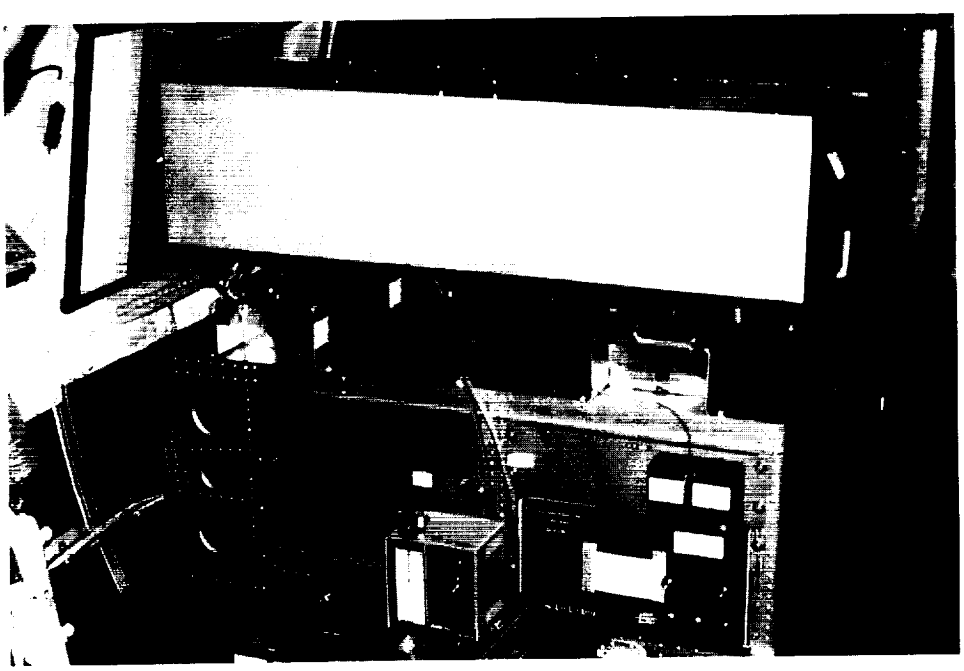

FIGURE 97.— 9.1-μm CW Doppler lidar installed aboard DC-8-72 aircraft at Ames Research Center, May 1990.

ELECTRICAL POWER SYSTEM FAULT STUDY

NASA/MSFC proposes to implement computer-controlled **fault injection** into an **electrical power system** breadboard to study the reactions of the various control elements of this breadboard, including the remote power controllers (RPC's), the algorithms, and expert systems in the control computers. To this end, a study of **electrical power system faults** is being performed to yield a list of the most common **power system faults**. The results of this study will be applied to a multichannel, high-voltage direct-current (dc) spacecraft power system called the large autonomous spacecraft **electrical power system** (LASEPS) breadboard (fig. 98).

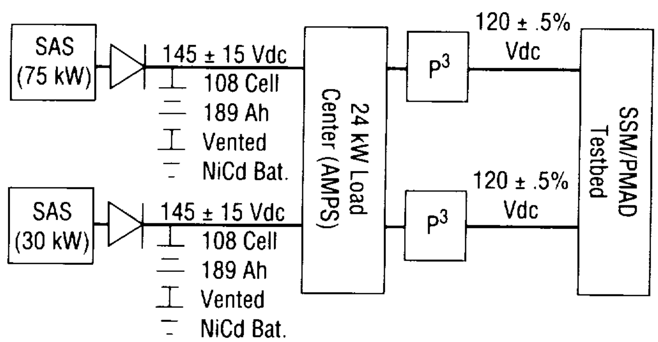

FIGURE 98.— Large autonomous spacecraft electrical power system (LASEPS).

The LASEPS breadboard is being created from two existing breadboards: the autonomously managed power system (AMPS) breadboard and the space station module/power management and distribution (SSM/PMAD) breadboard. The LASEPS breadboard will encompass complete power generation, storage, and distribution of power to the various loads. Preparations are being made to decrease the size of the AMPS battery to 108 cells to create one of the two 100–A buses of the LASEPS breadboard. In the meantime, the work on the programmable power processors (P^3) has been progressing. The two P^3 to be used to convert the power output from AMPS to the 120 V needed to operate SSM/PMAD are in place and are ready to be physically connected.[1]

The data used in the **electrical power system** fault study have come from both terrestrial and aerospace sources. The most common fault that is recorded in **electrical power systems** is a fault in the terminal-end user load. Some of the other common faults found in **electrical power systems** are:

- Short of bus to neutral or return
- Short of one bus or line to another
- Soft shorts of bus or line to return or ground
- Loss of ground to neutral connections
- Multiple neutral to ground connections
- Bus switch short
- Bus switch open
- Short of load to neutral or return
- Short of load to chassis or Earth ground
- Open circuit failure of load
- Soft short of load.

During the study, it was found that an analogy can be made between the neutral of the three-phase alternating current (ac) power lines and the return of the dc lines, as well as the Earth ground of the ac systems to the chassis ground in a dc system. The references to the neutral and return and the references to Earth ground and chassis ground in the above list refer to these analogies. More information about this part of the study can be found in a paper entitled "**Fault Analysis** of Multichannel Spacecraft Power Systems."[2]

The primary emphasis of this study in the past year has been on the batteries and solar arrays. Most of the information for this part of the study came from aerospace sources, although there are some ground-based uses for these systems. The following is a list of some of the solar array and battery faults that were found during this phase of the study:

- Solar array degradation
- Solar array panel short
- Solar array panel open
- Solar array electromagnetic interference
- Solar array parasitic plasma current power loss
- Solar array corona discharge
- Isolation diode short
- Isolation diode open
- Battery degradation
- Battery cell short
- Battery cell open
- Battery failure.

Many of these faults will be implemented by software simulation or control since the solar arrays are simulated and the battery operation is computer controlled. The most common of these are solar array and battery degradation and shorts.

Presently, no installed faults have been placed into the AMPS portion of the breadboard, but, during the activation of the breadboard, the following faults were found: communication faults, battery faults, and load faults. The results of the investigation dealing with these faults is discussed in a paper to be presented at the 1991 IECEC entitled "A Study of **Fault Injection** in Multichannel Spacecraft Power Systems."[1]

[1]Dugal-Whitehead, N.R., and Johnson, Y.B., "A Study of Fault Injection in Multichannel Spacecraft Power Systems," *1991 IECEC*, in press.

[2]Dugal-Whitehead, N.R. and Lollar, L.F., "Fault Analysis of Multichannel Spacecraft Power Systems," *1990 IECEC*, pp. 243–8.

N.R. Dugal-Whitehead/EB12
(205) 544-3304
Sponsor: Center Director's Discretionary Fund

Nickel Hydrogen Battery Expert System

The Electrical Division at NASA/MSFC is heavily involved in the testing of **batteries** for use in space flight. There was an **expert system**, titled nickel cadmium battery **expert system**-2 (NICBES-2), that was used to evaluate battery status and to provide decision support as to whether or not a change in the operation of the nickel cadmium battery, or batteries, is needed (i.e., reconditioning, a charging scheme change, or a load adjustment).[1] That **expert system** is now in the process of being converted to diagnose **nickel hydrogen batteries**.

The **nickel hydrogen** battery **expert system** (NIHBES) will reside on the same machine as NICBES-2 did previously. To date, the incoming data from the **nickel hydrogen** six-battery test-bed is being gathered from an RS232 connection that is controlled by the serial port process (fig. 99). Reference 1 provides more information on the system operation.

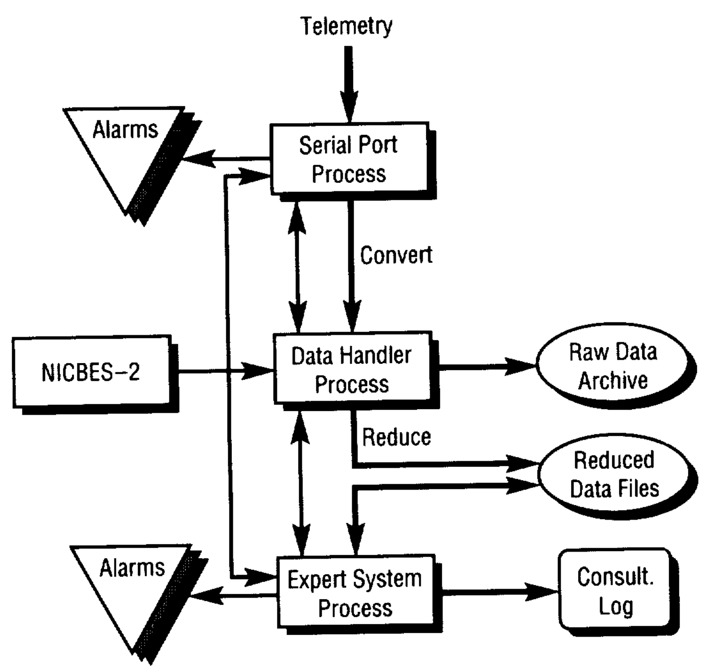

FIGURE 99.—NICBES-2 top-level structure.

The serial port process (SPP) has been modified to accommodate the new telemetry data format. Also, the data handler process (DHP) has been altered for data reduction computations based on the new telemetry format. Work is continuing on the **expert system** process (ESP) to enable it to accommodate **rules** for **nickel hydrogen batteries** and to expand the rule base. Currently, there are 40 **rules** consisting of 7 categories (charge, charge-status, device-status, recondition, temp-status, worm-status, and workload).[2]

There have also been hardware modifications to the system. The 90–MB hard drive in the Sun 386i/150 has been replaced with a 327–MB hard drive to enable the storing of more orbits for more accurate trend analysis.

An Apple LaserWriter laser printer has also been added to produce high-quality graphics printouts of the different graphic data. A typical NIHBES consultation is shown in figure 100.

[1]Bykat, A., "Expansion of Nickel-Cadmium Battery Expert System's Capabilities," Final Report on MSFC/NASA Grant NAG8–105.

[2]Shiva, S.G., "Nickel Hydrogen Battery Expert System," Final Report on NASA Summer Faculty Fellowship, Summer 1990.

Y.B. Johnson/EB12
(205) 544–3310
Sponsor: Advanced X-Ray Astrophysics Facility (AXAF) Program

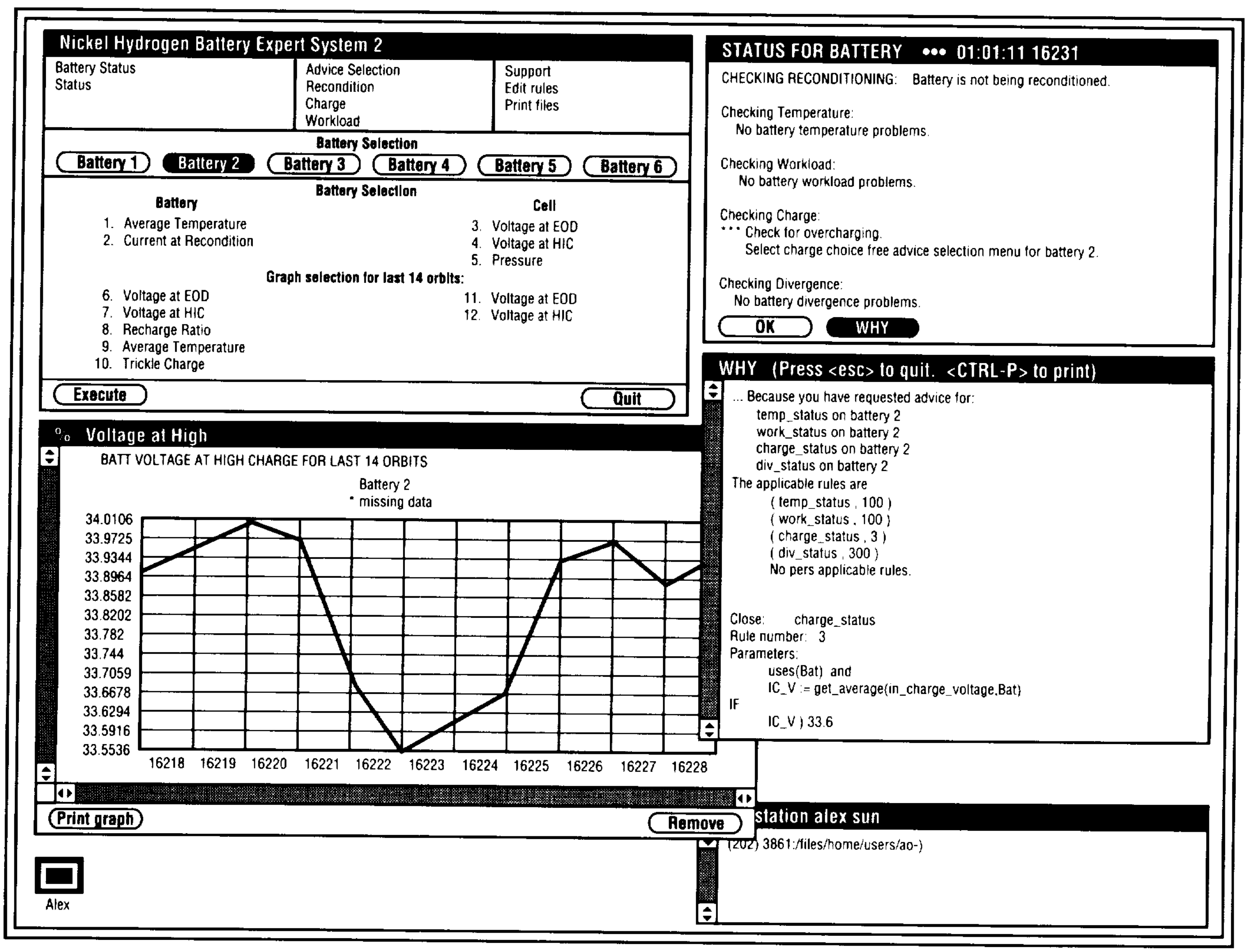

FIGURE 100.—NIHBES consultation.

Space Shuttle Wind Profiler

Knowledge of winds is required to reduce aerodynamic loads on the **space shuttle** during launch. Knowledge of winds is also required to safely land the unpowered orbiter. Balloons are currently used in both instances to produce the necessary wind profiles. These balloons require an hour to rise through the altitude range, sometimes drifting far from the area where the wind measurement is desired. As a result, the correlation between the actual winds encountered by the vehicle and those measured is reduced. NASA is investigating the potential of alternate wind sensors to produce more local wind measurement in less time to increase this correlation. **Laser radar (lidar)** is one technique under investigation.

Lidar has several advantages and disadvantages when compared to current launch and landing **wind profiling** systems. Among the advantages are: it can provide a faster update rate; it can provide higher spatial and velocity resolution; it is unaffected by ground clutter and can profile winds to ground level; and it is flexible and mobile, providing wind measurement at the desired location. However, **lidar** is dependent on entrained aerosols for backscattered signal. The aerosol distribution is variable and decreases with altitude. Other disadvantages include: **lidar** signals are blocked by clouds and, depending on frequency, suffer varying amounts of attenuation from atmospheric constituents including water vapor; and **lidar** velocity accuracy is dependent on signal-to-noise ratio, which decreases with range and is further degraded by atmospheric turbulence.

The primary **wind profiling** system for **space shuttle** launch is the jimsphere, a radar-tracked balloon. This system produces wind profiles to 18 km (60,000 ft) in all weather conditions at 30–m (100–ft) intervals with a velocity accuracy of 0.5 m/s (1.6 ft/s). A potential new system for launch **wind profiling** is the recently installed radar wind profiler, which is currently undergoing validation tests at Kennedy Space Center (KSC). It relies on atmospheric refractive index variations for backscattered signal and is insensitive to clouds and precipitation. Operating at 50 MHz and 1–μs pulsewidths, the radar wind profiler produces wind profiles to 18 km (60,000 ft) at 150–m (492–ft) height intervals with 1 to 2 m/s (3.3 to 6.6 ft/s) velocity accuracy. Three sequential fixed angle scans are used, producing a wind profile every 3 min. Ten profiles are averaged to produce a more accurate measurement of mean winds every 30 min. Landing **wind profiling** is accomplished using rawinsondes. Winds are measured at 152– or 305–m (500– or 1,000–ft) intervals to 30,478 m (100,000 ft) with 2 to 3 m/s (6.6 to 9.9 ft/s) velocity accuracy. Landing winds are also measured with the instrumented shuttle trainer aircraft. An anemometer network is used for measurement of surface winds for launch and landing.

To evaluate **lidar** as a sensor for **space shuttle wind profiling**, two **lidar** demonstrations were planned for 1991 at KSC. Each demonstration coincided with a shuttle launch to maximize the opportunity for comparison with existing **wind profiling** systems as well as with the actual shuttle launch performance. The **lidars** that were demonstrated are carbon dioxide (CO_2) and Nd:YAG, both operating at 0.8 J. Because of their availability, the **lidars** were selected to resolve performance issues associated with wavelength between the leading **lidar wind profiling** technologies (CO_2 and solid-state). Parameters that were compared included update rate, velocity accuracy, maximum altitude, altitude resolution, and all weather performance.

The Nd:YAG **lidar** system demonstration was scheduled for August. A demonstration of the National Oceanographic and Atmospheric Administration/Wave Propagation Laboratory CO_2 **lidar** system occurred April 1–9 at KSC in conjunction with the launch of STS–37. The system was set up midfield at the shuttle landing facility on a raised concrete pad adjacent to the runway. The site afforded good visibility in all directions, including a view of the shuttle glide slope. The site was 8 km (5 mi) from the launch pad and 20 km (12 mi) from the balloon launch facility at the Cape Canaveral Air Force Station. Numerous comparisons were made with the existing **wind profiling** systems including 8 jimspheres, 13 rawinsondes, and 28 shuttle trainer aircraft approaches. Daily comparisons were made with the radar wind profiler and the anemometer network. **Lidar** data were also collected during the shuttle launch. Analysis of the test data is under way. Figures 101 and 102 compare profiles collected by the jimsphere and **lidar**.

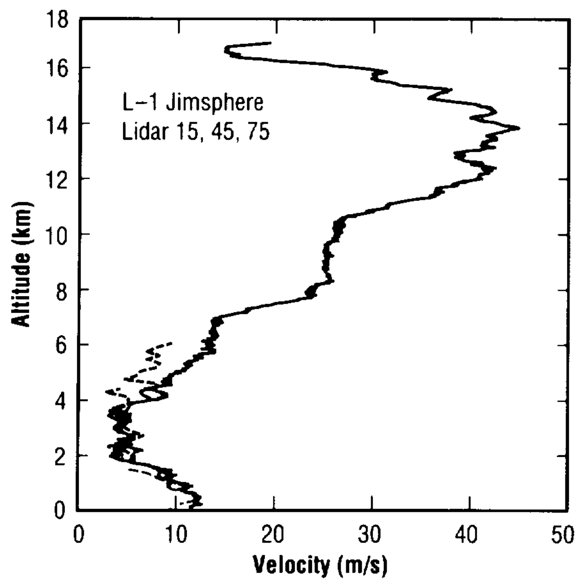

FIGURE 101.—Wind profiles, velocity versus height, comparing data collected by jimsphere with data collected by lidar.

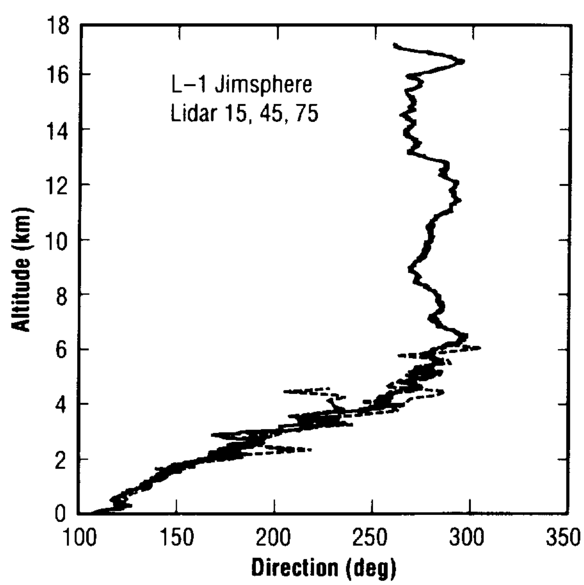

FIGURE 102.—Wind profiles, direction versus height, comparing data collected by jimsphere with data collected by lidar.

S.C. Johnson/EB23
(205) 544–3478
Sponsors: Office of Aeronautics, Exploration and Technology

COMPILING KNOWLEDGE BASES

Artificial intelligence techniques have become an important technology for the solution of some of the most difficult programming tasks. The dominant and most effective technology for developing such applications is to work in a multimechanism, integrated, knowledge-based system development environment. Unfortunately, systems developed in environments such as these are inappropriate for delivering many applications, particularly applications germane to space systems—they are not real-time systems, they carry the overhead of the entire development environment, and, particularly in light of space station requirements, they are not written in ADA.[1]

As reported in the 1990 Research and Technology report, research into a mechanism for **compilation** of **knowledge bases** into standard ADA is being done for NASA through a Small Business Innovation Research (SBIR) contract with IntelliCorp. Initially, this work was being done to accomplish a translation of **Knowledge Engineering Environment (KEE) knowledge bases** from their native LISP to ADA source. This strategy has been altered due to changes in the marketplace and a different emphasis on development environments. A new tool called **ProKappa** was introduced by IntelliCorp last year to replace **KEE**. **ProKappa**, although performing many of the same functions and processes as **KEE**, produces its **knowledge bases** in C language. One advantage of this type of product is the elimination of the often-expensive overhead of LISP development environments. The compiling **knowledge bases** project has been shifted to work on translation of C-based **knowledge bases** from **ProKappa** into ADA. The prototype tool that will be a product of this phase II SBIR effort is called PrkAda. There are two primary parts of PrkAda: (1) the core, which is an ADA library that supports an object-base functionality, and (2) the translation mechanism, which is a collection of Refine (a language-translation tool) routines for program analysis and transformation.[2]

The work on the ADA core has resulted in completion of the following elements:

- Definition of primitive data types
- List-processing primitives
- Hash tables
- Symbols
- Object, slot, and facet creation; slot and facet deletion
- Primitive value addition and deletion for slots and facets
- Inheritance, including all inheritance roles except for no-inheritance and monitor inheritance
- Methods
- Monitors
- Exception handling
- Application (object-base) reader
- **ProKappa** covering functions (those functions available to the user of the PrkAda; package; 2/3 done)
- Simple output
- Object names
- System initialization.

Research is also being accomplished on the ProTalk element of PrkAda. This ProTalk component is being designed to generate an efficient portable ADA code from the **ProKappa** source. The initial research for ProTalk is being done through Refine.

The research and development of this prototype system will continue through the summer of 1992 under the current funding.

[1]IntelliCorp, Inc., "Compiling Knowledge-Based Systems Specified in KEE to ADA," Phase II Proposal, August 1989.

[2]IntelliCorp, Inc., "Compiling Knowledge-Based Systems Specified in KEE to ADA," Quarterly Report, May 1991.

G.R. Higgins/EO41
(205) 544–5462
Sponsor: Office of Commercial Programs, Small Business Innovation Research

Computer Accessibility for the Visually Impaired

As stated in the 1990 Research and Technology Report, the research project on computer accessibility for the visually impaired is funded through the Center Director's Discretionary Fund at MSFC. This research involves evaluation of existing adaptive technologies mixed with a development effort using the **X-Windows** protocol. (**X-Windows** is a display environment that is commonly used to develop engineering work station **graphical user interfaces (GUI's)**.) During the past year, a grant has been made to the Georgia Institute of Technology to build a prototype system that provides audible access to software running in the **X-Windows** environment. This prototype has been named the Mercator project. Key requirements have been established, and a design for the system is being developed.

The prototype system is being designed to meet a basic goal of providing an audible and tactile interface to text-based applications hosted in a graphic environment. This audible interface will incorporate features not found in other more common speech-based applications for text environments. They include the following features.

- Location representation for screen objects based on sound moves in relation to where objects are displayed.

- Several algorithms are being investigated as potential means for tying display objects to audio that is produced in a 360°, two-dimensional sound spectrum. Variations in voice filtering and pitch may be utilized to differentiate between discrete display objects. This technology is currently available, but it requires more computer instructions than can be accomplished for real-time applications.

- Remapping of visual images to sound images that make sense in an audible environment.

- Many existing personal computer- (PC-) based screen access programs provide a method for a **blind** person to obtain information about what a sighted person sees on the screen. A design goal of the Mercator project is to represent existing visual images specifically for the audible environment. This will be accomplished without modification to the off-the-shelf software. This will require creation of new drivers that work in conjunction with the **X-Windows** routines. Current research subjects in this area include: the best way to map

X-Windows objects to sound objects, the control mechanisms needed for the **blind user,** the best methods to convey and perceive the audible environment, and the best ways to convey and perceive the tactile environment.

- Portability to many **X-Windows** environments.

  The Mercator project is being designed to run under the UNIX operating system. The core of the environment is being designed to provide transportability to other **X-Windows** environments. The aim is to make an audible environment that is functional on numerous types of work stations.

The design team has defined an object-oriented approach to be implemented in the C++ language for the Mercator project. The initial design concept is to create a process that will be interjected between the client/server processes of the **X-Windows** protocol. This Mercator process will pass all messages between the client/server processes for normal video output. It will also process the messages from client to server in order to produce the new audible/tactile environment for Mercator. This should make it possible to obtain all of the text that is being sent from the application to the display environment. Additionally, the messages will carry enough information to make it possible to map from the visual environment to the audible environment.

Other parts of the research include: mapping of video resource parameters into parameters that make sense for the audible display understanding of organizational techniques employed by the **blind** that are different from the desktop metaphor used as a standard part of **X-Windows**, processing of icons and other **X-Windows** artifacts, examination of the appropriateness of layered windows for the audible environment, examination of pointing device technologies, and examination of mechanisms and syntax for positional reference in the audible environment that are based on some unit of measure or regional characteristic.

The research team will be developing more proof-of-concept work over the summer of 1991. The basic requirements for the system have already been defined. The interface and design specifications will be available in the early fall of 1991. A working prototype is expected to be ready by the early spring of 1992.

G.R. Higgins/EO41
(205) 544–5462
Sponsor: Center Director's Discretionary Fund

The Earth-to-Orbit/ Solid-State Recorder

The Earth-to-orbit/**solid-state recorder** (**SSR**) is a research and development project managed by MSFC to develop a space-flight-qualified device potentially capable of storing 10 GB of data using **solid-state memory**. A contract was awarded to the Fairchild Space Company of Germantown, MD, on February 5, 1991, to help accomplish this task in two phases. Phase I involves a study of available **solid-state memory** technologies and results in a reduced capacity engineering unit to test proof of concept; phase II of the contract culminates in a space-qualified recorder with potential application with the space shuttle or Space Station *Freedom*.

The objective of the project is to advance technology in the area of digital **mass storage**, which will improve the availability of engine flight performance information, and to aid the evaluation of engine health monitoring. The evaluation of the health of a complex system like a **space shuttle main engine** (**SSME**) requires acquisition and postflight analysis of much sensor data, but technology used previously does not support the data storage requirements of future engine health monitoring systems and does not support operation in a high-vibration environment as is found near the **SSME's**. Because an **SSR** has no moving parts, unlike a tape recorder, it is ideal for space flight applications.

Minimum performance requirements for the **SSR** include an input rate of 20 MB/s, 8 channels of input, capability to read and write data simultaneously, and provision for a set of analog inputs to be recorded. The **SSR** will be capable of performing analog-to-digital data conversion without the need for external digitizing circuitry, and the analog inputs are expected to accommodate an input voltage range either from 0 to 5 V or 0 to 10 Vdc. The design rationale is that data from sensors such as strain gauges and thermocouples will be conditioned before reaching the **SSR**, and that the voltage ranges stated previously are sufficiently wide to allow the **SSR** to be used on a number of different programs and projects. Provision will be made for several large bandwidth analog inputs to store data from accelerometers from sources such as the **SSME**.

A technology study report discussing available **solid-state memory** alternatives will be completed by September 1991, and the engineering unit is projected to be completed by July 1992.

S.L. Bridge/EB33
(205) 544–8572
Sponsor: Office of Aeronautics, Exploration and Technology

Materials and Processes

AAOSS Beam Energy Measurements

The development of a neutral **atomic oxygen** (AO) beam system capable of simulating **low Earth orbit** (LEO) **AO** conditions is necessary to evaluate the susceptibility of spacecraft **materials** to **AO** degradation. Over the past few years, a system has been under development at Princeton **Plasma** Physics Laboratory (PPPL) in cooperation with MSFC for the purpose of developing an advanced atomic oxygen simulation system (AAOSS) that can simulate **5-eV AO**. Last year, a complete set of diagnostic tests was performed to measure the **AO** beam flux and flux distribution. Also, several material samples were exposed in the system in the **AO** beam, and the observed degradation of the **materials** was compared to similar materials exposed to **AO** on orbit. During the past year, work concentrated on measuring the **AO** beam energy and understanding the effects varying the material of the neutralizer plate and the bias of the neutralizer plate on the energy of the beam. Because of the past success of the system to reproduce observed material degradation caused by orbital **AO** and the ability of the system to deliver orbital fluences in a short period of time, the system was used for material testing to answer real material susceptibility questions regarding **AO** exposure in LEO.

AO beam energy measurements were made over a wide variety of neutralizer bias conditions (0 to –40 V) and plate **materials**. Because **plasma** instabilities caused by lowering the plate bias below 0 V made it difficult to collect needed plasma data used to determine the beam energy, data could not be taken below the targeted **5–eV** peak beam energy regime. The energy measurements were made in this facility using a quadrapole mass spectrometer (QMS) equipped with a cylindrical mirror energy analyzer. This instrument operates in two different modes: the first mode filters the neutral atom beam to only pass atoms of a certain atomic number and scan the energy distribution of the beam, and the second mode filters the beam according to the energy and scans the atomic mass of the beam. To date, most of the data have been done in terms of the first method.

The energy data of one test in which **AO** atoms were being reflected off a molybdenum plate are shown in figure 103. These data were taken with a neutralizer plate bias of –3 V and were corrected for any ambient **AO** in the vacuum chamber. The peak energy of this set of energy data occurs at 6.5 eV and the full-width-half-maximum (FWHM) beam energy spread is approximately 2 eV. The unusual abrupt stop of the energy data at the lower energies is caused by the subtraction of the background **AO** energy spectrum. These high-energy particles in the background are produced in the QMS ionizing chamber by dissociating the molecular oxygen atoms into atomic species. These high-energy atomic species are known as Frank-Condon atoms.

The data presented in figure 104 illustrate the effect that varying the bias voltage on the neutralizer has on the peak **AO** beam energy. The neutralizer plate was made of steel for this particular set of data. This figure plots the peak beam energy as a function of accelerating voltage, but the accelerating voltage is actually the sum of the **AO plasma** potential and the bias voltage. Typically, the **plasma** potential for this high-density **plasma** is about 20 to 25 V. Because the **plasma** potential remained relatively constant over a large range of bias potentials, the accelerating potential is a direct indication of the neutralizer plate bias. Interestingly, the lowest peak beam energy in this case is near 10 eV, but a peak beam energy of 6.5 eV was measured with a molybdenum neutralizer plate suggesting that the right selection of neutralizer plate material must be made to produce a **5–eV AO** beam.

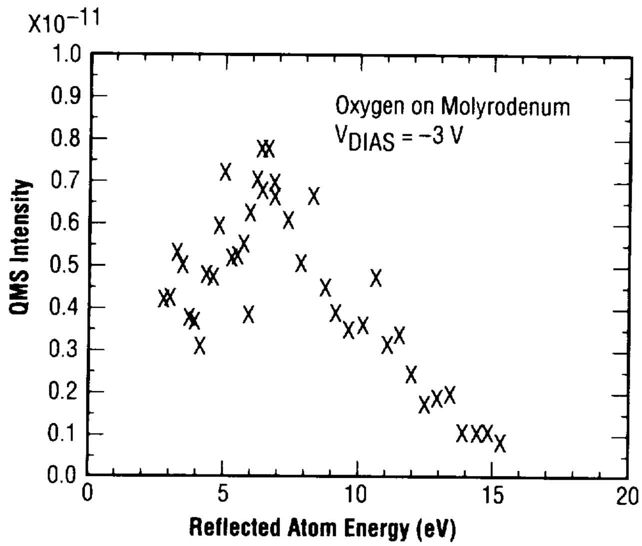

FIGURE 103.—Typical QMS beam energy data.

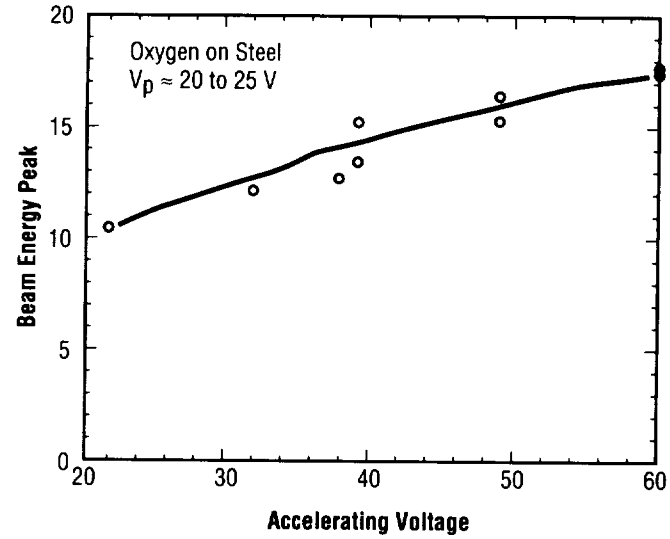

FIGURE 104.—Effect of accelerating voltage on peak AO beam energy.

J.A. Vaughn/EH12
(205) 544–9347
Sponsor: Office of Space Flight, Space Station *Freedom*

Advanced Powder Metallurgy Bearings for Cryogenic Applications

Advanced **powder metallurgy (P/M)** techniques have the potential to develop **bearing** materials that resist corrosion, wear, and rolling contact fatigue (RCF), and afford a viable solution to the problem of extending the service life of the **cryogenic turbopump bearings** of advanced rocket engines. Several **P/M** alloys were evaluated (under contract with Textron) in the areas of cylindrical RCF, five-ball RCF, stress corrosion cracking resistance, short rod fracture toughness, and both ambient and elevated temperature wear-resistance. The MRC–2001 alloy was found to possess the best combination of properties and was selected for further evaluation. A total of 40 full-size **bearings**, i.e., inner and outer raceways, and balls are being fabricated from MRC–2001 for testing in the MSFC **bearings** and seals materials tester.

The results achieved to date confirm the basic premise of this program that **P/M** processing, rather than conventional cast/wrought processing, will provide a superior metallurgy microstructure, regardless of the alloy being considered. When properly consolidated, the **P/M** microstructure is very fine and homogeneous, with small, uniformly distributed carbide particles (fig. 105). Furthermore, **P/M** processing provides the potential for alloy compositions that are simply not practical through conventional processing.

B.N. Bhat/EH23
(205) 544–2596
Sponsor: Office of Aeronautics, Exploration and Technology

FIGURE 105.—Powder metallurgy microstructure.

Advanced Sprayable Ablator for Solid Rocket Booster

The primary **insulation** in the exterior thermal protection system (TPS) for the space **shuttle's** solid rocket **boosters** (SRB's) has been evolving by strategic upgrades in its family of formulations called the Marshall sprayable **ablator** (MSA). Under the impetus of rising environmental concerns, the Materials and Processes Laboratory is currently engaged in a transitional development and a third MSA generation that means a fundamental innovation in material design. In 1981, MSA–1 became the nation's first aerospace spray-on **insulation** and soon displaced sheet cork on the SRB nose cap, frustum, and forward skirt as a faster and much more economical form of acreage **insulation**.

The 1989 modification, called MSA–2, was a more flexible rendition. Not limited to the 0.25–in thick layup of the parent material, MSA–2 expanded sprayable thermal protection to the SRB aft skirt, the last, largest, and hottest of the corked hardware. With MSA–2 now in flight, the Materials and Processes Laboratory has moved ahead to advanced developments that focus on safer and more environmentally compliant constituents. MSA–2A, a conservative variant of MSA–2, substitutes 1,1,1–trichloroethane for the latter's methylene chloride/perchloroethylene system. Some regions in the western United States already restrict or ban these particular solvents, so the MSA–2A alternative is being qualified as an immediate substitute if MSA–2 is withdrawn by an Environmental Protection Agency (EPA)/ Occupational Safety and Health Administration (OSHA) mandate in the near future. Equivalent properties have been verified; completion of an MSA–2A process sensitivity study will establish its optimum production ranges.

Over the long term, the Materials and Processes Laboratory's greater interest rests in the upcoming new formula that avoids chlorinated solvents altogether. With a base of a water-dispersible resin system, surfactants, defoamer, and fillers, MSA–3 represents a marked shift in technological direction. The preliminary breakthrough formulation (1990) produced a series of sprayed MSA–3 with strikingly similar physical and thermal properties to MSA–2. Optimization of the MSA–3

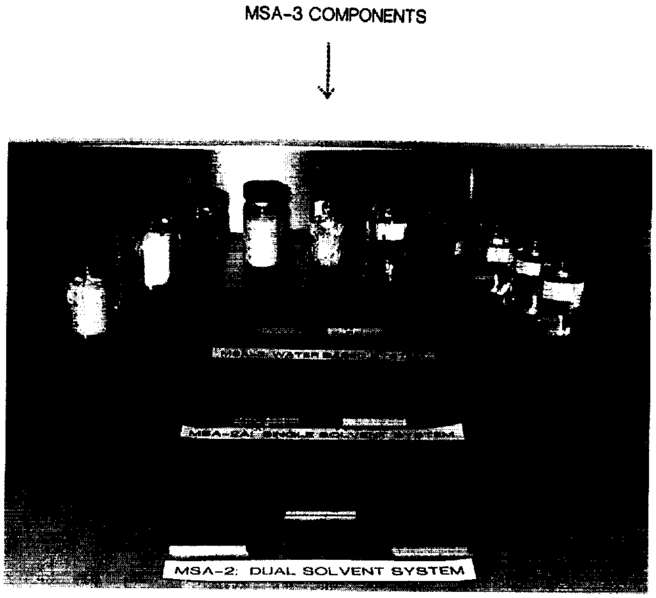

FIGURE 106.—The evolution of MSA to an environmentally compliant formulation.

process, currently in progress, will precede full-scale thermal verification. Figure 106 illustrates the transition from MSA–2 to MSA–2A/MSA–3 with samples of each formulation.

The Titan IV program is a second potential recipient of these "clean" materials, which offer assertive hazard avoidance in the interest of a cleaner environment.

C.N. Lester/EH43
(205) 544–4804
Sponsor: Office of Space Flight

Arc Plasma Expansion Caused by Dielectric Breakdown

The present baseline design for Space Station *Freedom* (S.S. *Freedom*) has a thin dielectric material (anodized aluminum) insulating the aluminum surface to control outer skin surface temperatures. Also, part of the current design is for the S.S. *Freedom* structure to be referenced to the negative side of the solar array. The solar array, which will electrically float in the **plasma**, will be driven mostly negative relative to the low-Earth orbit (LEO) **plasma**. This will make the negative end of the solar array 140–V negative of **plasma** potential and will drive the entire structure to the same relative potential. Because the anodic coating has a high resistivity, the entire–140 V will be dropped across the anodic coating. The thin anodic coating (0.2 mil) on the surface of S.S. *Freedom* does not have sufficient dielectric strength to withstand the applied voltage stress resulting in **dielectric breakdown**.

The anodic layer will store electrons in the conductive layer, and ions will gather on the outer surface from the **plasma** resembling one large capacitor. When an **arc** occurs, it breaks through the dielectric, dumping large amounts of electrons into the ambient **plasma** with sufficient energy to vaporize and ionize the surrounding aluminum, forming a dense **arc plasma**. The **arc plasma** expands and discharges the ion population on the outer surface of the dielectric to maintain a steady-state neutral condition. Because the S.S. *Freedom* structure with the thin dielectric coating has a large reservoir of electrons, there is potential for a lightning-type discharge (i.e., high current on the order of hundreds of amperes) to occur if the entire ion population on the surface can be discharged. The amount of electron current that can be transferred between the S.S. *Freedom* structure and the ambient **plasma** depends on the neutralization of the ion population on the surface by the expanding **arc plasma** and the return current from the ambient **plasma**. The tests described here only examine the **plasma expansion** phenomena.

Tests were conducted in a **plasma** chamber at MSFC (fig. 107) to determine the **expansion** rate of the **arc plasma** into the ambient **plasma**. An anodized aluminum plate, made to S.S. *Freedom* specifications, was biased –140 V and placed in an argon **plasma**. A 0.03–cm (0.01–in)

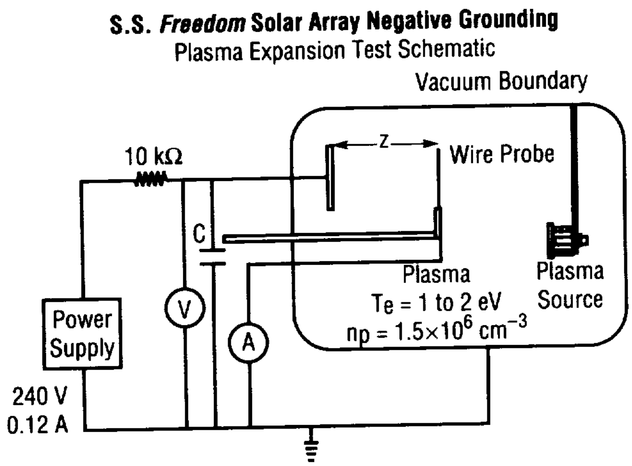

FIGURE 107.—Plasma expansion test chamber.

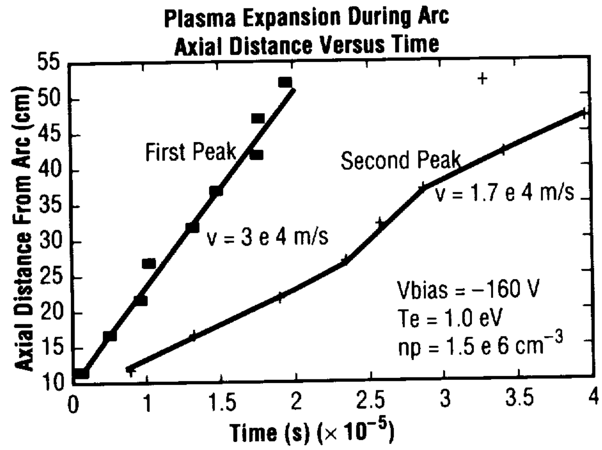

FIGURE 109.—Plot of current position versus time.

diameter wire Langmuir probe that was grounded was moved axially through the chamber while the plate arced. The Langmuir probe was connected through an ammeter to an oscilloscope to measure current transients as a function of time. The oscilloscope was triggered by measuring the voltage drop on the anodized plate, which would signal initiation of an **arc**.

The results from the **arc plasma expansion** test are shown in figures 108 and 109. The first figure (fig. 108) is a typical current-versus-time set of data recorded by the oscilloscope during an **arc**. This particular set of data was recorded with the probe placed 31.8 cm (12.5 in) from the anodized plate. This figure shows that an intense electron wave front passes the probe first, followed by a second, less-intense wave. The intensity of both fronts (i.e., 80 mA and 50 mA) is higher than can be supported by the thermal **plasma**. This type of wave structure was

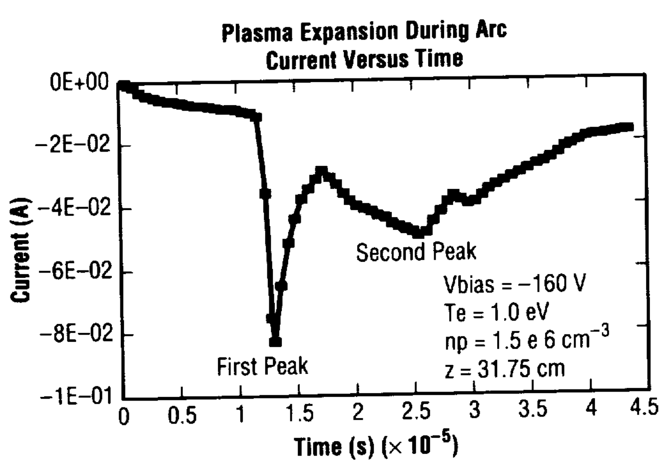

FIGURE 108.—Typical current-versus-time data.

typical of all data recorded during these tests. The time for the two wave fronts from the **arc plasma** to reach the Langmuir probe was plotted as a function of axial position and is shown in figure 109. This figure provides an indication of the velocity or the rate of **expansion** of the **arc plasma** into the ambient **plasma**. The electrons in the **plasma** that are more mobile than the ions are controlled by the electrostatic interaction of the ions. The velocities, which are an order of magnitude higher than ion acoustic velocities at these conditions, were computed for each wave front, and they are indicated in figure 109. Using the velocity of the first peak to calculate the kinetic energy in the first wave front, assuming aluminum ions, an energy of 127 eV is obtained; this is near the voltage bias of the plate (i.e., −160 V). This indicates that only a small amount of energy is going into vaporizing and ionizing the aluminum to produce a **plasma**.

The results of these tests indicate that, when an **arc** occurs, it produces an intense **arc plasma** that will expand at a rate given by the amount of energy dumped into the **plasma**. The **arc plasma** will expand at a velocity sufficient to discharge large surface areas of anodized aluminum over a short period of time.

J.A. Vaughn/EH12
(205) 544–9347
Sponsor: Office of Space Flight, Space Station *Freedom*

Arc Welding in the Space Environment

Welding can be a valuable process for fabrication and repair of metal structures in the space environment. As on Earth, more than one weld process may be required to satisfy potential **space welding** applications. Space Station *Freedom* will be the first application for welding to repair structural damage, plumbing leaks, and general maintenance. The Moon/Mars mission will also require joining of habitation structures and possible vehicle components.

Currently, the electron beam welding (EBW) process is the only process capable of operating in the **vacuum** of space, but the process is limited with respect to weld applications. For example, no apparatus is available to rotate an electron beam around a duct.

MSFC has undertaken a program to evaluate arc welding processes in a high **vacuum** environment (10^{-6} torr). **Vacuum** welding experiments are being conducted in a **vacuum** chamber with high gas-load capability (six 81–cm (32–in) diffusion pumps) belonging to MSFC's Low-Density Flow Facility. To date, the **gas tungsten arc** welding (GTAW) process has been evaluated using a hollow tungsten electrode. Inert gas at very low flow rates is used to transfer the arc to the workpiece. The process has shown promising results with definite potential for operating in a **vacuum**. The low-pressure arc reveals only slight variations in voltage with large changes in work to torch standoff distance (fig. 110). This is unlike the atmospheric collision-dominated plasma and more like a low-voltage electron beam. Technical issues resulting from the experiments center on torch design. Stray arcing and tungsten blockage were the main problems encountered.

A phase I Small Business Innovative Research (SBIR) contract with the Electric Propulsion Laboratory is currently under way in which an electric arc engine is being modified to act as a hollow electrode **gas tungsten arc (GTA)** torch. This contract addresses many of the problems associated with using an atmospheric **GTA** torch approach in **vacuum** applications.

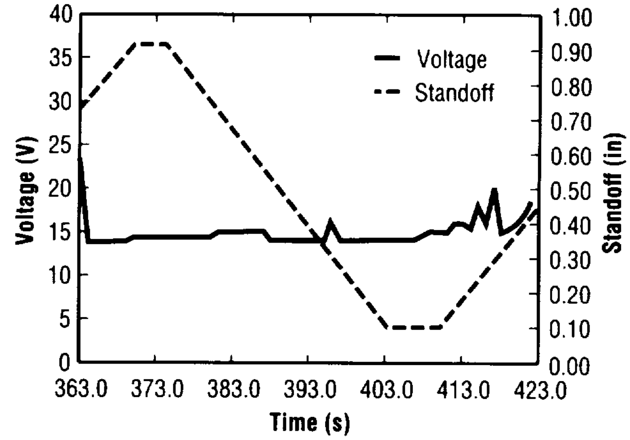

FIGURE 110.—Arc voltage/standoff versus time in vacuum ceriated tungsten, 6/26/90, 7th min.

The effects of zero-gravity are under study through the use of the NASA KC–135 aircraft. At present, no significant effects of gravity on weld quality have been identified. Weld joint gaps up to 1.5 times the thickness have been welded in the absence of gravity.

Presently, **gas metal arc** welding (GMAW) is being evaluated in **vacuum** application through another phase I SBIR contract.

C.K. Russell/EH42
(205) 544–2705
Sponsor: Office of Aeronautics, Exploration and Technology, and Office of Commercial Programs, Small Business Innovation Research

Advanced X-Ray Astrophysics Facility Coating Investigation

During FY91, considerable progress has been made in the Advanced **X-Ray** Astrophysics Facility (AXAF) coating investigation. The EB23 electron-beam (e-beam) evaporation box coating system was installed and activated during the latter portion of 1990. The Smithsonian Astrophysical Observatory (SAO) has performed **x-ray reflectivity** measurements for a substantial number of coated Zerodur and float glass flats. Many of the Zerodur flats were figured and polished by the Optical Systems Branch at MSFC. In addition to **x-ray reflectivity** measurements, other analytical techniques are being utilized to investigate surface morphology, film thickness, and coating density. These techniques include Wyco surface profile, scanning electron microscope (SEM), scanning tunneling microscope (STM) analyses at TRW, and Rutherford backscattering (RBS) analysis at SAO.

The overall goal of the AXAF coating investigation is to determine the optimum coating material, coating method, and coating procedures for the AXAF mirror elements. The **x-ray reflectivities** of **gold** (Au), **iridium** (Ir) and **nickel** (Ni) **coatings** on glass flats are being compared at various **x-ray** source energies and grazing angles. Coating methods include thermal evaporation from boats or crucibles, e-beam evaporation, sputtering, and ion-enhanced e-beam deposition. Deposition angle and deposition rate are two examples of coating procedure variations.

A.P. Shapiro/EB23
(205) 544–3488
Sponsors: Advanced X-Ray Astrophysics Facility (AXAF) Project Office and Office of Space Science and Applications

Carbon Phenolic Constituent Test Methodology and Specifications

In order to improve the reproducibility, reliability, and uniformity of **solid rocket motor** (**SRM**) **nozzles**, an industry advisory committee was established to review and refine the specifications and advance the test methodology of carbon-phenolic constituent materials, **prepreg**, and cured composite materials utilized in the manufacture of the **SRM nozzles**.

The industry advisory committee is represented by aerospace material suppliers, fabricators, and design organizations. These voluntary members contribute to the advisement tasks under study as follows:

- Perform round-robin testing for assessment of test accuracy and precision
- Recommend improved test methodology for consideration
- Provide access to corporate independent research and development activity.

Advisory tasks now under study include:

- Fabric **oxidation mass loss** test
- Phenolic resin advancement testing by nuclear magnetic resonance (NMR)
- Carbon assay testing by the Laboratory Equipment Company (LECO) equipment
- Carbon yarn electrical resistivity testing.

An example of the committee activity involves the development of a test procedure to measure carbon fiber **oxidation mass loss** rate by using the Arrhenius equation. A Perkin Elmer thermal gravimetric analysis (TGA) apparatus is used to measure **oxidation mass loss** rates at various temperatures, and the rates are plotted against 1/T. Figure 111 presents the results of round-robin testing between ICI/Fiberite, LPARL (Lockheed), and NASA/MSFC. All three facilities provided data that showed excellent agreement on temperature dependency. Laboratory to laboratory variance can be easily measured from the plots and attributed to a calibration offset. In particular, calibration of the Fiberite equipment was found to be 13 °C (55 °F) lower than at NASA/MSFC. It was concluded that location of the reference thermocouple is critical to achieving common laboratory to laboratory results.

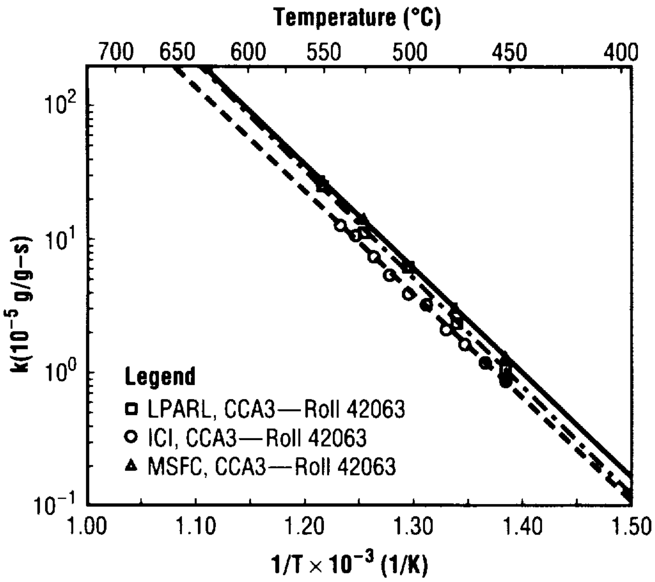

FIGURE 111.—Testing carbon fabric for oxidation mass loss.

The Arrhenius relationship was also used very effectively in measuring the catalytic effect of 3,000 parts per million sodium (Na) on carbon fabric **oxidation mass loss.** Table 3 summarizes the percent rate increase associated with oxidation temperatures 400 to 500 °C (752 to 932 °F). Most informative to the committee activity is the higher catalytic effect at lower temperatures. At 400 °C (752 °F), the mass loss rate is increased by 681 percent.

TABLE 3.—*Testing carbon fabric for oxidation mass loss*

Effect of Na on Oxidation Rate of Exp. 10B Fabric		
Temperature (°C)	A.R. Air Oxidation Rate* (g/g–s)	Influence of Na (% Rate Increase)
500	24.4×10^{-5}	102
475	16.5×10^{-5}	194
450	9.09×10^{-5}	258
425	5.61×10^{-5}	415
400	3.40×10^{-5}	681

* As Received

The Arrhenius temperature dependency has proven to be very effective in investigating oxidation sensitivity; however, the industry advisory committee consensus recommended a need for a simplified go/no-go procedure. Studies are currently under way to simplify the test procedure to meet the recommendation.

C.G. Upton/EH34
(205) 544–5755
Sponsor: Office of Space Flight

CO_2 Blast as an Alternative Cleaning Method for Space Flight Hardware

A high level of cleanliness is a typical requirement for the sensitive equipment routinely lifted into space. Most standard **cleaning** processes utilize a labor-intensive manual effort and require large amounts of environmentally hazardous and chemically dangerous **cleaning** agents. New, safer, and easier methods of **cleaning** must be developed to protect both humans and Earth. Recent additional Environmental Protection Agency (EPA) requirements necessitate an expeditious change in the way this type of **cleaning** is presently performed. The new methods should reduce the costs and processing time along with increasing personnel, hardware, and environmental safety.

In a joint effort between NASA, the U.S. Air Force (USAF), and the Martin Marietta Corporation (MMC), one environmentally safe **cleaning** method is being evaluated. This process uses carbon dioxide (CO_2) solidified in small pellets to blast the surface to be cleaned. As the pellets approach the substrate surface, the pellets compress and fracture. The small fragments quickly sublime and the resultant turbulent gases drive the **contamination** away from the surface. This process does not require any post drying or other additional processing. The pressure and mass flow rate are easily controllable to prevent peening damage to all but the thinnest of substrates. The experimental setup is shown in figure 112 .

This **cleaning** method utilizes CO_2, which is extracted from the waste gas stream created from other manufacturing processes. No additional gas is created that would contribute to the greenhouse effect. The **cleaning** system is automated by using a programmable robot. Therefore, personnel are not usually required to be in the same area as the CO_2 spray. This is beneficial since the spray generates sound levels above acceptable guidelines, which would require the system to be isolated from personnel or would require operators to wear proper hearing protection

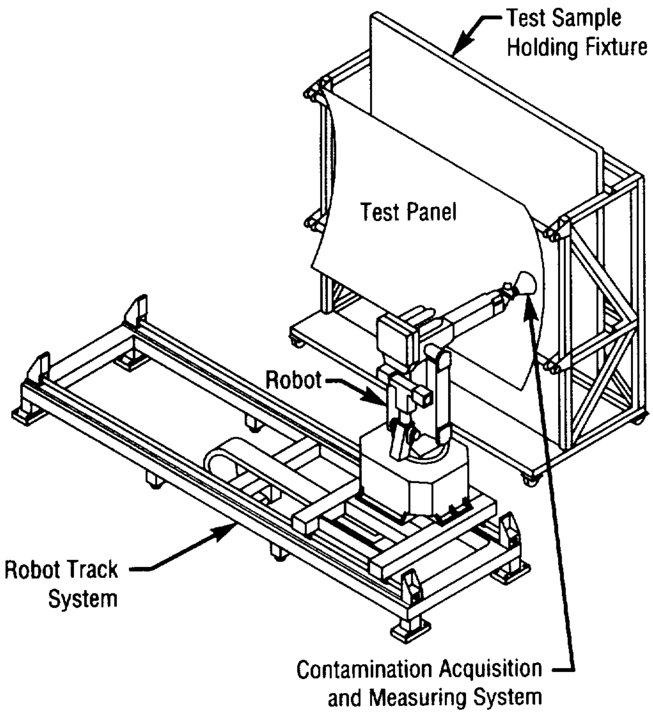

FIGURE 112.—Equipment setup.

when **cleaning**. Gaseous CO_2 levels in confined areas show a slight increase because of the sublimation process. Suitable ventilation would be required in the blast area if an operator is required to be present.

Tests performed at MSFC were conducted on small-scale test panels, large-scale mockup models, and actual hardware typically used in the refurbishment of solid rocket motors. Test panels were prepared by **cleaning** the surface in a certified laboratory to below 1 mg/ft^2. With a known cleanliness level, the test panels were then contaminated with a measured specific material. Measurements at the conclusion of the CO_2 blasting operation would then clearly indicate the effectiveness of the **cleaning** system. **Contamination** levels were measured with solvent flushes, tape lifts, cloth wipes, and a real-time **contamination** measurement method.

Preliminary results from **cleaning** a variety of substrate materials have shown that CO_2 **cleaning** systems are capable of eliminating or at least greatly reducing the amount of **chlorofluorocarbon** and chlorine-based **cleaning** fluids required. A variation in parameters can create fine molecular **cleaning** below 1 mg/ft^2 and can result in a highly efficient particulate removal rate. A more intense set of parameters, higher pressures, and mass flow rates may be used to remove gross **contamination** such as paint, adhesives, scaling, and insulation materials.

The success in automating the process results in the reduction of **cleaning** time by as much as 90 percent. The reduction in **cleaning** time results in a corresponding decrease in the labor costs. Material costs are also greatly reduced by this system. Since the CO_2 returns to its natural state in the atmosphere, no additional wastes except that which is removed from the substrate are generated, resulting in a much lower waste disposal cost. The system has proven to be reliable and gives high-quality results. A comparison between **cleaning** methods is shown in table 4. Preliminary **bonding** tests performed on panels cleaned by the CO_2 system have shown that the bond strength exceeds the standard requirements.

D.T. Hoppe/EH44
(205) 544–8836
Sponsor: U.S. Air Force and Office of Space Flight

TABLE 4.—*Comparison of cleaning methods*

Method	Cleaning Efficiency	Stripping Efficiency	Ozone Depletion	Environmental Hazard	Personal Hazard	Automated Processing
Vapor Degreasing	Very Good	No	No	Yes	Yes	No
Water Blast	Moderate	Very Good	No	Yes, With Walnut Shell Injection	High-Pressure Water	Yes
CO Blast	Very Good	Good	No	No	No	Yes
Aqueous Solution	Good	No	No	Slight	No	No

Compression-After-Impact Testing of Composite Materials

As part of MSFC's Polymers and Composites Branch's ongoing efforts to evaluate **carbon fiber composites** for foreign object **impact damage** susceptibility, two **compression-after-impact** (CAI) methods of testing are being used to help rank the various materials as to their ability to carry load after damage. This is vital information that the designer needs to know when using or selecting a material. One method involves the use of a honeycomb **sandwich beam** loaded in four-point bend, and the other method utilizes a version of the Illinois Institute of Technology Research Institute (IITRI) **CAI** fixture along with an antibuckling rig developed at the University of Dayton Research Institute.[1] Both of these methods allow the use of thin (down to eight-ply) laminates. This saves time and money, and gives more realistic results than the current standard **CAI** test that calls for 48–ply laminate, which is much thicker than needed for most design applications. In addition, a smaller load is needed to break the specimen that allows use of laboratory scale loading frames and much safer testing conditions.

The first **CAI** method uses the honeycomb **sandwich beam** (fig. 113). Since the beam strength needs to be determined by facesheet compressive failure, a very-high-density aluminum honeycomb core is used in the regions of the beam that experience the shear loads, and a lightweight honeycomb is used in the region that sees the bending moment, so, when impacted at its center, the composite facesheet is not supported by an extremely rigid base. Usually, this test is performed when data is being gathered for an end product that is a honeycomb structure. In this case, the density of the core used in the structure is the same as the density of the core in the middle section of the test specimen.

The other method of **CAI** testing utilizes a fixture designed at MSFC (fig. 114). This fixture uses wedge grips that are 7.62 cm (3.0 in) in width to shear load (as opposed to endload) a wide specimen with fiberglass end tabs. This eliminates the edge-brooming of fibers commonly seen in the current end-loaded **CAI** standard. This method is actually much like the IITRI **CAI** test method, only a much wider and longer specimen is used. The specimen has a gauge length of 10.16 cm (4.0 in), so a method to prevent global buckling of the specimen is needed. It had been shown previously that a long, thin composite specimen loaded in compression could be prevented from globally buckling by sandwiching it between two metal faceplates.[1] This technique was incorporated into the fixture with large cutouts in the faceplates to accommodate the damage area, i.e., protruding fibers, etc. This fixture has been used successfully for over 100 tests and gives undamaged compression strength values very near the value obtained by using the Celanese fixture standard, which uses an extremely small specimen.

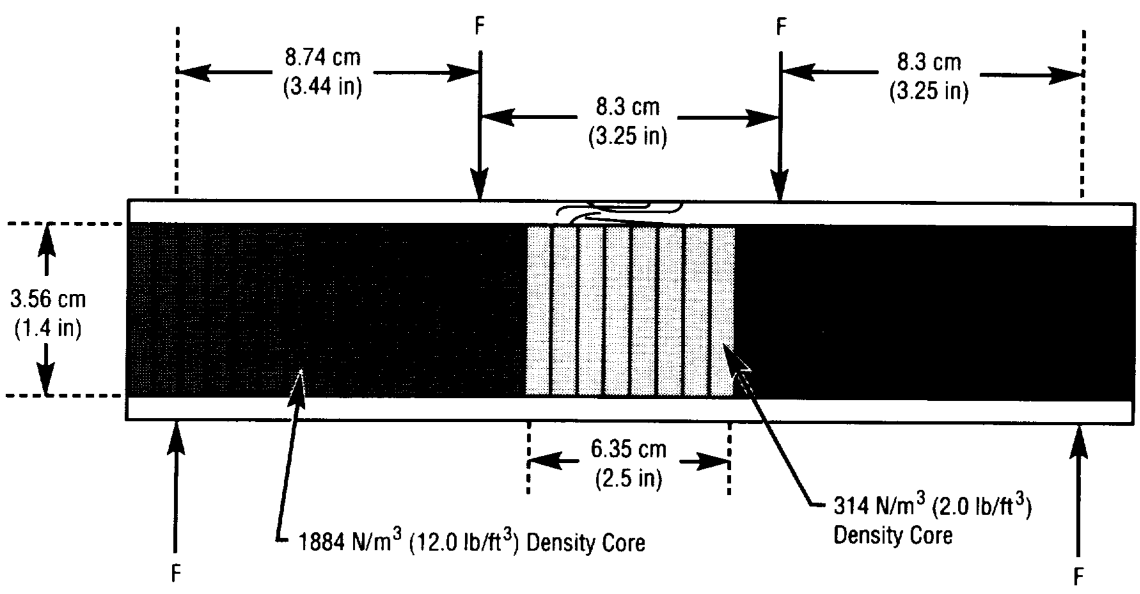

FIGURE 113.—Honeycomb core sandwich beam method of compression-after-impact.

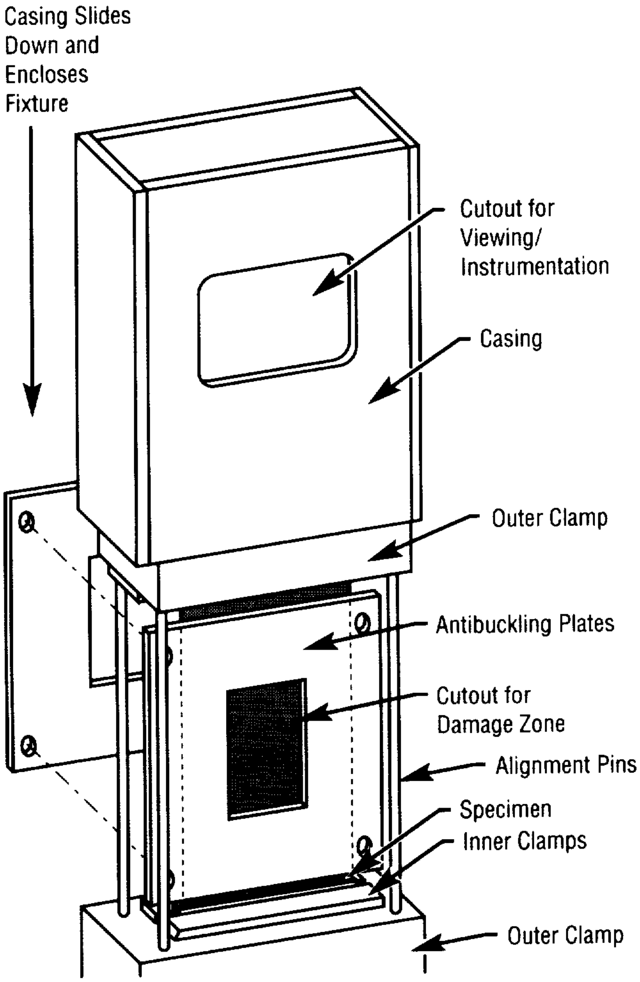

FIGURE 114.—Modified IITRI fixture for compression-after-impact testing.

Along with instrumented impact data and cross-sectional examination of the damage zone, the **CAI** data is another means used by the Polymers and Composites Branch to determine the **damage tolerance** of different composite materials.

[1]Sjoblom, P., and Hwang, B., "Compression-After-Impact: The $5,000 Data Point!" Proceedings, 34th International SAMPE Symposium, Reno, NV, May 8–11, 1989.

A.T. Nettles/EH33
(205) 544–2677
Sponsor: Center Director's Discretionary Fund

Development of Low Thermal Conductivity PAN-Based Fibers for SRM Nozzle Application

Commercial **polyacrylonitrile** (**PAN**)-based fiber is designed to meet the requirements of structural composites, which are generally tensile and modulus-driven. **Carbon fibers** used in **ablative** applications are unusual in that their design requirements are not generally driven by structural property requirements. **Ablative** applications require low thermal conductivity fiber to minimize char depth and backside temperature rise. The Materials and Processes Laboratory has initiated an effort to evaluate eight low thermal conductivity **PAN**-based carbon fiber candidates as potential replacements for traditional rayon-based carbon fiber in **ablative nozzle** applications. These candidates were manufactured from commercial precursor **PAN** fiber by Amoco, Hercules, Textron, and BASF Celanese. An extensive fiber characterization program was conducted to measure the properties of fibers from all sources at one test facility, Lockheed Palo Alto Research Laboratory, and to assess the relationship of fiber properties to subscale test performance. Low fiber thermal conductivity (measured by electrical resistivity) was established as the primary discriminator for this effort. Other fiber properties measured were density, moisture adsorption capacity, isopropanol adsorption capability, alkaline metal content, sodium equivalents, oxidation rate, carbon assay, ash content, tensile strength, tensile modulus, strain-to-failure, and the effect of high-temperature heat treatment (2,500 °C). A detailed description of test methodologies and the test results from the fiber characterization have been presented by Clinton, Pinoli, and Canfield.[1]

Performance testing of the eight **PAN** fiber candidates was performed by Thiokol Corporation/Wasatch Division using forty-pound-charge (FPC) subscale solid rocket motors. Erosion and char measurements are presented in tables 5 and 6, respectively, along with critical fiber and composite tag end properties. The propellant formulation for all motors was 88/20 hydroxyl terminated polybutadiene (HTPB), with an average burn time of approximately 33.2 s.

TABLE 5.—*Erosion rate performance in FPC tests with key fiber and composite tag end properties*

	Erosion Rate at Section B (45°)*	Composite Density (g/cm³)	Carbon Assay (%)	Fiber Density (g/cm³)	Activation Energy (kcal/mol)	2,500 °F Weight Loss (%)
Amoco 25	6.0	1.60	84	1.78	32.6	15.7
BASF DG-2	6.4	—	87	1.78	36.9	15.5
Herc LF-2	6.5	1.56	83	1.78	32.0	21.3
Amoco 23	6.7	1.55	84	1.78	32.7	16.3
AVCARB B-2	6.7	1.55	84	1.76	26.6	18.5
BASF DG-1	6.8	1.53	89	1.78	39.2	12.2
Herc LF-1	7.0	1.57	79	1.77	33.0	22.3
AVCARB G	8.1	1.50	75	1.65	26.8	28.2

* Scaled to FM5014 conditions (767 lb/in^2 average pressure)

TABLE 6.—*Char depth measurements from FPC tests with key fiber and composite tag end properties*

	Char Depth at Section B (45°)	Char Depth at Section C (90°)	Electrical Resistivity (ER)*	Resin Content		Carbon Assay (%)
				45° Part (%)	90° Part (%)	
AVCARB G	0.25	0.32	63,000	41	45	75
Herc LF-1	0.28	0.38	308	26	29	79
Herc LF-2	0.28	0.33	80	39	35	83
Amoco 23	0.28	0.40	88	30	32	84
AVCARB B-2	0.32	0.36	35	40	41	84
Amoco 25	0.34	0.44	61	35	29	84
BASF DG-1	0.40	0.48	27	30	32	89
BASF DG-2	0.48	0.55	35	39	—	87

* Current production lots of conventional shuttle-grade, rayon-based fabrics (CSA, CCA3 and VCL)

TABLE 7.—*Material spallation in FPC tests with key fiber properties*

Material	Spallation	Moisture Absorption (%)	Na (ppm)	Tensile Strength (lb/in²)	Strain (%)	Mod (lb/in²)
BASF DG-1	Yes	1.07	207	462k	1.54	25M
Amoco 25	Yes	3.70	9	320k	1.28	24M
Herc LF-2	Yes	3.60	940	411k	1.57	25M
AVCARB G	No	8.92	32	190k	1.77	10M
Herc LF-1	No	6.65	971	340k	1.53	21M
Amoco 23	No	5.66	5	348k	1.44	23M
AVCARB B-2	No	7.70	40	317k	1.48	21M
BASF DG-2		1.53	194	454k	1.61	24M

ppm–parts per million

Three of the materials exhibited spallation in the 90° section as presented in table 7 with other key fiber properties. The char depths in the 90° section were measured approximately 0.5–in aft of the interface with the 45° section. In the aft end, three materials charred through the entire section, BASF DG–1, BASF DG–2, and Amoco 25. This performance was attributed to the low values of electrical resistivity (higher conductivity) in the BASF materials. For the Amoco 25 material, poor quality prepreg and relatively low resin content were factors suspected to have influenced thermal performance.

Additional thermal performance data has been gained on the Hercules LF–2 material through the **PAN nozzle** development and qualification program for the Titan IV solid rocket motor upgrade (SRMU) at Hercules. This material has been fired in Minuteman III third stage and Hercules Brutus test motors. Preliminary results from embedded thermocouples indicate that the low thermal conductivity LF–2 composite compared favorably with rayon-based carbon phenolics in the same environment, and, in some instances, exceeded the thermal insulation performance of the rayon-based materials.[2]

In the second phase of this program, several candidates will be retested in the FPC motors due to uncertainty in the initial test results caused by several factors. Also, BASF will modify their process to produce a fiber candidate that meets target electrical resistivity values, and Textron Specialty Materials will provide spun versions of their candidate fibers in an attempt to increase thermal insulation capability. All successful candidates will be fired in the MSFC 2–in throat subscale solid rocket motor, and screening level thermal and mechanical properties will be generated at Southern Research Institute. Results of these efforts will be reported in 1992.

[1]Clinton, R.G., Pinoli, P.C., and Canfield, A.R., "Development of Low Thermal Conductivity PAN-Based Fibers for Solid Rocket Nozzle Application," JANNAF RNTS, Pasadena, CA, October, 1990.

[2]Wendel, G.M., "Update on PAN-Based Nozzle Ablative Qualification for Titan IV SRMU," JANNAF RNTS, Pasadena, CA, October, 1990.

R.G. Clinton/EH34
(205) 544–2682
Sponsor: Office of Space Flight

Diamond Film Production Using an Oxy-Acetylene Torch

Continuous films of **diamond** offer a number of outstanding material properties with practical application in aerospace system. **Diamond** boasts the highest hardness and the highest room temperature **thermal conductivity** of any known material. **Diamond** also possesses a small coefficient of thermal expansion and a low coefficient of friction.

Frequently, the dimensions obtained by plasma deposition systems are too small to be of practical use in aerospace applications. Recently, a number of laboratories have demonstrated the ability to deposit thin **films** of **diamond** using an oxy-acetylene torch.[1,2] This technique holds the promise of allowing deposition of continuous large-area coatings. Large-area **films** have not yet been produced, even on a laboratory scale. Research is directed toward understanding the processes underlying the nucleation and growth of these **films** and using the results to produce large-area continuous **films**.

The schematic (fig. 115) illustrates the intended setup for baseline production of continuous **diamond films**. **Films** are produced by obtaining the necessary gas mixture ratio with the mass flow controllers and then maintaining the sample in the narrow temperature region by use of the chill block, the optical pyrometer, and the relative distance from the torch tip to the sample surface. Only a narrow range of positions is allowable for the torch-to-sample distance, further limiting the system. Concurrent with obtaining and setting up the system, MSFC hopes to produce small-area **films** under conditions that will allow increases in quality and types of available substrates for deposition.

Using a preliminary setup, simply comprised of the mass flow controllers and a thermocouple, MSFC has reproduced some of the encouraging torch work reported in the literature.[3] MSFC has produced small islands of pure **diamond** crystals, and has just completed the setup for

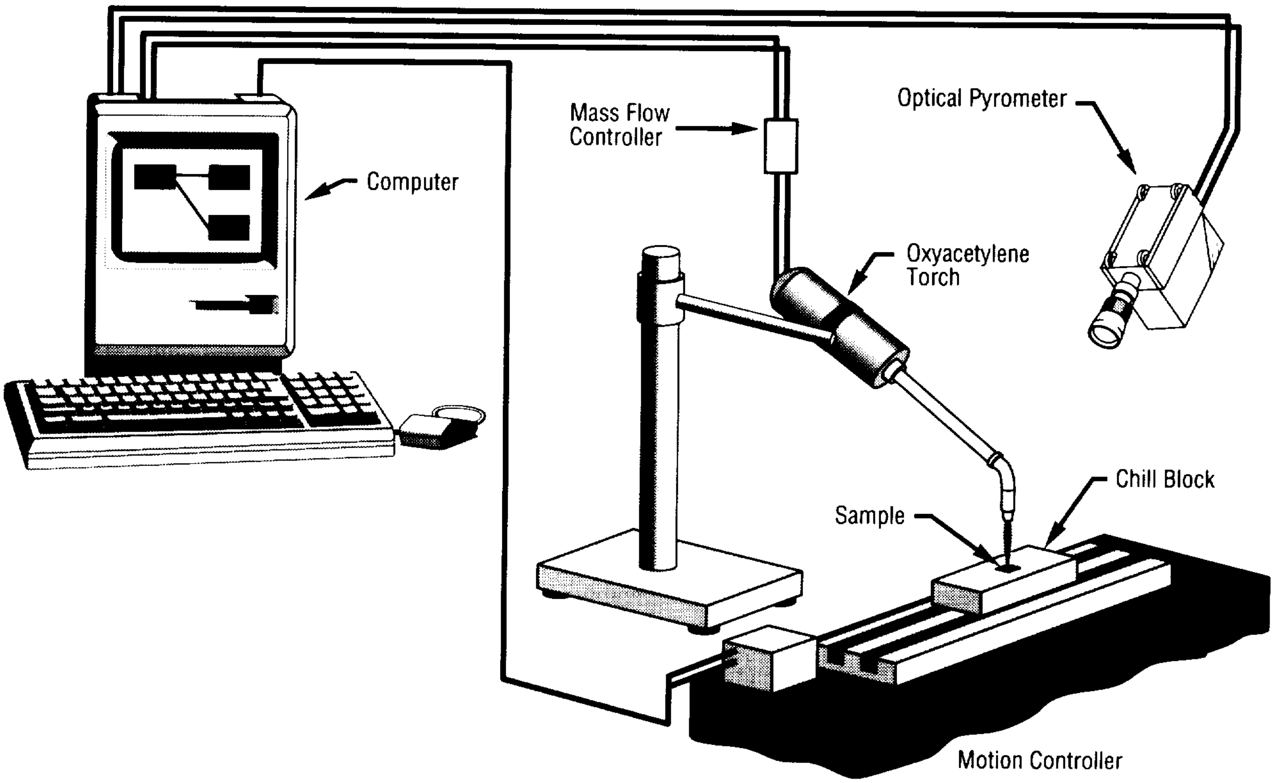

FIGURE 115.—Continuous diamond film production schematic.

microcomputer control of the deposition system to permit processed feedback signals to control the deposition process. Software has been written to control the optical pyrometer, and, hopefully, to soon control the flowmeters and the direct current power supply. These components will eventually be integrated into a process loop allowing for control of the system overall dynamics. During the next 6–mo period, MSFC will be adjusting fuel gases to improve the **film** quality.

Large area **diamond films** have applications in such diverse applications as micrometeoroid impact resistant windows, turbine blade edge coatings, cooling tube coatings, and nozzle and reentry surface coatings.

[1]Hanssen, L.M., Carrington, W.A., Butler, J.E., and Snail, K.A., "Diamond Synthesis Using an Oxygen-Acetylene Torch," *Materials Letters*, vol. 7, No. 7, 1988.

[2]Hirose, Y., Abstract, 1st International Conference on New Diamond Science and Technology, 1988, p. 38.

[3]Carrington, W.A., Hanssen, L.M., Snail, K.A., Oakes, D.B., and Butler, J.E., "Diamond Growth in O2+C2H4 and O2+C2H2 Flames," *Met TRANS*, vol. 20, July 1989, p. 282.

F.E. Roberts/EH34
(205) 544–1967
Sponsor: Office of Space Flight and Center Director's Discretionary Fund

Dielectric Breakdown of Spacecraft Surfaces Due to Plasma Interaction

With few exceptions, spacecraft flown to date have had power levels under a kilowatt and 28–V distribution systems. The **solar arrays** that convert sunlight into electrical power have typically operated between 30 and 36 V.

It has long been recognized that large spacecraft with much higher power levels will require **high-voltage solar arrays** to reduce the amount of current in the primary power system and, therefore, to operate efficiently. Space Station *Freedom* will be the highest power spacecraft that has been put into orbit. Its baseline design is for the **solar array** and the primary power system to operate at 160 Vdc and the secondary power distribution to the users to operate at 120 Vdc.

A spacecraft immersed in the low Earth orbit **plasma** must come to an equilibrium potential with this **plasma** such that there is no net current to the spacecraft. The electrons are very mobile and easy to collect whereas the ions are massive and difficult to collect. Therefore, in order to collect equal numbers of electrons as ions to the spacecraft, most of the voltage generated by the **solar array** will be negative of the local ionospheric **plasma** potential. This is a simplified description, and the actual equilibrium potential will depend on **solar array** design, the conducting area of the spacecraft, wake effects, and other variables.

Thin coatings are used on spacecraft and most of the surface of the space station is proposed to be anodized aluminum. If a spacecraft is grounded to the negative end of the **solar array,** then its structure will float negative of the local **plasma** potential; for the space station, this is approximately –140 V. If the converted surface or coating is a dielectric with a high resistivity, then the outer surface exposed to the **plasma** will be at the local **plasma** floating potential or within about a volt of local **plasma** potential. This leaves a large voltage drop across the dielectric. If the dielectric is thin enough so that it has insufficient dielectric breakdown voltage, then electrical breakdown of the surface will occur and **arcing** on the surface will result. For very large surfaces having such a voltage drop across thin dielectrics, the capacitance of the spacecraft can be quite large, storing large quantities of energy that potentially can be released during such an **arcing** event.

Anodized samples were tested in a **plasma** environment in such a configuration as shown in figure 116. The sample was biased negative relative to the **plasma** and data acquired for **arcing** onset and arc rate as a function of bias voltage relative to the **plasma**. These data are shown in figure 117. Data were also acquired on arc characteristics as a function of capacitance, which was meant to simulate the available capacitance that might be discharged on orbit. Arc currents of hundreds of amperes were observed, and the pit formed in the plate increased with the energy put into the arc. The plates tested were 6061 aluminum that had been chromic-acid-anodized. The conditions noted in figure 117 relate to the time the plates spent in the acid bath. Conditions A, B, and C are characterized by 30–, 25–, and 60–min time periods in the acid, respectively; all were hot-water-sealed. Condition D was the same as condition A except that it was unsealed. Condition E was the same as condition A except that it was aged at 49 °C (120 °F) for 6 d.

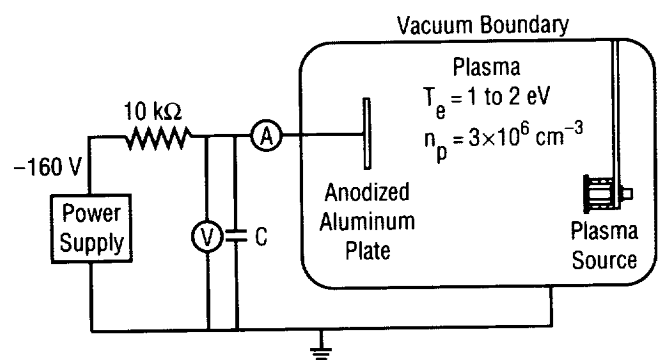

FIGURE 116.—Experimental configuration used for dielectric breakdown testing of anodized aluminum plates.

An arc will occur at the site of dielectric breakdown and the capacitance of the spacecraft will try to discharge through the arc. The underlying metal will have a net negative charge; an equal net positive charge will reside on the exterior of the dielectric surface. Current paths will have to close the circuit of negative charge flow from the structure to the outer surface. There are two basic mechanisms necessary for this to happen. When the **arc** occurs, a very dense **plasma** is formed at the **arc** site and will expand outward. This very dense and highly conductive **plasma** will be able to discharge a local area near the **arc**

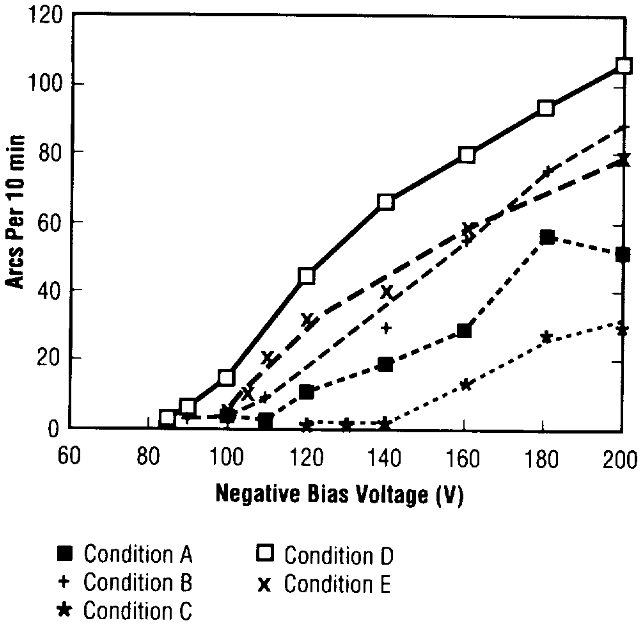

FIGURE 117.—Data of dielectric breakdown voltage of biased anodized plates in a plasma.

site. This may be on the order of meters. Secondly, as the negative charge tries to flow through the **arc** into the ambient **plasma**, a positive charge will exist on the outer surface of the dielectric. The electric field that develops will pull electrons from the ambient **plasma** to the surface until the positive charge is neutralized and this will complete the current path. Under steady state conditions, a thin **plasma** sheath on a large surface will limit the current to the random thermal current that can flow to a surface. A space station module in the maximum **plasma** condition will only be able to collect a few amperes in this case. In a transient case, such as an **arc**, the electric field will develop and will be able to collect the electrons within the volume it occupies, and, if the transient is fast enough, the ions will be frozen for a time. In this condition, **Debye shielding** will not occur and the electric field will be able to extend far out into the **plasma**. Therefore, large currents might be supported through an **arc** by such current return capability.

Experiments were conducted on the ability of a nearby surface area to discharge through an **arc plasma**. The test configuration and data are shown in figure 118. Figure 119 illustrates how an anodized plate was biased negatively but not allowed to **arc**. It charged as a capacitor and, when instantly grounded, a large current peak was measured, much more than could be supported by random thermal current to the surface. A typical data curve is also given in figure 119. The results indicate that the **arc** and ambient **plasmas** are able to provide large **current paths**, at least for sufficiently short transients.

These data indicate that spacecraft interactions with the ambient **plasma** where **high voltages** may be induced across anodized layers or other thin coatings must be considered carefully in the design and operation of future high-power spacecraft.

M.R. Carruth, Jr./EH12
(205) 544–7647
Sponsor: Office of Space Flight, Space Station *Freedom*

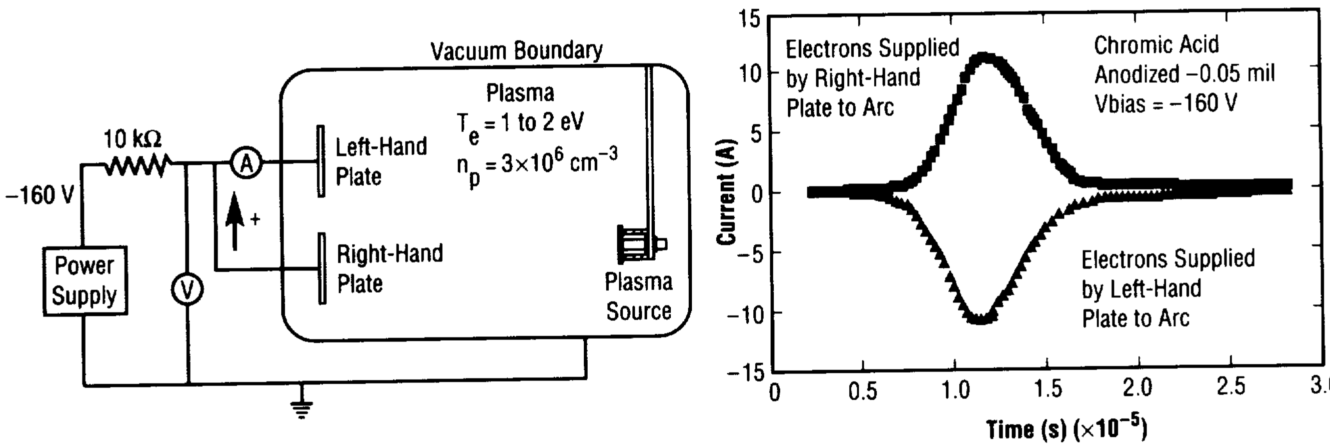

FIGURE 118.—Test configuration and current flow data showing discharge of a charged anodized plate when a dielectric breakdown occurs on a similar nearby plate.

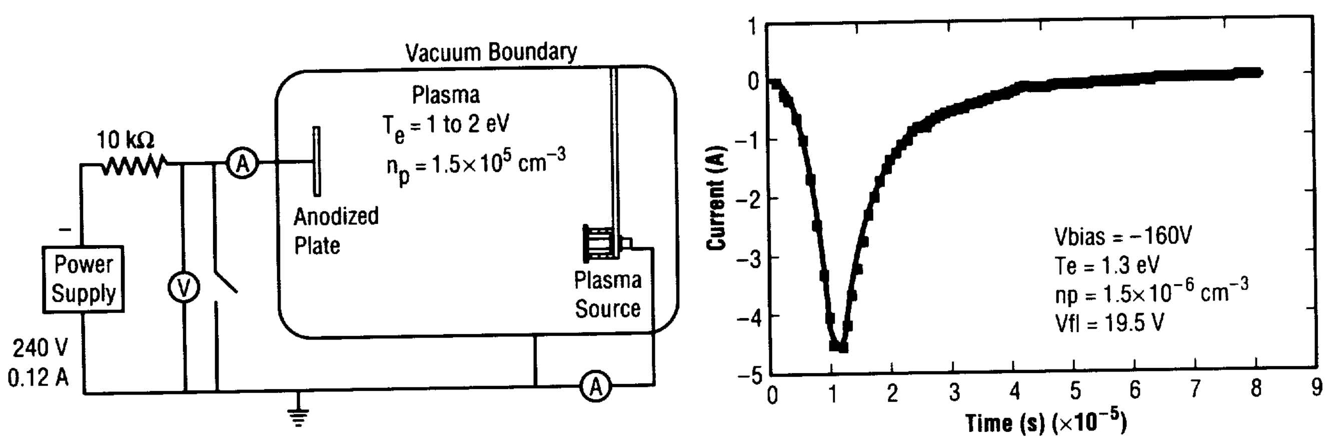

FIGURE 119.—Test configuration and current data for a biased plate suddenly grounded and the current supplied through the plasma.

Dual Property AISI 440C Bearing Race Using Localized Bore Retempering

Standard processing of American Iron and Steel Institute **440C alloy bearing** races for cryogenic propulsion systems involves thorough hardening and **tempering** to a hardness of Rockwell C (Rc) Scale 58–60. In that condition, the alloy exhibits high tensile strength (1,379 MPa (>200 K/in^2)) with relatively low fracture toughness (22 to 24 MPa $\sqrt{m}$ in (20 to 22 Ksi $\sqrt{in}$)) at room temperature and a moderate resistance to **stress corrosion cracking** (SCC). In addition, the thick cross section of typical cryogenic propulsion **bearing** races tends to develop tensile residual hoop stresses during the hardening treatment. Such stresses when combined with the tensile interference fit stress (172 to 207 MPa (25 to 30 K/in^2)) and the low fracture toughness can cause reduced **bearing** service life. In an effort to circumvent this limitation, a concept was devised to produce a dual-property **bearing** race consisting of a hard **bearing** surface (Rc 59 minimum) and a softer, tough, stress-relieved core using localized gradient retempering. The gradient retempering consists of localized induction heating of inner race bores to achieve the dual-property condition shown in figure 120. It is recognized that in order for the dual-property approach to be viable there must be a balance or compromise of the resultant properties (balanced toughness, **SCC** resistance, hardness, strength, and residual stresses) in the retempered bore.

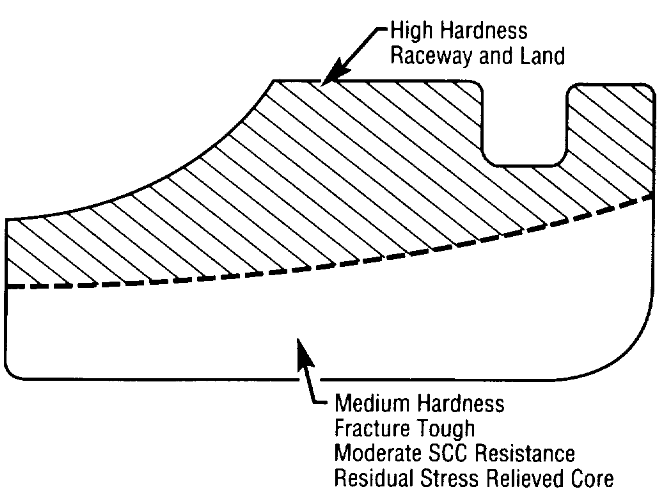

FIGURE 120.—Schematic illustration of the dual property condition in an ATD bearing inner race.

This may be challenging to achieve since opposing property changes occur with **tempering** temperature (fig. 121). The processing parameters necessary to produce a balanced set of properties (**SCC**, hardness, resistance, and fracture toughness) will be the primary determination of this research project.

Phase I of the research project is under way to demonstrate the feasibility of producing the dual-property condition by conducting localized heat trials initially on bolt specimens and later on cylindrical rings. Ring design will have a geometric representative of typical liquid propulsion cryogenic ball **bearing** inner races. The rings will be locally retempered to temperatures in the ranges of 260 to 400 °C (500 to 750 °F) and 538 to 677 °C (1,000 to 1,250 °F) while maintaining the raceway surface at 59 Rc. The room-temperature fracture toughness, hardness, and tensile properties will be characterized to identify the **tempering** range necessary to produce a balanced set of properties.

Phase II of the project will be to perform **SCC** tests on the gradient tempered rings of phase I. The rings will be mounted on an arbor at prescribed stress levels and **SCC**-tested in a humidity cabinet at 49 °C (120 °F), 100-percent humidity. Results of this phase of the project will be a major factor in influencing the decision to continue on with phases III and IV. Phase III will be to establish a method to yield the dual-property condition in a representative space shuttle main engine (SSME) ball **bearing** and phase IV will be to perform actual rig testing of the dual-property SSME ball **bearing** races of phase III.

R.A. Parr/EH22
(205) 544–2582
Sponsor: Office of Aeronautics, Exploration and Technology

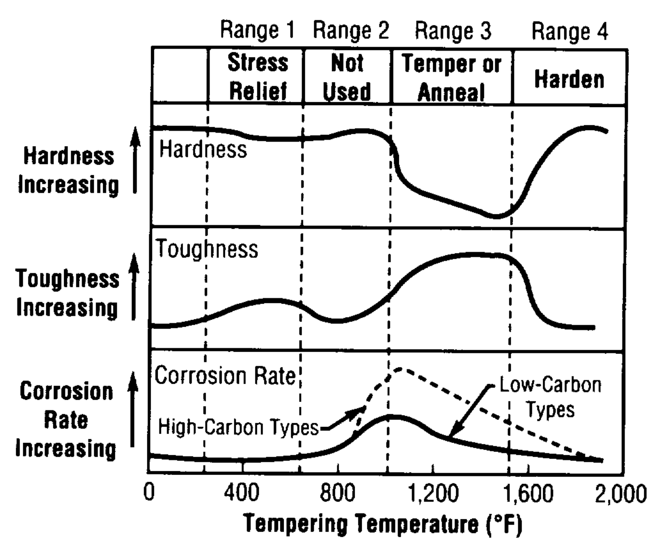

FIGURE 121.—Relation between properties and heat treatment.

Embedded Fiber Optic Sensors for Composite Structures

Composite materials offer several advantages over metals including higher stiffness, lower weight, and lower coefficients of thermal expansion. However, it is more difficult to detect damage and defects in **composite** laminates, especially since the damage is often not visible on the surface. A new sensor technique is being developed to alleviate the problem of damage detection and to perform in-service monitoring of the structure. This technique involves embedding optical fibers in the laminate as it is being manufactured, and using changes in the light transmission characteristics as a measure of damage, strain, temperature, or other physical quantity.

A considerable volume of experimentation with this concept has been performed and documented in journals and proceedings, but much remains to be done. The primary interests of the Materials and Processes Laboratory are damage detection, in-use monitoring of strain, and applicability to automated manufacturing processes. Preliminary work in these areas of interest includes the fabrication of **composite** bars by the pultrusion process with an embedded optical fiber, hand lay-up of several 10×10–in panels with embedded fibers, and tests performed on unembedded optical fibers to measure the attenuation of transmitted light when the fiber is compressed.

Pultruded bars 1/8–in deep and 1–in wide were fabricated with one multimode fiber centered within the bar. The optical fiber was undamaged and no visible defects were found in the bar. While the bar was fabricated, measurements of photocurrent decrease in the fiber were taken with a photodiode to determine if the fiber could transmit under conditions of high temperature and pressure and if the attenuation level could be used as an indicator of pressure or strain. The fiber continued to transmit throughout the process, and the photocurrent decreased as more of the fiber entered the die. Further work with the pultrusion process will include nondestructive evaluation of the bars to identify hidden defects, comparison of bend tests of parts with and without embedded fibers, and measurements of attenuation during fabrication using a calibrated optical power meter and an optical time domain reflectometer (OTDR).

Tests on unembedded fibers were conducted by compressing a known length of fiber with a known load and measuring the transmitted optical power. The purpose of this experiment was to examine the effect of the length of fiber under consideration, the repeatability of transmission measurements, and whether a compressed fiber would return to its original state. Results have been encouraging but more trials must be performed to draw a firm conclusion.

Future work with this technique will be conducted in conjunction with university researchers and with other science and engineering organizations. Beyond the workability of the method, questions regarding manufacturing and production techniques and implementation of the method in future programs will be addressed.

C.E. Wilkerson/EH44
(205) 544–8834
Sponsor: Center Director's Discretionary Fund

Feasibility of Atomic Oxygen Interactions Accelerated Testing

Spacecraft that will be in **low Earth orbit (LEO)** will be subjected to reactive **atomic oxygen (AO)** atoms with an energy near 5 eV, relative to the spacecraft. It is known that most materials will react with the oxygen, with some materials being very degraded in a short time in **LEO**. Because of the wide range of materials on spacecraft and the limited flight data, ground testing of materials to an **AO** environment is necessary. However, it is very difficult to reproduce **LEO** conditions in the laboratory. A study has been undertaken to quantify the difference in reactions between materials and **atomic oxygen** ions and neutrals at various energies in order to understand reaction mechanisms and to establish relative rates of reactions. If accelerated testing in the laboratory can be performed reliably using 30–eV ions or neutrals instead of 5–eV ground-state neutrals, then laboratory testing for long exposure will be more practical. In order to accomplish this, interaction mechanisms must be understood and the effects of ionization state and energy must be determined.

An **ion-beam** system with a grazing incidence neutralization process has been developed by Vanderbilt University for this study. Beams of ions and neutrals with variable energy from low energy to high energy are now routinely produced with this system, including beam energies of only a few electronvolts. Most of the work during development and checkout has been performed using nitrogen or other gases due to the lifetime limits resulting from the use of oxygen.

Optical emissions of the surface exposed to the incoming beam, as well as the emissions of desorbed atoms, are examined in order to obtain data on the surface reactions. Laser-induced fluorescence is also used to determine the energy and temperature of the atoms that have left the surface. Some of the studies performed to date have shown that the optical spectra from surfaces show marked differences when exposed to ion beams or neutral beams. Detailed studies with **AO** will only begin following complete operation and checkout of the system and studies with other gases of interest.

Examination of the effects on materials due to **AO** combined with ultraviolet radiation, and/or energetic electrons and protons are also being conducted. This will allow determination of the synergistic effects of these combined environments. The different energy put into the material surface may affect the chemistry of the interaction and produce effects that are not additive.

M.R. Carruth, Jr./EH12
(205) 544–7647
Sponsor: Office of Space Flight, Space Station *Freedom*

In Situ Contamination Effects Study

The **In Situ** Contamination Effects Facility in the Materials and Processes Laboratory at MSFC is being used to observe **optical effects** of **molecular contamination** and to compare results to analytical modeling. These results show that the useful range of acceptability of some spacecraft materials can be extended by defining the critical temperature at which molecular deposition onto an **optical surface** begins. Materials tested so far include silicone S–383, Z–306, viton V–747, engine pressure ratio (EPR) rubber E–692–75, and solithane 113.

This testing measures the time-dependence of the angular reflectance from molecularly contaminated **optical surfaces** in the vacuum ultraviolet (VUV). This time-dependence defines the in-plane VUV **bidirectional reflectance distribution function** (**BRDF**). The light-scattering measurements are accomplished **in situ** on **optical surfaces** in real time during deposition of molecular contaminants. The measurements are taken using noncoherent VUV sources with the predominant wavelengths being the krypton resonance lines at 1,236 and 1,600 Å. Detection of the forward- and backscattered light is accomplished using a set of three solar blind VUV photomultipliers.

The contamination study with the **In Situ** Contamination Effects Facility is a joint endeavor by The University of Alabama in Huntsville and MSFC.

R.C. Linton/EH12
(205) 544–2526
Sponsor: Office of Space Flight, Space Station *Freedom*

Long-Duration Exposure Facility Experiments and Orbital Materials Interaction Studies

The **Long-Duration Exposure Facility** (LDEF) continues to provide a wealth of information on the space environment and how materials react to that environment. Ongoing analysis of three **LDEF** experiments in the Materials and Processes Laboratory of MSFC provides new data on spacecraft thermal control, photovoltaic, and structural materials.

These three experiments are A0171, the solar array materials passive **LDEF** experiment; S0069, the thermal control surfaces experiment; and A0034, **AO** stimulated outgassing. All three of these experiments were mounted on or adjacent to the leading edge of the **LDEF** for maximum exposure to the impacting **AO** and orbital debris, as well as to ultraviolet (UV) radiation, hard vacuum, and thermal cycling.

About one-sixth of the **LDEF** experiment A0717 tray was devoted to composite-material tensile specimens. These specimens were thermally isolated from the mounting plate using polytetrafluorethylene (PTFE) washers. These washers protected a small area of the specimens from **AO** erosion. Profilometer traces then measured the amount of erosion (table 8). **AO** reactivity also increased optical diffusivity, eroded the matrix more than the reinforcing fiber, and left behind a thin layer of white ash.

Also included on the A0171 tray were solar cells with antireflectance-coated coverslips. Comparisons between preflight and postflight electrical properties show the preponderance of the data to indicate a 5– to 8–percent drop in maximum power output. Other materials presently being analyzed are adhesives, encapsulants, reflector materials, substrate strength materials, mast and harness materials, and thermal control coatings.

TABLE 8.—*Mass loss and thickness loss for A0171 composite samples*

Composite Materials (No. of Specimens)	Mass Loss per Area (mg/cm^2)	Average Thickness Loss (mil)	Atomic Oxygen Reactivity 10^{-24} cm/atom
HMF 322/P1700/±45°	18.46	4.7 to 11.5*	(1.9 to 4.6)
HMS 934/0°	11.79	2.50**	1.0
HMS 934/90°	11.31	2.70	1.1
P75S/934/90°	11.27	2.70	1.1
P75S/934/0°	10.29	2.80	1.1
"S" Glass-Epoxy	2.40	0.36***	0.14
Thermal Control Aluminized Taped "S" Glass-Epoxy	0.59	Indeterminate	--

* Matrix Erosion Much Greater Than Fiber
** Average of Rates From Two Ends of Sample; Contamination Likely on Forward End
*** Fibers Uneroded and Become Protective After Initial Matrix Mass Loss

The battery-powered, active **LDEF** experiment S0069 measured the spectral hemispherical reflectance of selected thermal control specimens. The optical testing instrumentation recorded 420 d of data before the batteries were depleted. Figure 122 shows the increase in solar absorptance of flight specimens versus ground simulation for S-13G-LO and Z-93 thermal control coatings. Also noted in this experiment were **AO** erosion of the silver/Teflon surfaces, thermal cycling damage to protective overcoatings, and fluorescence to UV light by some coatings. Calorimetric sensors also provided in-flight recordings of solar absorptance and infrared thermal emittance.

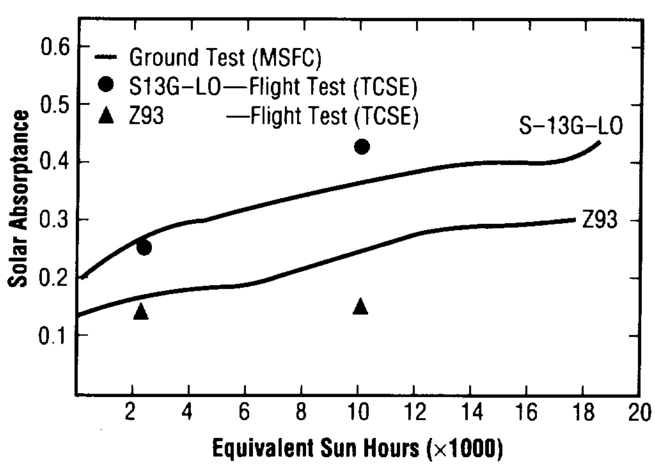

FIGURE 122.—Comparison of thermal control surfaces equipment (TCSE) flight data with ground simulation testing.

Experiment A0034 consisted of two identical one-sixth tray modules, exposing selected thermal control coatings to **LDEF** leading- and trailing-edge conditions. Optical mirrors were included adjacent to the thermal coatings for deposition of outgassing products. Analysis is continuing on the effects of **contamination** combined with the natural and manmade space environment on material performance. Ultraviolet grade windows and metal covers were provided for additional assessment of the effects on various environmental factors. Preliminary results indicate that **AO** is both a degrading and optically restorative factor in the thermo-optical properties of selected thermal control coatings. There is evidence of more severe optical degradation on collector mirrors adjacent to **AO**-exposed coatings.

A. Whitaker/EH11
(205) 544-2510
Sponsor: Office of Aeronautics, Exploration and Technology

NASA–23 Alloy Development

The alloy NASA–23 was formulated in the early 1980's as a **structural alloy** resistant to hydrogen embrittlement. It was designed to be as good as, or better than, Inconel 718, the most common **structural alloy** used in the **rocket engines** (e.g., space shuttle main engine). However, unlike Inconel 718, which is severely embrittled in hydrogen, NASA–23 is relatively immune to hydrogen embrittlement and can be used without a protective hydrogen barrier coating such as copper. Therefore, the use of NASA–23 in **rocket engine** components can result in substantial cost savings.

The NASA–23 alloy is currently being developed for the structural jacket of the advanced main combustion chamber, which is basically a **cast** structure. Therefore, strength, ductility, and **hydrogen resistance** in the **cast** condition are important for this application. Preliminary test data obtained with hot isostatically pressed, solution-treated, and aged **cast** NASA–23 test specimens indicated that the yield strength was relatively high (140 lb/in^2), but the ductility was moderate with 6–percent elongation. The goal was to achieve a minimum of 10–percent elongation without sacrificing strength.

Two approaches were used to improve ductility: (1) optimization of hot isostatically pressing and (2) modification of heat treatment. Hot isostatic pressing was optimized by raising the temperature to 1,204 °C (2,200 °F) from 1,177 °C (2,150 °F) and pressure to 25k lb/in^2 (from 15k lb/in^2). This resulted in a 30– to 40–percent improvement in ductility. The original heat treatment consisted of solution treating at 954 °C (1,750 °F), followed by aging—first at 718 °C (1,325 °F) for 8 h and then at 621 °C (1,150 °F) for 8 h. This resulted in the precipitation of eta phase at the grain boundaries, which apparently contributed to the low ductility. In an attempt to modify the heat treatment, a time-temperature-transformation (T–T–T) diagram was constructed for NASA–23. This diagram shows the precipitation of different phases in time-temperature space. Using a series of samples heat-treated at various times and temperatures, with subsequent microstructural examination using optical and electron microscopy, the time-temperature relationship for the precipitation of phases was determined. Based on this T–T–T diagram, the NASA–23 heat treatment was modified to a three-step aging treatment: 718 °C (1,325 °F) for 0.5 h, 621 °C (1,150 °F) for 4 h, and 732 °C (1,350 °F) for 4 h. This treatment minimized eta precipitation and reduced the volume fraction of gamma prime, the strengthening precipitate; and, it enhanced the ductility of NASA–23 to 15–percent elongation at acceptable strength levels.

B.N. Bhat/EH23
(205) 544–2596
Sponsors: Office of Aeronautics, Exploration and Technology and Office of Space Flight

New Portable Tensile Strength Test Equipment Developed at MSFC

Bond strength testing of **thermal protection system** (**TPS**) material on the external tank (ET) and solid rocket boosters (SRB's) is a vital part of flight preparation. Currently, bond strength tests are performed with a variety of pneumatically powered testing devices that have little control over displacement rates and might not have direct tensile load measuring capability.

The purpose of this effort, known as NASA electric portapull (NEP), is to develop a tensile strength test system that is lightweight, measures load directly and accurately, and has a controlled displacement rate. To generate greater standardization among **tensile test** equipment used on the various materials, the NEP is designed to be adaptable to many ablative materials.

There are three basic components to the NEP: a motor-driven pulling mechanism, a motor controller, and a data-acquisition system. To perform a test using the current prototype, the NEP is attached to the sample's test button using a spring-loaded gripper. Once the electric motor is running, its displacement rate is maintained at a selected value by closed-loop feedback control. The load is measured and recorded at a rate of 40 samples/second. The maximum tensile strength value is also held and displayed on the computer screen. The computer serves as the operator's input station and contains the software that controls functions such as the displacement rate and sampling speed.

A program to test the NEP against fixed location **tensile test** equipment, such as the Instron 1333 servohydraulic test system, is now under way. Tests comparing the tensile values for Marshall sprayable ablator (MSA) were obtained with the NEP to identically prepared samples tested on the Instron and to 2×2–in block samples tested on the Instron. Preliminary results show a closer correlation between the two test methods than has ever been achieved. There has also been a reduction in the measured tensile strength variance over a sample set compared to previous portable tensile strength test equipment. A sample of the results is shown in figure 123. Further tests will include statistically designed experiments to examine the effects of various processing and testing parameters.

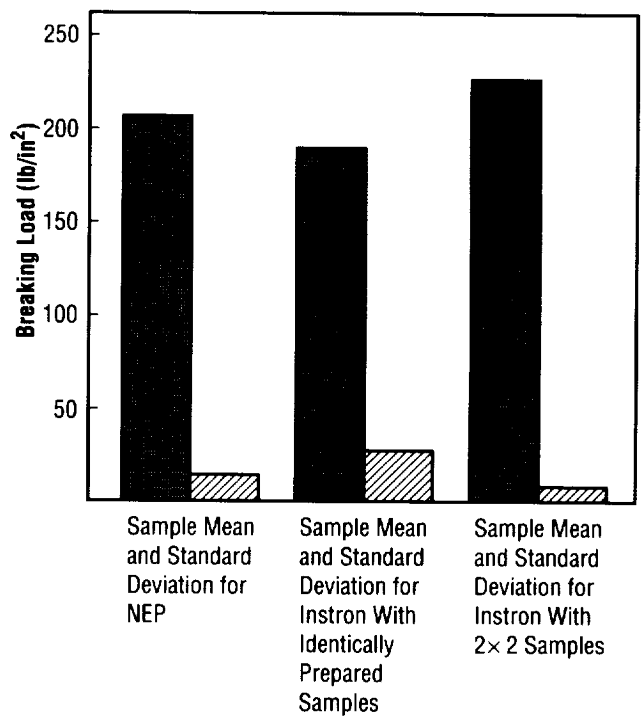

FIGURE 123.— Comparison of NEP and Instron data for tensile tests of MSA–2.

C.E. Wilkerson/EH44
(205) 544–8834
Sponsors: Office of Space Flight

NONMETALLIC TOOLS FOR MARSHALL SPRAYABLE ABLATOR TENSILE TEST BUTTON PREPARATION

A study was conducted to determine if an improved nonmetal tool could be found for the **Marshall sprayable ablator (MSA) coring cutters** used in the preparation of tensile test buttons. The **cutters** presently used are made of fiberglass with 16 teeth equally spaced at 22.5°. **Coring** is done by inserting the **cutter** into a guide and turning a knob affixed to the **coring cutter** by hand. **Nonmetallic cutters** are utilized to minimize any damage to the hardware metal surface and subsequent closeout processing. The tools tested in the study were evaluated on the basis of tear, wear, and overall durability.

Five candidate materials were selected and one **cutter** from each was made. The materials selected were polyvinyl chloride (PVC), Plexiglas, nylon, Textolite, and fiberglass. A steel **cutter** was also made for use as a standard. The **cutters** were made with 12 teeth each (30° apart) with a 0° front rake and a 10° end clearance. The inside diameter was bored to 28.65 mm (1.128 in) in order to leave a 6.4516 cm^2 (1 in^2) cored area. The **cutters** were run at about 75 r/min in a Gorton milling machine for each of the samples. The first tests involved 14 cored **MSA** samples by each **cutter** except the PVC, which totally failed early in the test and was eliminated from the study. Test specimens numbers 1 and 14 were saved for visual examination. Photomicrographs were made of the first and last **MSA** sample cored by each **cutter**. The photos were taken at a cross section to further evaluate the effect of the **cutter** on the **MSA** substrate. Subsequent tests without photomicrographs were conducted until a total of 75 samples were done with each **cutter**. The results of the tests are as follows, and are summarized in table 9.

TABLE 9.—*End clearance wear*

Test Material	Number of Samples	End Clearance Wear (%)
PVC	6	100
Plexiglas	75	100
Textolite	75	100
Fiberglass	75	50
Nylon	75	25

- PVC **cutter** totally failed at six cuts
- Plexiglass **cutter** cored 75 samples and the 10° end clearance was worn to 0°
- Textolite **cutter** cored 75 samples and the 10° end clearance was worn to 0°
- A fiberglass **cutter** cored 75 samples and the 10° end clearance was worn to 0° for a distance of 1.02 mm (0.04 in)
- A nylon **cutter** cored 75 samples and the 10° end clearance was worn to 0° for a distance of 0.51 mm (0.20 in)

The data show the percent of the 2.03-mm (0.08-in) wide 10° end clearance worn on each tooth after 75 cuts with each material tested. The test was conducted with the **cutter** going through the **MSA** and cleaning the substrate down to the paint. Some of the wear is attributed to varying pressures on the tool to obtain a clean cut at the substrate. As expected, no wear was visible on the steel **cutter**.

The three **cutters** experiencing the least wear, the Textolite, fiberglass, and nylon, were resharpened to their original condition for additional tests. This time 119 samples were cored with each **cutter**. A stop was set to mechanically end the **coring** just before hitting the substrate. The material cored was about 3.81-mm (0.15-in) thick. Visual examination and feel of the cutting teeth revealed very little wear on any of the three **cutters**. The Textolite maintained the sharpest edge followed by the fiberglass.

This study confirmed that presently used **nonmetallic coring** tools for **MSA** material are adequate for preparing tensile test buttons. The materials used in the study experienced normal wear and did not damage the **MSA** surface, as evidenced by the photomicrographs and visual inspections. However, further testing is recommended to establish correlations between **MSA** tensile strength, standard deviation, tool wear, and tool material.

W.E. Norton/EH44
(205) 544-2721
Sponsor: Office of Space Flight

Optical Properties Monitor

The **optical properties** monitor (OPM) is an experiment to provide a test-bed for studying the effects of both natural and induced environments in space on **optical** and **thermal materials**. A predecessor to the OPM experiment is the thermal control surfaces experiment (TCSE) flown on the Long-Duration Exposure Facility (LDEF).

Like TCSE, OPM will incorporate a rotating carousel design as illustrated in figure 124. This carousel will contain 160 samples, half of which will be exposed during launch and reentry, as well as during orbital change maneuvers. The carousel's other half will be exposed while in the designated orbit. **Material measurements** will include reflectance, transmittance, and scatter, while **environmental measurements** will include solar and Earth irradiance, molecular contamination, and atomic oxygen.

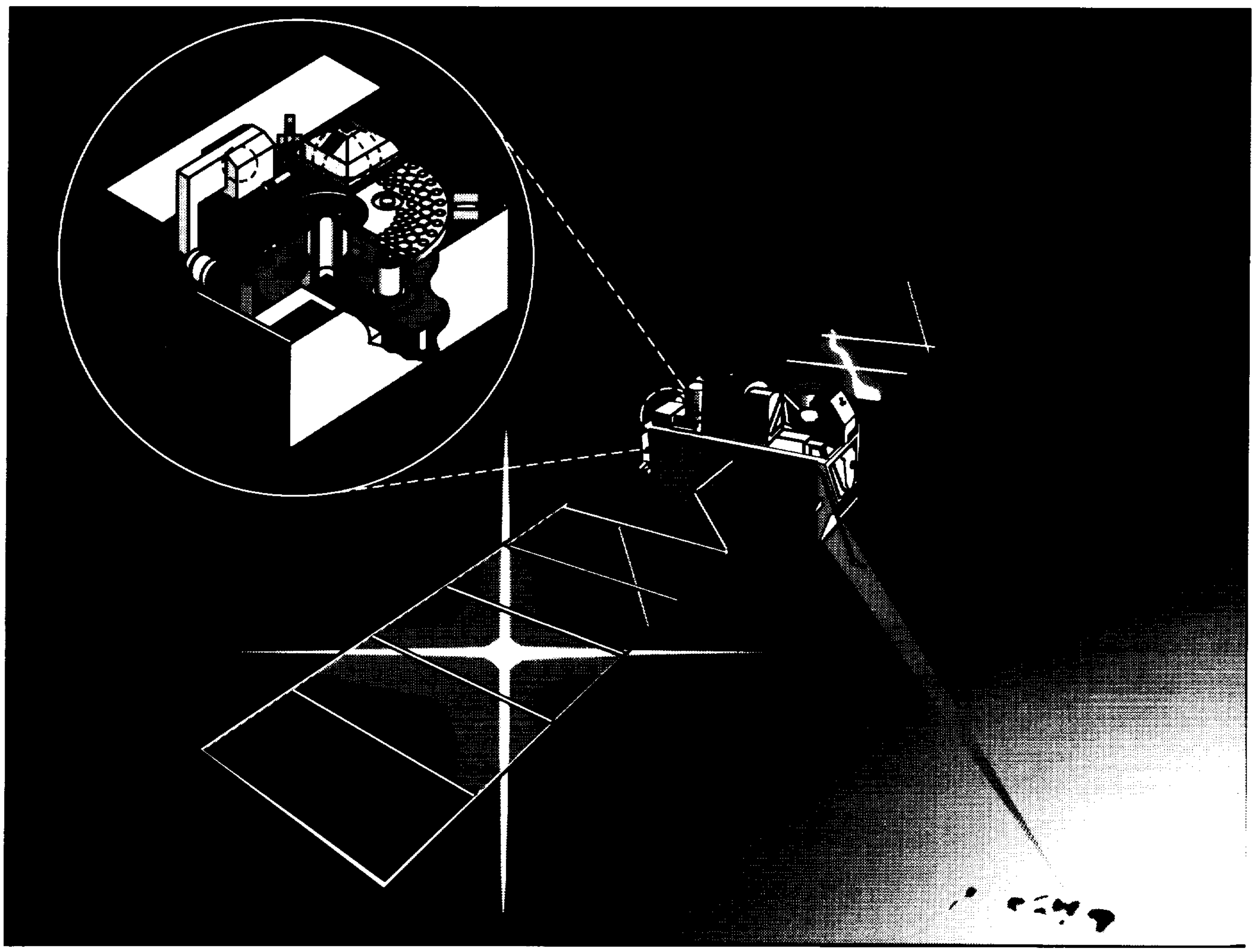

FIGURE 124.—OPM assembly.

This experiment is currently planned for flight on the **European retrievable carrier** (**EURECA**). The OPM/ **EURECA** configuration is depicted in figure 125. The **EURECA** spacecraft is carried to low Earth orbit by the space shuttle, released, and then boosted into a 500-km orbit. After approximately 6 mo at this orbit, the mission is completed by deorbiting to an altitude where the space shuttle retrieves the spacecraft and returns it to Earth.

Activities in FY91 included a feasibility study to determine the compatibility of OPM requirements with **EURECA** mission plans, and the initiation of a 1-yr experiment definition activity.

D.W. Cockrell/JA93
(205) 544-1279
Sponsors: Office of Science and Applications

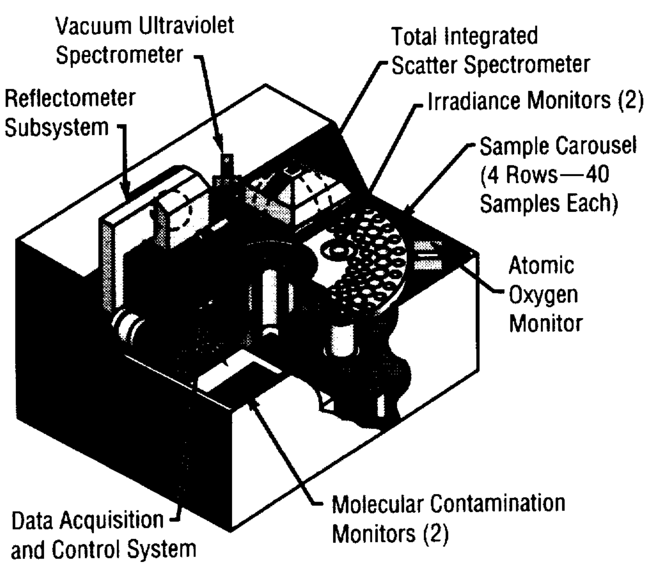

FIGURE 125.—OPM/EURECA configuration.

Optimization of Vacuum Plasma Spray Processing Through Kinematic Simulation

Event simulation for modeling manufacturing systems is an effective tool to increase production, improve quality, and reduce cost. The parameters effecting kinematics or dynamics of a process are embedded in routines that manipulate three-dimensional (3-D) graphical models and enable a complete simulation of the process. This **graphic simulation** can be executed (with different sets of parameters affecting it) to test concepts, set limits of motions and collision avoidance, and process optimization and verification.

Graphic simulations offer an approach for studying various manufacturing alternatives and strategies. By varying selected parameters in a controlled environment, various options can be studied rapidly. **Graphic simulation** provides an inexpensive insurance against costly mistakes and expensive delays.

This technology is being used in the design of tooling, process automation, and manufacturing verification of the vacuum plasma spray (VPS) formed main combustion chamber (MCC) for the space shuttle main engine/ space transportation main engine (SSME/STME) (fig. 126). To obtain optimum material deposition, the plasma spray gun must be positioned near perpendicular and approximately 28-cm (11-in) away from the MCC liner surface. By kinematic simulation of the process, the engineer verifies that the gun assembly, rotary table, and tooling works in a **coordinated motion** maintaining optimum spray parameters and avoiding any collision between tooling, part, and spray chamber.

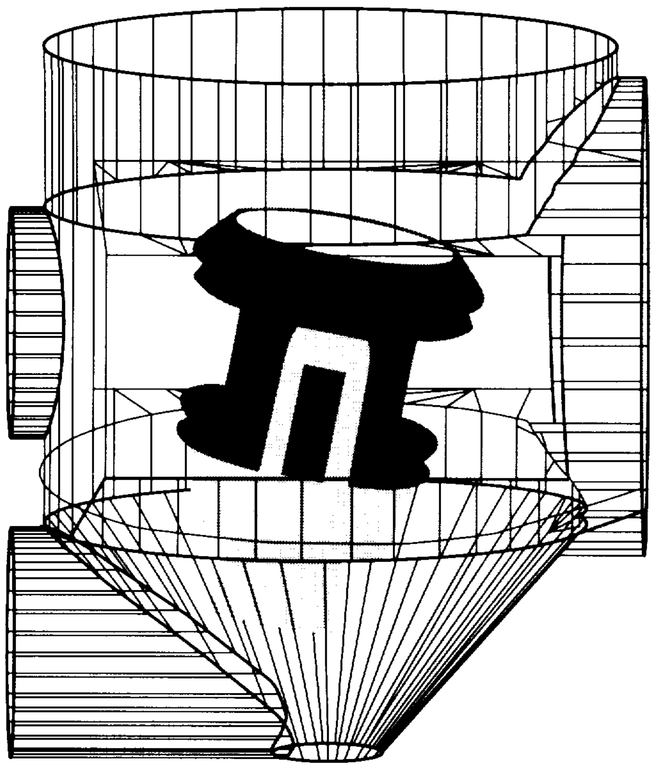

FIGURE 126.— Optimization and verification of the VPS for the MCC through 3–D graphic simulation.

The simulation also provides 3–D visual aides and mathematical coordinates to establish specifications for axis travel limits, geometrical modifications, and, tooling and device orientation. In addition to a computerized process verification, cost and time savings are accrued by debugging the process and conducting manufacturing runs using a computer, without material and utilities expense. Furthermore, the safety of the hardware and process equipment is verified prior to commencing the manufacturing sequence.

M.K. Babai/EH44
(205) 544–2795
Sponsor: Office of Space Flight

Particulate Contamination on Optical Surfaces

Detection and characterization of **particulate contamination** on **optical** surfaces is of utmost interest to those who have a need to model overall performance of **optical** systems. Among the various types of **optical** systems, those designed to operate using grazing incidence reflection may exhibit more substantial degradation of performance due to **particulate contamination**. In **x-ray optical** systems, such as the Advanced **X-Ray** Astrophysical Facility (AXAF), the small grazing angle will effectively magnify the fractional area obscured by foreign particles on the mirror surfaces.

In order to model the performance of the AXAF optics more accurately, measurements designed to characterize the **particulate contamination** will be performed. Experimental assessment of the relationship between **x-ray optical** performance and **particulate contamination** has so far been limited to studies involving the technology mirror assembly (TMA), a small-scale, **x-ray** telescope designed to simulate one pair of AXAF mirror elements. The TMA, known also as TMA–2, was optically examined in early 1990. Following the **optical** measurement, tape-lift samples were collected in order to allow high-resolution particle sizing via electron **microscopy** and **x-ray** elemental analysis. Another **optical** measurement is scheduled to be performed in late 1991 on the largest AXAF mirror pair contained in an assembly known as the verification engineering test article (VETA).

The TMA–2 **optical particulate contamination** measurement was performed using a custom-built device known as the TMA viewing mechanism (fig. 127), which is a periscope-style lens system. This instrument is capable of resolving particles as small as 3 µm (0.00012 in) in diameter. During this measurement, particles on the TMA mirror surfaces were photographed through 1.6 cm (0.63 in) access holes in the TMA inner cylinder baffles. The total **particulate** fractional area coverage, viewed from normal to the mirror surface and based on the portion of the mirror observed, was determined to be approximately 1×10^{-5} for the parabolic mirror and 5×10^{-6} for the hyperbolic mirror.

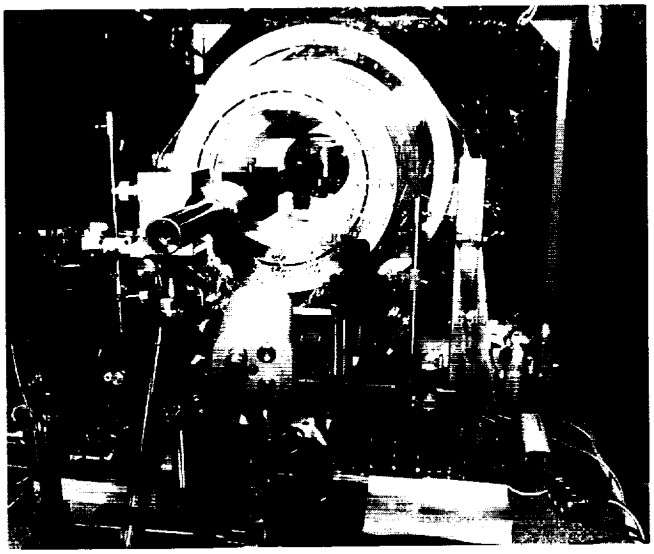

FIGURE 127.—TMA–2 optical particulate contamination measurement.

Concerning the TMA–2 tape-lift analysis, preliminary results from examinations of the first two tape lifts have recently been received. In this case, the measurement equipment was capable of resolving particles as small as 0.5 μm (0.000020 in) in diameter. The measured fractional area coverage appears to agree with the **optical** measurement to within an order of magnitude; however, further data analysis will be required. The primary elemental constituent was found to be stainless steel or stainless steel corrosion products.

To perform the VETA **optical** measurement, a new long-working-distance video microscope system is being designed and fabricated. This system should be capable of resolving particles as small as 0.5 μm (0.000020 in) in diameter. The measurement is planned to be performed on the VETA optics following **x-ray** performance testing at MSFC.

A.P. Shapiro/EB23
(205) 544–3488
Sponsors: Advanced X-Ray Astrophysics Facility (AXAF) Project Office and Office of Space Science and Applications

Pinhole Sputtering of Surfaces Exposed to the LEO Plasma

The current baseline design for Space Station *Freedom* (S.S. *Freedom*) specifies that the entire structure, including the modules and the truss, be "grounded" or referenced to the negative side of the solar array. Because the solar array will float (i.e., collect equal number of electrons as ions) in the low-Earth orbit (LEO) **plasma**, the potential of the solar array will be driven mostly negative due to the difference in ion and electron mobilities. Therefore, the negative side of the solar array will be at a potential of –140 V relative to **plasma** potential driving the entire conductive structure of S.S. *Freedom* to that potential. Also, the present baseline design is for the entire structure to be covered with a thin nonconductive layer (i.e., anodized aluminum) to control the surface temperature of the outer skin. Because of interactions between the low LEO **plasma** and micrometeoroid environments and the thin nonconductive layer, the anodized aluminum will develop defects in the dielectric surface either from dielectric breakdown or micrometeoroid debris impacts.

When a defect or **pinhole** develops in the dielectric exposing the high-voltage conductor to the **plasma**, a **plasma sheath** develops to allow the voltage to drop from –140 V on the exposed conductor to **plasma** potential (near 0 V). Figure 128 is an illustration of what the **plasma sheath** looks like in most cases. The **sheath** is usually on the order of a few centimeters in radius, which is orders of magnitude larger than the **pinhole**, and any

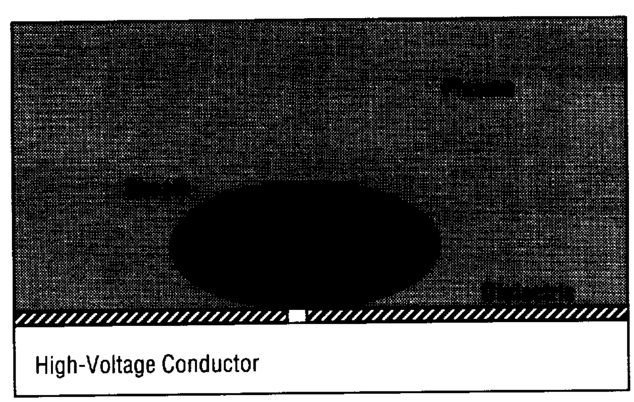

FIGURE 128.—Plasma sheath illustration.

ion near the **sheath** can be collected by the **pinhole**. The **sheath**, because of its large surface area, collects more ions from the **plasma** than would be possible by the **pinhole** itself. Also, the **sheath** acts like a **focusing** lens, tending to focus the ion current into the center of the hole. If the atomic oxygen (AO) ion sputter yields are sufficiently large, these high-energy ions will sputter the conductive metal, depositing the atoms on other sensitive surfaces.

Two separate tests were conducted in the laboratory at MSFC to investigate the **pinhole focusing** phenomena and to measure sputter yields of copper and aluminum being impinged by 150–eV AO ions. The initial **pinhole focusing** tests were done to measure ion **focusing** factor data to be included in modeling on the subjects (i.e., the increased amount of ion current collected over the thermal ion current). The **pinhole focusing** factor data were collected by immersing a glass substrate that had a vapor-deposited copper layer covered with 25.4 µm (1 mil) kapton in an argon **plasma**. The sample, which had a 0.535–cm (0.21–in) hole cut in the kapton, was biased –140 V with respect to the **plasma** and was exposed for 5 h. The sample was removed and examined using a three-dimensional (3–D) profiler to measure the depth and radius (fig. 129) of the hole. The data obtained from the 3–D surface profile were compared to the predicted hole diameter from a model. The model predicted that all the ions would be focused into a 0.2–cm (0.08–in) diameter hole, which compares very well to the data shown. The **focusing** factor calculated for the data of figure 130 was 27 or the 0.535–cm (0.21–in) hole collected 27 times ambient thermal ion current.

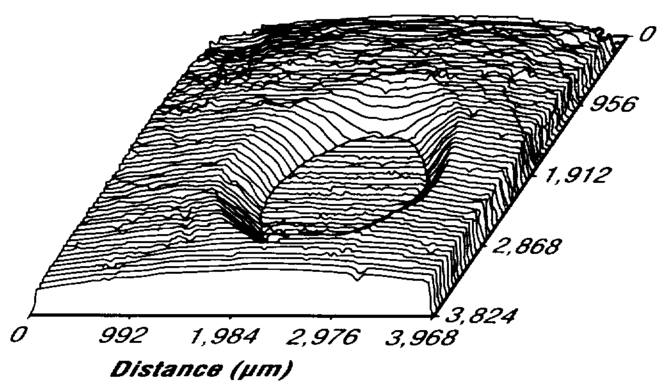

FIGURE 129.—Three-dimensional surface view of pinhole sputtering.

Because the LEO **plasma** does not contain argon ions and very little data on low-energy AO ion sputter yields were available, tests were conducted to measure AO sputter yields on aluminum and copper over an energy range of 50 to 200 eV. These tests were conducted by vapor coating thermoelectric quartz crystal microbalance (TQCM) crystals and exposing them to a known energy AO beam in the AO simulation system (AOSS) at MSFC. The yields were obtained by measuring the number of incoming ions and the mass loss from the TQCM crystals. The sputter yields measured during these tests are listed in table 10. These data can now be used to predict the sputter rate in the tiny **pinholes** that are enhanced by the **focusing** factors.

TABLE 10.—*AO sputter yield data*

Sputter Yield of Copper and Aluminum with AO Ions

Energy (eV)	Copper Sy	Aluminum Sy
50	0.019	0.056
100	0.052	0.061
150	0.229	0.097
200	0.528	0.130

Future work will center on measuring **focusing** factors for a wide range of hole diameters as small as 0.02 cm (8 mil). Also, the electric field in the **sheath** will be measured and compared to present models for validation. Once the models have been validated, computations of the **focusing** factor in space for any size hole can be made.

J.A. Vaughn/EH12
(205) 544–9347
Sponsor: Office of Space Flight, Space Station *Freedom*

Portable Spectroreflectometer

Increasingly complex and long-lifetime space missions require greater demands on the performance of spacecraft materials. The **spectral reflectance** properties of materials used on space and ground systems are critically important to their design and operation. Because of this, there is a need to control manufacturing processes and to assess the effects of exposure of materials to ground handling and the space environment.

Current instruments for measuring **spectral reflectance** properties of materials do not offer the portability or the accessibility required for such operations on space systems and other extant or proposed assemblies while retaining the high resolution necessary. Therefore, research is under way to develop a portable integrating sphere spectroreflectometer to measure the **spectral reflectance** of extended surfaces and assemblies. This instrument will be usable as a hand-held device for ground and space application and will also be adaptable for remote use via a **remote manipulator system (RMS)**.

Research to develop the conceptual and functional design of a portable spectroreflectometer has been completed, and the development of prototype instruments has begun. A model of the hand-held prototype instrument (fig. 130) will be field-tested for astronaut/instrument interface compatibility. The remotely operated prototype instrument will undergo intensive testing using a robot arm to simulate the **RMS**. These tests will determine the suitability of the design for routine use by NASA and commercial users. The flight designs will be based on the ground prototype units, but will require alternate packaging to facilitate astronaut use and **RMS** interfacing. Such space-qualified flight versions of the portable spectroreflectometer will be required for future NASA long-term missions, such as Space Station *Freedom* where astronauts must survey the condition of external **spacecraft surfaces** (i.e., thermal radiators, solar arrays, and thermal insulation) to determine when on-orbit servicing of critical surfaces is needed (fig. 131).

J.K. Norwood/EH12
(205) 544-8281
Sponsor: Office of Aeronautics, Exploration and Technology

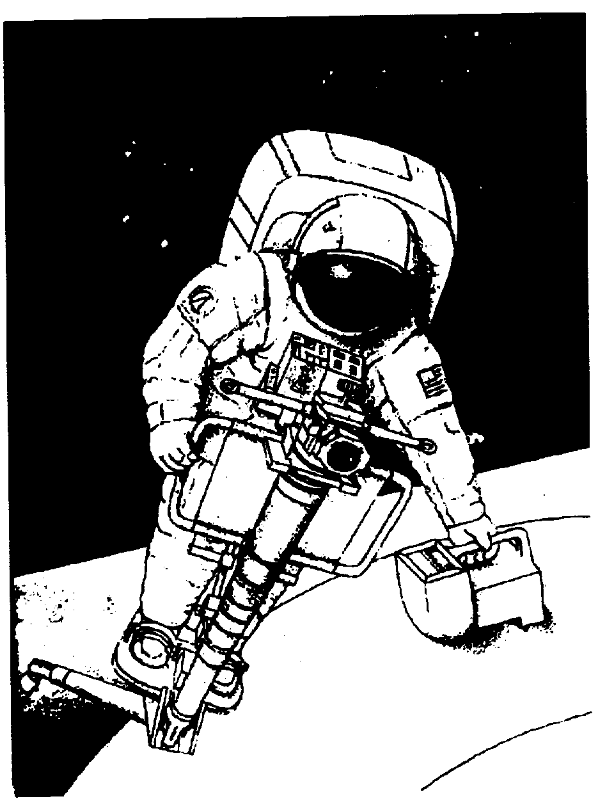

FIGURE 130.—Illustration of hand-held portable spectroreflectometer.

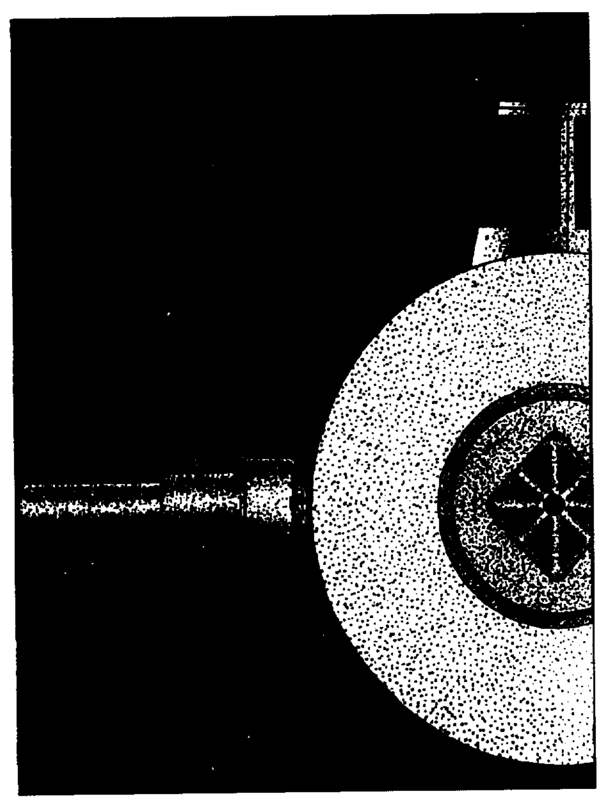

FIGURE 131.—Illustration of RMS portable spectroreflectometer.

PULTRUSION PROCESS CHARACTERIZATION STUDY FOR GRAPHITE/EPOXY

Advanced composites offer a wide variety of benefits for use in the aerospace industry, such as weight reduction, corrosion resistance, and higher stiffness. However, one major drawback with composites is the health hazard many of the fabrication processes and chemicals pose to the worker. In recent years, advanced resin systems have been designed that minimize the content of hazardous chemicals. These new resin systems, although improved, must still undergo qualification testing before being accepted by the aerospace industry for use on flight hardware. In an effort to investigate the reliability of a new resin system and to comply with the ever-changing Environmental Protection Agency (EPA) and Occupational Safety and Health Administration (OSHA) requirements, a **pultrusion** process characterization study was initiated. This study is being conducted with the aid of the University of Mississippi to determine the **pultrusion** characteristics of Shell Chemical's 9420/9470/537 non-**methylenedianiline** (MDA) **epoxy** resin system in a **graphite** fiber matrix. MDA is a suspected carcinogen and is on the EPA's right-to-know list.

Pultrusion is an automated process used to fabricate advanced composite structures. This process makes constant cross-sectional shaped parts by pulling fibers or fabric through a resin bath then through a heated die where the part cures (fig. 132). The simplicity of the production setup saves manufacture time, which, in turn, makes it a cheaper fabrication method. Compared to other methods of advanced composite manufacture, **pultrusion** is almost always the cheapest and fastest, since it eliminates time consuming lay-up procedures, limits the amount of tooling, and eliminates cure processing (fig. 133).

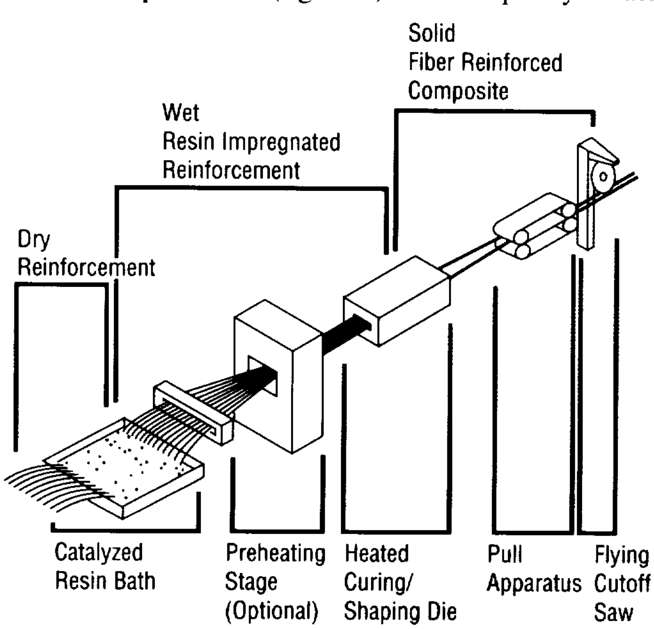

FIGURE 132.—Schematic of pultrusion process.

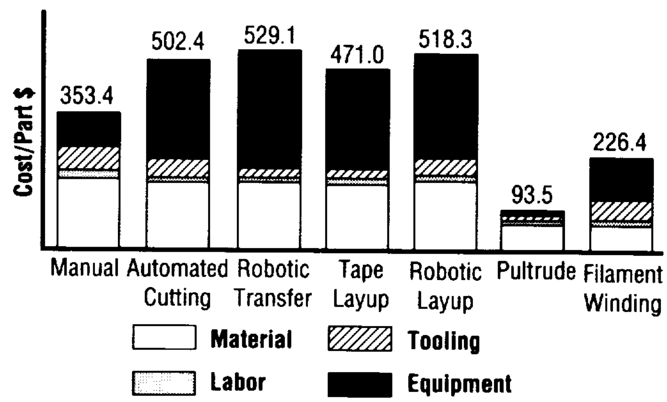

FIGURE 133.—Costs for a 4-ft^2, 24-ply part for an annual production of 2,000 parts.

During this study, a 1 × 1/8-in bar will be fabricated and five different **pultrusion** variables examined, including: (1) amount of filler in the resin, (2) percent **graphite** reinforcement, (3) pull speed of the pultruded product, (4) temperature of the first zone of heating, and (5) temperature of the second zone of heating. Included with the experiment is a finite element model of the **pultrusion** process. The model accurately predicts the temperature profile of the material throughout the length of the **pultrusion** die and locates the position of the transition of the material from the liquid to solid phase. The model will have a two-dimensional modeling capability and will provide a highly refined definition of the gel region of the material. The testing of the fabricated samples is currently in progress and is expected to be completed by the end of 1991.

W.M. McMahon/EH44
(205) 544-2802
Sponsor: Office of Space Flight, Space Station *Freedom*

Slit Digital Radiography for Analysis of Bondline Defects in Solid Rocket Motors

Under a Small Business Innovation Research (SBIR) task, Bio-Imaging Research of Chicago, IL, has teamed with MSFC to examine the feasibility of using a radiographics **nondestructive evaluation** method known as **slit digital radiography** to potentially inspect the first bondline between case and insulation in typical large **solid rocket motors** (**SRM's**). In past **SRM** programs, the first bondline has been nondestructively inspected by ultrasonic pulse-echo methods and by conventional film **radiography** techniques. This method of **slit digital radiography** has the potential to improve on the resolution of this **bondline** and to increase the probability of detection of common anomalies such as unbonds.

Discrete-element, x-ray detectors developed from medical computed tomography (CT) are being applied to industrial x-ray digital **radiography** (DR) and CT imaging. **Slit digital radiography** is a technique that may be applied to mapping density variations within rocket motor walls. This could replace the use of traditional film tangential **radiography** for inspecting the case-to-insulation **bondline**. The standard x-ray technique used today to image **bondline** defects in **SRM's** has an x-ray beam passing through the edge of the motor, tangent to the **bondline** circumference and detected by an area detector such as film or an x-ray image intensifier. While more effective than traditional radial x-ray techniques, this method has a difficult time imaging subtle defects because the area detector is exposed to a range of thicknesses, causing a wide range of background attenuating. In the **slit digital radiography** method, the rocket motor would be rotated as an x-ray beam passes through the **bondline** tangent to the detector array, creating a two-dimensional mapping of the **bondline** circumference. The small size of the detectors means this new technique can receive x rays through an essentially constant attenuation path and map **bondline** features against a constant contrast level. Small features will stand out and be easily identified. Line profiles are first taken at multiple angular positions as the test object is rotated, and the data are formatted into a two-dimensional image. The image will provide a circumferential mapping of the rocket motor **bondline** taken at the optimum x-ray exposure angle, with accurate information about the density and position of features within the bond.

The detectors that make this a potential **SRM** inspection tool were originally developed for medical CT. In this discrete element system, each detector has its own scintillator and photodiode, and an attenuating septa separates adjacent detectors. This significantly reduces both light and radiation crosstalk, which can cause defocusing in areas of excessive brightness or poor edge definition in traditional techniques that use film or image intensifiers. The detectors are instrument-grade elements that have a 16-bit or roughly 65,000 gray-level accuracy. After the necessary data correction processes, this accuracy generally results in a dynamic range of 10,000 to 1. Traditional systems, such as fluoroscopic screens have a contrast of 20 to 1. Even film, the standard in the **radiography** industry, has only a 100 to 1 dynamic range.

The **slit digital radiography** technique was proven feasible for small 10.2–cm (4–in) diameter cylinders that were configured with one **bondline** and had molded shim step wedges that simulated bondline defects. The shims ranged in thickness from 0.025 to 0.102 cm (0.01 to 0.04 in). Rods were used to simulate voids 0.076–cm (0.03–in) in diameter in the simulated propellant. All defects were imaged with sharp clarity.

The next step in this task will be to implement this system by modifying the existing advanced CT inspection system (ACTIS), located at MSFC's Productivity Enhancement Facility. The modification will be the installation of the software and hardware required to perform **slit digital radiography** concurrently with the CT capability. The hardware will consist of a turntable that will be able to rotate large rockets up to 38.1–cm (15–in) in diameter. The feasibility tests for this system will be performed on an inert HAWK missile that has simulated defects in its **bondlines** and propellant simulant.

The **slit digital radiography** technique, using a slit for a collimator, will initially be used to inspect this smaller motor to see if there is a potential use in scaling up the inspection tool to test large **SRM's** (shuttle class).

M.W. Suits/EH13
(205) 544–8336
Sponsor: Office of Commercial Programs, Small Business Innovation Research

Solid Rocket Booster Paint Technology

National health, safety, and environmental interests have compelled two **paint** system replacement programs, in progress under the auspices of the MSFC Materials and Processes Laboratory. Sprayable Environmental Protection Agency- (EPA-) compliant alternatives are being qualified to replace both the coating for the **shuttle booster's** aluminum substrate and the coating for the exterior insulation materials called the thermal protection system (TPS).

Current chemical deficiencies in the primer/topcoat system that provide direct **corrosion** protection for solid rocket **booster** (SRB) aluminum surfaces are the result of reducing solvents with unacceptable levels of **volatile organic compounds** (**VOC's**) and are a lead additive for curing. After application of TPS materials, a rubber-based outer paint protects the relatively porous thermal layer from the damaging effects of the Florida environment. The current TPS topcoat contains similar chemical deficiencies. Studies in progress will provide a low-**VOC**, high-solids system for the SRB aluminum substrate, and a low-**VOC**, water-based coat for the TPS. Shown in figure 134 are 12 aluminum substrate primer/topcoat test panels following 504 h of salt fog spray exposure (5-percent NaCl solution), and shown in figure 135 are two TPS topcoat test panels following 7 mo of exposure to Kennedy Space Center (KSC) beach environment.

Both programs are expected to be quickly eased into the production flow under material usage agreement (MUA) approvals. Initial application components for the new undercoat are likely to be the SRB aft skirt's thrust vector control reservoir, **booster** separation motors (BSM's), and aft heat shield.

Both qualification programs, currently at an advanced stage, are essentially similar. Each includes a broad-spectrum properties verification program that tests the candidates' adhesion to adjacent materials, ease of application, curing characteristics, durability during normal handling, and its resistance to the cycle of beach exposure, flight, and ocean submersion.

C.E. Henderson/EH43
(205) 544-2727
Sponsor: Office of Space Flight

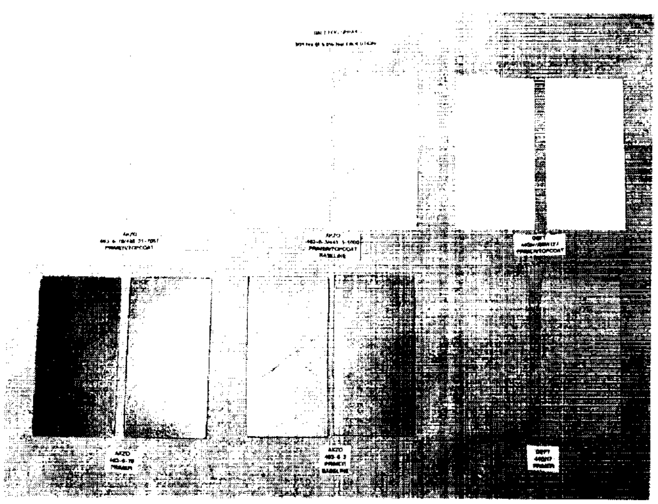

FIGURE 134.—Twelve primer/topcoat test panels following 504 h of salt fog spray exposure (5-percent NaCl solution).

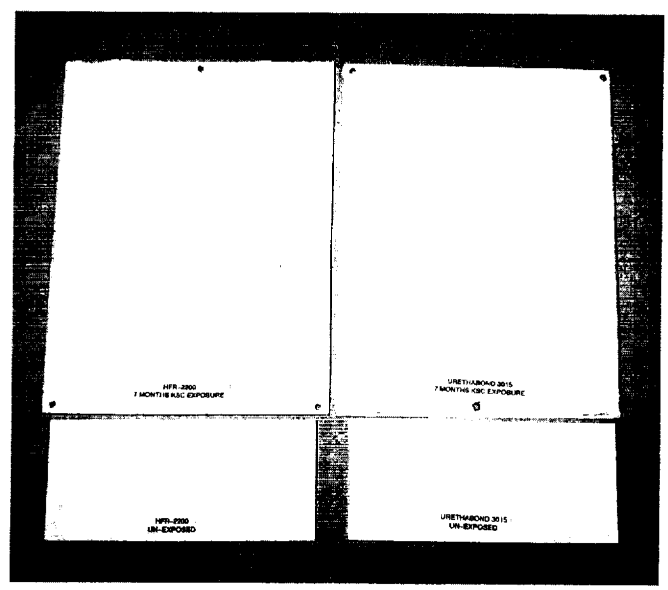

FIGURE 135.—Two TPS topcoat test panels following 7-mo exposure to KSC beach environment.

Thin-Film Electrostatic-Controlled Reflector

MSFC is developing a **thi-film** electrostatic **reflector**. Such lightweight **adaptive optic reflectors** could be deployed in space as infrared telescopes, radio antennae, or solar collectors. Previous work has been done at MSFC with **reflector** models to support study for the external tank gamma-ray imaging telescope (ET–GRIT). These preliminary design **reflectors** had curvature errors that were larger than allowed by system requirements. To remove these errors, an electrostatic control system was added to a seamless membrane design.

The approach was to form a 0.5–mil thick film into a spherical mirror mounted on a 5–ft diameter metal ring (fig. 136). The ring mount is sealed and slightly evacuated to pressurize the film into shape. The goal for this model was to achieve a 1–mrad surface curvature error over 90 percent of the **reflector** area. The curvature will be controlled by the pressure level and charged zone plates behind the **reflector** film. This curvature was measured by a laser scanning instrument.

The film curvature was first tested by pressurizing only. The measurement showed that the film to distort in the same manner as other **thin films**, but the error in this **reflector** was less than any yet tested and was within the required 1–mrad range. Application of voltage to the plates caused the film to respond by changing shape. The air-pressure deflection of the film limited the elasticity of the membrane, but there was noticeable improvement of the **reflector** figure by charging selected plates. With further refinement of the film material, this **adaptive optics** system will offer better control than similar segmented **reflectors**.

V.B. Huegele/EB23
(205) 544–3475
Sponsor: Center Director's Discretionary Fund

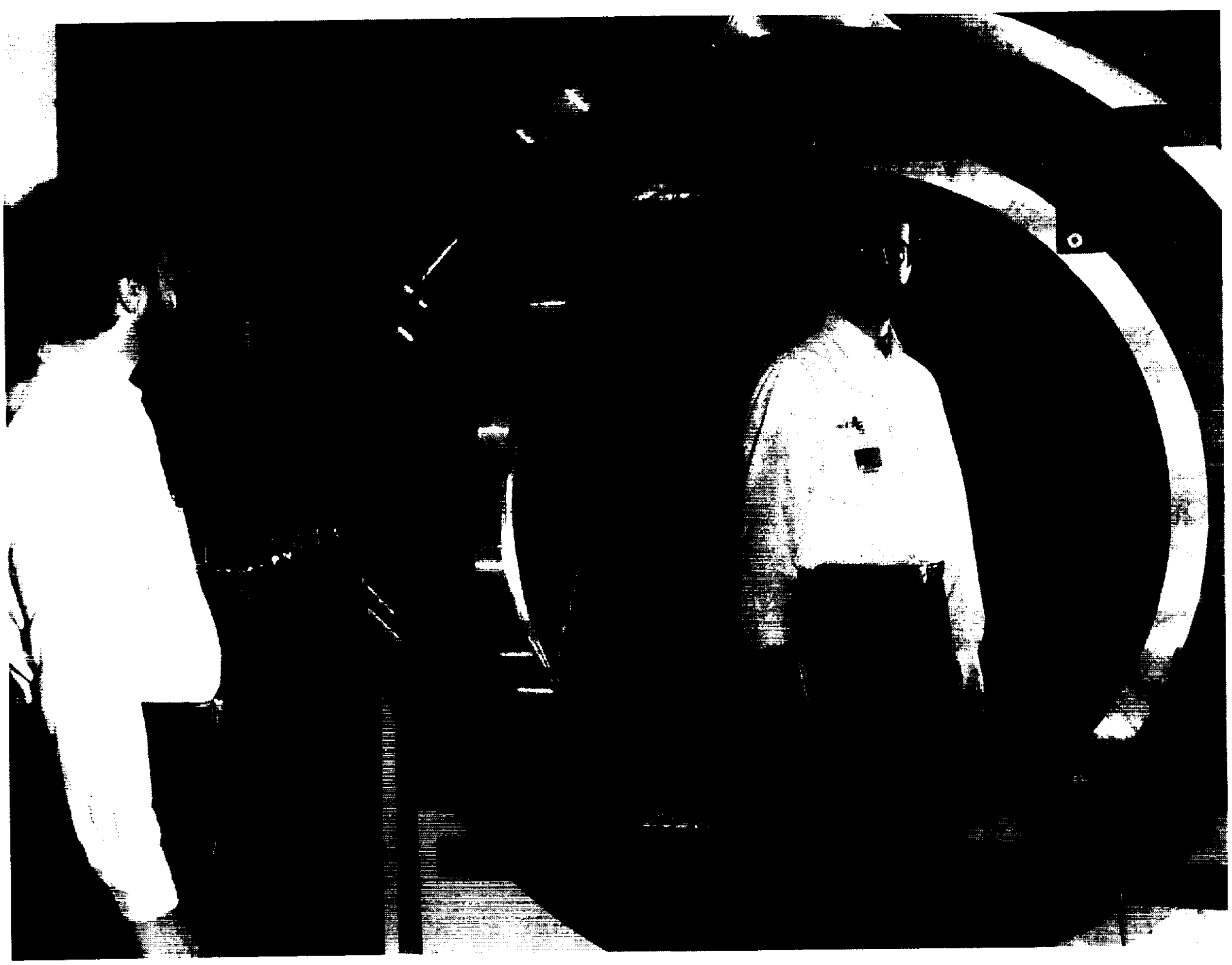

FIGURE 136.—Thin film electrostatic reflector.

Trowelable Ablator Development for Booster Structures

Ablative materials, which are part of the **thermal protection** system (TPS) for the space shuttle's solid rocket **boosters** (SRB's), function as heat shields to protect the vehicles during launch and reentry. A new TPS insulation, which is designated as the booster trowelable **ablator** (BTA), has reached flight stage. BTA (fig. 137) was developed at the Productivity Enhancement Complex as a replacement for the SRB's MTA–2 and K5NA closeout materials. (BTA is a thermal closeout and repair material compliant to Environmental Protection Agency

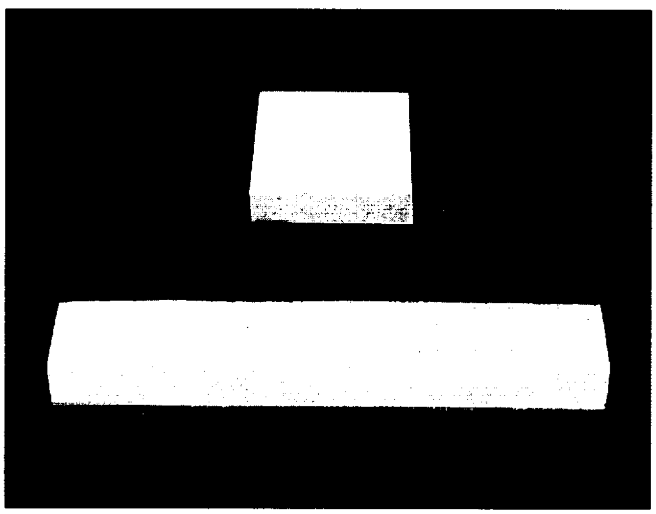

FIGURE 137.—Samples of BTA.

(EPA)/Occupational Safety and Health Administration (OSHA) standards.) MTA–2 was earmarked for cancellation after identification of a health hazard in its shell Z catalyst, the curing agent for its epoxy system. BTA is a remarkably safe, nonemitting formulation from an epoxy resin system known for superior adhesion; the resin is filled with inert glass eccospheres and ground cork, and cures at ambient conditions. Its potential displacement of K5NA, a commercial product, is influenced by practical considerations: with its inexpensive ingredients, BTA can be economically produced in-house and is more easily applied than K5NA, which is a hygroscopic material that sticks to operator gloves. Formable when uncured, BTA can be smoothed onto flat or contoured parts at a single-layer thickness up to 4 in. in the overhead position without slumping. It cures to a low-density, durable material (nominal 500 to 800 lb/in^2 flatwise tensile strength) that adheres well to acreage surfaces under stress. BTA's ablative properties are enhanced by mixing ingredients in a vacuum chamber. Thermal tests confirm low conductivity, slow recession rate, and a char integrity that will yield thermal stability during flight.

The first BTA will be flown in a high-heat region of the SRB aft skirt. The formulation is also being assessed for application on midbody motor segments. Although not a flight configuration at this time, the material can also be molded to insulate a contoured piece part.

In time, BTA is expected to yield a matrix of specialized **ablators** with wide applicability. Its successful development marks an assertive engineering trend to create alternatives to aerospace materials whose health and environmental deficiencies are no longer acceptable in this more enlightened era.

C.N. Lester/EH43
(205) 544–4804
Sponsor: Office of Space Flight

Vacuum Plasma Spray Deposition of SSME MFVH Copper Tie-In Bands

A vacuum **plasma** spray (VPS) process to apply the **copper** insulation tie-in bands to the surface of the **space shuttle main engine (SSME)** titanium main fuel valve housing (MFVH) has been developed. Due to the extremely low temperature of liquid hydrogen (217 °C (−423 °F)), the MFVH must be insulated. The polyurethane foam insulation is protected by an electrodeposited (ED) nickel **coating** that is anchored to the flanges of titanium housing. However, ED nickel will not adhere to titanium. This difficulty is overcome by depositing **copper** tie-down bands, to which the ED nickel will adhere, on the flanges. These **copper** bands were previously applied by air **plasma** spray. Oxidation of both the **copper** powder and the titanium surface during air **plasma** spray often resulted in brittle **coatings**, which failed to adhere well to the titanium. On the average, three applications were required to achieve one good **coating**. This problem was regarded as one of Rocketdyne's top−10 problems in the manufacture of the **SSME**. Unlike the air **plasma** spray processes, the VPS process consistently achieves a tenacious **coating** that does not peel away from the titanium.

The VPS process is conducted in a low-pressure, inert atmosphere inside a vacuum chamber (fig. 138). The **plasma** is generated by passing a carrier gas, a mixture of inert gases (80−percent argon and 20−percent helium) through a high-voltage, electric discharge. The resulting high-temperature **plasma** exits through a supersonic nozzle, and, in the low pressure (nominally 40 torr) environment, achieves velocities greater than Mach 3. The MFVH is heated with the **plasma** torch to 454 °C (850 °F) in the low-pressure, inert atmosphere (fig. 139). Oxides on the titanium surface are then removed by reverse polarity, transferred arc cleaning. Highly purified **copper** powder (−170/+325 mesh) is then injected into the **plasma** plume, which melts the **copper** particles and accelerates them toward the target. The length of the **plasma** plume is adjusted by varying the vacuum so that the particles remain in the plume long enough to become thoroughly softened, but not so liquid that they splatter on impact. The velocity obtained by the particles before impact onto the target is estimated at Mach 1.5 (approximately one-half the **plasma** velocity).

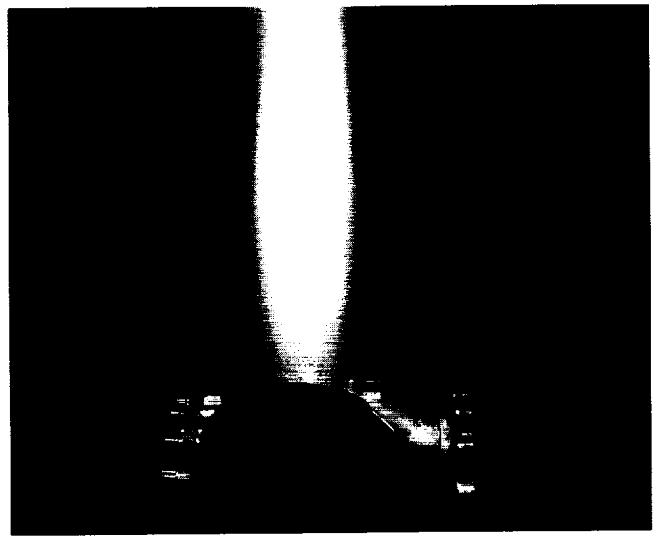

FIGURE 138.—Preheat of MFVH prior to VPS deposition of copper tie-in bands. Note that all areas except the band to be coated are masked to prevent copper deposition.

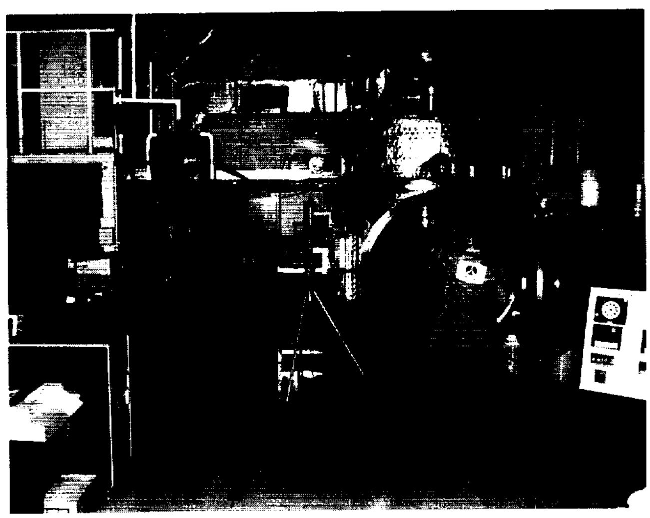

FIGURE 139.—MSFC vacuum plasma spray cell.

An engineering change proposal (ECP) has been approved, making the MSFC-developed VPS process the standard procedure for application of **copper** to the MFVH flanges. The first two VPS-sprayed MFVH's are scheduled to be installed on engines number 2034 and 2035, which are currently scheduled to be installed on the *Endeavour* for her maiden flight.

D.H. Burns/EH43
(205) 544−4807
Sponsors: Office of Space Flight and
Office of Aeronautics, Exploration and Technology

Vacuum Plasma Spray Fabrication of Main Combustion Chamber

The MSFC vacuum **plasma** spray (VPS) cell is engaged in the development of innovative VPS processes for the **fabrication** of aerospace **hardware,** such as main combustion chambers (MCC's). The VPS process is conducted in a low-pressure inert atmosphere inside a vacuum chamber. The **plasma** is generated by passing a carrier gas, a mixture of gases (argon plus small percentages of helium or hydrogen), through a high-voltage electric discharge. The resulting high-temperature **plasma** exits through a supersonic nozzle, and, in the low-pressure (nominally 40 torr) environment, achieves velocities greater than Mach 3. The target is heated with the **plasma** torch to a predetermined temperature before any material is deposited. Then, nonconducting materials (e.g., oxides or organic materials) are removed by reverse-polarity transferred arc cleaning. High-purity metal powder is then injected into the **plasma** plume, which melts the particles and accelerates them toward the target. The length of the **plasma** plume is adjusted by varying the vacuum so that the particles remain in the plume long enough to become thoroughly softened but not so liquid that they splatter on impact. The velocity obtained by the particles before impact onto the target is estimated at Mach 1.5 (approximately one-half the **plasma** velocity). Properties of material deposited by VPS are comparable with those of wrought material.

Early in this work, the MSFC VPS cell demonstrated the feasibility of VPS techniques in the manufacture of a low-cost space **shuttle** main engine (SSME) MCC using an "inside-out" spraying technique on subscale motors (fig. 140). In this process, the MCC **NARloy**-Z liner is sprayed onto a shaped mandrel, cooling channels are slotted, and then closed out with VPS **NARloy**-Z. After the channel closeout, a super alloy support jacket is built up by VPS. VPS **NARloy**-Z and Inconel-718 show properties comparable to wrought material at room temperature. At higher temperatures, the properties of

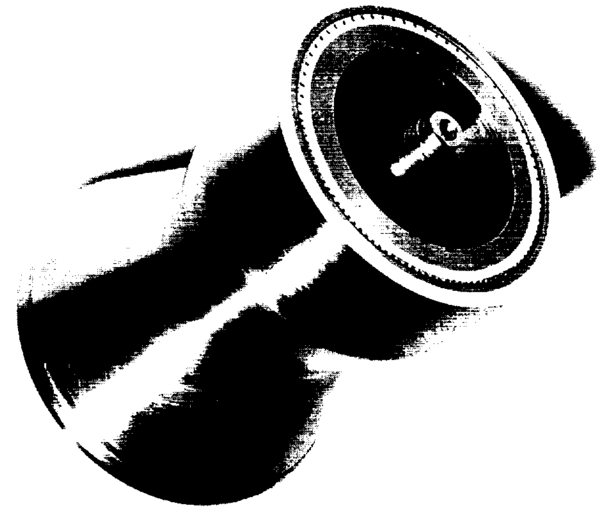

FIGURE 140.—A subscale motor fabricated by the VPS ("inside-out") technique.

NARloy-Z are somewhat degraded but are sufficient for some engine designs. Material properties of VPS **NARloy**-Z at elevated temperatures improve with reduced oxygen contamination in the powder.

A VPS **NARloy**-Z "calorimeter spool" hot wall liner for a subscale (40k) test engine has been fabricated and hot-fire tested with excellent results.

For a number of technical and economic reasons, the method chosen to fabricate a full-scale MCC requires the VPS **fabrication** of the MCC liner on the inside of a cast jacket. The VPS cell is now in the process of developing the techniques for spraying **NARloy**-Z onto an inner surface (fig. 141). (A variation of this technique will be used to fabricate the liner for a prototype SSME MCC.) The project goal is **fabrication** of a prototype improved MCC, which will be hot-fire tested on MSFC's technology test-bed (TTB) stand. A flight MCC based on this prototype will be manufactured by private industry using the processes developed at MSFC. MCC's fabricated by this method are scheduled to be included in the SSME block II engine change.

ORIGINAL PAGE
BLACK AND WHITE PHOTOGRAPH

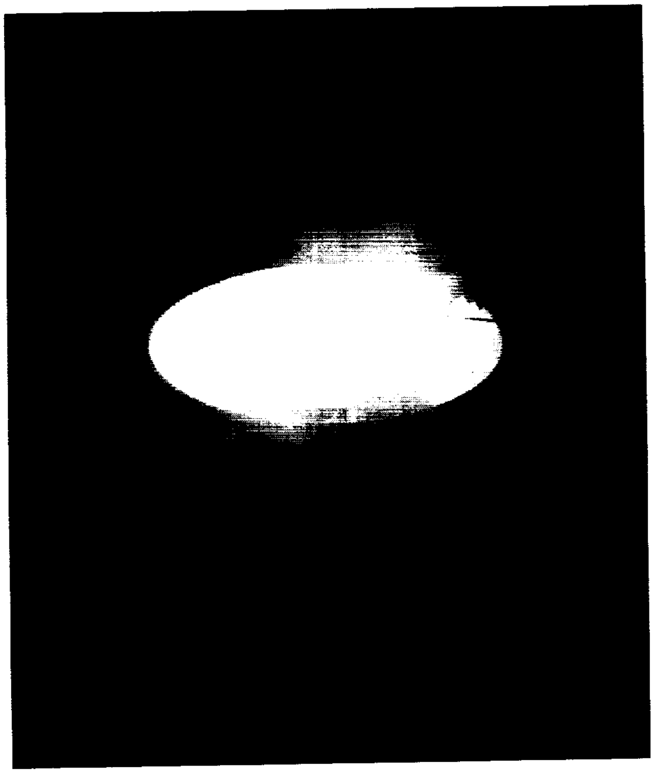

FIGURE 141.—VPS of NARloy-Z onto the inner surface ("outside-in" technique) of MCC throat section.

Fabrication of the SSME MCC by this method will eliminate most welds and all uninspectable welds and will also eliminate the costly and troublesome nickel electrodeposition process used in the current SSME MCC channel closeout. The use of the VPS **fabrication** method is projected to save at least $1.7M per engine compared to the current SSME MCC **fabrication** method and will reduce the **fabrication** time from more than 4 yr to approximately 1 yr.

ASM International's National Thermal Spray Conference, 1990, "Vacuum Plasma Spray Forming NARloy-Z and Inconel-718 Components for Liquid Rocket Engines."

D.H. Burns/EH43
(205) 544–4807
Sponsors: Office of Space Flight and
Office of Aeronautics, Exploration and Technology

Weld Process Modeling

The variable polarity **plasma** arc (VPPA) **welding** system plays a major role in fabrication of the space shuttle external tank and will also play a major role in fabrication of the space station. Mathematical **modeling** was undertaken to provide a basis for an intelligent multivariable control for the VPPA system. Models of the VPPA system are now being compared with empirical data (fig. 142). The computation compared with empirical data in the figure incorporates 7 parameters set by the weld operator (e.g., the standoff distance between the torch orifice and the workpiece), 7 parameters determined by the workpiece, and 10 parameters determined by the basic design of the system. The intended output of the model is the width and height of weld crown and root, respectively, but the model also yields voltages and other computable features of the system. Note that in the direct current electrode negative (DCEN) cycle interval, electrons flow from the electrode to the workpiece. In the direct current electrode positive (DCEP) interval, the current is reversed.

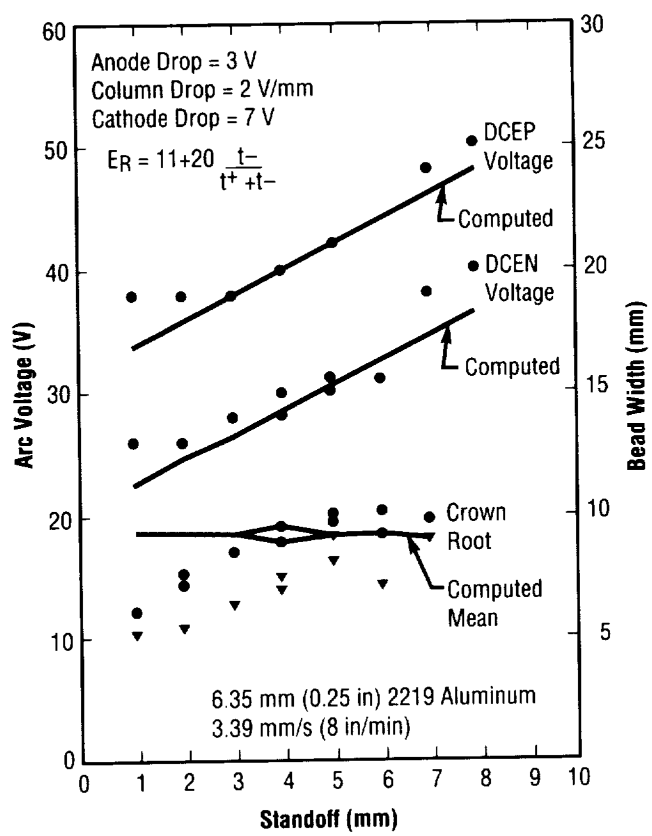

FIGURE 142.—Sample comparison of VPPA voltages and weld bead widths with computed values from a mathematical model.

Certain research issues have crystallized as foci of concentration in this study. Surface tension effects studies have already paid off in a qualitative understanding of the relation of undercutting and cutting to weld gas contamination that is useful in VPPA **welding** practice. A qualitative model of the effect of surface tension on the relative widths of the weld crown and root has also emerged. Field emission effects at the workpiece surface are thought to produce a significant part of the reverse polarity voltage and to be closely related to the cathodic cleaning action. A third issue is the effect of heat sinks including fixtures and geometry variations. A simple, approximate computation of the heat sink effect on the width of a weld caused by a boss on a plate near the path of the weld has been made. Lastly, more detailed **modeling** of the arc **plasma** physics is under way to account for voltage variations not explained through currently modeled features.

A theoretical model of the relation of the strength of a weld bead to its cross-sectional geometry is currently under experimental study. Pending validation, the strength versus bead geometry model offers an opportunity for improving or optimizing the weld bead cross section, while the bead geometry versus weld system parameters model can assist in the achievement of the desired section as well as in the stabilization of a controlled output.

A.C. Nunes/EH42
(205) 544–2699
Sponsor: Office of Space Flight

PROPULSION

COMBUSTION PROCESSES AND DENSE SPRAYS

The **combustion** processes of liquid oxygen (lox) with hydrogen under broad ranges (**subcritical**, critical, and **supercritical** conditions) of chamber pressure are being studied experimentally and theoretically. Experimentally, under different test conditions, the overall flame structures are observed by using two different flow visualization techniques: schlieren and laser-sheet. The former will be used to observe the change in the density gradient of the flame zone, and the latter to observe regions with a high water vapor concentration, which indicates the active reaction zones of oxygen with hydrogen. ($TiClO_4$ (titanium chlorine tetraoxide) is introduced in the combustor and reacts with water vapor to form submicron TiO_2 (titanium dioxide) particles, which are illuminated by the 30– to 60–ns laser sheet pulses.) In addition to flame structure, the temperature and infrared-active gas compositions are investigated with a fast-scan Nicolet 740 Fourier transform-infrared (FT–IR) system. The burning rate of lox is determined from the measured feed rate under different test conditions.

At present, the lox and hydrogen feed systems have been designed and implemented. The modification of an existing high-pressure optical combustor has been completed. Preliminary system checkout tests are now in progress.

Theoretically, an axisymmetrical model for simulating the evaporation and **combustion** processes of lox reacting with hydrogen under **supercritical** pressure conditions is being formulated. Important physical and chemical processes are treated in the model. These processes include the solubility of gas in the liquid, the vanishing surface tension and latent heat of vaporization at near-critical conditions, the so-called "drop-puff" phenomenon observed in droplet **combustion**, the real-gas effect, and the chemical kinetics of oxygen reacting with hydrogen.

In the observation of dense **spray** and mixing of impinging jets, two complementary advanced diagnostic techniques are being used to investigate the dynamic interaction in the near-injector region between impinging jets. These Techniques are: (1) real-time x-ray radiography, which is capable of penetrating the dense **spray**, and (2) laser-sheet-illuminated photography, which yields high-resolution photographs of the **spray** boundary and droplet regions.

Preliminary open atmosphere testing has been completed using the copper-vapor, laser-illuminated flash photography technique. High-resolution photographs were made using 30– to 60–ns exposure laser pulses to freeze the motion of the liquid jets and droplets. The testing was done using one of the interchangeable nozzle elements available. The chosen nozzle element had a 60° total angle. The tests were run for a full spectrum of flow conditions. Typical results under identical conditions are shown in figures 143 and 144.

FIGURE 143.—Photograph of like-on-like impinging jets. $Re_D = 9 \times 10^4$, fluid: water.

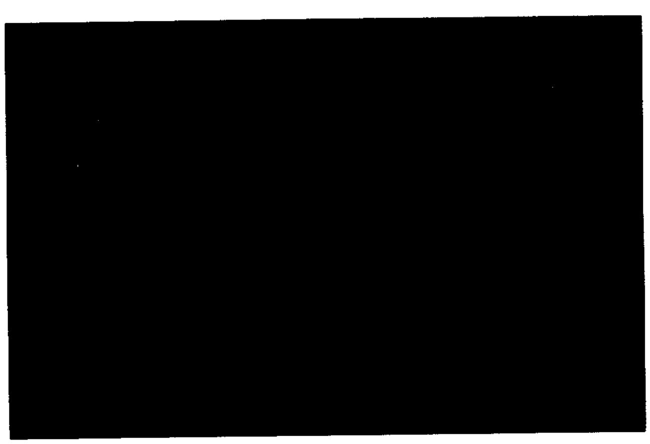

FIGURE 144.—Perpendicular to plane of impingement.

ORIGINAL PAGE
BLACK AND WHITE PHOTOGRAPH

The impingement of two low-speed liquid jets produces a thin "leaf" of liquid perpendicular to the plane of impingement. With increasing liquid velocity, the "leaf" structure disintegrates into smaller liquid fragments, i.e., ligaments and droplets, first at the outer edge then throughout. Photographs of the impinging jets were taken from the plane of impingement (fig. 143) and perpendicular to the plane of impingement (fig. 144) for this higher flow velocity case. These two figures represent the same flow conditions (Re_D of jets=9×10^4) and correspond to the regime in which the "leaf" is totally destroyed. In the plane of impingement (fig. 143), the total angle of the spreading postimpingement flow is less than the impingement angle of the two jets due to energy losses in the inelastic collision as well as surface tension effects. The spread angle in the perpendicular plane (fig. 144) is much larger. This spread angle is a function of jet Reynolds (Re_D) number and impingement angle. Liquid breakup occurs in a periodic manner, as shown in the wave-like formation of bands of liquid elements in figure 144. Efforts are under way to study the effects of impingement angle, flow Reynolds number, and Weber number on the outer structure of the jets, the **spray** pattern, and the droplet size distribution in the nondilute region.

This work is progressing under grant NAG8–174 at the Pennsylvania State University in University Park, PA.

K.W. Gross/EP55
(205) 544–2262
Sponsor: Office of Aeronautics, Exploration and Technology

Droplet-Turbulence Interactions in Vaporizing Sprays

An experimental study is in progress to study the behavior of liquid droplets under conditions typical of those encountered in liquid rocket combustion chamber sprays. Of particular interest is the understanding of droplet-**turbulence** interactions in vaporizing liquid sprays under subcritical and supercritical conditions. Quantitative information must be obtained on the turbulent transport processes and their effect on droplet drag, droplet dispersion in the flow field, droplet **vaporization**, and fuel mixing with the oxidant. Such data can be acquired from a flow field with known acoustic frequencies when an individual droplet or a **droplet spray** is injected (fig. 145). The projected data base will serve in the development of improved droplet-**turbulence** interaction submodels and the verification of analytical predictions.

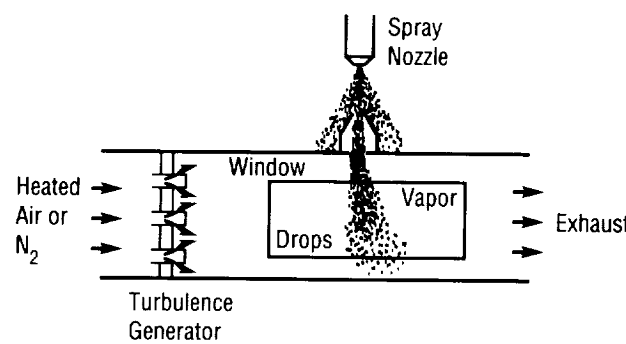

FIGURE 145.—Schematic of test configuration producing a droplet spray.

The essential components for the test facility have been constructed to allow operating conditions with air and propane up to pressures of 150 atm, temperatures of 500 K, gas velocities of 50 m/s, and acoustic frequencies of 1,000 Hz. With nonintrusive diagnostic techniques, such as fluorescence imaging, exciplex fluorescence, laser Doppler velocimeter, Raman scattering, and laser shadowgraphy, measurements can be made through a window in the gas flow duct. The variables of interest are: (1) gas properties, like average velocity and fluctuating components, pressure, and temperature; and (2) droplet properties of various fluids such as drop size, velocities, and surface conditions. The results accumulated to date are being documented for publication.

The experimental work is conducted by the Pennsylvania State University in University Park, PA, under Grant NAG8-160.

K.W. Gross/EP55
(205) 544-2262
Sponsor: Office of Aeronautics, Exploration and Technology

Formed Platelet Combustor Liner Construction Feasibility

Rocket engine combustion chambers must be cooled to withstand the severe, high-temperature environment that they contain. The construction of the **cooling liners** for the combustors is a time-consuming, intricate, and costly operation. Current practice employs the use of copper alloy liners with hundreds of axial grooves machined in the outer surface. These grooves are "closed out" by an electroforming process, usually using nickel, to form the cooling passages. Machining tolerance capability currently limits the minimum hot gas wall thickness to no less than approximately 0.635 mm (0.025 in) where wall temperatures are in the 732 °C (1,350 °F) range.

An alternate **cooling liner fabrication** approach is being investigated that has the potential for reducing liner fabrication time by an initial estimate of 50 percent and of improving the liner's cooling capability by lowering wall temperatures to 177 °C (350 °F). This alternate approach is based on the use of diffusion-bonded stacks of 0.20 mm (0.008 in) or greater sheets of copper alloy material, called platelets, which have been photo-etched to form cooling passages. The platelet stacks are formed into contoured sections by a stamping process and are joined to form the desired combustion chamber liner.

The investigation of the **platelet fabrication** approach has successfully demonstrated the forming of both zirconium copper and stainless steel panels with panel thickness to bend radius ratios of 0.044 to 0.22. These panels, ranging in thickness from 3.18 to 9.53 mm (0.125 to 0.375 in), have had hot wall thicknesses ranging down to 0.20 mm (0.008 in). A typical formed panel with panel cross sections is shown in figure 146.

A nozzle assembly sized to fit a 178-kN (40,000-lbf) thrust combustor is being fabricated for eventual hot testing to verify the design and fabrication approach and the thermal life cycle capability of the design. Four formed panels have been joined (fig. 147) to form the

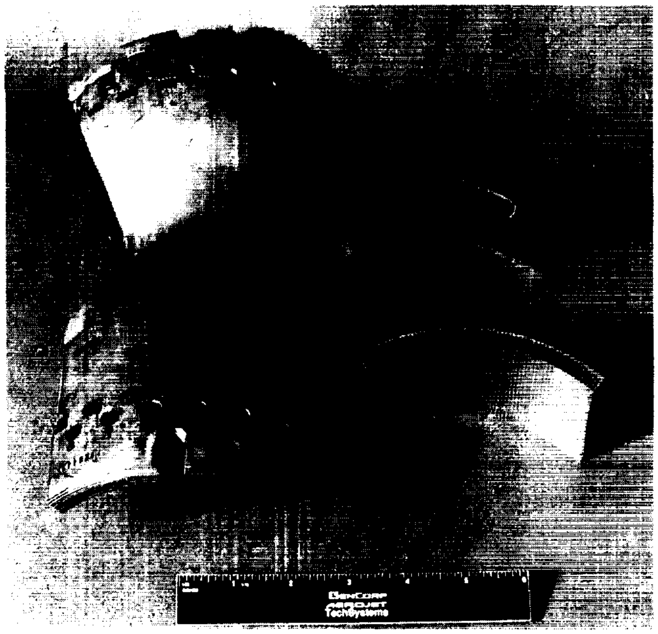

FIGURE 146.—Typical formed platelet cooling panel.

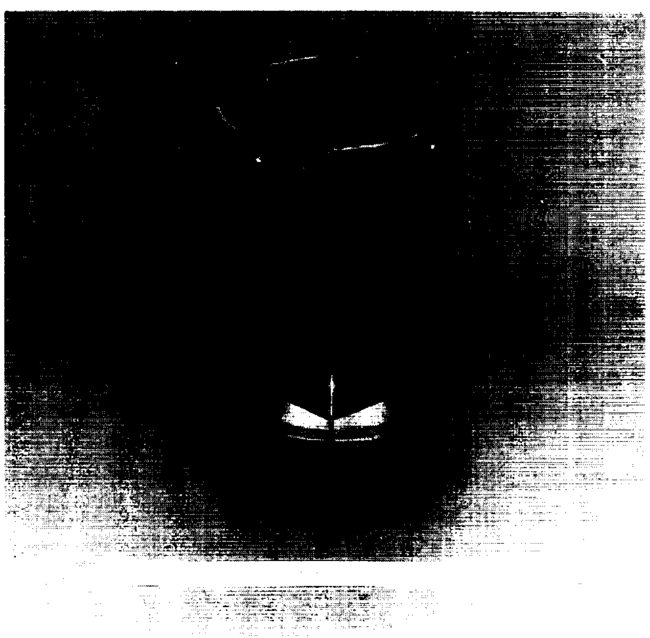

FIGURE 147.—Formed platelet cooling liner assembly.

complete **cooling liner**. The liner has been designed to operate at 20.7 MPa (3,000 lb/in^2 absolute) chamber pressure using hydrogen as the coolant. The predicted hot wall temperature is 371 °C (700 °F) with a predicted thermal life cycle capability of greater than 100 cycles.

F.W. Braam/EP52
(205) 544–7055
Sponsor: Office of Aeronautics, Exploration
and Technology

Injector Diagnostics Development

Research is being conducted to characterize the **injector** properties (i.e., droplet size distribution), droplet breakup, and **combustion** phenomena for single-element **injector** configurations. A pressurized, hot/cold flow test facility is being constructed for this purpose at MSFC.

This research is composed of measurement efforts for cold-flow characterization and hot-fire testing of **injector** assemblies for National Launch System (NLS) engine development. A two-dimensional stability research **combustor** will also be tested as part of the NLS effort to determine stability margins for liquid oxygen/hydrogen (lox/H_2) hardware development. The data acquired will be used to anchor computational fluid dynamics (CFD) codes currently under development.

Cold-flow data will be acquired for simulated **injector** sprays at 1,000 lb/in^{2}g using liquid nitrogen (LN_2) and gaseous nitrogen (GN_2) as simulant fluids. The initial test article will consist of a space shuttle main engine (SSME) preburner **injector** element. Droplets will be sized for this spray configuration using a phase Doppler particle sizer/velocimeter.

The hot-fire system will consist of a single-element hot-fire chamber with windows for **combustion** diagnostics and phase Doppler particle sizing measurements. A test-stand, laser-based diagnostic assembly is currently being designed for nonintrusive temperature measurements using an excimer-pumped dye laser for Raman **spectroscopy**. A dedicated laser Raman polychromator is under construction to allow high-speed determination of temperature and chemistry in the probe volume using the Raman spectra of H_2, water (H_2O), and oxygen (O_2) (fig. 148). Cooled photomultipliers and gated amplifiers are being procured to allow fast spectral data acquisition with minimum noise. Initial efforts have included laboratory studies of the Raman system for data reduction algorithm validation. A heater and pressurized cell is used for these studies to provide gases at known temperatures and pressures for calibration of the system.

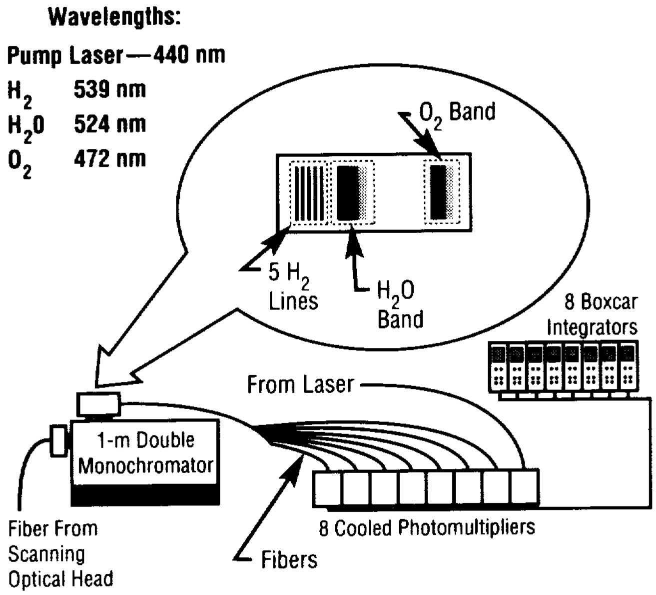

FIGURE 148.—Laser Raman polychromator data acquisition system.

A scanning optical head is also being developed for radial profiling of the single-element **injector** configuration. The system will utilize a single optic for focusing the laser beam and collecting the backscattered laser radiation. The collected signal will be coupled to the remote Raman polychromator via fiber optics.

R.H. Eskridge/EP55
(205) 544–7119
Sponsor: Office of Aeronautics, Exploration and Technology

Liquid Jet Atomization in Rocket Thrust Chambers

The space shuttle main engine (SSME) combustion chamber consists of many coaxial injection elements. These elements inject liquid oxygen (lox) and gaseous hydrogen (GH_2) into the thrust chamber. The primary **atomization** of the lox jet is caused by the large velocity and density gradients between the gas and liquid. The resulting liquid droplets evaporate and react with the GH_2. Previous studies have indicated that the calculation of spray combustion is very sensitive to the droplet initial conditions. Hence, the accurate prediction of breakup rate and drop size distribution is crucial to the successful prediction of the flow field in the combustion chamber.

Most of the previous studies used correlations based on the energy balance at the liquid-gas interface to calculate the breakup rate and drop size distribution. Presently, there is enough evidence to suggest that the breakup of a liquid jet occurs primarily due to surface wave instabilities; so, it is possible to calculate the breakup rate and droplet sizes from a fundamental instability wave analysis. This study deals with the development of computational fluid dynamics (CFD) submodels for **atomization** without employing any empirical correlations.

A novel jet-embedding technique is employed to couple the liquid jet and gas phase calculations. The one-dimensional (1–D) equations for the liquid jet core are solved to obtain the local jet velocity and shape. For this calculation, the momentum exchange between the gas and the liquid is modeled using a friction factor that is inversely proportional to the local jet Reynolds number. The mass breakup rate and the resulting droplet size distribution can be calculated from the most unstable surface wave growth rate and its wavelength. The gas phase calculations are performed using a CFD code. The calculated jet velocity and shape are used in specifying the boundary conditions for the gas phase calculation. The grid for the CFD code is dynamically adapted to the liquid jet core shape. The friction between the phases at the interface is automatically taken into account by applying a sliding wall (at local jet velocity) boundary condition.

The droplets from the gas-liquid interface are tracked in a Lagrangian frame of reference. The droplet momentum equation includes the local drag force, local pressure gradient force, and the body forces. The evaporation mass, exchange of momentum, and energy between the liquid droplets and the gas are included as source/sink terms for the gas equations. A finite-rate chemical model is used for the reaction of oxygen (O_2) and hydrogen (H_2). The predictions from these calculations are shown in figures 149 and 150. Figure 149 shows the isotherm contours for an SSME fuel preburner. A lox injection velocity of 24.4 m/s at 100 K and an (H_2) gas velocity of 213 m/s at 70 K are used in these calculations. The maximum temperature in figure 149 is about 3,800 K, which is close to the adiabatic flame temperature for an H_2-O_2 reaction. Figure 150, shows the velocity vectors in this SSME preburner design. A small recirculation zone near the face/wall corner is evident. To avoid the heat-up of the face plate due to this flow recirculation, the later designs use a gas bleed. The predictions from these calculations are in qualitative agreement with other predictions using the volume-of-fluid (VOF) approach.

This effort is being conducted by the CFD Research Corporation in Huntsville, AL, under contract NAS8-38425.

K.W. Gross/EP55
(205) 544-2262
Sponsor: Office of Commercial Programs, Small Business Innovation Research

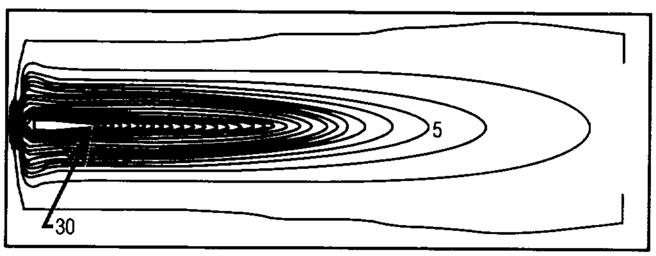

XY Plane 1

FMin. 1.000E+02
FMax. 3.824E+03

Contour Levels	Temp Contours	Contour Levels	Temp Contours
1	1.000E+02	9	1.127E+03
2	2.284E+02	10	1.256E+03
3	3.568E+02	11	1.384E+03
4	4.853E+02	12	1.513E+03
5	6.137E+02	13	1.641E+03
6	7.421E+02	14	1.769E+03
7	8.705E+02	15	1.898E+03
8	9.990E+02	30	3.824E+03

FIGURE 149.—Coupling jet-embedding and spray (constant temperature contours).

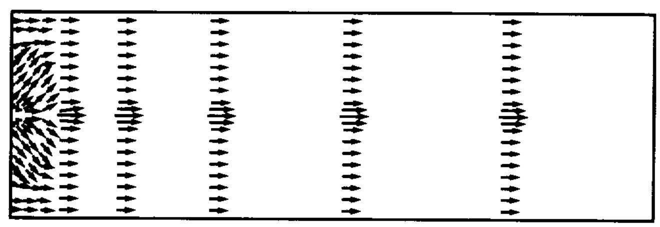

XY Plane 1
Velocity Plots
Velmin 5 172E+01
Velmax 2 056E+03

FIGURE 150.—Coupling jet-embedding and spray (velocity vectors).

National Launch System Propulsion Advanced Development

Advanced development research and technology activities to support National Launch System (NLS) propulsion definition studies were initiated in 1988. Efforts covered by the program are divided into the following categories, according to the nature of each task: liquid oxygen (lox)/hydrogen (H_2) engine, lox/H_2-lox/methane engine, liquid propulsion test facilities, and solid propulsion. The primary emphasis of the tasks is to support definition studies with demonstration and validation of design concepts, manufacturing processes, materials, and design techniques that will be employed to enable NLS propulsion to meet the program goals of high reliability, low cost, and operability. Particular effort is concentrated on producibility to allow dramatic cost reduction and quality increases compared to conventional propulsion systems. Testing is conducted at the MSFC Pressure Test Facility (Test Stand 116) and other facilities at the Stennis Space Center and the U.S. Air Force Phillips Laboratory.

Lox/liquid hydrogen (LH_2) activities include conduct of detailed trade studies, detailed design, fabrication, and testing of major engine components to fully investigate low-cost manufacturing processes, low-cost/producible/high-quality design concepts, and advanced manufacturing techniques. Emphasis will be placed on materials and materials fabrication processes that will support the selected approaches. The total effort will include the design, fabrication, and test of a lox turbopump (fig. 151), an LH_2 turbopump (fig. 152), and a brassboard controller/sequencer.

Lox/CH_4 activities have been discontinued (or rebaselined to LH_2) since it is no longer a candidate fuel for the **space transportation main engine** (**STME**) or the NLS. The total effort includes the design, fabrication, and test of the lox/LH_2 turbopump, thrust chamber assembly, and gas generator assembly.

Many of the liquid propulsion tasks have reached significant milestones during the past year. For example, testing began in February 1991 on a 580k–lb lox/hydrogen injector at MSFC Test Stand 116. These test results will validate design concepts and provide data for stability verification prior to the start of final design for the **STME** engine (fig. 153).

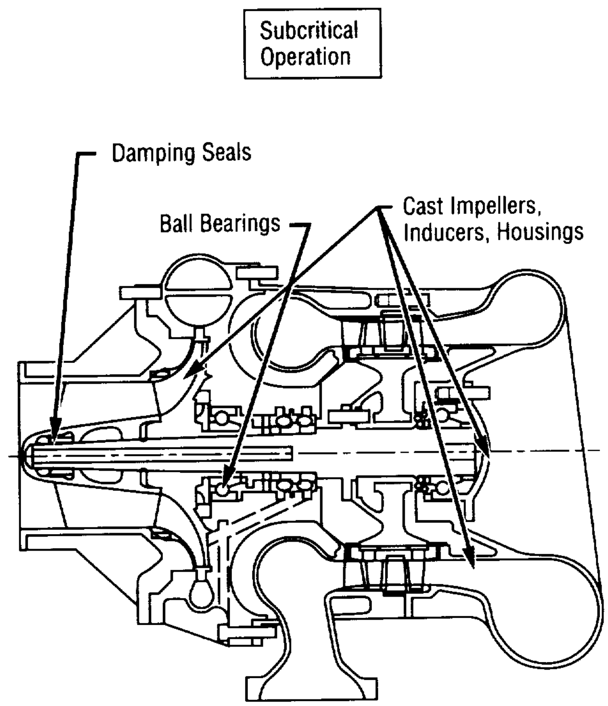

Speed: 8,600 r/min
Discharge Pressure: 3,239 lb/in^2 absolute (22,332 kPa)
Flowrate: 1,163 lb mass/s (527.5 kg/s)

Figure 151.—Lox turbopump.

Speed: 25,200 r/min
Discharge Pressure: 3,686 lb/in^2 absolute (25,414 kPa)
Flowrate: 192 lbm/s (87.1 kg/s)

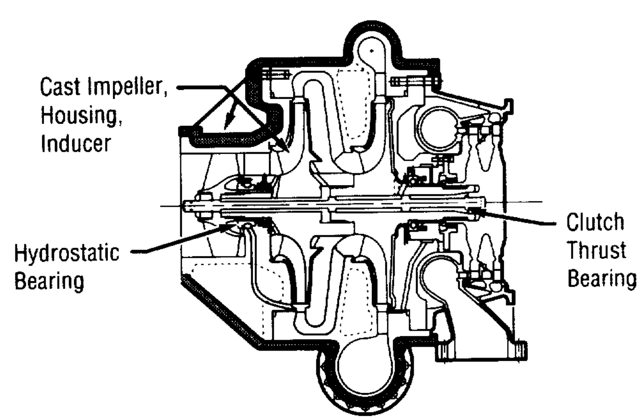

Figure 152.—LH_2 turbopump.

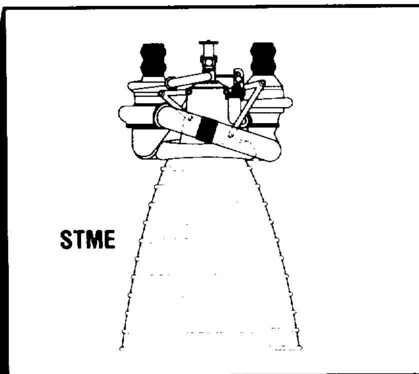

Categories	Engine Design Characteristics
Propellants	Lox/H_2
Demonstrated Reliability	0.99 at 90% Confidence
Thrust	583k lb (Vac) (2,593 kN)
Specific Impulse (I_s)	430.5 (Vac)
Weight	8,000 lb (3,629 kg)
Application	Expendable or Reusable Core or Booster
Chamber Pressure	2,250 lb/in^2 absolute (15,503 kPa)
Control	Open Loop

FIGURE 153.—Space transportation main engine.

Booster/core propulsion subsystems technology activities will provide definition of system architecture for low-cost auxiliary propulsion systems, definition of NLS design requirements and design criteria, design and validation of a prototype lox tank pressurization system remote from the engine, and demonstration of control authority and stability.

Solid propulsion activities center on technologies that support a monolithic-case, fixed-nozzle, clean-propellant booster concept selected by NLS studies as the candidate to best meet the goals of high reliability and low cost. Specific tasks are grouped into the categories of clean propellants, nozzle/case technologies, and motor element integration technologies. Clean propellant work will demonstrate high-rate, low-cost processing of low hydrochloric-acid content propellants. To support the demonstration, a pilot scale plant will be built, continuous processing methods will be operated, and moderately large-scale demonstration firings will occur. Hardware concepts that will improve the reliability and costs of nozzle cases, insulation, etc., will be selected, designed, and demonstrated on a small-scale basis to verify that the new concepts can meet goals. A task investigating castable nozzle is also being pursued, with subscale testing planned at MSFC next year.

J.L. Taylor, Jr./HA31
(205) 544–8824
Sponsors: Office of Space Flight

Nonintrusive Flowmeters for Rocket Engines

Flow measurements are essential to rocket-engine control and condition monitoring, providing more reliable engine operation. Nonintrusive **flowmeters** do not disturb the propellant flow, which could create potential hazards. Commercial, nonintrusive, **ultrasonic flowmeters** have typically been used to measure flow rates up to 9 m/s (30 ft/s) for noncryogenic liquids.

During this program, water flow rates up to 30 m/s (100 ft/s) have been obtained using this technique. In addition, **cryogenic** transducers are being developed, featuring survivability at liquid-nitrogen temperature, while providing good acoustic coupling. The **cryogenic** transducer survivability and **high-flow** measurements demonstrate that a nonintrusive, **ultrasonic flowmeter** has the potential of providing **cryogenic, high-flow** measurements for more reliable liquid-propellant rocket engine operation.

Ultrasonic flowmeters do not require a sensor to intrude into the flow path. Piezoelectric transducer pairs are attached to opposite sides of a duct, one upstream and one downstream (fig. 154). Each transducer pair transmits and receives **ultrasonic** pulses through the duct wall and the liquid. Flow velocity is measured by subtracting the upstream and downstream transit times of the **ultrasonic** pulses that travel through the duct diameter. This flowrate measurement technique has the advantage of depending only on the duct diameter and the separation of the transducer pairs, while being completely independent of the density, viscosity, pressure, temperature, and speed in sound liquid.

Commercially available nonintrusive, **ultrasonic flowmeters** have typically been used to measure flow rates up to 9 m/s (30 ft/s), lower than is required for high-power rocket-engine turbopumps. Furthermore, at

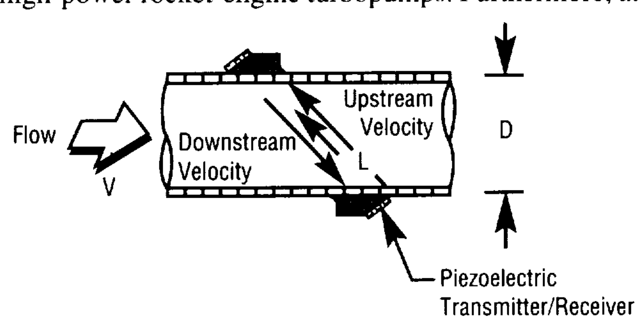

FIGURE 154.—Basic layout for transit-time flowmeters.

cryogenic temperature, acoustic coupling is poor due to freezing and cracking of the conventional **ultrasonic** couplants. At present, no nonintrusive, **ultrasonic flowmeter** capable of measuring high flow rates of **cryogenic** liquids is available commercially.

The flow in the duct of the space shuttle main engine (SSME) high-pressure, liquid-oxygen (lox) turbopump discharge has been used as the baseline for this program. The second phase of this program focuses on the development of transducers that will operate and survive in **cryogenic** environments. Seventeen combinations of piezoelectric crystals and bonding materials, including solders and epoxies, were tested after attachment to Inconel 718 wedges. Low-melting-point solders failed due to poor bonding with the Inconel 718 wedges. High-melting-point solders and brazes could not be used since the piezoelectric crystals would be permanently damaged. When cured, most of the epoxy bonds were several mils thick and frothy, the air bubbles extinguishing the **ultrasonic** signals. One particular epoxy provided excellent acoustic coupling with a very thin (less than 1 mil) bonding layer, and further tests were performed with these transducers.

The transducer wedges were attached with the epoxy to an Inconel 718 duct that was capped at one end. The duct was filled first with water, then with liquid nitrogen (LN_2). Comparison of the water and LN_2 signal amplitudes agreed to within 10 percent of the theoretical value, demonstrating that the epoxy bond did not crack or fail at **cryogenic** temperatures. Furthermore, the transducer bonds survived 12 thermal cycles from LN_2 to ambient temperature, and 25–g vibrations for 30 min with no apparent loss in bond integrity.

During the setup for high-rate **cryogenic** flow testing, it was found that the standard electronics being used were not receiving the signals properly. The system was re-instrumented using a pulse generator and oscilloscope, and it was found that a significant shift in anticipated frequency occurred, resulting in a low-amplitude, largely unusable signal. The cause of the observed phenomenon is not known but will be investigated. More work with the transceiver crystals may be required since these are unique to the project and were developed for this program. Flow-testing is dependent on the outcome of the sensor investigative effort.

W.T. Powers/EB22
(205) 544–3452
Sponsor: Office of Aeronautics, Exploration and Technology

Nonintrusive Hot-Gas Temperature Sensor

A program was performed to evaluate the potential of an infrared (IR) detector system for determining the **temperature** of the hot gas (hydrogen-rich water vapor) in the high-pressure turbopump discharge ducts of the space shuttle main engine (SSME). The **sensor** concept under evaluation utilizes the 2.6–μm water-band emission as the measuring standard in this application. This effort established potential **sensor** locations in the hot-gas manifold, analyzed the environmental constraints on the **sensor** design, and designed, fabricated, and laboratory-tested breadboard, **nonintrusive**, hot-gas **temperature sensor** hardware. The data analyses from these evaluations demonstrated the feasibility of this optical approach and showed a high degree of accuracy in **temperature** determinations of a laboratory flame. A preliminary design analysis effort was performed to recommend material candidates for housing and window substrates, and both thermodynamic and aero-thermodynamic analyses of the proposed **sensor** were performed.

Subsystem laboratory evaluations addressed the issue of the effects of varying mixture ratios in the flat-flame burner on the breadboard **sensor** performance. This technique was found to be quite independent of flame mixture ratio. Detailed design focused on the design specification issues with regard to the detector, its optical window, the sensor housing, and the **sensor** electronics.

Indium arsenide (InAs) detectors are current-generating, photovoltaic IR diodes sensitive to 1.0– to 3.6–μm wavelength radiation. This detector has a typical response frequency of direct current (dc) to 10 MHz, an inherently faster response time than that of the resistance **temperature** device (RTD) hot-gas **temperature sensor** presently in use in the SSME, and may allow more accurate thermal tracking of transient conditions in the turbopump discharge ducts.

Diamond remains the window material of choice for this application. Its relatively large thermal conductivity coupled with its relatively small thermal expansion coefficient results in a negligible **temperature** gradient and an acceptably low shear stress across the window. A series of design analyses of proposed diamond windows indicates that acceptable window thickness results from calculations utilizing typical SSME mainstage and transient conditions. The 125–MPa (20,000–lb/in^2) burst pressure requirement and 62.5–MPa (10,000–lb/in^2) proof pressure requirements for the current RTD hot-gas **temperature sensor** were included in these calculations.

The final design for the **sensor** (fig. 155) provides for the use of an InAs detector, and a foreoptic system having a diamond window and one or two sapphire lenses to concentrate the collected radiation onto the detector. This will be mounted in a housing compatible with its use on the SSME. Although the instrument reads out the **temperature** of hot gas, it must withstand some cryogenic cooling in its environment until the engine starts.

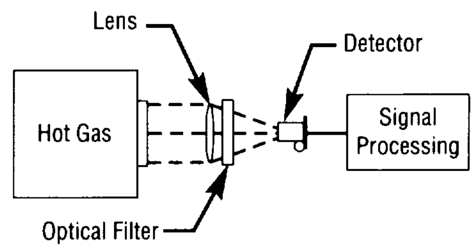

Figure 155.—Basic sensor layout.

The InAs detector would be supported by electronic circuitry, which may include the provision for a thermo-electric cooler for detector-temperature regulation. The electronics should be capable of operating under conditions of 70 °C (158 °F) ambient **temperature** and vibration levels of 30 g_{rms}.

The completed system will permit fast **temperature** measurement (1 kHz or better) and high accuracy so that **dynamic** reactions may be monitored and closed-loop control may be effectively enhanced.

W.T. Powers/EB22
(205) 544–3452
Sponsor: Office of Aeronautics, Explorations and Technology

Optical Leak Detection for Ground-Based Operations

There is clearly a need for a more rapid, thorough, and reliable **leak detection** approach for reusable rocket engines. The current approach used on the space shuttle main engine (SSME) involving soap solution is quite laborious, as well as incomplete, because only preselected points on the engine are inspected. An extension of this approach to all the hundreds of joints, welds, and brazes on the engine would be prohibitively time-consuming and impractical. An alternative approach has been utilized that consists of surrounding the entire engine with an airtight bag and testing helium leaks with a mass spectrometer. While more accurate and reliable for detecting the presence of leaks, this method is again quite laborious and gives no indication of where the leaks are occurring. If leaks are detected, bagging must still be followed by time-consuming soap solutions testing to identify the leak sources. The entire leak inspection process on the SSME consumes several work shifts and often must be repeated one or more times to reliably identify leaks and determine their sources. In contrast, turnaround times desired for future reusable space vehicles are on the order of 1 d or less, implying that total vehicle inspection times must be on the order of hours or less.

Of the techniques developed, **absorption-based optical leak detection** (fig. 156) is the most promising for ground-based operations. The component to be inspected is pressurized with a gas that strongly absorbs infrared (IR) light in a particular wavelength range. The component is then illuminated in that wavelength range by a tunable **IR laser**, and imaged with an **IR camera**. Leaking gas absorbs the laser light, showing up as a dark cloud in the IR camera image. Leaks from joints down to 4.1 mL (0.25 in^3/min) have been successfully imaged on an SSME nozzle in tests, using nitrous oxide (N_2O) as the tracer gas. These leaks were imaged at ambient temperature without a carbon dioxide (CO_2) laser or other external IR light source for illumination. The image was from 4.5 m (15 ft) away using a mercury cadmium telluride (HgCdTe) mid-IR imaging array system.

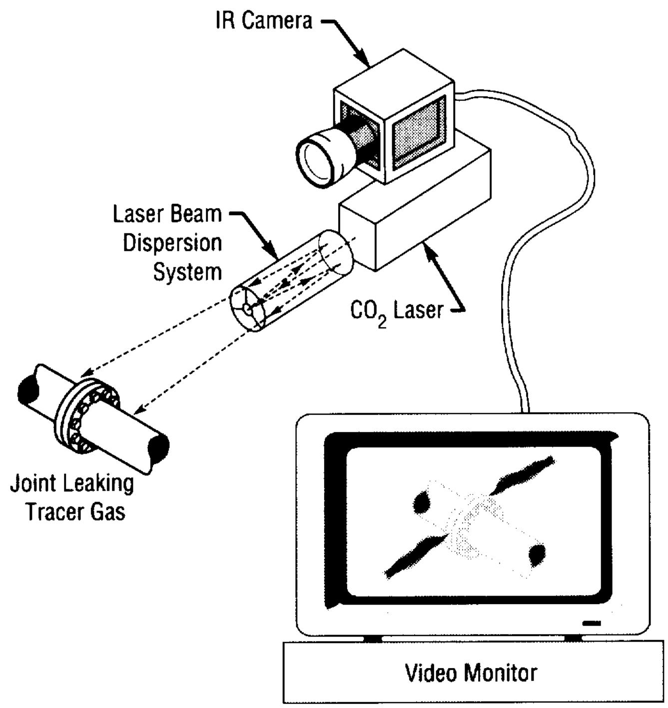

FIGURE 156.—Absorption-based optical leak detection.

Due to the recent hydrogen leaks on the space shuttle prior to launch, this **leak detection** task is under scrutiny for acceleration. This **optical leak detection** system should allow for a speedy turnaround time, returning the shuttle to flight in a matter of hours, not days or weeks.

M.L. Johnson/EB22
(205) 544–5519
Sponsor: Office of Aeronautics, Exploration and Technology

Optical Plume Anomaly Detector

Using the principle of exhaust **plume spectroscopy**, a system has been developed to monitor the health of the **space shuttle main engine** (SSME) during ground-test operation. Through the identification and interpretation of anomalous spectral activity, the optical **plume anomaly** detector (OPAD) system can provide real-time diagnostics of **engine** wear and/or component failure.

The OPAD employs two 0.5–m grating spectrographs, a 16–channel spectroradiometer (the polychromator), and a multichannel spectral analyzer (the spectrometer), which has two 2,048–element linear photodiode arrays at the exit plane of the dispersing instrument. The data acquisition and control system consists of four 80386 33–MHz computers: two at the test stand for instrument control and data preconditioning and two in the test support building providing data archiving and display and system control. A fiber optic data link connects the two sets. A more comprehensive description of the OPAD hardware is reported in the below-referenced publications.

OPAD efforts at present are concerned with data analyses. To date, the OPAD has acquired data on all 21 ground-level test firings of the **SSME** at the technology test-bed (TTB). The TTB OPAD spectrometer (reticon array spectrometer (RAS)) test results are shown in figure 157. Real-time displays, as well as oscillographic-type printouts,, provide quick look data for immediate scrutiny. Efforts to correlate any known **engine** performance **anomaly** support the Propulsions Lab's post-test review and provide valuable input necessary for system calibration. As an example, the OPAD data for TTB–020 indicated significant evidence of metallic species, primarily Cr, Fe, Mn, and Ni, throughout the test, suggesting component wear. Post-test inspection noted **engine** faceplate erosion. The faceplate is composed of Inconel 625, an alloy of Ni, Cr, Mo, Fe, Co, Mn, Ti, Al, Si, Nb, and Ta. In addition, nominal **engine** performance data support the data base for normal **plume** emissions.

An in-depth, quantitative analysis of the spectral data will be required to fully evaluate and monitor the state of the **engine**. In the current approach, a set of line-by-line radiative transfer models is being developed to relate observed spectral emissions to metallic species densities in the exhaust **plume**. The development of the radiative models is intensive and will require accurate

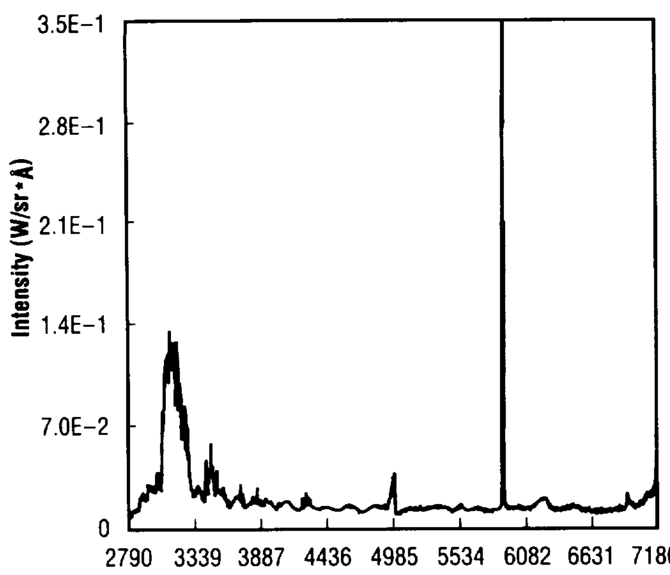

FIGURE 157.—TTB OPAD spectrometer (RAS) test results.

spectroscopic data, chemi-excitation rates, collision cross sections, and valid flowfield properties, primarily at the Mach disk. Also, since the metallic atoms readily react with the hydrogen-oxygen constituents, additional reactions must be included in the flowfield chemistry codes.

When completed, the models will be implemented to analyze the spectral data in realtime and/or in a post-test mode. The analysis will provide estimates of material composition alloy(s) identification, and mass flow erosion rates that may be compared to established red-line levels to detect **engine** or component failure. These data will be archived for future reference and statistical analysis and will provide valuable **engine** performance history.

Powers, W.T., and Zaccardi, V.A., "Status of OPAD Instrumentation Conference on Advanced Earth-to-Orbit Technology," MSFC, AL, May 17, 1990.

Wallace, T.L., and Cooper, A.E., "Summary of Data from OPAD Program—Conference on Advanced Earth-to-Orbit Technology," MSFC, AL, May 17, 1990.

W.T. Powers/EB22
(205) 544–3452
Sponsor: Office of Aeronautics, Exploration and Technology

Physical Processes of Injection and Atomization of Liquid Fuels

Under grant NAG-126 with Carnegie Mellon University, a series of experiments have been conducted to determine the fundamental physical processes of **injection** and **atomization** of **liquid fuels** for rocket combustion chambers. For coaxial injectors, liquid- and gas-flow rates have been progressively changed. Microphotography was used to obtain details of wave disturbances on liquid surfaces. Direct measurements were made of wavelength, amplitude growth rate, and frequency of wave propagation on liquid surfaces. Linear increases of wavelength and amplitude were found along the length of the liquid surface while frequency remained constant. Measured frequencies were in the range of those measured in combustion instability experiments. Final disintegration of liquid jets occurred in a sudden disruption, producing a shower of droplets with a wide range of drop sizes and velocities.

Detailed measurements have been made in the **sprays** using the phase Doppler particle analyzer (PDPA). Measurements of drop size, velocity, and number density are related to the disintegration process. Initiation of disturbances occurs in the injector or by interaction with the surrounding gas stream. The gas stream drives the waves and accelerates the liquid surface. Increasing turbulence intensity in the gas stream is a very effective means of reducing drop size. Large eddies from the gas stream penetrate into the liquid stream causing disruption, as shown in figure 158.

FIGURE 158.—Breakup of liquid jet by large eddy in coflowing gas stream.

K.W. Gross/EP55
(205) 544-2262
Sponsor: Office of Aeronautics, Exploration and Technology

Pressure-Velocity Algorithm for Fluid Flows

The current numerical method utilizing finite-difference or finite-volume techniques for solving fluid flows can generally be classified as density-based or pressure-based methods. Most density-based methods originated with external aerodynamics problems and retain density as a primitive variable that is governed by the continuity equation. However, the density-based methods, although very popular, are not suitable for efficiently solving low Mach number or incompressible flows. The flow fields encountered in typical rocket thrust chambers range from incompressible flow to supersonic flow conditions. It is desirable to have a unified algorithm covering all speed regions.

The quest for an all-speed capability goes back to the implicit continuous-fluid Eulerian (ICE) solution method formulated by the Los Alamos National Laboratory in 1973 using a pressure method in which pressure was used as a primary variable. For the last decade, most pressure-based methods have employed iterative techniques and have been applied mostly to low subsonic flows. In this study, a new **pressure-velocity algorithm**, suitable for fluid flows at all speeds, is derived based on the operator-splitting technique.

The split of the operator allows a different operation on different flow variables and establishes physically correct pressure correction equations. The resulting pressure correction is of a mixed type, i.e., elliptic for low-speed flows and hyperbolic for supersonic flows. The final pressure-velocity forms are general and can be integrated in finite-volume, finite-difference, or finite-element methods. The present **pressure-velocity algorithm** has been implemented in the computer code MAST (Multiphase All Speed Transient). Excellent solutions have been obtained for: incompressible driven cavity flows, unsteady vortex shedding flows, and subsonic, transonic, and supersonic flows over a bump. This method has also been applied to examine space transportation main engine (STME) subscale nozzle cooling problems and spray combustion calculations with swirling injection elements.

Several papers on this subject have been presented at conferences, and articles for publication in technical journals are in preparation. This analytical effort is in progress under grant NAG8–128 at The University of Alabama in Huntsville, AL.

K.W. Gross/EP55
(205) 544–2262
Sponsor: Office of Aeronautics, Exploration and Technology

SPACE SHUTTLE MAIN ENGINE EXIT DIAGNOSTICS

Photolysis of water (H_2O) with an excimer **laser** is being investigated as a means of **tagging** combustion-related flows for measurement of velocity by generation of a zone of enhanced OH concentration. A second pulsed ultraviolet (UV) **laser** is used to detect convection of the tagged zone by time-delayed electronic excitation of OH and spatial imaging of resultant **fluorescence**. This enhanced flow **tagging** method offers promise for measurement of velocity in rocket, gas turbine, supersonic combustion, and other applications where it is difficult or impossible to utilize other techniques. The specific applicability of the enhanced OH technique to supersonic or subsonic combustion flows depends on the photodissociation process and the kinetics of OH decay for given conditions. Laboratory studies of flames or heated flows containing water vapor are being conducted to characterize enhanced OH flow **tagging** for several applications, using an injection-locked, tunable excimer **laser** for excitation. Velocity measurement with this technique has been demonstrated in a small supersonic steam jet, and conceptual studies have shown that the method is attractive for velocity measurement in the exit plane of the space shuttle main engine (SSME).

For application to the high supersonic Mach number nozzle exit flow of the SSME, nitrogen (N_2) or H_2O diluted 1 atm hydrogen (H_2)/air premixed laboratory flames are being used to simulate exit plane stoichiometry and temperature. An injection-locked, narrowband, tunable 248 nm (KrF) excimer **laser** is used for photolysis of H_2O by a two-photon process. Enhanced OH **fluorescence** imaging results obtained with a Nd:YAG pumped-frequency, doubled-dye **laser** are shown in figure 159. The pulse energy of the KrF **laser** was about 200 mJ. The beam was focused over the burner to a spot size of 0.3 to 0.4 mm. Figure 159 shows spatial profiles of OH **fluorescence** obtained with the **lasers** positioned at two different heights above the surface of the premixed porous bronze plug burner. Near the burner surface (fig. 159), the bottom trace shows that the excimer **laser** itself induces a small amount of OH **fluorescence** during the photolysis process, which appears in a narrow spatial zone. (In figure 159, the temperature was about 1,200 K. The pulsed dye **laser** was unfocused and tuned to excite an O-O band OH transition near 308 mm. Fluorescence was detected through a 310–nm, 1.5–nm full-width-half-maximum (FWHM), 6–percent transmission filter.

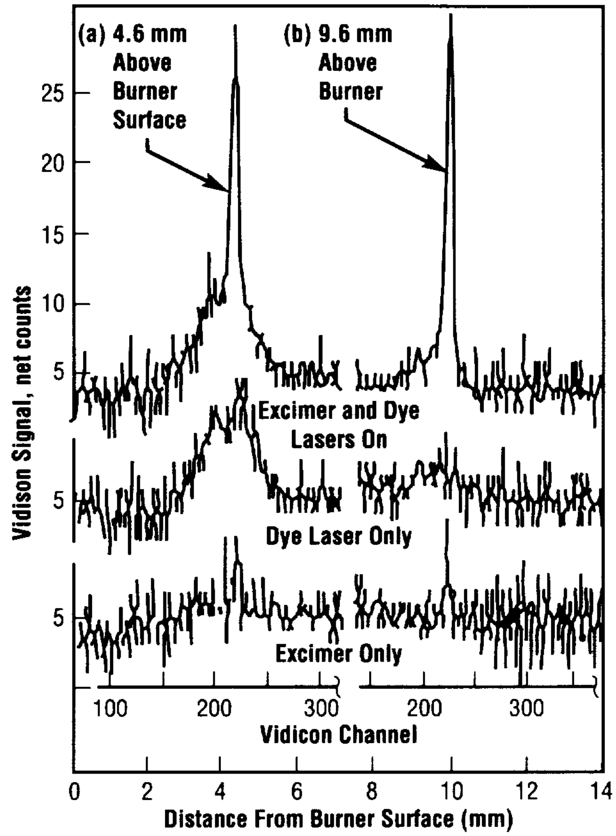

FIGURE 159.—Spatial imaging OH fluorescence in H_2/air, fuel-rich premixed flame.

The dye laser was time-delayed approximately 2 μs relative to the excimer laser.) The dye **laser**, tuned near 308 nm and pulsed approximately 2 μs after the KrF **laser**, induces a stronger OH **fluorescence** (middle trace) by itself from flame-generated OH, appearing in a broad zone, representative of the size of this unfocused beam (approximately 2 to 3 mm). The combined excimer-dye **laser** case (top trace) shows that the excimer-**induced** ground-state-OH concentration is much larger than the flame background OH. The tagged zone created by the focused excimer appears as a sharp spike on top of a broad background signal. The 2–μs time delay between dye and excimer **laser** signals is useful for the SSME application where velocities exceed 4,000 m/s (13,000 ft s). The flow velocity in the flame is less than 1 m/s (3.3 ft/s), too low to resolve in these studies, but the favorable enhanced OH lifetime results are evident.

The objective of current laboratory scale experiments was to measure the effect of intensity and tuning of the injection-locked KrF excimer **laser** on the level and decay of enhanced OH generated in the diluted H_2/air premixed flames over a 1– to 3–μs period (fig. 160). Enhanced OH is detected near 308 nm with a second

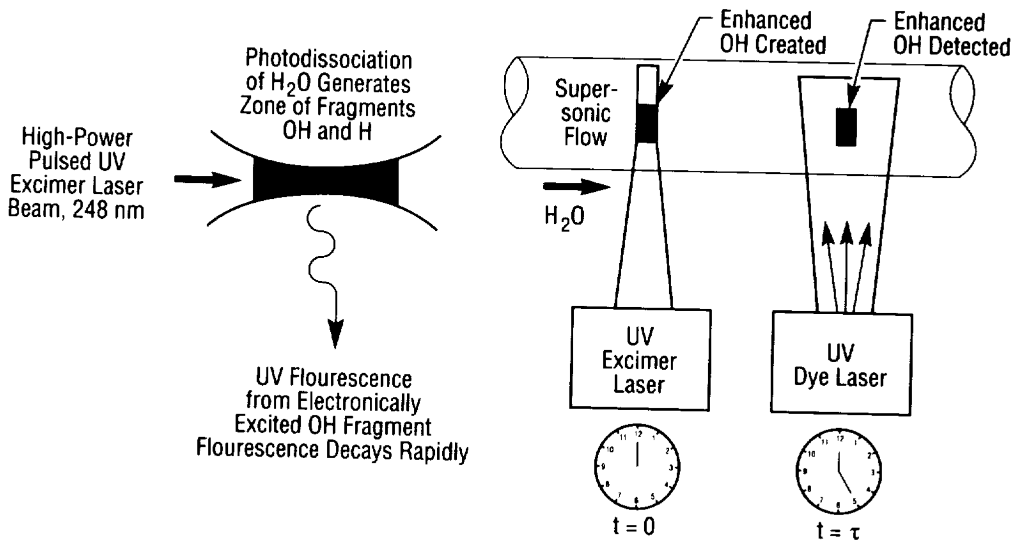

FIGURE 160.—Flow testing for velocity determination.

excimer **laser**, operating with XeCl. In an eventual field diagnostic system, it is planned to excite an OH 0,0 band transition directly with the output of this second excimer **laser**, operating in a line-narrowed tunable mode at 308 nm by injection-locking. Present results include some experience with this mode. Strong **fluorescence** from background has been observed that may correspond to OH transitions.

Focusing of the KrF beam for a rocket stand application will require significant standoff distances (approximately 7 m (25 ft)) and a large focal spot size (approximately 1 mm (0.4 in)). Preliminary experiments showed that significant enhanced OH could be detected when only 10 percent of the KrF beam was focused over the burner. Some experiments have required even lower intensities, which have been obtained by moving the focusing lens a few centimeters closer to the burner to obtain a larger beam diameter. Excitation spectra of OH **fluorescence** have been recorded in moist room air and in the N_2–diluted H_2/air flame. Results over a range of intensities suggest that photodissociative effects are more complex than in a low-pressure, room-temperature, water vapor cell.

Some quantitative, time-delayed measurements of enhanced OH excitation have been obtained with the tunable XeCl **laser** (308 nm) and photomultiplier tube (PMT). Analysis and interpretation of results are in progress.

L.R. Boedeker, "Velocity Measurement by H_2O Photolysis and Laser-Induced Fluorescence of OH," *Optics Letters*, vol. 14, 1989, p. 473.

Shirley, J.A., and Boedecker, L.R., "Nonintrusive Space Shuttle Main Engine Diagnostics," AIAA/ASME/SAE/ASEE 24th Joint Propulsion Conference (AIAA, New York, 1988), paper AIAA–88–3038.

Meijer, G., terMeulen, J.J., Andresen, P., and Bath A., "Sensitive Quantum State Selective Detection of H_2O and D_2O by (2+1) — Resonance Enhanced Multiphoton Ionization," *J. Chem. Phys.*, vol. 85, 1986, p. 6,914.

W.T. Powers/EB22
(205) 544–3452

Sponsor: Office of Aeronautics, Exploration and Technology

Space Shuttle Main Engine Prebumer Temperature Profiler

Laser-based diagnostic **instrumentation** is being developed to measure **temperature** profiles in the preburner combustion chambers. The staged combustion cycle used on the space shuttle main engine (SSME) burns liquid hydrogen fuel, rich with liquid oxygen, to generate gas to drive the propellant turbopumps. The pressures in the preburners are nominally 5,500 lb/in^2 absolute (34.5 MPa) and the **temperatures** are 800 to 1,700 K. The post-combustion gases are 89–percent molecular hydrogen and the balance is water vapor.

The main advantage of optical diagnostics for **temperature** measurements is that they are **nonintrusive** and, with judicious use, do not perturb the flow being measured. A physical probe inserted in the flow must be robust and of heavy construction to survive. For this reason, flow perturbation is unavoidable and instrument response time becomes long, i.e., seconds. The temporal response of laser techniques, however, is determined by the time required to acquire a sufficient number of single photons for an accurate measurement. With powerful lasers, the response time can be a small fraction of a second for the SSME preburner application.

A **nonintrusive** means of measuring **temperature** profiles in the SSME preburner is desired to support future combustor development and refinement. Raman scattering was selected for fuel preburner (FPB) diagnostics in a feasibility study. The condition of limited access existing in the preburner, the lack of particles in the flow, and the low-visible-neutral luminosity of the hydrogen-oxygen flame favor Raman diagnostics in the backscattering configuration. The fiber-optic Raman thermometer (FORT) (fig. 161) laser diagnostic system is designed to use optical fibers both to carry laser light for excitation to the combustor and to carry scattered light to remotely located equipment used for acquisition and analysis. This system permits measurement of the preburner **temperature** distribution across a diameter from an existing transducer port on the SSME preburner.

The FORT system consists of the following: (1) a high-power argon ion laser for excitation; (2) an optical head attached to the preburner that focuses light into the combustor and collects backscattered light; (3) a spectrograph and optical multichannel detector to disperse and rapidly detect the Raman-shifted radiation; (4) a computer system to acquire and analyze data; and (5) control **instrumentation** to position optics and thermally stabilize the head. The most unique aspect of the instrument design is the use of multimode optical figures to transmit backscattered radiation from the head to the spectrograph.

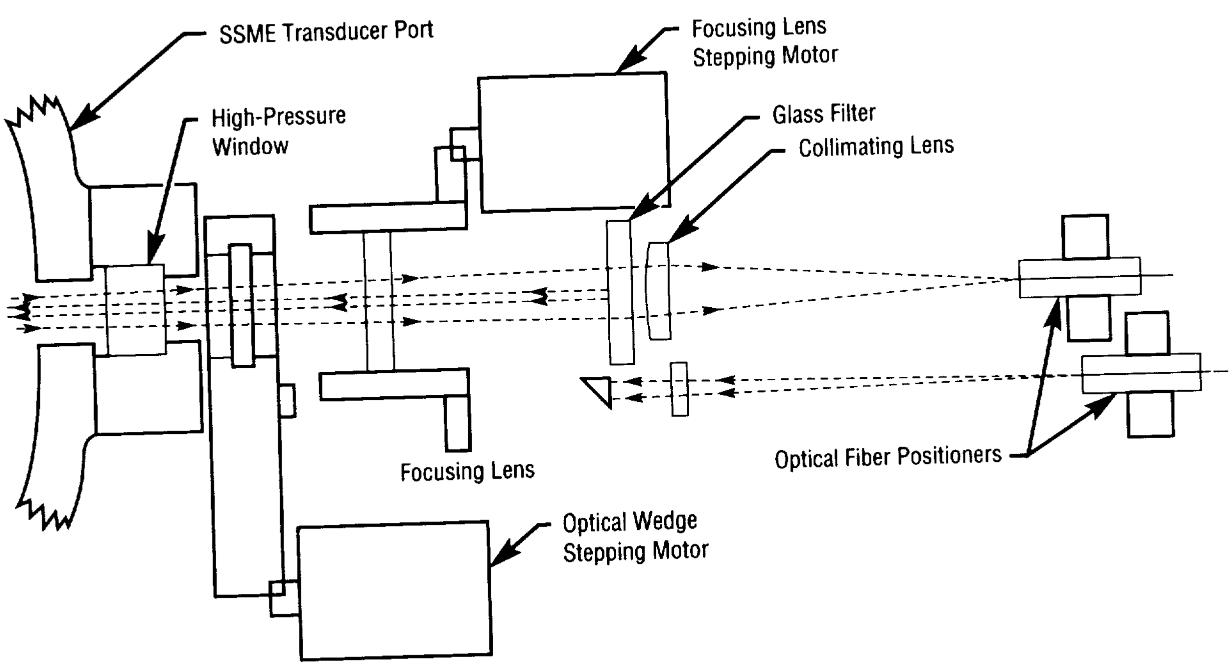

FIGURE 161.—Interior design of FORT optical instrument head.

The optical port, intended to be installed on an SSME technology test-bed (TTB) FPB, is a high-**temperature**, high-pressure, windowed test fixture designed to withstand SSME FPB operating conditions. The size and weight were kept as low as possible due to the severe vibration environment expected and the loading problems on the entire fiber-optic **temperature** profiling system. The final design was a 5-cm (2-in) diameter cylinder with a 3.55-cm (1.4-in) height, weighing only 0.454 kg (1 lb).

A computer model was constructed to evaluate the design for the effects of thermal shock. The model was used to determine the maximum **temperature** that the window is expected to be subjected to during the SSME FPB operation, approximately 426 °C (800 °F), with the **temperature** at the surface of the window expanded to be 115 °C (240 °F). Testing has determined that the window design can withstand the **temperatures** and pressures expected during normal SSME operation. The worst case **temperature** would occur in the event of failure of the purge system, possible raising the **temperature** to 760 °C (1,400 °F).

Testing verified that the design can withstand both extremely high **temperature** and high pressure simultaneously. Gas heated to between 760 °C (1,400 °F) and 790 °C (1,450 °F) and pressurized to 50 MPa (8,000 lb/in^2) was allowed to flow onto the face of the window. The **temperature** of the exiting **hot gas** and the test block was recorded downstream from the window. For this reason, the measured **temperature** is believed to be lower than the actual **temperature** at the window face. This allowed the entire body of the sight glass unit to reach high **temperature**, creating a more severe condition than expected on the SSME FPB. When installed on the SSME FPB, the cryogenic hydrogen in the liner is expected to keep the body of the sight glass unit at **temperatures** lower than experienced in these tests.

The initial tests of the fixture resulted in failures of the lenses due to the assembly procedure. Testing performed after changes demonstrated that the experimental design could withstand high **temperature** at 50 MPa (8,000 lb/in^2) for a time period significantly longer than a 600-s SSME test firing, with the exit **temperature** reaching a maximum **temperature** of 580 °C (1,075 °F).

Shirley, J.A., United Technologies Research Center: "Development of Fiber Optic Raman Diagnostics for SSME Preburner Temperature Measurements," Presented at 1990 Conference on Advanced Earth-to-Orbit Propulsion Technology, MSFC, AL, May 17, 1990.

Shirley, J.A., United Technologies Research Center: "Investigation of Breadboard Temperature Profiling Systems for SSME Fuel Preburner Diagnostics," 24th Joint Propulsion Conference, Boston, MA, July 12, 1989.

W.T. Powers/EB22
(205) 544-3452
Sponsor: Office of Aeronautics, Exploration and Technology

Space Shuttle Main Engine Propellant Path Leak Detection Real Time

The development, qualification, and reliability improvement testing of space shuttle main engines (SSME's) has resulted in the loss of a significant number of engines and associated resources, including project time. Each qualification or component improvement engine represents a critical program resource that includes the accumulated costs of all test time on the hardware. Loss of high-time, fleet-leader engines during ground testing has become more important as the SSME inventory matures. A study is under way to address one mode of engine failure that may be detected and analyzed with sufficient speed to save critical engine test hardware from destruction. This method uses optical sensors combined with computer image analysis and expert systems to detect **propellant leaks**.

Following the establishment of the feasibility of detecting hot/cold **leak** plumes in cold/hot backgrounds, efforts were directed toward temporal aspects of **leak** detection. Based on the assumption that a **leak** should appear in time on an **infrared (IR)** image as a sudden but persistent change in intensity (dark to light, or light to dark), this problem becomes that of detecting a step function in the presence of noise. The current work effort has focused on the time-varying behavior of **IR** light intensity at one point in the image, and a method for deciding whether a **leak** has occurred at that location within a given previous time interval. The processing technique, however, is applicable to full processing of video image data.

Development testing of this system involved its implementation onto digital **image processing** equipment in psuedo-real time. In addition, laboratory experiments have shown that simulated **leaks** are recordable with an **IR** video camera. One of the long-term goals of this study is the inclusion of spatial intensity variations in the image into the **leak** occurrence decision process because a **leak** should appear over an extended region in the image, not as just one point.

M.L. Johnson/EB22
(205) 544-5519
Sponsor: Office of Aeronautics, Exploration and Technology

Spray Combustion Simulation Phenomena in Liquid Rocket Engines

The variable thrust engine (VTE) of the orbital maneuvering vehicle (OMV) uses a **hypergolic** propellant combination of monomethyl hydrazine (MMH) and nitrogen tetroxide (NTO) as fuel and oxidizer, respectively. The propellants are pressure-fed into the **combustion** chamber through a single pintle injection element. Atomization of the liquid propellants is achieved by impacting the two jets at the exit of the pintle. The performance of this engine is dependent on a number of physical phenomena and their mutual interactions. The most important ones are atomization, **spray** dynamics, evaporation, mixing, and **combustion**.

Studies have shown that **spray** dynamics play a crucial role in influencing evaporation and mixing patterns within the combustor. This study was undertaken to develop advanced models for **spray** phenomena that can be incorporated into a computational fluid dynamics (CFD) code to analyze the flow field within the combustor. The **spray** solution is obtained in a Lagrangian frame of reference moving with the liquid droplets. The droplets are introduced with a presumed size distribution at the inlet of the combustor. The droplet trajectories in the gas field are influenced by the drag forces, the local gas pressure gradient, gas swirl (if any), and body forces. For evaporating **sprays**, the droplet sizes decrease and alter their trajectories. The effect of the droplets on the gas field is simulated as sources/sinks in the conservation equations of mass, momentum, and energy. The gas solution is obtained in an Eulerian frame of reference using a CFD model. Additional features of the **spray** model include two-liquid propellant capability, **spray** tracking in complex nonorthogonal geometries such as rocket engine combustors, and finite rate models for evaporation and heat transfer.

The **hypergolic** reaction between MMH and NTO is simulated with a chemical equilibrium model. The model considers the presence of 12 species (MMH, NTO, CO_2, H_2O, N_2, NO, OH, O, H_2, H, CO, and O_2) in the calculations. Figure 162 shows the computed temperature distribution in the **combustion** chamber and nozzle using a gas-gas model. The predictions of maximum and minimum temperature, Mach number, and pressure compare

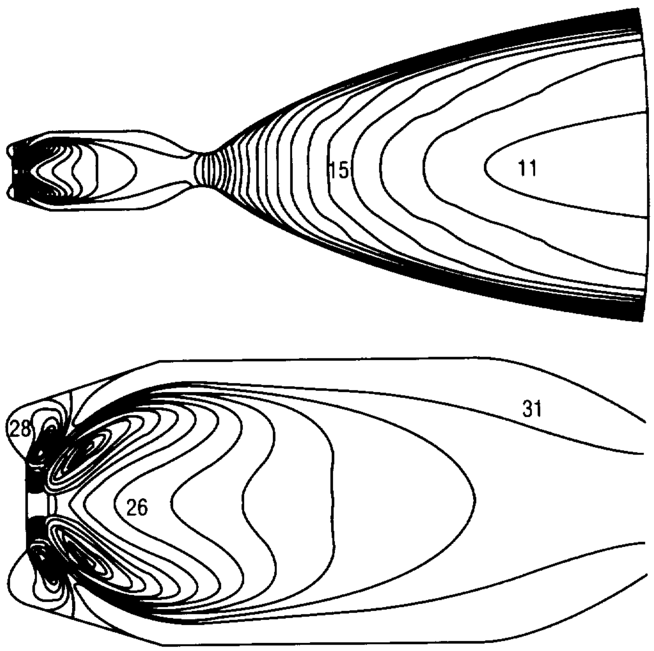

Contour Levels			
1	11	21	31
390.0000	1344.000	2298.000	3251.999
485.4000	1439.400	2393.400	
580.8000	1534.800	2488.800	
676.2000	1630.200	2584.200	
771.6000	1725.600	2679.600	
867.0001	1821.000	2775.000	
962.4001	1916.400	2870.399	
1057.800	2011.800	2965.799	
1153.200	2107.200	3061.199	
1248.600	2202.600	3156.599	

FIGURE 162.—Temperature distribution (gas-gas model).

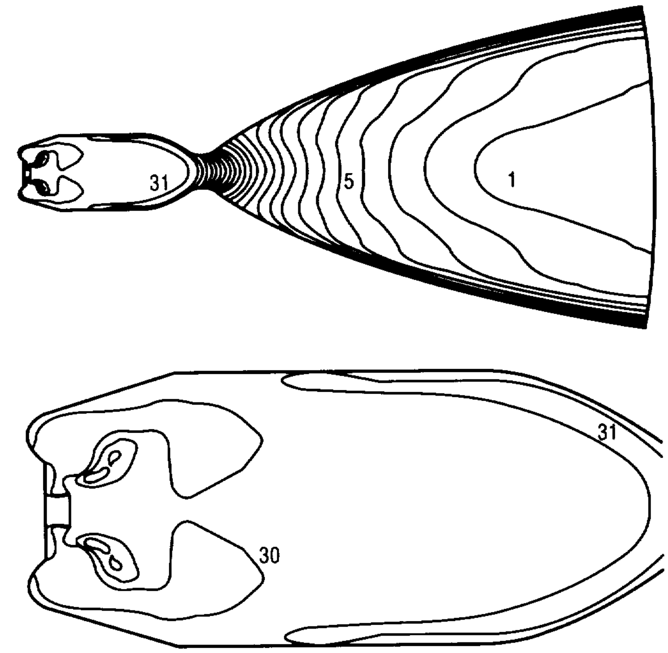

Contour Levels			
1	11	21	31
995.0000	1723.300	2451.600	3179.901
1067.830	1796.130	2524.430	
1140.660	1868.959	2597.260	
1213.490	1941.789	2670.090	
1286.320	2014.619	2742.920	
1359.150	2087.449	2815.750	
1431.980	2160.280	2888.580	
1504.810	2233.110	2961.410	
1577.640	2305.940	3034.240	
1650.470	2378.770	3107.071	

FIGURE 163.—Temperature distribution (spray model).

favorably with one-dimensional equilibrium (ODE) predictions for the same problem. Figure 163 shows the temperature distribution obtained from the **spray** model. The **spray** calculations predict a more or less uniform temperature distribution in the combustor. This indicates more efficient mixing due to the propellants being injected in the form of droplets. The gas-gas model, however, predicts high temperatures along the line of contact between the two propellants.

The **combustion** process is very sensitive to the boundary conditions of the problem. Injection of the propellants in the liquid state introduces additional physical processes that cannot be studied with a gas-gas model. The importance of different physical phenomena can be understood by performing detailed sensitivity analyses. The deficiencies in the model can be ascertained by comparison with test data. These comparisons can be used to further improve, refine, and calibrate the model to enhance its capabilities as a predictive tool.

Continuation of this activity is in progress at CFD Research Corporation in Huntsville, AL, under contract NAS8-37196.

K.W. Gross/EP55
(205) 544-2262
Sponsor: Office of Aeronautics, Exploration and Technology

The Chemical Kinetics of Liquid Oxygen/ Hydrocarbon Combustion

The combustion process in **liquid oxygen (lox)/hydrocarbon (HC)**-fueled liquid rocket engines can be broken into three steps: propellant atomization, propellant vaporization, and vaporized propellant combustion. At oxidizer-to-fuel mixture ratios used in liquid rocket engine main combustion chambers, it is typically assumed that the vaporized propellants are in chemical equilibrium, since the vaporization process is much slower than the finite rate chemical **kinetics**. However, if the mixture is fuel-rich, as is the case with gas generators and preburners, the combustion process becomes kinetically limited.

A Small Business Innovative Research contract, NAS8–38486, with Software and Engineering Associates, Inc., Carson City, NV, is addressing the combustion process (atomization, vaporization, and kinetic combustion) for fuel-rich **lox/HC** combustion in liquid rocket engine components. A primary concern of the computerized methodology being developed is the ability to predict sooting in gas generators. Soot prediction is important in gas generator design because excessive soot deposition can obstruct the nozzle throat or damage turbomachinery. However, limited sooting can provide an insulative coating that can protect machinery from high thermal loads. A carbon deposition program conducted by Aerojet for NASA/MSFC illustrates how a small change in operation conditions can cause a large increase in soot production.[1] Figures 164 and 165 show the large difference in sooting that results from a small change in mixture ratio (from 0.41 to 0.44 **lox**/propane).

The methodology being developed joins a spray vaporization model with a finite rate analysis to account for the interactions of the vaporization with the chemical **kinetics**. The **kinetics** mechanism uses a global cracking for rocket propellant-1 (RP–1) as well as a sooting scheme outlined by Frenklach.[2] The path to soot is dominated by the formation of successive polycyclic aromatic rings. When a sufficiently large ring is formed, it is assumed to go directly to soot.

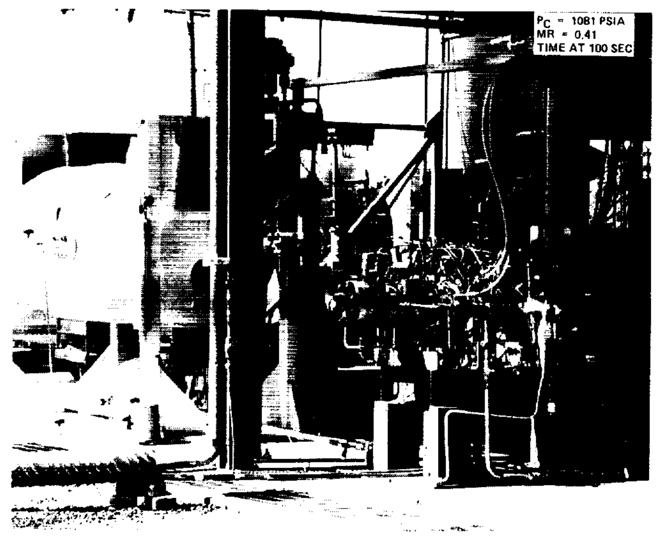

FIGURE 164.—Test 126 lox/propane.

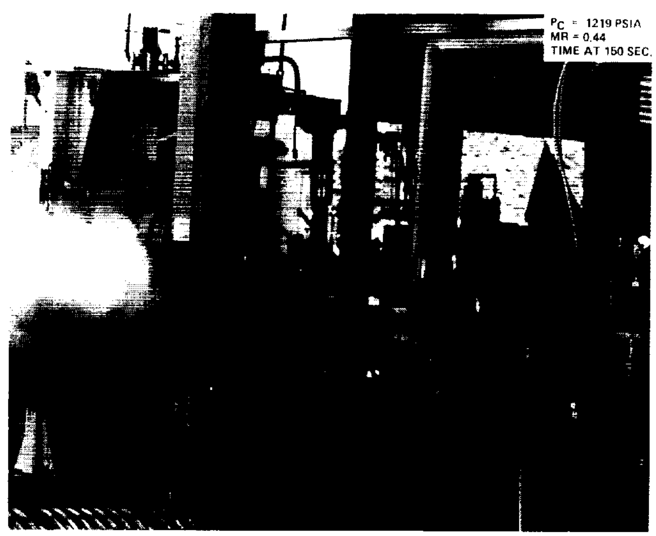

FIGURE 165.—Test 120 lox/propane.

The method has been compared to liquid rocket engine gas generator experiments using **lox**/RP–1, **lox**/propane, and **lox**/methane propellants. Predictions for sooting onset, and for relative sooting amounts, compare very well to the experiments.

[1]Hernandez, R., and Mercer, S.D., "Carbon Deposition Characteristics of LO$_2$/HC Propellants," AIAA-87-1855, 23rd Joint Propulsion Conference, June 29–July 2, 1987, San Diego, CA.

[2]Frenklach, M., Clary, D.W., and Ramachandra, M.K., "Shock Tube Study of the Fuel Structure Effects on the Chemical Kinetic Mechanisms Responsible for Soot Formation, Part 2," Final Report, NASA Report No. NASA-CR-174880, May 1985.

K.W. Gross/EP55
(205) 544–2262
Sponsor: Office of Aeronautics, Exploration and Technology

Turbulence Modeling for Liquid Rocket Thrust Chambers

Differences in flow-field solutions of computer programs for the same problem can be traced frequently to the **turbulence** model used in these codes. To overcome such situations in the future and to advance the current **turbulence** model capability, a study was conducted by The University of Alabama in Huntsville, AL, under contract NAS8–36955, D.O. 38. The effort was oriented to review various **turbulence** models used in existing liquid **thrust chamber** performance simulation programs and other sophisticated techniques. The study concluded that a useful **turbulence** model must be capable of treating inhomogeneous and anisotropic flow characteristics, which are present during the operation of a rocket motor. Such a quality is apparent in the Reynolds stress model (RSM), which was recommended as the most opportune approach.

At a workshop that was summoned to endorse the recommendation or promote a different method, other approaches were also discussed, such as: direct numerical solution (DNS), deterministic theory method (DTM), fractal technique, and probability density function (PDF). At the conclusion of the workshop, the recommended full RSM was favored by most of the experts present. This model can be developed with options such as the algebraic Reynolds stress and k-ε (kinetic energy) models to account for current computer limitations.

The results of this effort, which are documented in a final report, and a separate workshop are available.

K.W. Gross/EP55
(205) 544–2262
Sponsor: Office of Aeronautics, Exploration and Technology

Vortex-Shedding Flowmeter for Space Shuttle Main Engine

In order to measure the actual propellant flow in the space shuttle main engine (SSME), a meter of sufficient ruggedness to withstand the extremely **high velocities** encountered is required. Meters with moving parts are generally unacceptable and low pressure loss and meter weight are desired. **Vortex-shedding flowmeters** (fig. 166) were examined as candidates. They offer no moving parts, an output which is linear with flow (making them potentially more accurate at low flows than venturi meters), and are physically short. Their geometry is such that fewer modifications are required for installation.

Several designs have been built and flow-tested with water and air at velocities encountered within the SSME ducts. Most testing was done in ducts of 4.06– and 5.84–cm (1.6– and 2.3–in) internal diameter; testing is done in actual SSME ducts. Meters to be used with liquid

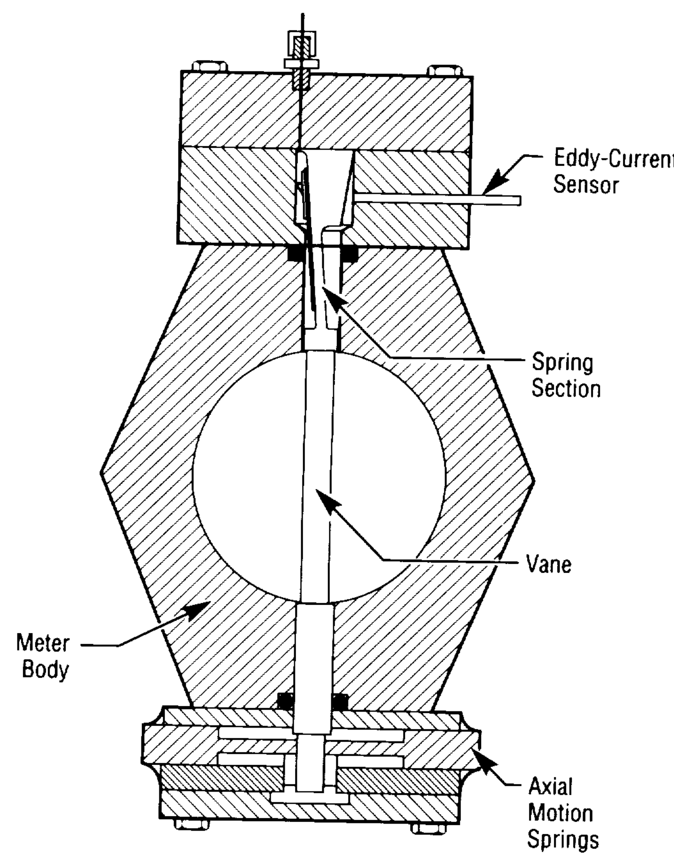

FIGURE 166.—Drawing of a typical vortex-shedding flowmeter.

oxygen (lox) are tested with water drawn from a high-head system owned by the city of Boulder, CO. Large heads are necessary to achieve the required velocities. Meters to be used with gaseous hydrogen (GH_2) are tested in high-pressure air systems provided by a testing laboratory. Correlations of GH_2 from the data obtained with air are computed for these tests.

The **vortex-shedding flowmeter** and its application to the measurement of flow in the ducts of the SSME have been introduced in previous reports. It has shown that it is possible to measure the flow in ducts with a **vortex-shedding flowmeter** that installs through an opposed pair of the standard 11.2–mm (0.44–in) diameter instrument ports used for the SSME ducts. A narrow signal spectrum line at constant flow can be obtained with no upstream flow conditioning in the duct. This has been demonstrated for liquids to average velocities of more than 30 m/s (98 ft/s). Successful airflow tests have indicated that air flows to at least 150–m/s (492–ft/s) average velocity can be measured in engine ducts with no upstream flow conditioning. The maximum gas flow is limited to this maximum by the properties of air. The limit for hydrogen (H_2) should be much higher.

A complete set of meters for use with the SSME has been designed; implementation of units for the lox side of the engine is under way. These units will be built as an in-house project for the technology test-bed. Sensors will likely be eddy-current proximeters qualified for lox-use. This configuration would be the flight prototype design. Initially, the meters will utilize their own electronics without interface to an engine controller.

Meters for use in H_2 require some more work. Calibration of these meters will be a problem due to the lack of adequate facilities that are convenient to use. It is probable that all meters will need to be calibrated in the ducts in which they will be used.

Siegwarth, J.D., "Vortex-Shedding Flowmeter for Measurement of Liquids at High Flow Velocities," *International Journal of Heat and Fluid Flow*, NIST/Boulder, 1988.

Siegwarth, J.D., "Vortex-Shedding Flowmeter Performance at High Flow Velocities," NBS Tech Note 1302, October 1986.

Siegwarth, J.D., "Vortex-Shedding Flowmeters for Space Shuttle Main Engines," Presented at the 1990 Conference on Advanced Earth-to-Orbit Propulsion Technology, MSFC, AL, May 17, 1990.

W.T. Powers/EB22
(205) 544–3452
Sponsor: Office of Aeronautics, Exploration and Technology

SPACE SYSTEMS

ADVANCED LIFE SUPPORT ANALYSIS

Advancements in **instrumentation** capabilities are needed to meet the specific needs of long-duration human missions, especially in the area of chemical composition monitoring. Features such as real-time response, low maintenance requirements, automatic calibration, and high reliability are of key importance.

The objective of this task is to continue a study by McDonnell Douglas Space Systems Company (MDSSC) for NASA to identify the **instrumentation** required for future life support systems and technologies to provide the needed capabilities. The data base of **environmental control and life support system** (ECLSS) technologies will be expanded to provide the basis for more detailed evaluation of the **instrumentation** requirements. Also, the data base of **instrumentation** technologies will be enhanced to include more detail.

An expanded data base of **instrumentation** technologies and further identification of **instrumentation** needs for additional ECLSS technologies including biological methods are the results of this study. This task is scheduled for completion in 1991.

P.O. Wieland/ED62
(205) 544-7215
Sponsor: Office of Aeronautics, Exploration and Technology

ADVANCED LIFE SUPPORT ANALYSIS FOR SPACE STATION *FREEDOM* EVOLUTION

Over the 30-yr design life of **Space Station *Freedom***, the facility will be expanded in size and capability. This will impact the **environmental control and life support system** (ECLSS) that will need to accommodate the new requirements. Understanding the requirements for life support and the impacts of changes on the ECLSS are essential to ensure that the changes can be accommodated. Incorporating features in the initial design that allow for growth will simplify accommodating the growth.

The objective of this task is to continue a study by McDonnell Douglas Space Systems Company (MDSSC) for NASA to evaluate the evolution of the ECLSS as **Space Station *Freedom*** grows. More detailed analysis will be provided of the interface requirements and **hooks and scars**, the effects of adding or relocating habitation or laboratory modules on ventilation will be evaluated, and cost/benefit trade studies will be performed on adding **hooks and scars**. The module patterns being considered as growth options for the ventilation analyses include the ones shown in figure 167, which were obtained from the Langley Research Center.

Currently, more detailed information is being added to the data base, intermodule ventilation is being evaluated, and other tasks are in progress. This task is scheduled for completion in 1991.

P.O. Wieland/ED62
(205) 544-7215
Sponsor: Office of Space Flight, Space Station *Freedom*

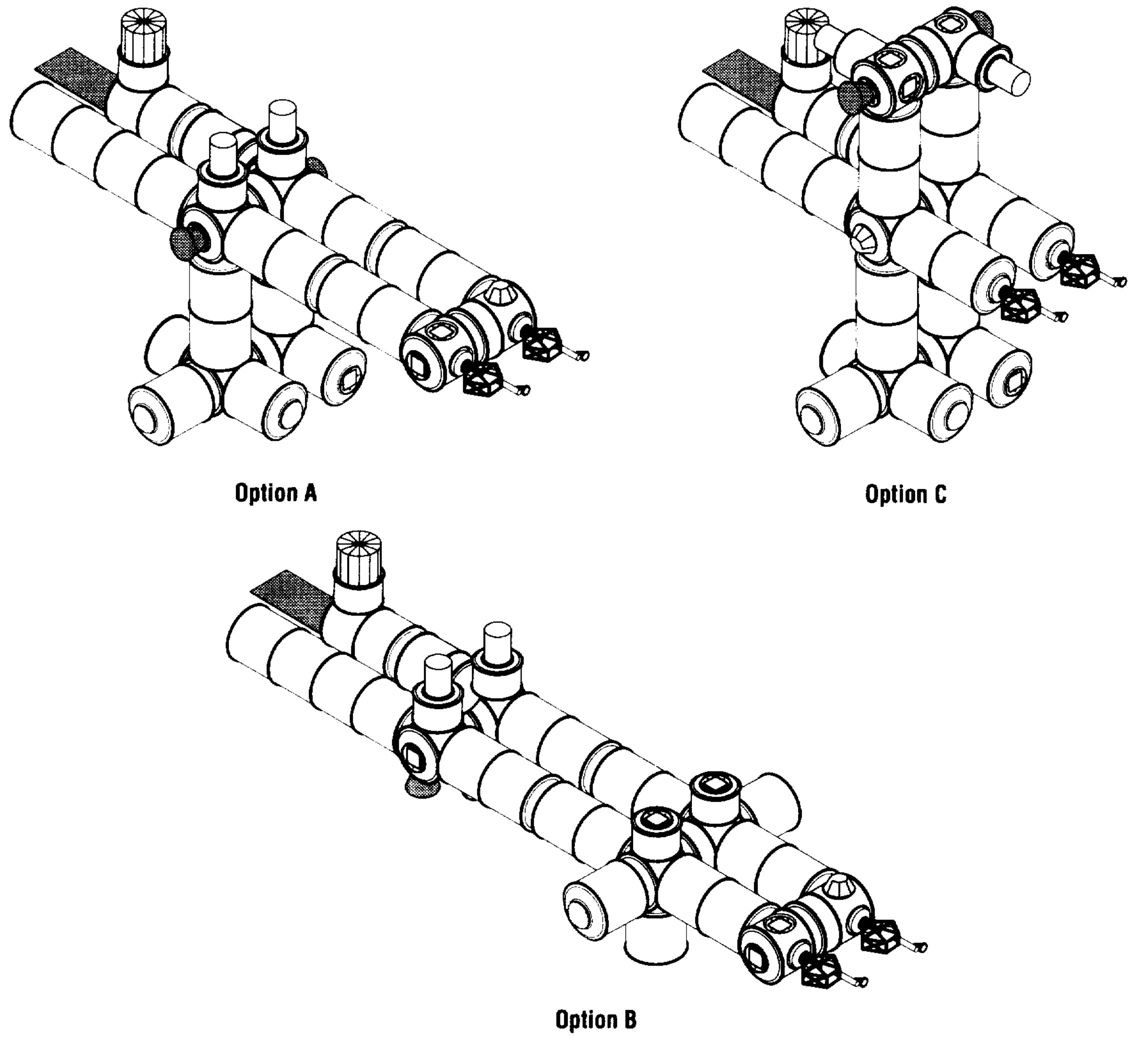

FIGURE 167.—Module pattern growth options.

Aerogel Processing of Ceramic Composite Membranes

Revitalizing the air, including recovering the oxygen (O_2) from carbon dioxide (CO_2), is essential for long-duration human exploration missions. This process requires many steps where proper mixtures must be maintained. This involves separating mixtures of gases into more pure streams of the components to achieve optimum operation. Innovative methods of performing this function are needed.

The objective of this task is to develop ceramic filtration membranes for **gas-phase separation** (e.g., CO_2 from nitrogen (N_2), O_2, water (H_2O) mixtures), which are capable of performing in high-temperature, high-pressure, oxidative, and corrosive environments.

Specific objectives are: to demonstrate that an **aerogel**-derived ceramic coating has the potential for ultrafiltration applications, and to demonstrate that the **aerogel**-infiltration technique provides a means of fabricating net-shape ceramic matrix composites.

The process of producing an **aerogel** glass membrane (fig. 168) begins with a soluble ceramic precursor of network-forming cations of metal alkoxides that form an ordered array. In an alcohol-water solution, the alkoxide groups are removed by acid- or base-catalyzed hydrolysis reactions and replaced with hydroxyl groups. Condensation reactions then yield macromolecular species in solution (the "sol" state). The polymers continue to grow by condensation until one macromolecule spans the solution (the "gel" state), which is easily recognized by a sudden increase in solution viscosity. By this process, the shape of the resulting gel can be precisely controlled using molds. The gel can be described as a viscoelastic material composed of interpenetrating solid and liquid phases. If the solvent is removed under supercritical conditions, shrinkage is minimized and the result is an aerogel. If drying occurs by evaporation of the solvent, the network collapses somewhat and the result is a xerogel. Further drying and shrinkage increases compressive stresses and shrinkage continues until a dense glass-like state is reached that can withstand the compressive stresses. An alternative pathway uses film deposition to produce a dense glass-like film. A stronger material can be produced by reinforcing with ceramic fibers with the potential of fabricating tough, low-cost, and high-performance membranes.

No results have been gathered to date.

P.O. Wieland/ED62
(205) 544–7215
Sponsor: Office of Commercial Programs, Small Business Innovation Research

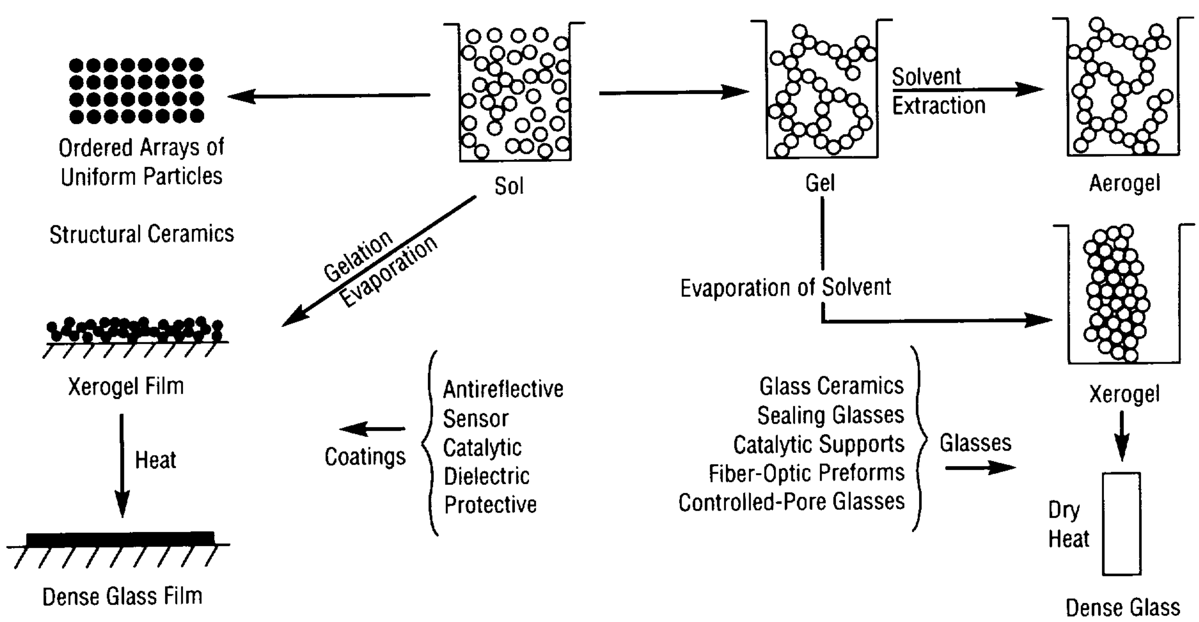

FIGURE 168.—Sol-gel glass forming process.

Alternative Illumination Technologies for the Human Habitation of Space

As NASA engages in longer-duration space missions and approaches a permanent manned presence in space, **lighting** systems will play a critical role in determining the **habitability** of human-occupied structures. To date, the **lighting** systems used in U.S. spacecraft have not taken advantage of the wide variety of light source and control technologies that are currently employed in Earth-based systems. While many of these new light source technologies offer NASA obvious advantages in terms of weight, volume, power consumption, and performance life over present systems, special consideration must be given to critical human factors such as spectral power distributions, chromaticity coordinates, and color-rendering capabilities of proposed sources, as well as resultant application considerations of direct glare, veiling reflections, and luminance distributions in the visual field.

As an in-progress phase I Small Business Innovation Research activity, these new technologies are being reviewed for applicability to manned space programs for both task and ambient **illumination** systems. Extensive photometric testing is near completion on several candidate sources, which will result in a comparative data base. These data are then being coupled with optical control devices (reflectors and refractors) to generate prototype luminaires using three-dimensional AutoCad. Photometric distributions and efficiencies are currently being generated for each luminaire using the Finite Element Luminaire Design software package. Luminaire performances in an interior environment are being analyzed using the Lumen-Micro software. Particular attention will be paid to surface luminance ratios and glare conditions.

Upon completion of the computer modeling and analysis, one or more of the candidate luminaires will be selected to be physically constructed as a mockup(s). The mockup(s) will be low-fidelity and will not be accurate enough to undergo photometric testing but will be effective for concept demonstration. The mockup(s) can then be integrated into the MSFC **Illumination** Laboratory upon phase I completion in the August 1991 timeframe.

B.C. Hayes/EO23
(205) 544–9276
Sponsor: Office of Commercial Programs, Small Business Innovation Research

Catalytic Methods Using Molecular Oxygen for Treatment of PMMS and ECLSS Waste Streams

Recycling of **waste water** is essential for long-duration human exploration missions in order to avoid prohibitive resupply or storage penalties. Some contaminants, such as urea, low molecular weight alcohols, and polar molecules, are not easily removed by existing methods and innovative methods of removing these compounds are of special interest.

The objective of this task is to develop a simple and energy-efficient method of oxidizing low molecular weight **organic contaminants** by using **molecular oxygen** with an appropriate catalyst to oxidize **organic contaminants** in situ at sterilization temperatures, approximately 121 °C (250 °F).

The proposed system is shown schematically in figure 169. An oxygen saturator, a **catalytic** reactor, and a membrane degasser are key elements. The oxygen saturator is designed to impart oxygen to the process stream at a concentration above the stoichiometric levels needed to oxidize the **organic contaminants** in the **catalytic** reactor. The membrane degasser is designed to remove carbon dioxide, sulfur dioxide, any nitric oxide compounds, excess oxygen, and other gaseous contaminants produced in the **oxidation** reactor. The polishing unibed consists of absorptive materials to remove any remaining contaminants.

The most effective catalysts for these conditions are ruthenium or platinum on carbon. Reduction of methanol and ethanol from 50 parts per million (p/M) to less than 1 p/M has been demonstrated at residence times of 1 to 3 min. Acetone has been identified as an intermediate byproduct of isopropanol **oxidation**. Preliminary success has been achieved at reducing acetone from 25 p/M to 5 p/M. A breadboard assembly (fig. 169) has been delivered to MSFC for use in the water recovery test. The assembly will be located downstream of the potable water processor.

P. O.Wieland/ED62
(205) 544–7215
Sponsor: Office of Commercial Programs, Small Business Innovation Research

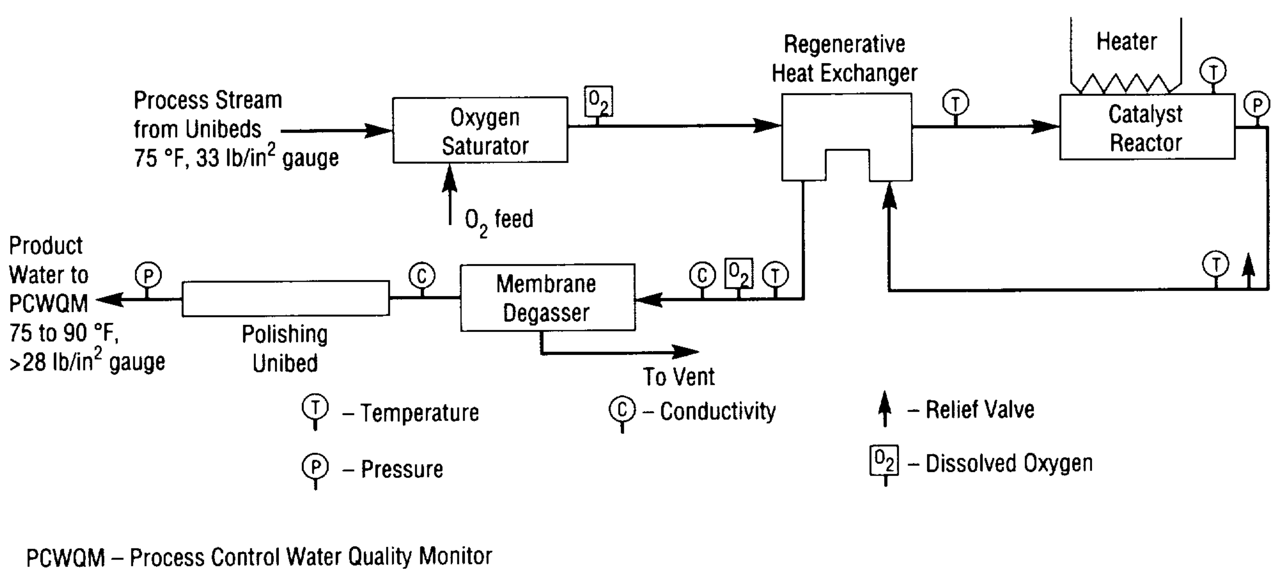

FIGURE 169.—Potable water catalytic oxidation assembly.

CO_2 Laser Research and Development

Investigations of candidate lasers for use of the **laser atmospheric wind sounder (LAWS)** continued in FY91. **LAWS** is a facility instrument slated for use as part of the **Earth-Observing System (EOS).** This research is funded by the Office of Aeronautics, Exploration and Technology (OAET) under the aegis of the Civil Space Technology Initiative (CSTI). The research consists of theoretical and experimental studies of lasers and laser radars (lidars) to establish the optimum technology for **LAWS**.

The FY91 research included work at MSFC, Langley Research Center (LaRC), the Jet Propulsion Laboratory (JPL), and the National Oceanic and Atmospheric Administration's Wave Propagation Laboratory (NOAA/WPL).

The work begun in FY90 by Electro-Optics Technology, Inc., to investigate novel concepts for **solid-state lasers** has continued by the award of a phase II Small Business Innovative Research (SBIR) grant. Similarly, Q-Source, Inc., has been awarded a phase II SBIR grant to continue studies of radio-frequency (RF) pumped carbon dioxide (CO_2) laser designs.

The laser breadboard concept for the **LAWS** instrument was endorsed by a panel of laser specialists from government and industry. These laser breadboards will verify that the proposed **LAWS** laser designs will be able to meet the requirements for lifetime, power, efficiency, spectral purity, and isotopic operation ($^{12}C^{18}O_2$).

Laboratory studies of the Pulse Systems, Inc., LP–140 sympathetic discharge laser and the Coherent Laser Systems hybrid-transversely-excited, electrical, atmospheric (TEA)/power amplifier laser continued during FY91. MSFC was assisted in this effort by collaboration with researchers at JPL and The University of Alabama in Huntsville. The results of these investigations were reported at the January 1991 Society of Photo-Optical Instrumentation Engineers (SPIE) Conference on high-power lasers.

Problem: Laser Discharge Causes CO_2 Dissociation and Rapid Power Loss

$$C^{18}O_2 \longrightarrow C^{18}O + 1/_2\,{}^{18}O_2$$

Solution: Develop High-Activity, Long-Life Catalyst to Regenerate Isotopic CO_2

$$C^{18}O + 1/_2\,{}^{18}O_2 \longrightarrow C^{18}O_2$$

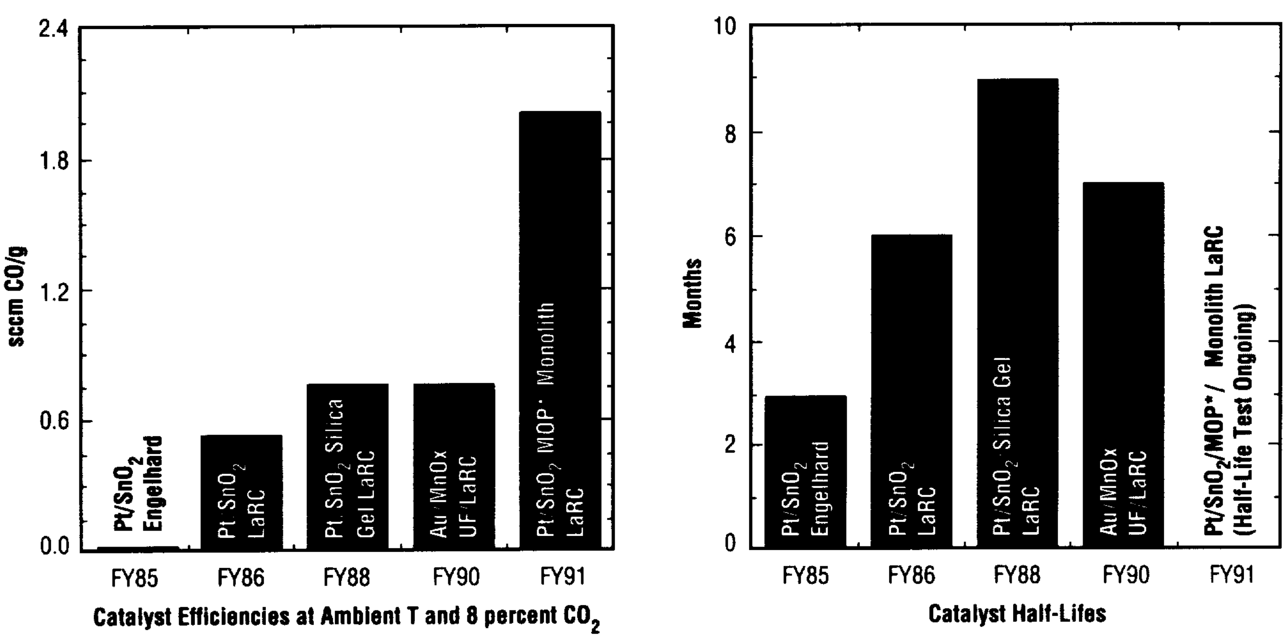

*MOP = Metal Oxide Promoter

FIGURE 170.—Catalytic activities and half-lives of various CO_2 laser gas catalysts.

Concurrently, an in-house effort has begun to combine numerical models for the optical resonator, gas flow loop, gas discharge kinetics, and the external electrical pulse-forming network (PFN) into an integrated model for **LAWS**-class lasers. The model outputs will be verified by comparison with laboratory measurements of the Pulse Systems, Inc., LP–140 laser and the Coherent Laser Systems hybrid-TEA/power amplifier system. This integrated model will be very useful during evaluation of the laser breadboard results and during preparation for the **LAWS** phase C/D effort.

CO_2 laser gas **catalyst** research at LaRC has verified the performance of the Pt/SnO2 **catalyst** in gas mixtures to be used in the **LAWS** lasers (fig. 170). This research is now directed at refining the procedures for depositing the **catalyst** materials on ceramic substrates suitable for use directly within the **LAWS** laser gas recirculation loop and on supplying sample quantities of the **catalyst** to the **LAWS** study contractors for use in the laser breadboard demonstrations.

Jaenisch, H., and Spiers, G., "Modifications to the LP-140 Pulsed CO2 Laser for Lidar Use," SPIE Conference on High-Power Lasers, Los Angeles, CA, 1991.

W.D. Jones/EB23
(205) 544–3479
Sponsor: Office of Aeronautics, Exploration and Technology

Development of a Conducting Tether for the Tethered Satellite System Electrodynamics Mission

The **tethered satellite system** (TSS) will be the first major space flight experiment involving two **tethered bodies** being controlled and equipped with data-collecting scientific instruments. The concept of tethering or connecting bodies together in space to explore their engineering applications and scientific merits has been studied for many years by the United States and foreign interests. The **TSS** is a joint endeavor between NASA and the Italian Space Agency, Agenzia Spaziale Italiana (ASI). It is being developed as a multiple-flight, reusable facility to deploy, control, and retrieve a tethered satellite from the space transportation system shuttle cargo bay. The orbiter-based equipment will provide the capability to deploy, control, and retrieve the satellite and will house a selection of scientific instruments. The tethered satellite will also house scientific instruments and support systems such as electrical power, data handling, attitude measurements and control, and an auxiliary propulsion system. The tether will provide the structural connection between the deployer (NASA-developed) and the satellite (ASI-developed).

Although the deployer system is designed to accommodate tether lengths in excess of 100 km (62 mi) for downward deployed atmospheric missions, a **conducting tether** of approximately 22 km (14 mi) in length has been developed for the initial **TSS electrodynamic mission**. The satellite will be deployed 20 km (12 mi) upward from the shuttle cargo bay (away from the Earth). The tether configuration selected is a multilayer insulated copper conductor with a stranded nomex core (fig. 171). The conductor is a 10–strand #34 American wire gauge (AWG), tin-coated copper bundle wrapped around the nomex core. Insulation for the conductor is provided by an extruded Teflon coating. Strength for the tether is

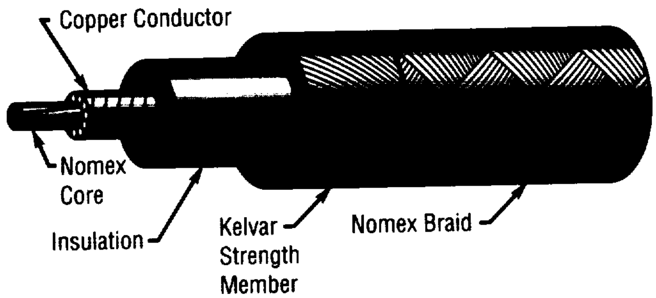

Diameter	2.54 mm (0.1 in)
Max Mass	8.2 kg/km (5.5 lb/kft)
Breakstrength	1780 N (400 lb)
Temp Range	−100 to +125 °C (−148 to +257 °F)
Elect Characteristics	Carry 1-A Current at 10 kV 0.2 Ω/m 5 mA (Max) Leakage
Max Elongation	5% at 1780 N

FIGURE 171.—TSS−1 electrically conductive tether.

provided through a braided Kevlar section outside the insulation with a final outer braid of nomex for monatomic oxygen protection. The tether characteristics are listed in the figure. For the first mission, the tether was developed by the Cortland Cable Company, Cortland, NY, under subcontract to Martin Marietta Corporation, Denver, CO, which is the **TSS** prime contractor for NASA/MSFC.

B.W. Nunley/FA31
(205) 544−6593
Sponsor: Office of Space Flight

DEVELOPMENT OF A MEMBRANE-BASED ATMOSPHERE CONTROL SUBSYSTEM

Maintaining optimum atmospheric mixtures in multichamber habitats will be increasingly challenging for Space Station *Freedom* as modules are added and for multichamber habitats on the Moon and elsewhere. In cases such as habitats with plant growth chambers, the optimum atmospheric mixtures may be different in different chambers; this requires controlled exchange between separate ventilation systems. Innovative methods of maintaining proper characteristics are needed.

The overall objective of this task is ultimately to develop a **membrane-based atmosphere control** (**MBAC**) subsystem. This subsystem, though designed for eventual use in extraterrestrial habitats, has a more immediate use by NASA in preparative research into integrated closed-loop habitats.

The aim of this research will be to develop a computer model for designing an **MBAC** subsystem. This will be a steady-state model, without time dynamics. The model will be tested and refined by building and operating a bench-scale apparatus that simulates the **MBAC** subsystem. Feasibility will be established by validating the model with data from the bench-scale apparatus. Toward this end, the following technical objectives have been defined:

- To develop a computer model of the **MBAC** subsystem that is sufficient for performing trade studies

- To build a bench-scale apparatus that simulates the **MBAC** subsystem, and then conduct a series of studies to validate and refine this computer model

- To incorporate data from actual plant chambers into the computer model.

A schematic of the bench-scale apparatus is shown in figure 172. Pure oxygen and nitrogen will be supplied to a gas-blending apparatus that utilizes a Linde model FM4575 multichannel flow controller and flowmeter modules. The mixed gas composition and feed pressure to the membrane module will be controlled through

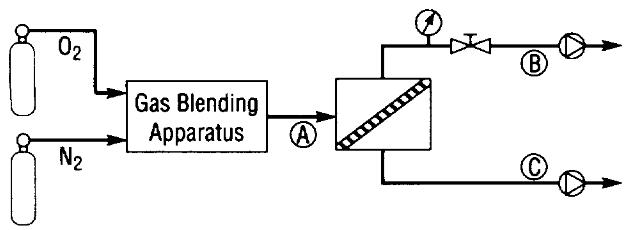

FIGURE 172.—Membrane-based atmosphere control subsystem test apparatus.

throttle valves on the gas-blending apparatus. The composition of the mixed gas feed and of the permeate and the retentate will be monitored by taking samples at points A, B, and C for analysis by gas chromatography. The bench-scale apparatus will be operated under steady-state conditions chosen to simulate anticipated operating scenarios. Test data will then be used to validate the computer model.

No results have been gathered to date.

P.O. Wieland/ED62
(205) 544–7215
Sponsor: Office of Commercial Programs, Small Business Innovation Research

Habitable Atmosphere Contaminant Monitoring

In order to sustain life in a closed-cycle habitable atmosphere, such as long-duration, manned space flight missions, **atmospheric** composition is of critical importance. A system to warn of the buildup of toxic hazardous constituents in **near real time** is a must. One effort nearly at the prototype design/brassboard delivery point takes the approach of modifying commercial analysis equipment linked together in tandem. This effort extends that technology. The instrument under development uses a combination of two advanced technologies: gas chromatograph with **mass spectrometer** (GC/MS) detector and tandem mass spectrometry. The gas chromatograph **mass spectrometer/mass spectrometer** (GC/MS/MS) will use a dual-column gas chromatograph in conjunction with the two **MS's** to eliminate ambiguity in qualitative analysis, and also to provide speed of analysis in **near real time**. The instrument will be greatly miniaturized in comparison to existing instrumentation.

The sample processing subsystem consists of the gas chromatograph, the enrichment cartridge, the injection port, and the inlet, which is a membrane separator. Testing of each of the system elements, with the exception of minor refinements, has been completed and is ready for incorporation into the subsystem and into the demonstration prototype.

The tandem **MS** subsystem is in the final phase of development and testing. Refinement to the subsystem elements has continued during this period. The precision alignment assembly has been fabricated and tested and is complete, together with the major components of **MS–1**. The ion source is being modified as a result of further ion optics modeling, which revealed that improved ion focusing can be achieved with the introduction of an additional extraction lens at the entrance aperture of the ionization volume. The addition of this lens will improve the "brightness" of the source, thus increasing the intensity of the ion beam that is produced.

The primary emphasis of this final phase will be the integration of the major subsystems into the demonstration prototype configuration and completion of the **MS** subsystem characterization, including the performance of the ion source with the new extraction lens. This next period will also include completion of the testing of the microchannel plate and the electric sector of **MS–2**.

M.L. Johnson/EB22
(205) 544–5519
Sponsor: Office of Commercial Programs, Small Business Innovation Research

Laser Atmospheric Wind Sounder

The **laser atmospheric wind sounder** (LAWS) is a Doppler **laser radar (lidar)** system for direct tropospheric **wind** measurements from space. The global **wind** profiles from **LAWS** will significantly contribute to global change science as a part of the **Earth observing system** (EOS).

Selected as one of five major facility instruments, **LAWS** is a candidate for the **EOS-B** platform. Currently, two competing phase B contractor teams have completed feasibility studies and have recently begun preliminary design of the instrument for a sun-synchronous (polar) platform (fig. 173). In parallel, both contractors are breadboarding a full-scale **laser** transmitter to address **laser** technology and component life issues. Together, these phase-B efforts will move **LAWS** significantly closer to the hardware development phase targeted to begin in FY94.

The **LAWS** instrument uses a single-frequency, pulsed, carbon dioxide (CO_2) infrared **laser** operating at 9.11 μm with pulse lengths of 2.5 to 3.5 μm. In addition, the coherent **lidar** system uses a scanning and transmit-and-receive telescope, heterodyne detector to determine the Doppler shift in the signal backscattered from aerosols or cirrus cloud particles, and a signal processing system. The combination of the telescope scanning pattern and spacecraft motion allows the same atmospheric volume to be viewed from different look angles. The line-of-sight measurements from different look angles can then be combined to produce a horizontal **wind** velocity vector for the particular cell being observed.

R.R. Jayroé, Jr./JA92
(205) 544–1968
Sponsors: Office of Science and Applications

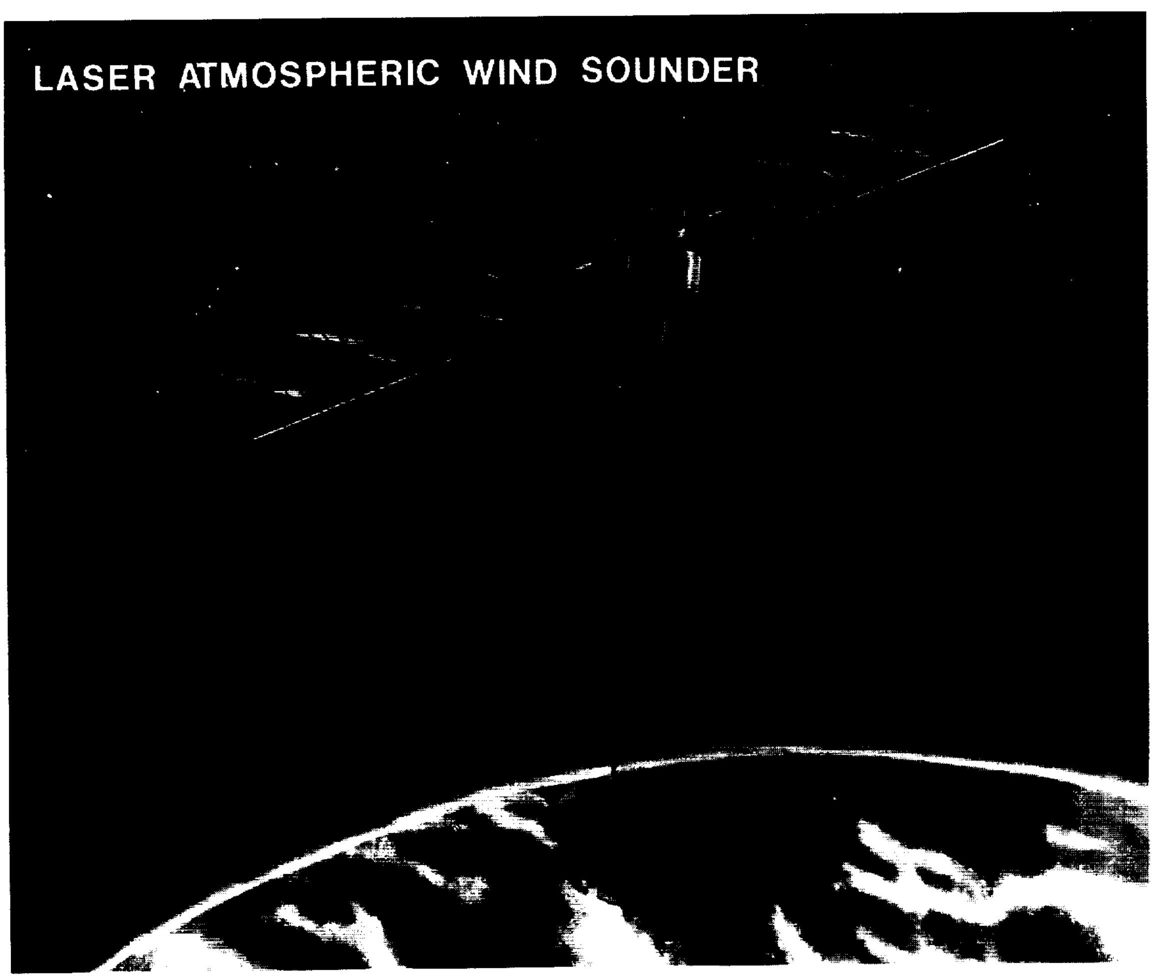

FIGURE 173. —Artist's conception of LAWS instrument.

Multifiltration Computer Model

Recycling of **waste water** is essential for long-duration human exploration missions in order to avoid prohibitive resupply or storage penalties. Some **contaminants,** such as urea, low molecular weight alcohols, and polar molecules, are not easily removed by existing methods, and innovative methods of removing these compounds are of special interest. **Multifiltration** (MF) is an existing method that could be improved.

The objective of this task is to develop a transient **computer model** that predicts breakthrough curves for the various **contaminants** expected to be found within the Space Station *Freedom* **waste water** effluent. The model is based on the current design of the **MF** subsystem, which consists of a series of beds, each of which contains a different sorbent material intended to extract particular contaminants from a waste stream. Each bed will be modeled with a different algorithm tailored to the type of material in that bed and the type of contaminant removal process occurring (e.g., carbon adsorption, cation exchange, anion exchange). The fundamental equations governing the mass transfer relations for each sorbent material type will be used. A flow chart of the modeling technique is shown in figure 174. A large majority of the work of developing a model of this nature revolves around data gathering. As shown by the flow chart, most of the development work will involve laboratory experiments to gather the required breakthrough data. Once developed, the resulting **computer model** will be used to evaluate the effect of various **contaminants** on product water quality as functions of the **MF** operating parameters (e.g., flowrates, contaminant concentrations, sorbent material characteristics, temperature, and pressure).

The majority of the work completed to date includes the characterization of **waste water** and bench-scale equilibrium testing for sorbent loading capacities. This task is scheduled to be completed in 1991.

P.O. Wieland/ED62
(205) 544–7215
Sponsor: Office of Space Flight, Space Station *Freedom*

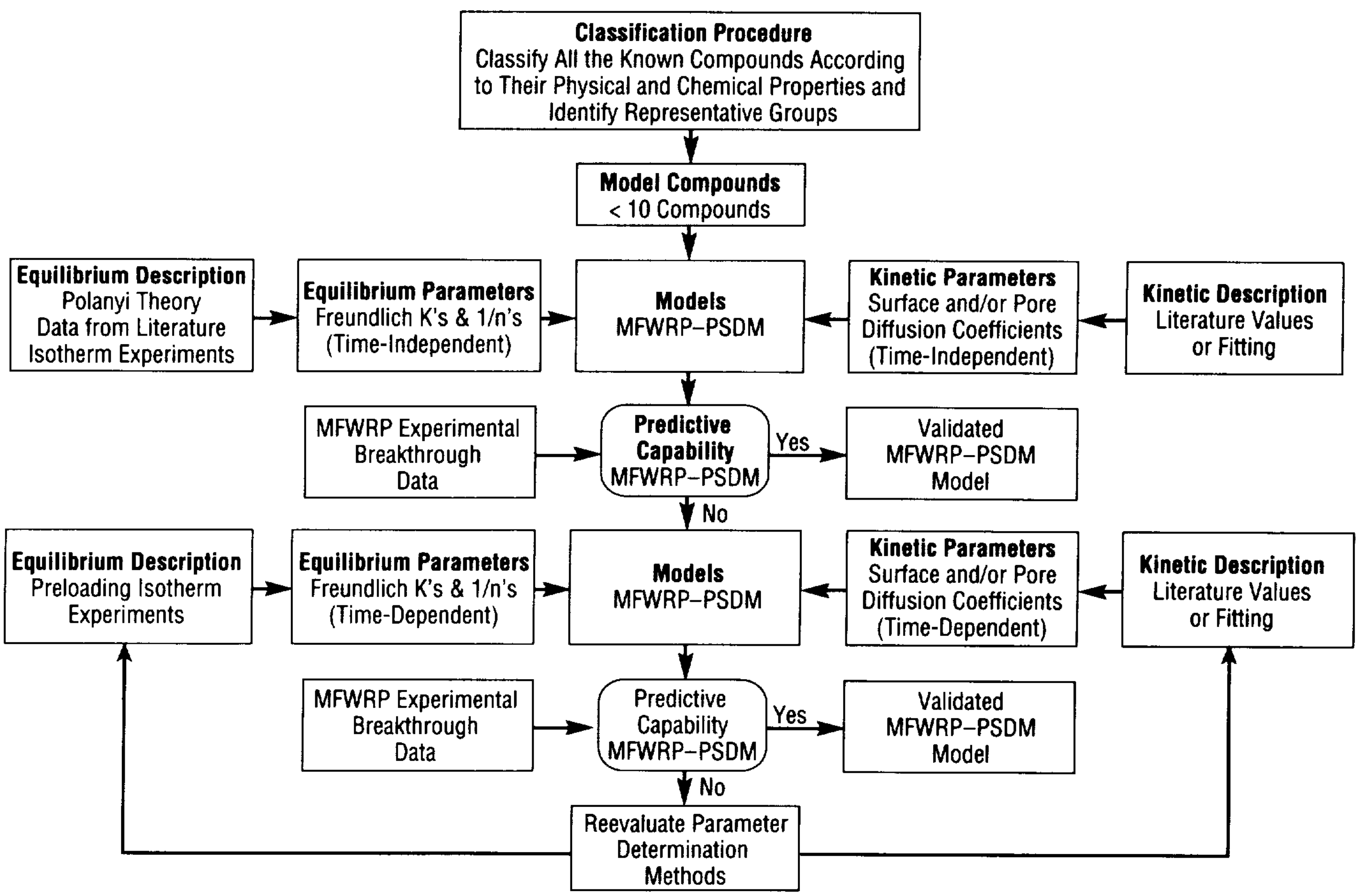

FIGURE 174.—Multifiltration modeling approach.

Nonazeotropic Binary Refrigerant Mixtures for Heating Space Station Hygiene Water

Personal hygiene on the space station requires a source of moderate temperature potable water. The current baseline design for heating the **hygiene water** is to use cartridge heaters on each of the individual devices that use the **hygiene water**. There are four such devices: a shower, a handwasher, a dishwasher, and a clothes (laundry) washer. A contract under the NASA Small Business Innovation Research (SBIR) program is being conducted to study the feasibility of using a **nonazeotropic** binary refrigerant mixture as the working fluid for a **heat pump** that would transfer waste heat from a thermal bus to the **hygiene water**. This **heat pump** would be incorporated into a centralized **hygiene water** supply system and would replace the cartridge heaters as the heat source for the **hygiene water**. Utilization of the **nonazeotropic** binary refrigerant mixture **heat pump** system has the potential of significant power savings and cost benefits over the cartridge heaters.

Binary refrigerant mixtures are made up of two refrigerants. Azeotropic binary refrigerant mixtures (azeotropes) act similar to a pure fluid. **Nonazeotropic** binary refrigerant mixtures, when used in refrigeration cycles, differ from pure fluids or azeotropes in two significant ways:

- The compositions of the liquid and vapor phases will be different during the phase change processes
- During constant pressure evaporation and condensation, the phase-change processes occur over temperature ranges rather than isothermally as in conventional systems (fig. 175).

With proper system design, one or both of these operating characteristics can be used to accomplish energy savings. The second operating characteristic, nonisothermal phase change, is the only characteristic utilized for the NASA SBIR contract described here. Nonisothermal phase change is used to increase the coefficient of performance (COP) of the refrigeration cycle. This process is sometimes referred to as cycle enhancement and stems from the minimization of the normal heat transfer penalties, which are necessary to accomplish heat transfer.

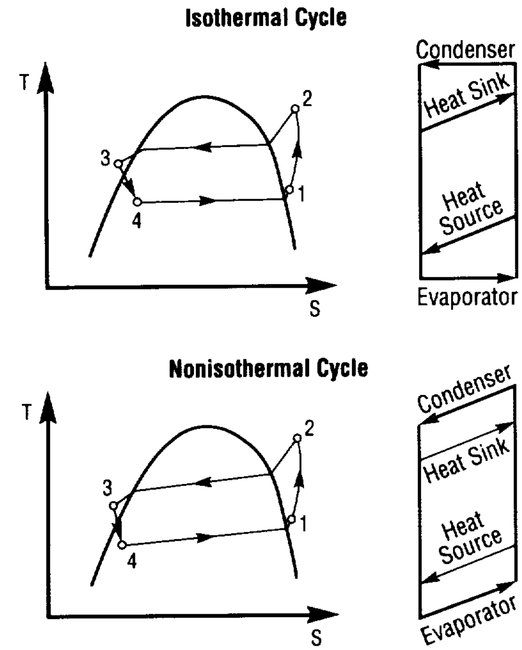

FIGURE 175.—Difference between isothermal cycle and nonisothermal cycle.

Typically, as much as half of the original ultimate COP, as defined by the source and sink temperatures, is degraded in accomplishing heat transfer.

The closer the average condensing and evaporating temperatures are to the source and sink temperatures, the greater the COP. This can be accomplished by increasing the area of the heat exchanger. However, for pure and azeotropic refrigerants that exhibit an isothermal phase change, the benefits of reducing the temperature gradient have diminishing returns. Real-world heat sinks and heat sources typically have significant temperature gradients. Increasing the heat transfer area forces the heat sink and heat source temperature profiles to more closely match the refrigerant temperature profile. For isothermal refrigerants, increasing the heat transfer area forces the heat source and heat sink to become more isothermal. In many **heat pump** applications, it is advantageous to increase the temperature of the heat sink fluid exiting the condenser. However, this becomes increasingly more difficult with isothermal cycles as heat transfer area is increased.

This is where the nonisothermal phase change operating characteristic of **nonazeotropic** binary refrigerant mixtures becomes useful. The composition of the two refrigerants can be chosen such that the temperature gradient during phase change on the refrigerant side matches the temperature gradient on the water side. The COP could then be increased though increased heat transfer area without adversely effecting the source or sink gradients.

The main tasks to be accomplished during this SBIR contract are the following:

- Select two refrigerants and a composition that would have a temperature profile similar to the temperature profile of the **hygiene water** loop
- Design a compressor that would operate reliably in a zero-gravity environment
- Size the condenser and evaporator heat exchangers to achieve an optimal COP and to achieve the desired refrigerant-side and water-side temperature gradients for the thermal bus and the **hygiene water** loop.

Experiments on the system that was designed under this SBIR (fig. 176) showed the actual COP of the system to be around 7.0. The expected life-cycle cost of the **heat pump** (not including research and development costs) is predicted to be 60 percent less than that of the cartridge heaters. The expected peak power of the **heat pump** is predicted to be 99 percent less than that of the cartridge heaters.

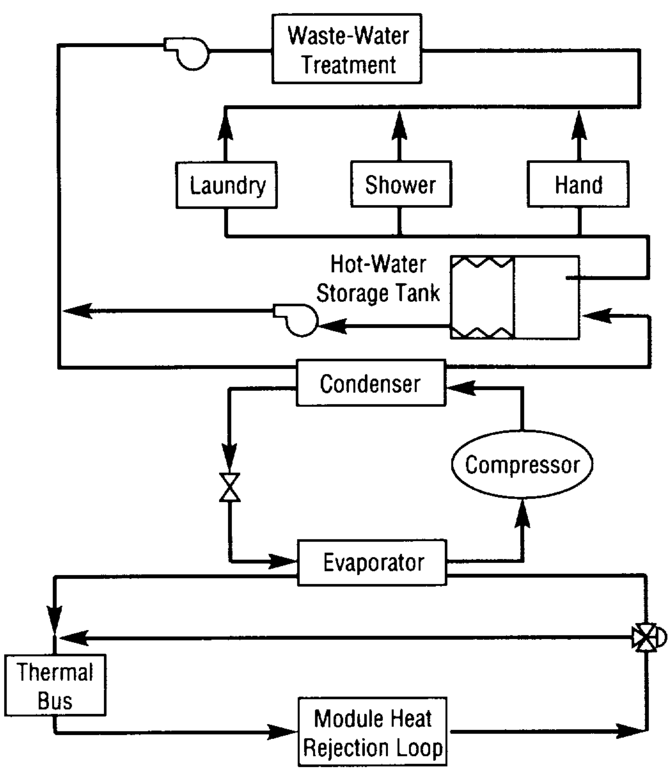

FIGURE 176.—Flow diagram for heat pump water heater.

Atwood, T., "The ABC's of NARB's (Nonazeotropic Refrigerant Blends)," *ASHRAE Transactions*, vol. 91, Part 2, 1985.

D.G. Westra/ED63
(205) 544–3120
Sponsor: Office of Commercial Programs, Small Business Innovation Research

ORGANIC CONTAMINANT MONITOR

Recycling of **waste water** is essential for long-duration human exploration missions in order to avoid prohibitive resupply or storage penalties. Contamination of water supplies is a major concern, and monitoring the levels of these contaminants is essential.

The objective of this task is to develop a device to monitor **organic contaminants** over a wide range of concentrations in water. The proposed method is an **acoustic plate mode (APM)** device that is sensitive to mass changes. The feasibility of using an **APM** device will be determined by fabricating and testing the device with known concentrations of organic compounds.

The major parts of the **APM** device are shown schematically in figure 177. This technique relies on the ability to monitor small mass changes that occur on the device surface while it is immersed in water. As the mass of the surface in contact with the liquid changes due to adsorption of organic compounds, the characteristics of the wave propagated by the input transducer also change. These changes are detected by the output transducer and can be used to identify characteristics of the organic compounds.

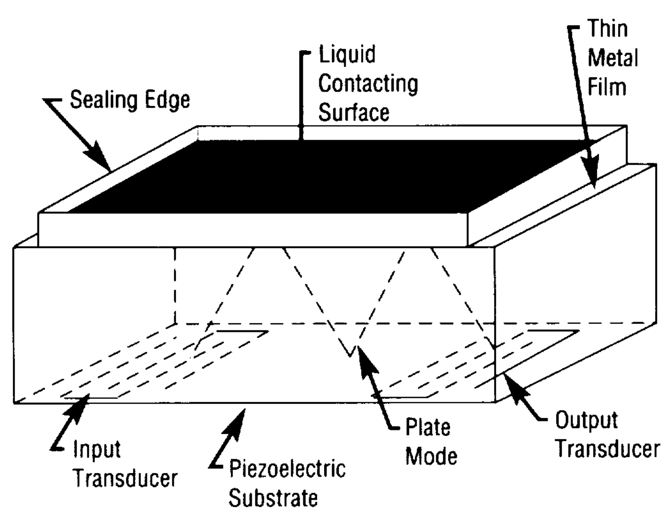

FIGURE 177.—Acoustic plate mode device schematic.

Specific objectives of this project are:

- To determine the plasma polymerization parameters for the active surface
- To design and fabricate an **APM** test probe
- To measure the mass changes that occur due to different **organic contaminants**
- To design a prototype **APM** device for fabrication and testing.

The test probe is being assembled and plasma polymerization techniques are being evaluated.

P.O. Wieland/ED62
(205) 544–7215
Sponsor: Office of Commercial Programs, Small Business Innovation Research

Phenomenological Molecular Sieve Model

The technology selected for removing carbon dioxide (CO_2) from the atmosphere on Space Station *Freedom* uses **molecular sieves**. Existing **analytical models** are based on empirical data that are very specific as to material and operating conditions. This limits the ability to analytically evaluate the performance under different conditions.

The objective of this task is to develop an improved **analytical model** of the four-bed **molecular sieve** (4BMS), which is capable of predicting performance when operating conditions (e.g., cycle time, temperatures, etc.) or hardware (e.g., bed size, etc.) are changed. The approach (shown in figure 178) is to accurately model the adsorption and desorption processes in the

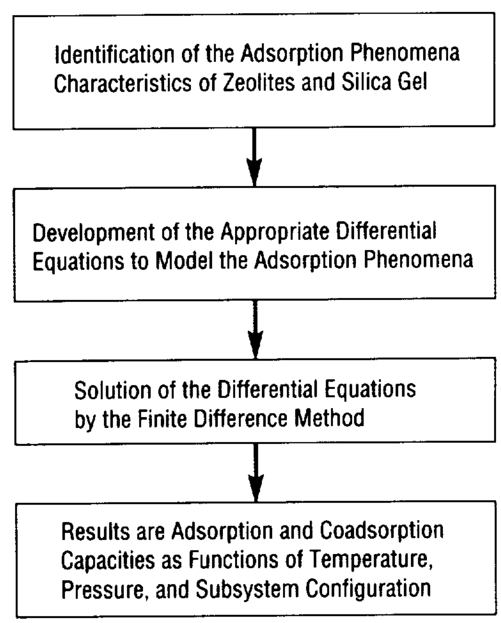

Previous models use a lumped capacitance approach. This is dependent on empirical data for a specific condition and for a specific configuration, as well as for a specific material and packed-bed data.

The new model will not require empirical data for the configuration or the operating conditions, only for material and packed-bed characteristics.

FIGURE 178.—Phenomenological molecular sieve modeling approach.

molecular sieve material. Previous models have used approximate (lumped parameter) techniques that are limited to a single set of conditions for which experimental data is available to verify the results. These models are not capable of accurately predicting the effects of unusual conditions or changes in hardware configuration or operating conditions.

The anticipated result will be a model that is useful as a design tool to optimize the 4BMS design and operational parameters, and, as an analysis tool, to evaluate the effects of off-nominal conditions. Model construction has been initiated, and completion is expected in 1991.

P.O. Wieland/ED62
(205) 544–7215
Sponsor: Office of Space Flight, Space Station *Freedom*

Programmable Heater Control Circuit

Current spacecraft heater control is accomplished with mechanical thermostats and analog circuitry. When temperatures must be controlled to strict limits, analog circuits are used. Mechanical thermostats are utilized when high power is required and/or precise temperature control is not required. Neither device (mechanical thermostats or analog circuitry) provides the capability to be reconfigured during flight, and, in both cases, spacecraft temperature data is obtained by running a sensor (usually a thermistor) to the location of concern from the spacecraft's central processor. This adds significant complexity and weight to the spacecraft. In order to eliminate these problems, the **programmable heater control circuit** is being developed.

The **programmable heater control circuit** is a solid-state, programmable, **spacecraft heater controller**. This device will allow the control circuit temperature sensors to be used as flight temperature data. The development effort will also produce a **spacecraft heater controller** that can be reprogrammed while the vehicle is in flight.

One configuration of the **programmable heater control circuit** is depicted in figure 179. The **hybrid integrated circuit** will be able to control up to four resistance heaters using eight temperature sensors. The temperature data from the sensors will be sent to the spacecraft's central computer over a time-multiplexed data bus. All control algorithms are performed by the microcontroller along with any performance calculations (e.g., duty cycle, status, power consumption, etc.) required for spacecraft health monitoring. Software can be reconfigured while in flight by ground controllers. The new software is sent to the spacecraft central processor then downloaded to the **programmable heater control circuit**. In addition to the built-in microcontroller, the **programmable heater control circuit** has an internal direct-current-to-direct-current (dc-to-dc) converter to deliver 5–V power for the electronics and 15–V power for the sensors from the spacecraft 28–V power bus. This reduces the number of power buses required to operate the device. An optional configuration will not have this built-in feature and can be utilized where the additional buses are readily

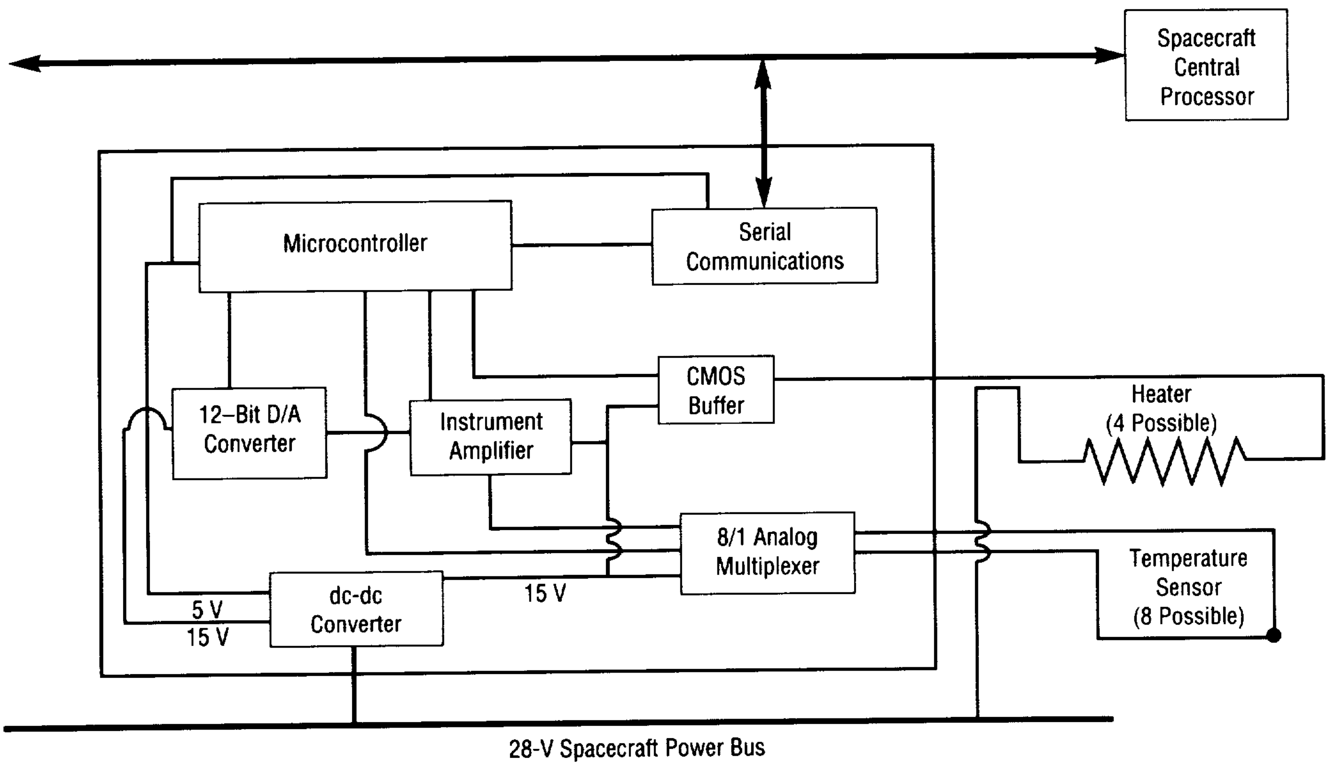

Figure 179.—Programmable heater control circuit with internal dc-to-dc converter.

available. Commands to operate the heaters are passed from the microcontroller to a complementary metal oxide semiconductor (CMOS) buffer. Temperature data input is controlled by the microcontroller via a 12–bit digital-to-analog (D/A) converter.

The hardware design and development, software design and development, and associated testing of the **programmable heater control circuit** are being conducted as a joint effort between the Structures and Dynamics Laboratory and the Electronics and Information Systems Laboratory. Manufacture of the device will be handled by independent electronics contractors.

The **programmable heater control circuit** will provide future spacecraft with state-of-the-art, programmable, active thermal control. This will allow spacecraft to readily respond to in-flight temperature anomalies by reprogramming the heater controllers.

D.M. Bryan/ED64
(205) 544–4265
Sponsor: Center Director's Discretionary Fund

Removal of Contaminants From Experiment Waste Water Using Immobilized Enzymes

Recycling of waste water is essential for long-duration human exploration missions in order to avoid prohibitive resupply or storage penalties. Some contaminants, such as urea, low molecular weight alcohols, and polar molecules, are not easily removed by existing methods, and innovative methods of removing these compounds are of special interest.

The objective of this task is to develop a device using **immobilized enzymes** to catalyze low molecular weight contaminants that are not efficiently removed with existing adsorption technologies. Targeted compounds include ethanol, methanol, isopropanol, and urea. **Enzymes** will be used to oxidize these contaminants into compounds that can be efficiently removed by existing methods. Figure 180 schematically shows the sorbent beds designed to catalyze urea and alcohols. The sorbents are identified and the functions of each are given.

Two **enzymes** were focused on: urease (for removal of urea) and alcohol oxidase (for removal of methanol, ethanol, and related contaminants). Both **enzymes** successfully catalyzed the contaminants and good performance was demonstrated. Continued development led to fabrication of prototype reactors that have been tested in the **environmental control and life support system** (ECLSS) test-bed at MSFC, and may have application on board Space Station *Freedom*. Test results show that the **enzymes** successfully reduced the targeted compounds to concentrations below their detection limit. Additionally, 80 percent of the total organic carbon (TOC) was removed (in most cases to less than 1 part per million (p/M)), indicating that other **organic contaminants** (probably glycols and aldehydes) were also being removed.

P.O. Wieland/ED62
(205) 544–7215
Sponsor: Office of Commerciall Programs, Small Business Innovation Research

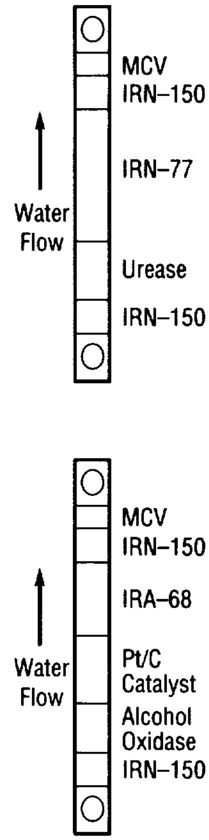

Urease Unibed

Sorbent	Volume	Function
IRN–150	60 cm³ (3.7 in³)	Iodine Removal
Urease	200 cm³ (12.2 in³)	Convert Urea to Ammonia
IRN–77	750 cm³ (45.8 in³)	Remove NH_3 as NH_4^+
IRN–150	60 cm³ (3.7 in³)	Protect From I_2 Back Flow
MCV	60 cm³ (3.7 in³)	Microorganism Control

Alcohol Oxidase Unibed

Sorbent	Volume	Function
IRN–150	60 cm³ (3.7 in³)	Iodine Removal
Alcohol Oxidase	200 cm³ (12.2 in³)	Convert Alcohol to Aldehyde
Platinum/ Carbon Catalyst	360 cm³ (22.0 in³)	Convert Aldehyde to Organic Acid
IRA–68	750 cm³ (45.8 in³)	Remove Organic Acid
IRN–150	60 cm³ (3.7 in³)	Protect From I_2 Back Flow, Scavenge Aldehyde, Organic Acid
MCV	60 cm³ (3.7 in³)	Microorganism Control

MCV – Microbial Check Valve
IRN – Material Designation
IRA – Material Designation

Figure 180.—Immobilized enzyme water treatment unibed.

Small Expendable Deployer System

The small expendable deployer system (SEDS) is a lightweight, spinning-reel type system designed to deploy a payload attached to the end of a 20–km (12–mi) long **tether**, which is cut and discarded after use. The key objectives are to validate the design concept and study the dynamics of **tether deployment**. SEDS weighs about 39 kg (85 lb), including the **tether** weight of 7 kg (15 lb). The **tether** is made from a high-strength, low-density, polyethylene fiber called SPECTRA. SEDS will fly on a Delta II launch vehicle in late 1992. Hardware development was completed in 1989 on the mechanical systems and in 1991 on the electrical systems. Both will be tested in early 1992. Analysis and planning leading up to the physical integration of SEDS into the Delta II began in 1991 and will continue until the launch.

During flight, the payload, weighing 23 kg (50 lb), will be deployed toward Earth. Payload instruments are an accelerometer, a tensiometer, and a magnetometer (for orientation information). The experiment will last about 2 h, ending when the **tether** is fully deployed and has swung to a near-vertical position, pointing toward Earth. The **tether** is then cut, allowing it and the payload to reenter the Earth's atmosphere. The SEDS concept is shown in figure 181.

Numerous future applications of SEDS are being considered. One is the routine deorbiting of Space Station Freedom waste materials, packaged in small, lightweight containers that can be folded for easy storage during shuttle trips to the station. Another is the generation of **artificial gravity** in a small capsule at the end of the **tether**. This is done by slowly spinning the **tether** with masses at each end, i.e., the capsule and a propulsive device. The most obvious use of SEDS will be to place instruments in the 90– to 120–km (56– to 75–mi) altitude region for upper atmospheric research.

J.K. Harrison/FA34
(205) 544–0629
Sponsor: Office of Space Flight

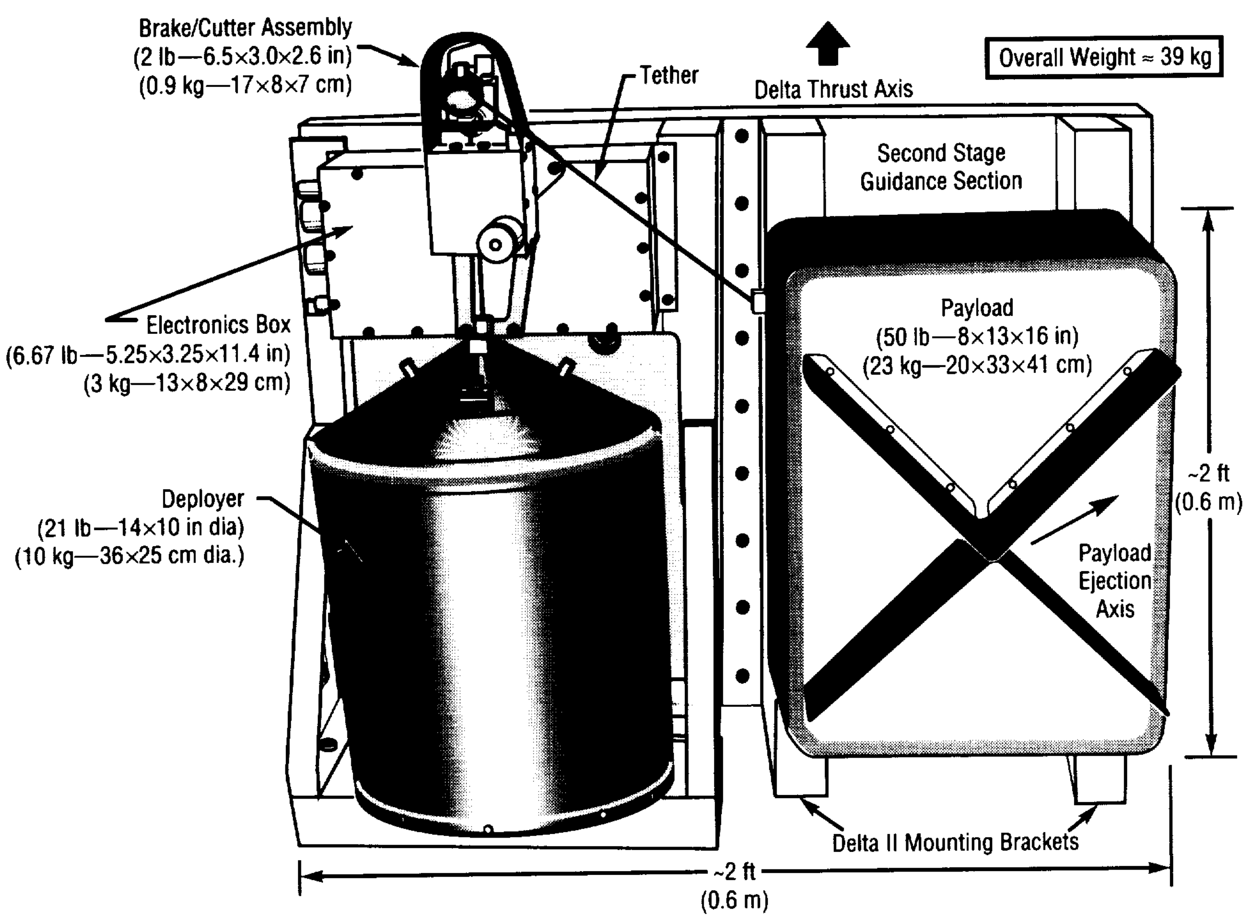

FIGURE 181.—SEDS configuration in Delta II launch vehicle.

Thin-Membrane Sensors

Recycling of **waste water** is essential for long-duration human exploration missions to avoid prohibitive resupply or storage penalties. Contamination of water supplies is a major concern, and monitoring the levels of these **contaminants** is essential.

Thin **membrane sensors** can potentially be used for rapid and highly sensitive detection of hazardous agents (chemical and biological) in water, with an electrochemical transduction mechanism that permits miniaturization and direct or remote electronic readout. The essential features are a thin membrane and a biochemical switch as shown in figure 182.

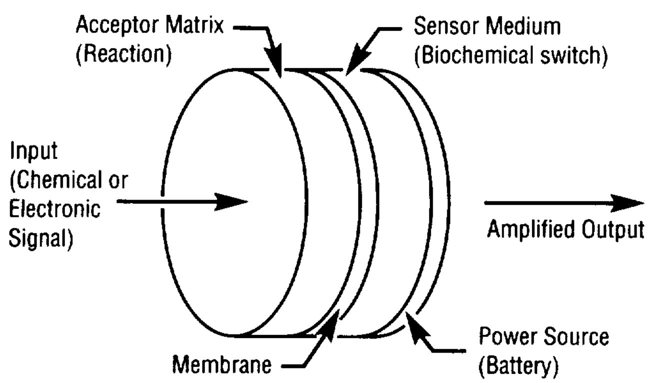

FIGURE 182.—Thin-membrane sensor concept.

The key objective of this project is to verify a suitable transducing membrane that can be incorporated into an electronic output device.

Further objectives are to develop and fabricate laboratory prototypes and to evaluate their usefulness for detecting biological and chemical hazards. Specific tasks are: transduction of major biological/chemical target processes; development and production of laboratory devices; and validation and demonstration of the prototypes.

The feasibility of preparing a durable membrane composition loaded with sufficient gate material to support a triggered current flow approaching 1 A/m^2 (0.09 A/ft^2) has been demonstrated. Durability relative to withstanding large (i.e., 6 to 16 V) overvoltage excursions and physical stresses was demonstrated.

P.O. Wieland/ED62
(205) 544–7215
Sponsor: Office of Commercial Programs, Small Business Innovation Research

Trace Contaminant Monitoring

Trace contaminants in spacecraft atmospheres are a major concern for long-duration human exploration missions due to potential health hazards of long-term exposure. Even small levels of some substances may have detrimental effects over time and these **contaminants** must be monitored to ensure that safe levels are maintained.

The objective of this task is to perform the necessary technology reviews and trade studies in order to recommend a trace **contaminant monitoring** concept for further development. Specifications will be developed for a breadboard system having improved capabilities. The approach for the trades analysis is shown in figure 183.

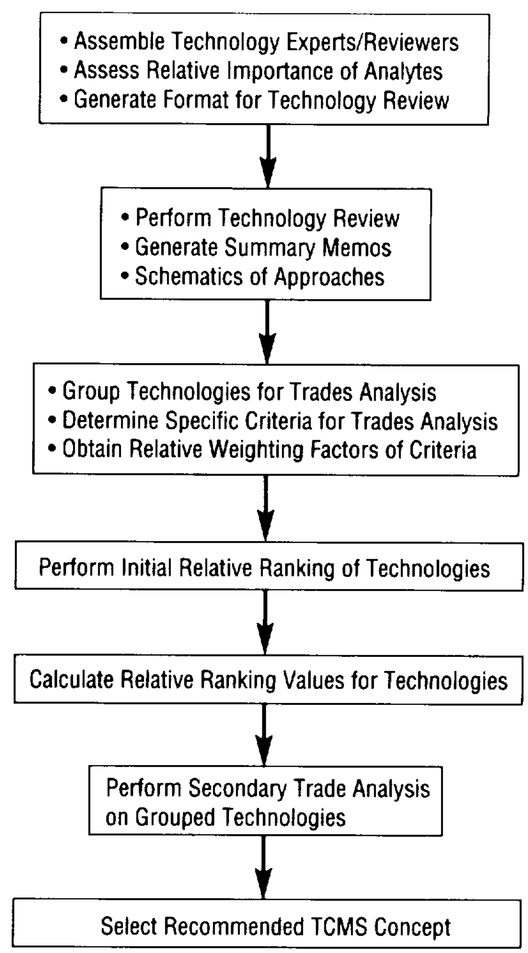

FIGURE 183.—Approach for trace contaminant monitoring trades analysis.

This task includes: reviewing candidate technologies; performing appropriate trade studies and analytical assessments with regard to functional, design, safety/hazard, and logistical criteria; selecting a concept and design; developing the design specifications for a breadboard system; and summarizing the results, including specifications, in a report.

To date, no results have been recorded.

P.O. Wieland/ED62
(205) 544-7215
Sponsor: Office of Aeronautics, Exploration and Technology

Ultrasonic Decomposition of Organic Molecules in Water

Recycling of **waste water** is essential for long-duration human exploration missions in order to avoid prohibitive resupply or storage penalties. Some contaminants, such as urea, low molecular weight alcohols, and polar molecules, are not easily removed by existing methods and innovative methods of removing these compounds are of special interest. Ultrasonic decomposition of organic molecules in water is one such method.

The objective of this task is to demonstrate the feasibility of using ultrasonic energy to simultaneously **degas** a water stream and decompose trace **organic contaminants** in the stream into compounds that are easier to remove. The effectiveness will be evaluated with organics (e.g., methanol, ethanol, isopropanol, acetone, formaldehyde, formamide, urea) and surface active agents (e.g., sodium dodecylbenzene sulfonate). The extent of **organic decomposition** is measured by the quantities of the decomposition products (acetate and formate ions). Free-gas effects will be evaluated with 1 at of air (20-percent oxygen (O_2) 80-percent nitrogen (N_2)), 5-percent carbon dioxide (CO_2) (5-percent CO_2, 95-percent N_2), and 5-percent air (1-percent O_2, 99-percent N_2).

Evaluations of **ultrasonic decomposition of organic compounds** have begun with methanol, ethanol, and acetone. Completion of this task is scheduled for 1991.

P.O. Wieland/ED62
(205) 544-7215
Sponsor: Office of Space Flight, Space Station *Freedom*

Structures and Dynamics

A Comparison of Single-Cycle Versus Multiple-Cycle Proof-Testing Strategies

Although **proof testing** is generally not the preferred method of crack detection, it has proven useful as a supplement to conventional nondestructive evaluation (NDE) methods. The objective of **proof testing** is to screen out gross manufacturing or material deficiencies and provide additional quality assurance of delivered hardware. Typically, only pressure loads are applied during the proof test, and these are generally scaled-up by a proof factor. Based on demonstrated success on a number of space shuttle main engine (SSME) components over the years, five-cycle **proof testing** has been adopted as a standard practice.

Potential benefits of **proof testing** must be weighed against the possibility of inflicting additional undetected damage on the component through subcritical crack growth or stable tearing upon loading. Since the application of **proof testing** to brittle materials results in little or no stable crack growth, multiple-cycle **proof testing** (MCPT) is unnecessary. On the other hand, MCPT is generally applied to tougher materials that exhibit significant stable crack growth. Figure 184 clearly demonstrates that the character of the material's resistance curve (**R-curve**) is important to MCPT behavior and holds the key to proper selection of an optimum proof-test strategy.

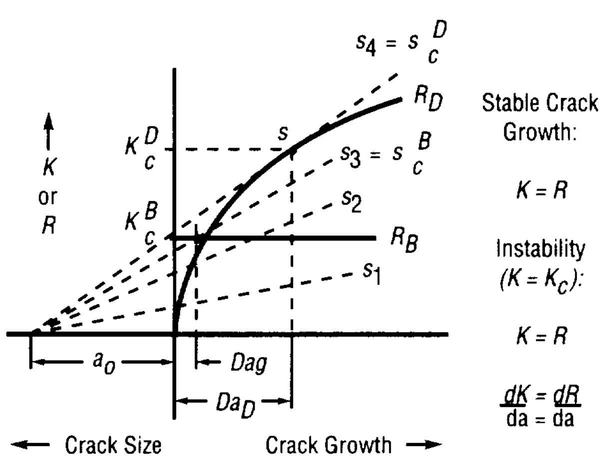

FIGURE 184.—Influence of R-curve on stable crack growth in brittle (B) versus ductile (D) materials.

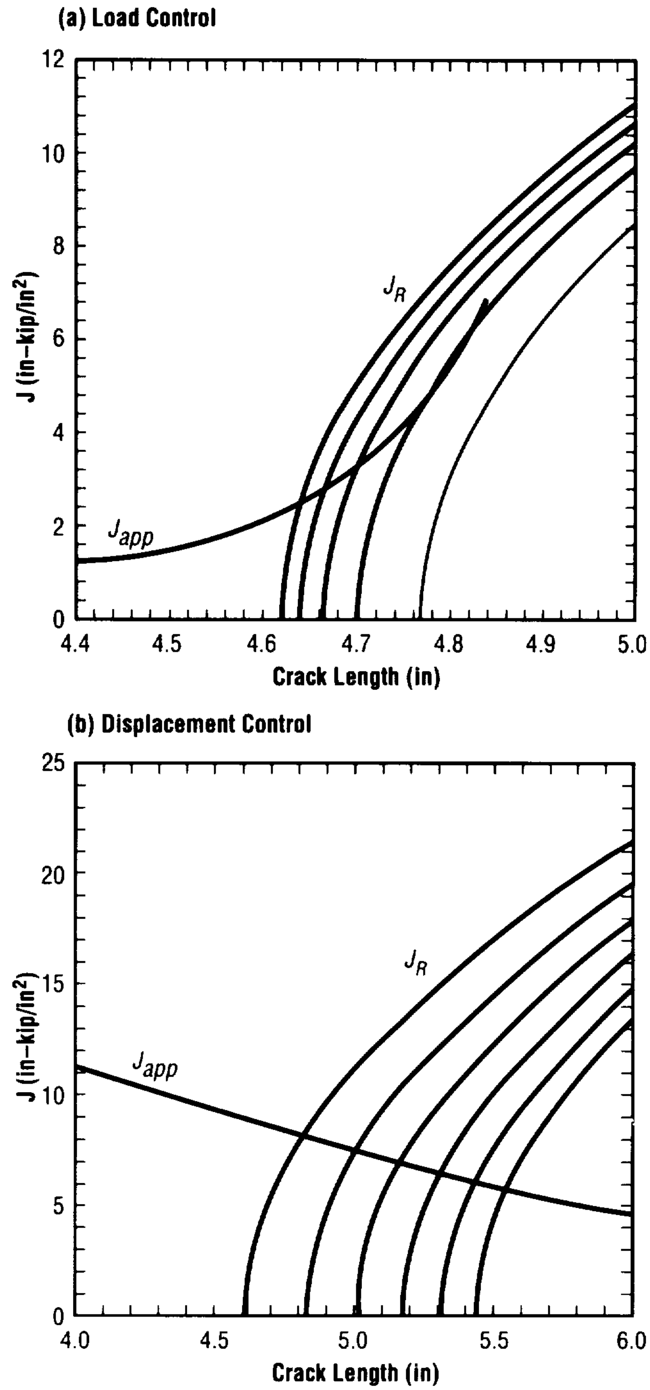

FIGURE 185.—Simulated MCPT.

A computer code was written that numerically simulates MCPT under a variety of conditions. The code, written in standard FORTRAN-77, essentially conducts quantitative comparisons of the material **R-curve** and the applied **J-curve** (J_{app}) by a suitable overlaying of the two. The code checks for noninitiation or failure on that cycle and then calculates the extent of stable crack growth. The complex nonlinear form of both curves requires the use of iterative numerical schemes.

An MCPT for a simulated compact tension specimen under pure load control is illustrated in figure 185(a). The single J_{app} curve corresponds to the given proof load. The five **R-curves** represent different proof cycles, each emanating from the appropriate initial crack length. Each new initial crack length is determined by the intersection of the applied **J-curve** with the **R-curve** for the previous proof cycle. Likewise, an MCPT under pure displacement control is shown in figure 185(b). Here the J_{app} value decreases slowly and nearly linearly with crack length, and no failure occurs on any of the five proof cycles.

The specific amount of crack growth during any load-controlled or displacement-controlled MCPT is a function of the specific applied loads or displacements. In general, displacement-controlled tests do possess a greater potential for extensive stable crack growth than load-controlled tests.

Hudak, S.J., and McClung, R.C., "A Comparison of Single-Cycle Versus Multiple-Cycle Proof Testing Strategies," Contractor Report 4318, NAS8-37451, August, 1990.

H.M. Lee/ED25
(205) 544-7245
Sponsor: Office of Aeronautics, Exploration and Technology

Advanced Code Development for Rocket Propulsion System

As a part of the overall objective of developing **numerical simulation** capability for **liquid rocket engines**, an effort is continuing for developing advanced incompressible and compressible **Navier-Stokes** codes. Several basic flow solvers have been developed in the past. During the past year, these codes have been enhanced to meet the demand for future high-performance computing capability, as well as to increase the code capability for simulating various complicated physical phenomena and geometries.

The INS3D-LU code, which is based on the lower-upper symmetric Gauss-Seidel implicit algorithm, has been ported to **parallel architecture**. The performance has been investigated using different grid sizes. It has been observed that the performance increases as the grid size increases reaching 1.2 GFLOPS using eight processors of Cray YMP and 2M grid points (fig. 186).

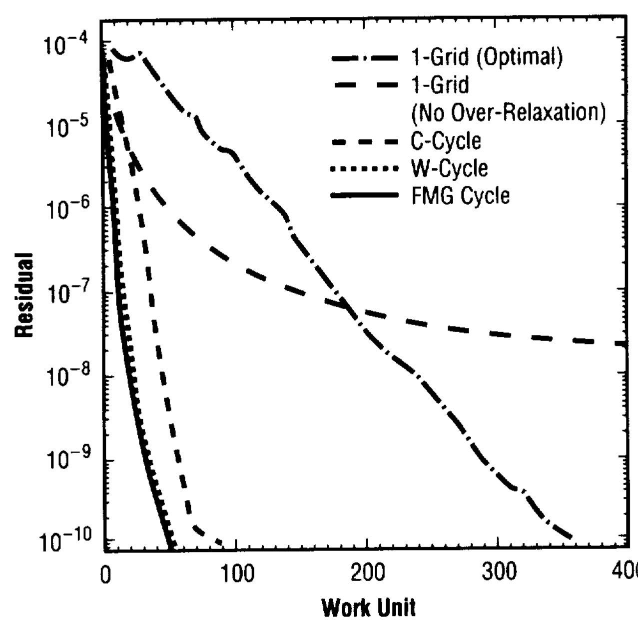

FIGURE 186.—Parallel processing of INS3D-LU on Cray YMP.

For **transient flow analysis**, the INS3D–FS code has been developed. During the past year, the speed of this code was enhanced by implementing a multigrid technique to the Poisson solver part. As shown in figure 187, the full multigrid (FMG) cycle accelerates the convergence by a factor of three over the optimal single grid case.

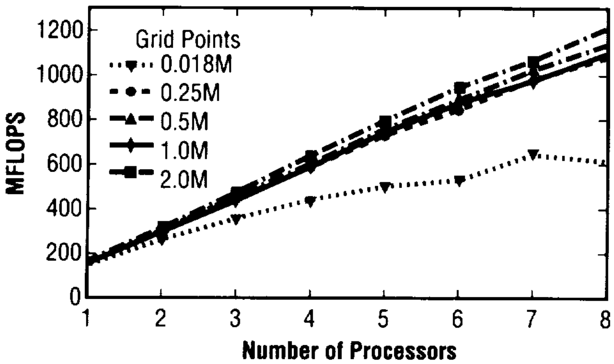

FIGURE 187.—Convergence history of multigrid cycling methods for INS3D–FS.

The INS3D–UP code, which is based on upwinding and the line Gauss-Seidel algorithm, was further developed by implementing a chimera grid scheme for simulating multiple moving domains.

To analyze **combustion-related flow**, a compressible **Navier-Stokes** code, CENS3D, is being developed that can handle chemical reactions in a computationally efficient manner. The performance under perfect gas condition is excellent. Further development is under way to include various chemistry models.

G.A. Wilhold/ED31
(205) 544–2651
Sponsor: Office of Aeronautics, Exploration and Technology

ADVANCED CONTROL EVALUATION OF STRUCTURES (ACES)

The Advanced Control Evaluation of Structures (ACES) Facility, located in the high-bay area of building 4619, has been significantly upgraded over the past year and has been used extensively in the development of advanced controller design, **system identification**, and fault detection and identification techniques. Guest investigators (GI's) from Purdue University, Massachusetts Institute of Technology (MIT), and Arizona State University used the laboratory for conducting experiments to further their research under the GI program under the direction of the Langley Research Center.

The most significant improvement made to the facility was the remodeling of the control room, which included the installation of a raised floor. Rearranging the equipment and running the cabling underneath the new floor provides a more efficient use of space and increases the users accessibility to the data processing equipment. A number of improvements were made to the computer system, including both software and hardware enhancements. The controller implementation algorithms were improved for efficiency, a ramp to zero feature for all disturbances was added, and data transfer software was developed. A nine-track tape drive was added to facilitate the collection of large quantities of data. Antialiasing filters were designed, fabricated, and installed in the real-time data processing system to improve performance. Sensor and actuator improvements were also accomplished.

In the area of advanced controller design and **system identification** techniques, researchers designed and implemented an **H-infinity controller** on the ACES structure. The performance of the controller was marginal, however, due to the requirement of an extremely high fidelity model to effect the design of the controller. A model of such fidelity does not exist for ACES due to the extremely complex nonlinear behavior of the system. The resulting failure of the controller led to the development of a promising **system identification** technique for multi-input, multi-output systems. The determinantal modeling and residue matrix identification techniques have been developed to extract system models from

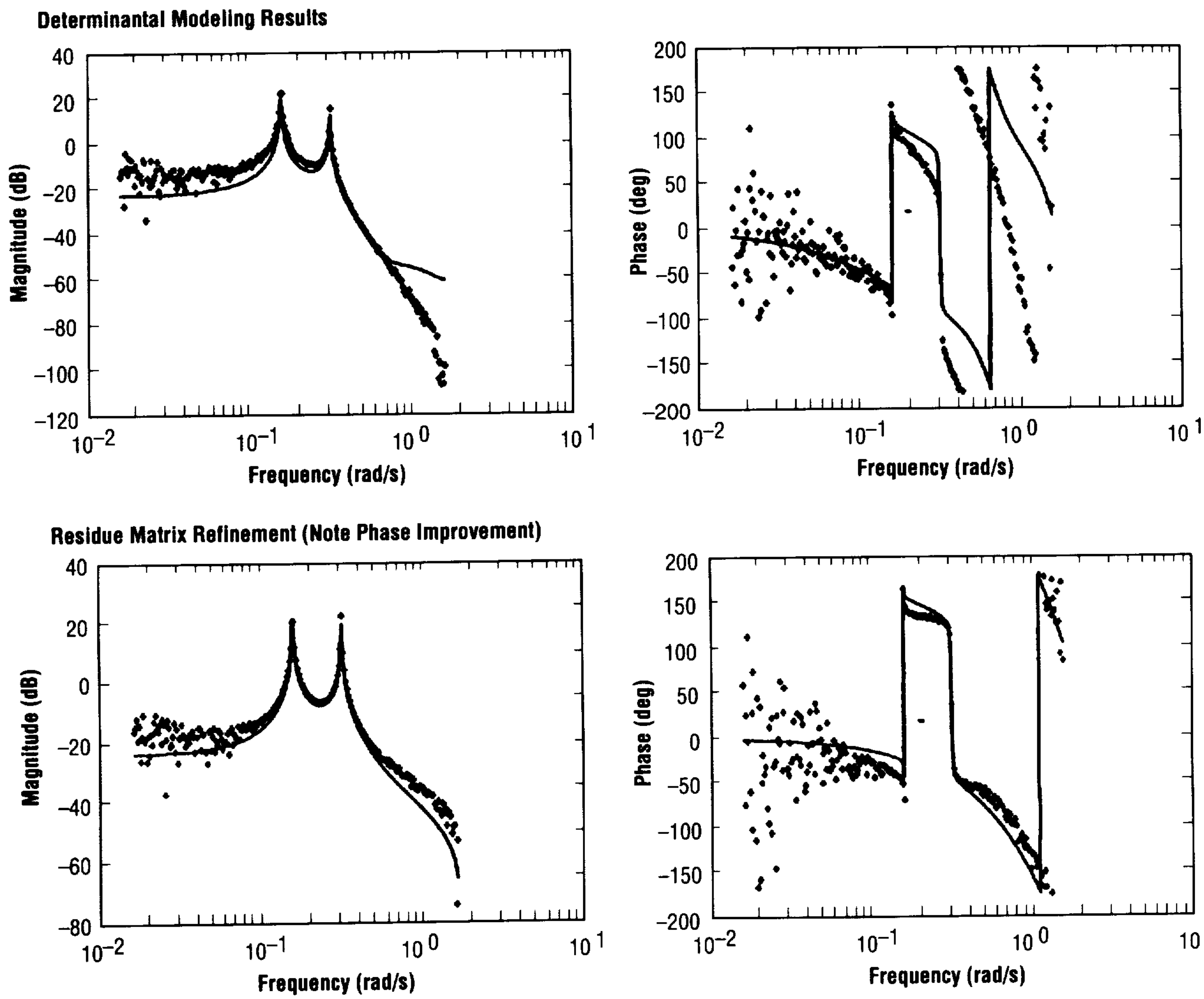

FIGURE 188.—Examples of models derived via determinantal and residue matrix methods.

experimental data. As shown in figure 188, the determinantal modeling technique provides an excellent fit to the magnitude response. Application of the residue matrix identification technique greatly improves the phase response match. Further, techniques to develop controller designs based exclusively on experimental frequency response data have also been developed under the ACES program.

One of the more significant results to come from the GI program is the **failure detection** and identification (FDI) methodology developed by researchers from MIT. Generalized parity relationships that have null residuals under system-nominal conditions are used to detect failures. Experimental data from the ACES facility were used in analyses in which sensor failures were simulated. A sample result is shown in figure 189. Note the failure is indicated by the significant increase in the magnitude of the parity relationship.

Another **system identification** methodology developed under the ACES program is the **Q-Markov cover** with frequency partitioning. The method is particularly applicable to closed-loop systems in which the controller is the only known quantity, (i.e., the plant and the disturbances, as well as their kinematic relationships, are to be

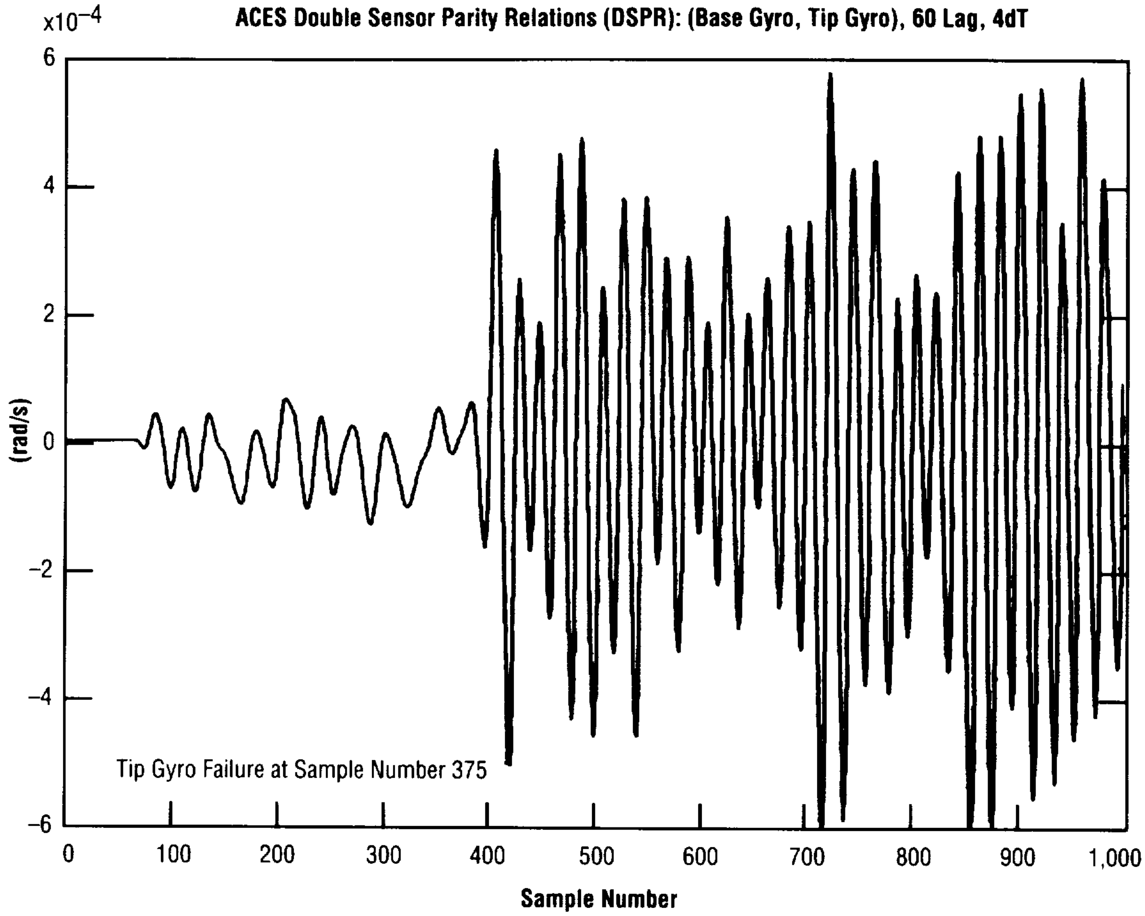

FIGURE 189.—Example of ACES tip gyro failure detection.

identified). This methodology was applied to data taken from the Hubble space telescope (HST) for the purpose of developing the model that was used to perform the controller redesign, which was necessary due to the solar panel disturbances.

In further support of the HST controller redesign, the ACES facility was configured to emulate the telescope dynamics to verify the proposed transfer function test methodology. The objectives were to validate proposed methods of extracting open-loop plant models from closed-loop data and to develop, test, and validate analytical tools in the ACES facility prior to HST on-orbit tests. Excitation profiles were evaluated on the flight-class hardware present in the facility.

A.P. Bukley/ED12
(205) 544–0054

Sponsor: Office of Aeronautics, Exploration and Technology

Aeroheating Flight Instrumentation

The objective of this project was to design and fabricate stacked ceramic **heat flux gauges** to be used on launch vehicles. The **gauges** were developed to reduce or eliminate the **temperature** mismatch between the **gauge** and surrounding TPS material that is normally associated with copper **heat flux gauges**. This was accomplished by thermally matching the ceramic **gauge** material to the surrounding structure/ablator.

Gauges have been developed that consist of two stacked ceramic disks with thin platinum/platinum 10-percent rhodium thermocouples located on the face of each disk. A copper slug heat sink serves as the base of the **gauge** with a chromel/alumel thermocouple used to measure the base **temperature**. The surface **temperature** of the **gauge** is capable of reaching 1,093 °C (2,000 °F). Two different density **ceramic materials** were used to provide a variation in surface **temperature** response characteristics (Thermo-Sil 50® with a density of 801 kg/m^3 (50 lbm/ft^3)and Masrock® with a density of 1842.3 kg/m^3 (115 lbm/ft^3). A perspective view of the proposed flight **gauge** is shown in figure 190.

The **gauges** were calibrated in the laboratory to determine **gauge** temperaure response and **gauge** measuring capability. A thermal math model was constructed for each **gauge** using the laboratory calibration data. This thermal math model is used in conjunction with the **gauge temperature** response to measure **heat flux**. The results of a typical laboratory calibration run are shown in figure 191. The results of this research effort were reported by Palko (1990).

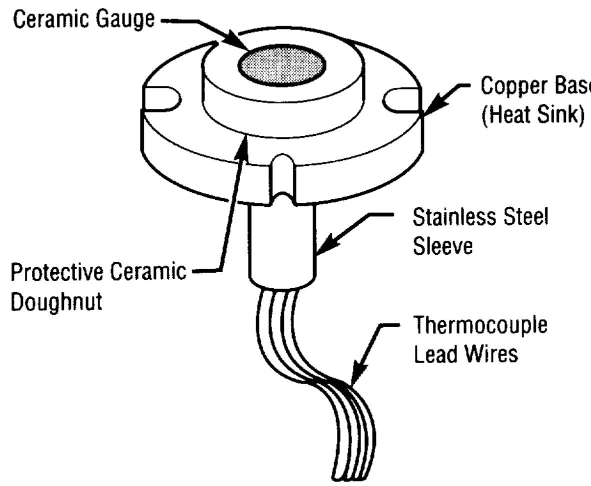

FIGURE 190.—Perspective view of the proposed flight gauge.

Palko, R.L., "Aeroheating Flight Instrumentation, NASA Small Business Innovation Research (SBIR) Phase II, Development, Fabrication, Calibration, and Evaluation," Final Report, NAS8-37409, REMTECH, Inc., RTR 199-02, August 1990.

L.D. Foster/ED33
(205) 544-1589
Sponsor: Office of Commercial Programs, Small Business Innovation Research

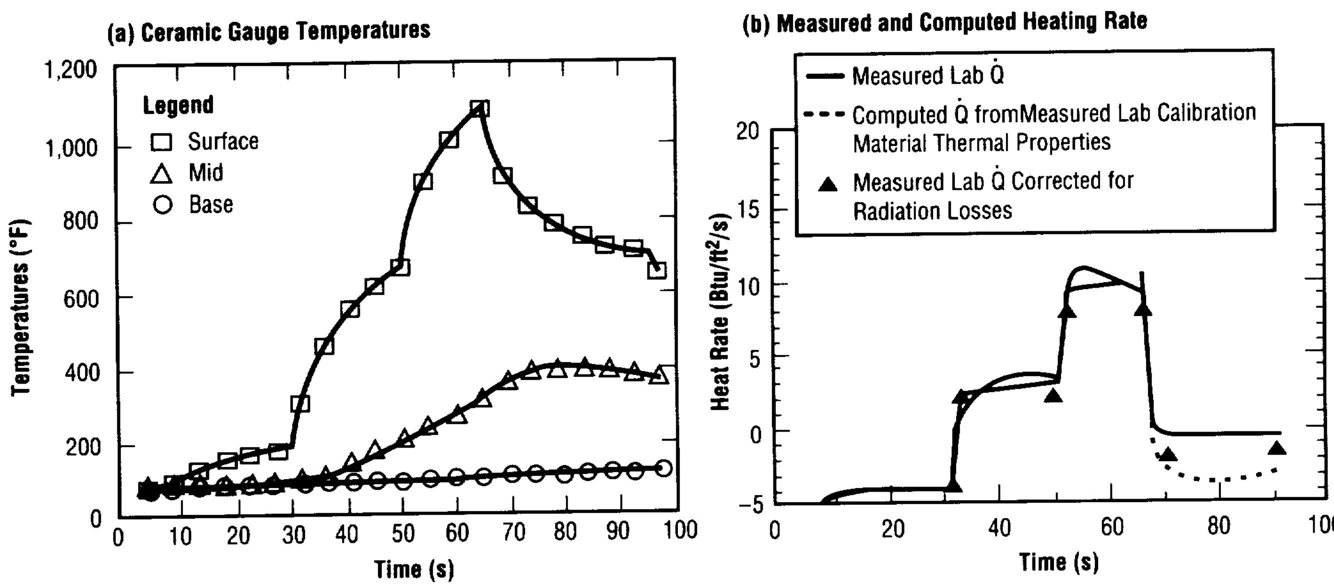

FIGURE 191.—Laboratory calibration data.

An Active Magnetic Suspension for Space-Based Microgravity Vibration Isolation

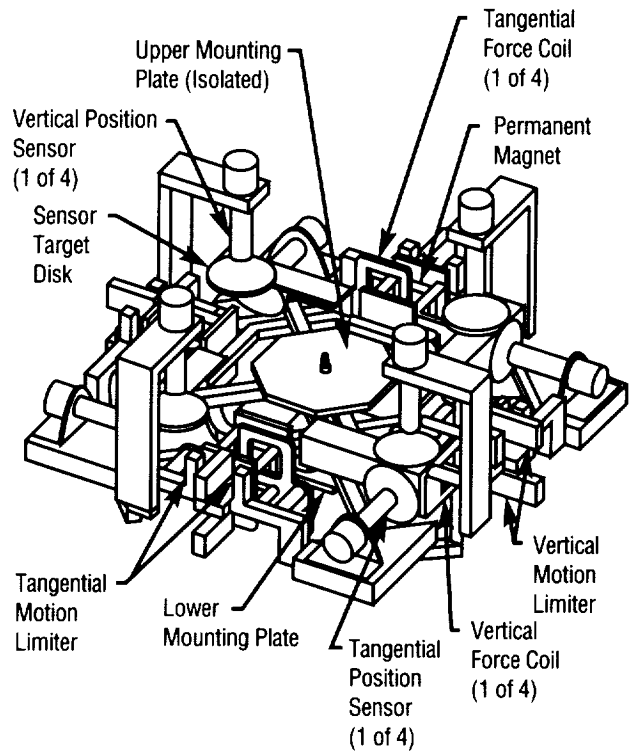

FIGURE 192.—SATCON Corp. 6–DOF magnetic suspension.

Space vehicle accelerations often exceed microgravity experiment requirements and many experiments must be isolated from the vehicle structure. Active isolators can best isolate vibrations at low frequencies, can balance directly applied forces, and can be changed to match individual experimental requirements. Lorentz force magnetic actuators are particularly well-suited because they are reliable, mechanically simple, linear, stable, and are easy to integrate with electronics. An integrated six-degrees-of-freedom (6–DOF) isolator using Lorentz force actuators has been designed, built, and tested and can be used for **space station** applications. The cylindrical design has radial magnetic fields at each end produced by permanent magnets. A six-layer winding in the annular air-gap produces forces and torques in 6–DOF. Nonlinear isolator control algorithms were developed to improve isolation from low-amplitude vibrations by varying suspension stiffness. These controllers were tested on a single DOF test-bed that reduces spurious microgravity accelerations. The test-bed was modified to evaluate the 6–DOF actuator.

The isolator was designed for **space station** microgravity experiments that must be isolated from accelerations caused by thruster firings, crew motion, acoustics, etc. This requires an actuator stroke of at least 1 cm (0.4 in), a minimum of 100–Hz bandwidth, and at least 1 N (0.22 lbf) of force for a 500–kg (1,100–lb) experiment. Testing showed that the isolator prototype exceeded the requirements with excellent damping characteristics. Figure 192 shows the isolator, which measures 45–cm (17.7–in) wide by 45–cm (17.7–in) deep by 8–cm (3.2–in) high and weighs 9.5 kg (21 lb). Power consumption is less than 5 W.

Fenn, R.C., Downer, J.R., Gondhalekar, V., and Johnson, B.G., "An Active Magnetic Suspension for Space-Based Microgravity Vibration Isolation," presented at the 1990 ASME Winter Annual Meeting, November 26–30, 1990.

R.C. Ferebee/ED23
(205) 544–1520
Sponsor: Office of Commercial Programs, Small Business Innovation Research

Buckling of Composite Beams

The objective of this research effort is to characterize the behavior of open-section composite structural elements under bending, axial, and combined axial/bending loads. Of particular importance, and an area that is to be thoroughly examined in this study, is the effect that **laminate layup** has on a beam's load-carrying capabilities. This also includes an investigation into the fabrication of laminated beams with unsymmetric laminates, which offer the advantage of minimizing the inherent bending/torsion coupling in beams of open cross sections. Additionally, composite beam manufacturing techniques will be studied to determine their effect on the load-carrying capability of open-section members.

The research effort is divided into two phases: phase I will feature both flat- and open-section beams subjected to bending loads only, while phase II will introduce both axial and a combination of axial and bending loads into the beams. Both phases will include the fabrication, pre- and post-test nondestructive evaluation (NDE), and analysis of the test results. In each of these phases, the layup of the individual plies will be unsymmetric in nature. It is this layup (orientation, angle of plies, and number of plies) that will be controlled to give the **open-section composite beams** the ability to carry greater loads than their metallic counterparts and to resist torsion.

Shown in figure 193 are the flat- and open-section beams to be used in phase I of the research under way to characterize behavior of composite structural elements under stress. Four beams of each of the three open sections will be fabricated by each of three manufacturing techniques. The flat beams are comprised of 24 plies of composite material, with each ply being 0.0132–cm (0.0052–in) thick, for a total thickness of 0.3175 cm (0.125 in). The flat beams are 38.1 cm (15 in) in length and 5.08–cm (2–in) wide. The open structural elements will be similar in cross sections with lengths of 76.2 cm (30 in). The dimensions and cross sections for the beams were chosen based on potential for future use, stackability, and ease of manufacturing. Phase I testing will consist of loading the cantilevered beams (both flat- and open-section) in bending. Strain and deflection gauges are to be mounted strategically along the beams to give an accurate assessment deformation of the beams under a given load.

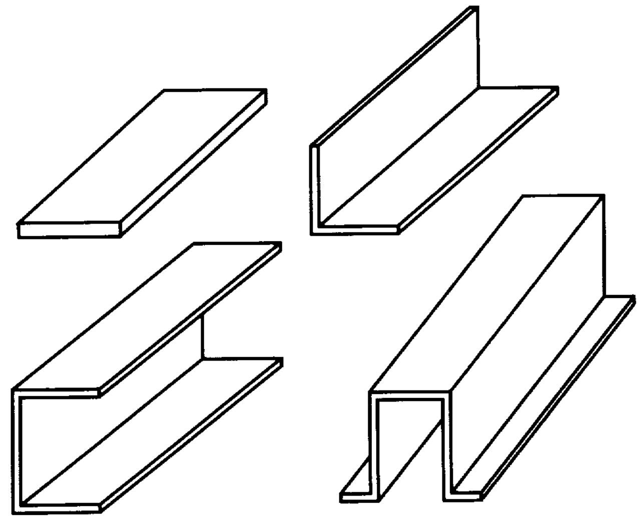

FIGURE 193.—Flat- and open-section beams to be used in phase I.

The flat beams for use in phase I have been fabricated and are undergoing load testing, with fabrication, NDE, and testing of the open-section beams scheduled for June 1991. Data from both sets of tests will be analyzed by Structures and Dynamics Laboratory personnel. Supporting analysis will be conducted by Albert Zvarick, a Vanderbilt University graduate student, under a graduate student research grant awarded by MSFC. Results of this study effort will enhance MSFC's knowledge of composite material structural design. The desired end product of this 2–yr effort is a procedure or code that would use interlaminar shear stresses, normal shear stresses, and in-plane stresses to make predictions on the failure of open-section beams. The procedure would also provide for the sizing of the composite structural members and selection of the optimum ply-angle layup and number of plies needed for a given load case.

P.E. Thompson/ED52
(205) 544–7017
Sponsor: Center Director's Discretionary Fund

CFD Flow Analysis of Bearings, Seals, and Material Tester

The bearings, seals, and material tester (BSMT) is a test vehicle being used at MSFC to evaluate the performance of conventional rolling contact bearings. **Computational fluid dynamics** (CFD) analysis of the flow fields inside the BSMT cavities and manifolds is being done with the following objectives: to estimate the hydrodynamic loads on the bearings; to provide inlet and exit flow conditions for the calibration and evaluation of bearing models; and to recommend feasible design modifications for BSMT to simulate conditions of advanced turbopumps of various Earth-to-orbit (ETO) transfer vehicles.

Axisymmetric analyses of the baseline BSMT inlet and exit cavities predicted large parasitic inward loads in excess of 13.35 kN (3,000 lbf) on the bearings. The pumping action of the slinger wall creates a strong vortex, causing a pressure drop of over 689.1 kPa (100 lb/in^2) in the inlet cavity No. 1 leading to lower pressures in the exit cavity. To reduce this axial load on the bearings, it is proposed that baffles be placed in the inlet cavities (fig. 194) to isolate the throughflow from the slinger wall, reducing pressure drop on the load-carrying wall. Computational analysis of inlet cavity No. 1 with the baffle and the exit cavity were performed, with the REFLEQS–2–D (1) code, to assess the effect of a baffle on the axial load. Results suggest that the axial load should be practically eliminated, with the baffle extended inward to the radius of the outer race.

Three-dimensional (3–D) computational analysis of the BSMT inlet cavity No. 1 has also been performed. The two-dimensional computations did not include the temperature probe that is always present inside the inlet cavities during the operation of the BMST. The flowfield inside the cavity was simulated with the REFLEQS–3–D (2) code assuming axisymmetric inflow and boundary conditions. Preliminary 3–D computations of inlet cavity No. 1, with the probe inserted, show the flowfield to be asymmetric, with large pressure gradients at the probe location. Compared to the baseline case, (i.e., no probe), the pressure drop inside the cavity appears to have been significantly reduced to approximately 344.55 kPa (50 lb/in^2) due to the presence of the probe.

Future plans include 3–D analysis of the exit cavity both with and without a temperature probe. Axial loads will then be recomputed from 3–D results.

Smith, C.E., Ratcliff, M.L., Przekwas, A.J., and Habchi, S.D., "Validation of an Advanced Turbulent Combustion Code: REFLEQS," Presented at the Seventh Space Shuttle Main Engine CFD Workshop, NASA MSFC, Huntsville, AL, 1989.

Przekwas, A.J., et al., "REFLEQS-3-D: A Computer Program for Turbulent Flows With and Without Chemical Reaction; Volume 1: User's Manual," CFDRC Report GR-89-4, 1990.

G.A. Wilhold/ED31
(205) 544–2651

Sponsor: Office of Aeronautics, Exploration and Technology

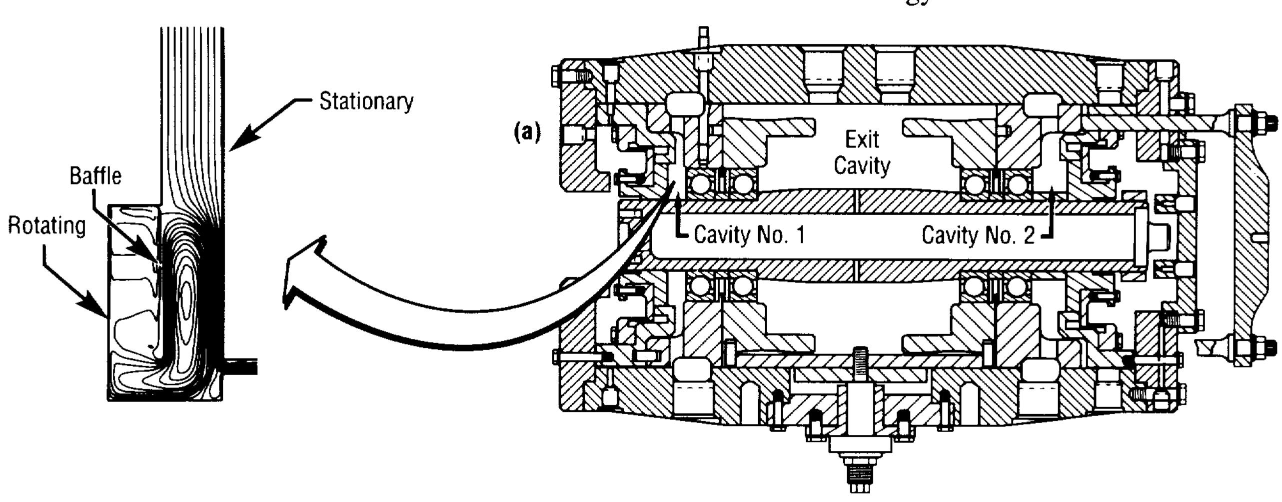

FIGURE 194.—MSFC BSMT and predicted streamlines in cavity No. 1 with a baffle.

Combustion Chamber Analysis Code

This project focuses on the development of an **analysis tool** capable of accurately predicting the flow, heat transfer, and chemical reaction characteristics of **combustion chambers** in **liquid rocket engines**. The latest relevant **numerical techniques** are used, including: strongly conservative formulation in curvilinear coordinates, collocated grids, high-order spatial and temporal discretization, and advanced pressure-based solution algorithms. The Eulerian-Lagrangian approach is used for the representation of **two-phase flows**. Several options for turbulence models and combustion models (including finite rate multistep chemistry and chemical equilibrium) are included and being tested in the two-dimensional (2–D) code.

The **two-phase flow** (spray) combustion model has the capability of tracking two types of liquid droplets (i.e., fuel and oxidizer) in the chamber. The droplet motion is

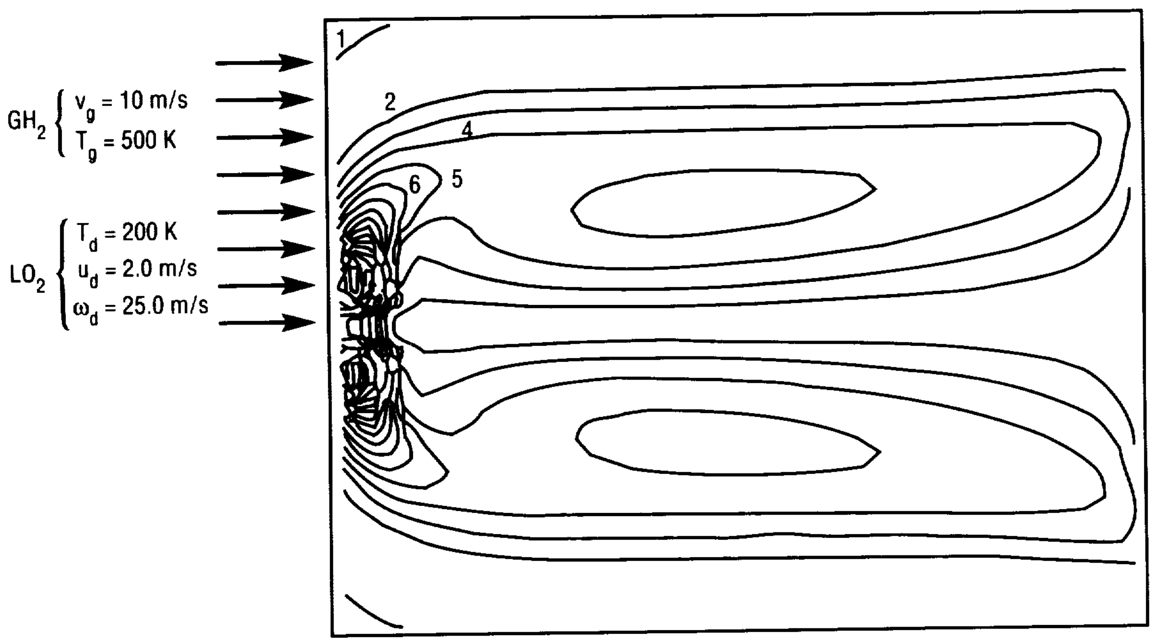

Contour Levels

1	.00002953
2	1.554
3	3.107
4	4.661
5	6.215
6	7.769
7	9.322
8	10.880
9	12.430
10	13.980
11	15.540
12	17.090
13	18.640
14	20.200
15	21.750
20	29.520

FIGURE 195.—Swirl velocity distribution.

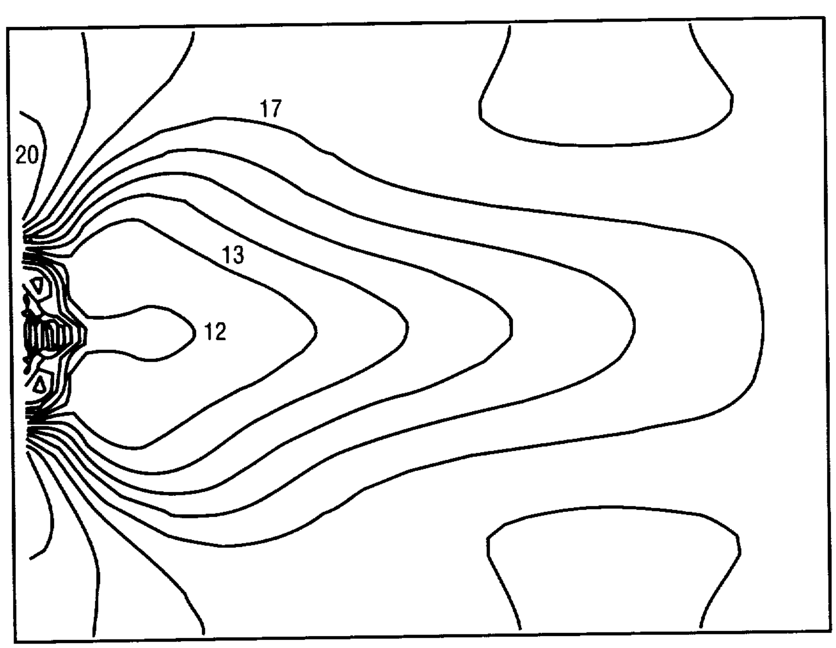

Contour Levels

1	−19.810
2	−18.540
3	−17.270
4	−16.010
5	−14.740
6	−13.470
7	−12.210
8	−10.940
9	−9.672
10	−8.405
11	−7.139
12	−5.872
13	−4.605
14	−3.338
15	−2.071
20	4.262

FIGURE 196.—Pressure distribution.

affected by friction (with gas), body forces (such as gravity), swirl, and the local gas pressure gradient. The Lagrangian spray formulation has been extended to nonorthogonal body-fitted coordinates through appropriate coordinate transformation.

One of the demonstration test calculations is for the shear/swirl injector configuration. Figure 195 shows the swirl velocity contours in a liquid oxygen-gaseous hydrogen (lox-GH_2) combustion chamber. The gas velocity is uniform and axial at the inlet of the chamber. The droplets are injected slightly away from the axis with an axial and a tangential component of velocity. The centrifugal force (due to the swirl) causes the droplets to move radially outward. The gas field develops a swirl through frictional interaction with the droplets. Figure 196 shows the relative pressure distribution in the chamber. The swirl induced in the gas (by the droplets) leads to a low-pressure region near the axis.

The remaining work will emphasize the extension of 2–D code to **three-dimensional** (3–D) situations and implementation of more advanced physical models for sprays, atomization, and turbulence.

G.A. Wilhold/ED31
(205) 544–2651
Sponsor: Office of Aeronautics, Exploration and Technology

Computational Fluid Dynamic Analysis for High-Altitude Hypersonic Vehicles

The overall objective of this program is to develop a **computational fluid dynamics** (**CFD**) computer code to analyze the flow about high-altitude **hypersonic** vehicles, in general, and the **aeroassist flight experiment** (**AFE**) vehicale, in particular. The code, HANA (**hypersonic** analysis of aerobrakes), solves the time-dependent, compressible **Navier-Stokes** equations with coupled finite-rate chemistry and thermal **nonequilibrium**. The code solves these equations using an LU-SGS implicit algorithm with the chemical source Jacobian approximately diagonalized.[1] The resulting algorithm requires no matrix inversions making it more efficient, particularly with chemistry models having a large number of chemical species. The HANA code uses multiple zones of i,j,k-ordered grids whose solutions are patched together at common boundaries. The multiple-zone nature of the code allows the analysis of more geometrically complex vehicles than would be possible with a single-zone code.

The HANA code uses a general chemistry model with the species properties and reaction rates specified by the user in the input file. This allows the program to be used to calculate chemically reacting flows of gases other than air. However, this report will concentrate on flows of air.

The HANA code has been verified for several **hypersonic** flows, with both ideal gases and real gases.[2] Two cases are presented in this report. The first case is an ideal gas calculation and the second is a thermochemical **nonequilibrium** calculation.

The first verification case is a Mach 10 airflow past a 0.022 scale model of the **AFE** vehicle. This model was tested at NASA Langley Research Center (LaRC). The data from these tests consist primarily of surface heat transfer and pressure distributions on the aerobrake surface and the cylindrical payload. A three-zone mesh (fig. 197) was used for this case. The calculated pressure and heat transfer distributions on the aerobrake surface show good agreement with the experimental data. The least favorable comparison is along the 270° ray where the maximum difference is about 15 percent. The heat transfer distribution on the payload also compares well with

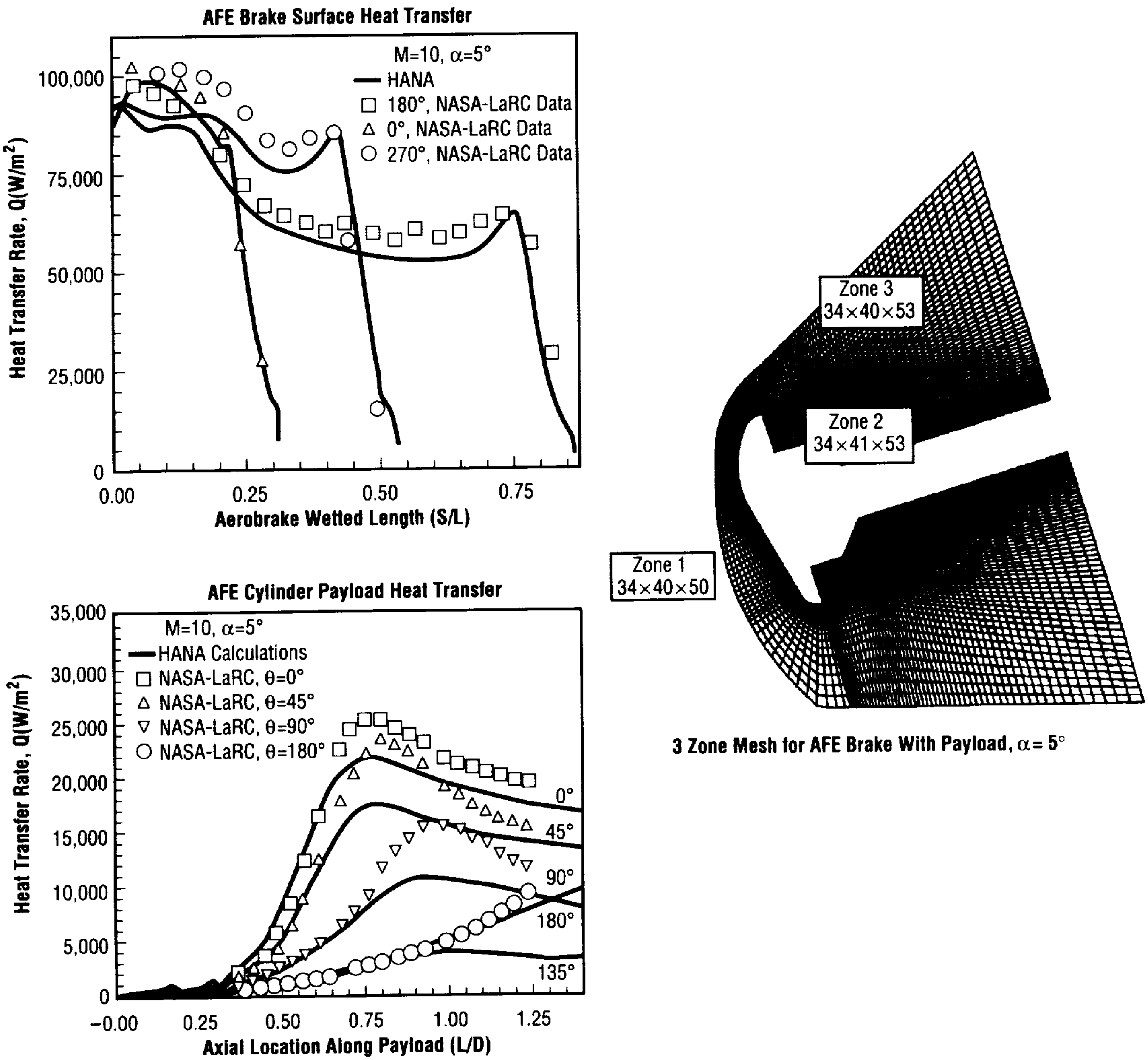

FIGURE 197.—AFE model scale vehicle test case, M=10.

the data. The magnitudes of the peaks are somewhat underpredicted, but the rise in heat transfer occurs at the correct location indicating that the computed location of shear layer impingement is accurate.

The second verification case is a sphere-cone probe that was tested during the radio attenuation measurement (RAM)-C III flight experiment in the 1960's. The computations were performed assuming real air in thermochemical **nonequilibrium**. Park's chemistry model for air is used. This model uses 11 species: 5 neutral species, 5 ionic species, and electrons. Figure 198 compares the computer results for the peak electron number density with the data measured axially along the body at Mach 33 at an altitude of 76.3 km (47.4 mi). The general trends and the magnitude are in very good agreement with experimental data.

The next objective of the present program is to improve the accuracy of the HANA code for very low-density (high-altitude) flows. As the freestream density is reduced, the continuum assumption breaks down first in the Knudsen layer, a region near the wall whose thickness is the local mean free path of the gas. The noncontinuum

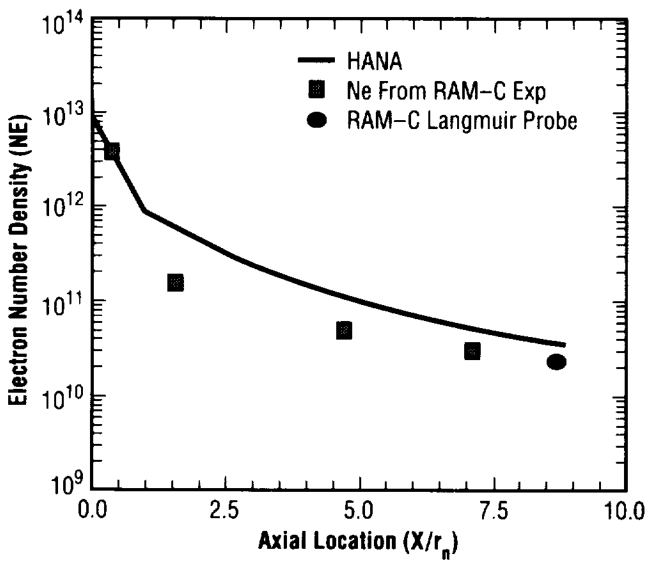

FIGURE 198.— Comparison of measured and computed peak electron number density in the boundary layer of the RAM–C III probe.

behavior of the flow in the layer may be approximated by using surface slip boundary conditions, which specifies jumps in velocity, temperature, and species concentrations at the wall. The surface slip boundary conditions in HANA are being generalized and improved. A second aspect of very low-density flows is that the thickness of the shock wave is significant. The **Navier-Stokes** equations do a poor job of modeling the detailed shock wave structure, but recent studies have shown that the Burnett equations, which extend the **Navier-Stokes** equations, in combination with rotational **nonequilibrium**, do a comparatively good job.[3] Therefore, the augmented Burnett terms are being added to the viscous stress and heat conduction terms in the HANA code, and a transport equation is being added for the rotational energy of the molecules.

[1]Eberhardt, S., and Imlay, S., "A Diagonal Implicit Scheme for Computing Flows with Finite-Rate Chemistry," AIAA Paper No. 90–1577, June 1990.

[2]Imlay, S.T., Roberts, D.W., and Soetrisno, M., "Nonequilibrium Thermo-Chemical Calculations Using a Diagonal Implicit Scheme," AIAA Paper No. 91–0468, January 1991.

[3]Lumpkin, F.E. III, and Chapman, D.R, "Accuracy of the Burnett Equations for Hypersonic Real Gas Flows," AIAA Paper No. 91–0771, January 1991.

C.M. Seaford/ED33
(205) 544–1596
Sponsor: Office of Commercial Programs, Small Business Innovation Research

Computational Fluid Dynamics Methodology for Fast Transients

Analysis of nonlinear combustion instability problems requires the use of nonoscillatory, high-accuracy numerical algorithms. Development of numerical methods for the treatment of high-speed flows has received much attention during the last 10 yr. Methods are now available that are capable of simulating compressible flows in two and three dimensions in complex geometries. A comprehensive assessment study was performed under a phase I Small Business Innovation Research (SBIR) project in which all advanced shock capturing **computational fluid dynamics** (**CFD**) techniques were implemented and tested for one-dimensional test problems, such as shock tube and resonant tube simulations.[1,2] In the present project (follow-up phase II SBIR), selected schemes are being further developed and tested for two- and three-dimensional flows.

The algorithms being used in the study are of second-order accuracy in time and, at least, second-order accuracy in space, and include the total variation diminishing (TVD), essentially nonoscillatory (ENO), and Godunov approaches. Some of the results have been presented at the Ninth **Computational Fluid Dynamics** Working Group Meeting, held at NASA MSFC, April 16–18, 1991.

Figures 199 and 200 show samples of simulations that have been performed for the purpose of algorithm comparison. Figure 199 shows transient reflection of a strong shock off a solid boundary. Of particular importance is the correct presentation of the flowfield near the solid boundary and the formation of the unstable jet.

Figure 200 shows the nonlinear resonant acoustics within a chamber cross section in the form of multiple wave reflections induced by an initially plane pressure wave. The scattering of a plane wave by the curved walls prevents formation of shocks and leads to formation of large-amplitude, undissipative pressure waves. Existence

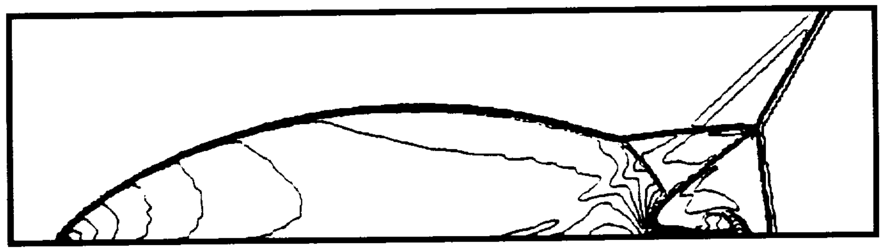

FIGURE 199.— Strong shock reflection off a solid boundary. Density contours for second-order Godunov method CFL=0.8.

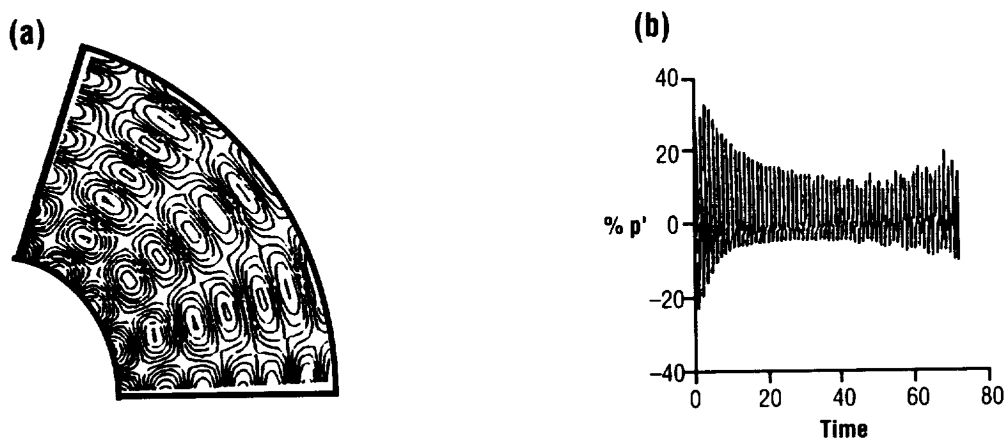

FIGURE 200.— Propagation of an initially plane wave in an annular cylinder. (a) Density contours at later stages. (b) Pressure history on a cylinder wall.

of such pressure waves can have an adverse effect on the performance of liquid rocket engines; therefore, it is essential that a numerical simulation can correctly account for the formation and behavior of such pressure waves. The data represented by figure 200 were generated using third-order Chakravarthy-Osher TVD at CFL=0.6.

[1]Przekwas, A.J., Yang, H.Q., McConnaughey, P., and Tucker, K., "Assessment of Shock Capturing Schemes for Resonant Flows in Nonlinear Instability Analysis," AIAA-90-2358, 1990.

[2]Yang, H.Q., Pindera, M.Z., and Przekwas, A.J., "Assessment of Advanced Numerical Schemes for Multidimensional Fast Transient Compressible Flows With Moving Waves and Discontinuities," 9th Annual CFD Working Group Meeting, NASA MSFC, 1991.

G.A. Wilhold/ED31
(205) 544-2651
Sponsor: Office of Commercial Programs, Small Business Innovation Research

Cyclic Plastic Crack Growth Prediction

High-performance space propulsion systems, such as the space shuttle main engine (SSME), are required to operate under severe loading conditions that frequently extend beyond elastic material response. Therefore, **fracture-mechanics**-based **life predictions** must consider the **elastic-plastic** and fully plastic regimes of **crack growth**. Over the last 25 yr, a large volume of research dealing with **crack growth** in the **elastic-plastic** and fully plastic regimes has been accomplished. Unfortunately, no single governing parameter has been identified that is widely accepted for the **elastic-plastic** and fully plastic regimes, like the stress intensity factor K for the elastic regime. Present analytical tools do not confidently provide the ability to perform life analysis on SSME components loaded well beyond elastic response. Although controversial from a theoretical viewpoint, the cyclic extension of the **J-integral** and ΔJ and its variants are the most widely used parameters for cyclic **crack growth** outside the elastic regime.

The objectives of this research program are to develop new solutions of the **J-integral**, to develop practical algorithms using ΔJ and its variants for **cyclic plastic crack growth** analysis, and to develop a verified analytical tool for structural engineers. In addition, the theoretical controversy in applying ΔJ beyond its mathematical limits will be studied by evaluating other proposed governing parameters used in the **elastic-plastic** and fully plastic regimes that are more complicated to formulate and use.

A comprehensive literature review of the use of the **J-integral** in **elastic-plastic** and fully plastic regimes of monotonic **crack growth** will be conducted with the goal of developing a library of existing **J-integral** solutions. New solutions that enhance the applicability of the **J-integral** and ΔJ and its variants for monotonic and cyclic **crack growth** will be developed. The solutions to problems of interest in SSME analysis will be emphasized.

Algorithms that enhance the use of **J-integral** and DJ and its variants will be developed. The effects of crack closure, stress ratio, stress amplitude, and material properties on crack opening and closing behavior will be considered. Schemes to incorporate this information into the estimation of governing parameters will be developed. Practical algorithms for calculating cyclic **crack growth** under variable load histories will be developed. Interaction effects resulting from crack closure, plastic strain, and residual stresses near the crack-tip will be considered. A major task will be to account for combined loadings, time, and temperature effects. Prediction of the onset of final crack instability resulting in failure will be developed. Laboratory test data and analytical methods will be used to establish limits and accuracy.

Other existing candidate parameters will be reviewed. The suitability of a parameter to correctly characterize the crack driving force in a theoretical sense and to predict cyclic **crack growth** for **elastic-plastic** and fully plastic regimes will be evaluated. Additionally, the suitability of a parameter for estimation and ease of calculation will be evaluated. A relative ranking of the existing parameters will be made.

C.D. Wilson/ED25
(205) 544–5430
Sponsor: Office of Aeronautics, Exploration and Technology

Design of Portable Powered Seat Lift Prototype

The need to develop a portable device to assist persons with **degenerative hip or knee joints** in sitting and standing was identified to the MSFC **Technology Utilization** Office. During research and brainstorming of seat lift concepts, guidelines for the range of motion required were established by conducting a video tape study of several people standing and sitting in front of a grid. The result of the study indicated that the sitting and standing motions even for people of average height require a large range of motion from an assist device. This is the largest driver of the mechanism design.

With the knowledge of the large range of motion required from a compact machine, the conceptual design effort for the **portable powered seat lift (PPSL)** was initiated using concepts and research of gear, motors, and pneumatic and hydraulic systems. Research began for a suitable mechanism by setting a couple of groundrules for the operation of the **PPSL**. The first of these was the control method; the user had to be able to rely on the **PPSL** for support during the entire lift cycle, even if the user decided to stop after rising up halfway. This meant that the mechanism had to be rigid and become completely immobile when the switch was released, which drove the design to a purely mechanical linkage and away from pneumatic actuation. An electric motor driving through a large gear reduction was chosen. The least expensive and most powerful direct current (dc) motor available was obtained from a hobby shop. This motor,

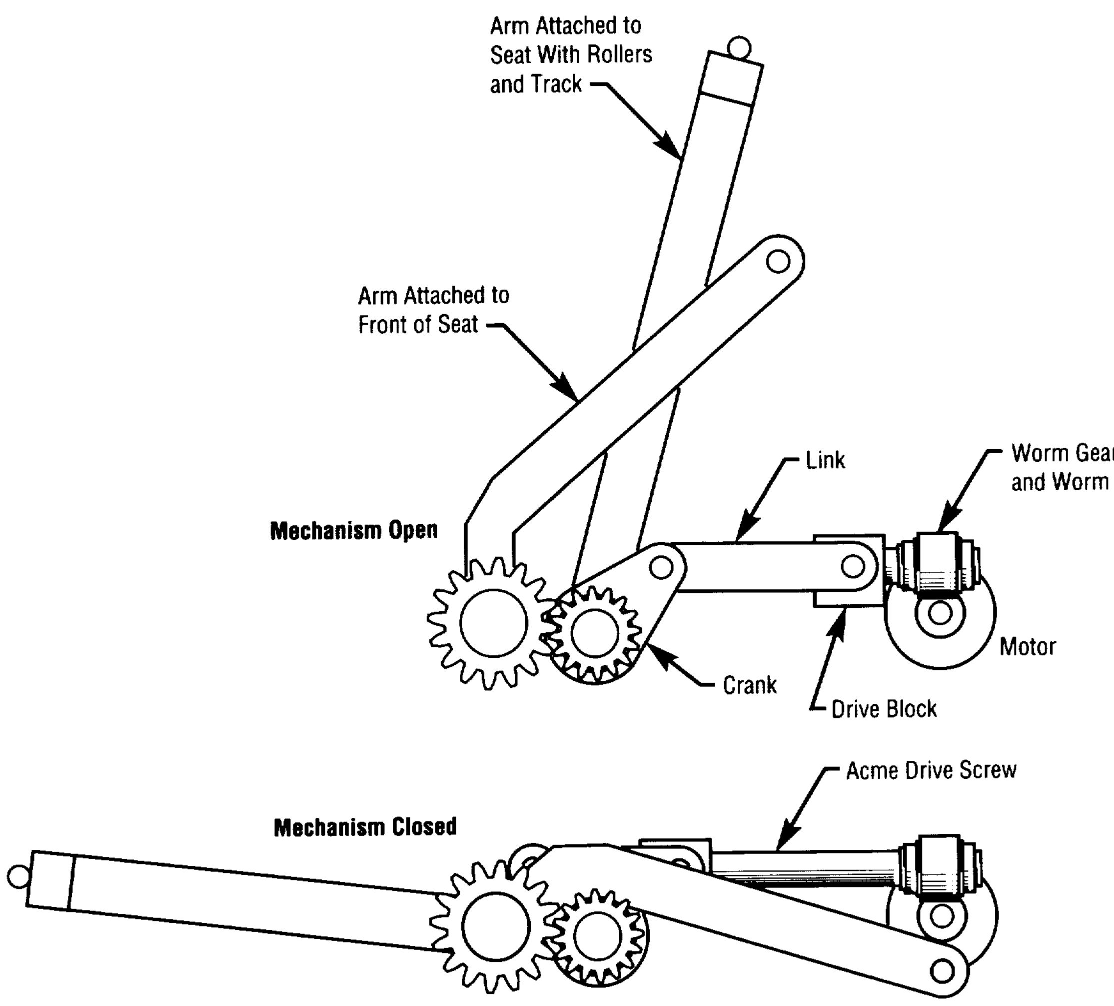

FIGURE 201.—The linkage mechanism of the PPSL.

intended for use on model planes, is lightweight and uses standard, readily available, rechargeable batteries. The next ground rule of the design was simplicity—reduce the number of parts to an absolute minimum. The design had to be a simple, rugged, one degree-of-freedom mechanism capable of lifting a 300–lb person to nearly standing and folding to a maximum thickness of 2.5 in. The linkage chosen to meet these criteria is illustrated in figure 201. The major components are the two integral arm-shaft pieces, which provide the moving link between the base and the top of the **PPSL**. To maximize the range of motion, the arms cross over, with the forward arm being part of the rear shaft and vice-versa. This allows the arms to be longer, thus allowing the top of the seat to rise more as the arms sweep up towards each other. To achieve a positive one degree-of-freedom of the linkage, the two shafts are geared together with spur gears integrally machined into them. The gear ratio between the shafts was selected to provide the appropriate steep tilt angle of the seat at its fully extended position. This gearing also requires that only one of the shafts be driven to operate the linkage. The system chosen to perform this task is a version of the crank-slider mechanism in which the shaft is turned by crank arms welded to it; the crank arms are driven by links pinned to them and to a drive block. The drive block is constrained to move along a track and is driven by an Acme screw running through its center. The screw is turned by a worm gear that is integrally machined onto its end, and the worm gear is turned by a matching worm fixed to the motor shaft.

The overall outward appearance of the **PPSL** (fig. 202) is not unlike a thin brief case that the user would carry by the handle and lay down on the seat before sitting. The user would then have the option of using the **PPSL** to assist in sitting by first raising the seat with the control switch, or simply sitting on the folded unit. When the user decides to stand, the user simply grasps the built-in handholds at the rear corners, and operates the control switch that is located under the right handle. The seat then rises, lifting the user to nearly standing in 5 to 10 s. Soft foam edges protect the user's fingers if they are shut in the **PPSL** as it lowers, and thin foam set padding will provide some comfort while seated.

The drawings for this prototype are complete, and a working model will be fabricated to serve as a demonstration tool.

B.C. Weddendorf/ED52
(205) 544–4304
Sponsor: Office of Commercial Programs,
Technology Utilization Office

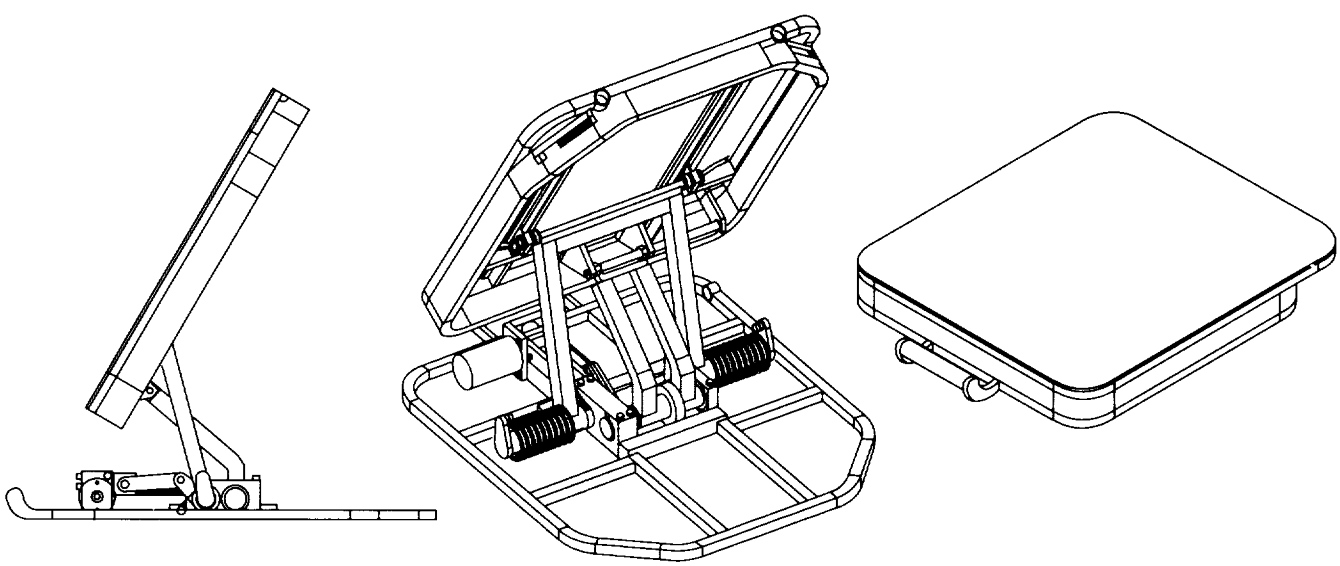

FIGURE 202.—The overall outward appearance of the PPSL.

Development of State-of-the-Art Proof-Test Methodology

The Durability Analysis Branch (ED25) of MSFC has, for some time, had an interest in **proof-testing** methodology, especially as it relates to components of the **space shuttle main engine** (SSME). Most components of the **SSME** (including the main combustion chamber, the powerhead, and the turbopumps) undergo proof testing to ensure their structural worthiness. A thorough understanding of proper **proof testing** methodology is vital for ensuring safe, reliable operation of these and other critical **SSME** components.

The primary objective of **proof testing** is to verify the quality of a component, especially those of the type mentioned in the previous paragraph. Testing is used by ED25 to check the various attributes that contribute to the overall quality of an engine component, such as: workmanship, analysis validity, and material quality assessment.

The third item, material quality assessment, is of particular interest to ED25. Among other things, this item particularly relates to the issue of screening for cracks that have the potential for propagation to failure during normal service. To account for these cracks in the material, the discipline of **fracture mechanics** must be employed.

A **proof test** is usually conducted alongside a nondestructive evaluation (NDE) (to inspect for cracks) and a **fracture mechanics** analysis (to determine the critical crack length at which the crack can no longer withstand both the **proof testing** and service conditions). During a **proof test**, a proof load (a prescribed overload) is applied to the **SSME** component. This load is sufficient to cause a certain crack growth or lengthening. Should this proof load cause the part to either structurally fail, or to develop cracks (as determined by NDE) that exceed the critical crack length (as determined by **fracture mechanics**), then that part is considered to have failed its **proof test**. However, there is a weak link to the approach just described. There are many possible variables that can affect the accuracy of the estimated critical crack length whose influence on the **fracture mechanics** analysis and on **proof testing** is not fully understood.

The Durability Analysis Branch (ED25) at MSFC has begun to take steps to correct this deficiency. ED25 has initiated a procurement request with the eventual goal of awarding a contract to develop a state-of-the-art **proof-testing** methodology that can be applied to the **SSME**, as well as to future rocket motors. The scope of this investigation will be limited to metal components of the type found in the current **SSME**. The eventual goal of this contract is to produce a document that can assist an engineer in developing an optimum **proof-test** plan for the component in question.

It will take a significant effort to develop a **proof-test** philosophy as outlined above. The following must be accomplished in order to have a state-of-the-art **proof-test** methodology:

- Review current **fracture mechanics** techniques, **proof-test** variables, and structural geometry considerations as to their impact on proof testing, as shown in figure 203;
- Select which items in figure 203 will be the most suitable for use in a **proof-test** philosophy
- Prepare an actual methodology to utilize the items selected from figure 203
- Develop and implement a test program to establish the validity of the testing philosophy proposed in the third step
- Write a **proof-test** methodology handbook based on conclusions from the test program.

- R-curve approach to proof test evalution
- Number of proof-test cycles
- Proof test load factor
- Proof hold times and stable crack growth
- Selection of test fluid and temperature
- Effect of proof test on fatigue crack growth
- Crack growth through two different materials (welded)
- Pre- and post-test NDE requirements
- Damage accumulation
- Pre-existing flaw populations
- Overload retardation
- Material variability with emphasis on tough ductile ones
- Effects of complex geometries
- Thickness

FIGURE 203.—Proposed proof-test parameters.

The contractor to develop the **proof-test** philosophy, as outlined above will be selected by fall 1991. The contract should be completed by fall 1995.

C.L. Denniston/ED25
(205) 544–7248
Sponsor: Office of Aeronautics, Exploration and Technology

Empirical Prediction of Pressure Wall Temperature Change Due to Hypervelocity Impact Damage to Multilayer Insulation

The manmade orbital debris environment poses a threat to all orbiting spacecraft. Since the great majority of orbital debris cannot be avoided, the current approach is to place a shield around the spacecraft to reduce the effects of the orbital debris impact. The shield breaks up the incoming particle thus dispersing the material over a wider area and reducing the energy density (energy per unit area). Because of this dispersion, the impacts that penetrate the shield will cause a significant amount of damage to the spacecraft's **multilayer insulation** (**MLI**).

The object of this project is to develop a user-friendly, graphically interfaced, microcomputer-based program, **MLITemp**, that will predict the temperature rise or drop of the pressure wall of Space Station *Freedom* due to hypervelocity impact damage to the **MLI**.

Thermal degradation tests of damaged **MLI** from **hypervelocity impacts** in the thermal vacuum chamber at MSFC were performed at the beginning of FY91, and the computer code **MLITemp** is being developed based on interpolations/extrapolations of the results from these thermal tests.

Pressure wall temperature changes will be predicted considering the location of the damage on the spacecraft and the position of the spacecraft relative to the Sun and Earth. A finite difference technique is used to calculate the temperature profile in the spacecraft pressure wall based on **MLI** damage predictions. **MLITemp** also predicts the rate of condensate formation, which can lead to electrical and fungus growth problems. This program will be completed by August 1991.

K.B. Hayashida/ED52
(205) 544-4308
Sponsor: Office of Space Flight, Space Station *Freedom*

Expendable Lightweight, Low-Cost Composite Intertank

As the United States develops a new launch system to complement the space shuttle and to meet foreign competition, **composite** material can play a vital role. The structural element selected to demonstrate this is the **intertank**. The **intertank** is the section of the vehicle between the oxidizer tank and the fuel tank. A structurally efficient **intertank** has the synergistic effect of requiring less propellant and results in an overall smaller, more efficient vehicle. Since the **intertank** stays with the vehicle all the way to orbit, more payload can be delivered to orbit with a lighter **intertank**. The **composite intertank** can also be built by an automated process. Preliminary studies show the **composite intertank** with a low-cost option, as compared to a traditional metal **intertank**.

The reference vehicle (fig. 204) is similar in size and layout to the space shuttle's external tank. The liquid hydrogen fuel tank stands as the base, the **intertank** is in the middle, and the liquid oxygen oxidizer tank is stacked on the **intertank**. The reference vehicle also has engines mounted on the bottom of the fuel tank and the payload mounted on top of the oxidizer tank. The **intertank** is a primary load path for the entire vehicle, supporting the heavy oxidizer and payload while handling flight

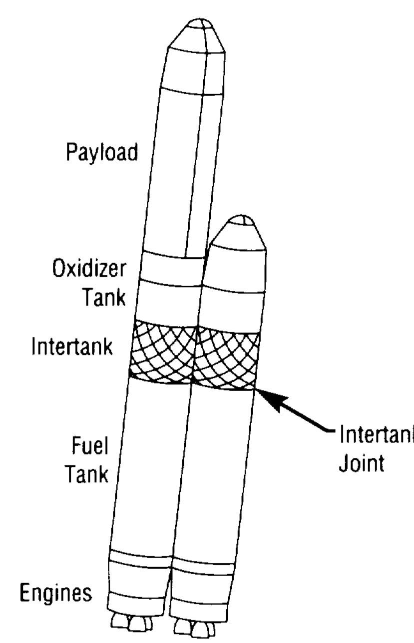

FIGURE 204.—Reference vehicle.

bending loads. The critical portion of the **intertank** is the joint region. The **intertank** joint provides the mechanical attachment to the fuel tank at cryogenic conditions.

A honeycomb sandwich is considered the best construction technique for this application. **Composite** sandwich skins meet the strength requirements, and an aluminum honeycomb core provides ample load transfer between the skins. In the joint region, the honeycomb is truncated, and the **composite** skin is built up to manage the flexure loads.

Honeycomb sandwich construction also lends itself to automated fabrication. Automated fabrication greatly reduces the man-labor usually associated with **intertank** construction, which reduces cost. Another major low-cost and bold manufacturing approach is using a nonautoclave cure. While highly loaded **composite** structures typically undergo an autoclave cure, no existing autoclave is capable of containing the large diameter **intertank**. Therefore, the **intertank** design incorporates vacuum-bag jacket pressure in an oven cure process.

Based on a set of preliminary test panels, an enhanced design has been established. A set of panels, like the panel shown in figure 205, will be fabricated to exhibit an automatic **tape-laying** capability to produce the structure within design tolerances.

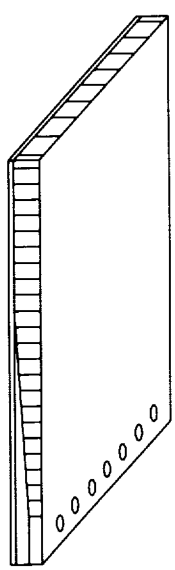

FIGURE 205.—Intertank joint test panel.

Benefits from this study apply to more than space vehicle structures. Any project could take advantage of considering use of **composites** for primary structure, automated layup, and nonautoclave cure.

D.B. Ford/ED52
(205) 544–2454
Sponsor: Office of Space Flight, National Launch System

FRACTURE MECHANICS LIFE ANALYTICAL METHODS VERIFICATION TESTING

The critical components of oxygen (O_2)/hydrogen (H_2) components, such as the space shuttle main engine (SSME), are to be designed for several hours of life in numerous environments and stress fields. The NASCRAC™ computer code was developed to accurately predict life in critical components based on flaw growth concepts. The code must give efficient and accurate results to predict the serviceability and lifetime of hardware. In order to report life predictions with confidence and reliability, the computer code itself must be thoroughly verified. **Fracture mechanics** test verification methods, procedures, and specimens are being developed and/or tested to verify the NASCRAC™ code. Two methods of approach will be utilized: perform the new test to compare with code results, and analyze existing data and compare with code results.

The following types of analyses are to be verified:

- "a" versus "k" calculations
- "a" versus "J" calculations
- Life calculations by fatigue **crack growth**
- Calculation of tolerable crack size
- Calculation of crack opening area
- Life calculation by creep **crack growth**
- Proof-test logic
- Tearing instability.

Verification testing of the above will include simple and complex loadings, variable thickness effects, multi-degree-of-freedom (DOF) **crack growth**, finite width effects, crack front shapes, stress gradients, low- and high-cycle fatigue, and crack transitioning. All stress intensity and J-integral solutions contained in the code (fig. 206) will be verified.

The code currently contains capabilities for analysis of **crack growth** under spectrum loading by the use of the Wheeler and Willenborg retardation models. These two models will be test-verified by using multi-DOF cracks under complex loadings. The observed fatigue life will be compared to that predicted by NASCRAC™.

Standard specimens

+ Compact tension specimen
  Round compact-type specimen
  Arc-shaped specimen
  Standard three-point bend specimen

Through-thickness cracks in planar bodies

+ * Crack in an infinite plate
+ * Center-cracked panel
+ * Single-edge crack in a plate
+ * Double-edged crack in a plate
+ * Axial (inside) crack in a hollow cylinder
  * Radial crack (inside) in a hollow disk
  * Radial crack (outside) in a hollow disk
  Through crack from hole in a finite plate
  Through crack from hole in a lug

Through-thickness cracks in "shells"

Through crack in a sphere
Through crack in a cylinder—axial
Through crack in a cylinder—circumferential

One DOF cracks in bodies of revolution

+ * Circumferential crack (inside) in a hollow cylinder
  Circumferential crack in a solid cylinder
  Circumferential crack (outside) in a hollow cylinder
  Edge rack in a solid circular bar

Buried cracks

* Buried elliptical crack (4DOF)

Corner cracks

Quarter-circular crack from hole in a plate
Quarter-circular crack from hole in a lug
* Quarter-elliptical corner crack in a plate

Surface cracks

* Semi-elliptical surface crack in a plate
* Semi-elliptical surface crack (inside) in a hollow cylinder

User-defined crack depth versus k-tables

User-defined a_1 versus k-tables

User-generated influence functions

* Denotes a solution that includes influence functions
+ Denotes j-solutions

FIGURE 206.—Summary of stress intensity and J-integral solutions in NASCRAC™.

The NASCRAC™ code also provides for calculation of redistribution of stresses due to plasticity in the vicinity of a stress concentration. The elastic-plastic stress redistribution feature in the NASCRAC™ code allows calculation of **stress intensity factors** and computation of fatigue life for structural details that have experienced localized yielding prior to cracking. This feature is applicable to cases of localized or contained plasticity. The stress strain fields near a notch with a circular root or other stress concentration under monotonic loading and under cyclic loading will be measured from strain gauges located on the specimens. The measurements will be compared to results from elastic-plastic finite element models and NASCRAC™ predictions. Both the Neuber and equivalent energy methods incorporated in NASCRAC™ will be evaluated.

The growth of a crack introduced after shakedown to elastic conditions (then grown under cyclic loading) will then be compared with NASCRAC™ predictions. A literature survey of the growth of cracks from stress concentrations loaded into the plastic zone will then be performed and compared with NASCRAC™ predictions.

Failure Analysis Associates: NASCRAC™, NASA Crack Analysis Code.

R. Stallworth/ED25
(205) 544–7189
Sponsor: Office of Aeronautics, Exploration and Technology

Ground Test Facility Development

The objective of this program is to develop a **ground test facility (GTF)** in which large structures characteristic of future space platforms can be analyzed and controllers can be designed and tested. Key **control structure interaction (CSI)** methodologies will be demonstrated in the **CSI GTF**. The initial structural configuration in the **CSI GTF** will be that of the proposed **controls and structures experiment in space (CASES)**. The **CASES** experiment is a proposed space shuttle-based flight experiment in which a 32–m (105–ft) boom supports an occulting plate that points towards a star to perform an x-ray experiment. The control objective is to maintain alignment of the occulting plate at the tip with the detector at the boom base on the space shuttle. Control authority is provided by two-axis thrusters at the boom tip, a two-axis set of angular momentum exchange devices (AMED's) at a mid-point on the boom, a three-axis set of AMED's at the boom tip, and a roll tip motor.

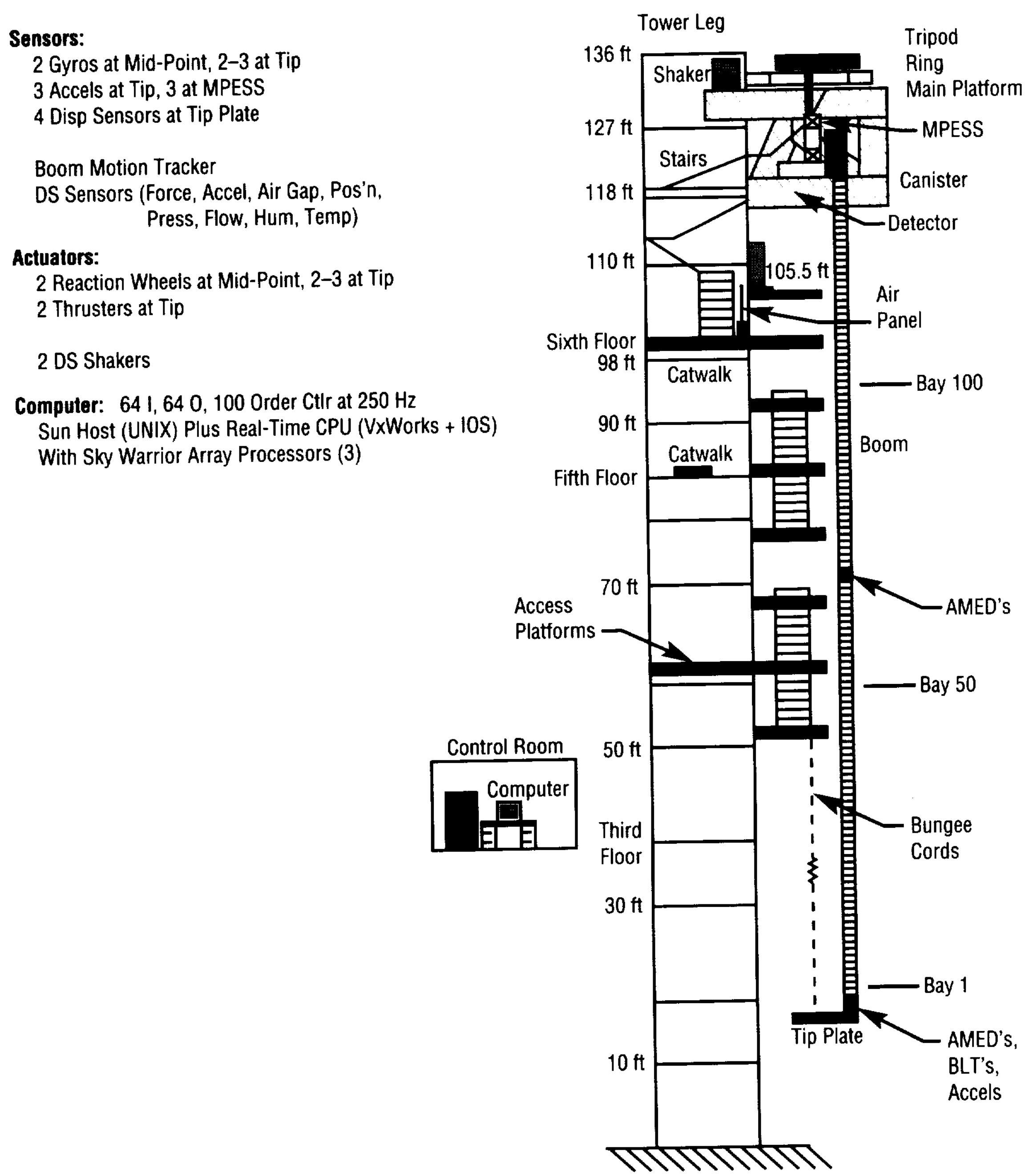

FIGURE 207.—Schematic of the CSI GTF.

Primary objectives of the flight experiment are to investigate **CSI** methodologies applied to a large space structure (LSS), to perform guest investigator (GI) programs to test and evaluate LSS control and system identification (ID) techniques, and to enable comparisons between ground predictions and flight results.

Figure 207 is a schematic of the **CSI GTF** in the **CASES** configuration. Except for the roll tip motor, this will be the baseline **GTF** configuration. The primary focus of the activity associated with the **CSI GTF** development over the last year has been the integration of the various structural components comprising the facility. The major facility modifications are complete. The main platform, 6.7×7.6 m (22×25 ft), at the 40–m (132–ft) level supports the entire system (e.g., disturbance system and experiment). Eight access platforms, 2.4×2.7 m (8×9 ft), with stairs and ladders provide access to the upper portion of the boom. The test article is the 32–m (105–ft) solar array flight experiment-I (SAFE–I) boom, which was modified in 1990 for the **GTF**. Modal and dynamic deployment tests on the boom were completed this year, with the resulting data used for refinement of the **GTF** computer models.

The boom is attached to a simulated mission peculiar experiment support structure (MPESS). **Modal tests** on the MPESS were performed prior to attaching the boom canister. The MPESS/boom configuration is attached to a tripod that floats on an air-bearing system, which consists of an epoxy-filled ring and three air bearings mounted to the tripod. The tripod supports the experiment through the simulated MPESS and the ring provides a flat surface on which the air bearings float. The tripod, ring, air bearings, and the MPESS and boom were all lifted into place on the platform in early 1991. Disturbances are provided via two electromagnetic shakers that move the tripod. A mechanical interface to connect the shakers to the tripod has been designed, the components have been obtained, and integration has been initiated. The disturbance system will be fully operational in July 1991.

Two orthogonal thrusters will be used primarily for pointing the boom in the flight experiment, but will be used for **vibration suppression** in the ground experiment. Three bidirectional linear thrusters have been designed, obtained, and tested. The AMED's will be used for **vibration suppression** at a midpoint and at the tip of the boom. The midlength AMED package will consist of two motors attached to reaction wheels and 2 two-axis gyros. The tip AMED package will have three motors with reaction wheels and 2 two-axis gyros. The AMED's have been designed and detailed mechanical drawings have been completed, with fabrication and integration currently in progress.

The custom-designed **real-time computer system** was delivered in January 1991. Computer integration into the facility is in progress. A number of custom electronic circuits including a multiplexer, a demultiplexer, filters, signal conditioning, AMED's electronics, and the power supply system have been designed, fabricated, and tested in the last year. Sensor integration is also on-going. It is expected that the baseline **GTF** configuration will be fully operational by the end of August 1991.

Detailed modeling and simulation of the **CSI GTF** have been completed. The finite element model of the tripod and ring has been developed and compared to the modal test results. The boom model has been developed and exercised. The TREETOPS dynamic system simulation code and Matlab simulations are used for evaluation of lab designs and for fine-tuning the final configuration.

A.P. Bukley/ED12
(205) 544–0054
Sponsor: Office of Aeronautics, Exploration and Technology

Joint NASA/MSFC-Sandia National Laboratories Hypervelocity Impact Testing

Due to the continuously growing and increasingly dangerous orbital environment, one of the primary design considerations for space structures is shielding systems to protect against **micrometeoroid and orbital debris (M/OD)**. The most recent **M/OD** environment model defines the average velocity or orbital debris to be 10.3 km/s (23,040 mi/h) and that of micrometeoroids to be 18 km/s (40,267 mi/h). As a result of this and preceding environment definitions, there has been great interest in evaluating shielding concepts at these velocities, but these impact velocities are not obtainable through conventional projectile launcher technology.

Recently, Sandia National Laboratories (SNL) demonstrated the capability to launch near 1-g (0.035-oz) flat plates to velocities in excess of 10 km/s (22,370 mi/h) through the use of a modified two-stage **light gas gun**. As a result of this demonstrated capability, NASA/MSFC and SNL established a joint effort to further develop this capability and to evaluate the performance of thin aluminum "Whipple" shields at impact velocities of 9.5 to 10.4 km/s (21,252 to 23,265 mi/h).

The test program conducted consisted of impacting thin aluminum Whipple shields with an aluminum flat plate traveling approximately 10 km/s (22,370 mi/h). Upon impact of the flat plate on the shield, a photographic record was created from the debris cloud formation, propagation across the standoff distance, and impact on the back wall structure. A photographic record was also created of the rear face of the back wall structure for evidence in the event of a perforation.

The Whipple shield concepts tested under the joint effort consisted of a 0.127-cm (0.050-in) 6061-T6 aluminum bumper with a 0.3175-cm (0.125-in) 2219-T87 aluminum back wall separated by a 10.16-cm (4.0-in) standoff. An additional test was conducted using a titanium flier plate.

The test has identified the **ballistic limit** (e.g., the point, identified by a combination of diameter and velocity of projectile, that will just penetrate the back wall structure) for this shielding system concept at 10.4 km/s (23,265 mi/h) to be a 12.7-mm (0.50-in) diameter by 0.88-mm (0.035-in) thick flat plate projectile. Traditionally, the **ballistic limit** curves have been defined for spherical projectiles; therefore, further analysis is required to convert the "critical" flat plate into an equivalent "critical" sphere.

In addition to the experimental portion of this program, SNL is also performing computational analyses of **hypervelocity** impacts from "critical" particles, as determined from the Wilkinson and Cour-Palais (1990) penetration equations, using a three-dimensional hydrodynamics code, CTH, which was developed by SNL. The results from these analyses are to be used to evaluate the accuracy of each penetration predictor. The results from the experimental tests will be used to "baseline" the CTH code to increase confidence in CTH analyses performed at even higher velocities.

S.A. Hill/ED52
(205) 544-4106
Sponsor: Office of Space Flight, Space Station *Freedom*

Lightweight Composite Heat Pipes

Weight reduction of **radiator** systems is essential for future space missions. Lightweight systems not only enhance payload capabilities but also offer improved heat rejection with minor weight impacts. **Heat pipes** are often integral components of these designs and can comprise significant portions of overall weight.

Heat pipe exteriors are typically constructed from aluminum tube and/or extruded aluminum shapes. Replacing these elements with **composite** materials in combination with aluminum powder wicks can result in weight savings. Under this NASA Small Business Innovation Research (SBIR) program, a prototype **composite heat pipe** was developed. The prototype consisted of a 25–mm (1–in) diameter tube, 610–mm (24–in) in length, constructed from carbon fiber/epoxy **composite**. The capillary wick was a polymer-bonded aluminum powder. Ammonia was selected as the working fluid for the prototype development.

Composite resin and working fluid compatibility was a major concern for this development. Testing on various resin samples indicated none were totally immune to the effects of anhydrous ammonia. To minimize working fluid contact with the resin, an aluminum foil liner was bonded to the **composite** tube's interior between the tube and capillary wick, as seen in figure 208. The foil lining also ensures the tube's vacuum capability and serves as a noncondensable gas barrier. The compatibility of epoxy resins and ammonia remains a concern and will be further assessed in future development testing.

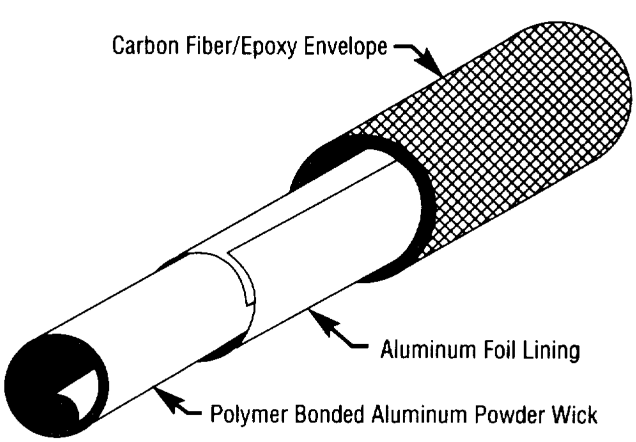

FIGURE 208.—Composite heat pipe construction.

Three designs of tube closures were investigated, including an end closure fabricated into the tube during the **composite** manufacturing process. However, due to the nature of the process, only one end of the tube could be closed by this technique. For prototype development, a domed aluminum cap was bonded to the tube ends' interior surfaces. This same type of aluminum-to-**composite** joint will be further developed to fabricate lengthy **heat pipes** from **composite** tube sections.

Performance testing of the **composite heat pipe** was conducted with a 5°, gravity-aided orientation. In this configuration, the prototype transported 370 W (1,260 Btu/h) with no indication of wick dryout. While the design was not optimized for performance, the results did indicate that (1) a **composite** pressure envelope was a viable alternative to aluminum tubing, (2) fabrication of polymer-bonded powder wicks was possible in **composite** tubes, and (3) vacuum tight end closures were demonstrated. Future development will address design optimization.

W.A. Till/ED63
(205) 544–7205

Sponsor: Office of Commercial Programs, Small Business Innovation Research

Mechanical Joints for In-Space Assembly and Construction

The objective of the in-space assembly and construction research and technology project is to develop the technology required to assemble and construct space vehicle components in orbit. A goal of this project is to minimize extravehicular activity (EVA) and maximize automation methods. The methods defined to meet these objectives are as follows: develop methods for constructing large vehicle components in space; develop joint concepts for constructing and assembling components in space; develop the ability to manipulate, position, and assemble large massive components in space; and define the infrastructure to accomplish the construction, joining, and assembly of vehicles in space.

MSFC has identified a 37–m (120–ft) diameter tetrahedral **aerobrake** truss as a focus problem. Using this **aerobrake** structure, requirements for developing joining methods and assembly concept technologies were developed.

The significant developed requirements were that each truss member be capable of supporting a ±444.8–kN (±100,000–lb) axial load, be assembled laterally, correct a misalignment (due to thermal, assembly, and manufacturing tolerances) of ±0.508 mm (±0.020 in), be **robot-compatible** and astronaut-compatible, and be lightweight. A mechanical joint was designed to meet these requirements, and seven joints were fabricated. Of these seven joints (fig. 209), three are 2219–T6 aluminum, two are 6AL4V titanium, and two are the advanced composite material silicon/carbide aluminum metal matrix composite (MMC). Two tests have been designed to determine the structural characteristics of the MSFC **mechanical joint** concept. The first test is designed to determine the ultimate load-carrying capability of the joint. The second test is a torque test to determine the amount of torque required to assemble the joint and provide the minimum required preload.

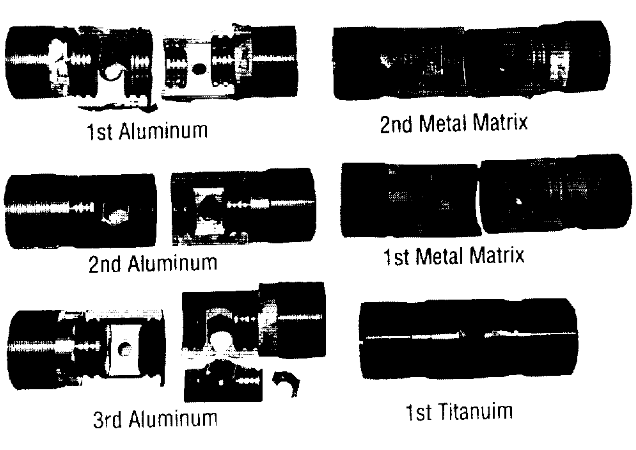

Figure 209.—MSFC in-space assembly and construction.

The results of the ultimate strength tests are found in table 11. (A titanium joint was tested to the ultimate capacity of the tensile/compression machine, ±533.7 kN (±120,000 lb), and no appreciable strains or displacements were recorded.) Fixture test hardware has been designed for a larger test machine to determine the ultimate load-carrying capability of the two remaining titanium joints.

Table 11.—*Joint torque to achieve 445 kN preload*

1st aluminum joint	240.2 kN (54,000 lb)
2nd aluminum joint	266.8 kN (60,000 lb)
3rd aluminum joint	422.5 kN (95,000 lb)
1st titanium joint	533.7 kN (120,000 lb)
1st MMC joint	311.3 kN (70,000 lb)
2nd MMC joint	471.5 kN (106,000 lb)

The torque test to determine the assembly and final torque requirements has been performed on all seven joints. The joint is designed to compensate for a ±0.508–mm (±0.020–in) axial misalignment. In this design, the **mechanical joint** is metallic, and the strut is a 381-cm (150.0–in) graphite epoxy tube with a modulus of elasticity of 275.7 kN/m^2 (40 Mlb/in^2). Approximately 22.2 kN (5,000 lb) is required to produce a deflection of ±0.508 mm (±0.020 in). A test has been designed to determine the torque required to provide this load. The test specimen was placed in a tensile test machine, and a 2.2–kN (500–lb) load was applied to the joint resulting in a gap between the two mating pieces. Then, the specimen was torqued until the gap was reset to its initial condition, and the torque was recorded. The load was increased to cause a gap increase, and, again, torque was applied to reset to the initial condition; the torque was recorded. This was continued until the load reached approximately 22.2 kN (5,000 lb). The torque required to assemble the joints ranged from 22.5 N/m (200 lb/in) to 45.2 N/m (400 lb/in), with the titanium being the easiest to assemble and the aluminum and MMC being the most difficult to assemble.

During the ultimate load test, a washer-type load cell was placed under the head of the bolt of the joint to record bolt load. The bolt-load versus applied-load was recorded. To effectively join structural elements, the amount of locking load (preload) should be greater than the maximum load the connection will experience, but less than the yield strength of the bolt. Using the data generated from the six ultimate strength tests, the torque required to achieve a preload of ±444.8 kN (±100,000 lb) is presented in table 12.

TABLE 12.—*Joint ultimate strengths*

1st aluminum joint	1,050.7 N/m (9,300 lb/in)
2nd aluminum joint	6,270.0 N/m (5,550 lb/in)
3rd aluminum joint	Data not compiled
1st titanium joint	813.4 N/m (7,200 lb/in)
1st MMC joint	406.7 N/m (3,600 lb/in)
2nd MMC joint	728.7 N/m (6,450 lb/in)

F.P. Thomas/ED52
(205) 544–4936
Sponsor: Office of Aeronautics, Exploration and Technology

Multibody Modeling, Verification, and Controls

The primary focus of the 5–yr multibody modeling, verification, and controls (MMVC) program, initiated in November 1990, is the verification of the **TREETOPS** analysis code via experimental data to be obtained in the MMVC laboratory under development at MSFC. **TREETOPS** is a menu-driven program used to model and analyze **flexible multibody structures** exhibiting either open- or closed-tree topologies. The menu program also provides the facility to provide gains for a standard proportional-plus-integral-plus-derivative (PID) controller or to include a user-defined controller. The verification process is a key step in advancing toward the computational controls activity, also conducted under this research and technology program, which will enhance the **TREETOPS** suite of routines to include various model reduction techniques, improved computational efficiency, thermal effects, and expanded controller design capability to include inverse dynamics and **model reference adaptive control**. Figure 210 depicts in flow-chart form the general methodology to be employed in the MMVC program.

TREETOPS embodies many complex **modeling features** that must be validated for various **multibody** configurations. Some of the features to be examined are body flexibility to include large motions with small and large flex, interface degree-of-freedom to include point and line interfaces undergoing translation and rotation, geometric stiffness to include gravity and foreshortening, and constraints to include prescribed motions and closed-tree topologies. The top-level design of a basic set of experiments that emphasizes critical **modeling features** presently included in **TREETOPS** is completed. Beginning with a simple single-beam experiment and expanding to multiple beams, joints, and various topologies, the experiments will grow in complexity as each modeling feature is examined. The final experiment will feature a test article traceable to an Advanced X-Ray Astrophysics Facility (AXAF) –type flight vehicle. Detailed designs of the experiments are in progress.

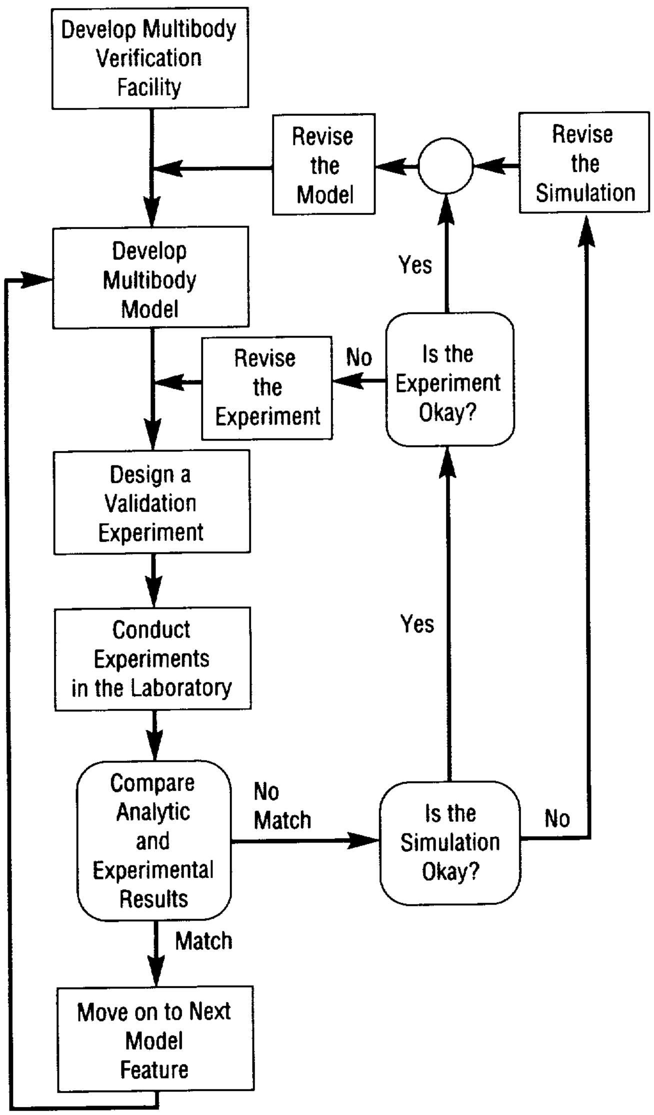

FIGURE 210.—MMVC methodology.

Critical to the experiments is the design and development of a test facility. A facility concept plan has been developed that details three candidate configurations for the test article support structure. After conducting modal tests on the platform on the west side of the control room between the high bays in building 4619 (on which the MMVC experiments will be conducted), the optimal configuration for the experiment support structure has been determined. Additional structure will be added to the platform to provide a support for the test articles. The final facility concept plan is in draft form. Detailed experiment support structure designs based on the modal test data and simulation analysis are in progress.

A **real-time closed-loop system (RTCLS)** will be an integral part of the laboratory. Its function will be to process the sensor inputs, implement the controller, and provide the **real-time** output signals to the actuators. The basic design of this system has been completed and component selection is in progress. Integration of the **RTCLS** will be accomplished by early 1992.

A.P. Bukley/ED12
(205) 544–0054
Sponsor: Office of Aeronautics, Exploration and Technology

Plume Impingement Evaluator

Research is being conducted to develop a **vacuum plume impingement** evaluator using the **plume impingement computer program (PLIMP).**[1] The **PLIMP** code simulates a complex configuration as a series of simple shapes, and computes the impingement environment by orienting the surfaces (shapes) in a rocket **exhaust plume**. The evaluator provides an analyst with the capability for rapid assessment of thruster impingement scenarios, thus offering a spacecraft or satellite designer an opportunity to simulate and assess impingement effects on hardware prior to flight. The research was divided into three areas: code modification/validation, graphics development, and plume handbook.

PLIMP modifications and enhancements have been made to provide more detailed output information, metric input/output options, improved shading, and the ability to order and analyze two-phase impingement solutions in a single execution. The **PLIMP** code was modified to accept plume flowfields generated using the source flow plume model generator (SFPGEN). The advantages of using SFPGEN to produce a flowfield for **PLIMP** are: the flowfield is portable between different computers; the flowfield requires considerably less computer storage than existing flowfield solutions; the **PLIMP** calculations are faster; and the source flow plume can be determined for much larger distances than are practical using other codes.

Selected analytical/experimental data comparisons have been performed to demonstrate the validity of the analytical (**PLIMP**) approach to plume impingement analysis. One comparison case involved tests conducted at the Arnold Engineering Development Center Rocket Test Facility J2A Test Cell[2] to determine the thermal and pressure effects of rocket-exhaust impingement on surfaces at 300,000–ft simulated altitude. A flat plate was placed at various angles and distances from the rocket and was subjected to the exhaust plume. Heating rates and surface pressures on the flat plate for three experimental test configurations were analyzed.[3] Good agreement between the analytical results and experimental data was obtained as shown in the heating rate comparison of figure 211.

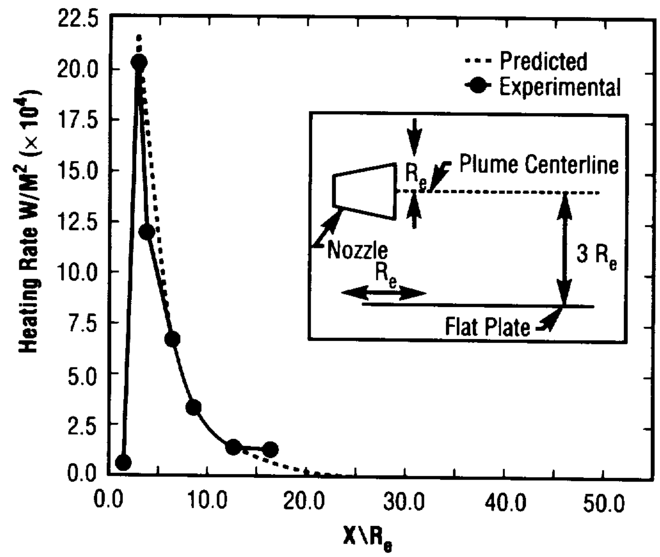

FIGURE 211.—Analytical/experimental heating rate comparison along the engine centerline.

One objective of this research was the development of a pre/post processing graphics system utilizing the enhanced **National Center for Atmospheric Research (NCAR) graphics** package. The enhancement enables the user to view three-dimensional (3–D) geometric object(s) with color contours representing surface conditions such as temperature, pressure, heating rate, etc. Previously, NCAR did not have a 3–D general surface drawing capability. The developed software assumes the surface to be composed of N polygons, each read into the algorithm and depth-sorted according to the projection of its centroid onto the eye Z-vector. Once sorted, the polygons are projected onto the eye vector's X-Y plane for screen drawing. The color contours are determined by varying the hue as a function of the intensity of the surface condition parameter. Each individual plane is assigned a color; no interpolation is performed.

The preprocessing graphics system provides the capability to view the individual shapes or the composite body (with or without shading) prior to **PLIMP** execution to ensure correct model geometry. **PLIMP** output was modified to read directly into the postprocessing subroutines, which generate vertices, depth sort, and draw to the screen. The user can type the ONE command to execute the entire graphics package.

A plume handbook detailing the processes necessary to perform rapid assessment of plume impingement scenarios is the principal output of this research. The handbook will consist of two volumes: one volume will describe the overall process of generating plume impingement environments with **PLIMP** from various plume flowfield sources, and the second volume is an updated **PLIMP** specific input/output guide.

One objective in developing the handbook was to establish a data base of precomputed plume flowfields that can be used by **PLIMP** to predict high-altitude, plume-induced environments. This will provide quick-look assessment capability for common plume impingement problems. Examples of some of the plume flowfields included in this data base through on-line storage or tape/hard disk are: space shuttle reaction control system (RCS), space shuttle main engine (SSME), space station RCS, orbital maneuvering system (OMS) RCS, and aeroassist flight experiment (AFE) RCS. A list of available plumes will be provided in volume 1.

[1]Wojciechowski, C.J., and Penny, M.M., "Development of High-Altitude Plume Impingement Analysis for Calculating Heating Rates, Forces, and Moments," Lockheed Missiles and Space Co., Huntsville, AL, LMSC–HREC D162867–1, March 1971.

[2]Piesik, E.T., Koppang, R.R., and Simkin, D.J., "Rocket-Exhaust Impingement on a Flat Plate at High Vacuum," J. Spacecraft, vol. 3, No. 11, November 1966.

[3]Prendergast, M.J., "Analytical/Experimental Data Comparison of Rocket-Exhaust Impingement on a Flat Plate at High Vacuum," REMTECH Technical Note RTN 214–01, November 10, 1990.

P.R. Sulyma/ED33
(205) 544–1601
Sponsor: Office of Commercial Programs, Small Business Innovation Research

Pre- and Postprocessing Techniques for Determining Goodness of Computational Meshes

Numerical modeling techniques have become indispensable in the study of almost all types of engineering phenomena. Three of the most common techniques—**finite difference**, **finite volume**, and **finite element** methods—have been applied to a wide range of boundary value problems, particularly in the solid and fluid mechanics fields.

In order for a computational analysis to yield meaningful results, however, careful attention must be paid to each step of the modeling process. First, a set of governing equations must be obtained that adequately describes the relevant physics of the problem being studied. For example, the incompressible form of the Navier-Stokes equations should not be selected when studying fluid flows exhibiting high Mach numbers. Then, suitable material properties must be collected and meaningful boundary conditions prescribed. All of these steps can be performed without selecting a numerical technique and with little or no knowledge of these techniques.

Once a **numerical model** has been chosen, however, the user's expertise in using the selected technique and his or her experience with the particular problem become vital factors necessary for producing meaningful results. For example, considerable expertise is needed during the construction of the computational mesh in order to determine the appropriate cell size, shape, and spectral approximation, as well as the necessary cell clustering to obtain an approximate solution that adequately resolves the desired features of the problem. Finally, once the approximation has been computed, it must be carefully examined in order to provide some assurance concerning its accuracy. This last step is the most difficult to perform and generally relies heavily on the experience the user has with the problem being solved.

Research and design has begun on a mesh and solution analysis tool that would greatly simplify the process of generating acceptable meshes and analyzing approximate solutions. This program would accept the mesh and solution data produced by **finite element, finite difference,** or **finite volume** methods for two- and three-dimensional problems in heat transfer, linear elasticity, Euler flow and incompressible, as well as compressible, Navier-Stokes flow. Mesh analysis functions would include identification of tangled and/or distorted cells, identifying regions of the mesh as candidates for potential cell clustering. Both user-specified and automatic forms of mesh clustering would be available.

Error estimation functions would include calculation of overall, as well as cell-wise, estimates of the error in the approximate solution for each of the problem classes. These estimates will be expressed in the absolute units of the solution or as a percentage of the solution.

Finally, this program will provide techniques with which a given approximate solution can be improved or enhanced, yielding another approximation of higher quality.

During the initial phase of this work, the main focus has been on the development of reliable **error estimation** techniques for linear elasticity, steady-state heat conduction, and incompressible flow. A simple example for steady-state heat conduction is provided when the calculated error estimates are used to repeatedly subdivide elements, resulting in the mesh shown in figure 212. This process took an initial mesh of 10 bilinear elements with an approximate solution of about 20–percent overall error and reduced the error to less than 0.6 percent. Figure 213 shows the cell-wise distribution of estimated error in the approximate solution for this improved mesh.

G.A. Wilhold/ED31
(205) 544–2651
Sponsor: Office of Commercial Programs, Small Business Innovation Research

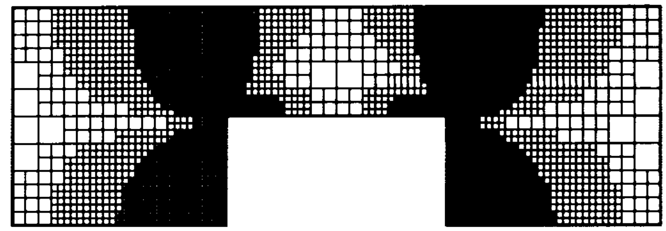

FIGURE 212.— Computational mesh for heat conduction example produced by subdividing elements with large estimated errors.

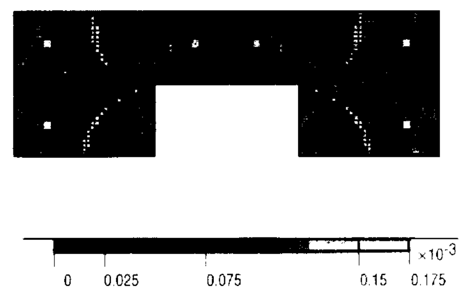

FIGURE 213.— Cell-wise distribution of error estimates for a heat conduction problem.

Rarefied Gas Aerodynamic Bridging Procedures

The overall objective of this study is to develop improved **bridging procedures** to better define the **aerodynamics** of spacecraft operating in the hypersonic **rarefied flow** regime. The aeroassist flight experiment (AFE) spacecraft is planned to fly in this regime in 1996 to collect critical measurements to improve our understanding of the flow dynamics in this region. An underlying objective of this study is to provide AFE with a best estimate of its **aerodynamics**.

Two major tasks of this study are: (1) improve the Kotov, *et al.*, (1982) bridging techniques; and (2) determine a best estimate of the preferred **gas/surface interaction** (**GSI**) model to use in the bridging procedure. Progress in the latter task is the subject of this report.

It was demonstrated early in the study that rarefied **aerodynamics** are very sensitive to the **GSI** model assumed in the **aerodynamic** computations. The most common practice today is to assume the diffuse **GSI** model. The hard question is: is such an assumption warranted or justifiable? The answer to this question was sought in a review of nearly 250 references addressing the subject of **GSI**. Specifically, direct experimental measurements of the momentum accommodation coefficients on materials similar to those used in spacecraft were sought at conditions comparable to the orbital environment. Only six sources were found that met the above criteria. The data sets obtained from those six sources are shown in figure 214 and the reference sources are listed in table 13. While there appears to be some obvious outliers and a fair amount of scatter, there does appear to be a consistent trend with surface incidence angle in figure 214.

Curve fits (17 different models) of those trends were developed and used in the Schaaf and Chambre free-molecular pressure and shear equations to compute the body forces on several geometries of interest. The drag results of a sphere are tabulated in table 14 by **GSI** model number (**GSI** models 3 and 6 are for diffuse and specular, respectively).

TABLE 13.—*Sources of momentum accommodation coefficient measurements*

Data Set	Source
1, 2, 12, 13	Knechtel, E.D. and Pitts, W.C., "Experimental Momentum Accommodation on Metal Surfaces of Ions Near and Above Earth-Satellite Speeds," *Rarefied Gas Dynamics*, Proc. Sixth Int. Symp., Academic Press, 1969, vol. I, pp. 1,257–1,266.
3–6	Doughty, R.O. and Schaetzle, W.J., "Experimental Determination of Momentum Accommodation Coefficients at Velocities up to and Exceeding Earth Escape Velocity," *Rarefied Gas Dynamics*, Proc. Sixth Int. Symp., Academic Press, 1969, vol. II, pp. 1,035–1,054.
7–9, 14	Knechtel, E.D. and Pitts, W.C., "Normal and Tangential Momentum Accommodation for Earth Satellite Conditions," *Astro. Acta* 18, 171, 1973.
10	Mair, W.N., Viney, B.W., and Colligon, J.S., "Experiments on the Accommodation of Normal Momentum," *Rarefied Gas Dynamics*, Proc. Fifth Int. Symp., Academic Press, 1967, vol. I, pp. 187–198.
11	Lin, S-M, Sharma, P.K., and Knuth, E.L., "Satellite Drag Coefficients Calculated from Measured Distributions of Reflected Helium Atoms," *AIAA J.*, No. 17, 1979, pp. 1,314–1,319.
15	Musanov, S.V., Nikiforov, A.P., Omelik, A.I., and Freedlender, O.G., "Experimental Determination of Momentum Transfer Coefficients in Hypersonic Free Molecular Flow and Distribution Function Recovery of Reflected Molecules," *Rarefied Gas Dynamics*, Proc. Thirteenth Int. Symp., Plenum Press, 1985, vol. I, pp. 669–676.

TABLE 14.—*Computed sphere drag coefficients*

Model No.	C_D	Model No.	C_D
1	1.7601	11	1.9132
2	1.8283	14	2.0173
3	2.0472	15	1.7601
4	2.3961	16	1.7358
5	1.8027	17	1.8709
6	1.9921	Hurlbut-Sherman	2.0951
7	1.9814	Nocilla A	2.1126
8	2.2120	Nocilla B	1.9060
9	1.9442	Nocilla C	2.0275
10	1.5953	Nocilla D	2.1665

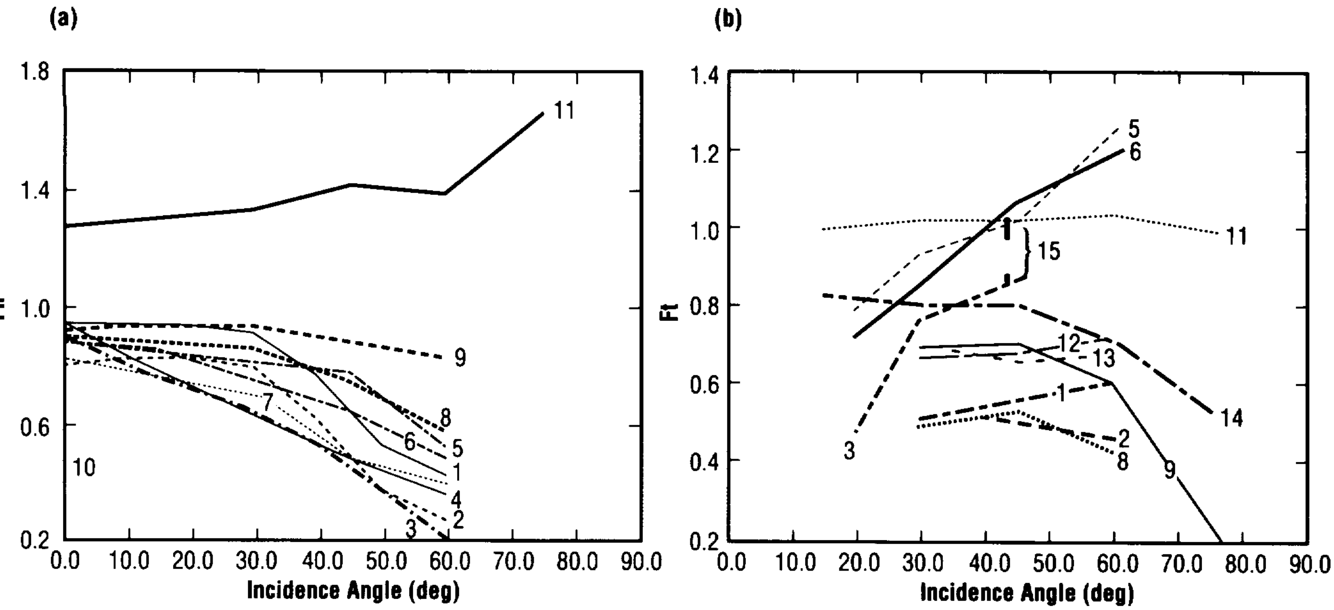

FIGURE 214.—Normal and tangential momentum accommodation coefficient measurements. (a) Normal accommodation coefficient; (b) Tangential accommodation coefficient.

In addition to the curve-fit models, five models based on the Nocilla analytical model were included in the computations. One of the Nocilla models was taken from Hurlbut and Sherman; the others were devised in this study.

Despite the wide variance of the **GSI** models, all the results are within ± 20 percent of the mean (larger differences were observed for the other geometries studies), suggesting that the integrated force on a sphere is not very sensitive to the **GSI** effects—an observation to be borne in mind in planning **GSI** experiments on the tethered satellite program. A second observation is that the measurement-based results suggest a drag coefficient less than 2.0, which is outside the classical limits predicted by the diffuse and specular values once thought to bound the possible range of values. The values for **GSI** models 4, 8, and 10 are considered outliers and were eliminated from computations on other geometries.

The **aerodynamics** of the sphere-cone, wedge, and AFE were computed also. Shown in figure 215 is the resultant lift-to-drag (L/D) ratio for these geometries. By evaluating the results for the emergence of a consensus among the several **GSI** models, several additional outliers become apparent. Also, the diffuse **GSI** model (3) produced significantly different **aerodynamic** characteristics. These observations precipitated the decision that, based on the present results, **GSI** model 17 was selected as the preferred one to use for preliminary **aerodynamic** design computations until more precise **GSI** information becomes available.

The differences shown in figure 215 for the AFE are quite dramatic compared to the diffuse values presently used. It should be noted, however, that the effects shown here are for the free-molecular regime only; but the differences shown in this regime are compounded into the rarefied regime by diminishing amounts to zero at the continuum end through the **bridging procedures**.

Much additional work is urgently needed in this area, and a continuation of this study will be considered.

Kotov, V.M., Lychkin, E.N., Reshetin, A.G., and Schelkonogov, A.N., "An Approximate Method of Aerodynamic Calculation of Complex Shape Bodies in a Transition Region," Thirteenth International Symposium of Rarefied Gas Dynamics, vol. 1, 1982, pp. 487–494.

Nocilla, S., "The Surface Re-Emission Law in Free Molecule Flow," *Rarefied Gas Dynamics*, Proc. Third International Symposium, Academic Press, vol. 1, 1963, pp. 327–346.

Hurlbut, C.F., and Sherman, F.S., "Application of the Nocilla Wall Reflection Model to Free-Molecule Kinetic Theory," *Phys. Fluids*, vol. 11, 1968, p. 486.

Knox, E.C., Collins, F.G., and Liver, P.A. II, "Engineering Assessment of Gas/Surface Interactions in Free-Molecular Aerodynamics," AIAA 91–1747, AIAA 22nd Fluid Dynamics, Plasma Dynamics, and Lasers Conference, Honolulu, HI, June 24–26, 1991.

C.M. Seaford/ED33
(205) 544–1596

Sponsor: Office of Commercial Programs, Small Business Innovation Research

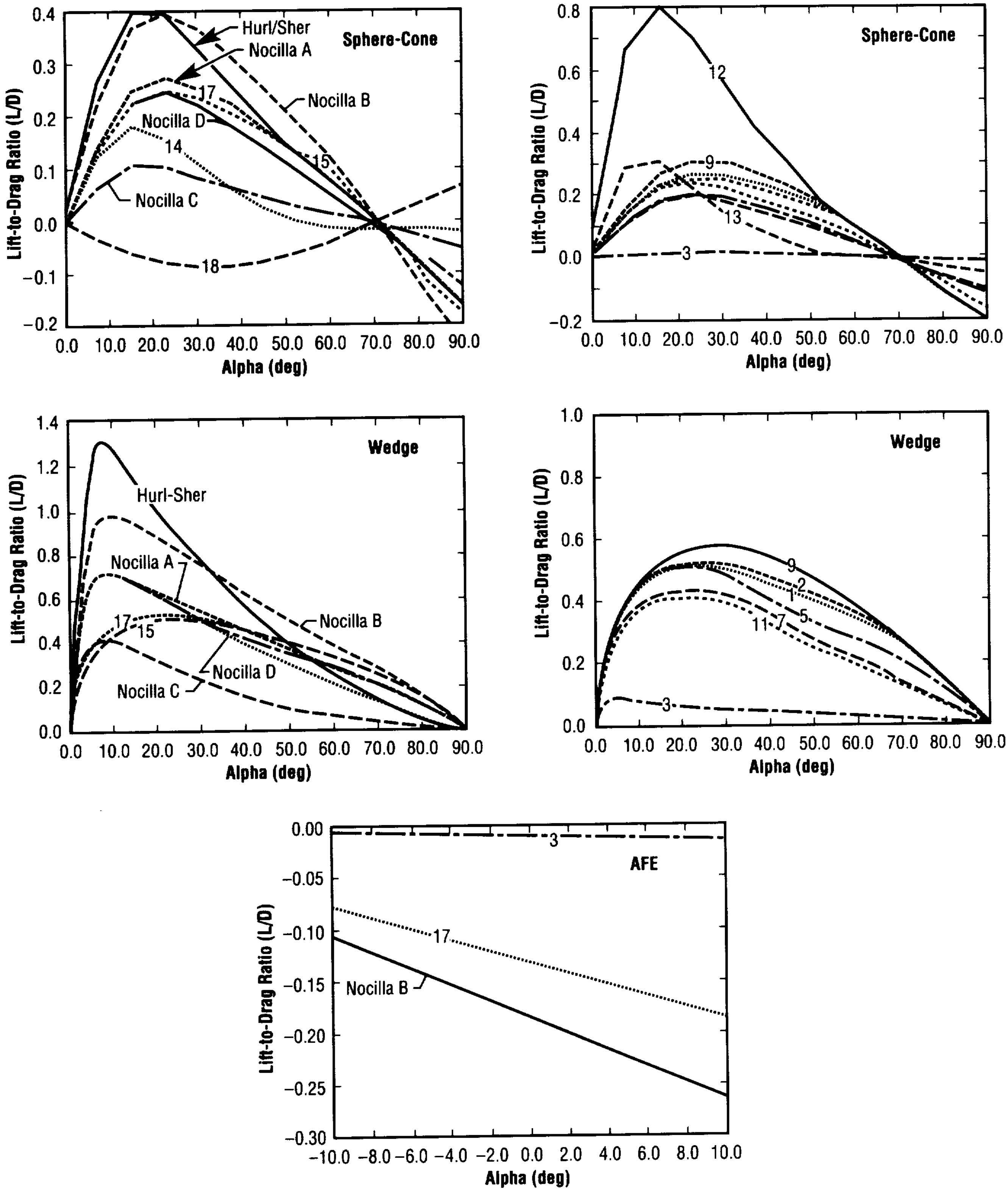

FIGURE 215.— Computed L/D ratio for sphere-cone, wedge, and AFE geometries versus angle-of-attack using GSI models indicated on plots.

Space Flight Gas Temperature Probe

An omnidirectional, flow-capturing probe is being developed that will provide explicit determination of the induced **gas temperature** of the **launch vehicle** base region plume throughout ascent. The flight probe(s) will be flown as **instrumentation** on a space shuttle flight and will provide **gas temperature** data at critical base locations. The probe will be mounted to the orbiter base heat-shield substructure through an opening in one of the high-temperature reusable surface insulation tiles (fig. 216).

The uniqueness of the probe lies in its sensitivity to a wide range of vehicle base flow conditions and the error compensation provided by multiple sensors. **Gas temperature** probes used in the past to measure ascent environments were shielded thermocouples with large radiation and conduction errors and large time constants, which prohibited accurate measurement of base region **gas temperature**. Base **gas temperature** measurement, coupled with measurements of total and radiation heating rate during ascent, enables validation of **base heating** environment design predictions and assessment of the adequacy of the base region thermal protection system.

Based on extensive thermal modeling, flow analyses, and vibration analyses performed during the initial phase of this research, a gas probe design was developed that included the following features:

- Four spiral shields (to prevent radiation from line-of-sight to the sensors) with openings to route the base gas from any direction into and through the probe
- A large circular heat sink base to maintain cold end temperatures on the sensors and absorb heat conducted from the shields
- A removable insert to facilitate assembly and protect the sensors
- The choice of Inconel 617 as the primary material to meet the shield maximum temperature limits, and, because of its good machining, welding and thermal conduction characteristics
- The choice of S-type thermocouple sensors, Pt-Pt 10-percent Rh, to minimize oxidation of the exposed thermocouple wires.

An exploded view of the final design components is shown in figure 217.

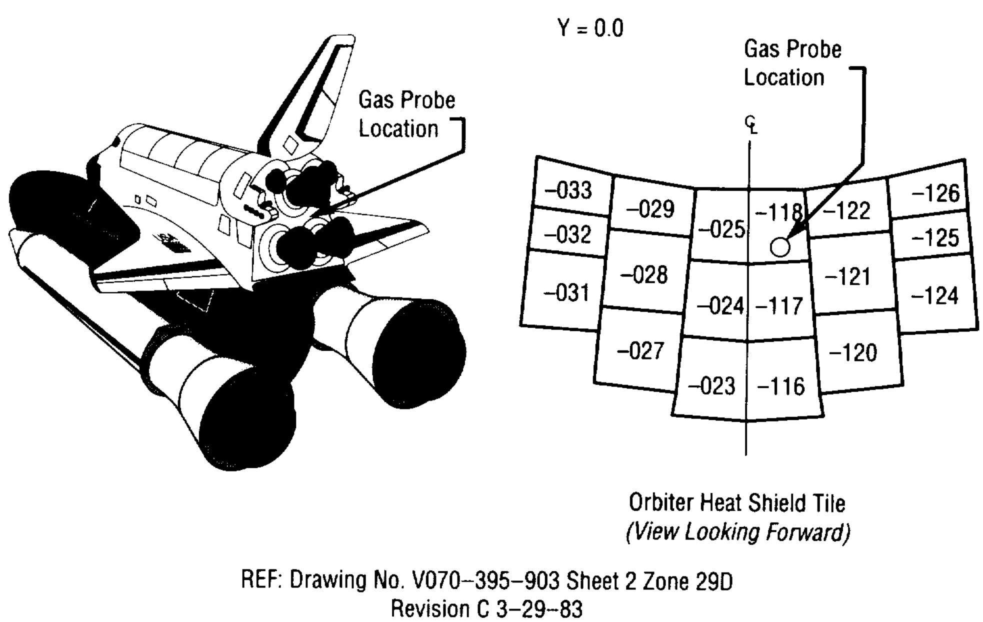

FIGURE 216.— Assembled gas probe mounted to Orbiter base heat shield.

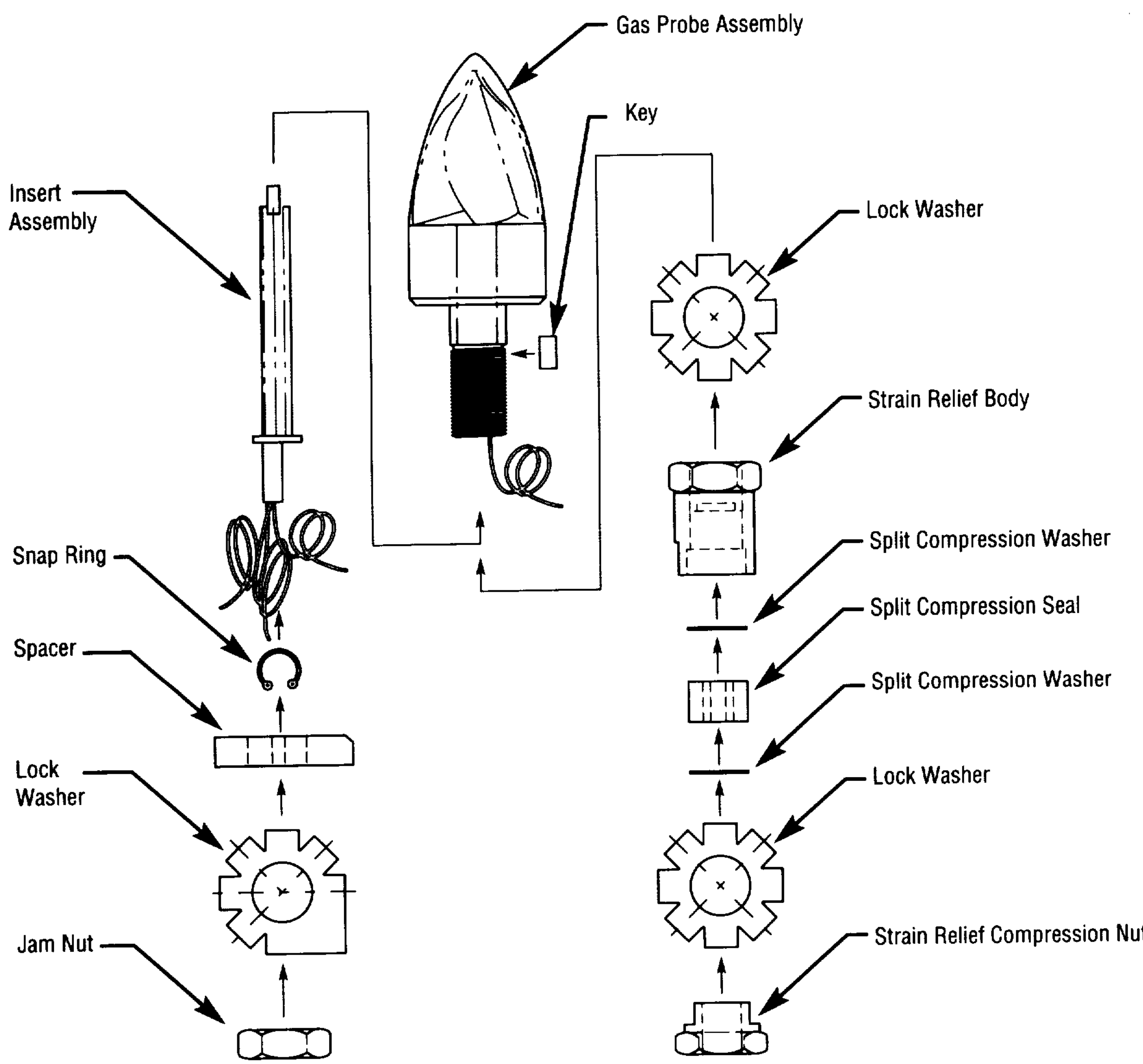

FIGURE 217.—Gas probe design components.

In order to validate the design, the following development tests were performed:

- Proof-of-concept test to demonstrate that low-speed flow will enter and exit the probe under a variety of initial flow conditions

- Thermal loads test to demonstrate the survivability of the probe after exposure to the maximum ascent **base heating** environment, and to validate the thermal model and measure the thermal responses

- Vibro-acoustic test to demonstrate the survivability of the probe after exposure to the maximum ascent vibro-acoustic environment.

Additional tests were performed during the program to better understand Inconel 617 welding characteristics and to choose final potting materials for the insert/sensor design. The development tests demonstrated that the spiral shield concept works well under a variety of flow conditions and that the probe can easily survive and function properly when exposed to simulated ascent **thermal** and vibration **environments**.

L.D. Foster/ED33
(205) 544-1589
Sponsor: Office of Commercial Programs, Small Business Innovation Research

Static Deflection Studies of the Solid Rocket Motor Aft Dome/Nozzle Joint

Structural analyses were conducted using the NASA **structural analysis** system (NASTRAN) to determine relative **deflections** at the O-rings in the solid rocket motor (SRM) aft dome/nozzle joint. The results of the study were verified through the use of the transient pressure test article (TPTA) using measured data from the test at MSFC. The TPTA test series was used to verify the aft case/nozzle joint math model by making slight changes to the model to accurately represent the TPTA configurations.

The basic modification to the math model was removing the math model representation of the nozzle and fixing the boundary conditions at the fixed housing/nozzle interface in all translational directions except the X-direction. An isometric view of the **finite element** model is shown on figure 218, which has 22,050 degrees-of-freedom.

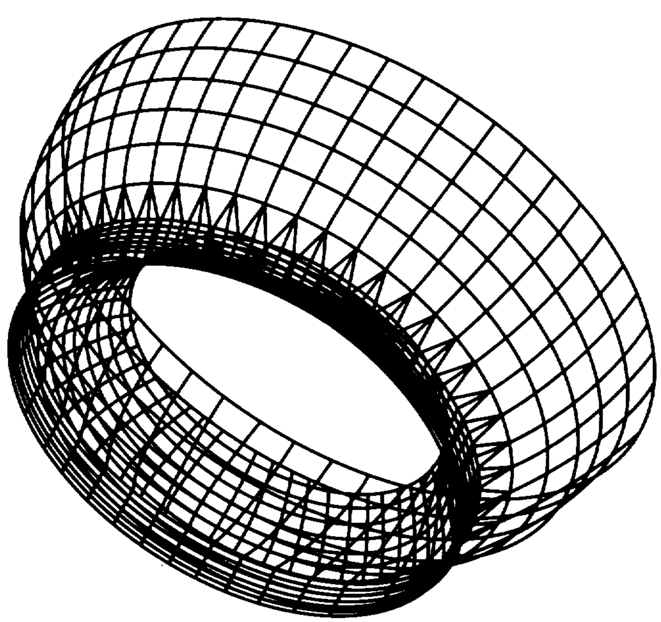

FIGURE 218.—SRB aft dome/nozzle joint dynamic model.

Plates, bars, rods, and solid elements were used to model the complete joint structure. The math model was developed in the full 360° configuration to allow for unsymmetrical loading and checking results in an unsymmetrical fashion to be sure the worst case was enveloped. The primary purpose of the model was to provide **deflections** along the vertical face at locations of the primary O-ring and the radial bolts (fig. 219). Figure 219 shows a section of the aft dome/fixed housing interface, with these locations shown as dots or gridpoints on this vertical face. For example, a dot (also a grid point) located at station –50.587 in is at the centerline of the

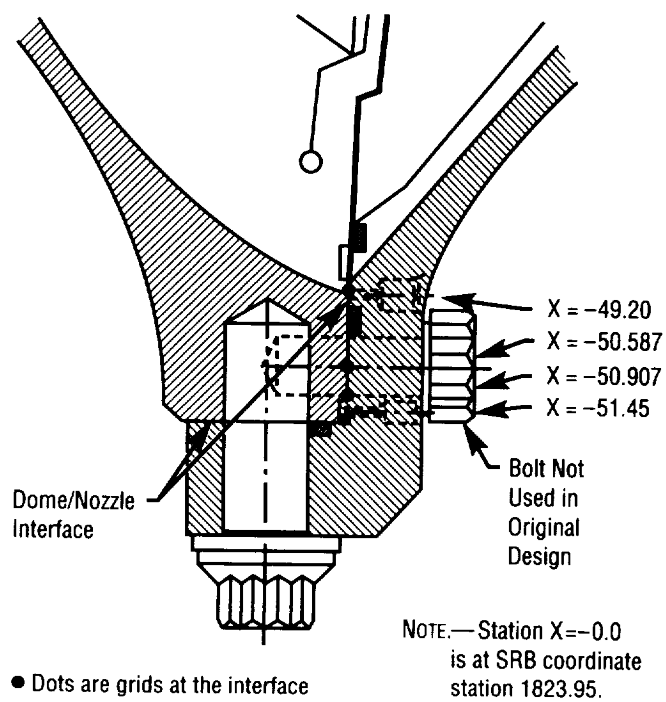

FIGURE 219.—X-location of gridpoints in gap.

radial bolts. The deflection gauge locations used in the TPTA test were at the same circumferential locations as the model where grid points were retained. The plot in figure 220 shows the individual data points from the first TPTA test and analytical results from the model connected with a line. The two sets of data are plotted together to show the similarity between test results and analysis results. Analytical results envelope test data, which show that the model is conservative for studying joint behavior. These **deflections** were caused primarily by the applied internal pressure of the TPTA, which was approximately 900 lb/in^2. The analytical and experimental results closely match. This comparison provides confidence in analytically predicting the gap **deflections** during flight, and is considered a step forward in the use of finite element modeling techniques for large complex structures. It is recommended that this type of study be conducted in the future on all O-ring interfaces for high-pressure SRM's.

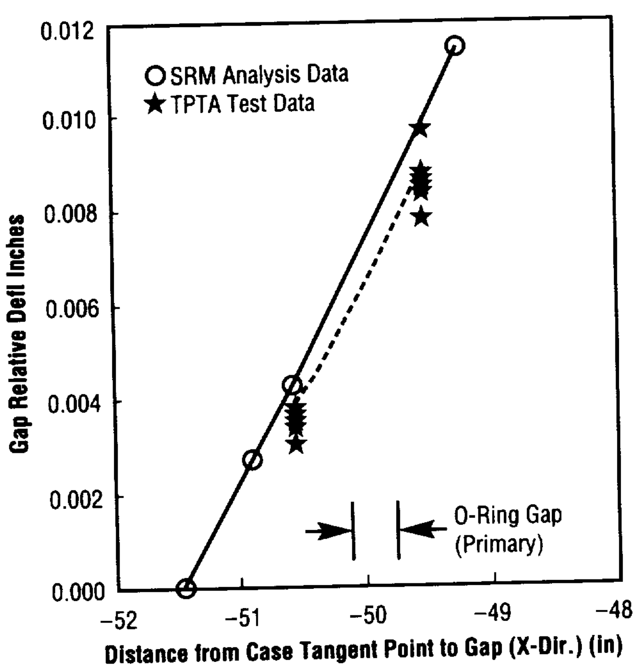

FIGURE 220.—Static gap between fixed housing and aft dome—TPTA test.

D.C. Christian/ED23
(205) 544–1517

Sponsor: Office of Space Flight

Structural Damage Prediction and Analysis for Hypervelocity Impacts

The purpose of this contracted effort with the Martin Marietta Corporation (MMC) and the University of Dayton Research Institute (UDRI) is to develop a design and analysis methodology handbook and a **user-friendly computer program** for quantifying wide-area **damage** to a module wall structure due to impact by a meteoroid or space debris particle. The severity of impact-induced **damage**, including module wall bulging, penetration, hole formation, and crack growth, will be predicted in relationship to the size, velocity, obliquity, and **probability** of occurrence of meteoroid and space debris particles.

In this effort, the contractor team will use the existing MSFC **hypervelocity** test data base, material modeling techniques, and additional testing to develop prediction techniques for module wall **damage**. The UDRI portion of this effort centers around modeling of the debris cloud generated from impact with outer bumper materials. In support of this effort, tests have been performed at the UDRI light gas gun facility using a "soft" x-ray system to characterize particle mass and velocity distributions within debris clouds from various bumper impact conditions. Figure 221 shows the typical resolving capability of the UDRI flash x-ray system.

The MMC portion of this effort is twofold: to perform a structural analysis of the effect of various debris cloud impacts on wall structures and to predict the **probability** of characterized impact **damage** levels from the projected meteoroid and space debris environment. Dr. N. Elfer of MMC is being assisted by Mr. A. Rajendran of UDRI in characterizing three distinct wall-failure modes—wall penetration, hole formation in excess of a 10-cm (4-in) diameter, and critical cracking of module walls. Finite element computer codes (HULL and NASTRAN) will assist in this analysis. Once the

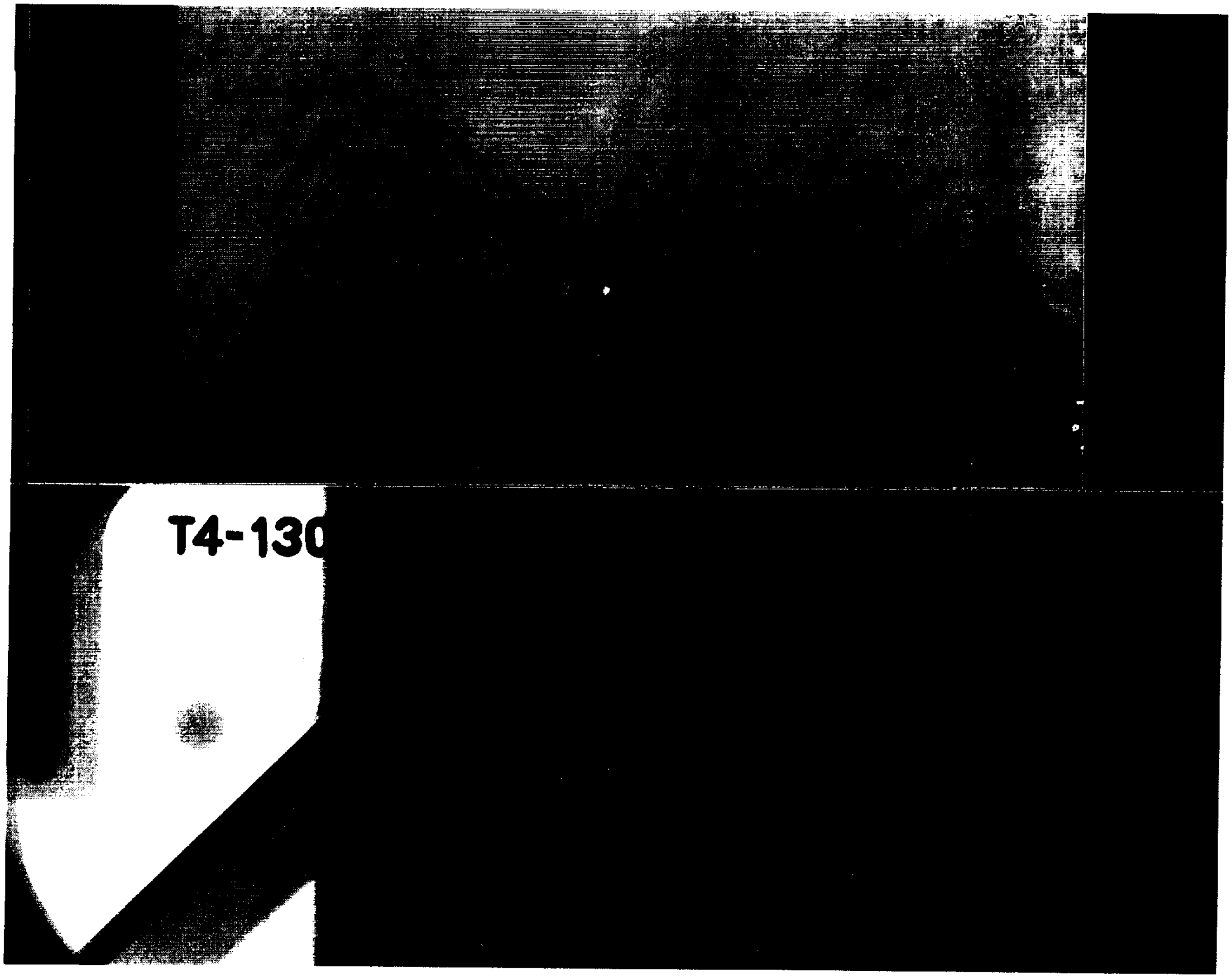

FIGURE 221.—Typical resolving capability of the UDRI flash x-ray system.

mechanisms are better understood for these three failure types, Dr. Elfer will characterize the diameters, velocities, and obliquities of particles expected to cause these **damage** types for at least two distinct shield design types. A **user-friendly computer program**, based on the existing Bumper code, will be developed to analyze for the **probability** of these structural failure types given spacecraft geometry, orbit, and other mission profile inputs.

Completion of the contract is expected in September 1992.

J.E. Williamsen/ED52
(205) 544-7007
Sponsor: Office of Space Flight, Space Station *Freedom*

ORIGINAL PAGE
BLACK AND WHITE PHOTOGRAPH

Thrust Chamber Life Prediction

A **design** tool has been developed to estimate the **life** of a liquid propellant rocket engine thrust **chamber**. The inner wall of a thrust **chamber** is subjected to an extreme thermal-mechanical load cycle. Failures typically occur along the inner wall. These failures are characterized by the progressive thinning and eventual rupture of the inner (hot gas) wall. Finite element techniques can be used to model the thinning of the hot gas wall. These techniques are very time- and resource-consuming. It is not practical to use these methods for sensitivity analysis and trade studies required during preliminary **design**.

A **design** tool is needed that can provide reasonable estimates of **chamber life**, and is also quick and easy to use. Existing analytical **design** techniques, which account for plastic strain ratcheting and creep, have been incorporated into a small, easy-to-use computer program.[1,2] A minimum of input data is required, and can be easily generated by hand or by another computer program. This program is currently being used to **design** the coolant channels for an advanced main combustion **chamber** (AMCC). Typical results are shown in figure 222 for a trade study looking at the effect of number of coolant channels (from 320 to 520) on **chamber life**. Inputs to this program were automatically generated by flow-thermal models of candidate coolant channel **designs**. As a result of this cyclic **life** sensitivity study, the machinists are challenged to attempt new techniques to cut thinner coolant channel grooves for greater cyclic **life** in the AMCC inner wall.

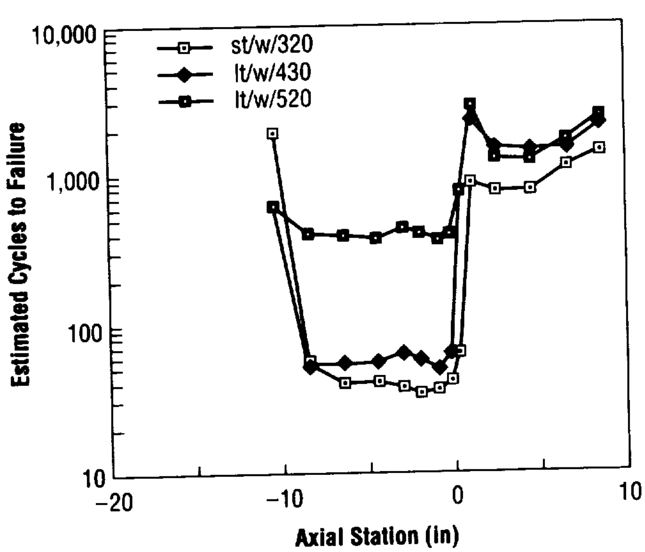

FIGURE 222.—Predicted thrust chamber liner life.

J.M. Price/ED25
(205) 544–4645

Sponsor: Office of Space Flight

[1]Porowski, J.S., Badlani, M., Kasraie, B., O'Donnell, W.J., and Petersen, D., "Development of a Simplified Procedure for Thrust Chamber Life Prediction," NASA CR–165585, October 1981.

[2]Badlani, M., Porowski, J.S., O'Donnell, W.J., and Petersen, D., "Development of a Simplified Procedure for Rocket Engine Thrust Chamber Life Prediction with Creep," NASA CR–168261, October 1983.

Index of Contacts